

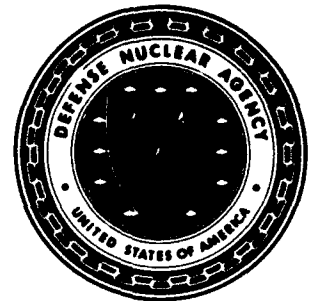
AD-A285 581



74



**Defense Nuclear Agency
Alexandria, VA 22310-3398**



DNA-TR-92-163

Investigation of Single Event Upsets in Silicon and GaAs Structures Using Reaction Calculations

**Peter J. McNulty
Clemson University
117 Kinard Laboratory of Physics
Clemson, SC 29634-1911**

September 1994

Technical Report

**DTIC
ELECTE
OCT 16 1994
S G D**

3298
94-32346

CONTRACT No. DNA 001-88-C-0189

**Approved for public release;
distribution is unlimited.**

DTIC QUALITY INSPECTED 5

9410 002

Destroy this report when it is no longer needed. Do not return to sender.

PLEASE NOTIFY THE DEFENSE NUCLEAR AGENCY,
ATTN: CSTI, 6801 TELEGRAPH ROAD, ALEXANDRIA, VA
22310-3398, IF YOUR ADDRESS IS INCORRECT, IF YOU
WISH IT DELETED FROM THE DISTRIBUTION LIST, OR
IF THE ADDRESSEE IS NO LONGER EMPLOYED BY YOUR
ORGANIZATION.



DISTRIBUTION LIST UPDATE

This mailer is provided to enable DNA to maintain current distribution lists for reports. (We would appreciate your providing the requested information.)

- ☐ Add the individual listed to your distribution list.
- ☐ Delete the cited organization/individual.
- ☐ Change of address.

NOTE:

Please return the mailing label from the document so that any additions, changes, corrections or deletions can be made easily. For distribution cancellation or more information call DNA/IMAS (703) 325-1036.

NAME: _____

ORGANIZATION: _____

OLD ADDRESS

CURRENT ADDRESS

TELEPHONE NUMBER: () _____

DNA PUBLICATION NUMBER/TITLE

CHANGES/DELETIONS/ADDITIONS, etc.)

(Attach Sheet if more Space is Required)

DNA OR OTHER GOVERNMENT CONTRACT NUMBER: _____

CERTIFICATION OF NEED-TO-KNOW BY GOVERNMENT SPONSOR (if other than DNA):

SPONSORING ORGANIZATION: _____

CONTRACTING OFFICER OR REPRESENTATIVE: _____

SIGNATURE: _____

CUT HERE AND RETURN



DEFENSE NUCLEAR AGENCY
ATTN: IMAS
6801 TELEGRAPH ROAD
ALEXANDRIA, VA 22310-3398

DEFENSE NUCLEAR AGENCY
ATTN: IMAS
6801 TELEGRAPH ROAD
ALEXANDRIA, VA 22310-3398

REPORT DOCUMENTATION PAGEForm Approved
OMB No. 0704-0188

Public reporting burden for this collection of information is estimated to average 1 hour per response including the time for reviewing instructions, searching existing data sources, gathering and maintaining the data needed, and completing and reviewing the collection of information. Send comments regarding this burden estimate or any other aspect of this collection of information, including suggestions for reducing this burden, to Washington Headquarters Services, Directorate for Information Operations and Reports, 1215 Jefferson Davis Highway, Suite 1204, Arlington, VA 22202-4302, and to the Office of Management and Budget, Paperwork Reduction Project (0704-0188), Washington, DC 20503

1. AGENCY USE ONLY (Leave blank)		2. REPORT DATE 940901		3. REPORT TYPE AND DATES COVERED Technical 881001 - 920310	
4. TITLE AND SUBTITLE Investigation of Single Event Upsets in Silicon and GaAs Structures Using Reaction Calculations				5. FUNDING NUMBERS C - DNA 001-88-C-0189 PE - 62715H PR - RV TA - RA WU - DH052100	
6. AUTHOR(S) Peter J. McNulty					
7. PERFORMING ORGANIZATION NAME(S) AND ADDRESS(ES) Clemson University 117 Kinard Laboratory of Physics Clemson, SC 29634-1911				8. PERFORMING ORGANIZATION REPORT NUMBER	
9. SPONSORING/MONITORING AGENCY NAME(S) AND ADDRESS(ES) Defense Nuclear Agency 6801 Telegraph Road Alexandria, VA 22310-3398 RAEE/Palkuti				10. SPONSORING/MONITORING AGENCY REPORT NUMBER DNA-TR-92-163	
11. SUPPLEMENTARY NOTES This work was sponsored by the Defense Nuclear Agency under RDT&E RMC Code B4662D RV RA 02232 RAEE 3400A 25904D.					
12a. DISTRIBUTION/AVAILABILITY STATEMENT Approved for public release; distribution is unlimited.				12b. DISTRIBUTION CODE	
13. ABSTRACT (Maximum 200 words) Two procedures were developed to obtain the dimensions of the sensitive volume: one using charge collection measurements and the other proton Seu cross sections measured at different energies and angles of incidence. The CUPID simulation codes play an important role. They have been made user friendly and received adequate documentation. The methodology has been extended to single event latch-up and displacement damage.					
14. SUBJECT TERMS Energy Deposition Charge Collection Spallation Reactions CUPID Sensitive Volume Displacement Damage Single Event Upsets Single Event Latch-Up				15. NUMBER OF PAGES 342	
				16. PRICE CODE	
17. SECURITY CLASSIFICATION OF REPORT UNCLASSIFIED	18. SECURITY CLASSIFICATION OF THIS PAGE UNCLASSIFIED	19. SECURITY CLASSIFICATION OF ABSTRACT UNCLASSIFIED	20. LIMITATION OF ABSTRACT SAR		

UNCLASSIFIED

SECURITY CLASSIFICATION OF THIS PAGE

CLASSIFIED BY:

N/A since Unclassified.

DECLASSIFY ON:

N/A since Unclassified.

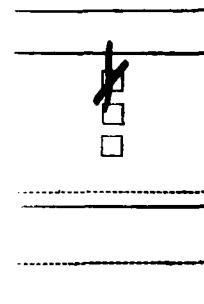
SUMMARY

This was an experimental/theoretical study of the basic physics of radiation induced single-event phenomena with a view towards improving the accuracy of SEU rate predictions. It included an analysis of SEU testing and the theoretical basis of the algorithms used in calculations. Experimental tests of the First-Order Model indicate that, to a good approximation, the relevant SEU parameters needed for accurate predictions of the SEU rate to be expected in space are the dimensions of the sensitive volume, the critical charge, and the shape of the response curve, i.e., the plot of the SEU cross section versus the effective LET of the incident ion. However, to apply the First-Order Model effectively, the correct values for the dimensions of the sensitive volume must be used along with the corresponding correct value of the critical charge. Procedures for determining the cross sectional area of the sensitive volume and its thickness using charge collection were developed. When done correctly, not only should the SEU tests carried out with heavy ions be consistent with the proton tests, but either data set, if obtained with sufficient statistics, can be used to estimate the SEU parameters. This report details the correct procedures to be used and provides examples of applications.

The CUPID codes were tested by comparison of simulations with the results of charge - collection measurements as part of this investigation, and they were found to correctly predict the energy-deposition in a parallel array of microvolumes, each having dimensions typical of the SEU-sensitive structures of CMOS and NMOS devices. The codes become useful for confirming the dimensions of the sensitive volumes from SEU measurements on working devices and for estimating the correct value of the critical charge. The codes were modified to make them user-friendly to workers familiar with, but not expert on, an IBM PC computer.

The CUPID codes were also modified to extend them to applications to neutron-induced SEUs with mixed success. The codes predict the distribution of energy depositions within the sensitive volume but underestimate the total number of events generated as a result of exposure to a given fluence. This may be partially the result of carrying out the tests at neutron energies below those for which CUPID was designed.

CUPID was originally designed to explain and predict the energy deposition through ionizations within microvolumes which results from the nearby spallation reactions. However, an important class of radiation-induced phenomena is due to the non-ionizing component of energy deposition by charged particles emerging from the spallation reactions. The non-ionizing energy loss produces an increase in the dark current across the depletion regions as a result of displacement damage. Spallation reactions can result in such large concentrations of displacement damage around the end of the trajectory of the recoiling nuclear fragment that single event non-ionizing energy loss events become a design limitation for applications of CCDs to satellite communications and hyperspectral imaging.



Availability Codes	
Dist	Avail and / or Special
A-1	

CONVERSION TABLE

Conversion factors for U.S. customary to metric (SI) units of measurement

To Convert From	To	Multiply
angstrom	meters (m)	1.000 000 X E-10
atmosphere (normal)	kilo pascal (kPa)	1.013 25 X E+2
bar	kilo pascal (kPa)	1.000 000 X E+2
barn	meter ² (m ²)	1.000 000 X E-28
British Thermal unit (thermochemical)	joule (J)	1.054 350 X E+3
calorie (thermochemical)	joule (J)	4.184 000
cal (thermochemical)/cm ²	mega joule/m ² (MJ/m ²)	4.184 000 X E-2
curie	giga becquerel (GBq)*	3.700 000 X E+1
degree (angle)	radian (rad)	1.745 329 X E-2
degree Fahrenheit	degree kelvin (K)	$t_K = (t_F + 459.67)/1.8$
electron volt	joule (J)	1.602 19 X E-19
erg	joule (J)	1.000 000 X E-7
erg/second	watt (W)	1.000 000 X E-7
foot	meter (m)	3.048 000 X E-1
foot-pound-force	joule (J)	1.355 818
gallon (U.S. liquid)	meter ³ (m ³)	3.785 412 X E-3
inch	meter (m)	2.540 000 X E-2
jerk	joule (J)	1.000 000 X E+9
joule/kilogram (J/Kg) (radiation dose absorbed)	Gray (Gy)	1.000 000
kilotons	terajoules	4.183
kip (1000 lbf)	newton (N)	4.448 222 X E+3
kip/inch ² (ksi)	kilo pascal (kPa)	6.894 757 X E+3
ktap	newton-second/m ² (N-s/m ²)	1.000 000 X E+2
micron	meter (m)	1.000 000 X E-6
mil	meter (m)	2.540 000 X E-5
mile (international)	meter (m)	1.609 344 X E+3
ounce	kilogram (kg)	2.834 952 X E-2
pound-force (lbf avoirdupois)	newton (N)	4.448 222
pound-force inch	newton-meter (N-m)	1.129 848 X E-1
pound-force/inch	newton/meter (N/m)	1.751 268 X E+2
pound-force/foot ²	kilo pascal (kPa)	4.788 026 X E-2
pound-force/inch ² (psi)	kilo pascal (kPa)	6.894 757
pound-mass (lbm avoirdupois)	kilogram (kg)	4.535 924 X E-1
pound-mass-foot ² (moment of inertia)	kilogram-meter ² (kg-m ²)	4.214 011 X E-2
pound-mass/foot ³	kilogram/meter ³ (kg/m ³)	1.601 846 X E+1
rad (radiation dose absorbed)	Gray (Gy)**	1.000 000 X E-2
roentgen	coulomb/kilogram (C/kg)	2.579 760 X E-4
shake	second (s)	1.000 000 X E-8
slug	kilogram (kg)	1.459 350 X E+1
torr (mm Hg, 0°C)	kilo pascal (kPa)	1.333 22 X E-1

*The becquerel (Bq) is the SI unit of radioactivity; Bp = 1 event/s.

**The Gray (Gy) is the SI unit of absorbed radiation.

TABLE OF CONTENTS

Section		Page
	SUMMARY	iii
	CONVERSION TABLE	iv
1	INTRODUCTION	1
1.1	FORMAT OF REPORT	1
1.2	OBJECTIVES OF STUDY	1
1.3	BASIC MECHANISMS	2
1.4	RELATIONSHIP TO SEU	2
1.5	ACCURATE DETERMINATION OF SEU PARAMETERS	3
1.6	NEUTRON STUDIES	3
1.7	DOCUMENTATION OF CUPID	3
1.8	APPLICATION TO NEW PHENOMENA	4
2	CHARGE COLLECTION -- THE BASICS	5
2.1	INTRODUCTION	5
2.2	CHARGE COLLECTION MEASUREMENTS	8
3	MEASUREMENTS ON DEVICES: CHARGE COLLECTION SPECTROSCOPY	11
4	THE CUPID MODEL AND APPLICATIONS TO SEU	13
5	APPLICATIONS TO OTHER SINGLE-EVENT PHENOMENA	16
6	CUPID MODIFICATIONS AND DOCUMENTATION	18
6.1	INTRODUCTION	18
6.2	USER-FRIENDLY VERSION OF CUPID FOR PCs	18
7	REFERENCES	19

Appendix

A	PREDICTING SINGLE EVENT PHENOMENA IN NATURAL SPACE ENVIRONMENTS	A-1
B	CHARGE COLLECTION MEASUREMENTS AND THEORETICAL CALCULATIONS FOR PARTIALLY DEPLETED SILICON DEVICES	B-1
C	CHARGE COLLECTION IN HI2L BIPOLAR TRANSISTORS	C-1
D	CHARGE COLLECTION IN PARTIALLY DEPLETED GaAs TEST STRUCTURES INDUCED BY ALPHAS, HEAVY IONS, AND PROTONS	D-1
E	PULSE-HEIGHT ANALYSIS SYSTEM	E-1
F	MODELING CHARGE COLLECTION AND SINGLE EVENT UPSETS IN MICROELECTRONICS	F-1
G	COMPARISON OF CHARGE COLLECTION AND SINGLE EVENT UPSETS IN MICROELECTRONICS	G-1
H	MICROBEAM ANALYSIS OF MOS CIRCUITS	H-1
I	CHARGE COLLECTION AT LARGE ANGLES OF INCIDENCE ..	I-1
J	DETERMINATION OF SEU PARAMETERS OF NMOS AND CMOS SRAMS	J-1
K	CHARGE COLLECTION AND SEU SENSITIVITY FOR GaAs BIPOLAR DEVICES	K-1
L	PROTON-INDUCED SPALLATION REACTIONS	L-1
M	SEU PARAMETERS AND PROTON-INDUCED UPSETS	M-1
N	TEST OF SEU ALGORITHMS AGAINST PRELIMINARY CRRES SATELLITE DATA	N-1
O	PROTON-INDUCED SEU IN CMOS/SOS	O-1
P	PROTON AD HEAVY-ION UPSETS IN GaAs MESFET DEVICES	P-1

Q	QUANTITATIVE COMPARISON OF SINGLE EVENT UPSETS INDUCED BY PROTONS AND NEUTRONS	Q-1
R	SOFT FAILS IN MICROELECTRONIC CIRCUITS DUE TO PROTON-INDUCED NUCLEAR REACTIONS IN MATERIAL SURROUNDING THE SEU-SENSITIVE VOLUME	R-1
S	SINGLE AND MULTIPLE PROTON-INDUCED NIEL EVENTS IN SILICON	S-1
T	SIMPLE MODEL FOR PROTON-INDUCED LATCH-UP	T-1
U	MICRODOSIMETRY IN SPACE USING MICROELECTRONICS CIRCUITS	U-1
V	CHARACTERIZING COMPLEX RADIATION ENVIRONMENTS USING MORE (MONITOR OF RADIATION EFFECTS)	V-1
W	USER MANUAL FOR THE CUPID CODE	W-1

SECTION 1

INTRODUCTION

1.1 FORMAT OF REPORT.

The research carried out under this contract has resulted in a number of publications and manuscripts submitted for publication. Where appropriate, those papers have been briefly summarized in the text in order to present the material clearly. In other cases, the papers describe details less important to this narrative. All papers developed under this contract are included as appendices. Other papers are mentioned that describe work which followed tangents that were peripheral to the goals of the project, such as the biological implications of the models developed for microelectronics. These are described briefly and one complete review manuscript is included as an appendix.

The text is divided into two parts; one experimental, the other theoretical. Each part begins with a description of the basic measurements and models involved and leads to the implications for Single Event Upsets (SEU) or other single event phenomena, and includes recommendations for improvements in testing or predicting event rates.

1.2 OBJECTIVES OF STUDY.

The main goal of the project was to develop a quantitative understanding of how changes in technology affect the sensitivity of the device to single event phenomena, particularly upsets. Retrograde doping, dielectric isolation, and trench structures are examples of such potentially important technologies. This analysis required ways to determine the dimensions of the sensitive volume and the critical charge from experimental measurements. The approach used was charge collection. A number of papers describing the charge collection techniques developed in this laboratory are incorporated in the appendices.

The CUPID code was to be modified to include neutron-induced spallation reactions, was to be extended to calculations for GaAs devices, was to be made user-friendly and modified to run on IBM-type personal computers. Documentation was to be developed for the CUPID code and the theoretical formalism described. A User Manual for CUPID was developed.

The code was also to be modified to handle non-ionizing energy loss (NIEL) events. This was completed under the contract, and is currently being applied to single and multiple event NIEL events in CCDs under a subcontract from Kodak.

It was also proposed that the problem of SEU problems in avionics be addressed. This was one reason for developing the ability to handle neutron-induced upsets. A complete analysis of the avionics problem is being prepared for an invited talk at the American Nuclear Society.

1.3 BASIC MECHANISMS.

The immediate cause of any Single Event Phenomena (SEP) is either the traversal of an SEU-sensitive junction by an energetic heavy ion or traversals by secondary charged particles emerging from a nearby spallation reaction. Each charged particle traversing a reverse-biased junction generates a trail of ionizations along its trajectory. These charges are known to form a transient current through the junction which in turn causes a momentary drop in the bias drop across it. The amount of charge collected during the pulse, the time profile of the current across the junction, and the cross section for initiating the pulse are complicated functions of the particles linear energy transfer, its angle of incidence, and the doping profiles on both sides of the junction. There have been a considerable number of investigations into the details of charge collection because of the role it plays in the onset of SEPs (for a review, see McNulty, 1990 or Sexton, 1992). A copy of the first reference is included in this report as Appendix A. The approach followed in this study was to use the First-Order Model as a benchmark and test for deviations from its predictions.

The First-Order Model (1) ignores the details of the charge collection process and replaces them with simple parameters that characterize the device's sensitivity to Single Event Upsets (SEU). The model assumes the SEU-sensitive junctions can be represented by a sensitive volume, the dimensions of which are chosen such that the charge generated within the sensitive volume equals the charge actually collected across the junction. The sensitive volume is not necessarily an identifiable structure on the device, but should be considered as a mathematical artifice used for convenience in calculations. The model states that an upset occurs if, and only if, more than some threshold amount of energy is deposited within the sensitive volume. The details of how that energy is deposited and the time profile for the charge crossing the junction are assumed to be irrelevant. This is essentially the same assumptions adopted by (Binder et al., 1975) and (Pickel and Blandford, 1980) for cosmic-ray upsets and (McNulty et al., 1980) for proton-induced upsets.

1.4 RELATIONSHIP TO SEU.

The First-Order Model is the basis of the CREME model of cosmic-ray induced SEUs (Adams, 1983) and the CUPID model of proton-induced upsets (McNulty et al., 1981). Calculations using CREME and CUPID are straightforward because the only input

parameters are the dimensions of the sensitive volume and the critical charge. The shape of the response curve for the device can be incorporated into the SEU-rate predictions simply by assuming that the device contains a large number of sensitive volumes with identical dimensions but different values of the critical charge. The relative number having each value of the critical charge can be obtained from the response curve. Predicting SEUs based on the shape of the response curve requires that the shape of the curve be accurately determined. Unfortunately, pressures of beam time and costs induce almost all test groups to make certain approximations. The first assumption is that the charge collected across the junction increases with the secant of the angle of incidence; the second is that the measured SEU cross section decreases with the angle of incidence as the cosine decreases because the projected area of the junction decreases with cosine. Both of these assumptions will be shown in what follows to be incorrect under some circumstances. The second assumption is often incorrect for modern devices. Predicting SEU rates accurately requires that systematic errors in the plot of the response curve characterizing devices be corrected.

1.5 ACCURATE DETERMINATION OF SEU PARAMETERS.

Two techniques were developed under this contract for determining the dimensions of the sensitive volume. One involves charge collection with heavy ions using an accelerator or alpha particles from an Americium source under vacuum. The second method involves simple SEU measurements using protons at a variety of energies and angles of incidence. The true test that the dimensions are correct is that both the heavy-ion data and the proton data can be fit with the same assumptions for the dimensions of the sensitive volume and the critical charge. Both techniques are described below. Where both proton and heavy-ion testing were possible, the experience of this laboratory was that the proton value of the critical charge had smaller error limits.

1.6 NEUTRON STUDIES.

CUPID simulations of the charge collection in thin (2.5 μm) surface-barrier detectors were in excellent agreement with the energy spectrum, but they were not in agreement with the total number of events. The simulations and the experiments were carried out at 14 MeV which is at too low an energy for accurate calculations with CUPID. The neutron-induced spallation reaction at that energy is probably considerably higher at that energy than the value obtained by treating the target nucleus as a Fermi gas of free nucleons, as is done in CUPID. The codes were used to improve some models developed by Boeing to treat neutron-induced SEUs in avionics.

1.7 DOCUMENTATION FOR CUPID.

Since we anticipate the use of CUPID for determining the dimensions of the sensitive volume and the value of the critical charge from proton SEU measurements, it was important that users have some understanding of spallation reactions, how they are modeled in CUPID, and how to use the codes.

1.8 APPLICATION TO NEW PHENOMENA.

When this project began, Single-Event Latchup (SEL) was an effect of concern for cosmic rays but not for protons. The recoiling nuclear fragment was not considered to have sufficient recoil energy to generate enough electron-hole pairs to turn on the parasitic transistor. The feature sizes of modern circuits are much smaller, however, and proton-induced SEL has been observed both in space and in the laboratory (Goka et al., 1991; Adams et al., 1992). A test of proton-induced SEL against the First-Order Model showed that agreement between the CUPID predictions and the test data taken at different angles of incidence were possible only for specific value of the thickness of the sensitive volume. This value agreed with the thickness of the p-well obtained from reverse engineering the part. The techniques involved are similar to those developed under this contract for proton-induced SEUs and are described below.

The First Order Model has been adopted by others (Bond et al., 1983) for application to mutations in biological cells. This raised the question of what the dimensions of the sensitive volume for biological cells are. Although not directly funded for this application, some university-supported effort using tools and insights developed under this contract was spent to estimate the dimensions. The similarity of models for radiation effects on microelectronics components and biological cells led to another university supported effort to develop a microdosimeter from arrays of p-n junctions made using the techniques of commercial lithography. These microdosimeters are described in the text since they take advantage of the approaches developed under this contract.

The following sections expand on the items briefly introduced in this section. Section 2 describes the experimental studies, Section 3 covers the theoretical modeling and simulations, and Section 4 describes the modifications to CUPID and the documentation to the program.

SECTION 2

CHARGE COLLECTION -- THE BASICS

2.1 INTRODUCTION.

Testing the First-Order Model turns out to be difficult because a rigorous test requires one to specify the dimensions of the sensitive volume. Because the sensitive volume does not correspond to any visible structure on the device, at least one of its dimensions, usually the thickness, is not typically known with any certainty. Unfortunately, the SEU rate is particularly sensitive to the smallest dimension of the sensitive volume which is usually the thickness. This is true even when the value of the critical charge is scaled with the thickness so that the two devices would have the same response curve for their test data. This is illustrated in Fig. 2.1 which is a CREME calculation of the SEU rates to be expected in deep space for two sensitive volumes having the same lateral dimensions and different thicknesses. In general, thicker sensitive volumes are less sensitive to cosmic-ray upsets according to CREME. Therefore, deviations from the measured SEU rates may be explained by the incorrect value of the thickness of the sensitive volume being used. As mentioned above, the value of the critical charge estimated from the response curve depends on the thickness assumed for the sensitive volume because the critical charge Q in pC is obtained from the threshold LET_{th} from:

$$Q = LET_{th}(\text{MeV cm}^2/\text{mg}) \times \rho(\text{mg}/\text{cm}^3) \times t(\text{cm}) / 22 \text{ MeV/pC} \quad (2.1)$$

where:

ρ = the density of silicon

t = the thickness of the sensitive volume

It is essential to conduct any test of the First-Order Model using proper values of the dimensions of the sensitive volume and, therefore, the correct value of the critical charge. This required developing techniques for determining the dimensions experimentally. Theoretical and experimental approaches were tried. The experimental approach, charge collection, will be discussed first in Section 2.2. Papers describing this work in some detail are included as Appendices B through D. Overviews of those papers follow the lead-in material for Section 2.2.

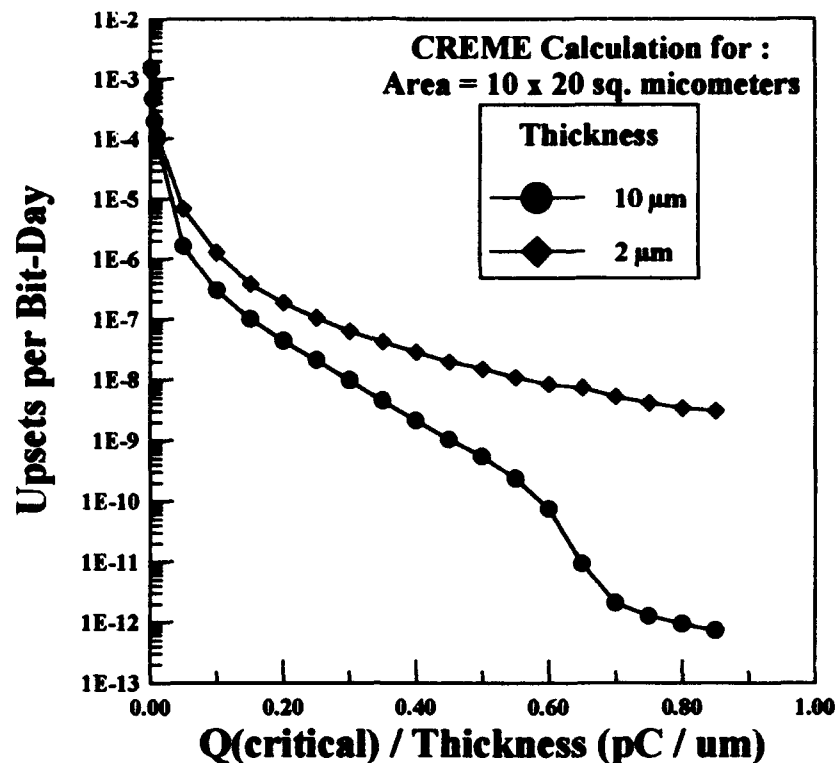


Fig. 2.1. CREME simulations of the Errors per bit per day for two devices having the same lateral dimensions of the sensitive volume, different thicknesses, and the same value of LET_{th} . The cross section is plotted versus the ratio of the critical charge to the thickness of the sensitive volume so that the abscissa value corresponds to the same value of LET for both devices.

Appendix E describes the pulse-height system which has been used at Clemson with an alpha source and a vacuum system designed for charge collection measurements. The same electronics is used at heavy-ion and proton accelerators. The theoretical approach to estimating the dimensions of the sensitive volume involves computer simulations. It is described in detail in Appendix F which is a paper "Modeling Charge Collection and Single Event Upset in Microelectronics." A brief overview is included here to help the reader through this material.

Appendix E: R.A. Reed, "Clemson University Pulse-Height Analysis System -- A Guide for Beginning Students in Radiation Physics."

This guide describes the methods for making charge collection measurements using the equipment and vacuum systems in our laboratory. It is very detailed and provides sufficient information for building as well as using such a system. The ion source in this case is an Americium source. The experiments are carried out in a vacuum system which is also described. This technique represents the cheapest way to estimate the dimensions of the sensitive volume and is, therefore, presented in some detail.

Appendix F: P. J. McNulty, W.G. Abdel-Kader, and J.E. Lynch, "Modeling Charge Collection and Single Event Upsets in Microelectronics," Nuclear Instruments and Methods in Physics Research B61, 52 - 60 (1991).

This paper outlines a simple model for determining the dimensions of the sensitive volume from the process information for the device. The model is applied to a DRAM and the results are found to be in agreement with the charge collection measurements for that device. This paper also shows how to use CUPID simulations and the proton-induced SEU cross section to predict the critical charge. Applying the procedures at three incident proton energies results in critical charges in good agreement.

2.2 CHARGE COLLECTION MEASUREMENTS.

In this study charge collection measurements were carried out with the same test equipment as is used for measuring pulse-heights in solid state nuclear detectors. The experimental configuration used for these measurements is shown in Fig. 2.2. Care should be taken to ensure that the time constants of the preamplifier correspond roughly to the switching speed of the circuit elements. These measurements can be carried out on individual test structures, arrays of test structures in parallel, and between the power pins of functional devices. If the exposures are to parallel beams of identical particles from accelerators, the peaks in the spectra provide information on the various p-n structures connected in the circuit.

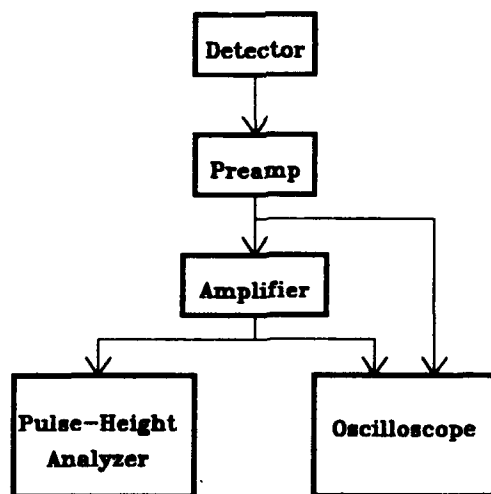


Fig. 2.2. Experimental configuration used for charge collection measurements.

The following section describes charge collection measurements on test structures.

Measurements on Test Structures.

The pulse-height spectrum obtained from measurements on a single test structure from the Honeywell RICMOS process is shown in Fig. 2.3. The spectrum is quite noisy which is unusual for test structure measurements. However, a clearly defined peak is observed when measurements are carried out during irradiation. Two exposures were carried out: one under bias and the other under no bias. Even in the absence of bias the peak is clearly observed. This is because the built-in bias across the junction is sufficient to produce a depletion region of reasonable strength. Applying bias shifts the peak about 20% to higher channel numbers corresponding closely to the increase in the thickness of the sensitive volume due to the increase in the thickness of the depletion region. This indicates that the depletion width for this technology represents only a small fraction of the sensitive volume, and that there is a significant diffusion component to the charge collected. The area of the junctions at which the pulses originate can be obtained from the ratio of the number of events under the peak to the fluence of incident particles. The thickness of the sensitive volume can be obtained from the peak position using range energy tables or from the slope of the peak position versus the LET of the incident particle. There is clearly a broad spread of charge collection pulses resulting from exposure to identical particles all arriving with the same incident LET. This spread is probably due to the small size of the junction -- each particle has a unique position relative to the edges of the junction. As junctions decrease in dimensions, the spread should increase. The theoretical basis for charge collection and a description of the technique is described in considerable detail in Appendix A.

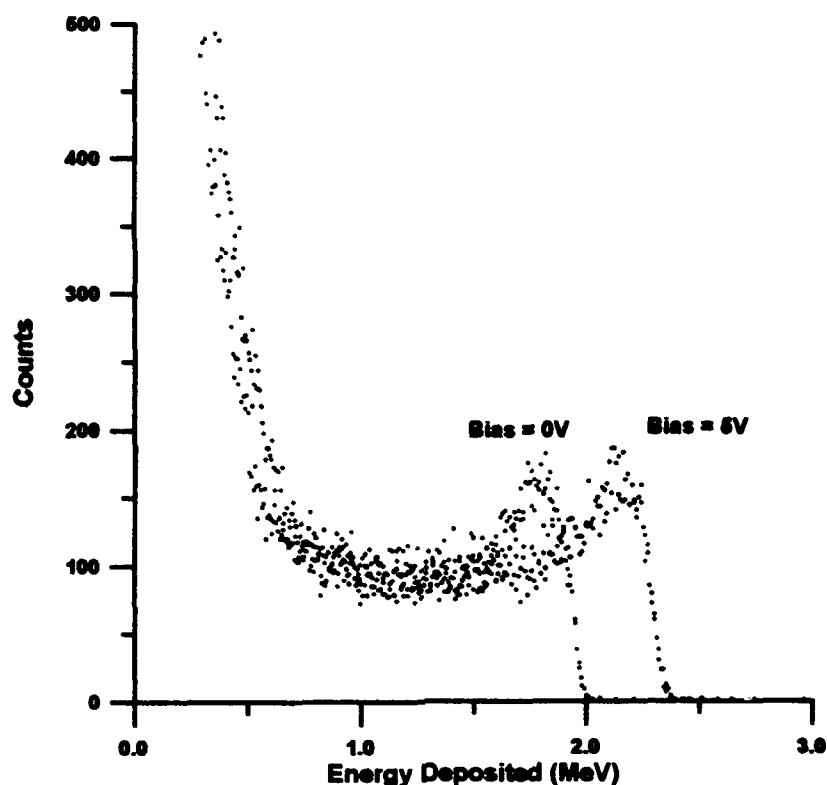


Fig. 2.3. Charge collection spectra obtained from Honeywell RICMOS test structures of the drain-substrate junction under bias and no bias.

The three appendices listed below are papers published under this contract. Brief overviews are presented here to help the reader through the published material.

Appendix B: W.G. Abdel-Kader, S.S. El-Teaty, and P.J. McNulty, "Charge Collection Measurements and Theoretical Calculations for Partially Depleted Silicon Devices," Nucl. Instr. and Methods in Physics Research B56/57, 1246 - 1250 (1991).

This paper applies the procedures for charge collection in devices that are the detectors for the PHA experiment on CRRES. The amount of charge collected at the junction is used to determine the thickness of the sensitive volume for that junction. A simple analytic expression provides reasonable agreement with the charge collection measured with alphas. When the dimensions estimated from the charge collection were used in Monte-Carlo simulations of charge generation in the sensitive volume through proton spallation reactions, the results were in agreement with experiment.

Appendix C: P.J. McNulty, M.H. Yaktien, J.E. Lynch, and W.M. Weber, "Charge Collection in HI2L Bipolar Transistors," IEEE Trans. Nucl. Sci. NS-35, 1613 - 1618 (1988).

This paper represents the first time charge collection was used on test structures in order to determine the dimensions of the sensitive volume of a device and its corresponding value of the critical charge.

Appendix D: S.S. El-Teleaty, P.J. McNulty, W.G. Abdel-Kader, and M. Yaktien, "Charge Collection in Partially Depleted GaAs Test Structures Induced by Alphas, Heavy Ions, and Protons," J. Appl. Phys. 69, 475 - 480 (1991).

This paper describes charge collection measurements on test structures exposed to a variety of radiations, different bias values, and two doping levels. The dimensions of the sensitive volume determined for some Rockwell GaAs test structures were used in simulations of charge collection by proton-induced nuclear reactions using the CUPID codes. Comparison of the results with experimental data yields agreement.

SECTION 3

MEASUREMENTS ON DEVICES: CHARGE COLLECTION SPECTROSCOPY

INTRODUCTION.

There are two types of pulse-height analysis possible for devices exposed to radiation. If there is only one type of junction, the peaks in the spectra provide information on the radiation field which can be quite complex. This is the traditional application of silicon detectors. The other application is to take a complex device and expose it to a uniform beam of energetic charged particles from a radiation source or an accelerator and interpret the peaks as coming from the different junction types on the device. This latter approach applied to commercial devices is collectively referred to as Charge Collection Spectroscopy. It ranges from simple spectra obtained with devices dominated by one junction type such as NMOS SRAMs to the more complex spectra of CMOS devices. Even among CMOS devices, the analyses vary in complexity, p-well CMOS being more complicated than n-well CMOS.

The techniques of charge collection spectroscopy are described in a series of papers presented as the following sections. A brief overview is included here to help the reader through the material.

Appendix G: P.J. McNulty, D.R. Roth, W.J. Beauvais, W.G. Abdel-Kader, and D.C. Dinger, "Comparison of the Charge Collecting Properties of Junctions and the SEU Response of Microelectronic Circuits," *Int. J. Radiat. Instr., Part D, Nucl. Tracks Radiat. Meas.* **19**, 929 - 938 (1991).

The charge-collection spectrum for NMOS memories exposed to monoenergetic ions is shown to be dominated by a single peak. The peak corresponds to ion traversals of the drain, SEU-sensitive junction for the device. The cross sectional area of the junction can be estimated from the number of counts under the peak, and the thickness of the sensitive volume can be obtained from the peak position.

Appendix H: P.J. McNulty, W.J. Beauvais, D.R. Roth, J.E. Lynch, A. Knudson, W.P. Stapor, "Microbeam Analysis of MOS Circuits," in Radiation: Effects on Components and Systems-- Proceedings of the First European Conference on Radiation and Its Effects on Devices and Systems, J.P. Charles and A. Holmes-Siedle, Eds. (IEEE Piscataway, NJ, 1991) pp. 435 - 439.

A RICMOS CMOS SRAM was exposed to energetic ions. Two peaks were observed. Exposures through a microbeam show that both peaks are the result of ion traversals of the different junctions in the memory cell.

Appendix I: P.J. McNulty, W.J. Beauvais, R.A. Reed, D.R. Roth, E.G. Stassinopoulos, and G.J. Brucker, "Charge Collection at Large Angles of Incidence," IEEE Trans. Nucl. Sci. NS-39, 1622 - 1629 (1992).

Charge collection by p-n junctions with at least one small dimension in a p-well CMOS SRAM deviates from the geometric assumptions common to most SEU testing: that the amount of charge collected increases with the secant of the angle of incidence, that the number of events decreases as the cosine, and that it does not matter which axis the device is rotated about to increase the effective LET.

Appendix J: P.J. McNulty, W.J. Beauvais, and D.R. Roth, "Determination of SEU Parameters of NMOS and CMOS SRAMs," IEEE Trans. Nucl. Sci. NS-38, 1463 - 1470 (1991).

Procedures for determining the SEU parameters for advanced memory devices are developed for CMOS and resistor-loaded NMOS SRAMs.

Appendix K: M.H. Yaktien, P.J. McNulty, J.E. Lynch, D.R. Roth, J.F. Salzman, and J.H. Yuan, "Charge Collection and SEU Sensitivity for Ga/As Bipolar Devices," IEEE Trans. Nucl. Sci. NS-36, 2300 - 2304 (1989).

Charge collection was measured across the base emitter heterojunction to test certain assumptions of the First-Order Model. The observed dependence of pulse heights on the angle of incidence and the LET is consistent with the hypothesis that the charge collected equals the product of the LET and the pathlength through a sensitive volume of fixed dimensions. The data suggested that the switch from devices made from MBE to those made with MOCVD resulted in an increase in the thickness of the sensitive volume from 0.11 to 0.25 microns with a corresponding increase in SEU sensitivity.

SECTION 4

THE CUPID MODEL AND APPLICATIONS TO SEU

INTRODUCTION.

Most potential users of the CUPID simulation codes are not familiar with the theory of spallation reactions and may not be comfortable with simulation codes. At the request of the agency, we addressed this concern in two ways. CUPID was made user friendly and adapted to the common IBM form of PC. The modifications to make CUPID more user-friendly and to improve its documentation are described in Section 6. The problem of making users familiar with the basic mechanisms of proton-induced SEUs and the theoretical formalism upon which CUPID is based is addressed in this section.

The theoretical formalism is outlined in Appendix L which is a review of the theory of spallation reactions. It is an invited paper for a special issue of the International Journal of Radiation Physics and Chemistry. This paper illustrates significant features of the spallation reactions by means of CUPID simulations. The fact that the residual nuclear fragments tend to recoil in the forward direction following the spallation reaction, leads to the great difference in the SEU cross sections measured at normal and grazing angles of incidence for devices with thick sensitive volumes and little difference in cross section for devices with very thin sensitive volumes. This paper predicts that the SEU cross section depends strongly on the incident energy, the angle of incidence, and the smallest dimension of the sensitive volume, the thickness for bulk and epi devices.

The paper in Appendix M applies the results of that analysis to a particular device, the AMD 93L422, to illustrate how this sensitivity can be used to determine the smallest dimension of the sensitive volume from the energy and angular dependencies of the SEU cross section. Once the dimensions of the sensitive volume are known, the value of the critical charge can be easily obtained from the measured SEU cross section at any incident energy. Comparison for five devices of the values of the critical charge obtained using protons with the values obtained using heavy ions shows that the proton values have smaller margins of uncertainty. Appendix M is a summary of this work prepared for the 1993 NSREC Conference. Predictions of SEU rates in space should be improved if the proper SEU parameters are used in the calculations. This is shown in Appendix N which reports on the comparison of theory and experiment for the preliminary data available from the first 400+ orbits of the CRRES satellite.

The importance of proton-induced SEUs is illustrated in Appendix O which is a paper describing proton-induced SEU in a CMOS/SOS circuit. This paper disproved the accepted wisdom that a device with a measured threshold LET above 10 MeV cm²/mg, the maximum LET for the spallation recoils, is immune to proton-induced SEUs. It is the energy deposited within the sensitive volume that determines whether the device upsets

and not the LET of the charge crossing the junction. Rare spallation reactions can generate large energy depositions. The tests described a device implemented using radiation hardened CMOS/SOS technology. There are now a number of cases where the conventional wisdom regarding proton sensitivity is violated. It is important to note that CUPID simulations carried out before the CMOS/SOS tests indicated proton upsets at a very low cross section, which is what was observed.

Modifications were made in the CUPID model to extend the calculations to GaAs circuits and to events initiated by neutron-induced spallation reactions. Some results of these efforts are included in the papers which form Appendices P and Q. Since the following sections are papers submitted to or already published in journals, a brief overview is included here to help the reader through the material.

Appendix L: P.J. McNulty, W.G. Abdel-Kader, and G.E. Farrell, "Proton-Induced Spallation Reactions," submitted as an Invited Paper to SPACE RADIATION ENVIRONMENT AND EFFECTS, a special issue of the International Journal of Radiation Physics and Chemistry, L. Adams, Ed.

This paper describes the kinematics of the spallation reactions, the mechanism behind proton-induced single event phenomena. Computer simulations using CUPID are used to illustrate the kinematics of the spallation reaction and the resulting energy deposition in microvolumes which have dimensions typical of the sensitive volumes of modern devices.

Appendix M: P.J. McNulty, W.J. Beauvais, and W.G. Abdel Kader, "SEU Parameters and Proton-Induced Upsets," submitted for presentation at the 1993 Nuclear and Space Radiation Effects Conference.

This paper illustrates how the SEU cross sections measured at various incident proton energies and angles of incidence are very sensitive to the thickness of the sensitive volume and the critical charge required for upset. It demonstrates procedures of determining the thickness of the sensitive volume and the critical charge from the measured SEU cross sections.

Appendix N: P.J. McNulty, W.J. Beauvais, W.G. Abdel-Kader, E.G. Mullen, K.P. Ray, and S. El-Teleaty, "Test of SEU Algorithms Against Preliminary CRRES Satellite Data," IEEE Trans. Nucl. Sci. NS-38, 1642 - 1651 (1991).

This paper describes the preliminary results from SEU studies in the Microelectronic Package on the CRRES satellite. The orbit was highly elliptical and exposed the devices in the experiment to both the trapped protons in the inner radiation belt and the cosmic rays of deep space. Two experiments are compared with predictions based on the algorithms CUPID and CREME. These were the Ratemeter experiment which measured SEU rates in DRAMs and the PHA experiment which measured the pulse-height spectrum from a small silicon photodiode. These experiments were chosen because the dimensions of the sensitive volumes were well established in both cases. The data in the inner belts are in relatively good agreement with AP-8 combined with CUPID to simulate the spallation

reactions. Differences between experiment and theory are consistent in the two cases suggesting that AP-8 underpredicts the environment by roughly a three. The deep-space data was in good agreement with the CREME predictions.

Appendix O: J.C. Pickel, B. Lawton, A.L. Friedman, and P.J. McNulty, "Proton-Induced SEU in CMOS/SOS," J. of Radiat. Eff. 7, 67 - 76 (1989).

This paper describes experiments on proton-induced SEUs in 16K CMOS/SOS SRAMs. Analytic predictions based on CUPID simulations are consistent with the experimental results. The implications for SOI technologies are discussed.

Appendix P: T.R. Weatherford, E. Petersen, W.G. Abdel-Kader, P.J. McNulty, L. Tran, J.B. Langworthy, and W.J. Stapor, "Proton and Heavy Ion Upsets in GaAs MESFET Devices," IEEE Trans. Nucl. Sci. NS-38, 1450 - 1456 (1991).

This paper describes an NRL study on the proton energy dependence of the SEU cross sections for GaAs MESFETS. Clemson supported the effort by determining the thickness of the sensitive volumes using our charge-collection techniques and equipment. CUPID simulations were also carried out to determine the values of the critical charge from SEU measurements to predict how the cross sections would have varied if the values of the critical charge given by SPICE had been correct.

Appendix Q: E. Normand, W.J. Stapor, P.J. McNulty, W.G. Abdel-Kader, and M.H. Yaktien, "Quantitative Comparison of Single Event Upsets Induced by Protons and Neutrons," IEEE trans. Nucl. Sci. NS-38, 1457 - 1462 (1991).

This paper examines the SEU susceptibility of microchips to neutrons on both experimental and theoretical grounds. It involves a collaborative effort between Boeing, NRL and Clemson. It represents a beginning analysis of one of the key issues for SEUs in avionics.

Appendix R: S. El-Teleaty, P.J. McNulty, W.G. Abdel-Kader, and W.J. Beauvais, "Soft Fails in Microelectronic Circuits Due to Proton-Induced Nuclear Reactions in Material Surrounding the SEU-Sensitive Volume," Nucl. Instr. and Meth. in Physic Res. B40/41, 1300 - 1305 (1989).

This paper describes the measurement of charge collection resulting from proton-induced spallation reactions in well-defined sensitive volumes with and without material surrounding the sensitive volume. The results are in agreement with the predictions of the CUPID simulation codes over a range of energies from 37 to 154 MeV. Proton spallation simulations which ignore the contributions from reactions in the surround can seriously underestimate the SEU rate.

SECTION 5

APPLICATIONS TO OTHER SINGLE-EVENT PHENOMENA

INTRODUCTION.

Single-event phenomena are common to any structures which have microscopic dimensions and which store or process information. This is true for biological organisms as well as manmade circuits. It is very exciting to find that the First-Order Model appears to provide a reasonable quantitative model for all of the ones studied to date. This section describes applications of the First-Order Model and CUPID to Single Event Latchup (SEL) and displacement damage resulting from spallation reactions. The CUPID predictions show that large Non-Ionizing Energy Loss (NIEL) depositions in a microvolume are possible from spallation reactions. These rare stochastic events can happen at any time during the exposure and represent a potential design limit for some applications of CCDs to satellite communications and hyperspectral imaging. CUPID was modified under this contract to handle NIEL events. A collaborative effort with Kodak, the model was extended to multiple events corresponding to long intense exposures. The applications also included Kodak devices which were supported under a different contract. Because the basic changes in the model were carried out under this contract, a report describing the work with Kodak is included in Appendix S.

This report also includes in Appendix U a description of applying the same single event formalism to biological phenomena including the very important case of mutations. The biological studies were not supported by the contract, but have obvious overlap. The biological applications of the First-Order Model are outlined for completeness.

If biological mutations can be explained by models resembling the First-Order Model and they have dimensions common to those of the circuit elements of microchips, then single-event phenomena in microchips can be used to monitor radiation hazards for biological organisms, namely mankind. Microdosimeters were developed using parallel arrays of p-n junctions, some on SRAMs. Again, this work was carried out on university funds and was supported under this contract, but since it is an example of applying models and concepts developed for circuit elements under the contract, a short description is included in Appendix U for completeness. Moreover, at least one of the figures used was obtained for other purposes under the contract.

The following appendices are manuscripts prepared for submission to journals or for conferences. Brief overviews are presented here to help the reader through the material.

Appendix S: L. Chen, P.J. McNulty, W.G. Abdel-Kader, T.L. Miller, and D. A. Thompson, "Single and Multiple Proton-Induced NIEL Events in Silicon," submitted to the 1993 Nuclear and Space Radiation Effects Conference.

Displacement damage from exposure to protons has two large components: the cumulative effects of many small elastic nuclear events, and the rare large contributions from spallation reactions. Spallation reactions can contribute large amounts of non-ionizing energy loss (NIEL) in a small volume element. These rare events pose a design limitation for applications of CCDs to satellite communications and hyperspectral imaging. CUPID was modified to handle NIEL events and extended to include multiple events in an array. The results are in good agreement with previous experimental results.

Appendix T: P.J. McNulty, W.G. Abdel-Kader, W.J. Beauvais, L. Adams, E.J. Daly, and R. Harboe-Sorensen, "Simple Model for Proton-Induced Latch-Up," submitted for the 1993 Nuclear and Space Radiation Effects Conference.

This paper explores the possibility of explaining proton-induced latch-up by the First-Order Model. Accordingly, latch-up occurs, if and only if, more than some threshold amount of energy is deposited within the sensitive volume. Simulations were carried out for a number of values of the thickness of the sensitive volume for both normal incidence and grazing incidence. Presumably, the correct thickness is the value which best fits the data with the same value of the critical charge. The best fitting thickness turns out to be the thickness of the p-well, the presumed sensitive volume for latch-up.

Appendix U: P.J. McNulty, D.R. Roth, W.J. Beauvais, W.G. Abdel-Kader, and E.G. Stassinopoulos, "Microdosimetry in Space Using Microelectronic Circuits," in Biological Effects and Physics of Solar and Galactic Cosmic Radiation, C.E. Swenberg, Ed., (Plenum) to be published.

This paper compares the SEU in microelectronic circuits with similar phenomena in biological organisms, and the similarities and differences are discussed. Both types of phenomena appear to obey the First-Order Model at least approximately. This general applicability of the model appears to reflect the need of each system to operate despite the noise inherent in the storage and processing of information within microscopic volume elements.

Appendix V: P.J. McNulty, D.R. Roth, E.G. Stassinopoulos, and W.J. Stapor, "Characterizing Complex Radiation Environments Using MORE (Monitor of Radiation Effects)," in Proceedings of the Symposium on Detector Research and Development for the Superconducting Super Collider, T. Dombeck, V. Kelly, and G.P. Yost, Eds. (World Scientific, Singapore, 1990) pp. 690 - 692.

SECTION 6

CUPID MODIFICATIONS AND DOCUMENTATION

6.1 INTRODUCTION.

In the preceding sections, applications have been described for the CUPID simulation codes which go considerably beyond its intended purpose which was to test the First-Order Model for proton-induced SEUs. CUPID has been shown to be useful in determining the thickness of the sensitive volume and the value of the critical charge. It has been extended to SEL and single event NIEL. Moreover, there were requests for copies from other laboratories. Unfortunately, the original CUPID was developed in earlier times when the documentation of software was not routinely done and the codes did not transfer easily from one computer to another. In order to make CUPID available in a form easily used by others, three changes had to be made. The codes had to be able to be run on a personal computer in order to be truly portable. They had to be made user-friendly in the modern sense, i.e., menu driven. Finally, the codes had to be documented. All three have been accomplished under the contract. The code is now used by groups at the following laboratories: Aerospace Corp., the European Space Agency, IBM, the Naval Research Laboratory, and copies are being prepared for a laboratory at West Point and in Great Britain.

6.2 USER-FRIENDLY VERSION OF CUPID FOR PCs.

The new version of CUPID runs the simulation code for a sensitive volume with dimensions specified by the user nested within an outer volume of silicon whose dimensions are also specified. The user also must specify the energy of the incident protons and the relative number of iterations to be carried out. The output is in the form of a plot of the integral cross section versus the energy deposited in the sensitive volume, i.e., the plot of the cross section for depositing at least energy ϵ versus ϵ . If the critical charge is located on the abscissa in energy units, the corresponding ordinate coordinate is the SEU cross section. The output is also available in list form. The details of using the program are described in Appendix W.

SECTION 7

REFERENCES

- Adams, J.H., "The Variability of Single Event Upset Rates in the Natural Environment," *IEEE Trans. Nucl. Sci.* NS-30, 4475 - 4480 (1983).
- Adams, L., E.J. Daly, R. Harboe-Sorensen, R. Nickson, J. Haines, W. Schafer, M. Conrad, H. Greich, J. Meckel, and T. Schawall, "A Verified Proton-Induced Latch-Up in Space," *IEEE Trans. Nucl. Sci.*, to be published.
- Binder D., C.E. Smith, and A.B. Holman, "Satellite Anomalies from Galactic Cosmic Rays," *IEEE Trans. Nucl. Sci.* NS-22, 2675 - 2680 (1975).
- Rond, V.P., and M.N. Varma, "A Stochastic Weighted Hit Size Theory from Cellular Radiobiological Action," in Proceedings of the Eight Symposium on Microdosimetry, J. Boos and H.G. Ebert, Eds., (Commission of the European Committees, 1983) pp. 423 - 438.
- Goka, T., S. Kuboyama, Y. Shimano, and T. Kawanishi, "The On-Orbit Measurements of Single Event Phenomena by ETS-V Spacecraft," *IEEE Trans. Nucl. Sci.* NS-38, 1693 - 1699 (1991).
- McNulty, P.J., "Predicting Single Event Phenomena in Space," in 1990 IEEE Short Course: Microelectronics for the Natural Radiation Environments of Space, (IEEE NPSS Radiation Effects Committee, 1990) pp. 3-1 to 3-93.
- McNulty, P.J., G.E. Farrell, R.C. Wyatt, P.L. Rothwell, R.C. Filz, and J.N. Bradford, "Upset Phenomena Induced by Energetic Electrons and Protons," *IEEE Trans. Nucl. Sci.* NS-27, 1516 - 1522 (1980).
- McNulty, P.J., W.J. Beauvais, D.R. Roth, J.E. Lynch, A. Knudson, and W.P. Stapor, "Microbeam Analysis of MOS Circuits," in Radiation Effects on Components and Systems -- Proceedings of the First European Conference on Radiation and Its Effects on Devices and Systems, J.P. Charles and A. Holmes-Siedle, Eds. (IEEE Piscataway, NJ, 1991) pp. 435 - 439.
- Pickel, J.C., and J.T. Blandford Jr., "Cosmic-Ray Induced Errors in MOS Memory Cells," *IEEE Trans. Nucl. Sci.* NS-28, 3962 - 3967 (1980).
- Sexton, F.W. "Measurements of Single Event Phenomena in Devices and ICs," in 1992 IEEE Short Course: Measurement and Analysis of Radiation Effects in Devices and ICs, (IEEE NPSS Radiation Effects Committee, 1992) pp. 3-1 to 3-55.

Wyatt, R.C., P.J. McNulty, Toumbas, P., Rothwell, P.L., and Filz, R.C., "Soft Errors Induced by Energetic Protons," IEEE Trans. Nucl. Sci. NS-26, 4905 - 4910 (1979).

APPENDIX A

PREDICTING SINGLE EVENT PHENOMENA IN SPACE

P.J. McNulty

Published as part of the 1990 IEEE Short Course: Microelectronics in the Natural Environments of Space (IEEE NPSS Radiation Effects Committee, 1990) pp. 3-1 to 3-93.

PREDICTING SINGLE EVENT PHENOMENA IN NATURAL SPACE ENVIRONMENTS

**P.J. McNulty
Clemson University
Clemson, SC 29634-1911**

ABSTRACT

Modern microelectronics are known to be subject to a variety of single-event phenomena, the most quantitatively understood being the single-event upset. Circuits upset because they consist of a skillfully arranged array of p-n junctions, and when ionizing particles traverse reverse-biased p-n junctions, they cause sudden swings in the bias across the junction. These pulses are large enough that particle detectors are also made of p-n junctions. Many of our circuits on current spacecraft are detecting cosmic rays and trapped protons with unfortunate consequences. The physics of particle detectors is applied to typical microelectronic junctions to elucidate the basic mechanisms behind the current models for predicting SEU rates. Procedures for predicting upset rates in space from accelerator test data are described and the potential accuracy of these algorithms discussed.

TABLE OF CONTENTS

1. INTRODUCTION

- 1.1 Background**
- 1.2 Single Event Effects**
 - 1.2.1 Latchup**
 - 1.2.2 Snapback**
 - 1.2.3 Burnout**
 - 1.2.4 Single Event Upset**
- 1.3 Vulnerability of Satellites**
- 1.4 SEU Sensitive Structures**

2. REVERSED-BIASED JUNCTIONS

- 2.1 Particle Detectors**
 - 2.1.1 Dimensions of the Sensitive Volume**
- 2.2 Microelectronic Junctions**
 - 2.2.1 Charge Collection**
 - 2.2.2 Threshold Dependence on LET**
 - 2.2.3 Charge Collection Dependence on LET**
 - 2.2.4 Sensitive Volume**
 - 2.2.5 Track Structure Effects**

3. MEMORY CELLS

- 3.1 Charge Collection Measurements**
- 3.2 Dimensions of the Sensitive Volume**

4. EXPERIMENTAL SIMULATION OF SEUs

- 4.1 Method**
- 4.2 Analysis**
- 4.3 Typical Results for Heavy Ions**
- 4.4 Proton-Induced Upsets**

5. FIRST-ORDER MODEL

6. ALGORITHMS FOR PREDICTING SEU RATES

6.1 Cosmic Rays

6.2 Trapped Protons

7. SOURCES OF INACCURACY

7.1 Shape of the Threshold-Response Curve

7.2 Track Structure

7.3 Lot-To-Lot Variations and Process Changes

7.4 Differences in Test Boards, Applied Bias, etc.

7.5 Uncertainties in the Natural Radiation Environments

7.6 Shielding

8. HOW ACCURATE ARE SEU PREDICTIONS?

8.1 Deep Space

8.2 Low-Earth Orbit

8.3 Predicting Proton Response From Heavy Ion Data

8.4 Conclusions

9. ACKNOWLEDGEMENTS

1. INTRODUCTION

1.1 Background

The advent of large-scale integration (LSI) in semiconductor electronics was based on industry's ability to produce memory and logic elements with microscopic dimensions. Increasing the number of transistors on a chip as technology passed through VLSI was accomplished by shrinking still further the dimensions of the circuit's memory elements. As their dimensions became microscopic the circuit elements became sensitive to ionizing radiation in an entirely new way. It was discovered that circuits incorporating these micro-elements could have their electrical state, and hence their logic state, altered as a result of a single interaction with an energetic cosmic-ray particle (1). Logic states become more sensitive as their dimensions decrease because smaller differences in charge storage on the junctions separate the two different logic states of the element. The energy difference required to switch states also depends on the bias and the speed at which the device is to be switched. The product of the number of gates and the clocking frequency is defined to be the functional throughput rate (FTR). Petersen and Marshall (2) point out that, as the FTR of commercial devices increases, the energy of the individual gates must be decreased in order to limit the power dissipation. This is illustrated in Fig. 1 for past and near future trends in commercial devices. The information stored in modern devices is represented by such small amounts of energy that the information can often be changed by the passage of a cosmic-ray particle or, in some instances, an alpha particle.

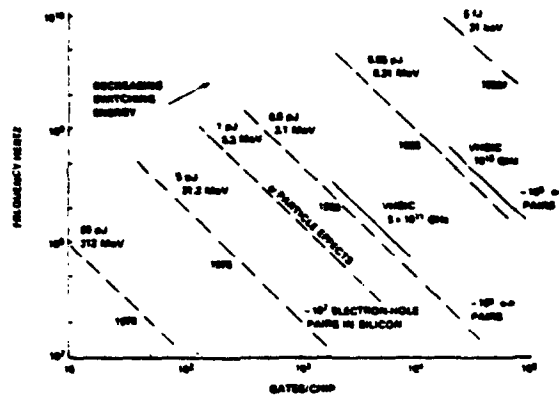


Fig. 1 Trends in microelectronic switching energy as FTRs increase.



Fig. 2 Cosmic ray nucleus in nuclear emulsion.



Fig. 3 Nuclear reaction in nuclear emulsion.

The generation of large amounts of charge at critical locations on the die of a chip can alter the electrical, and hence the logic state, of the local element. Concentrations of charge are generated along the trajectories of cosmic-ray ions and at the locations of spallation reactions. Figure 2 shows the trajectory of a heavily ionizing cosmic-ray ion through nuclear photographic emulsion which was flown in space and subsequently developed. The cosmic-ray particle is probably a member of the iron group and comes to rest at the lower left corner of the figure. Traversal of certain junctions on a circuit by such a particle would be sufficient to induce changes in the electrical state in any circuit element except those specifically hardened against such changes. Figure 3 shows a similar "photo" of a cosmic-ray induced spallation reaction where the target nucleus is either a silver or a bromine nucleus. Nuclear reactions such as this have also been shown to upset circuit elements (3,4). The largest concentration of charge is generated along the trajectory of the recoiling nuclear fragment (5).

1.2 Single Event Effects

Such densely ionizing events are far apart in both space and time and, as a consequence, any effects in the natural radiation environments of space must be due to a single such event, hence the names single-event effects or single-event phenomena. Single-event effects (SEE) can be characterized as either hard or soft according to whether or not there is permanent damage. The soft error or single-event upset (SEU) involves a change in the information stored on the device with no significant damage to the circuit element. Examples of hard errors, listed in Fig. 4, include elements which can no longer change states (frozen bits), latchup, snapback, direct burnout of circuit elements in power MOSFETS, and displacement damage events which generate noise (6).

TYPES OF HARD ERRORS

- Burnout of power MOSFETS
- Gate rupture
- Latchup resulting in high current
- Frozen bits
- Noise source in CCDs
- Snapback

Fig. 4 Types of hard errors.

1.2.1 Latchup

The characteristics of latchup are outlined in Fig. 5, and they are described in more detail in Ref. (7). Latchup requires that a path of ionization be connected across an array of at least three junctions connecting four regions of alternating doping (p and n). This requirement is most often satisfied in CMOS circuits. Both p-n-p and n-p-n parasitic bipolar transistors are inherent in the bulk CMOS architecture. If the base region of one transistor is the same material as

the collector of the other, these bipolars combine to form a p-n-p-n-type silicon-controlled rectifier, or SCR, in parallel with the CMOS inverter. When the CMOS IC operates normally, the p-n-p-n stays "off", i.e., in a high impedance state. However, the traversal of the base region of either bipolar transistor by a high LET particle can result in a sufficient number of minority carriers being injected into the base of the parasitic bipolars to put the p-n-p-n structure into its low impedance state, thereby latching the cell (8-10).

CHARACTERISTICS OF SINGLE EVENT LATCHUP

- CMOS circuits
- Turn on of SCR transistor
- Requires P-N-P-N paths
- Threshold LET similar to SEU

Fig. 5 Characteristics of single-event latchup.

1.2.2 Snapback

Another SEE which results in a high current mode state is called snapback (10). While qualitatively similar to latchup in terminal behavior, snapback does not require the p-n-p-n structure. It has been observed in discrete n-channel devices. It is initiated by charges generated in the p-well surrounding n-channel FETs. A drain avalanche current is induced and maintained by minority carriers from the source. The source to drain voltage necessary to sustain snapback is well below the avalanche voltage of the device.

1.2.3 Burnout

Single-event burnout has been observed in MNOS programmable memories (11) and MOSFET power transistors (12). These phenomena have been studied in the laboratory but have yet to be reported as occurring in space. In both cases, the heavy ion creates a permanent low resistance path between the gate and the substrate when it passes through junctions with high voltage present. The LET and the electric field have to exceed some minimum value for burnout to occur. Burnout of power MOSFETs is characterized in Fig. 6 and described in detail in Ref. (12). The direct catastrophic effects of hard errors in the devices themselves can often be avoided by changing the chip design to reduce the probability of turning on parasitic transistors, by modifying circuits to limit the currents flowing into the chip, and by permanent fault maps by which the computer avoids damaged memory locations.

BURNOUT OF POWER MOSFETS

- Two targets
 - Junctions
 - Oxide
- Junction more sensitive
- Results in burnout of junction
- N channel more sensitive than P channel

Fig. 6 Burnout of power MOSFETs.

1.2.4 Single Event Upset

Even if the circuit is not damaged or permanently altered, there can still be an alteration in the stored information resulting in a change in the system's instructions. See Fig. 7. The change can occur as a result of a bit upset, i.e., a change in the information stored at some register or memory location. A second source of soft error is the generation of a transient signal which then poses as a bit of new information. This in turn becomes stored somewhere or is acted upon by the system. Distortions in the instructions can cause systems to malfunction in a number of ways, including the turning on and off of rockets or other critical systems. The results can, in some cases, be catastrophic.

TYPES OF SOFT ERRORS

- BIT UPSETS IN MEMORY CELLS OR REGISTERS
- TRANSIENT SIGNALS IN LOGIC OR SUPPORT CIRCUITRY

Fig. 7 Types of soft errors.

Most studies of SEUs have involved memories and register arrays. Since the gates of logic circuits can also be switched from one electrical state to the other, they are also susceptible to SEUs. Logic circuits pose a problem in analysis, however. The change in the electrical state of a single gate can propagate errors through a chain of gates without the error being apparent from the outside. This was illustrated by Tim May (13) in a series of electron microscope photographs (Fig. 8) which show the propagation of errors through the Intel 80186 microprocessor. The voltage levels and, therefore, logic states of the gates of the microprocessor are represented as light and dark areas on the photographs. The fault-free micrograph of the device is shown in the first image of the top row. The next image shows

the same micrograph with a single fault introduced. No difference is noticeable. The third image in the top row is the difference between the first two, i.e., the lighted points representing those pixels which appear in one image but not the other. The light spot in image 3 represents the gate location with different states in the first two images, thus showing the location of the original error. A single lighted point can barely be discriminated from photographic reproducing noise in the figure.

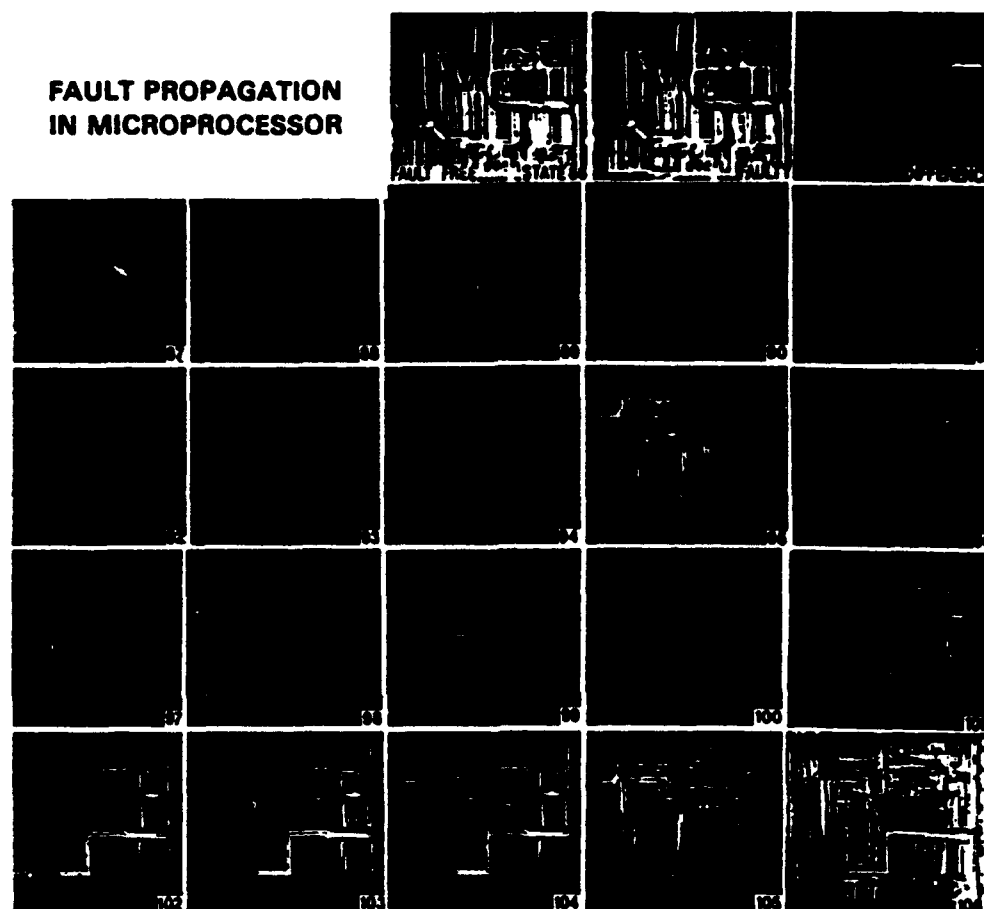


Fig. 8 Fault propagation in Intel 806186 microprocessor. Light and dark areas represent different voltage states on the first two SEM photographs. The first represents a fault-free state and the second the same state with a single error introduced. Remaining images are the difference between the fault-free state and the faulty state after the same number of machine cycles.

The microprocessor then operated normally and micrographs were taken after each machine cycle. Each numbered image in Fig. 8 represents the difference between the fault image and the fault-free image after the same number of machine cycles. Light points then represent errors or differences in logic states between the fault and fault-free versions at that machine cycle. The error points spread over the images, contract, then spread again in complicated patterns. It takes a large number of machine cycles, in this case about 100, for any of the errors to reach a bondpad. Only after an error reaches a bondpad is the problem observable to the world outside of the chip.

The detection and correction of errors on microprocessors are obviously very difficult and, as a result, they are more serious than memory upsets. They are also much more difficult and expensive to analyze than memory upsets. Newberry points out that there are at least three different types of errors possible in logic chips including the bit upset, the lost data word, and the lost data path (14). The lost data path can be particularly serious since sometimes the device must be powered down and then restarted from initial conditions before it will work properly again (15).

1.3 Vulnerability of Satellites

Present demand by system designers for electronic components which are faster, have higher density, and use less power results in the use of circuits with increased sensitivity to single-event effects. The SEU is the most common and troublesome of the SEEs observed by satellite operations. It is also the best studied. As a result, they are the most understood quantitatively. SEUs will be emphasized in discussions of the ability to predict SEE phenomena because any conclusions regarding predictive ability will almost certainly apply also to hard errors.

A broad range of existing satellites have experienced SEUs. Detailed discussion of the impact on all the different programs is beyond the scope of this tutorial. However, the three programs listed in Fig. 9 illustrate the different types of impact single-event phenomena can

have on a satellite program. The first generation TDRS satellites were designed without concern for SEEs and had, as a consequence, a number of SEU-sensitive bit locations which are critical to satellite operations. When one of these bits is upset by a cosmic ray or a proton-induced spallation reaction, the satellite sometimes responds inappropriately for its mission, requiring ground-based intervention. Upsets requiring intervention were frequent enough to require extra personnel on standby in order to prevent the satellite's breaking communication, leading to mission failure.

IMPACT OF SEU ON SOME RECENT SATELLITE SYSTEMS

- **REQUIRES RETROFIT BEFORE LAUNCH
(GALILEO)**
- **REQUIRES FREQUENT GROUND-BASED
INTERVENTION (TDRS)**
- **INTERFERES WITH PERFORMANCE
(HUBBLE SPACE TELESCOPE)**

Fig. 9 Examples of SEU impacts on satellites.

The system designers for Galileo based designs of critical satellite systems around components which were later found to be SEU sensitive. The problem was discovered well before launch, but replacing a few devices without impacting other systems on the satellite required changes which cost over \$15M and resulted in considerable delay in the launch. The recently launched Hubble Space Telescope includes SEUs among its problems. There is cause for concern that the rate of SEUs is sufficiently high that despite frequent ground-based intervention there may be performance interference.

1.4 SEU Sensitive Structures

Reverse-biased junctions are essential components of both micro-electronic circuits and particle detectors. Both silicon and GaAs circuits have been shown to be sensitive to SEUs as summarized in Fig. 10. A wide range of particle types can generate the large local concentrations of charge necessary to effect at least some circuits (Fig. 11). SEUs have been shown to be induced by uncharged particles such as energetic neutrons (3,17,18) and high-energy gamma rays (17), but only traversals of certain reverse-biased junctions by heavy ions and proton-induced nuclear reactions, at or near the junction, are believed to contribute significantly in space (Fig. 12). Heavy-ion traversals should dominate for circuits flying in deep space. In low-earth orbits, spallation reactions between trapped protons and the silicon nuclei of the crystal will dominate for all but the least sensitive devices. Browning et al (19) has suggested that proton-induced fission of fissionable contaminants in the materials making up the device may lead to proton-induced upsets and hard errors in even the most SEU insensitive devices flown in space.

CIRCUIT TYPES EFFECTED BY SEU PHENOMENA

SILICON:

- CMOS
- DRAM
- BIPOLAR
- NMOS

GALLIUM ARSENIDE:

- JFET
- MESFET
- H⁺L

Fig. 10 Types of circuits subject to soft errors.

TYPES OF RADIATION KNOWN TO INDUCE SEU.

HEAVY IONS

PROTONS

NEUTRONS

GAMMAS

IMPORTANT IN SPACE

HEAVY IONS

PROTONS

Fig. 11 Types of radiation known to induce SEUs.

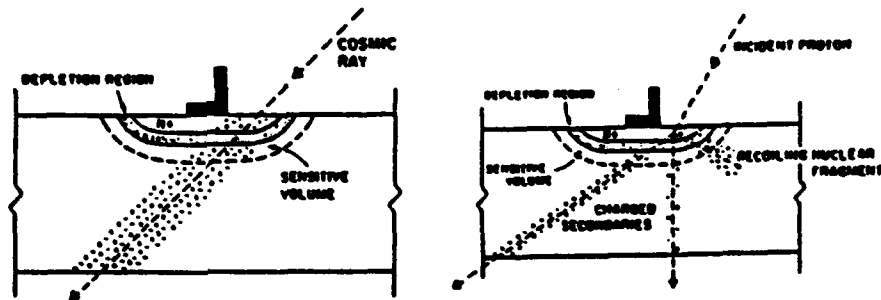


Fig. 12 Important mechanisms for SEUs in space. a) Heavy ion traversal of a reverse-biased junction. b) Spallation reaction at or near the junction.

Reducing the size of the junctions makes them harder to hit, but, as mentioned above, it also makes them more sensitive to upsets. The amount of charge which must be collected across the junction to upset the circuit element is called the critical charge. It is related to the switching energy. For unhardened devices, the critical charge has been shown by Petersen (2) to decrease as the feature size is reduced. Figure 13 illustrates this dependence on the feature size characterizing the technology for various device types. Presumably smaller feature sizes are accompanied by smaller, lower-capacitance junctions. The

lower the capacitance the smaller the difference between the values of stored charge representing the two electrical states of the element. Devices can be hardened against SEUs either by reducing the amount of charge that will be collected across the junction or by increasing the amount of charge necessary to upset the element. A discussion of hardening is beyond the scope of this tutorial. The reader is referred to recent reviews edited by Kerns and Shafer (16).

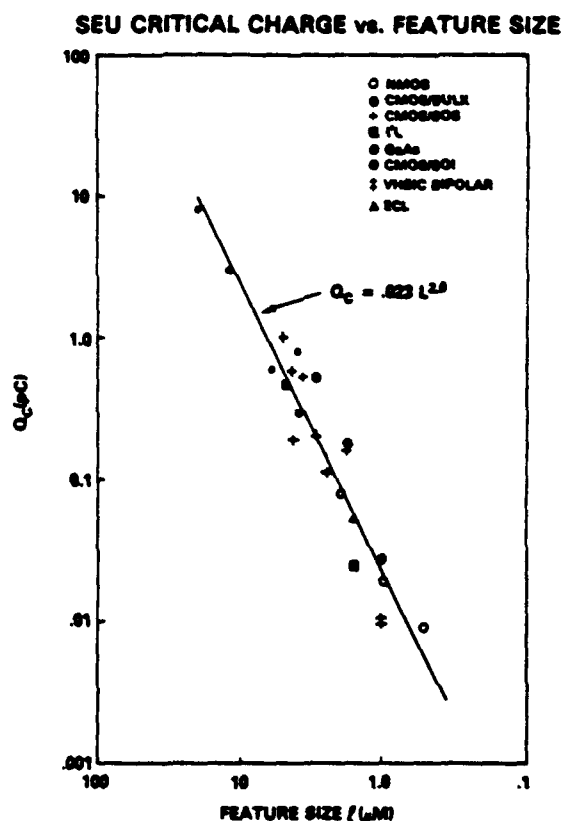


Fig. 13 Dependence of the critical charge on feature size.

While the SEU will be the example used in discussions, it is hoped that the procedures outlined for predicting SEUs will eventually be applicable, at least in part, to other single-event phenomena. Figure 14 outlines the information needed to accurately predict SEU rates in space. Of course, the relevant components of the radiation environment must be known. In deep space this means the charge and energy spectra of the cosmic rays. In low-earth orbits concern is primarily with the protons trapped in the radiation belts. These are discussed in the earlier article by E.G. Stassinopoulos. The analysis of predicting SEU rates begins with a discussion of the collection of charge by the SEU-sensitive junctions.

NEEDED TO CALCULATE SEU RATES

- CHARGE, MASS, AND ENERGY OF PARTICLES
- DIMENSIONS OF SENSITIVE MICROVOLUMES
- DETAILS OF THE CHARGE GENERATION AND COLLECTION
- RESPONSE OF THE CIRCUIT

Fig. 14 Information needed to predict SEU rates in space accurately.

2. REVERSE-BIASED JUNCTIONS

The reverse-biased junction formed at the interface between regions of a silicon crystal which have different doping characteristics is the basis for both the diode action required for the operation of the transistors forming modern microelectronic circuits and the particle detection characteristics which lead to SEUs. A depletion region consisting of layers of positive and negative charge appears on opposite sides of a junction, as shown in Fig. 15. The depletion region grows larger when the junction is reversed-biased, becoming smaller in the absence of external bias, and thinning down to the point of disappearance as the device is forward biased. See the lower portion of Fig. 15. The charges in the layers making up the depletion region are fixed to the donor and acceptor atoms on either side of the junction and consequently, the thickness of the depletion region depends on the doping levels on both sides. The higher the doping density, the thinner the depletion region is on that side of the junction. Strong electric fields connect the charges on either side with the direction of the field lines oriented perpendicular to the junction. In the absence of external disturbances, the electric field does not extend beyond the depletion region. Charges generated as electron-hole pairs within the depletion region or individual charges wandering into the depletion region are accelerated under the force of the field with electrons and holes attracted to opposite sides. This flow of current across the junction results in a measurable decrease in the voltage difference across the junction. This voltage swing due to charge collected across an n-p junction is the basis of the operation of solid-state silicon and germanium particle detectors as well as the mechanism for SEUs in microelectronic circuits.

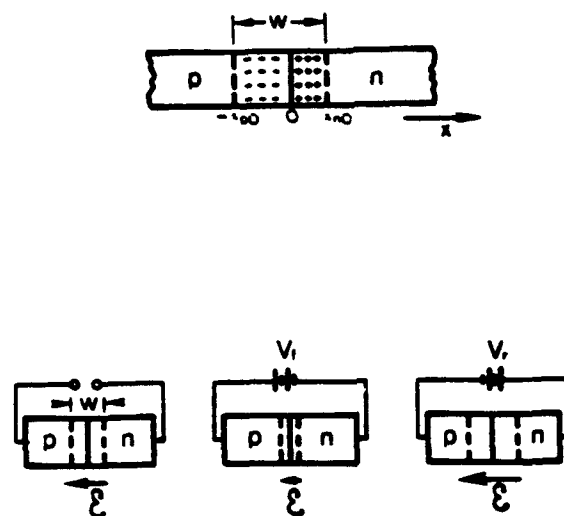
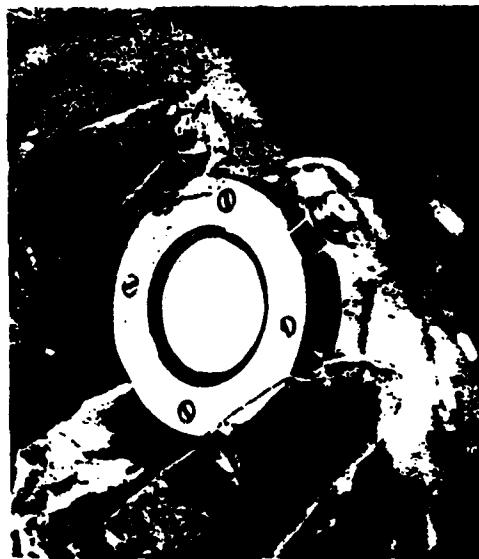


Fig. 15 Schematic of a reverse-biased junction.

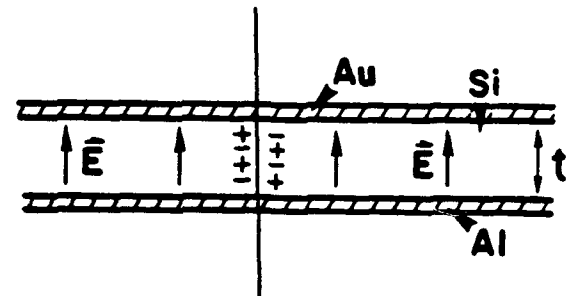
2.1 Particle Detectors

The easiest example of charge collection to analyze quantitatively is the case of the fully depleted surface-barrier detector. A photo of a silicon surface-barrier detector consisting of a biased p-n junction with metallic surface electrodes along with a schematic of its cross section is shown in Fig. 16. The circuitry necessary to measure and record the amount of charge collected as a result of the junction being traversed by a charged particle is outlined in Fig. 17. If the detector is fully biased, the depletion region fills almost the entire volume of the silicon, and all the electrons and holes are accelerated under electric fields toward their respective terminals by the electric field. The resulting pulse of voltage versus time seen on the oscilloscope has the narrow shape characteristic of fully depleted detectors. The measured shape of these fast pulses typically reflects the impedance characteristics of the device and the measuring circuits as well as the

time profile of the charge collection. The preamplifiers used in pulse-height analysis have long time constants relative to the time required for the charge collection and the time constants of the device. As a result, the pulse height of the signal emerging from the preamplifier is proportional to the integral of the pulse from the detector, which means that the signal entering the amplifier is proportional to the charge collected across the junction. The shaping amplifier increases the pulse height so that it lies within a range of values suitable for sorting by the pulse-height analyzer. See Knoll (18) for a detailed discussion of the operation of particle detectors and pulse-height analyzers.



(a)



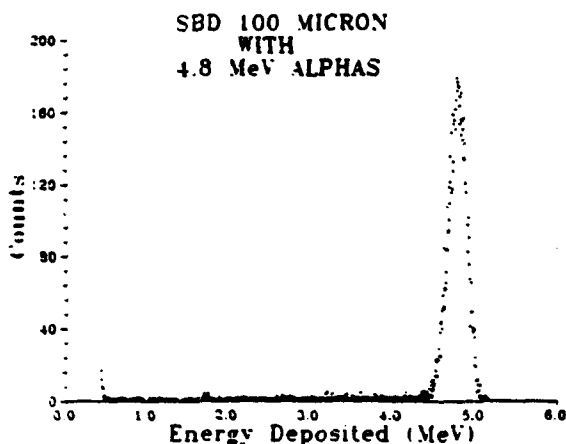
(b)

Fig. 16 a) Photograph of a surface-barrier detector. b) Schematic of a fully depleted version in cross section.



Fig. 17 Circuit used for pulse-height analysis.

Figure 18a shows a typical pulse-height spectrum obtained when the detector in Fig. 16 is irradiated with identical monoenergetic heavy ions. Charge collection is plotted on the abscissa in the units of energy deposition typically used in radiation physics. The equivalency between charge collected and energy deposited is based on the fact that, for most particles, the number of electron-hole pairs generated along the path of an ionizing particle is proportional to the energy deposited along the trajectory. The average energy deposited per ion pair generated is 3.6 eV for silicon and 4.8 eV for GaAs with the result that 1 pC of each charge sign is generated when 22.5 MeV of energy is deposited in silicon, and 1 pC in GaAs requires an average deposition of 30 MeV.



UNITS OF CHARGE COLLECTION

pC - 1E-12 Coulombs
MeV - 1E+6 Electron volts

CONVERSIONS

1pC = 22.5 MeV (Si)
1pC = 30 MeV (GaAs)

(a)

(b)

Fig. 18 a) PHA spectrum for a fully depleted detector exposed to 4.8 MeV alphas at room temperature. b) Units of charge collection.

2.1.1 Dimensions of the Sensitive Volume

The spectrum in Fig. 18a can be used to confirm the area of the sensitive volume of the detector. The sensitive volume is defined to be that region of the silicon within which the charges generated by the traversing particles are efficiently collected at the junction. For the surface-barrier detector, the sensitive volume is virtually the entire slab of silicon. Only the charge generated within the ultrathin dead layers formed under the electrodes by the highly doped regions of the ohmic contacts is not collected. The ratio of the number of events under the peak to the fluence of incident particles equals the area of the active or sensitive volume of the detector.

The charge collected across a junction traversed by a charged particle depends on the amount of charge generated along the particle's trajectory. These ionizations occur as a result of collisions between the

incident particle and the atomic electrons of the medium and other collisions between the secondary electrons and atomic electrons. As a result of the proportionality between the numbers of electron-hole pairs generated and the total energy lost in all collisions with the atomic electrons that exist for most particles, the linear energy transfer (LET) represents both the energy deposited in the medium per unit pathlength and the number of pairs generated per unit pathlength. There are, as a result, a number of equivalent representations or units for the LET. These are summarized in Fig. 19. A related concept which is often useful in characterizing the SEU sensitivity of a device is the "Effective LET" which is defined in Fig. 20. If the position of the peak of the pulse-height spectra obtained with the detector and experimental setup, shown in Figs. 16 and 17, is plotted versus the Effective LET of the incident particle, a linear curve that passes through the origin should be obtained in a well calibrated system, as illustrated in Fig. 21. A linear system means that the charge collected is proportional to the Effective LET. The slope of the curve is the product of the density of silicon (2.32 g/cm^3) and the thickness of the sensitive volume of the detector. Therefore, for fully depleted detectors at least, there are ways of experimentally determining the dimensions of the active or sensitive volume of the silicon.

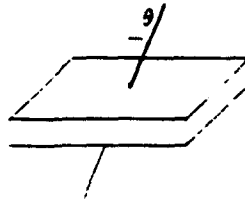
EQUIVALENT REPRESENTATIONS OF LET

REPRESENTATION	UNITS
Stopping power $\frac{dE}{dx}$	$\text{MeV cm}^2/\text{mg}$
Energy deposited per unit length	$\text{MeV}/\mu\text{m}$
Charge generated per unit length	$\text{pC}/\mu\text{m}$
Electron-hole pairs per unit length	$(\mu\text{m})^{-1}$

Fig. 19 Equivalent representations of LET.

EFFECTIVE LET

$$\text{LET}_{\text{EFF}} = \text{LET} \sec \theta$$



Equivalent to the LET times the pathlength divided by the thickness.

Fig. 20 Definition of effective LET for a thin detector.

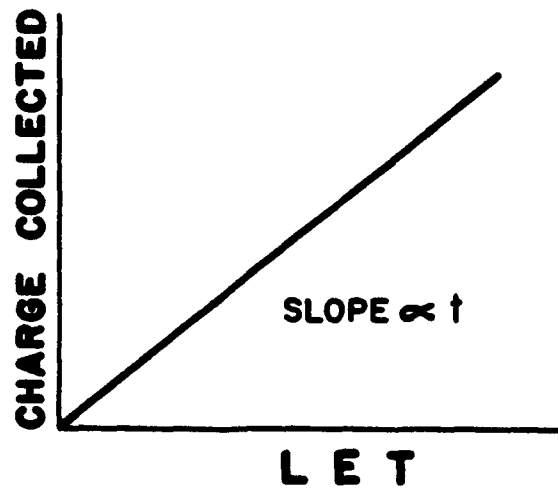
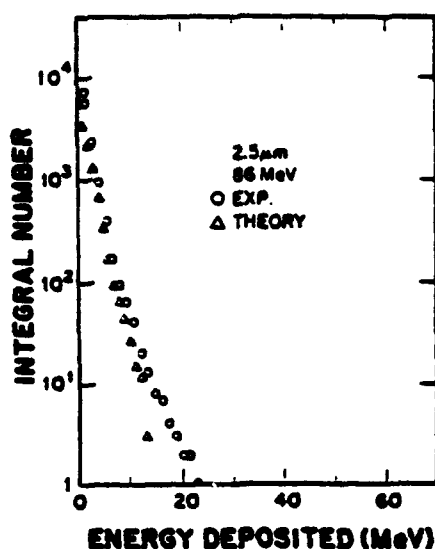
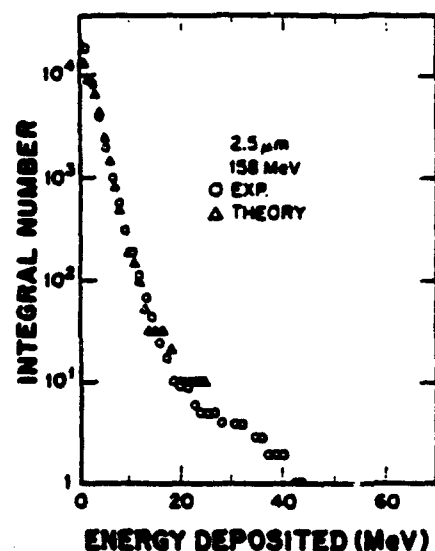


Fig 21. Charge collection versus LET for thin fully-depleted silicon surface barrier detectors exposed to energetic heavy ions.

Surface barrier detectors with thicknesses greater than the range of the monoenergetic heavy ions being used in studies of charge collection can be used to calibrate measuring systems since the energy deposited in the sensitive volume is well defined in that case. One advantage of working with thin fully depleted detectors is that models of energy deposition by different radiations can be tested in well defined sensitive volumes. Examples are shown in Fig. 22 where the measured integral energy-deposition spectra are compared with the results of the CUPID simulation codes (5,21). The spectra are plots of the number of events in which at least some energy E is deposited versus E . This format for displaying is useful for data analysis because, according to the sensitive-volume approach, a circuit element upsets when more than a critical charge is deposited in the sensitive volume. Dividing the ordinate by the fluence gives the cross section for depositing at least that energy. The ordinate then becomes the cross section for upsetting a device with a critical charge given by the abscissa. Data taken in this manner has been found to be useful for testing other Monte-Carlo models (22) and semiempirical models (23). The smaller the sensitive volume, the larger the relative contribution the recoiling nuclear fragments makes to the energy deposited in the sensitive volume.



(a)



(b)

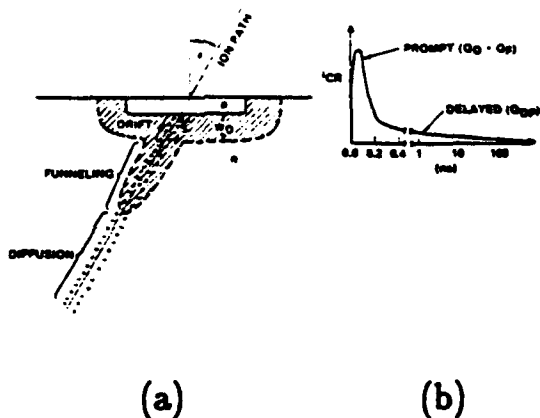
Fig. 22 Integral number of events, in which at least energy E has been deposited in a detector versus E . The active sensitive volume of the detector is a cylinder with a cross sectional area of 25 mm^2 and a thickness of $2.5 \text{ } \mu\text{m}$. The experimental data was obtained with an Ortec surface-barrier detector and the theoretical simulations were carried out using CUPID.

2.2 Microelectronic Junctions

The charge collection at an SEU-sensitive junction in a microelectronic circuit is more complicated than it was for the fully depleted detectors discussed above because the circuit junctions are only partially depleted and are much smaller in area than those on the detectors. The phenomena involved in charge collection across a small partially depleted junction are outlined in Fig. 23. The passing particle generates numerous electrons and holes along its trajectory creating a cylindrical sheath of charge about the trajectory which acts as an

electrical short through the depletion region with the inner regions of the cylinder being shielded from the electric fields by reorientation of the outer charge. The entire column of charge expands radially by ambipolar diffusion until the charge density level reaches the doping density of the medium. At that point, the electric fields penetrate the sheath and accelerate the charges towards their respective electrical contacts. This latter is the so-called funneling action (25-30). Eventually the funnel collapses and subsequent charge is collected by the slow random motion typical of diffusion. As a result, the pulse across such a junction has a time sequence which is quite different from the case of the fully depleted detector discussed earlier. Figure 23b illustrates the drift and diffusion components of the charge-collection current as a function of time. Diffusion contributes a slowly arriving component to the total charge collected at the junction which would not be present in the fully depleted detector.

DEPENDENCE ON LET



- Depletion region
 $\propto LET$
- Funnel
 $\propto (LET)^y \quad 1 \leq y \leq \frac{4}{3}$
- Fast diffusion
 $\propto LET ?$

Fig. 23 a) Schematic of a particle traversing a junction showing portions of the trajectory where charge is collected by drift and diffusion. b) Charge collection across junctions versus time. Portions of the pulse due to drift and diffusion are illustrated. c) Dependence of the charge collection components on LET.

2.2.1 Charge Collection

Measurements of the time sequence of charge collection on junctions with microscopic dimensions are difficult but progress is being made (31-43). The sensitivity of the circuit to the temporal pattern of the currents making up the charge collection pulse is also being studied with SPICE simulations (44-51) in attempts at providing reliable predictions of SEU rates. The information required for accurate SPICE predictions of SEU sensitivity are outlined in Fig. 24. The current situation is that extensive SEU testing is required to develop the correct equivalent circuits for the SPICE models, but once the circuit elements are established for a device, SPICE simulations appear to handle changes in the time constants reasonably well (52).

SPICE PREDICTIONS OF SEU SENSITIVITY

REQUIRED INFORMATION:

- Temporal sequence of charge collection
- Accurate equivalent circuit for device
- Time constant for circuit

Fig 24 Requirements for SPICE predictions of SEU sensitivity.

A simplifying assumption, which is presently being made for most SEU-rate predictions, is that upsetting a given circuit requires collecting at least some threshold amount of charge within a period of time determined by the time constants of the circuit. This is the so-called critical charge. With the circuits typical of today's technology, the critical charge includes all of the depletion-region and funnel portions of the drift component and some part of the diffusion component. Estimating what fraction of the diffusion component of the charge collected contributes to upsetting the device requires comparison of

oscilloscope traces of the charge-collection pulses with the circuit's relevant time constants. Circuits like DRAMS in the static mode include all the diffusion as well as the drift components, while circuits with switching speeds of a few nanoseconds or less would include little or no diffusion. It is difficult to specify the appropriate time constants for determining the fraction of the charge collected which contributes to upsetting a given device. It must be less than the recovery time or the switching time but how much less is not easily known by the purchaser of the device. Since resistor loaded NMOS circuits have slow recovery times they are sensitive to most of the diffusion components. CMOS circuits used in space typically have switching speeds between 20 nsec and 500 nsec, and as a result, they are sensitive to the early portion of the diffusion component, as well as the drift components. Abdel-Kader et al. (53) discusses the relative contributions of the drift and diffusion components of the charge collected for a small junction in bulk silicon.

There are other complications in the charge collection at partially depleted junctions beyond the extension of the temporal pattern induced by the diffusion component. Measurements of the prompt component of the charge collected with large area junctions (25-27,30) suggest that the drift and diffusion components may have a nonlinear dependence on LET. See Fig. 23c. The drift component from charge generated inside the depletion region should exhibit proportionality between charge collection and the LET until the LET values are so high that recombination becomes important or the charge collected approaches the fixed charge making up the junction and the depletion region collapses. The drift component from outside the depletion region is taken as linear by Hu (25). It is taken as nonlinear by Oldham and McClean (26,27,30) but their later paper does not rule out linearity. This is an important point. Fully depleted detectors showed a linear relation and the detector could be modeled as a sensitive volume of silicon where the charge generated within the sensitive volume equals the charge collected across the junction. A nonlinear dependence on LET would mean that the dimensions of the sensitive volume depend on the LET of the incident particle.

The charge collection by junctions which have microscopic dimensions is further complicated by the phenomena illustrated in Fig. 25. It shows particles hitting the depletion region of a junction, hitting the edge, and missing the junction entirely. Particles traversing the central region of the junction provide a number of events with about the same value of charge collected. These events form the peak in the pulse-height distribution in Fig. 26 which shows the pulse-height spectrum measured with a test-structure of a CMOS drain-substrate junction. The peak in the spectrum is clearly observable at the high-energy end of the spectrum. Particles traversing unprotected edges of the junction experience enhanced charge collection (35). As junctions decrease in size, the events at the edge become a larger fraction of the data. Defects in the junction are another possible cause of enhanced charge collection. Events in which the particle misses the junction, so that either no drift component or a reduced drift component occurs, may still have a significant amount of charge collected at the junction through diffusion. These events lie on the low-energy side of the peak in Fig. 26. A small number of enhanced charge collection events on the high-energy side of the peak are also visible.

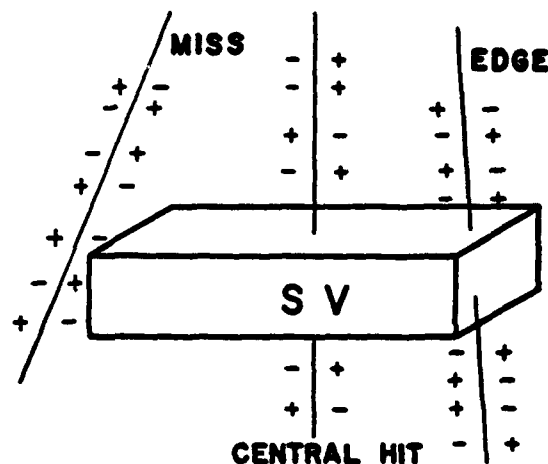


Fig. 25 Sensitive volume illustrating direct hit, miss, and edge-hit events.

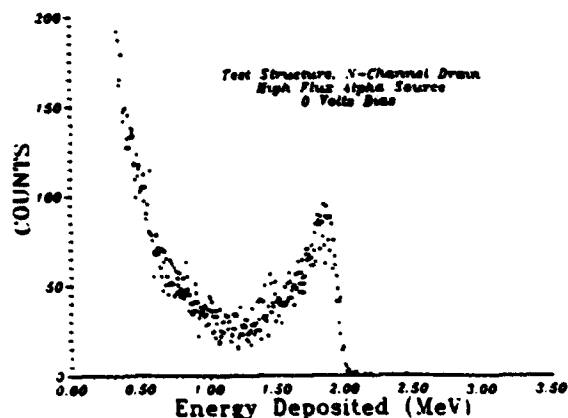


Fig. 26 Measured pulse-height spectrum for a drain-substrate test-structure junction of a CMOS circuit exposed to 4.8 MeV alphas. The peak corresponds to direct hits on the junction, while the events to the left of the peak correspond to alphas missing the junction, and the events to the right of the peak correspond to enhanced charge collection events, possibly the result of edge effects or defects.

2.2.2 Threshold Dependence on LET

Let it be assumed that a device having SEU-sensitive junctions which are identical to the above test structure will upset if more than some critical charge is collected but not otherwise. Let it be further assumed that the value of the critical charge corresponds to the position on the pulse-height spectra marked Q_c in Fig. 27. Let particles be incident with LET values of x , $2x$ and $3x$. The lower figure illustrates how the cross section for pulses exceeding Q_c varies with the incident particle's LET. Since for an LET value of x none of the pulse delivers more charge than Q_c , the number of events in which threshold is exceeded for that LET must be zero. If the particle's LET is doubled to $2x$, the pulse-height spectrum shifts to higher energies in the middle figure on top so that the peak position coincides with the

critical charge. This means there will be a sharp rise in the number of times that threshold is exceeded between $LET = x$ and $LET = 2x$, as illustrated in the lower figure, and that the steep rise continues until LET values are reached where the entire peak lies to the right of Q_c , as it does for $LET = 3x$.

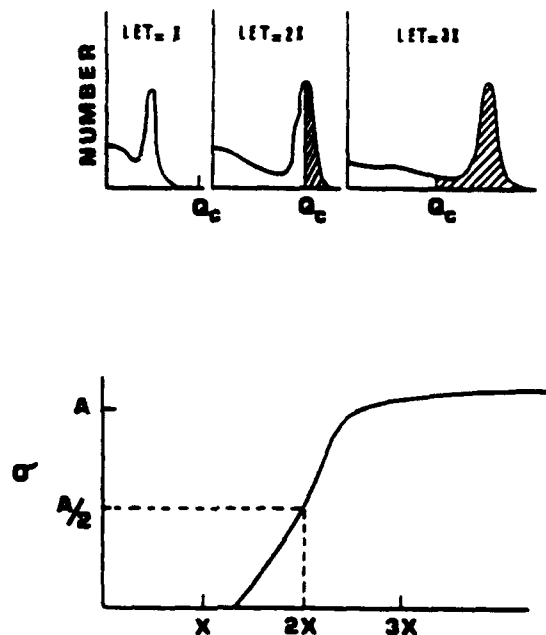


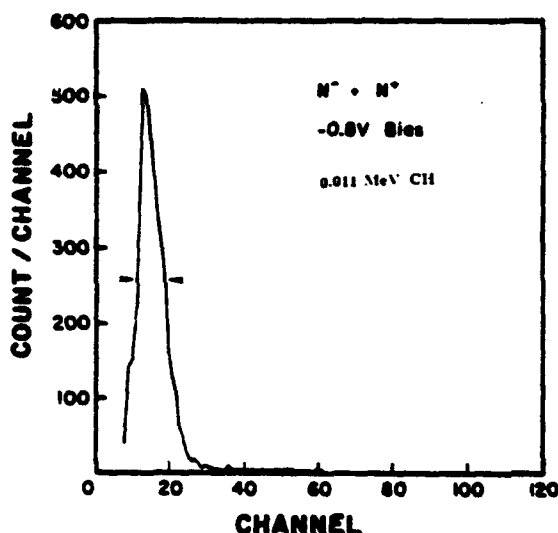
Fig. 27 Schematic representation of pulse-height spectra obtained by exposure of the same device to particles at an $LET = x$, $LET = 2x$, and $LET = 3x$. Q_c represents the critical charge for that device. The bottom plot is of the cross section for depositing at least Q_c versus LET for the same device. The shape of the cross section curve is determined by the shape of the peak in the charge-collection spectra shown above.

The shape of the threshold response curve in the lower figure of Fig. 27 is determined by the shape of the peaks in the pulse-height spectra for the device. The cross section would be zero for LET values up to and including x . It remains zero until the LET values of the few

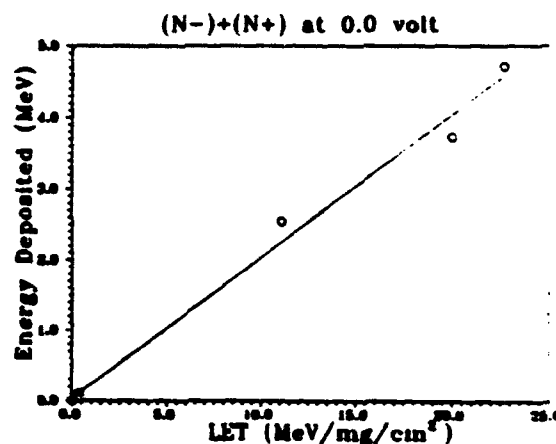
enhanced charge-collection events which exceed the critical charge are reached. The cross section is much smaller than the geometric cross section at this point. As the LET increases so that a fraction of the events making up the peak exceed the critical charge, the cross section increases rapidly. The ratio of the number of events under the peak in Fig. 27 to the fluence should be the area of the junction as it was earlier for the particle detector. Therefore, the cross section after the sharp rise in LET should be just above the geometric cross section of the junction A, as shown in the lower figure. Beyond $LET = 3x$, the cross section continues to increase but the rise is now more gradual. This gradual increase is due to the events in which the particle misses the junction but the charge collected exceeds the critical charge anyway.

2.2.3 Charge Collection Dependence on LET

The charge collection spectra obtained with a GaAs junction on a test structure is shown in Fig. 28a. The position of the peak is plotted versus the LET of the incident particle in Fig. 28b. All of the data was obtained with the particles incident normal to the surface (54). The relationship is one of proportionality just as it was for the fully depleted detector in Fig. 21. A further test of the applicability of the concept of Effective LET is provided in Fig. 29 where the peak position in the charge-collection spectra for GaAs heterojunction test structures exposed to heavy ions is plotted against the Effective LET, i.e., the product of the LET and the secant of the angle of incidence. Data at different values of the Effective LET were obtained by changing the angle of incidence for two ion species. The fit of the data in Fig. 29 to a straight line is consistent with the assumption that the charge collected is proportional to the product of the LET and the pathlength through a parallelepiped to the junction. This is consistent with the data of Shanfield et al. (40).



(a)



(b)

Fig. 28 a) Pulse-height spectrum obtained with a GaAs junction on a test structure exposed to energetic heavy ions. b) Plot of peak position versus LET. All the data points were obtained at normal incidence.

2.2.4 Sensitive Volume

The linear relationship between charge collected and LET exhibited in Figures 28 and 29 is a necessary condition for the concept of the sensitive volume with constant dimensions being applicable to SEU modeling. Without a linear relationship between the charge collected and the LET, the sensitive volume would have to be assigned dimensions which depend on the incident particle's LET which would seriously limit its usefulness as a calculational tool. The use of a sensitive volume is common to the standard procedures for calculating SEU rates in space. The sensitive-volume approach is outlined in Fig. 30. It is important to remember that, useful as the sensitive volume is

in modeling and predicting SEUs, for most devices there is no structure on the device that corresponds to the sensitive volume. It is a mathematical artifice. Its dimensions are chosen such that the charge generated within the sensitive volume by energy-loss processes equals the charge collected across the junction. The fact that the charge collection data for some junctions is proportional to the Effective LET over a wide range of angles does not mean that it must be valid for all devices. In particular, it has not been demonstrated for some modern devices which have submicron feature sizes. It may turn out that the appropriate sensitive volume is not a parallelepiped for these structures (55) or that the sensitive-volume approach itself is not valid for all technologies.

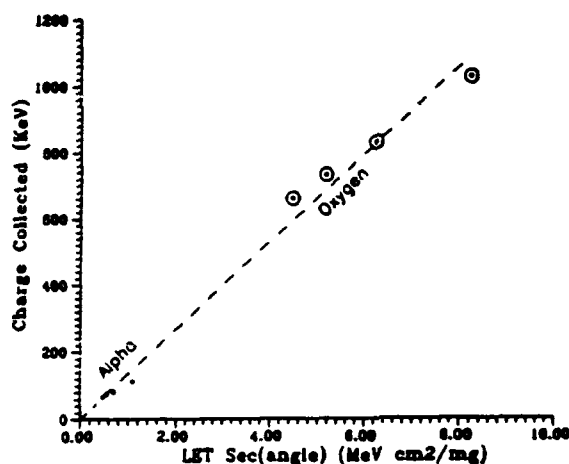


Fig. 29 Charge collection versus LETsec θ for GaAs heterojunction on a test-structure. The effective LET was varied by changing the angle of incidence for the two ion species.

SENSITIVE VOLUME

- MATHEMATICAL ARTIFICE - Charge Generated Within SV Equals Charge Collected Across Junction
- Lateral Dimensions Same as Junction
- Thickness has Three Components
 - 1 Depletion Width
 - 2 Depth of Funneling
 - 3 Thickness Equivalent to Diffusion
- Diffusion Component Estimated from RANDOM WALK

Fig. 30 Sensitive volume associated with SEU sensitive junctions.

2.2.5 Track Structure Effects

The LET of a particle depends on the charge and speed of the incident particle as well as the density and atomic number of the medium through which it passes. Particles with different charge and speeds can have the same LET. Often particles with different energies and charge but the same LET result in the same SEU response from a circuit. However, differences in SEU response are sometimes observed for particles with the same LET but very different energies. This is apparently due to differences in the pattern of ionizations generated in the original track around the trajectory which can result in substantial differences in the charge collected at the junction (56-58), especially when one track is generated by a stopping particle and the other by an energetic ion with considerable residual range. This is illustrated in the charge collection measurements carried out with particles of similar LET but different kinetic energies. The results are described in Table 1 which is taken from Ref. (56). For the Sandia device, there is little difference in the charge collection between the different energies at the same LET. However, significant differences are observed for the CMOS/SOS structures. These differences are attributable to differences in track structure in the two cases, i.e., differences in the radial pattern of the initial charge generation about the particle tra-

jectories. Calculations, also from Ref. (56), of the radial distributions of the initial charge distribution about the trajectory of ^{58}Ni in silicon at two different energies for which the particle has about the same value of LET are illustrated in Fig. 31.

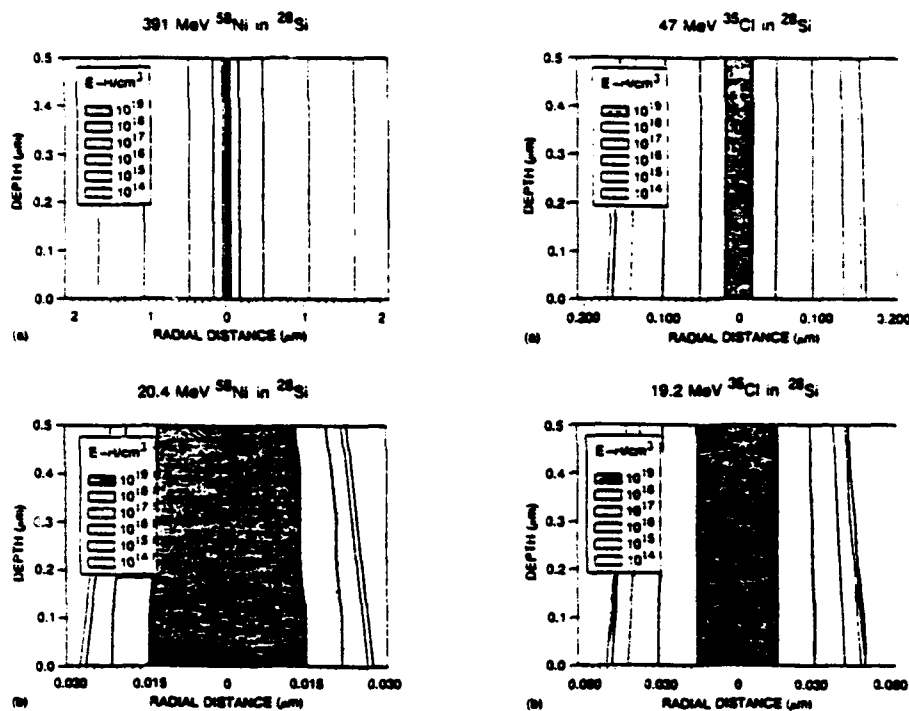


Fig.31 Results of calculation of the density profile of charge generated about the track of an energetic Ni ion traversing Si at four different energies. The curves show the electron-hole pair distribution in bins from 1E19 to 1E14 pairs/cm³ (56).

Table 1. Calculated and measured energy deposition in MeV in the sensitive volume of the CMOS/SOS and Sandia structures. Also given is the ratio of the energy deposition at the higher beam energy (HE) to that of the lower beam energy (LE). For each of the three cases the first line is the calculated energy deposition and the second line is the measured deposition. Ref. (56)

	Nickel Beams		Ratio HE/LE	Chlorine Beams		Ratio HE/LE
	405 MeV	34.8 MeV		57.2 MeV	29.6 MeV	
CMOS/SOS Gate	2.53	2.35	1.077	1.93	1.8	1.072
	1.05	0.67	1.57	0.65	0.47	1.38
CMOS/SOS Drain	2.53	2.4	1.054	1.92	1.84	1.043
	1.73	1.2	1.44	1.18		1.34
Sandia	4.92	4.51	1.093	3.75	3.46	1.085
	5.16	4.02	1.28	3.49	2.99	1.17

3. MEMORY CELLS

The elements that make up logic circuits are composed of p-n junctions of the type described above. Given the proper process information, the charge collecting characteristics of the SEU-sensitive junctions making up the device may be estimated theoretically (53). However, such information is often not available and, if available, does not take lot-to-lot variations into account. Sometimes approximate information can be obtained directly from the devices themselves. This is illustrated below for a resistor-load NMOS memory, an important technology for space applications. They are also important because SEU-sensitive structures, the drain-substrate junctions, are similar in construction to the SEU-sensitive drain-substrate junctions in CMOS. CMOS is an essential component of most spacecraft systems because of its low power requirements. Therefore the techniques applied here to NMOS should also be applicable to CMOS, albeit in a less straightforward manner (59). The memory element for an NMOS SRAM used in space is typically the resistor-load, four-transistor cell of the type shown in Fig. 32a.

3.1 Charge Collection Measurements

Figure 32b shows one of the NMOS FETs in cross section. The SEU-sensitive junctions in each memory cell of the NMOS SRAM is the drain-substrate junction which is reverse biased because the corresponding FET is turned off. In normal operation, only one reverse-biased drain-substrate junction in each memory latch of the two is SEU sensitive. The SEU sensitivity alternates between the two inverters as the memory states switch. If the device is not under bias, all the junctions become reverse-biased to the extent of the built-in biases across the junctions. Moreover, particle strikes across the junctions connected between VDD and VSS result in transient voltage swings between those lines, even in the absence of external bias. Therefore, if the VDD and VSS pins of an NMOS SRAM are connected to the same electronics as used for detectors, as illustrated in Fig. 33, the SRAM should behave like a parallel array of partially depleted particle detectors with the detector junctions being the potentially SEU-sensitive drain-substrate junctions (60).

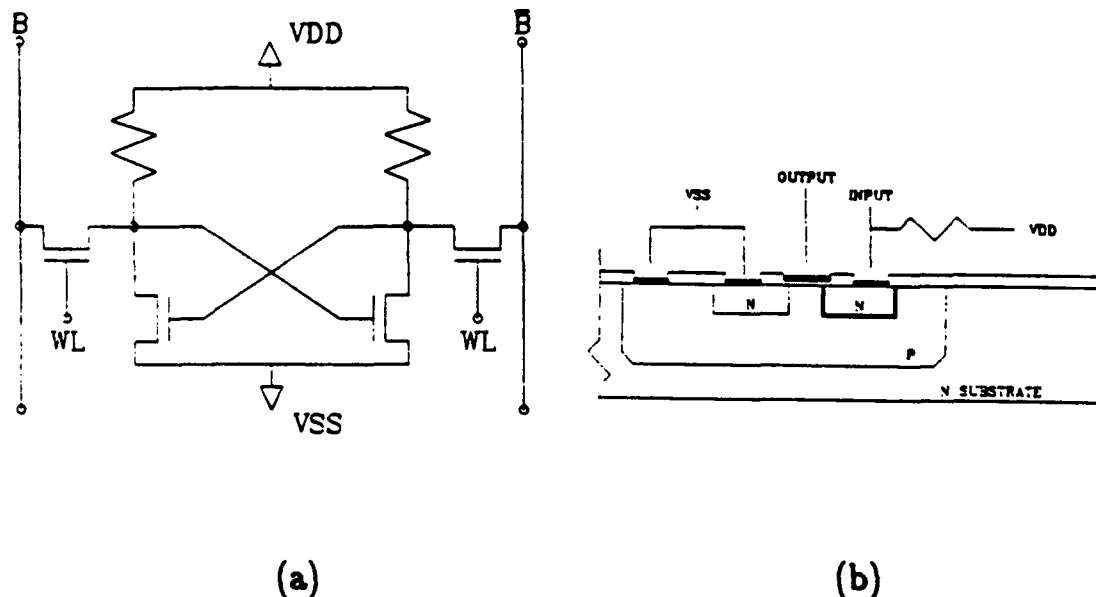


Fig. 32 a) Schematic of a resistor load NMOS memory cell. b) Cross section of one of the inverters.

Schematic for experimental configuration used for irradiations.

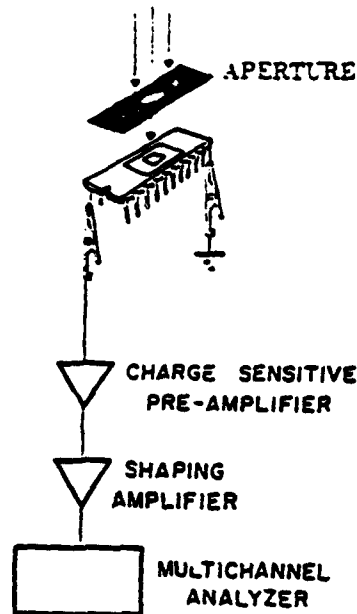


Fig. 33 Experimental configuration used for charge-collection measurements on the power lines of the memory cells.

3.1.1 Dimensions of the Sensitive Volume

The pulse-height spectrum obtained when the memory cells of an NMOS SRAM are exposed to 4.8 MeV alphas is shown in Fig. 34. The spectrum consists of events at 32,768 similar junctions, each having dimensions of a few microns on a side. The cross sectional area of the individual junctions can be estimated from the ratio of the number of events under the peak to the fluence divided by the number of junctions.

$$\text{Area} = \text{Events} / (\text{Fluence} \times \text{Number of Junctions})$$

The results are consistent with each junction having about $137 \mu\text{m}^2$ in area which agrees with the value of $160 \mu\text{m}^2$ obtained from the plateau value of the SEU cross section by Kolasinski et al. (61) within the limits imposed by the uncertainty in the fluence.

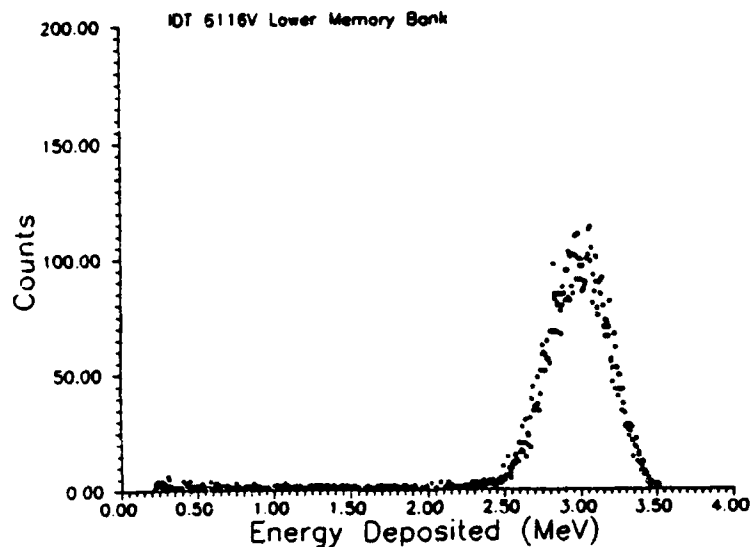


Fig. 34 Pulse-height spectrum obtained when a portion of the memory cells of an NMOS SRAM (IDT6116V) is exposed to 4.8 MeV alphas.

The thickness of the sensitive volume can be estimated from range-energy tables. If $R(E_i)$ is the range of the particle entering the sensitive volume with energy E_i and $R(E_i - E_d)$ is the residual range of the particle after it deposited energy E_d in traversing the sensitive volume, the pathlength l through the sensitive volume can be estimated from:

$$l = R(E_i) - R(E_i - E_d)$$

At normal incidence, this pathlength should equal the thickness of the sensitive volume. The thickness obtained for this device is $13.5 \mu\text{m}$.

An independent check on whether this provides a useful estimate of the dimensions of the sensitive volume can be carried out by comparing the pulse-height spectrum measured by exposing the device to 148 MeV protons to simulations of the energy-deposition spectrum obtained from CUPID. The comparison is shown in Fig. 35. The agreement is quite reasonable considering the error in the area introduced by the uncertainty in the fluence of the alpha source.

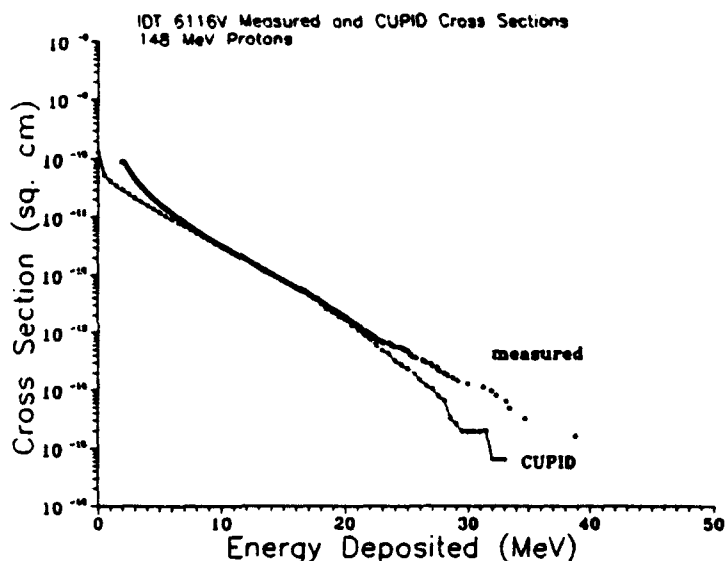


Fig. 35 Integral cross section for depositing at least some energy E in a sensitive volume versus E . The theoretical simulations were CUPID simulations assuming a parallelepiped sensitive volume with $11.7 \mu\text{m} \times 11.7 \mu\text{m} \times 13.5 \mu\text{m}$ dimensions. The experimental measurements were obtained from measurements on the IDT6116V divided by the number of relevant junctions.

The dimensions of the sensitive volume associated with the SEU-sensitive junctions on other devices can be determined in this way also (54,59,62,63). However, the spectra are more complicated and the results obtained, at least for CMOS (59), are still a subject of some controversy.

The position of the peaks in the charge-collection spectra change with the angle of incidence in a manner which is consistent with the expected changes in the particle's pathlength through the sensitive volume (40,62,63). That pathlength should be proportional to the product of the thickness of the sensitive volume t and the secant of the angle of incidence, at least for small angles.

$$l = t \sec \theta$$

This assumption that the pathlength and, therefore, charge collection increased with the secant of the angle of incidence, is fundamental to all models which incorporate the use of a sensitive volume as outlined above. Furthermore, it forms an essential part of the standard procedure for measuring threshold which is described in a later section.

For the IDT6116V the value of the thickness obtained from charge collection and range-energy tables (64) is $13.5 \mu\text{m}$ which exceeds the thickness of the p-well. The SEU sensitive drain is collecting charge from the substrate as well as the p-well. In standard CMOS, the well competes with the charge collected at the drain. Twin-well CMOS has one FET for which the well does not inhibit charge collection and may facilitate it.

4. EXPERIMENTAL SIMULATIONS OF SEUs

4.1 Method

The SEU phenomena can best be studied quantitatively in random access memories (RAMs), although it can be argued that their occurrence is potentially more damaging when they occur in a CPU or other logic circuits. Experimental simulation of SEUs requires connecting the memories to circuits in a manner similar to their actual application in space, including at least occasional read-write commands. A typical experimental configuration used for SEU testing is shown in Fig. 36. The computer not only exercises the device under test (DUT) but records the data, plots the location of the event on the die, and determines whether it was a single-upset or multiple-upset event. The DUTs are exposed to energetic particles at nuclear particle accelerator facilities. Exposures to high-energy ions including energetic protons are carried out under air at cyclotrons or larger alternating gradient accelerators. Exposures to the lower-energy heavy ions typically used for SEU tests are carried out under vacuum. The vacuum chamber at the Tandem Van de Graaff facility at Brookhaven National Laboratory provides plenty of space for sequential, simultaneous, and complete system irradiations. Despite its size, the time for pumping down to the required vacuum levels is relatively short. The facility is user friendly after brief training.

There is an extensive literature on experimental measurements of SEUs with most of it published in the IEEE Transactions on Nuclear Science and presented at this conference. The student is referred to the last 10 years of that journal for a complete list of references. An extensive but not complete list has been compiled by S. E. Kerns (65). In particular, there is an annual article on the latest trends in single-event phenomena results. See Ref. 65 for the most recent version.

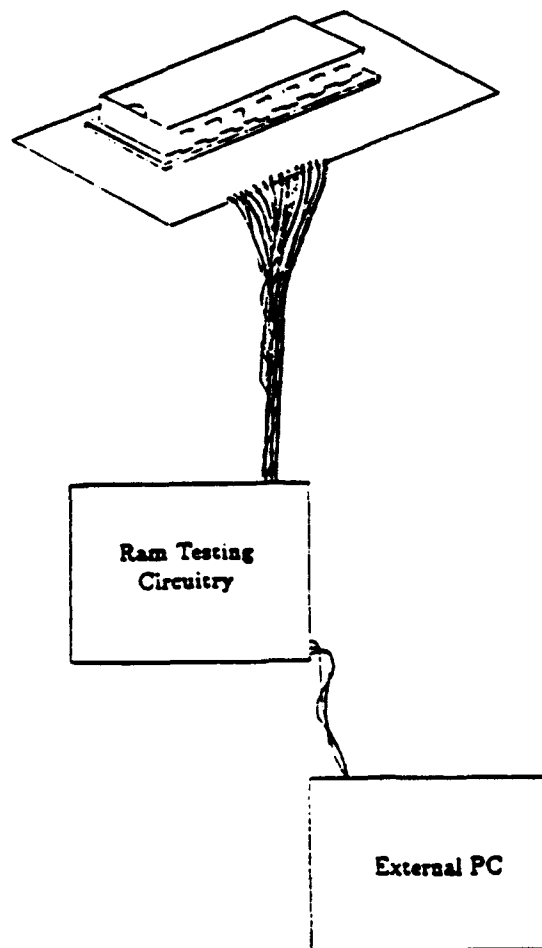


Fig. 36 Experimental configuration for exposure of memories and logic devices to energetic charge particles at accelerator facilities. The DUT remains a functioning part of a test circuit or computer during irradiation.

4.2 Analysis

As the exposure is being carried out, the appearance of an SEU is reported to the investigator by the computer and its location is plotted on the topographical bit map as illustrated in Fig. 37. To

separate multiple upsets induced in a single event from multiple independent events, the data is examined for multiple upsets found within two memory-search cycles. This subset of events is then searched by the computer for neighboring events on the topographical map. For some technologies, adjacent locations on the topographical map may not be nearest neighbors on the die. For example, in DRAMs all the multiple upset events examined on a mask-level map were found to have memory cells which were nearest neighbors of the type shown schematically in Fig. 38 despite the fact that they often had small spaces between them on the topographical map of Fig. 37. Multiple upset events have been observed with ions incident normal to the surface of the device as well as at larger angles (67). Therefore, the ion does not have to traverse more than one junction to upset more than one cell. A more recent analysis of multiple upset events in DRAMs has been carried out by Zoutendyk et al (68,69) and multiple upset events have been studied in CMOS and NMOS (61,62).

A possible explanation for multiple upset events is provided by Figs. 26 and 27 which shows the charge collection by a test structure junction. If threshold lies at energies below the peak, the ions that miss the junction can still result in charge collecting events which exceed the upset threshold.

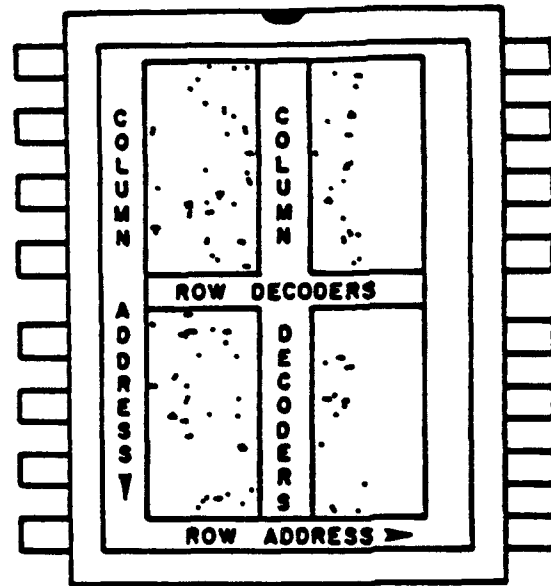


Fig. 37 Topographical map of error obtained on a commercial DRAM exposed to heavy ions under conditions where the die was partially shadowed by the edge of the package well.

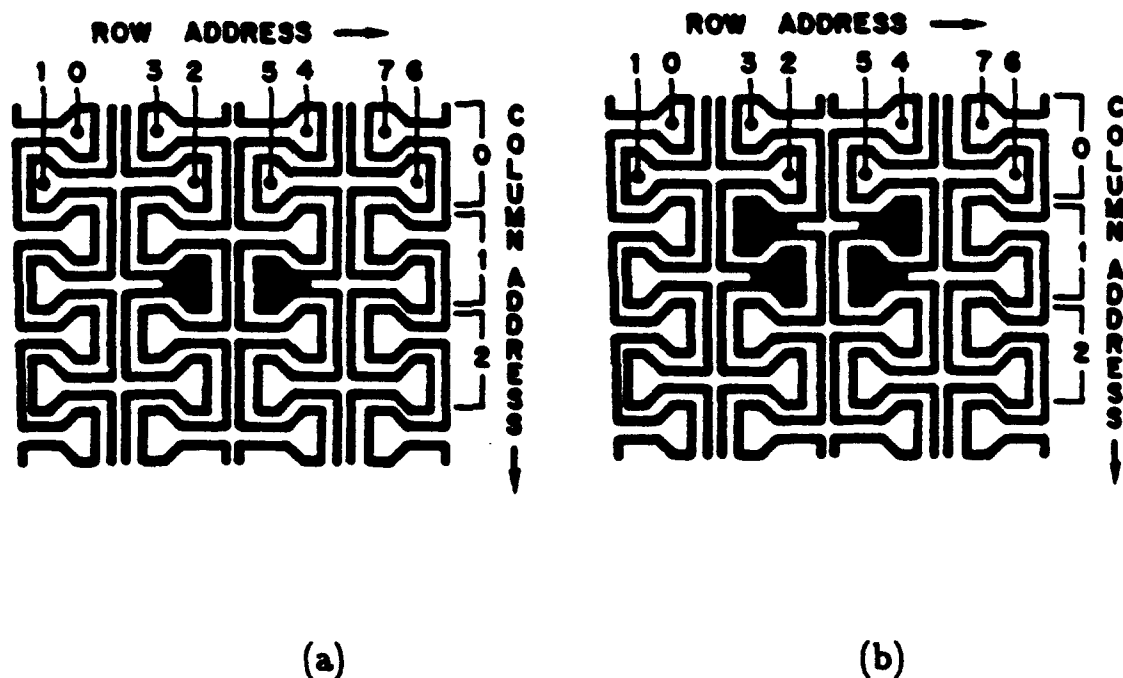


Fig. 38 a) Double upset event exhibited on a mask-level map. b) Quadruple error.

Two versions of the SEU cross section are being used to characterize devices, often without the authors clearly specifying which one is intended. These alternative definitions are listed in Fig. 39. Only the event cross section should be expected to match the dimensions of the sensitive volume, and it should match in the low-LET portion of the plateau before "miss" events become significant.

SEU CROSS SECTIONS

ERROR

$$\sigma_{ER} = \frac{\text{NUMBER OF ERRORS}}{\text{FLUENCE}}$$

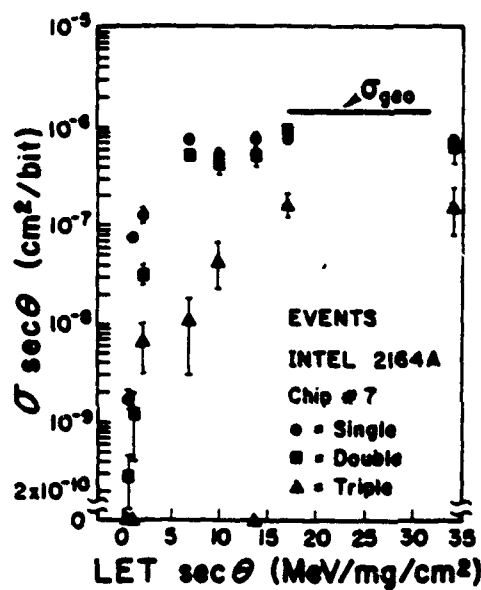
EVENT

$$\sigma_{EV} = \frac{\text{NUMBER OF EVENTS}}{\text{FLUENCE}}$$

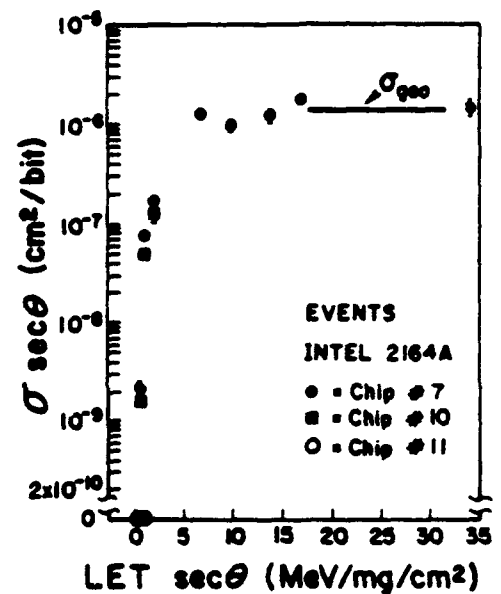
Fig. 39 Definitions of SEU cross sections.

To reduce the number of changes in accelerator beams and their energies which are costly in both time and money, the approach typically used in experimental SEU simulations is to make numerous changes in the particle's angle of incidence, thereby changing the particle's pathlength through the sensitive volume. The results are then plotted as the product of the measured cross section per bit and the secant of the angle of incidence versus the Effective LET, defined above as the product of the LET and the secant of the angle of incidence. One such plot is shown in Fig. 40a where the cross section for single-upset, double-upset, and higher-order events are plotted versus Effective LET for a 64K DRAM (67). The geometric correction for the cross section attempts to correct for the reduction in the cross sectional area of a junction projected on a plane perpendicular to the incoming beam. This is a fairly standard practice, but may not be proper for the next generation of devices. Some thought should be given before using this geometrical correction on devices like modern bulk CMOS where the lateral dimensions have shrunk until they are comparable to the thickness. At LET values near threshold, the particle would have to traverse the junction to upset the device, and since the depletion region is thin, the SEU cross section would still be

close to the projection of the junction area on a plane perpendicular to the beam direction. At high LET values the particle may miss the junction and still cause an upset. In that case increasing the angle of incidence should only have a small and complicated effect on a projection of the junction area which the sensitive volume presents to the beam.



(a)



(b)

Fig. 40 a) Cross section for events in which one or more memory cells upset corrected for angle of incidence versus Effective LET. b) Event cross section versus Effective LET for the same device type. Plateau cross section agrees with geometric cross section of the memory cell.

The use of Effective LET on the abscissa reflects the common assumption of an increase in the particle's pathlength through the sensitive volume as the angle of incidence increases. Changing the Effective LET by varying the angle of incidence is convenient when searching for threshold, and it is far less expensive than having to change particle

species or incident energy for every new value of LET. As mentioned in the previous section, the use of Effective LET assumes that the pathlength increases with the secant of the angle of incidence. This is only true if the sensitive volume is a parallelepiped and until the pathlength becomes comparable to the lateral dimensions of the sensitive volume. Therefore, the dimensions of the sensitive volume should be kept in mind when carrying out heavy-ion simulations and applying these geometric corrections.

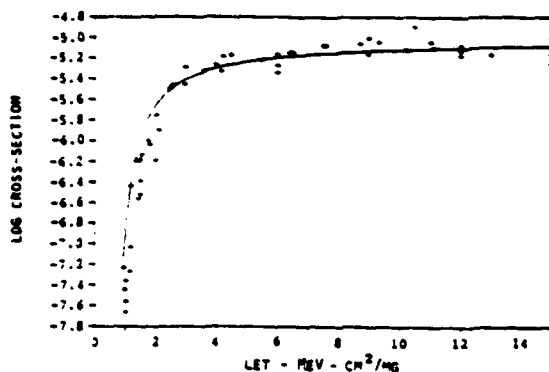
4.3 Typical Results for Heavy Ions

The SEU event cross section should rise with LET until it reaches a plateau value. This plateau should correspond to the cross sectional area of the SEU-sensitive junction. Figure 40b plots the event cross section versus the Effective LET for the same device type. The cross sectional area of the junction is represented as a horizontal line for comparison. Obviously, the agreement for the Intel 2164A is quite good.

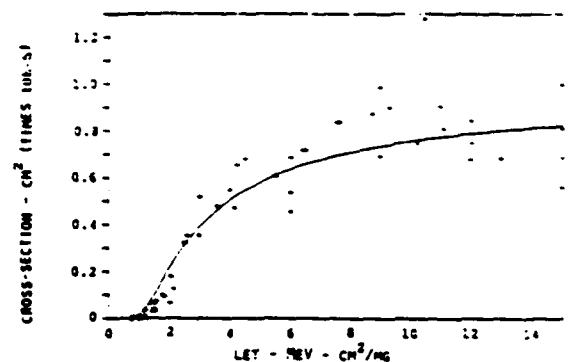
In Fig. 41 the measured SEU cross section is plotted versus the Effective LET for the Fairchild 93L422, a bipolar RAM in common spacecraft use (70). The SEU problem in the Hubble Space Telescope resides in the 93L422. This device is of particular interest because it is one of the few devices where the critical charge determined from circuit simulations agrees with measurements (70). The measurements are also typical of data characterizing a wide range of devices. The classic "S"-shaped threshold is apparent in the linear plot. The semilog plot is the more common form of presenting SEU-threshold data. There is a steep rise in the cross section as the LET reaches threshold.

The shape of the threshold curves in both Fig. 40b and Fig. 41 are in qualitative agreement with what is to be expected based on the earlier discussion of the charge collection at a single SEU-sensitive junction (See the discussion for Figs. 25 through 27). The upsets begin with a few events at LET values just below threshold, presumably due to the type of rare enhanced-charge-collection events seen

with test structures. These are followed at slightly higher LET by a sharp rise in the SEU cross section followed by a slower rise at higher LET. It would appear, qualitatively at least, that the shape of the initial fast rise reflects the broad, charge-collection peak observed with test structures and that the slow continuation is the result of "miss" events. The cross section at the transition from sharper rise to the gradual rise of the plateau is approximately equal to the geometric cross section of the SEU-sensitive junction. In cases where there is more than one sensitive junction, the eventual plateau would be higher and the shape of the curve reaching it more complicated. The plot of SEU cross section versus Effective LET for the IDT6116V NMOS SRAM is plotted in Fig. 42. The horizontal line represents the area of the junctions calculated from the number of events under the peak of the charge collection spectrum for the device (Fig. 33) as described earlier.



(a)



(b)

Fig. 41 Cross section versus Effective LET for the 93L422 on a) semi-log plot and b) linear plot. (Smith and Simpson, Ref. 70)

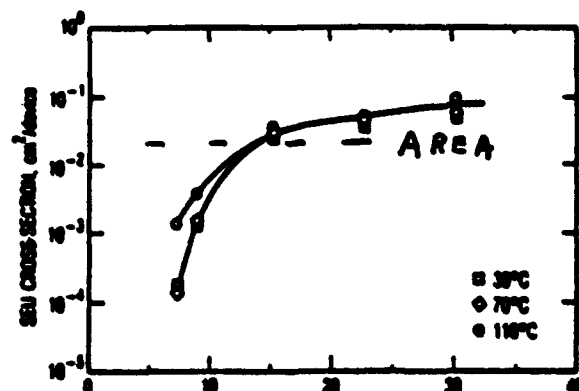
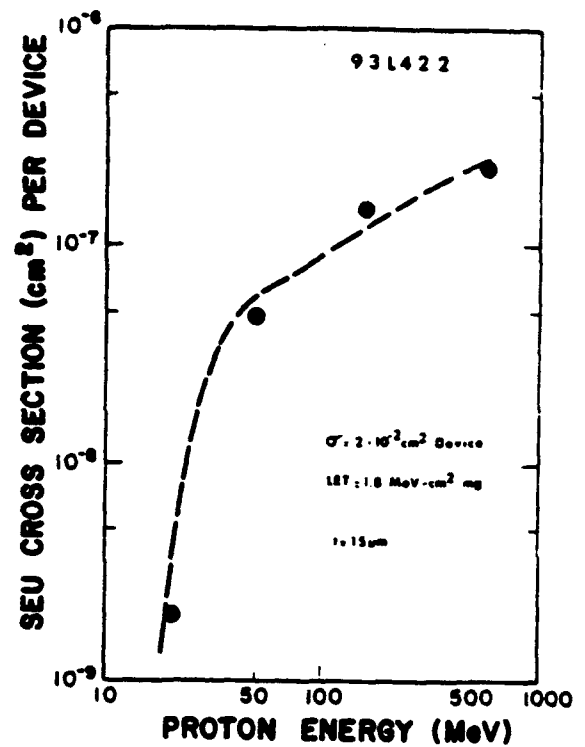
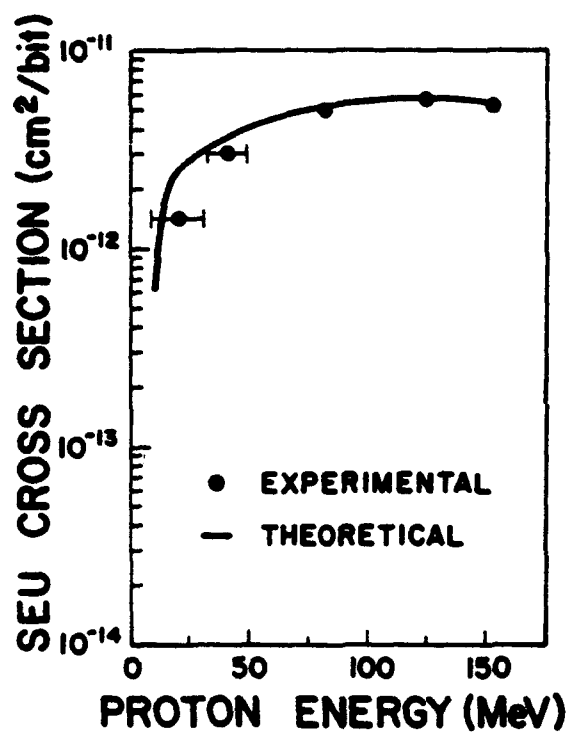


Fig. 42 Cross section versus Effective LET for the NMOS device, the IDT6116V exposed to heavy ions (61). The transition between sharply rising cross section and plateau on the experimental curve agrees with the geometric area of the SEU-sensitive junction, as measured by charge collection off the power line and marked by a horizontal line in the figure.

4.4 Proton Induced Upsets

Experimental simulations for proton-induced upsets are carried out in the same manner as for heavy ions, but because the localized concentration of charge necessary to upset a circuit element requires a nuclear spallation reaction, the cross section increases with the incident proton energy rather than decreasing as its LET and total nuclear cross section decrease. This increase in cross section with incident proton energy is illustrated in Fig. 43 with data obtained with the DRAM and the bipolar device. There is a sharp rise in the SEU cross section at low incident proton energies followed by a plateau at energies above 100 MeV, presumably reflecting the cross section for spallation reactions which are sufficiently energetic to result in recoiling nuclear fragments with sufficient recoil energy to deposit at least a threshold amount of energy in the sensitive volume.



(a) (b)
 Fig. 43 Cross section versus incident proton energy for a) the DRAM of Fig. 40 and b) the bipolar device of Fig. 41.

5. FIRST-ORDER MODEL

The simplest model (1,4,5,71,72) which incorporates the sensitive volume approach is summarized in Fig. 44. The dimensions of this equivalent sensitive volume should be chosen such that the charge generated along the portion of the particle's trajectory that lies within the sensitive volume equals the charge actually collected at the junction. The amount of charge generated by each particle traversing the sensitive volume is calculated, using the product of the LET, the density of the semiconductor, and the particle's pathlength within the sensitive volume, if the LET is constant. Range-energy tables should be used if the LET varies significantly along the portion of the trajectory which lies within the sensitive volume. If more than a critical (threshold) amount of charge is generated within the volume, the memory cell upsets; if less charge is generated, it does not upset.

FIRST ORDER MODEL OF SEU

1. SENSITIVE VOLUME

CHARGE GENERATED = CHARGE COLLECTED
DRIFT AND DIFFUSION INCREASES DIMENSIONS

2. THRESHOLD

CRITICAL CHARGE OR CURRENT
ALL OR NONE

Fig. 44 First-order models of SEUs.

The sensitive volume approach implies that all the sensitive junctions have the same dimensions and that all the memory cells have the same sensitivity. This assumption requires that VLSI devices have uniform sensitivity to upsets across the die. This is tested for a 256K DRAM in Fig. 45 which plots the number of upsets versus bias in the absence of radiation. At high voltages there are no upsets, and as the bias is reduced, there is a sudden transition from no upsets to all the cells upsetting. The vast majority of memory elements on the device changed state within a very narrow voltage range, suggesting that the concept of a single critical charge for all the elements on the die may in fact be viable for commercial devices. The gradual rise of the SEU cross section may be due to the fact that traversals of the junction by identical particles do not result in the identical amounts of charge being collected. This intrinsic spread in the charge collected for incident particles of the same LET was discussed earlier.

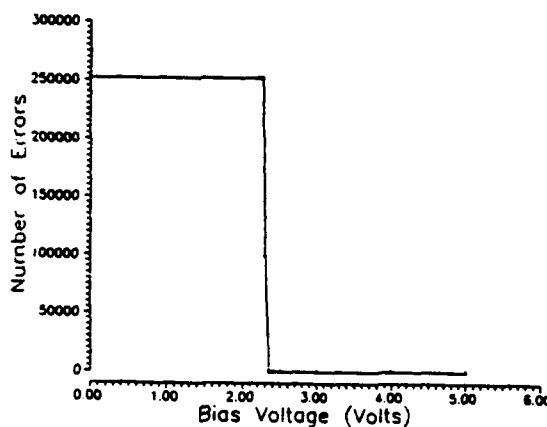


Fig. 45 Number of upsets in the absence of radiation versus bias. Measurements were carried out on an Intel 2164A DRAM.

6. ALGORITHMS FOR PREDICTING SEU RATES IN SPACE

6.1 Cosmic Rays

Computer codes available for calculating SEU rates in space as a result of cosmic-ray traversals and spallation reactions are listed in Fig. 46. The CRIER (Cosmic-Ray-Induced Error Rate Analysis) code was the original cosmic-ray code developed to predict SEU rates in space (72) and is maintained by S-Cubed Corporation. The CREME (Cosmic-Ray-Effects on Microelectronics) (73) and the CRUP (Cosmic Ray Upset Program) (74) are both from the Naval Research Laboratory and are generally available. Since the three codes are in reasonable agreement with one another, the discussion in what follows will be restricted to CREME, but much of what is said applies to the other codes as well. All three involve algorithms which use the sensitive volume approach outlined earlier. The dimensions of the sensitive volume must be specified by the user. The user also specifies the critical charge which must be generated (or threshold amount of energy which must be deposited-conversion 3.6 eV/ion-pair) in the sensitive volume to upset the circuit element. The number of elements per device, the shielding about the circuit, and the radiation environment the spacecraft is expected to fly in must also be specified.

CALCULATION OF SEU-RATES

1. MECHANISM

- SEU-SENSITIVE JUNCTIONS
- EVENTS of INTEREST
 - *Cosmic Ray Traversals*
 - *Proton Induced Reactions*

2. CHOICE OF ALGORITHM

- COSMIC RAYS
 - CREME*
 - CRUP*
 - CRJER*
 - PETERSEN's FORMULA*
- PROTONS
 - CUPID*
 - A-CURVES*

3. INPUT TO CODES

CIRCUIT

- *Critical Charge*
- *Dimensions of SV*

ENVIRONMENT

- (Adams 90% Worst Case)*
- South Atlantic Anomaly*

SHIELDING

Fig. 46 Codes and algorithms available for calculating SEU rates.

For a flare-free environment in deep space, the radiation environment can generally be represented as a mixture of solar maximum and solar minimum with the relative amounts depending on what period in the solar cycle the flight takes place. The cosmic-ray spectrum for solar minimum is shown in Fig. 47. The deep space environment is harsher than this most of the time. Solar maximum is a maximum only for the quiet or flare-free environment. The program calculates equivalent LET spectra for the particles incident on the spacecraft from the solar minimum spectrum or whatever spectrum is appropriate for the environment and time period. Then the cord-length distribution of trajectories through the sensitive volume, and the corresponding energy-deposition spectra are calculated. The number of

events per day in which more energy is deposited than the value of the critical charge (at 3.6 eV per ion pair) becomes the upset rate for that device. The energy deposited in the sensitive volume by each traversing particle is taken to be the product of the LET, the density of the medium, and the pathlength through the sensitive volume. The effects of flares can only be included in advance by specifying the relative abundances of the species comprising the radiation components of the flares and their energy spectra. In our present state of knowledge, that is impossible to do in advance. The errors per bit day calculated using CREME and CRUP for a device exposed to Adams' 90% worst-case environment (75) is plotted in Fig. 48 for dimensions of the sensitive volume which are typical of base-emitter heterojunctions in GaAs bipolar devices (43,76). The two codes modified for GaAs are in essential agreement.

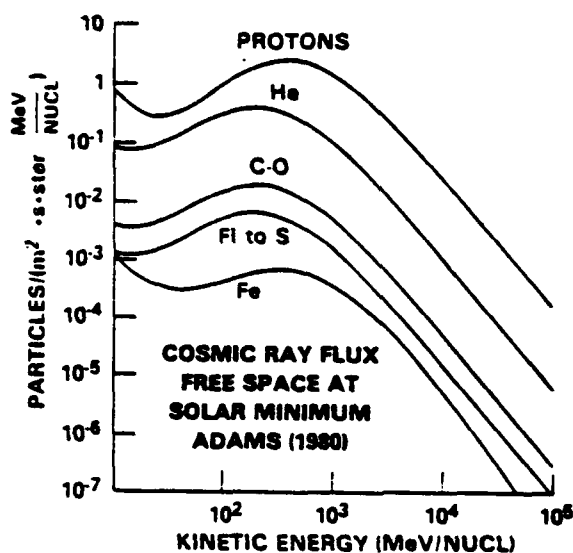


Fig. 47 Cosmic-ray spectrum - Adams' model for deep space at solar minimum.

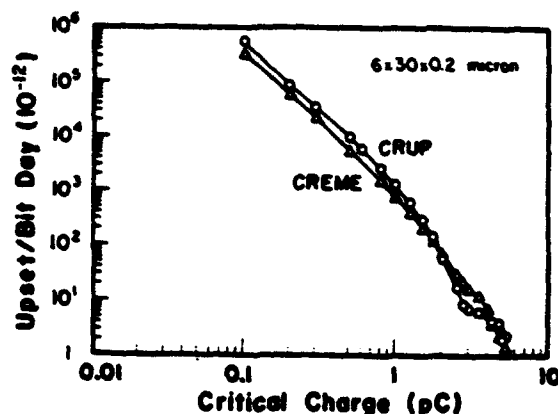


Fig. 48 CREME calculation of errors-per-bit-day versus critical charge for device dimensions typical of HI^2L bipolar GaAs.

The chance that a given heavy ion will upset a device depends on its LET and its pathlength within the sensitive volume. Heinrich (77) suggested plotting the integral flux of particles having at least some value of LET versus that value of LET. This form is convenient for workers trying to estimate some types of radiation effects. Figure 49 shows the Heinrich plot for deep space, as generated by Adams (75). The percentage labels on the curves reveal the fraction of time the deep space environment exceeds the integral flux levels given by that curve. The bottom curve represents solar minimum with no flare activity while the uppermost curve represents a very intense flare. The equivalent spectrum of high LET particles for a low-earth environment (77) is presented in Fig. 50.

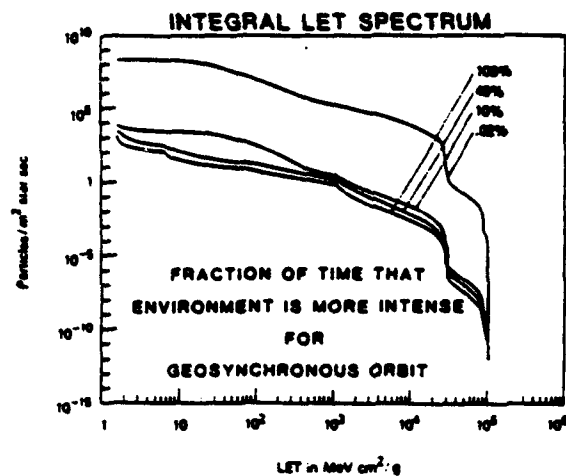


Fig. 49 Integral LET spectra for different deep space environments. Percentages represent the fraction of the time the environment exceeds that curve (75).

LET SPECTRA OF COSMIC-RAY NUCLEI

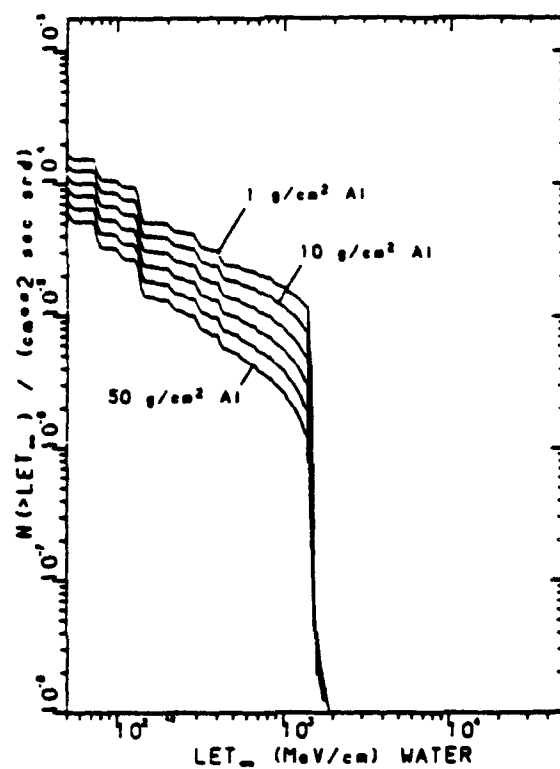


Fig. 50 LET spectra for a low earth orbit (Heinrich). LET is expressed in units of interest to biologists.

The simplest approach to estimating the SEU rate for a device flown in deep space is to use the Petersen formula. Only the dimensions of the sensitive volume and the critical charge must be specified or, alternatively, the plateau value of the SEU cross section and the threshold LET (78). The formula provides an estimate for Adams' 90% worst-case environment. In terms of critical charge Q_c in pC, the SEU rate R in errors per bit-day is given for silicon by the following expression:

$$R = 5 \times 10^{10} \frac{a \times b \times c^2}{Q_c^2}$$

where a , b , and c are the dimensions of the sensitive volume in microns.

The corresponding formula for GaAs is given by the following expression:

$$R = 3.5 \times 10^{10} \frac{a \times b \times c^2}{Q_c^2}$$

6.2 Trapped Protons

Proton-induced spallation reactions result in a broad range of charge generations within the sensitive volume even when all the reactions were induced by protons of one incident energy. The current versions of CUPID (5,21,79) require the user to provide the incident proton energy, the dimensions of the sensitive volume, and the dimensions of an external volume throughout which the spallation reactions occur; the external volume contains the sensitive volume and at least 4 microns of additional semiconductor as illustrated in Fig. 51. CUPID's output is in either of two forms: one is the differential spectrum of the energy depositions in the sensitive volume; the other is an integral cross section for depositing at least some energy E plotted versus the value of E . The integral form is more useful in SEU studies since it provides cross sections for events exceeding some threshold energy deposition. Examples of the integral form were shown in Figs. 22 and 34. The theoretical curves in both cases represent the cross section for depositing at least some energy E versus E in a sensitive volume with the dimensions specified. The agreement with charge-collection

measurements, for both the full-depleted surface-barrier detector of Fig. 22 and the partially-depleted drain-substrate junctions in the IDT 6116V of Fig. 34, generates some confidence in the code output.

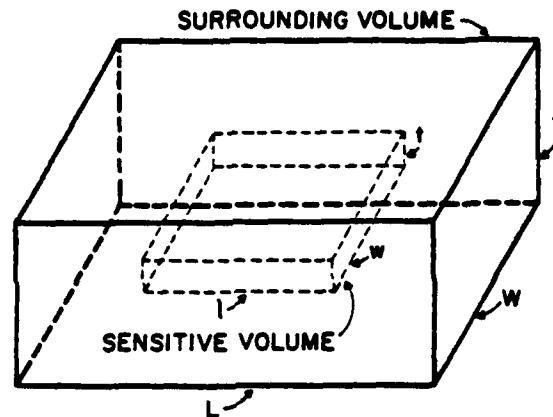


Fig. 51 Schematic showing the sensitive volume and the surrounding external volume whose dimensions must be specified for CUPID.

The integral cross section output of CUPID can also be interpreted as a plot of the cross section for upsetting a device with the specified dimensions and a critical charge given by the abscissa. Theoretical calculations carried out this way have led to good agreement with experimental data for a number of devices over a wide range of incident proton energies. Two examples of SEU cross section predictions are shown in Fig. 43 for the Intel 2164A DRAM and the 93L422, a bipolar SRAM. Again, the agreement is quite good. Similar agreement has been found for NMOS and CMOS devices (59,60).

Most of the energy deposited in a micro volume by a nearby spallation reaction is delivered by the recoiling nuclear fragment, at least for the large events that lead to upset (5,21,79). These nuclear fragments are similar to cosmic rays with moderately high values of LET. The average LET of each fragment can be calculated from the ratio of its energy to its range divided by the density of silicon. The distribution of average LET for nuclear fragments emerging from spallation reactions induced by 131 MeV protons was calculated using CUPID and plotted in Fig. 52. The upper end of the spectrum is at an LET of about $10 \text{ MeV cm}^2/\text{mg}$. This value of LET had been found to be the threshold LET which serves as a boundary between devices accepted as proton sensitive and proton insensitive.

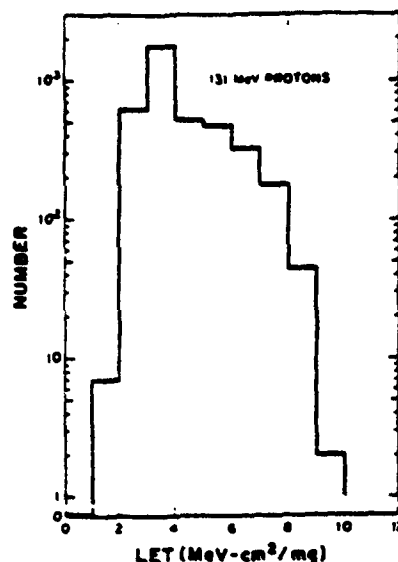


Fig. 52 Distribution of average LET for recoiling nuclear fragments emerging from spallation reactions induced by 131 MeV protons. Average LET is defined to be the energy of the residual fragment divided by its range.

This form of CUPID is adequate for predicting SEU rates for exposure to monoenergetic proton beams from accelerators incident perpendicular to one face. Exposure to proton energy environments with complex energy spectra and varying angles of incidence requires modification of the codes which is underway. The energy deposited in spallation reactions is only weakly dependent on the angle of incidence of the incident proton, but variations of a factor of two with the angle have been observed (61,80). The dependence on the angle of incidence may be the result of the fact that the recoiling nuclear fragments tends to recoil in the forward direction as shown in Fig. 53 (81). The codes currently available can be used to approximate the complex environments of the inner belts by representing the incident protons as a series of monoenergetic exposures at different energies

with the relative flux of each exposure dependent on the distribution of incident proton energies in the environment. A paper at this conference (82) compares CUPID simulations combined with the NASA model, AP8, to the spallation-reaction events measured with the J^{*} dosimeter on the DMSF satellite (83). The agreement was within 25% for four detectors having two different critical charges, two different geometries, and four different shield thicknesses.

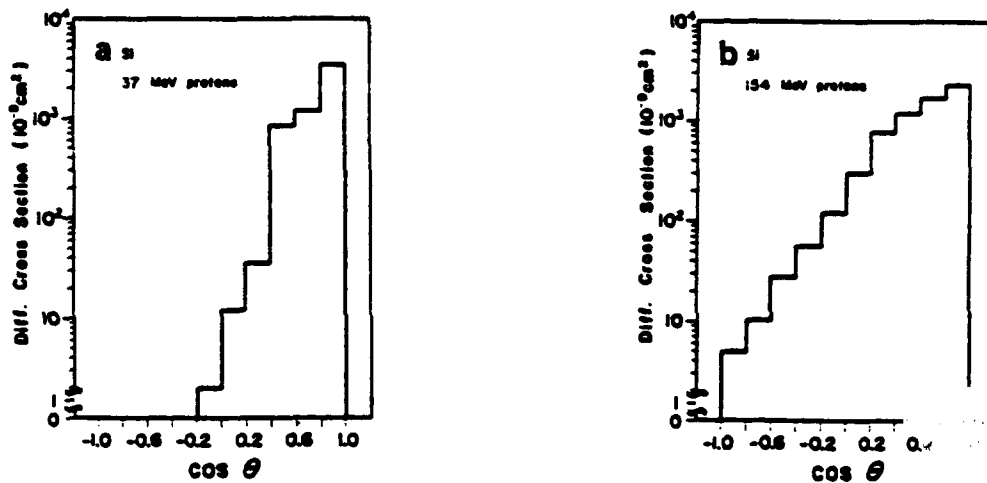


Fig 53 The angular distribution of the recoil nuclei from nuclear reactions induced by protons incident at (a) 37 MeV and (b) 154 MeV. Distribution obtained from CUPID simulations (81).

An alternative approach to predicting SEU rates in the radiation belts involves using the A curves of Bendel and Petersen (85) which are plotted in Fig. 54. To use the A curves, the measured SEU cross section is plotted versus incident proton energy in Fig. 54a and the value of A for the closest fitting curve noted. The corresponding SEU rate due to energetic protons trapped in the inner radiation belt is then obtained from their plot of SEU rate versus altitude in Fig. 54b for devices having various A values. One difficulty with this approach has been the fact that many devices do not exhibit an SEU depen-

dence which parallels the curves in Fig. 54a. This is being addressed in their new two-parameter model to be presented at this conference. See also Ref. 91.

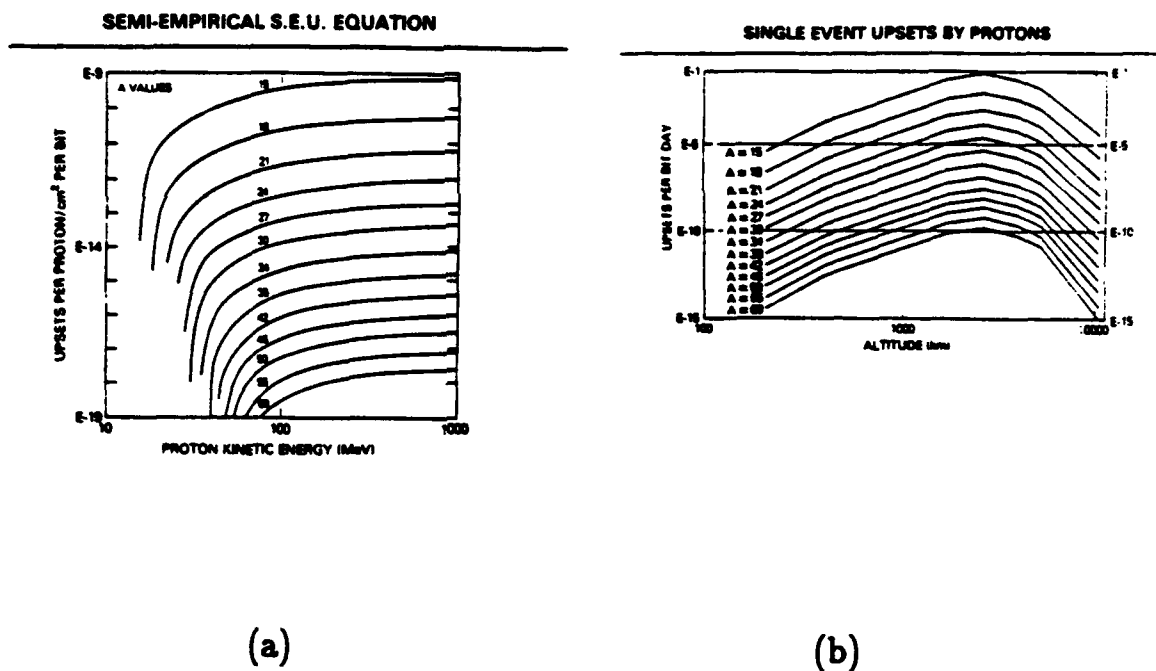


Fig. 54 a) The A curve of Petersen and Bendel. The measured cross section versus energy determines the proper A value to use. b) Error rates as a function of altitude for devices with different A values.

7. SOURCES OF INNACURACY

7.1 Shape of Threshold

Despite the absence of evidence for a variation in the critical charge across commercial devices, the largest source of inaccuracy in SEU calculations results from representing the device as a collection of identical circuit elements, all with the same critical charge. Such an assumption leads to a stepfunction threshold as illustrated by the dashed curve in Fig. 55, while the measured cross section for SEUs in real devices typically increases with Effective LET as the solid curve. The "S" shape of the solid curve is probably caused by the fluctuations in the amount of charge collected at the junction, even when exposed to identical particles. This "S" shape would be more obvious in a linear plot like Fig. 41b. In Monte-Carlo simulations, SEU thresholds are too often treated as single stepfunctions. This assumes that particles with the same LET and pathlength always generate the same amount of charge within the sensitive volume, an assumption which was shown above to be incorrect. The simplest procedure for resolving this difficulty is to represent the identical circuit elements as having identical dimensions but different thresholds. The number of elements to be assigned each value of threshold can be estimated by fitting the cross section versus LET curve by a series of steps, as illustrated in Fig. 55, with the difference in height between successive steps determining the relative number of elements assigned, as a threshold LET, the value midway between steps. Figure 55 also compares the errors-per-bit-per-day calculated using CREME under two assumptions: first, a single threshold for all elements and, second, different thresholds for subpopulations of the elements with the relative numbers and thresholds given by the steps in Fig. 54. The latter should be the more accurate calculation.

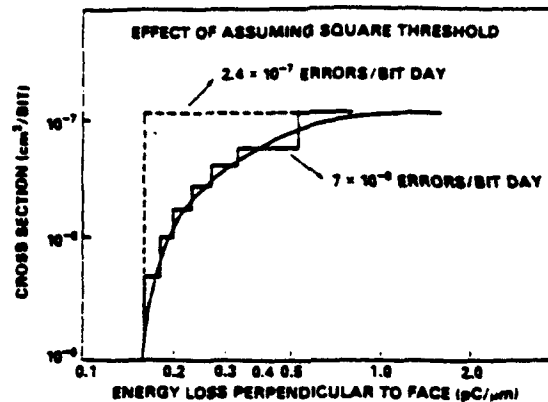


Fig.55 Comparison of a stepfunction threshold in a plot of SEU cross section versus LET with a threshold-response function which is typical of real devices(78).

This procedure can be applied to the SEU cross section data of the Intel 2164A DRAM in Fig. 56. The weightings given by the steps in the figure were incorporated into the CUPID calculations used for the theoretical curve in Fig. 43a. The manufacturer provided a critical charge for this device. The threshold LET can be estimated by dividing the critical charge by the pathlength through the sensitive volume which can be estimated from process information (53). The value obtained is represented in the figure by a triangle. It is in good agreement with the data. A single-threshold calculation based on this value of the critical charge resulted in CUPID simulations which were a factor of two below the experimental data. Calculations of the SEU rate to be expected for this device flying in Adams' 90% worst-case environment are presented in Table 2. Again, there is a factor of ten difference between the single-threshold calculation and the multiple-threshold calculation. As can be seen in Table 2, the Petersen formula using multiple thresholds provides a better estimate than CREME using a single threshold. According to the results in Table 2, the best

single threshold approximation is the value of LET corresponding to a cross section 25% of the plateau value. According to Petersen (85), this best fit by the LET at 25% - 30% of plateau is true of a broad range of devices.

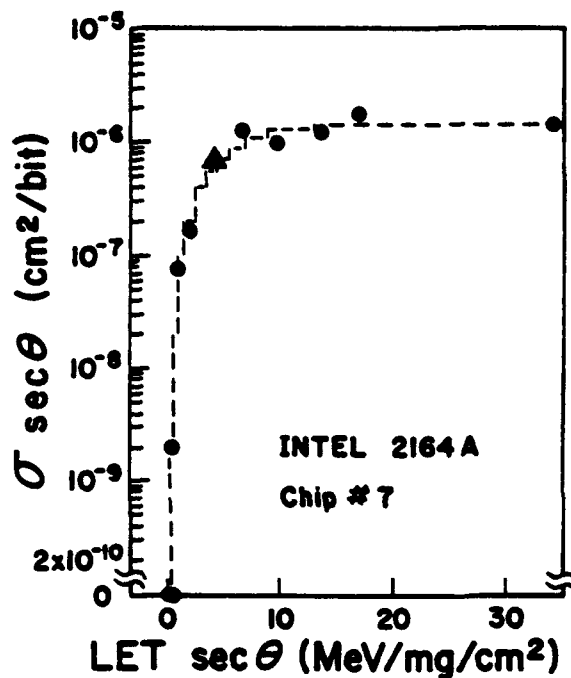


Fig.56 SEU cross section versus Effective LET for a DRAM fitted by a series of steps. The height of each step represents the product of the cross section area of the sensitive volume assigned to the junction times the fraction of elements having a threshold at or below the value of LET.

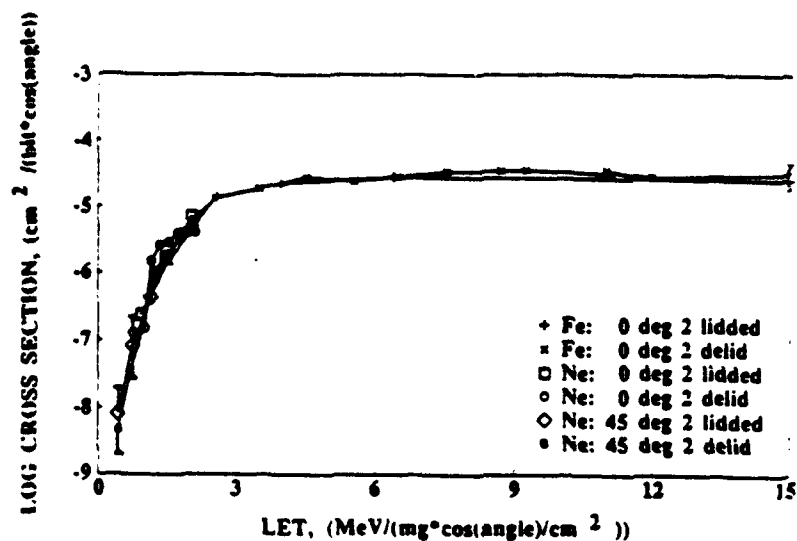
TABLE 2.

ALGORITHM PREDICTIONS FOR 2164A (Adams 90% Worst Case Environment)		
Technique	Approximation	Errors/Bit-Day
Detailed Calculation	Single (50%)	3.3E-5
	Multiple	2.7E-4
Petersen Formula	Single (50%)	3.7e-5
	Single (30%)	5.5e-5
	Single (.1%)	2.7e-3
	Multiple	1.65E-4

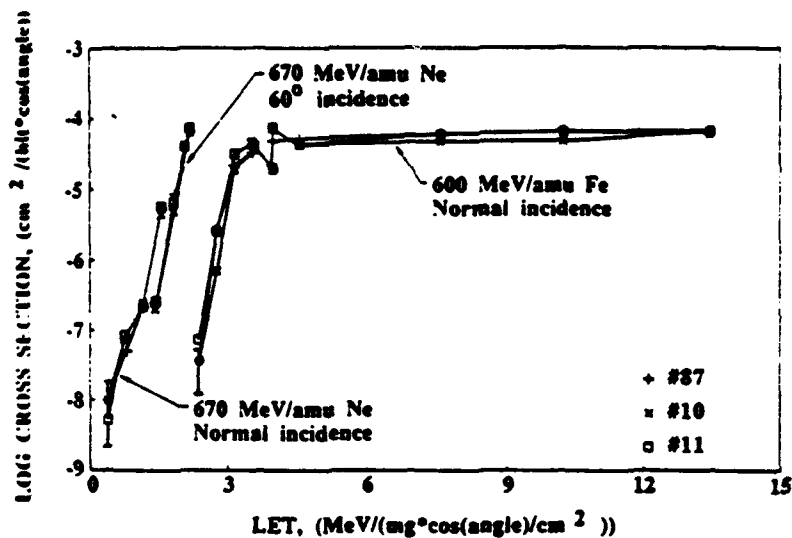
7.2 Track Structure

Heavy ions with different values of charge and kinetic energy but the same value of LET have been shown to produce different charge-collection spectra when incident on the same junction (56) and different threshold LETs for exposures of the same device (86). Presumably these differences are due to differences in the initial radial distribution of charge along the trajectory. They are most pronounced when comparing low-energy ions with high-energy ions with the same LET. An example is shown in the threshold curves in Fig. 57. The low-energy ions have kinematic limits on the energy which can be transferred in individual collisions with the atomic electrons of the media. This confines the pattern of primary and secondary radiations to a narrower region about the trajectory. This effect on track structure can be seen in Fig. 2 where the track is seen to thin down as the trajectory nears the end of the range in the bottom of the photograph. Most of the current SEU testing is carried out using low-energy particles whose tracks would definitely lie within the "thindown" region illustrated in Fig. 2, but most cosmic rays encountered in space are energetic and not thindown tracks. Only for devices with high thresholds LETs in the regions values where the integral LET spectra exhibit sharp falloff with further increases in LET (see Fig. 49) would low-energy

ions play a significant role in upsetting the device in deep space. However, data obtained with thindown tracks should be more appropriate for correlating SEU parameters between heavy ions and protons.



(a)



(b)

Fig. 57 Comparison of SEU cross sections plotted versus LET for low-energy ions and high-energy ions with similar LET values. a) The SEU response function for the 93L422 is seen to scale as the secant of the angle of incidence and exhibits no species dependence. b) The SEU response function for the 27LS00 exhibits a pronounced species dependence and does not scale as the secant of the angle of incidence Ref. (86).

The problem of track-structure effects is being addressed by the new heavy-ion test facility being planned at Brookhaven National Laboratory. This new facility will use high-energy ions thereby ensuring that particles at all LET values have similar track structure. The availability of high-energy ions with greater penetrating power will have the further advantages that SEU testing can be carried out in air, thereby avoiding the expense and delays of carrying out the experiments under vacuum, and that irradiations can be carried out at angles of incidence up to and including grazing. Careful studies of charge collection as a function of large angles should allow tomographic views of the sensitive volume.

7.3 Lot-To-Lot Variations and Process Change

New lots of parts may have different SEU characteristics than previous lots because of deliberate or inadvertent process changes or because of changes in foundry, personnel, or equipment. Differences of a factor of ten in the proton SEU cross sections have been observed with the IDT 6116V (80). This possibility of variability has necessitated repeated testing of the same part type when they are used in different essential programs.

7.4 Differences in Test Boards, Applied Bias, etc.

Differences in SEU response due to changes made in the circuit components making up the remainder of the test system of which it is a part is an area with limited information. Certainly the test protocol, for example the rate at which the cells are addressed, can effect the measured cross sections.

7.5 Uncertainties in the Natural Radiation Environment

It is appropriate to end a discussion of single-event phenomena with a discussion of the uncertainties in our knowledge of the particles actually incident on our device. Obviously, our ability to predict the response of a circuit most strongly depends on our ability to predict the particles which will be incident on it, and yet space consists of very complicated radiation environments. Solar flares and magnetic

disturbance can result in dramatic temporary changes in the radiation incident on the spacecraft and, consequently, the SEU rates. There is also a slow variation in the environments from solar minimum to solar maximum, which should result in corresponding increases in SEU rates in deep space and over the poles, and decreases in the portions of low-earth orbits where the spacecraft penetrates the radiation belts. This is an 11 year cycle and longer trends cannot be ruled out. The temporal variations in the cosmic-ray environment were illustrated in Fig. 49 where the LET spectra which are exceeded for different fractions of the time were displayed.

Current NASA models of the radiation environments are static models which only handle the dynamic variations described above by long term averaging. The codes for the cosmic-ray environment which serve as the input for CREME are probably valid to within a factor of two for averages of the environment. It is, of course, necessary to provide the proper mix of the solar maximum and the solar minimum in calculations. Also, AP8, the NASA code of the proton environments, may have errors of a factor of two in the high-energy proton environments for low-earth orbits. The J* dosimeter recently characterized the low-earth orbit of the DMSP satellite in terms of the energetic nuclear reactions which would lead to SEUs in microelectronic devices (83). The data was found to be in excellent agreement with the predictions of the AP8 model of the proton environment combined with CUPID's predictions of the number of spallation events which deposit at least 40 MeV and 70 MeV in the detectors (82).

7.6 Shielding

The most complicated part of any calculation of single event phenomena for a device flying on a satellite is taking into account the shielding provided by material between the device and the outer walls of the spacecraft. The changes in the LET spectra for devices behind different amounts of isotropic shielding are shown in Fig. 50. On real spacecraft, the shielding is not isotropic, however. The amount of material the cosmic ray or trapped proton must traverse depends on the direction of incidence. In low-earth orbit the earth provides

considerable shielding. Often, the spacecraft is spinning. Fortunately, shielding codes are usually generated as a part of spacecraft design and if free-space calculations suggest the possibility of a problem, the designer can take advantage of the codes to improve his analysis.

8. HOW ACCURATE ARE SEU PREDICTIONS?

8.1 Cosmic Rays

Relatively good agreement between predictions, based on heavy-ion accelerator data, and cosmic-ray spaceflight data have been reported by Binder (87), Smith and Simpson (70), and Blake and Mandel (88). These predictions were for a small number of devices in different satellite programs and included geosynchronous orbits and low-earth polar orbits. Binder developed a simple analytic expression for upset rates which by folding in the appropriate integral LET spectra provided estimates for three devices on the Global Positioning Satellite, including the AM 93L422. Blake and Mandel (88) used CREME to predict SEU rates for the Harris HM6508, a 1K SRAM in a low-earth polar orbit. Smith also carried out an analytical approach which took the different projections of the sensitive volume into account for the Fairchild 93L422. In all cases, the agreement was well within a factor of two. Although the details of the calculations were different in each case, all of the calculations were consistent with the CREME approach outlined earlier; in particular, the path-length distribution was taken into account.

A comparison of the three approaches leads to some tentative conclusions regarding SEU-rate predictions. First, the devices must be well characterized by thorough accelerator testing so that the response curve for the cross section versus LET is well defined. It is essential that the shape of the response curve be taken into account in calculating SEU rates. This is best done by fitting the response curve and weighting the calculations as subpopulations with different thresholds, as described above. A more risky alternative is to use a single threshold that takes this shape into account. Petersen recommends assigning the single threshold to the value of LET corresponding to the point on the response curve which is 25% to 30% of the plateau value. The response curve for the HM6508 did not exhibit a plateau and Blake and Mandel chose a value that appears to be about 50% of the highest value. In general, the more detailed calculations are warranted. In any event, the detailed response curve is needed if only

to determine the proper value to set for the single threshold. Poorly defined response curves generates uncertainties that can easily lead to errors of an order of magnitude or more.

Second, the pathlength distribution of particle trajectories must be incorporated into calculations. This is automatically done in CREME and was included in the calculations of Binder (87) and Smith and Simpson (70).

Third, corrections must be made for the appropriate time period in the solar cycle. Smith and Simpson (70) found a variation of a factor of 2.4 between maximum and minimum over the 11 year solar cycle.

Fourth, Multiple-upset events must be identified both in space and in the laboratory tests. There is, as yet, no accurate model for predicting the multiplicity of an event.

8.2 Trapped Protons

The use of CUPID and the Bendel-Petersen curves for predicting SEU rates was discussed in some detail earlier. Alternative approaches have recently become available. Bion and Bourrieau (89) have recently developed a simulation program which give fits to the measured Fairchild 93L422 and the Intel 2164A response curves which are comparable to the fits shown earlier for CUPID. When the model was applied to data from a polar-orbiting satellite (90) the agreement was within 20%. Shimano et al (91) have modified the Bendel-Petersen curves from a one-parameter fit to the proton response curve to a two-parameter fit. This gives them a correspondingly improved agreement with the measured in-orbit SEU rates for the 93419 RAM. The fact that CUPID, combined with the NASA AP8 model of the trapped protons, gave good agreement with the J^{*} Dosimeter data from the DMSP satellite instills confidence in CUPID's ability to perform SEU rate calculations accurately. It should be noted that the SEU rate predictions that are reported to be in agreement are for devices which are well characterized at accelerator facilities.

8.3 Predicting Proton Response From Heavy Ion Data

An earlier discussion outlined the procedure for using heavy-ion data as input to the CUPID simulation codes in order to predict the proton-cross-section versus incident-energy response function (67). For this to work, the identity of the SEU-sensitive junction must be known, and the dimensions of its associated sensitive volume determined. The critical charge can then be estimated from the heavy-ion data. This is a thorough test of the understanding of the basic mechanisms and the algorithms used for calculations. The agreement obtained for CUPID was excellent for two devices, as shown earlier (67). Bion and Bourrieau (89) have developed simulation codes of the same general type as CUPID. They also find that one can use the heavy ion data to predict the proton data. Again, the detailed shape of the response curve must be taken into account for accurate calculations.

There have been recent attempts to reverse this procedure, i.e., use the proton data to predict the heavy-ion threshold; they have met with some success (59,60,62,63). However, threshold alone is only sufficient for the roughest of calculations. It is necessary to specify the shape of the response curve for accurate predictions. It may be possible to determine the shape by charge collection measurements on test structures or the devices themselves. In any event, this approach is controversial and should be tested carefully at a number of different laboratories before being implemented.

8.4 Conclusions

Accurate calculations of SEU rates have been carried out by procedures of the type described in this tutorial. They require accurate models of the environment, detailed characterization of the part by extensive SEU testing, and a reasonable knowledge of the electrical operation of that device. There should be some confidence that, in the not too distant future, the single-event hard errors will be equally reliable. Of course a skeptic might argue that there has been a significant weakness in the successful calculations of SEU rates in space

to date which inhibits full confidence because they were carried out after the fact. Knowing the correct answer might introduce subtle unconscience bias in the choice of the value of the threshold LET or the dimensions of the sensitive volume which improves the agreement. Calculations based on the total response function rather than a single threshold should be immune to this criticism. In any case, this skepticism will be tested in the near future when the CRRES satellite is launched. A number of groups have been invited to place predictions on a wide range of parts in the public domain before the satellite is launched. Pick up your parts list from your friendly CRRES representative and join the fun! In addition to providing careful flight data on a number of parts which are important to the space program, CRRES will also have a variety of experiments on board which will measure the environments including the energy of the particles.

Despite the genuine successes of the first-order model, there are reasons to suspect that it may have problems with this generation of devices. The feature sizes are reaching dimensions where the thin parallelepiped may not describe the shape of the sensitive volume (55). Enhanced charge collection will become increasingly important, as the junctions become smaller, whether it is due to edge effects (35) or defects. The pulse-height spectra observed when charge collecting from the junctions will become more complicated as we enter the "microdosimetry" regime with the advent of submicron feature sizes. The loss of the simple geometric relationships which connect the cross section with the angle of incidence and the charge collected with the angle of incidence will make future testing and analysis more complicated. Multiple upsets are becoming more important, requiring greater sophistication in both the accelerator experiments and in recording of space data. Improved understanding of basic mechanisms of multiple-upset events is needed. This tutorial ends then, appropriately enough, with a partial list of SEU-related problems which require attention.

• UNEXPLAINED PHENOMENA

Multiple Upsets

Angular Dependence

Charge Collection versus LET

Enhanced Charge Collection Events

Fig. 58. SEU Phenomena in need of quantitative models.

9. ACKNOWLEDGEMENTS

Helpful conversations and materials from Ed Petersen and Bill Stapor of NRL are greatly appreciated. Conversations with the graduate students and research associates in the Clemson laboratory played a big role in the formulation of some of the ideas expressed here. However, any errors or omissions are purely my own.

I would particularly like to express my sincere appreciation to Wagih Abdel Kader, David Roth, and Patricia McNulty for their help and advice in putting this manuscript together.

REFERENCES

1. D. Binder, C.E. Smith, and A.B. Holman, "Satellite Anomalies from Galactic Cosmic Rays" IEEE Trans. Nucl. Sci. NS-22, 2675-2680 (1975).
2. E Petersen and P. Marshall, private communication.
3. C.S. Guenzer, E.A. Wolicki, and R.G. Allas, "Single Event Upset of Dynamic Rams by Neutrons and Protons," IEEE Trans. Nucl. Sci., NS-26, 5048-5052 (1979).
4. R.C. Wyatt, P.J. McNulty, P. Toumbas, P.L. Rothwell, and R.C. Filz, "Soft Errors Induced by Energetic Protons," IEEE Trans. Nucl. Sci. NS-26, 4905-4910 (1979).
5. P.J. McNulty, G.E. Farrell, R.C. Wyatt, P.L. Rothwell, R.C. Filz, and J.N. Bradford, "Upset Phenomena Induced by Energetic Protons and Electrons," IEEE Trans. Nucl. Sci. NS-27, 1516-1522 (1980).
6. J.R. Srour, Z. Stanfield, R.A. Hartmann, S. Othmer, and D.M. Newberry, "Permanent Damage Introduced by Single Particles Incident on Silicon Devices," IEEE Trans. Nucl. Sci. NS-30, 4526-4532 (1983).
7. B.L. Gregory and B.D. Shafer, "Latch-up in CMOS Integrated Circuits," IEEE Trans. Nucl. Sci. NS-20, 293-299 (1973).
8. W.A. Kolasinski, J.B. Blake, J.K. Anthony, W.E. Price, and E.C. Smith, "Simulation of Cosmic-Ray Induced Soft Errors and Latchup in Integrated Circuit Computer Memories," IEEE Trans. Nucl. Sci. NS-26, 5087- 5091 (1979).
9. K. Soliman and D.K. Nichols, "Latchup in CMOS Devices from Heavy Ions," IEEE Trans. Nucl. Sci. NS-30, 4514-4519 (1983).
10. D.K. Nichols, W.E. Price, M.A. Shoga, J. Duffey, W.A. Kolasinski, and R. Koga, "Discovery of Heavy-Ion Induced Latchup in CMOS/Epi Devices," IEEE Trans. Nucl. Sci. NS-33, 1696 (1986).

11. J.T. Blandford, Jr., A.E. Waskiewicz, and J.C. Pickel, "Cosmic-Ray Induced Permanent Damage in MNOS EAROMs," IEEE Trans. Nucl. Sci. NS-31, 1568-1570 (1984).
12. A.E. Waskiewicz, J.W. Groninger, V.H. Strahan, and D. M. Long, "Burnout of Power MOS Transistors with Heavy Ions of Californium-252," IEEE Trans. Nucl. Sci. NS-33, 1710-1713 (1986).
13. T.C. May, "Dynamic Fault Imaging of VLSI Random Logic Devices," presented at the 1984 International Reliability Symposium, Los Vegas, Nevada, April 2-5, 1984.
14. D.M. Newberry, private communication.
15. C.S. Guenzer, A.B. Campbell, and P. Shapiro, "Single Event Upsets in NMOS Microprocessors," IEEE Trans. Nucl. Sci. NS-28, 3955-3958 (1981).
16. S.E. Kerns, B.D. Shafer, L.R. Rockett, Jr., J.S. Pridmore, D.F. Berndt, N. van Vonno, and F.E. Barber, "The Design of Radiation-Hardened ICs for Space: A Compendium of Approaches," Proceedings of the IEEE 76, 1470-1509 (1988).
17. C.S. Guenzer, R.G. Allas, A.B. Campbell, J.M. Kidd, E.L. Petersen, N. Seeman, and E.A. Wolicki, "Single Event Upsets in RAMs Induced by Protons at 4.2 GeV and Protons and Neutrons below 100 MeV," IEEE Trans. Nucl. Sci. NS-27, 1485-1489 (1980).
18. J.N. Bradford, "Single Event Error Generation by 14 MeV Neutron Reactions in Silicon," IEEE Trans. Nucl. Sci. NS-27, 1480-1484 (1980).
19. J.S. Browning, J.E. Gover, T.F. Wrobel, K.J. Hass, R.D. Nasby, R.L. Simpson, L.D. Posey, R.E. Boos, and R.C. Block, "Hard Error Generation by Neutron Induced Fission Fragments," IEEE Trans. Nucl. Sci. NS-34, 1269-1274 (1987); J.S. Browning, private communication.

20. G.F. Knoll, *Radiation Detection and Measurement*, John Wiley & Sons, New York, NY 1989.
21. P.J. McNulty, G.E. Farrell, and W.P. Tucker, "Proton-Induced Nuclear Reactions in Silicon," *IEEE Trans. Nucl. Sci.* NS-28, 4007-4012 (1981)
22. R.N. Hamm, M.L. Rustgi, H.A. Wright, and J.E. Turner, "Energy Spectra of Heavy Fragments in the Interactions of Protons with Communication Materials," *IEEE Trans. Nucl. Sci.* NS-28, 4031-4017 (1981).
23. K.W. Fernald and S.E. Diehl Kerns, "Simulation of Proton-Induced Energy Deposition in Integrated Circuits," paper presented at the Conf. on Nuclear and Space Radiation Effects, Snowmass Village, CO, 1987.
24. P.J. McNulty, R.C. Wyatt, G.E. Farrell, R.C. Filz, and P.L. Rothwell, "Proton Upsets in LSI Memories in Space," in *Space Systems and Their Interactions with the Earth's Space Environment*, H.B. Garrett, and C.P. Pike Eds., Vol. 71 of Progress in Aeronautics and Astronautics, (MIT Press, Cambridge, MA, 1980) pp 413-433.
25. C. Hu, "Alpha-Particle-Induced Field and Enhanced Collection of Carriers," *IEEE Electron Device Lett.* EDL-3, 31-34 (1982).
26. F.B. McLean and T.R. Oldham, "Charge Funneling in N- and P- Type Substrates," *IEEE Trans. Nucl. Sci.* NS-29, 2018-2023 (1982).
27. T.R. Oldham and F.B. McLean, "Charge Collection Measurements for Heavy Ions Incident on N- and P- Type Silicon," *IEEE Trans. Nucl. Sci.* NS-30, 4493-4500 (1983).
28. M.A. Hopkins and J.R. Srour, "Measurements of Alpha-Particle-Induced Charge in GaAs Devices," *IEEE Trans. Nucl. Sci.* NS-30, 4457-4463 (1983).

29. M.A. Hopkins and J.R. Srour, "Charge Collection Measurements on GaAs Devices," IEEE Trans. Nucl. Sci. NS-31, 1116-1120 (1984).
30. T.R. Oldham, F.B. McLean, and J.M. Hartman, "Revised Funnel Calculations for Heavy Particles with High dE/dx ," IEEE Trans. Nucl. Sci. NS-33, 1646-1650 (1986).
31. A.B. Campbell, and A.R. Knudson, "Charge Collection Measurements for Energetic Ions in Silicon," IEEE Trans. Nucl. Sci. NS-29, 2067-2071 (1982).
32. A.B. Campbell, A.R. Knudson, P. Shapiro, D.O. Patterson, and L.E. Sieberling, "Charge Collection in Test Structures," IEEE Trans. Nucl. Sci. NS-30, 4486-4492 (1983).
33. R.M. Gilbert, G.K. Ovrebo, J. Schifano, and T.R. Oldham, "Charge Collection in N-Type GaAs Schottky-Barrier Diodes Struck by Heavy Energetic Ions," IEEE Trans. Nucl. Sci. NS-31, 1570-1573 (1984).
34. A.R. Knudson, A.B. Campbell, P. Shapiro, W.J. Stapor, E.A. Wolicki, E.L. Petersen, S.E. Diehl, J.R. Hauser, and P.V. Dressendorfer, "Charge Collection in Multilayer Structures," IEEE trans. Nucl. Sci. NS-31, 1149-1154 (1984).
35. P.J. McNulty, W.G. Abdel-Kader, A.B. Campbell, A.R. Knudson, P. Shapiro, F. Eisen, and S. Roosild, "Charge Collection in GaAs Test Structures" IEEE Trans. Nucl. Sci. NS-31, 1128-1131 (1984).
36. A.B. Campbell, A.R. Knudson, W.J. Stapor, P. Shapiro, S.E. Diehl, and J. Hauser, "Charge Collection in CMOS/SOS Structures," IEEE Trans. Nucl. Sci. NS-32, 4128-4130 (1985).
37. A.R. Knudson, A.B. Campbell, J.R. Hauser, M. Jessee, W.J. Stapor, and P. Shapiro, "Charge Transport by Ion Shunt Effect," IEEE Trans. Nucl. Sci. NS-33, 1560-1564 (1986).

38. A.L. Ward, "Avalanching in Single-Event Upset Charge Collection in Semiconductor Diodes," IEEE Trans. Nucl. Sci. NS-33, 1552-1559 (1986).
39. R.S. Wagner, J.M. Bradley, C.J. Maggiore, J.G. Beery, and R.M. Hammond. "An Approach to Measure Ultrafast-Funneling-Current Transients," IEEE Trans. Nucl. Sci. NS-33, 1651-1655 (1986).
40. Z. Shanfield, K.S. Kitasaki, M.M. Moriwaki, and D.E. Campbell, "Angular Dependence of Charge Funneling in Si and GaAs Devices," IEEE Trans. Nucl. Sci. NS-34, 1341-1346 (1987).
41. W.T. Anderson, A.R. Knudson, F.A. Buot, J.P. Kreskovsky, H.L. Grubin, and A.B. Campbell, "Experimental and Theoretical Study of Alpha-Particle-Induced Charge Collection in GaAs FETs," IEEE Trans. Nucl. Sci. NS-34, 1326-1331 (1987).
42. R.S. Wagner, N. Bordes, J.M. Bradley, C.J. Maggiore, A.R. Knudson, and A.B. Campbell, "Alpha-, Boron-, Silicon-, and Iron-induced Current Transients in Low-Capacitance Silicon and GaAs Diodes," IEEE Trans. Nucl. Sci. NS-35, 1578-1584 (1988).
43. P.J. McNulty, M.H. Yaktieen, J.E. Lynch, W.M. Weber, H.T. Yuan, and J.F. Salzman, "Charge Collection in GaAs Bipolar Transistors," IEEE Trans. Nucl. Sci. NS-35, 1613-1618 (1988).
44. L.W. Nagel, "Spice 2: A Computer Program to Simulate Semiconductor Circuits," University of California Memo No. ERL-M520 (May 1975).
45. S.E. Diehl, A. Ochoa, Jr., P.V. Dressendorfer, R. Koga, and W.A. Kolasinski, "Error Analysis and Prevention of Cosmic-Ion Induced Soft Errors in Static CMOS RAMs," IEEE Trans. Nucl. Sci. NS-29, 2032-2039 (1982).

46. R.L. Johnson, and S.E. Diehl, "An Improved Single Event Resistive-Hardening Technique for CMOS Static RAMs," IEEE Trans. Nucl. Sci. NS-33, 1730-1733 (1986).
47. S.E. Diehl, J.E. Vinson, B.D. Shafer, and T.M. Mnich, "Considerations for Single Event Immune VLSI Logic," IEEE Trans. Nucl. Sci. NS-30, 4501-4507 (1983).
48. S.E. Diehl, J.E. Vinson, and E.L. Petersen, "Single Event Upset Rate Predictions for Complex Logic Systems," IEEE Trans. Nucl. Sci. NS-31, 1132-1138 (1984).
49. R.L. Johnson, Jr., S.E. Diehl, and J.R. Hauser, "Simulation Approach for Modeling Single Event Upsets on Advanced CMOS SRAMs," IEEE Trans. Nucl. Sci. NS-32, 4122-4127 (1985).
50. T.R. Weatherford, J.R. Hauser, and S.E. Diehl, "A Study of Single Events in GaAs SRAMs," IEEE Trans. Nucl. Sci. NS-32, 4170-4175 (1985).
51. M.G. Buehler and R.A. Allen, "An Analytical Method for Predicting CMOS SRAM Upsets with Application to Asymmetrical Memory Cells," IEEE Trans. Nucl. Sci. NS-33, 1637-1641 (1986).
52. S.E. Kerns, L.W. Massengill, D.V. Kerns, Jr., M.L. Alles, T.W. Houston, H. Lu, and L.R. Hite, "Model for CMOS/SOI Single-Event Vulnerability," IEEE Trans. Nucl. Sci. NS-36, 2305-2310 (1989).
53. W.G. Abdel-Kader, P.J. McNulty, S. El-Teleaty, J.E. Lynch, and A.N. Khondker, "Estimating the Dimensions of the SEU-Sensitive Volume," IEEE Trans. Nucl. Sci. NS-34, 1300-1304 (1987).
54. S. El-Teleaty, W.G. Abdel-Kader, P.J. McNulty, M.H. Yaktien, "Charge Collection in Partially Depleted GaAs Test Structures Induced by Alphas, Heavy Ions, and Protons," submitted for publication.

55. J.B. Langworthy, "Depletion Region Geometry Analysis Applied to Single Event Sensitivity," *IEEE Trans. Nucl. Sci.* **NS-36**, 2427-2434 (1989).
56. W.J. Stapor, P.T. McDonald, A.R. Knudson, A.B. Campbell, and B.G. Glagola, "Charge Collection in Silicon for Ions of Different Energy but Same Linear Energy Transfer," *IEEE Trans. Nucl. Sci.* **NS-35**, 1585-1590 (1988).
57. E.J. Kobetich and R. Katz, "Width of Heavy Ion Tracks in Emulsion," *Phys. Rev.* **170**, 405-411 (1968).
58. P.J. McNulty, "Track Structure Effects at P-N Junctions in Microelectronic Circuits," *Nucl. Tracks Radiat. Meas.* **16**, 197-204 (1989).
59. P. J. McNulty, W.J. Beauvais, D.R. Roth, and J. E. Lynch, "Determination of SEU Sensitivity of CMOS Devices by Charge Collection Measurements" submitted for publication.
60. P.J. McNulty, D.C. Dinger, D.R. Roth, and W.J. Beauvais, "Characterization of SEU Sensitivity Through Charge Collection Measurements," in preparation.
61. R. Koga, W.A. Kolasinski, J.V. Osborn, J.H. Elder, and R. Chitty, "SEU Test Techniques for 256K Static RAMS and Comparisons of Upsets Induced by Heavy Ions and Protons," *IEEE Trans. Nucl. Sci.* **NS-35**, 1638-1643 (1988).
62. P.J. McNulty, D.R. Roth, W.J. Beauvais, and J.E. Lynch, "Charge Collection Measurements on CMOS Devices" in preparation.
63. J.E. Lynch, P.J. McNulty, and M. Yaktien, "Comparison of Charge Collection and SEU Cross Sections for VLSI Devices Exposed to Heavy Ions and Energetic Protons," submitted for publication.
64. U. Littmark and J.F. Ziegler, *Handbook of Stopping Cross-Sections for Energetic Ions in All Elements*, Pergamon Press, Elmsford, NY, 1980.

65. S.E. Kerns, "Transient-Ionization and Single-Event Phenomena," in *Ionizing Radiation Effects in MOS Devices and Circuits* T.P. Ma and P.V. Dressendorfer Eds. (John Wiley & Sons, New York, NY, 1989) pp. 485-576.
66. D.K. Nichols, L.S. Smith, G.A. Soli, R. Koga, and W.A. Kolasinski, "Latest Trends in Parts SEP Susceptibility From Heavy Ions," *IEEE Trans. Nucl. Sci.* NS-36, 2388-2397 (1989).
67. J.M. Bisgrove, J.E. Lynch, P.J. McNulty, W. Abdel-Kader, V. Kletnieks, and W.A. Kolasinski, "Comparison of Soft Errors Induced by Heavy Ions and Protons" *IEEE Trans. Nucl. Sci.* NS-33, 1571-1576 (1986).
68. J.A. Zoutendyk, H.R. Schwartz, R.K. Watson, Z. Hasnain, and L.R. Nevill, "Single-Event Upset (SEU) in a DRAM with ON-Chip Error Correction," *IEEE Trans. Nucl. Sci.* NS-34, 1310-1315 (1987).
69. J.A. Zoutendyk, L.D. Edmonds, and L.S. Smith, "Characterization of Multiple-Bit Errors From Single-Ion Tracks in Integrated Circuits," *IEEE Trans. Nucl. Sci.* NS-36, 2267-2274 (1989).
70. E.C. Smith, and T.R. Simpson, "Prediction of Cosmic-Radiation-Induced Single-Event Upsets in Digital Logic Devices On Geostationary Orbit," TRW Final Report, November 2, 1987.
71. J.C. Pickel, and J.T. Blandford, Jr., "Cosmic Ray Induced Errors in MOS Memory Cells," *IEEE Trans. Nucl. Sci.* NS-28, 3962-3967 (1980)
72. J.C. Pickel, and J.T. Blandford, "CMOS RAM Cosmic-Ray-Induced Error-Rate Analysis," *IEEE Trans. Nucl. Sci.* NS-28, 3962-3967 (1981).
73. J.H. Adams, Jr., A.J. Tylka, and B. Stiller, "LET Spectra in Low-Earth Orbit," *IEEE Trans. Nucl. Sci.* NS-33, 1386-1389 (1986).

74. P. Shapiro, Naval Research Memorandum Report # 5901 (1986).
75. J.H. Adams, "The Variability of Single Event Upset Rates in the Natural Environment," IEEE Trans. Nucl. Sci. NS-30, 4475-4480 (1983).
76. J.F. Salzman, P.J. McNulty, and A.R. Knudson, "Intrinsic SEU Reduction From Use of Heterojunctions in HI2L Transistors," IEEE Trans. Nucl. Sci. NS-34, 1676-1679 (1987).
77. W. Heinrich, "Calculation of LET Spectra of Heavy Cosmic Ray Nuclei at Various Absorber Depths," Radiation Effects 34, 143-148 (1977).
78. E.L. Petersen, J.B. Langworthy, and S.E. Diehl, "Suggested Single Event Upset Figure of Merit," IEEE Trans. Nucl. Sci. NS-30, 4533-4539 (1983).
79. G.E. Farrell and P.J. McNulty, "Microdosimetric Aspects of Proton-Induced Nuclear Reactions in Thin Layers of Silicon," IEEE Trans. Nucl. Sci. NS-28, 4007-4012 (1981).
80. W.J. Stapor, private communication.
81. S. El-Teleaty, P.J. McNulty, W.G. Abdel-Kader, and W.J. Beauvais, "Soft Fails in Microelectronic Circuits Due to Proton-Induced Nuclear Reactions in Material Surrounding the SEU-Sensitive Volume," Nucl. Instr. and Meth. in Physics Research B40/41 1300-1305 (1989).
82. P.J. McNulty, W.J. Beauvais, M.S. Gussenhoven, and E.G. Mullen, "Comparison of Spallation-Reaction Simulations with DMSP Satellite Data," IEEE Trans. Nucl. Sci. submitted for publication.
83. M.S. Gussenhoven, E.G. Mullen, R.C. Filz, D.H. Brautigam, and F.A. Hanser, "New Low-Altitude Dose Measurements," IEEE Trans. Nucl. Sci. NS-34, 676-683 (1987).
84. W.L. Bendel and E.L. Petersen, "Predicting Single Event Upsets in the Earth's Proton Belts," IEEE Trans. Nucl. Sci. NS-31, 1201-1205 (1984).

85. E.L. Petersen, private communication.
86. T.L. Criswell, D.L. Oberg, J.L. Wert, P.R. Measel, and W.E. Wilson, "Measurement of SEU Thresholds and Cross Sections at Fixed Incidence Angles," IEEE Trans. Nucl. Sci. NS-34, 1316-1321 (1987).
87. D. Binder, "Analytic SEU Rate Calculation Compared To Space Data," IEEE Trans. Nucl. Sci. NS-35, 1570-1572 (1988).
88. J.B. Blake and R. Mandel, "On-Orbit Observations of Single Event Upset in Harris HM-6508 1K RAMS," IEEE Trans. Nucl. Sci. NS-34, 1616-1619 (1986).
89. T. Bion and J. Bourrieau, "A Model for Proton-Induced SEU," IEEE Trans. Nucl. Sci. NS-36, 2281-2286 (1989).
90. L. Adams, R. Harboe-Sorensen, E. Daly, and J. Ward, "Proton-Induced Upsets in the Low-Altitude Polar Orbit," IEEE Trans. Nucl. Sci. NS-36, 2339-2343 (1989).
91. Y. Shimano, T. Goka, S. Kuboyama, K. Kawachi, T. Kanai, and Y. Takami, "The Measurement and Prediction of Proton Upset," IEEE Trans. Nucl. Sci. NS-36, 2344-2348 (1989).

APPENDIX B

CHARGE COLLECTION MEASUREMENTS AND THEORETICAL CALCULATIONS FOR PARTIALLY DEPLETED SILICON DEVICES

Charge collection measurements and theoretical calculations for partially depleted silicon devices *

W.G. Abdel-Kader, S.S. El-Teleaty¹ and P.J. McNulty

Department of Physics and Astronomy, Clemson University, Clemson, SC 29634-1911, USA

Charge collection measurements were carried out using partially depleted silicon devices. The amount of charge collected at a given junction can be used to estimate the thickness of the sensitive volume to be associated with that junction. The assumption that the charge generated within this sensitive volume equals the charge collected at the junction forms the basis of current methods of predicting SEU rates for components exposed to the natural radiation environments of space. A simple analytic expression provides reasonable agreement with the experimental results of charge collection with alphas. When the dimensions estimated from this expression were used in Monte Carlo simulations of charge generation in the sensitive volumes through proton-induced spallation reactions, the results were found to be in good agreement with measured charge collection spectra.

1. Introduction

Soft errors or single event upsets (SEU) result when ionizing particles traverse SEU-sensitive reversed-biased junctions in microelectronic circuits. These particles can be isolated cosmic rays or secondary particles emerging from nearby spallation reactions. The standard models [1-3] for SEUs assume that circuit elements change their electrical and hence their logic states when more than some critical charge is collected at the junction within a response time determined by the circuit parameters. The charge collected has a fast drift component which includes the charge generated in the depletion region of the junction and the charge brought in by funneling [4]. Expressions for the thickness of the depletion layer in terms of the doping concentration on both sides of the junction and the applied bias are given in most texts on semiconductor physics [5]. Hu [6] and Oldham and McLean [7] have derived expressions for charge collection by funneling which are in reasonable agreement with experimental measurements. Hu's model leads to a thickness value for the drift layers which is independent of the stopping power or linear energy transfer (LET) of the incident particles. This constant thickness is assumed in all of the current algorithms for calculating SEU rates in space.

In many important device technologies, the largest component of the charge collected arrives by diffusion.

Previous estimates of this component and the corresponding thickness of the sensitive volume involved random walk modeling using computer simulations [8]. A simple analytic expression has been recently derived [9] to provide an alternative estimate of the charge collection by diffusion assuming random walk. The equivalent thickness t of the layer of the sensitive volume corresponding to diffusion is given in ref. [9]:

$$t = \frac{1}{2} \left[v_d \tau - l_f - (v_d^2 \tau^2 + a^2)^{1/2} + (l_f^2 + a^2)^{1/2} \right], \quad (1)$$

where v_d is the diffusion velocity, τ is the minority carrier lifetime, l_f is the funneling length and a is the radius of the junction. In fast devices, only the charge collected within the time constants of the circuit contribute to upsetting the circuit element. In that case, the time constant (possibly estimated from the switching speed) of the circuit should be used instead of τ . Eq. (1) was derived for a particle incident along the axis of symmetry perpendicular to the plane of the junction. Somewhat different values would be obtained for other trajectories, but this expression is useful for estimating a value to be used in the SEU models which assume that the sensitive volume is a rectangular parallelepiped.

SEU cross sections, calculated for memory cells of DRAM devices using the thickness of the sensitive volume estimated from this formula and a cross sectional area obtained from the heavy-ion SEU cross section, were in good agreement with the SEU cross sections measured with energetic protons [8]. In this paper, we present experimental measurements of the diffusion component of the thickness and compare the values obtained with the calculated values for a p-i-n diode. Also, the pulse-height spectra of the charge col-

* Work supported by the Air Force Geophysics Laboratory and the DNA Single Event Radiation Effects Program.

¹ Department of Physics and Atmospheric Sciences, Jackson State University, Jackson, Mississippi.

lection (energy deposition) measurements obtained in exposures of UV100 and the YAG444 p-i-n photodiodes to beams of energetic protons are compared to Monte Carlo simulations using the CUPID (Clemson University Proton Interactions in Device) code. The code simulates the nuclear spallation reactions induced by energetic protons and calculates the energy deposition within a sensitive volume having dimensions given by the junction area and the thickness determined by eq. (1).

2. Experiment

Fig. 1 is a schematic diagram of the experimental setup. Alpha particles from an ^{241}Am source were used to calibrate the system and to measure the thicknesses of the sensitive volume to be associated with the SEU-sensitive junction. The alpha exposures were carried out in a vacuum chamber. The multichannel analyzer calibration was carried out before and after the experimental measurements using silicon surface-barrier detectors (50 or 100 μm thickness) biased at voltages appropriate for being fully depleted. The proton exposures were carried out at the Harvard cyclotron where energies of 158 MeV were available for irradiation. Lower energies were obtained by degrading the beam by making it traverse layers of lucite. UV100 and YAG444 silicon p-i-n diodes were used in the charge collection measurements. A p-i-n diode consists of highly doped p and n layers with a high resistivity i region in between. The i region is either an intrinsic semiconductor or a very low doped p or n layer. The thickness of the i layers of both detectors are well beyond the 26 μm range of the ^{241}Am alphas used in this study. The p-i-n diodes used in these experiments, the UV100 and the YAG444, are planar diffused silicon

photodiodes. The i region of the UV100 and the YAG444 diodes are low doped n and p layers, respectively. Each p-i-n diode is normally operated at zero or reverse bias. The width of the depletion layer could be controlled by changing the value of the applied bias.

Any electron-hole pair created in the depletion region will be separated and collected efficiently by the electric field. The major portion of the depletion region lies on the lightly doped high resistivity side of the junction. Charges created outside the depletion region are collected by either funneling, diffusion, or both. Both the UV100 and YAG444 are optical sensors and, as such, have sensitive junctions with areas which are much larger than those typical of microelectronic devices. While optical sensors do not upset as such, radiation-induced noise is an important concern in certain environments including space. The active area of the UV100 is 5.1 mm^2 and the active area of the YAG444 is 1.0 cm^2 . In this experiment, the device surface was aligned normal to the beam path while the energy-deposition spectra are recorded by the pulse-height analyzer (PHA). The PHA data was recorded on digital tape and floppy disks.

Two sets of measurements were carried out. In the first set, the pulse-height spectrum obtained with 5.3 MeV alphas from an ^{241}Am source were used to estimate the thickness of the sensitive volume corresponding to the total charge collection. The peak position obtained from the energy-deposition spectrum was converted to a thickness value using range-energy tables. This step was repeated over a range of different bias values including forward and reverse bias. The bias was applied through the preamplifier circuit. In the case of forward bias where small but significant currents flow, a major fraction of the bias drop is across resistors inside the preamplifier and only a small fraction of the voltage drop is across the detector. The current increases dramatically as the voltage approaches forward bias, and there is eventually no further decrease in the peak position with increased bias. At this point the charge collection should be dominated by diffusion. Moreover, the noise in the spectrum increases dramatically at forward bias. The important parameters in the measurements are the peak positions measured on the ordinate in fig. 2 at reverse bias and at forward bias because the relative contributions of the drift and diffusion components of the charge collection can be determined from them. The ordinate value at forward bias provides the component corresponding to diffusion while the value at reverse bias is the sum of the drift and diffusion components.

The second set of measurements tested the CUPID simulation codes [3] against experiment. For this set, the pulse-height spectra were recorded while the devices were exposed to proton beams from the Harvard Cyclotron. The proton measurements were carried out

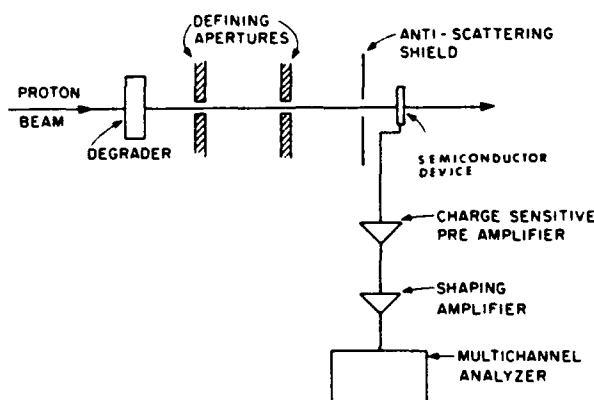


Fig. 1. Experimental configuration for proton irradiations of a semiconductor device.

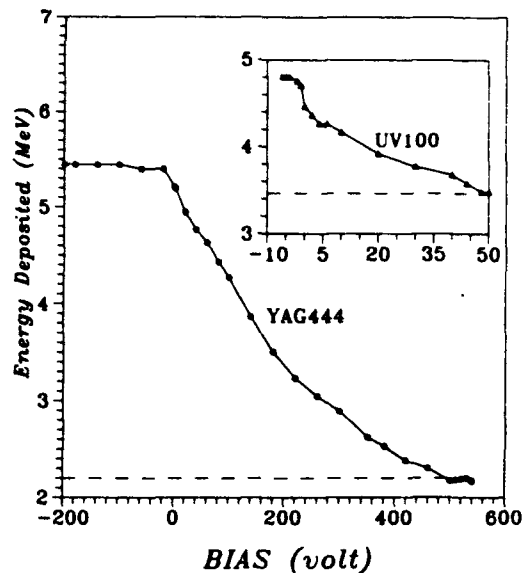


Fig. 2. The position of the peak in the energy-deposition spectra obtained with ^{241}Am alphas versus the bias voltage applied through the preamplifier for the UV100 and YAG444. The energy deposition can be converted to equivalent thickness of charge collection using range-energy tables.

at zero and reverse bias, values for which the depletion widths are given by the manufacturer.

3. Results

Table 1 lists the equivalent thicknesses for the charge collection mechanisms (drift, funneling and diffusion) of two p-i-n diodes (the UV100 and the YAG444). These numbers are calculated using the equations in ref. [9]. The sum of the three thicknesses will give the total thickness of the sensitive volume for each device. The critical charge and the dimensions of the sensitive volume are required by most of the existing codes for calculating the single event upset rate in space. The area is taken to be the area of the junction.

The charge collection obtained with alpha particles was measured as a function of the reverse and forward bias voltages. Fig. 2 shows the peak channel from the alpha spectra plotted versus the applied voltage for the UV100 and the YAG444. It shows that the amount of energy deposited decreases with increasing bias, presumably because of the decrease in the depletion width. The peak channel of the alpha spectrum corresponds to the most probable value of the energy deposited. This value is convertible to the charge collected or the equivalent charge collection length. At the highest nominal forward bias (+50 V for UV100 or +560 V for YAG444) the current increases sharply and the measured energy deposited no longer decreases with increasing bias. At this forward bias the contributions from charge collected by drift should be minimal and the contribution of diffusion dominates the collection mechanisms. The horizontal dashed line which best represents this region is extended to intersect the y-axis in fig. 2. The value at this point of intersection represents the energy deposition corresponding to charge collection by diffusion. This value can be converted to a corresponding thickness using range-energy tables. The value obtained for the UV100 is 18 μm . The theoretical value obtained using eq. (1) is 14 μm . The difference between the theoretical and experimental value is just over 20%. The corresponding values for YAG444 are 14 and 12 μm , a difference of 14%.

The thickness of the depletion region of the UV100 at zero bias is 6.0 μm and the funneling length should be 2.0 μm according to ref. [6]. Adding these values to the value of the thickness corresponding to diffusion, one obtains the total theoretical equivalent thickness of the sensitive volume of the UV100. The value obtained, 22 μm , agrees with the thickness of 23 μm estimated from the alpha-deposition spectrum for the same device at zero bias.

The thickness of the depletion width at zero bias for the YAG444 is 22 μm and the funneling length is 66 μm using Hu's model [6]. The equivalent diffusion thickness is estimated to be 14 μm using eq. (1). The total thickness should therefore be 102 μm . Unfor-

Table 1

The equivalent thicknesses for the charge collection mechanisms (drift, fast drift or funneling and diffusion) of p-i-n diodes (UV100 and YAG444). The third column represents the measured thickness of the sensitive volume using the alpha deposition spectrum.

Device type	Bias voltage [V]	Alpha measured [μm]	Depletion width [μm]	Funneling length [μm]	Thickness equivalent diffusion [μm]	Total thickness [μm]
UV100	0.0	23.4	6.0	2.0	14.3	22.3
UV100	-5.0	N/A	22.0	6.6	14.3	42.9
YAG444	0.0	N/A	22.0	66.0	14.0	102.0

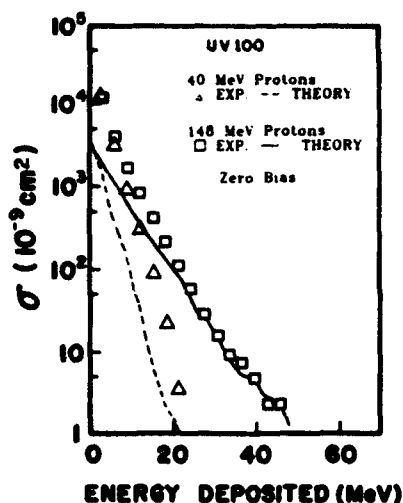


Fig. 3. Comparison between experimental measurements and the CUPID code simulations at 0 V UV100 p-i-n diode exposed to 40 and 148 MeV incident proton energies. The ordinate is the cross section for depositing at least the amount of energy given by abscissa.

tunately no experimental measurements could be done for the total thickness because of the short range of alphas from ^{241}Am which is only about 26 μm .

An indirect test of the thickness of the equivalent sensitive volume can be obtained by comparing measurements obtained with energetic protons with simulation calculations carried out using the dimensions of the sensitive volume estimated above. The area of the sensitive volume is assumed to be the area of the junction. Fig. 3 shows CUPID calculations of the integral cross section for collecting at least some value of charge versus that value of the charge, where the charge collected is given in energy deposition units (1 MeV = 44 fC). The area and the thickness of the sensitive volume are inputs to the code besides the energy of the incident protons. The experiments were carried out at zero bias and the values of the thickness of the sensitive volume from table 1 were used in the CUPID simulations. The agreement between the simulation and the experimental charge-collection spectra for the UV100 shows that these techniques provide values of the dimensions of the sensitive volume which are useful in simulations even for large area devices.

The comparison for -5.0 V are shown in fig. 4. The total equivalent thickness for the UV100 at -5 V is 43 μm . Again, the experimental values exceed the theoretical at low incident energies. The algorithms in CUPID are only designed for incident energies above 50 MeV. However, the model appears to provide a reasonable lower limit to the energy-deposition spectra even at energies below 50 MeV. The close agreement at higher energies is evidence for the validity of our estimate of

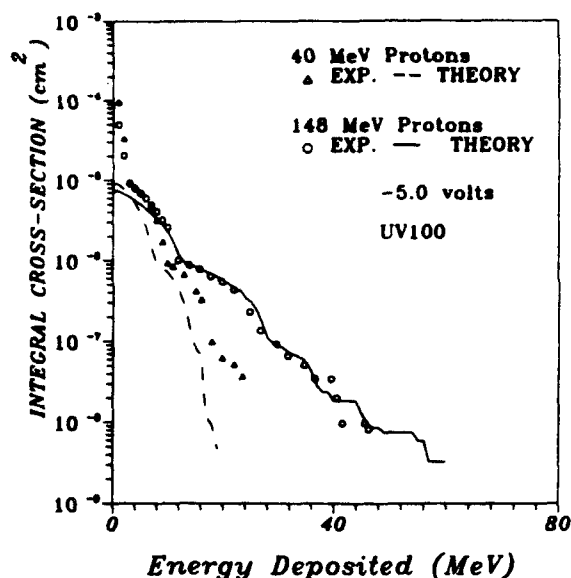


Fig. 4. Comparison between experimental measurements and the CUPID code simulations at -5.0 V for UV100 p-i-n diode exposed to 40 and 148 MeV incident proton energies.

the thickness as well as the usefulness of the codes. Fig. 5 compares the plots of integral cross section versus the energy deposited (charge collected) obtained from CUPID simulations with the curve obtained from experimental measurements with the YAG444. There is considerably poorer agreement at 148 MeV in this case than was true for the UV100. The theoretical shapes are

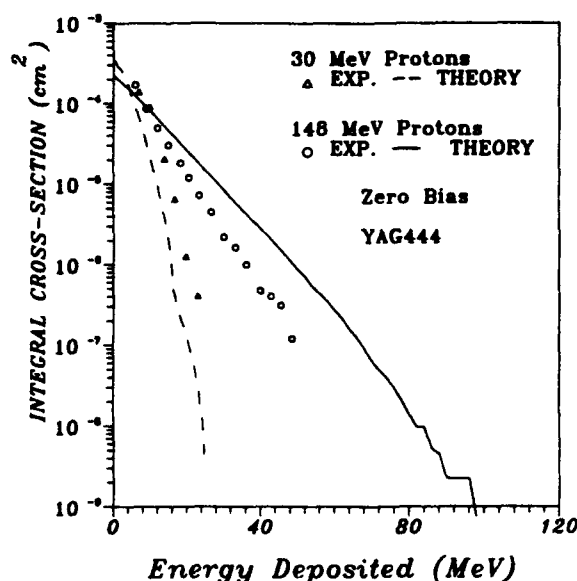


Fig. 5. Comparison between simulations using the CUPID codes and experimental measurements at 0 V bias for the YAG444 p-i-n diode exposed to 30 and 148 MeV incident proton energies.

XVII. RADIATION PROCESSING

similar to the experimental spectra at low incident proton energies for both detectors but there is a significant difference in the number of events. At 148 MeV the number of events are in reasonable agreement, but the shape differs from the experimental spectrum for the YAG444 while the fit is excellent for the UV100.

4. Conclusion

Comparison between the thickness measured from the alpha spectrum obtained with the UV100 at zero bias and the value estimated by using the equations in ref. [9] shows good agreement which implies that the technique can be used to estimate the thickness for partially depleted devices, particularly if the doping concentration is well defined. The bias voltage and the area of the junction are also required. A procedure for separating the diffusion component from the drift component of the charge collection is described. Reasonable agreement with the expressions given in ref. [9] is obtained. The agreement of the charge collection measurements with the CUPID calculations, which use the dimensions of the sensitive volume predicted by the technique, confirms the ability of the CUPID code to simulate the energy deposition for partially depleted devices. The poor agreement for the partially depleted YAG444 device at zero bias may be due to an error in the correct thickness of the equivalent sensitive volume. The thickness of the sensitive volume of the unbiased

YAG444 is greater than the range of the alphas from ^{241}Am and so could not be measured directly with the alphas from a radioactive source.

Acknowledgements

The help of Andy Koehler and his staff at Harvard Cyclotron with proton exposures is greatly appreciated.

References

- [1] D. Binder, E.C. Smith and A.B. Holman, *IEEE Trans. Nucl. Sci.* NS-22 (6) (1975) 2675.
- [2] J. Pickel and J.T. Blandford, Jr., *IEEE Trans. Nucl. Sci.* NS-27 (2) (1980) 1006.
- [3] P.J. McNulty, G.E. Farrell, R.C. Wyatt, P.L. Rothwell, R.C. Filz and J.N. Bradford, *IEEE Trans. Nuc. Sci.* NS-27, (6) (1980) 1516.
- [4] C.M. Hsieh et al., *Proc. IEEE Int. Reliability Phys. Symp.*, Orlando, FL, 1981, p. 38.
- [5] S.M. Sze, *Physics of Semiconductor Devices*, 2nd ed. (Wiley-Interscience, New York, 1981).
- [6] C. Hu, *IEEE Electron Device Lett.* EDL-3 (1982) 31.
- [7] F.B. McLean and T.R. Oldham, *IEEE Trans. Nucl. Sci.* NS-29 (1982) 2018.
- [8] W.G. Abdel-Kader, P.J. McNulty, S. El-Teleaty, J. Lynch and A.N. Khondker, *IEEE Trans. Nucl. Sci.* NS-34 (1987) 1300.
- [9] P.J. McNulty, W.G. Abdel-Kader and J.E. Lynch, *Nucl. Instr. and Meth. B*, to be published.

APPENDIX C

CHARGE COLLECTION IN GaAs H₁₂L BIPOLAR TRANSISTORS

CHARGE COLLECTION IN HI^2L BIPOLAR TRANSISTORS

P. J. M'Nulty, M.H. Yaktieen, J.E. Lynch and W. M. Weber*
Clarkson University, Potsdam, NY 13676

and

Clemson University, Clemson, SC 29634-1911

and

H.T. Yuan and J.F. Salzman

Texas Instruments

Dallas, TX 75266

ABSTRACT

Charge collection measurements were carried out on HI^2L transistors in GaAs in order to determine the thickness of the equivalent sensitive volume to be used in calculating SEU rates for this technology and to set a new lower limit to the critical charge. The measurements were in the form of pulse-height spectra measured between the base-emitter and collector-emitter contacts upon exposure to energetic protons, alphas, and sulfur ions. The sulfur data is consistent with the SEU-sensitive junction being the base-emitter junction with an equivalent sensitive volume of thickness $0.1 \mu m$ for high LET particles. This value of the thickness of the equivalent sensitive volume is a factor of two thinner than the value previously used to estimate error rates in space and is a factor of three thinner than estimates based on alphas which have lower LET. Comparison of the proton charge-collection data with earlier SEU measurements results in a revision of our estimate of the lower limit to the critical charge for HI^2L gate arrays to a value which is higher than previous estimates by more than a factor of two. The combination of reduced charge collection and higher critical charge implies that this technology will be considerably harder to SEUs than previously believed.

INTRODUCTION

Texas Instruments' HI^2L bipolar GaAs gate arrays configured as shift registers have been shown to be very resistant to single event upsets (SEU) induced by energetic ions with moderately high values of linear energy transfer (LET) at normal incidence (1). The explanation proposed for this hardness to SEUs was reduced charge collection at the base-emitter junction due to it being a heterojunc-

tion. The heterojunction allows higher doping and, hence, a thinner base. Inefficient charge collection prevents the contribution to the base current from being sufficient to both forward bias the base-emitter junction and to steer current from one transistor to the next. The gate arrays were laid out in crystals grown by molecular beam epitaxy (MBE) and there is the question of whether the charge collected would be similarly reduced in crystals grown by MOCVD. A schematic of the HI^2L transistor is shown in Fig.1. The base-emitter junction consist of a heterojunction while the base contact forms a junction with the emitter in the AlGaAs layer.

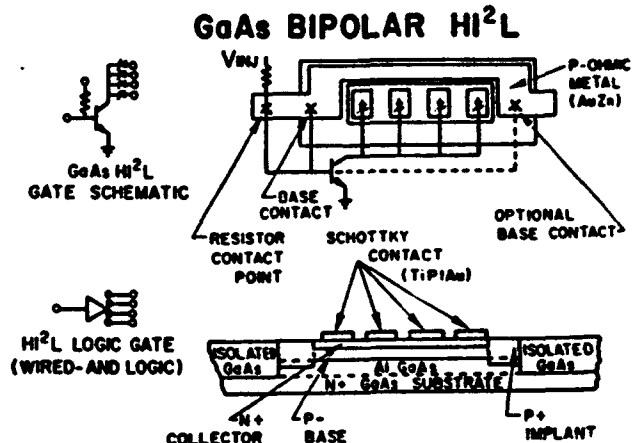


Fig.(1) Schematic of HI^2L transistor.

Only two SEUs were observed in the earlier experiments and both were coincident with power surges associated with shutter openings, one of which tripped other computer equipment. The paucity of SEU events made it impossible to determine the error rates to be expected in space with this technology because the values of the thickness of the equivalent sensitive volume (SV) and the critical charge to be used in calculations were left unresolved. Even if both events were accepted as valid, i.e. induced by ions, the resulting cross sections are smaller than expected from the lateral dimensions of the sensitive

* Currently at the University of Arizona, Tucson, AZ 85721

junction. The thickness of the equivalent SV was estimated from design considerations to be about $0.2 \mu\text{m}$ and when this value was combined with lower limits on the critical charge determined from heavy-ion measurements and used in CREME (2) and CRUP (3) simulations to determine upper limits on the error rates to be expected in Adams' 90% worst-case environment (2), the results (1) suggested that the device is intrinsically hard with most of the simulated errors resulting from ions traversing the SV at large angles with respect to normal incidence.

This paper reports on charge collection measurements made on HI^2L transistors exposed to particles of different LET and subjected to the nuclear reactions induced by energetic protons. Direct measurements of charge collection at the junction following traversal by beam particles of known charge, mass, and energy are used to determine the vertical dimension of the SV associated with the junction. Test structures implemented in crystals grown by both MBE and MOCVD techniques were studied to determine whether the amount of charge collected differs between the two crystal types. Because the base structures are so thin in these devices, charged particles have to have long path lengths within the SV in order to deposit much energy. Since recoiling nuclear fragments from fragmentation reactions have high LET and traverse the junction at all angles of incidence, they provide an efficient method of inducing large pulses across the junction. The pulse height spectra of charge collected at the base-emitter junction during proton irradiation were measured and the data plotted as an integral cross section for collecting at least some value of charge Q versus Q . The critical charge, Q_c , can then be estimated by assuming Q_c to be the value of Q for which the cross section for depositing at least Q_c equals the SEU cross section per transistor for the functioning device. In other words, if n SEU events are observed in a given exposure and a charge-collection spectra is obtained over an identical exposure, then we assume that the n largest charge-collection events, measured in the same exposure, would initiate SEUs and the lowest value of Q obtained for these n events becomes the critical charge. Unfortunately, since no SEUs had been observed in the earlier proton irradiations, the charge-collection spectra could not be used to determine the critical charge directly. However, the data could be used to establish a new lower limit on its' value.

EXPERIMENTAL MEASUREMENTS

In this experiment, charge collection at the base-emitter junction was measured for alpha particles from an Americium source in two ways: First, the time profiles of typical pulses were measured using a Tektronix 7912AD Transient Digitizer. The device under test was biased through a Tektronix FET probe (Model P6201) with the output from the probe connected to the digitizer. Alpha traversals initiated transient pulses across the biased junction which were recorded by the digitizer circuit. The measurements were carried out in a heavily shielded room with batteries used to apply biases. These precautions were necessary to reduce the reception of electromagnetic noise from the power line and other sources. The resolution of the system was limited by the probe but remained under 2 nsec. Figure 2 shows a typical sequence. The voltage given by

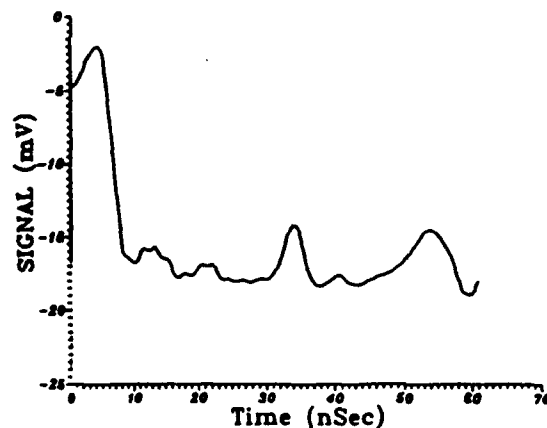


Fig.(2) Time profile of pulse obtained with transistor exposed to 5.46 Mev alphas.

the ordinate is proportional to the current at that time interval after the alpha strike. The large signal following $t = 0$ represents the charge collected immediately after an alpha strike. While the pulse profile shown reflects the time constants of the measuring network as well as the sequence of charge collection, the measurements do establish that essentially all the charge collected from an alpha strike is collected within 10 nsec. Beyond 10 nsec the signal is indistinguishable from the background signal obtained with the source removed. Since all or most of the charge is collected promptly, slower circuitry can be used to measure the total charge collected in each event.

The experimental configuration shown in Fig. 3 was used to measure the total charge collected in individual events. This is the standard configuration

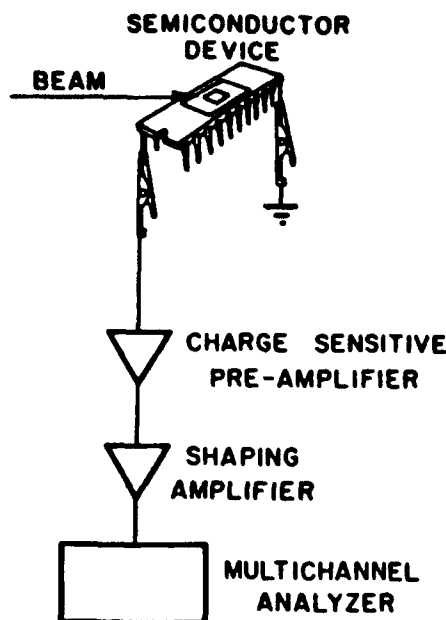


Fig.(3) Schematic of setup for charge collection measurements on test-structure transistor.

for measuring events in nuclear solid state detectors. A charge-sensitive preamplifier was connected across the leads to the base-emitter junction with the base biased at 0.8 V through the preamplifier and the emitter connected through the substrate to ground. The collector was biased at 2 V. The signals from the preamplifier were amplified and then sorted according to pulse height in the PHA (pulse-height analyzer). The location of an event on the PHA, i.e. the voltage of each signal emerging from the amplifier, is proportional to the charge collected in that event. The PHA system was calibrated using fully depleted surface barrier detectors and pulsed (See Ref. 6). Note that charge collection is often expressed in terms of the more familiar units of energy deposition (MeV) used here. To convert from MeV to pC divide by 30.

Exposures to 148 MeV and 70 MeV protons were carried out at the Harvard Cyclotron. For the proton irradiations the transistors were inside an aluminum can with walls 0.025 in. thick. The irradiations to 32.9 MeV sulfur ions were carried out under vacuum at the Tandem Van de Graaff accelerator at the University of Pittsburgh. The alpha irradiations were carried out with an Americium source under vacuum at Clarkson University and repeated at each of the accelerator facilities as a test that the calibration was maintained. All exposures described in this paper were carried out at normal incidence.

RESULTS

Figure 4 shows the charge-collection spectrum measured across the base-emitter junction during exposure of a single transistor to alphas. The values of charge collected are traditionally expressed in terms of the units of energy deposited, MeV. The median value of the charge collected expressed this way is 0.074 MeV where $1\text{ MeV} = 33\text{ fC}$. The width of the peak in the charge-collection spectra shown in Fig. 4 is not due to noise or leakage current which was determined to be below 1 Kev by removing the alpha source. It may be the combined result of the differences in path lengths through the sensitive volume due to the angular spread of the alphas emerging from the source, differences in energy deposition due to straggling, and possible variation in charge collection due with location of the point of traversal within the base. The corresponding spectrum obtained with sulfur ions which have a smaller angular dispersion and generate far more electron-hole pairs

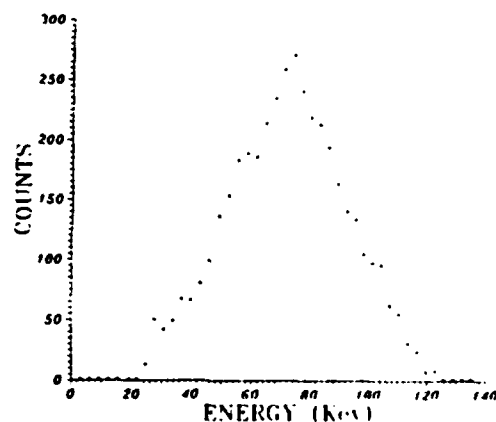


Fig.(4) Typical pulse-height spectra of pulses measured using setup shown in Fig. (3) with the device exposed to alphas.

per traversal is shown in Fig. 5a. It has a narrower peak than the alpha spectrum.

Models which use the computational artifice of replacing each SEU-sensitive junction by an equivalent SV assume either that the charge collected at the junction in energy-deposition units equals the product of the LET of the particle in MeV per micron and its' pathlength through the SV or they do a comparable calculation using range-energy tables (2-4). Therefore, the thickness of a thin SV can be obtained from the ratio of the energy deposited and the LET of the particle at the level of the junction. The value of the thickness obtained this way and the spread in thickness corresponding to the spread in energy depositions observed in Fig. 4 are listed in Table 1.

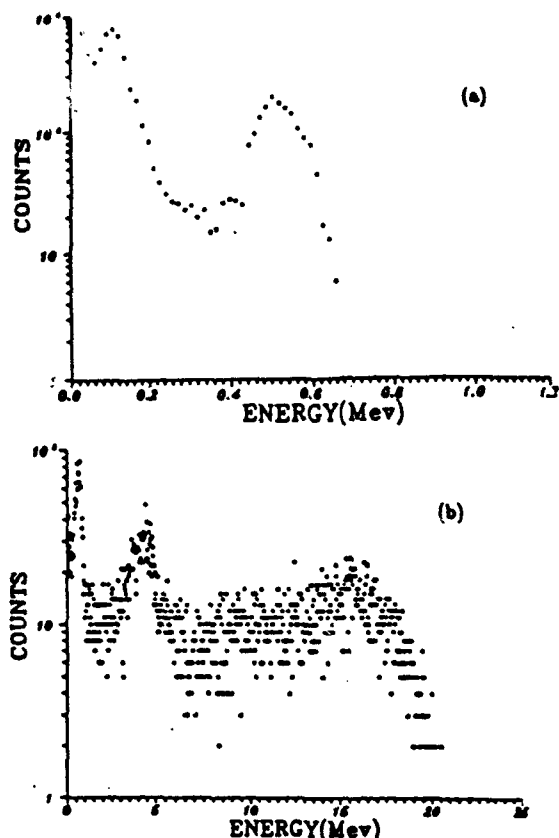


Fig.(5) Charge collection pulse-height spectra for individual HPL transistor exposed to 32.9 MeV Sulfur ions obtained for measurements across a) base-emitter junction and b) collector-emitter contacts.

DEVICE TYPE	NUM. OF TRANS.	FANOUT	BEAD.	INCIDENT ENERGY (MeV)	ENERGY DEPOS. (MeV)	EQUIV. THICK. (μm)
Indiv. Trans.*	1	1	ALPHA	3.29	0.074	0.174000
Sh. Trans.*	20	4	ALPHA	3.29	0.004	0.004000
Sh. Trans.+	20	1	ALPHA	3.29	0.004	0.004000
Indiv. Trans.*	1	1	SULFUR	32.9	0.51	0.114001

* MBE
+ MOCVD

Table(1) Charge collection and equivalent thicknesses.

Similar measurements were carried out for arrays of nineteen transistors. Two arrays were tested. The transistors in one array had a fan-out of 4, meaning that each transistor had four Schottky diode connections as shown in Fig. 1, while the other array had one long diode per transistor. Table 1 shows no difference in charge collection between the two fanouts.

There is about a 13 % difference between the energy deposited in the MBE and MOCVD materials. This may be due to differences in the junctions or due to the fact that there are nineteen transistors in parallel in the MOCVD material as opposed to a single transistor in the MBE crystal. Even if the difference between the value of the energy deposited in the individual transistor and the value obtained for the nineteen transistor arrays is attributed entirely to differences in charge collection at MBE and MOCVD heterojunctions, it amounts to less than a 15 % difference. This is important because it means that switching between MBE and MOCVD material which have different doping profiles across the heterojunction results in only small differences in charge collection. Moreover, such a small difference between the single transistor and the arrays of nineteen transistors, gives some confidence that charge collection data obtained with test structures does represent the charge collection to be expected in functioning circuit elements.

The charge-collection pulse-height spectra obtained for a single HPL transistor exposed to 32.9 MeV sulfur ions are shown in Figs. 5a and 5b for measurements across the base-emitter junctions and between the collector and emitter contacts, respectively. There are two peaks in Fig. 5a. One peak represents ion traversals of the base-emitter heterojunction while the other probably represents traversals of the junction in the AlGaAs between the emitter and the base contact (See Fig. 1). We assume in what follows that the higher energy signals represent charge collection at the base-emitter heterojunction because the doping level in the base is lower than in the base contact. Then, the peak at higher energy depositions corresponds to charge collection at the base-emitter junction of 17 fC or an energy deposition of 0.51 MeV. Assuming an LET of 4.8 MeV/ μm (5), this implies an equivalent thickness of the sensitive volume for the base-emitter junction of 0.11 μm . The lower peak is at roughly 3 fC or 0.1 MeV.

The corresponding spectra measured across the collector and emitter contacts is shown in Fig. 5b. The highest peak is at 15.5 MeV. These transistors were designed to have a gain of about 25 between input signals at the base to output at the collector. If one assumes that the signal originates as charge collected across the base-emitter heterojunction and that the gain of the transistor is 25, the 15.5 MeV peak corresponds to collecting 21 fC or

0.6 MeV across the base-emitter junction. If, again, an LET of 4.8 MeV/ μm is assumed, one obtains an equivalent thickness of the SV of 0.13 μm in reasonable agreement with the value of 0.11 μm obtained directly off the base-emitter junction. Both the base and collector signals appear, therefore, to be dominated by the charge collected across the base-emitter junction. The spectra measured at the collector has less definition than that measured at the base, probably the result of measuring from only one of the four Schottky contacts (See Fig. 1). This introduced a wide dispersion in path lengths travelled by charge reaching the collector.

The peak values of the charge collected for the different irradiations are compared in Table 1 in units of energy deposition along with the corresponding values of the equivalent thickness of the SV. The value of the equivalent thickness obtained for the sulfur irradiations is significantly smaller than that obtained for alphas on the same transistor. More data at different LET values are needed to confirm that the thickness decreases with increasing LET but a similar decrease with increasing LET has been reported for silicon devices (6). Such a decrease would indicate a significant increase in recombination with increasing LET.

The pulse-height spectrum obtained from measurements of charge collection across a single base-emitter junction exposed to 70 MeV protons is shown in Fig. 6. This is an integrated spectrum with the number of events in which energy E was deposited plotted versus E. The largest deposit of energy measured during an exposure of the transistor to a fluence of 7.1×10^{11} protons/cm² is 9.4 MeV or 313 fC. The absence of errors in a previously reported

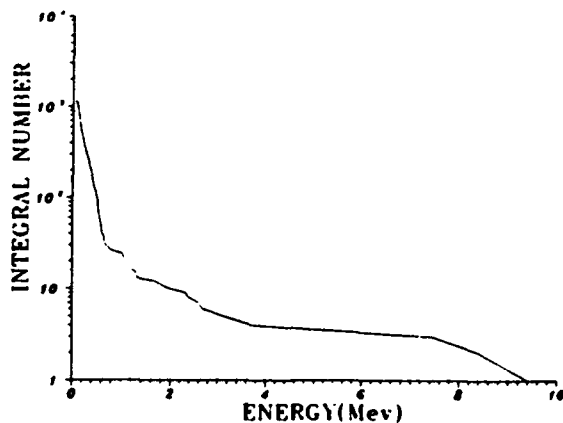


Fig.(6) Charge collection pulse-height spectra obtained across base-emitter junction for transistors exposed to 70 Mev protons.

irradiation of a 4K gate array containing 320 SEU-sensitive transistors would suggest that a lower limit to the critical charge can be set at least at the highest value measured in this experiment 313 fC.

PROJECTED ERROR RATES

The new lower limit on the critical charge and the new values for the thickness of the sensitive volume to be associated with the base-emitter junction can be used to improve our estimate of the error rates to be expected in space. First, the errors per bit-day for Adams' 90 % worst-case environment can be obtained from Peterson's formula, as modified for GaAs in Ref. 1. Using the lateral dimensions of the base-emitter junction given in Ref. 1 as those of the SV and the thickness of the SV obtained from this work, we obtain error rates of 6.7×10^{-9} , 4.3×10^{-8} , and 5.7×10^{-8} errors per bit day for thicknesses of 0.11 μm , 0.28 μm , and 0.32 μm , respectively. The small difference between the second and third values suggest that switching between MBE and MOCVD should only have a small impact on the error rates to be expected in space if charge collection is the only factor involved. The large difference between the first error rate and the other two means that the uncertainty in which value of the thickness of the SV should be used introduces large uncertainties in the error rate.

The dependence of the error rate in Adams' 90 % worst-case environment on the value of the critical charge is illustrated in Fig. 7 which compares plots

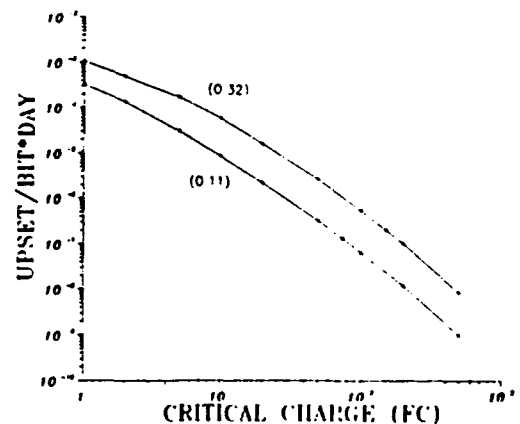


Fig.(7) Error rate versus critical charge for H^2L transistor with thicknesses of 0.11 μm and 0.32 μm .

of the error rates given by the CREME codes (2) for a SV having the lateral dimensions of the base and thicknesses of 0.11 and 0.32 μm . If we assume that the 0.11 μm value of the equivalent thickness is more typical of the high LET particles which cause upsets, the error rate from Fig.7 for a critical charge of 313 fC is 3.2×10^{-9} . A more conservative estimate obtained from using the thickness determined from the alpha data, i.e. the curve labeled 0.32 in Fig. 7, is 2.5×10^{-8} . Comparison of the two curves in Fig. 7 provides further illustration that a large uncertainty in error rate over a wide range of critical charge results from the lack of certainty regarding the thickness of the sensitive volume.

SUMMARY

Comparison of charge collection measurements across the base-emitter junction carried out on HI^2L transistors does not show significant differences in charge collection between junctions in MBE and MOCVD grown crystals. The pulse-height spectra appear to confirm that the base-emitter junction has a thin sensitive volume associated with it. Moreover, the values of the thickness of the sensitive volume obtained with low-LET alphas are greater than the value obtained with 32.0 MeV sulfur ions which has a much higher LET. This may be the result of increased recombination along the track of high LET particles. Since long exposures to 63 MeV protons do not result in SEUs (1) and measurements reported here show charge collection pulses of as high as 313 fC during less intense proton exposures at similar energies, one can set 313 fC as a new lower limit to the critical charge. Using this value for the critical charge and the thickness of the sensitive volume obtained from the sulfur irradiations in CREME calculations, one obtains an upper limit to the projected error rate in Adams' 90 % worst-case environment of 3.2×10^{-9} , a value much lower than our previous estimate of 7×10^{-7} . Ion irradiations at higher LET will be necessary to determine the actual critical charge for these shift registers. Further studies of charge collection as a function of LET and angle of incidence are planned.

ACKNOWLEDGEMENTS

This work supported by the Defense Nuclear Agency under contract DNA001-86-C-0076. We gratefully acknowledge help and advice with the digitizer measurements from G.K. Ovrebo of Harry Diamond Lab.

Help from Art Campbell and Al Knudson of NRL with the heavy ion measurements is also gratefully appreciated as was the help and cooperation of the staffs of the Harvard Cyclotron and the Pittsburgh Tandem Van de Graaff facility.

References

- [1] J.F. Salzman, P.J. McNulty, and A.R. Knudson
IEEE Trans. Nucl. Sci. NS-34,
- [2] J.H. Adams Jr. IEEE Trans. Nucl. Sci. NS-30,
4475 (1983).
- [3] P. Shapiro Naval Research Laboratory Report
Memorandum Report No. 5901 (1986).
- [4] G.E. Farrell and P.J. McNulty, IEEE Trans.
Nucl. Sci. NS-29, 2012 (1982).
- [5] U. Littmark and J.F. Ziegler *Handbook of Range
Distributions for Energetic Ions in All Ele-
ments*, J.F. Ziegler Ed. (Pergamon Press, New
York, 1980).
- [6] J.E. Lynch, P.J. McNulty, and Mohamed Yak-
tween, IEEE Trans. Nucl. Sci., this issue.

APPENDIX D

CHARGE COLLECTION IN PARTIALLY DEPLETED GaAs TEST STRUCTURES INDUCED BY ALPHAS, HEAVY IONS, AND PROTONS

Charge collection in partially depleted GaAs test structures induced by alphas, heavy ions, and protons

Shadia El-Teleaty,^{a)} W. G. Abdel-Kader, P. J. McNulty, and M. H. Yaktien
Department of Physics and Astronomy, Clemson University, Clemson, South Carolina 29634-1911

(Received 4 June 1990; accepted for publication 10 September 1990)

Charge-collection measurements on test structures were carried out for events induced by alphas, heavy ions, and proton-induced nuclear reactions over a variety of bias values and for two doping levels. Analysis of charge-collection pulse-height spectra provides the shape and dimensions of the sensitive volume associated with the single-event upset (SEU) sensitive junctions. The critical charge is determined by the circuit design. The critical charge and the dimensions of the sensitive volume are required by all the existing codes dealing with the calculation of SEU rates in natural space environments. The dimensions of the sensitive volume determined for some Rockwell GaAs test structures were used in simulations of charge collection by proton-induced nuclear reactions using the Clemson University Proton Interactions in Devices codes. Comparison of the results with experimental data yields agreement.

I. INTRODUCTION

The mechanism by which single-event upset (SEU) events are initiated in Si and GaAs circuits is the collection of more than a critical charge at a reverse-biased junction within some time interval after the junction is traversed by an ionizing particle. This interval is determined by the time constants of the circuit of which the junction is a part. Circuits can be hardened against SEUs by increasing the critical charge, altering the time constants of the circuit, or introducing fault-tolerant algorithms into the system architecture. However, the application of any of these fixes with a minimum of performance tradeoff requires precise knowledge of the SEU rates to be expected before and after the fix. This, in turn, requires a quantitative understanding of the charge collection at the SEU-sensitive junctions of the circuits.

The Clarkson University Proton Interactions in Devices (CUPID) codes have been shown to accurately predict the charge generation in fully depleted Si surface-barrier detectors over a wide range of incident proton energies where the thickness of the detectors was varied from 2.5 to 97 μm .¹⁻⁴ However, the codes have never been proven to work for GaAs devices nor have they been tested against measurements with partially depleted structures in either GaAs or Si. The codes have been shown to be useful in predicting proton-induced SEUs from first principles for Si devices for which sufficient process information was known and for which sufficient heavy ion data were available. These devices included SEU-sensitive structures which were partially depleted. The approach was to assume the validity of the first-order model used in all SEU algorithms for calculating rates in space,⁵⁻⁷ i.e., represent the SEU-sensitive junction by an equivalent sensitive volume. This sensitive volume extends on both sides of the junction by an amount at least equal to the space-charge layers which make up the depletion region. In order

to be useful in modeling SEU sensitivity, the dimensions of the sensitive volume should be independent of the linear energy transfer (LET) of the incident charged particle. The sensitive volume is a mathematical artifact; its dimensions are chosen such that the charge generated within the sensitive volume equals the charge collected across the junction. This paper presents the first published results from a comparison of CUPID⁴ calculations with charge-collection measurements in GaAs field-effect transistor (FET) struc-

II. EXPERIMENTAL PROCEDURE

The experimental setup used for these measurements is shown in Fig. 1. All the proton exposures were carried out at Harvard University's Cyclotron using protons with incident energies from 25 to 158 MeV. The heavy ion exposures were done using the Tandem Van de Graaff accelerator at the University of Pittsburgh. The GaAs Fat FET test structures are tested for two different types: one lightly doped (N^-) and one heavily doped ($N^- + N^+$). The difference between this study and the previous study³ is that the devices in Ref. 3 were fully depleted Si devices and the only contribution to the charge collected was the drift component

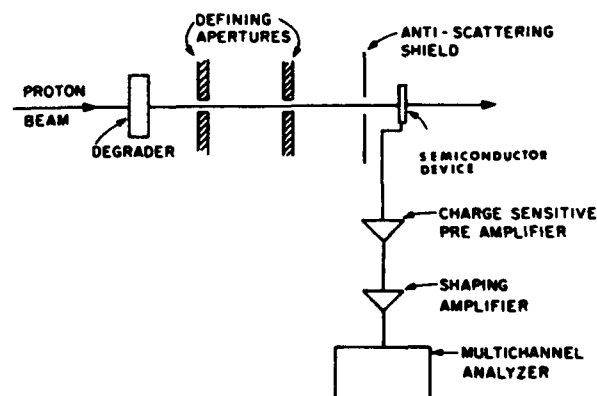


FIG. 1. Schematic diagram of the experimental setup.

^{a)} Presently at Jackson State University, Dept. of Physics and Atmospheric Sciences, Jackson, MS.

due to the collection of electron-hole pairs generated in the depletion region. In this study, the devices are partially depleted and there are two extra components contributing: the field-assisted drift (funneling)^{8,9} and diffusion.¹⁰ Also, the test structures are made from GaAs, not Si.

GaAs Test Structure: The gates of the Rockwell (1K RAM) GaAs MESFET Fat FET test structures¹¹ were negatively biased with the source and drain grounded. Test structures were available with light (N^-) and heavy (N^+) doping under the gate electrode. The Fat FET test structures were much larger in area but otherwise were processed identically to the normal FET used in memory elements. The lateral dimensions of the Fat FET structure are $145 \mu\text{m} \times 350 \mu\text{m}$. The effective thickness of the sensitive volume varies with bias especially when the lighter doping is used because the width of the depletion region depends on the bias across the junction.

Use the CUPID codes to predict the charge collection in partially depleted test-structure devices, it is first necessary to estimate the thickness of the sensitive volume associated with the junction from the pulse-height spectra obtained with exposure to Am^{241} alphas. Figures 2(a) and 2(b) show examples of the charge-collection spectra for GaAs test structures exposed to alphas. The effect of bias has been to shift the peak to larger values of charge collection and to broaden the distribution. Figures 3(a), 3(b), and 3(c) show the spectra from exposure of the heavily doped devices. Here the effect of bias is far less because the width of the depletion region is less sensitive to bias for highly doped materials.

Notice that in both Figs. 2 and 3 there is a pronounced tail of energetic events. Because the data were obtained with small test structures and relatively slow sources, these high-energy pulses are not due to pulse-pileup. These events are believed to be due to enhanced charge collection at the edge of the test structure junction of the type previously observed with microbeams.¹¹

The position of the peak provides a rough estimate of the effective thickness of the sensitive volume. A particle incident on the junction with energy E has a range $R(E)$ which can be determined from Ziegler's Tables.¹² If the charge collected at the junction in energy units ($30 \text{ MeV} = 1 \text{ pC}$) is E_D , then the thickness of the equivalent sensitive volume is given by

$$t = R(E) - R(E - E_D). \quad (1)$$

Similarly, the high-energy tail can be used to estimate the dimensions of the small enhanced-collection regions¹¹ at the edges of the $145 \mu\text{m} \times 350 \mu\text{m}$ structure.

Typical charge collection spectra obtained from exposures to heavy ions are shown in Figs. 4, 5, and 6 for the $N^- + N^+$ test structure. Again, there is evidence of a small number of enhanced charge-collection events. The noise levels were higher inside the vacuum chamber at the Van de Graaff accelerator.

III. RESULTS

Figures 7(a) and 7(b) plot the position of the peak of the charge collection spectra versus the incident particle's

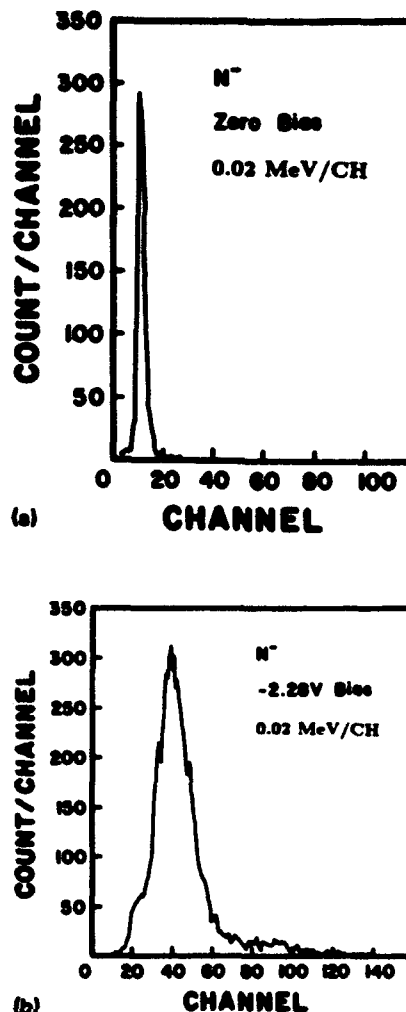


FIG. 2. Charge-collection spectra for N^- test structure exposed to Am^{241} alphas at different gate biases (a) 0 V and (b) -2.28 V .

LET for exposures carried out at normal incidence. The heavy ion data were all taken at the Tandem Van de Graaff Facility while the alpha data were obtained in the relatively noise-free environment of a vacuum chamber in our laboratory. The solid curve represents a linear fit to all the data including the origin. The fit is consistent with the peak position in the charge collected being proportional to the LET. The slope of the curve is the product of the density and the thickness of the sensitive volume. Proportionality between charge collected and LET is an assumption made for all current algorithms for calculating SEU rates. The thickness of the equivalent sensitive volume obtained this way includes contributions to the charge collection from funneling and diffusion and is, therefore, thicker than the depletion width. The assumption that the charge collected at the junction that generated within a sensitive volume whose dimensions are independent of LET appears to be reasonable for GaAs over the range of the LET values corresponding to the abundant cosmic rays. Figure 8 shows how the energy deposition changes with the bias voltage for different ion exposures. The alpha exposures and charge-collection measurements were carried out using a shielded $4.8 \text{ MeV } \text{Am}^{241}$ source.

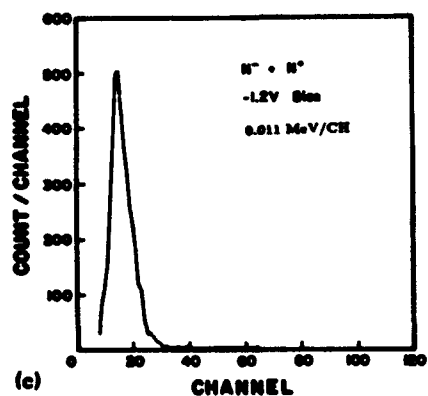
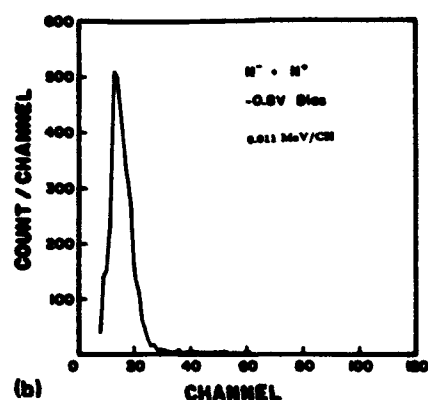
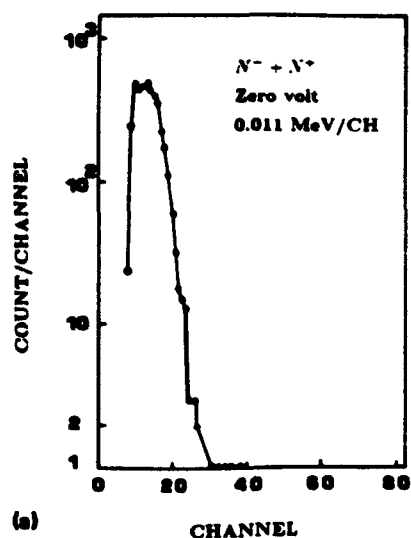


FIG. 3. Charge-collection spectra for $N^- + N^+$ test structure exposed to Am^{241} alphas at different gate biases (a) 0 V, (b) -0.8 V, and (c) -1.2 V.

If the reverse-biased junction is to be replaced by a sensitive volume in SEU-rate predictions, the charge collected must be proportional to the product of the LET and the path length through the sensitive volume. The path length increases for small angles with the secant of the angle of incidence measured with respect to the normal. This proportionality between the charge collected and the product of the LET and the secant of the angle of incidence is confirmed in Fig. 9 for another GaAs test structure, a heterojunction used

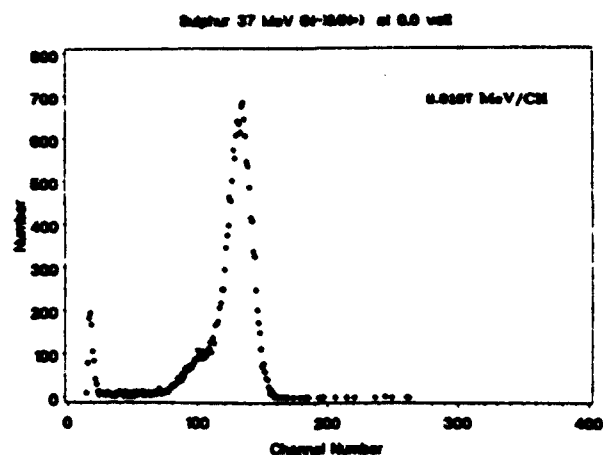


FIG. 4. Charge-collection spectra for $N^- + N^+$ test structure exposed to 37 MeV sulphur at 0 V.

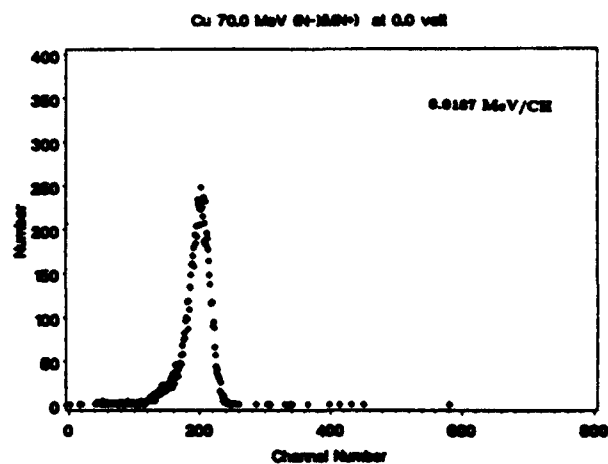


FIG. 5. Charge-collection spectra for $N^- + N^+$ test structure exposed to 70 MeV copper at 0 V.

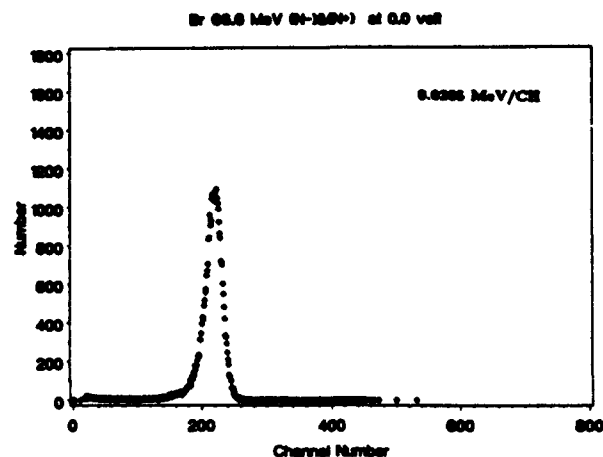


FIG. 6. Charge-collection spectra for $N^- + N^+$ test structure exposed to 66.6 MeV bromine at 0 V.

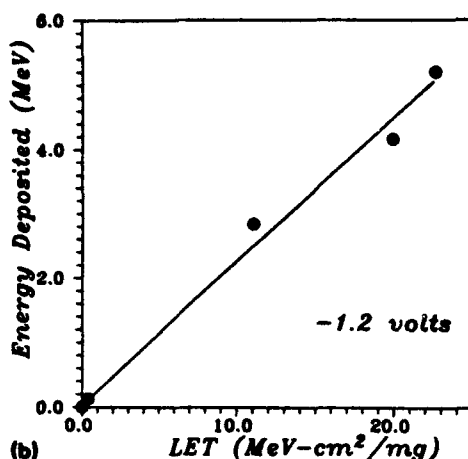
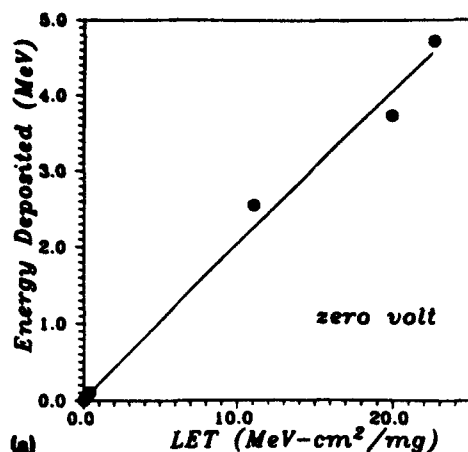


FIG. 7. Relative charge-collected across the gate vs the LET of the incident particle for an $N^- + N^+$ GaAs test structure with bias of (a) 0 V and (b) -1.2 V.

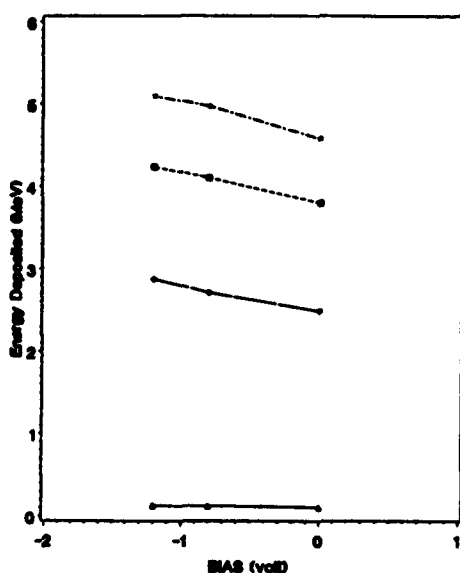


FIG. 8. Energy deposition across the junction vs the applied bias on the gate for different incident particles. The solid triangle, solid diamond, solid square, and star represent alpha, sulphur, copper, and bromine ions, respectively.

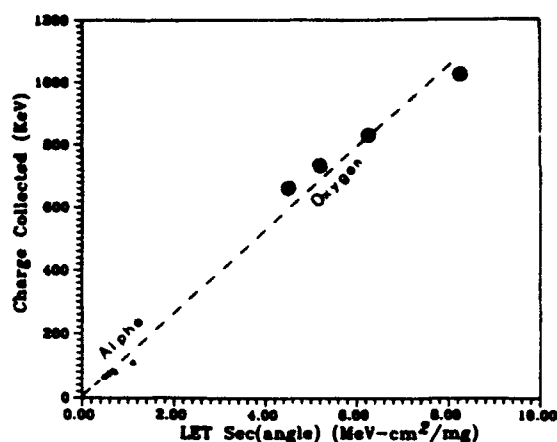


FIG. 9. Relative charge collected (energy deposited) across the gate vs the product of the LET and the secant of incidence for 4.8 MeV alphas and 20 MeV oxygen. The dashed line represent the linear fit for the data. The solid triangles and solid circles represent the experimental data for alpha and oxygen, respectively.

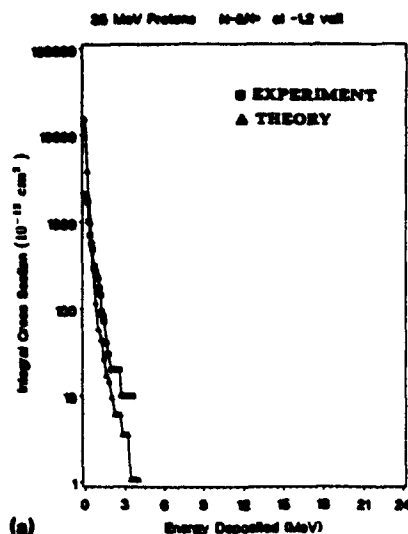
in Texas Instruments HI2L bipolar gate array. The data were taken with 4.8 MeV alphas and 20 MeV oxygen nuclei at different angles of incidence.

Figures 10 and 11 compare the charge-collection spectra obtained for energetic protons incident on the two test structures with theoretical simulations of the energy deposition in the respective sensitive volume as a result of proton-induced spallation reactions. The simulations were carried out using the CUPID codes for GaAs. The comparisons for the heavily doped $N^- + N^+$ test structures are shown in Figs. 10(a)–10(c), while those for the lightly doped N^- are shown in Figs. 11(a) and 11(b). The GaAs version of the CUPID codes have a problem at lower incident energies (less than 70 MeV) because the wrong total number of events is predicted. For this reason, the comparisons below 70 MeV are done by normalizing the model calculations to the total number of events to be expected in the sensitive volume plus surround obtained from the known total cross section. The normalization is not required for higher energies. The fit between theory and experiment is good.

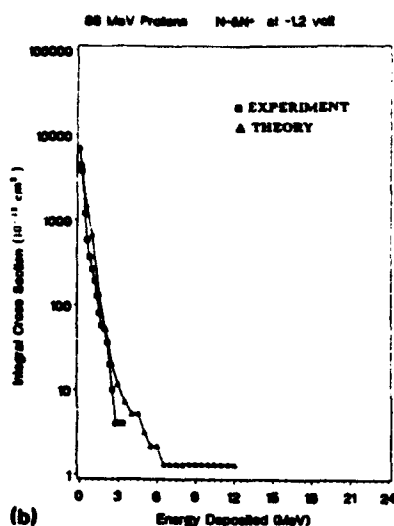
An interesting feature of the comparisons is that at low incident proton energies the model predicts that the pulse-height spectra falls with increased energy depositions more sharply than the experimental data.

IV. CONCLUSION

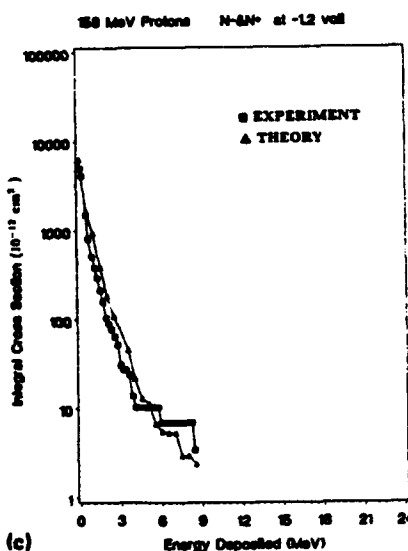
The CUPID codes used with a sensitive volume whose dimensions are determined by simple charge-collection procedures, appear to be reasonably accurate in simulating the charge collection at GaAs junctions in test structures for high incident proton energies. More work is needed for low proton energies but the assumption of little or no change from higher energies appears to be reasonable. The model predicts fewer high-energy depositions at low incident proton energies than is observed experimentally. The CUPID codes have now been tested by this method for a number of



(a)

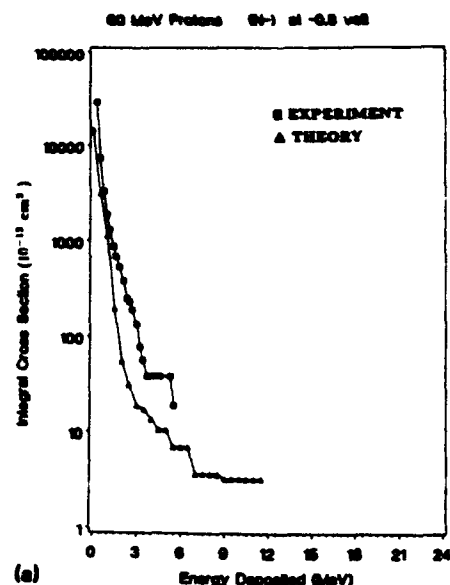


(b)

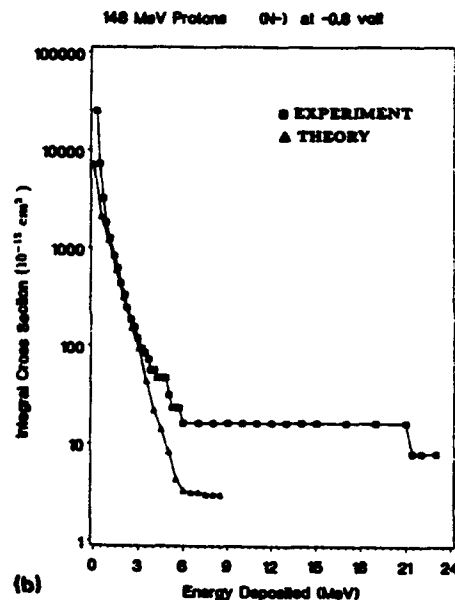


(c)

FIG. 10. Comparison between the experimental measurements (solid square) and the CUPID calculations (solid triangle) for $N^- + N^+$ GaAs test structures at -1.2 V for different proton exposures (a) 25 MeV, (b) 86 MeV, and (c) 158 MeV.



(a)



(b)

FIG. 11. Comparison between the experimental measurements (solid square) and the CUPID calculations (solid triangle) for N^- GaAs test structure at -0.8 V for different proton exposures (a) 60 MeV, and (b) 148 MeV.

simple devices. The GaAs tests are described in this manuscript and the silicon tests in Refs. 1-3. All the devices tested so far have simple structures.

ACKNOWLEDGMENTS

The help of the staff of the Harvard Cyclotron and the University of Pittsburgh's Tandem Van de Graaff accelerator are gratefully acknowledged. We would like to thank the Rockwell Corporation and, in particular, Fred Eisen, for providing the test structures and the processing information. This work was supported by the Air Force Geophysics Laboratory and the DNA SEU Program.

- ¹ P. J. McNulty, G. E. Farrell, and W. P. Tucker, IEEE Trans. Nucl. Sci. NS-28, 4533 (1981).
- ² G. E. Farrell, and P. J. McNulty, IEEE Trans. Nucl. Sci. NS-29, 2012 (1982).
- ³ S. El-Teleyat, G. E. Farrell, and P. J. McNulty, IEEE Trans. Nucl. Sci. NS-30, 4394 (1983).
- ⁴ G. E. Farrell, P. J. McNulty, and W. Abdel Kader, IEEE Trans. Nucl. Sci. NS-31, 1073 (1984).
- ⁵ J. Pickel and J. T. Blandford, Jr., IEEE Trans. Nucl. Sci. 1006 April (1980).
- ⁶ James H. Adams, Jr., IEEE Trans. Nucl. Sci. NS-30, 4475 (1983).
- ⁷ P. Shapiro, Naval Research Laboratory, Memorandum Report 5901 (1986).
- ⁸ C. Hu, IEEE Electron Device Lett. EDL-3, 31 (1982).
- ⁹ F. B. McLean and T. R. Oldham, IEEE Trans. Nucl. Sci. NS-29, 2018 (1982).
- ¹⁰ S. Kirkpatrick, IEEE Trans. Electron Devices ED-26, 1742 (1979).
- ¹¹ P. J. McNulty, W. G. Abdel-Kader, A. B. Campbell, A. R. Knudson, P. Shapiro, F. Eisen, and S. Roosild, IEEE Trans. Nucl. Sci. NS-31, 1128 (1984).
- ¹² U. Littmark and J. F. Ziegler, in *Handbook of Range Distributions for Energetic Ions in All Elements*, edited by J. F. Ziegler (Pergamon, New York, 1980).

APPENDIX E

PULSE-HEIGHT ANALYSIS SYSTEM:

A GUIDE FOR BEGINNING GRADUATE STUDENTS IN RADIATION PHYSICS

**CLEMSON UNIVERSITY
PULSE HEIGHT ANALYSIS SYSTEM**

**A GUIDE FOR BEGINNING STUDENTS
IN RADIATION PHYSICS**

**Prepared by:
R. A. Reed**

FORWARD

Introduction:

Welcome to the wonderful world of charge collection. The system you are about to use was developed by several people over a long period of time. The methods used to make charge collection measurements on microelectronic devices were derived from techniques used to make these same measurements on surface barrier detectors. An overview of charge collection techniques as applied to surface barrier detectors can be found in Glenn Knoll's book entitled *Radiation Detection and Measurements*. This group's paper entitled "Comparison of the Charge Collecting Properties of Junctions and the SEU Response of Microelectronic Circuits" *Nucl. Tracks Radiat Meas.*, Vol. 19, 1991 contains information about charge collection and its application. This manuscript is intended to be used as a guide for beginning students. The best way you can learn the skills necessary to perform accurate charge collection measurements is to "just do it", over and over again. Following the steps in this guide will hopefully get you started in the proper direction.

PREFACE

A Word About Syntax:

Commands that you type at the command line are depicted in this guide by capital bold face letters. The "^" symbol denotes a blank space. An example of a command is GR^1,6. First type the letters "G" "R", then press the space bar followed by "1" ", "6".

Functions represented on the keypad are depicted in this guide by capital bold face italicized letters. There are two types of keystrokes. The syntax used is (1) *KEY* \Rightarrow press the key once then release it and (2) *KEY1+KEY2* \Rightarrow press key number 1; while holding it down press key number 2 then release both of them.

What can I destroy?

Following the guidelines listed below will ensure that minimum damage is done to the equipment.

1. Do not turn the screws on the ADC labeled "U" or "Z".
2. Do not touch the active area of a surface barrier detector.
3. Do not use the high bias supply to bias up a device other than a surface barrier detector.
4. Do not bias a surface barrier detector above the recommended voltage level.
5. Do not apply a negative bias to a surface barrier detector.
6. Normally chips are not biased. If you think a chip should be biased, check with someone who knows.
7. Do not loosen or tighten any of the bolts on the vacuum chamber unless you have prior approval. You have prior approval to use a circular flange to mount the pre-amplifier BNC plate onto the vacuum chamber.
8. Handle the goniometer and device brackets with care.
9. Wear rubber gloves when handling source mounts or any object that has come in contact with the sources.
10. Do not touch the source.
11. Do not remove the sources from the charge collection area.
12. No food or drinks are allowed in the charge collection area.

After you read through the guide you should reread these guidelines. It is recommended that you understand each of these guidelines before you begin using the Pulse Height Analysis (PHA) system. Following these guidelines is mandatory.

CHAPTER 1: PULSE HEIGHT ANALYSIS SYSTEM (GENERAL INFORMATION)

The Pulse Height Analysis (PHA) system (Figure 1) has eight components. They are:

1. Vacuum Chamber.
2. Preamplifier.
3. Shaping amplifier.
4. Multichannel Analyzer (MCA).
5. Pulse Generator.
6. High bias supply.
7. HP power supply.
8. Voltmeter.

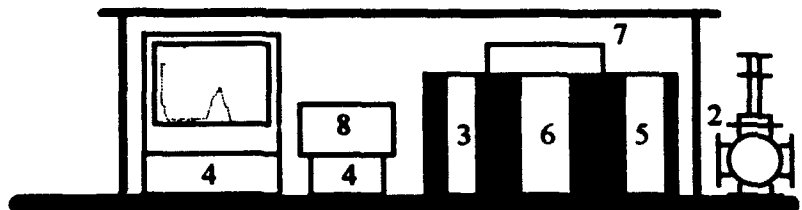


Figure 1. The PHA system.

The charge that is generated within the Sensitive Volume (SV) of the Device Under Test (DUT) creates a current that can be monitored on the power lines of the device. The preamplifier (2; inside the vacuum chamber) integrates the current over time. The result is a voltage pulse that is proportional to the charge. The voltage pulse is then passed through the shaping amplifier (3). Its purpose is to create a voltage pulse that is identifiable by the MCA. The MCA (4) digitizes the pulse height and increments the count number in the proper channel with the larger voltage pulse heights appearing farther to the right on the MCA screen.

Why are we doing this? Well, the digitized voltage pulse height is proportional to the charge that was collected in the SV. Therefore, if the MCA is calibrated, one can find the energy deposited within the SV by an ion interaction. Information obtained from the PHA system can be used to determine the following important characteristics of a device.

1. The ion's path length through the sensitive volume (SV) (i.e., the thickness of the SV). Use DEAD3.EXE to determine the path length and thickness of the SV.
2. The total projected area of the SV onto a plane perpendicular to the beam. Use the MCA or CUP2.EXE to determine the Counts Under the Peak (CUP). Then the area = CUP / fluence. CUP2.EXE will calculate the area if the proper fluence and angle are contained in the configuration file.
3. Possibly, the number of different junction types connected between V_{ss} and V_{dd} (i.e., more than one peak appears in spectra).

Read the Nuclear Tracks paper if you want more information on these topics. This paper is a good general review of SEU.

CHAPTER 2: MULTICHANNEL ANALYZER

The MCA (Figure 2) has five main components. They are:

1. Screen.
2. Keyboard
3. Keypad.
4. ADC.
5. Floppy drive.

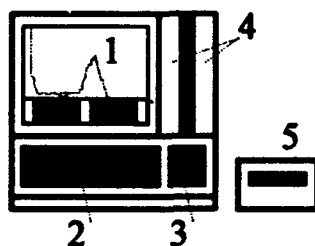


Figure 2. The MCA.

The ADC:

Up to four ADC's can be plugged into the MCA (Figure 1). However, if all four ADC's are in place the MCA will be loaded down and will not operate. At the present time only two are in place (they are numbered). ADC#1 is recommended. The numbers identify the "memory" ADC that is associated with a "physical" ADC. The MCA stores the signals converted by the "physical" ADC#1 into the "memory" ADC#1. You can divide each "memory" ADC into six groups (see The Keyboard). This allows you to perform six different runs without saving the spectra to a floppy disk. To display the spectra stored in an ADC group: repeatedly press the *ADC* button on the keypad until the desired "memory" ADC is selected then repeatedly press the *GRP* button on the keypad until the desired group is selected. The active ADC group is the one that is displayed on the screen. The active ADC group number is shown at the top of the screen. Look for "SP = #1 / #2" (#1 is the active ADC and #2 is the active group). To begin acquiring data select the desired active ADC group then press *INIT+ACQ*. The acquiring ADC group is the one that data is stored into if data acquisition is in progress.

There is only one setting on the "physical" ADC that needs to be adjusted. This is the Lower Level Discriminator (LLD). The LLD is used to cut off conversion of low voltage pulses, thereby reducing the number of noise pulses converted. If the LLD is set too low, then the ADC spends most of its time processing noise. To adjust the LLD, insert a small flathead screwdriver into the hole marked "L" (the one that does not have tape over it). Turn the screw clockwise to increase the LLD and counter-clockwise to decrease the LLD. **DO NOT TURN THE SCREWS MARKED "U" OR "Z".**

The Light-Emitting Diode (LED) scale is a visual reading of how often the ADC is converting voltage pulses. The LED has two modes that can be used, 100% and 25%. The LLD is properly adjusted when the bottom LED (25% mode) light is the only one that is lit and the noise rate is approximately the same as the data collection rate. If there is less than 1% dead time, the data set is probably good. (Note : $\% \text{ dead time} = (\text{realtime} - \text{livetime}) * 100 / \text{livetime}$. Livetime and realtime : defined in The MCA Screen section of this chapter.) If all the LED's are lit when in 100% mode and no data is being collected, move the ACQ-STRB switch on the ADC to the "off" position then back to the "acquire" position. This resets the ADC.

Normal settings for the dials and switches on the ADC are:

COIN-ANTI switch ~ OFF
CONV. GAIN dial ~ 4K

ACQ-STRB switch ~ ACQ
LED MODE switch ~ 25%

The Keyboard:

The keyboard is used to enter commands at the command line. The command line is located at the top of the screen. A few of the more commonly used commands are defined below.

Commands:

MO^1,PHA -- Set ADC#1 to PHA mode.
GR^1,6 -- Divide ADC#1 into 6 groups. The ADC group division must be less than 7.
TRA^1,FILENAME.RAW -- Transfer the spectra in the active ADC group to a floppy disk.
TRA^FILENAME.RAW,1 -- Transfer a pulse height spectra from a floppy disk to the active ADC group. Make sure that the spectra shown on the screen can be deleted.
TD -- Transfer a record of the livetime of the previous run to channel #1 of the active ADC group. (Note: Enter this before TRA if you wish to save the livetime for a run.)
LM^#### -- Position the left mark in channel ####.
LE^#### -- Set the energy value (keV) of the channel where the left mark is positioned to ####.
RM^#### -- Position the right mark in channel ####.
RI^#### -- Set the energy value (keV) of the channel where the right mark is positioned to ####.
CC^#### -- Position the cursor in channel ####.
CE^#### -- Position the cursor in the channel with an energy value (keV) of ####.
LI^HH:MM:SS -- Set the maximum livetime for the current run. When the livetime reaches HH:MM:SS the run will stop. To perform this command the MCA must not be acquiring data and the current livetime must be less than the desired value.
DDA -- List the files stored on the floppy disk in drive A. (Same as DIR on a PC.)
DA^DD-MMM-YY -- Set the current date.
TI^HH:MM:SS -- Set the current time.

If a letter is mistyped, press the RUB OUT key. The command line cursor will move back one space. See the ND77 operator's manual for a complete list of the commands.

The Keypad:

The keypad is a set of hot keys that perform various functions. Some of these functions are defined below.

Keypad functions:

ADC -- Toggle the active ADC.

GRP -- Toggle the active ADC group.

INIT+ACQ -- Initiate and terminate data collection. Data will be stored in the active ADC group.

INIT+ERAS -- Erase the data stored in the active ADC group. **CAUTION: If this key sequence is pressed and you have not saved your data, it will be lost.**

XPND RGN -- Zoom in on the region between the left and right marks. To return to a full screen view press the **XPND RGN** key again.

↑↓ -- Change the y-axis scale.

MARK SPAN -- Move the right mark.

MARK POSI -- Move the left and right marks.

CRSR -- Move the cursor.

PAGE -- Toggle the screen type.

± -- Change the direction of movement for the cursor and the marks. Also, change between increment and decrement for the **ADC**, **GRP**, **PAGE** and **↑↓** keys.

See the ND77 operator's manual for a complete list of the functions represented by the keys on the key pad.

The Floppy Drive:

The floppy drive uses 360k, DOS formatted floppies. To save the data set that is stored in the active ADC group type **TRA^1,FILENAME.RAW**. Using the **RAW** extension is not necessary, however if you wish to use the program **ND_NEWER.EXE** you must use this extension (Chapter 9). **ND_NEWER.EXE** converts the MCA data file to a ASCII file. ASCII format is used by most plotting programs. To recall a saved spectra type **TRA^FILENAME.RAW,1**. Make certain that the spectra stored in the active ADC group can be deleted. To list the files stored on a floppy disk type **DDA**. A directory of the floppy disk will scroll across the bottom of the screen. To return to a normal view press the **PAGE** key on the keypad until the desired screen is shown.

The MCA Screen:

Figure 3 shows a typical alpha spectra that was collected from a Surface Barrier Detector (SBD). The y-axis of the screen is counts and the x-axis is channel number (or energy). Each time an alpha particle strikes the SBD a voltage pulse is created. The pulse passes through the analog electronics and is converted, linearly with its height, to a digital number by the ADC. Then the MCA classifies the digital pulse and increases the count number in the appropriate channel. Classification goes from left to right (i.e., a relatively large pulse will increase the count in a channel on the right). Most of the alpha particles striking the SBD caused the peak at the right.

Counts caused by voltage pulses created by the noise in the system are seen on the far left. The data points between the peak and the noise are believed to be caused by alphas with a lower energy than the ones that produced the large peak or alphas which hit the dectector at an edge of the SV. The low energy alphas may have passed through a thicker portion of the material used to seal the source, thereby losing some of their energy along the way.

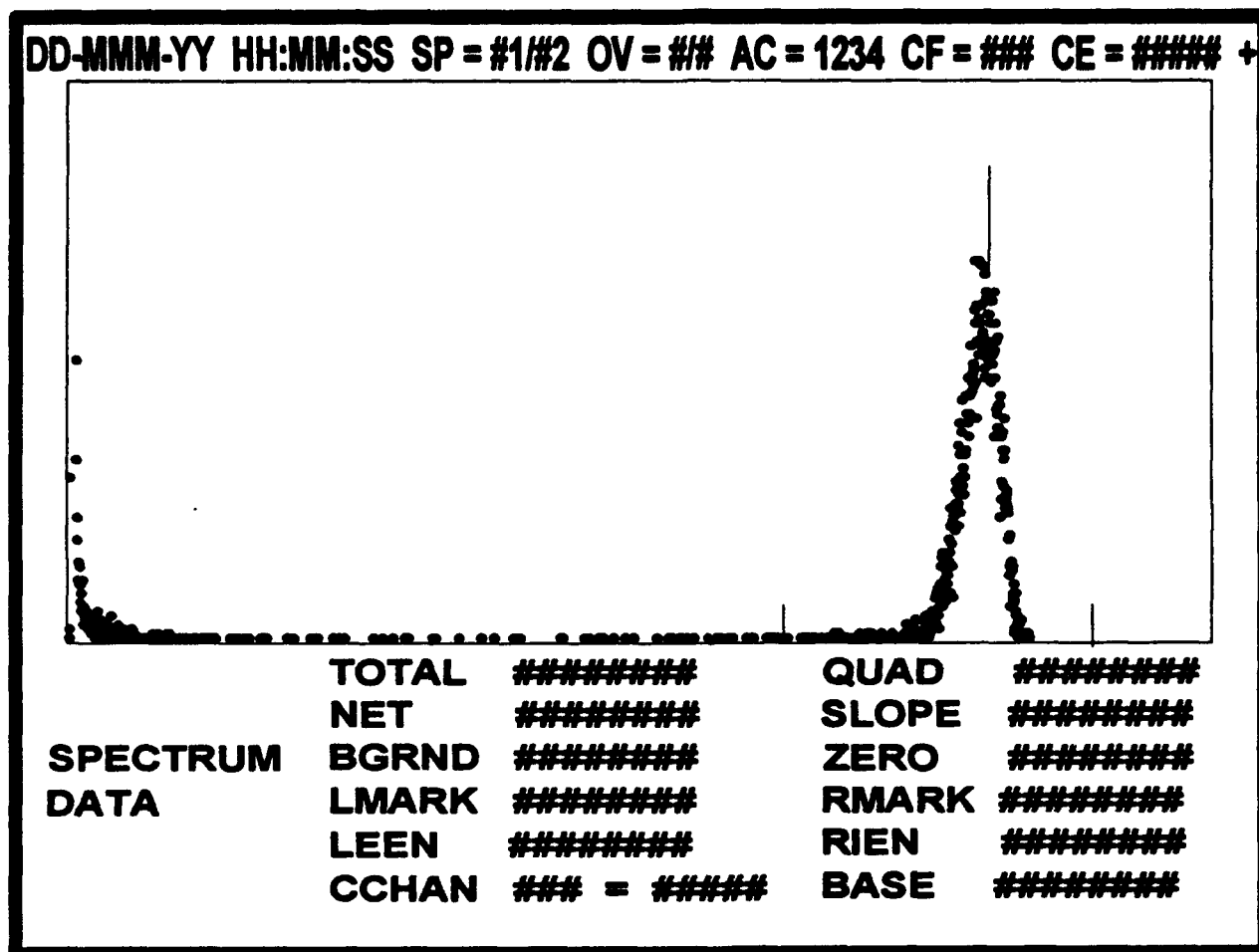


Figure 3. MCA screen #1.

The three vertical lines (Figure 3) are, from left to right, the left mark, cursor and right mark, respectively. The region of the spectra defined by the left and right marks is zoomed in on when the *XPND RGN* key is struck. To move the left and right mark press and hold the *MARK POSI* key. To move the right mark press the *MARK SPAN* key. To move the cursor press the *CRSR* key. To change the direction of movement of the cursor, right mark or both marks press the \pm key.

The information of interest at the top of the screen:

SP = #1/#2 -- This entry tells which ADC (#1) group (#2) is the active ADC group (i.e., the spectra shown on the screen is stored in the defined ADC group).

AC = 1234 -- The number that is blinking in this entry is the "memory" ADC used to store data currently being acquired by "physical" ADC.

CF = ### -- The y-scale of the MCA screen. Changing this entry will change the number of data points shown on the screen.

CE = ##### -- The energy value (keV) where the cursor is positioned.

The information of interest at the bottom of the screen:

TOTAL -- Total number of counts between the left mark and right mark.

NET -- Total number of counts above a line drawn from the lower end of the left mark to the lower end of the right mark.

BGRND -- Total number of counts below a line drawn from the lower end of the left mark to the lower end of the right mark.

LMARK -- Channel number where the left mark is positioned.

LEEN -- Energy value (keV) where the left mark is positioned.

CCHAN -- The first number is the channel number where the cursor is positioned. The second number is the total number of counts in that channel.

RMARK -- Channel number where the right mark is positioned.

RIEN -- Energy value (keV) where the right mark is positioned.

The *PAGE* key can be used to change the information that is shown on the screen. One of the more useful screens is shown in Figure 4. The entry ACQGRP tells which group of the "memory" ADC is used to store data currently being acquired by "physical" ADC. Livetime is the total conversion time of the "physical" ADC. Realtime is the actual acquire time of the "physical" ADC. See the ND77 operator's manual for complete definitions of the entries on these and other screens.

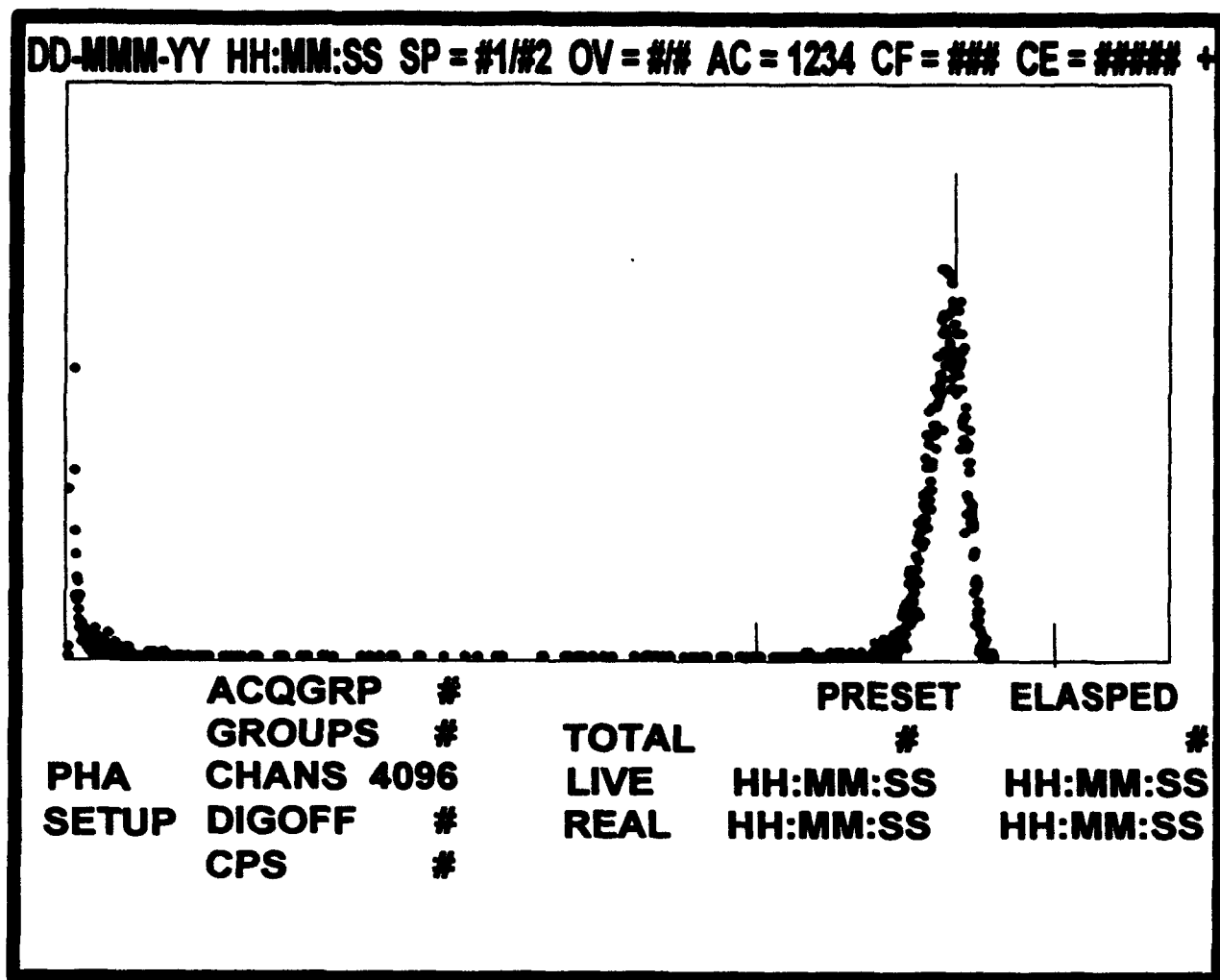


Figure 4. MCA screen #2.

Initialization of the MCA:

Listed next are the commands typed at the command line to initialize the MCA. This needs to be done only when you power up the MCA.

1. **MO^1,PHA**
2. **GR^1,6** (optional)
3. **DA^DD-**MMM-YY**** (optional)
4. **TI^HH:MM:SS** (optional)
5. Select the ADC and group you wish to use by pressing the **ADC** and **GRP** keys.
6. Turn on the floppy drive.

CHAPTER 3: VACUUM CHAMBER:

Figure 5a is a front view of the chamber and Figure 5b is a top view of the chamber. The vacuum chamber has six main parts. They are:

1. Goniometer assembly.
2. Pre-amplifier.
3. Source mounting rod.
4. Vent valve.
5. Exhaust valve.
6. Pump (not shown).

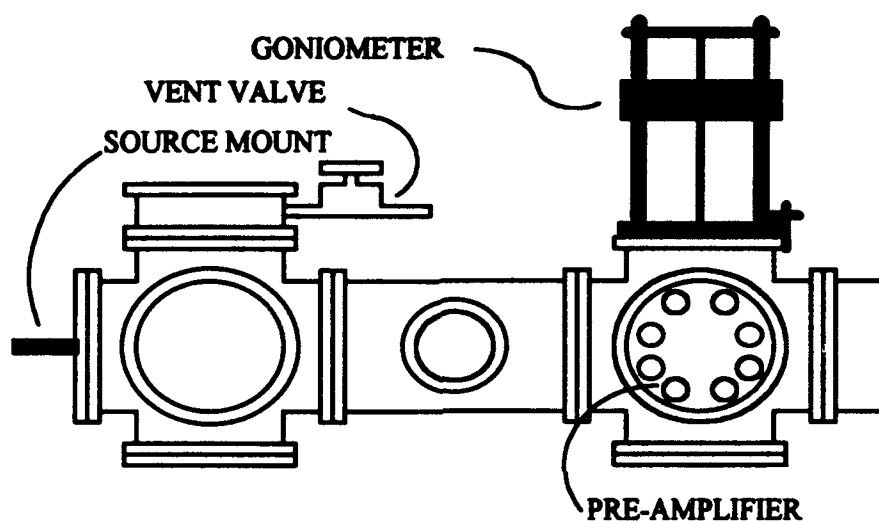


Figure 5a. Front view of the vacuum chamber.

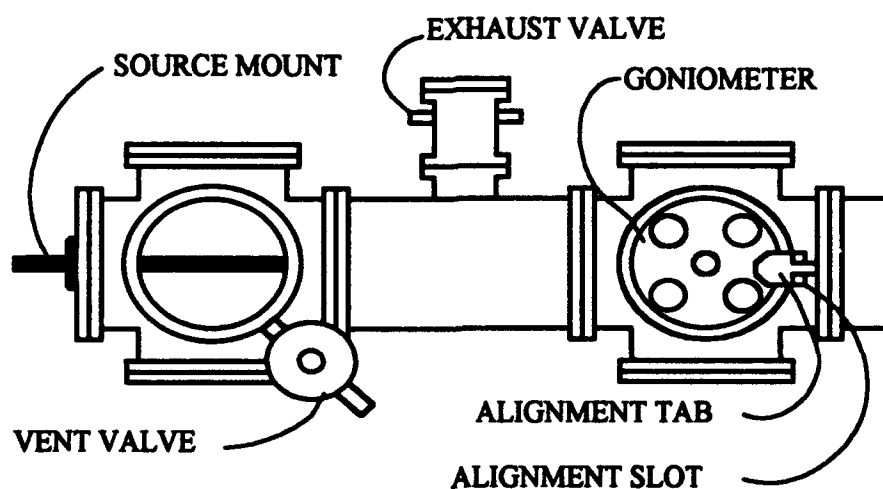


Figure 5b. Top view of the vacuum chamber.

Currently there are two view ports mounted on the chamber. If light is allowed in the chamber during a charge collection measurement, the device will generate an increased amount of noise. Covering the view ports with aluminum foil will eliminate this photon induced noise.

Venting and Exhausting:

Turn the exhaust and vent valves (Figure 5) all the way when opening or closing them.

Procedure for exhausting the vacuum chamber:

1. The vacuum pump is off and the chamber is vented.
2. Close the vent valve (clockwise).
3. Close the exhaust valve (clockwise).
4. Insert the vacuum pump's electrical plug into an outlet (the pump will start).
5. After a few seconds have passed, open the exhaust valve (counter-clockwise).
6. Listen for leaks.
7. The vacuum gauge pressure should be less than 100 mtorr (?) .

Procedure for venting the vacuum chamber:

1. The vacuum pump is running and the chamber is exhausted.
2. Close the exhaust valve (clockwise).
3. Slowly open the vent valve (counter-clockwise).
4. Unplug the vacuum pump.

The Source:

Our lab has four sources.

<u>SOURCE TYPE</u>	<u>ENERGY</u>	<u>NAME</u>	<u>MOUNT</u>
Americium -- alpha	4.80 MeV	Source	Metal cylinder -- centered
Americium -- alpha	4.96 MeV	Cold	Metal rectangle -- off center
Americium -- alpha	4.43 MeV	Hot	Metal circle -- off center
Cesium -- gamma	0.66 MeV	Gamma	Plastic disk

The 4.8 MeV alpha source is believed to be the most reliable source we have at this time. **Always wear rubber gloves when handling sources, mounts or any object that comes into contact with a source. Never touch a source.** Store all the sources in the Plexiglas box. You do not need to remove the source from the vacuum chamber when the system is not being used. Calibration of the source energy should be performed once every year (Chapter 7). Positioning the source so that it is as close as possible to the device will increase the rate at which data is recorded.

The goniometer Assembly:

The goniometer assembly (Figure 6) is used to measure the angle of incidence of the particles. There is a list posted on the wall above the vacuum chamber that relates the goniometer angle values to the actual values. Placement of the goniometer assembly is crucial for accurate angle

measurements. The alignment tab should be placed in the alignment slot (Figures 5 & 6). Mounting a microelectronic device on the goniometer device bracket is explained in the Chapter 8. Mounting of a SBD is explained in Chapter 6.

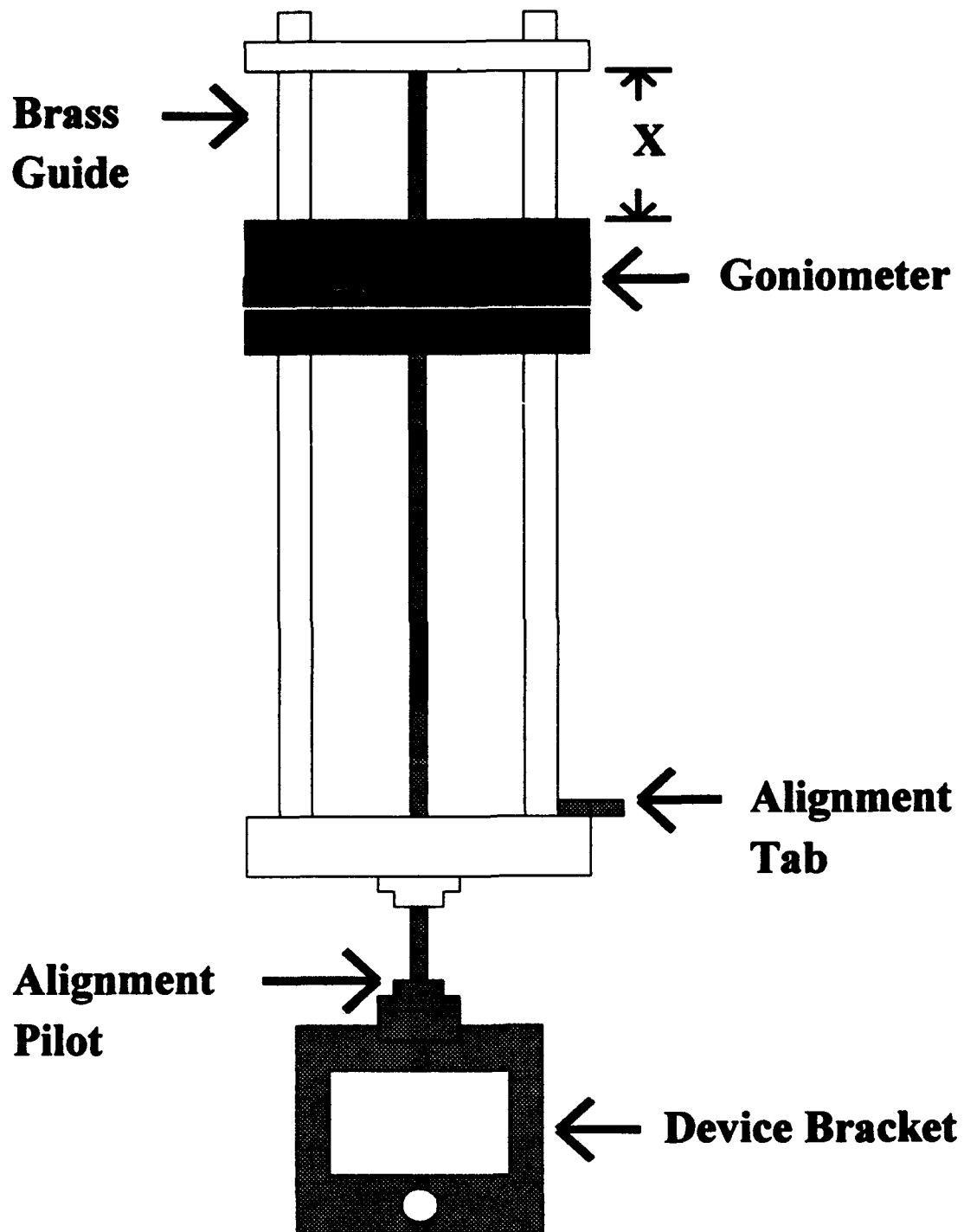


Figure 6. The goniometer assembly.

The Pre-Amplifier:

The Pre-amplifier is mounted on the inside of the vacuum seal plate shown in Figure 5a. It is a charge sensitive amplifier. The output voltage pulse is proportional to the charge. It is desirable that the time constant of the preamplifier be roughly that of the switching speed of the device for CMOS or NMOS memories. For CCD structures or dynamic memories the time constant should be very long. The alpha cable that extends out of the Faraday cage is used to connect the DUT to the pre-amplifier. There should be a Mircodot connector soldered to the alpha cable. Connecting a DUT to the pre-amplifier is described in Chapters 6 and 8. The connections made to the BNC connectors are explained in the Chapter 5. The HP power supply voltage (Figure 1) for the pre-amplifier should be set at 6.00 volts. Small deviations from 6.00 volts can effect the results.

CHAPTER 4: THE NIMBIN

The NIMBIN is a housing and power supply for the shaping amplifier, high bias supply and pulse generator (Figure 1).

The Shaping Amplifier:

The shaping amplifier magnifies the voltage pulse received from the pre-amplifier. It also creates a gaussian pulse that has a height that is proportional to the height of the input pulse, i.e., the charge collected. Normal settings for the dials and switches on the shaping amplifier are as follows:

BLR switch ~ CENTER	GAIN dial ~ variable
POS-NEG switch ~ POS (this can vary)	FINE GAIN dial ~ 0.5
MODE switch ~ GAUSS	SHAPING TIME dial ~ variable

Increasing the gain will cause the voltage pulse heights produced by the shaping amplifier to be larger. Therefore, the MCA classifies the pulses into larger channels. Changing the gain dial will cause the peak position to shift. The advantage is the optimization of the MCA screen. Changing the gain dial has no effect on the energy per channel calibration of the MCA (see Chapter 7).

The shaping time dial sets the amount of time the shaping amplifier looks at the incoming pulse. You can use this dial to eliminate noise. Changing the shaping time dial *does* affect the energy per channel calibration of the MCA.

The High Bias Supply:

The high bias power supply is used to apply bias to SBD. Positive bias should be applied to all SBDs in our current stock. The voltmeter can be used to ensure that the SBD is biased to the manufacture's recommended value. Use channel B on the high bias supply. Never use the high bias supply to bias a device.

The Pulse Generator:

The pulse generator produces a voltage pulse that is defined by the settings on the dials and switches. When the pulse generator is calibrated to let's say 4.8 MeV, it produces a voltage pulse that emulates the pulse caused by an 4.8 MeV ion strike. This pulse is used to make the energy per channel calibration of the MCA. Chapter 7 discusses how the pulse generator is calibrated and how it is used to calibrate the MCA.

Normal Settings for the dials and switches on the pulse generator are as follows:

MODE switch ~ REP	FREQUENCY dial ~ variable
RANGE switch ~ 1V	AMPLITUDE dial ~ variable
POL switch ~ NEG (this can vary)	RISE TIME dial ~ 1 μ sec
REF switch ~ INT	FALL TIME dial ~ 200 μ sec
ATTEN switches ~ variable	NORMALIZE dial ~ 10.0

If the frequency dial is set to EXT it is off, otherwise it is producing a pulse at the designated frequency.

CHAPTER 5: ELECTRICAL CONNECTIONS

Figure 7 shows the electrical connections that need to be made when performing charge collection measurements. These connections are the same for all DUT's. Each component of the PHA system is outlined with a dotted box. The name of the component is in the upper left hand side of the box. A circle represents a BNC connection and a square represents a screw clamp connection. The thick line represents connections made with alpha cable. The medium line is the outer ground wire of the alpha cable and the thin line is the inner copper wire surrounded by an insulator. The connection between the ADC ~ signal and the oscilloscope ~ input is optional.

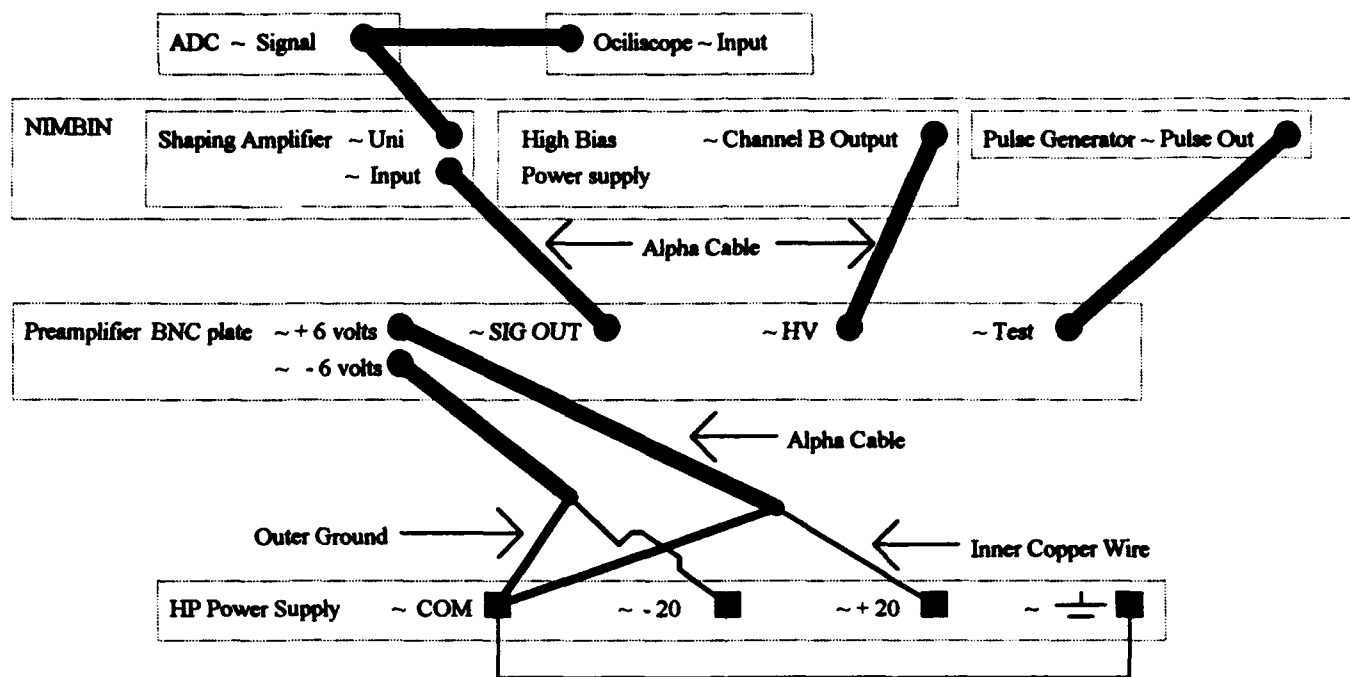


Figure 7. Electrical connections.

Connecting the DUT to the pre-amplifier is discussed in Chapters 6 and 8.

CHAPTER 6: SURFACE BARRIER DETECTORS

A surface barrier detector is a layer of n-type material with a thin gold contact evaporated on top of the n-type layer. The evaporation process produces a high density of electron traps at the surface which forms a p-n type junction. The depletion region will extend deep into the n-type material when the SBD is reversed biased (Figure 8). When a constant bias is applied across the junction the depletion region thickness will increase to some constant value. An incident ion will deposit all of its energy within the depletion region if and only if the region's thickness is larger than the ion's range. A typical SBD thickness is $100\mu\text{m}$. The range in Si of a 4.8 MeV alpha particle is approximately $22.14\mu\text{m}$. Therefore, all of its energy (or generated charge) is deposited within the depletion region. This charge creates a voltage pulse that passes through the analog electronics, then it is sent to the MCA. The relationship between the energy deposited and the charge generated in Silicon is 22.5 MeV energy deposited creates 1pC of charge.

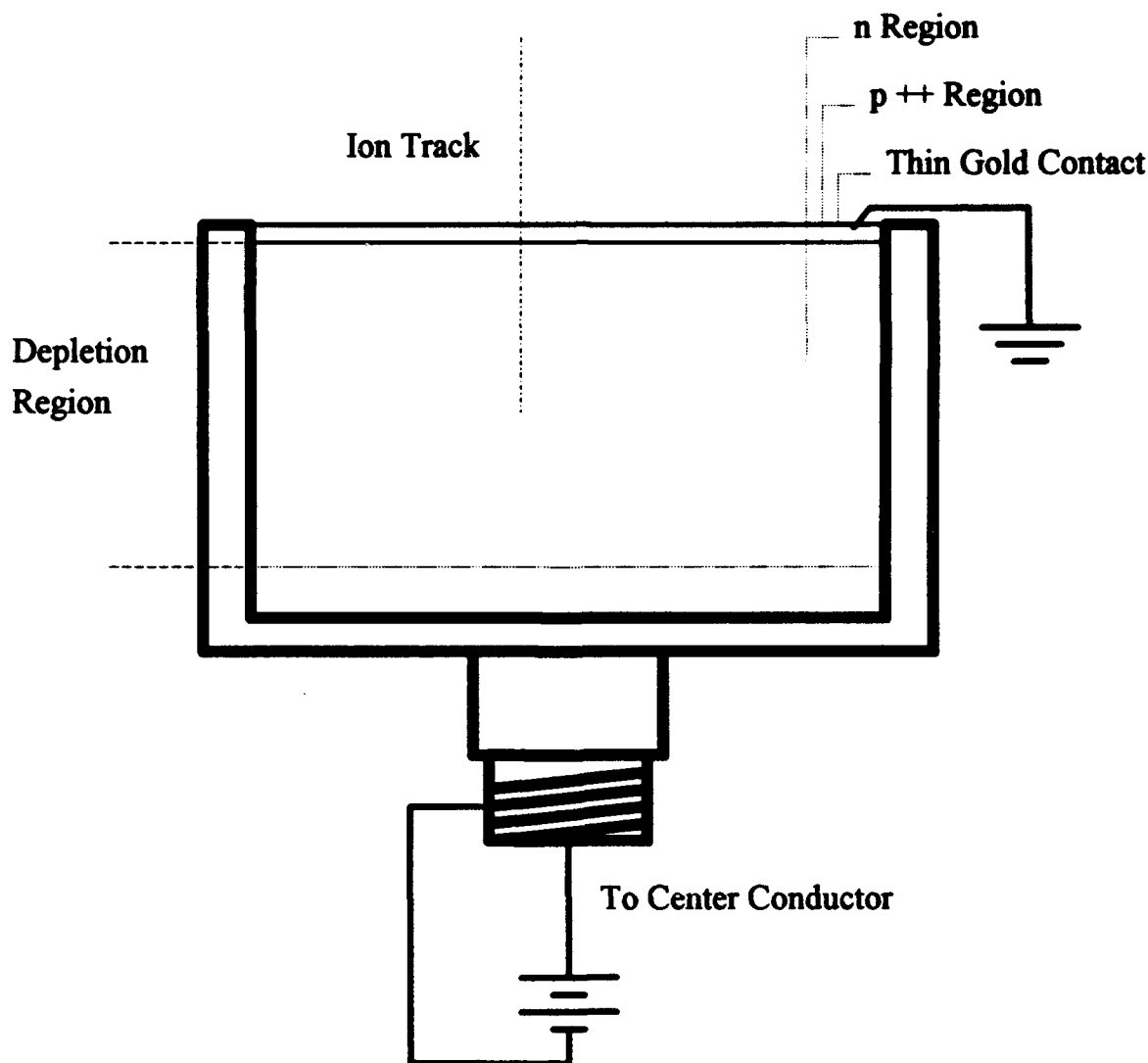


Figure 8. Cross-sectional view of a SBD. Note that dimensions are not to scale.

SBD Charge Collection Measurement:

Listed below is a set of instructions on how to make charge collection measurements on a SBD.

A. Mount the SBD onto the Goniometer Assembly:

1. Mount device bracket #2 (Figure 9) onto the goniometer alignment pilot (Figure 6). Make certain that the alignment pins are inserted into the correct holes. There should be an ink mark on the device bracket that is to be aligned with the ink mark on the alignment pilot. Do not force the device bracket onto the alignment pilot.
2. Mount the SBD bracket onto the device bracket (Figure 10). The SBD bracket is a brass rectangle with a hole drilled in it the size of the SBD. The hole is off center, align the center of the hole with the centering markings on the device bracket. The SBD bracket should be mounted on the side opposite to the plane of rotation.
3. Insert the SBD into the hole and tighten the set screw (Figure 10). *Do not over tighten the set screw.* The SBD should be positioned so that the plane of the active area is in the plane of rotation.

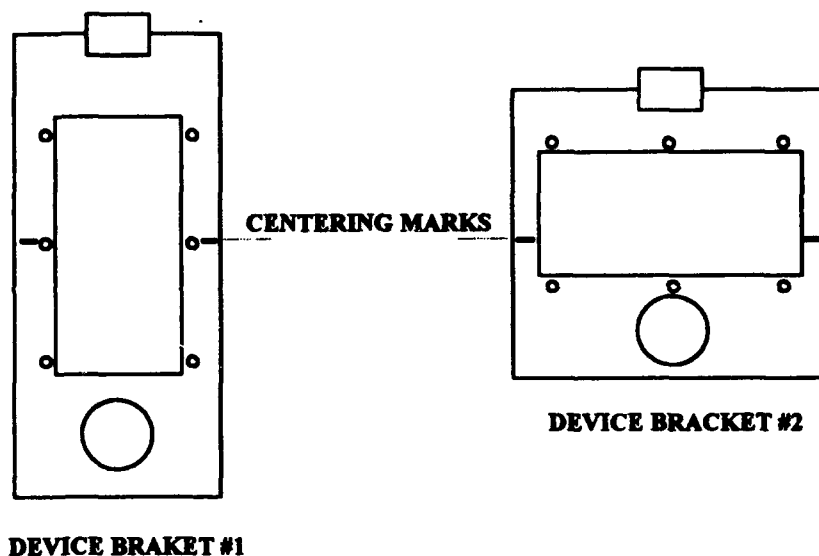


Figure 9a. Device brackets.

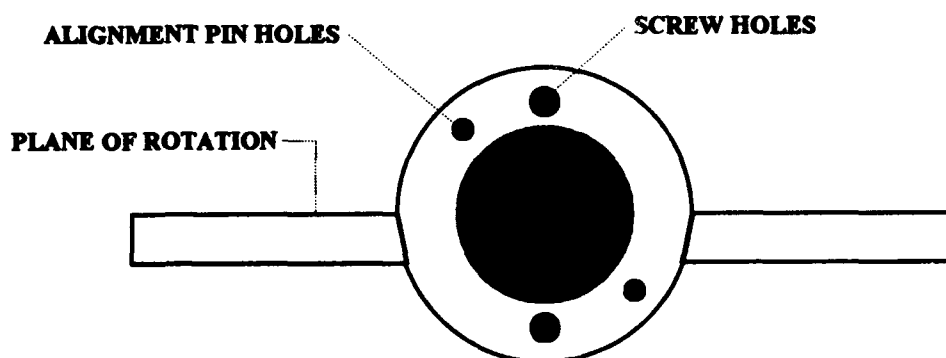


Figure 9b. Top view of a device bracket.

DEVICE BRACKET

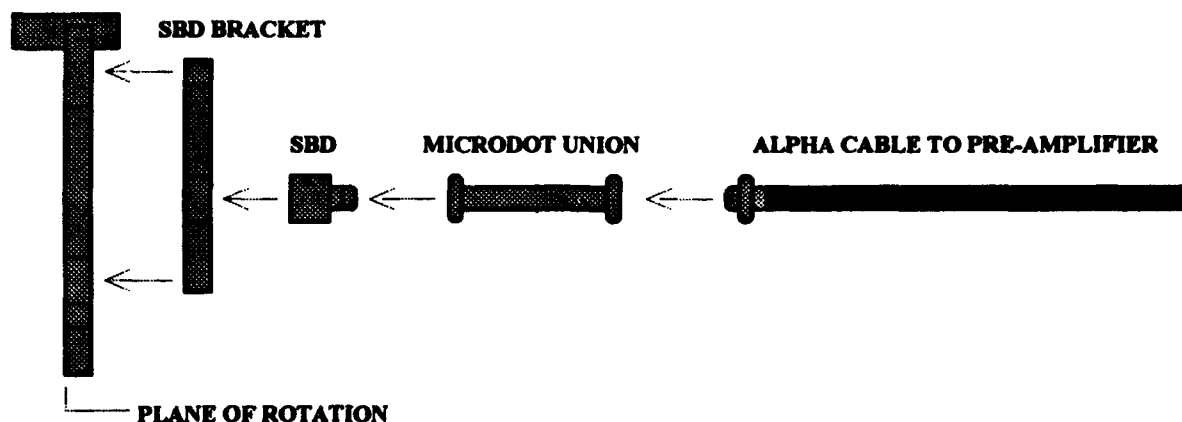


Figure 10. Schematic of SBD mounting.

- B. Place the goniometer assembly on the proper vacuum chamber opening. Make certain that the alignment tab is inserted into the alignment slot (Figures 5 and 6).
- C. Connect the Microdot connections shown in Figure 10.
- D. Place the pre-amplifier BNC plate on the proper vacuum chamber opening.
- E. Mount a flange around the BNC plate.
- F. Exhaust the vacuum chamber.
- G. Set the angle of incidence to the desired value (normally 0 degrees). Make certain not to pull on the alpha cable between the pre-amplifier and the SBD.
- H. Position the SBD in the center of the chamber. If the SBD is aligned with the centering marks then the distance X in Figure 6 is 1.72 inches.
- I. Cover all the view ports with aluminum foil.
- J. Use alligator clip wires to ground all the components.
- K. Make all the electrical connections described in Chapter 5. Detach the alpha cable between the high bias supply and the BNC plate at the BNC connector attached to the high bias supply.
- L. Turn on the MCA, NIMBIN, HP power supply, multimeter and oscilloscope (optional).
- M. Initialize the MCA (Chapter 2).
- N. Set the shaping amplifier dials and switches to the values recommended in Chapter 4.
- O. Set the shaping time to 10 μ sec.
- P. Set the shaping amplifier gain to the desired value (normally 50).
- Q. Set the pulse generator frequency dial to EXT. This is the off position.
- R. Turn the high bias supply on and set it to zero. Use the multimeter to measure the output of the high bias supply.
- S. Reconnect the high bias supply to the BNC plate.
- T. Slowly bias the SBD to the recommended value (see the manufacturer's specification sheet).
- U. Use the multimeter to measure the output of the HP power supply. Disconnecting the multimeter will reduce the signal to noise ratio.
- V. Press the *INIT+ACQ* keys. This begins data acquisition.
- W. Adjust the LLD (see Chapter 2).
- X. Adjust the shaping amplifier gain so that the peak appears as far to the right as possible (see Chapter 4). Pressing *INIT+ERAS* clears the screen.

Y. After a sufficient amount of data has been collected press *INIT+ACQ* keys. This stops the data acquisition process.

In your lab book record the high bias supply setting, HP power supply setting, angle of incidence, shaping time, gain, peak position channel number, livetime and the SBD used. After the data set is complete, slowly unbias the SBD and turn off all the equipment. Place the SBD in its case. Do not touch the active area of the SBD.

Figure 11 is a plot of a typical spectra obtained from a SBD when irradiated by 4.8 MeV alpha particles. The channel that the peak appears in is determined by the energy of the alpha particles, the gain and shaping time settings of the shaping amplifier, and other component settings. If all the electronic properties of the system remain the same, the peak will appear in the same channel anytime a data set is collected. The peak position is approximately channel 2030. Events occurring near channel 2030 are 4.8 MeV events.

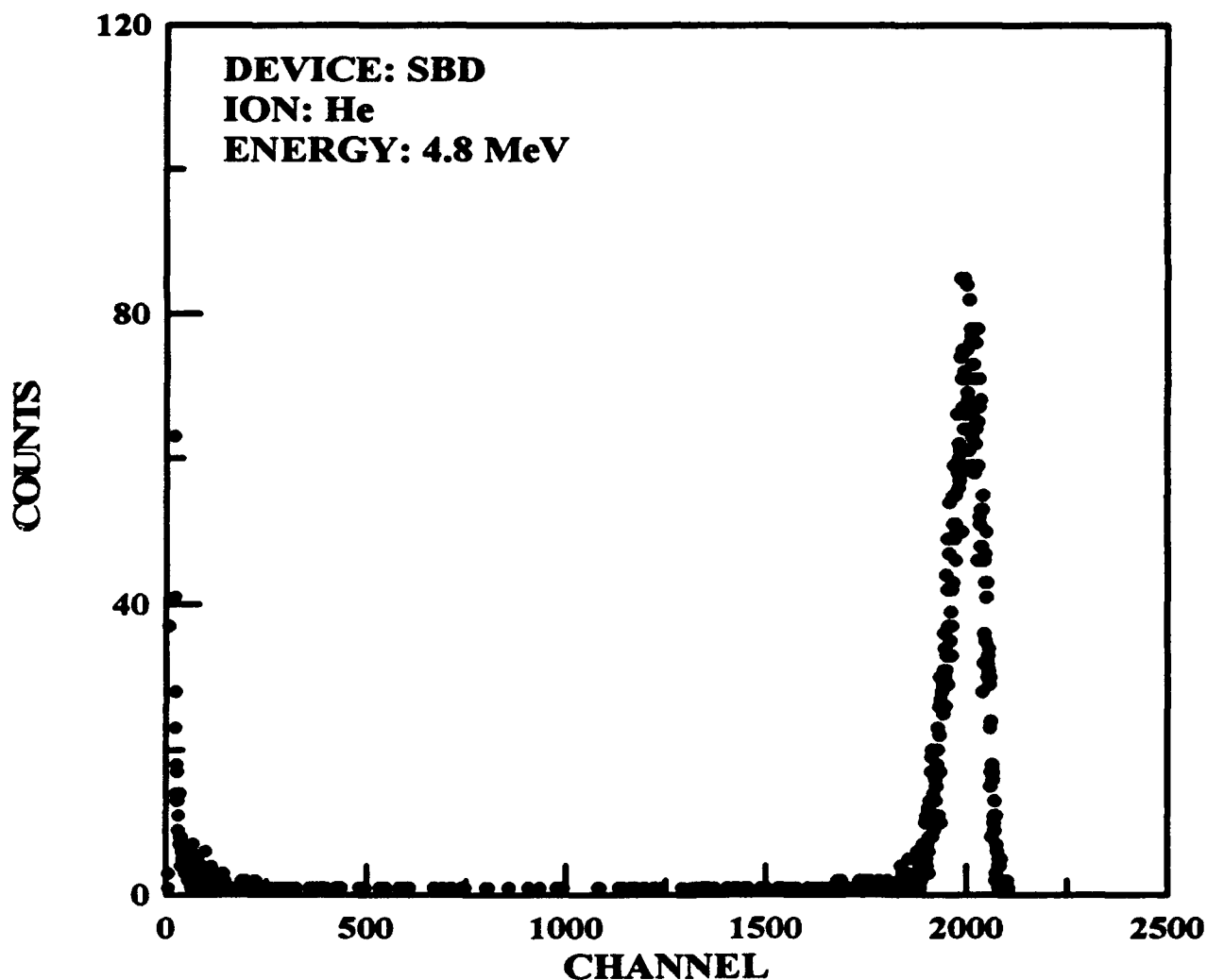


Figure 11. Charge collection spectra from a SBD.

CHAPTER 7: CALIBRATIONS

There are several calibrations. The following list gives the type of calibration and how often each should be performed.

<u>Component</u>	<u>Calibration</u>	<u>Frequency</u>
Source	Flux	As Needed
Source	Energy	Yearly
Pulse generator	Energy Representation	Daily
MCA	Energy per Channel	Beginning of a Run
MCA	Dead Channel	Yearly
Goniometer	Angle	Yearly

Flux Calibration of a Source:

Using a SBD to calibrate the flux of a source is described below.

1. Mount the source on the source mounting rod (Figure 5).
2. Move the source as close to the SBD as possible.
3. Perform a charge collection measurement (Chapter 7).
4. Measure the distance between the source and the SBD.
5. Determine the counts under the peak.
6. Change the distance between the source and the SBD.
7. Repeat steps 3 through 6 until the source is at a maximum distance from the SBD.
8. Generate a plot of the flux versus the inverse square of the distance.

Five or six distances should be sufficient for a good data set. Figure 12 is a plot of the flux versus the inverse square distance between the 4.8 MeV alpha source and the SBD.

$$\text{Flux} = \text{CUP} / (\text{Active Area} * \text{Livetime})$$

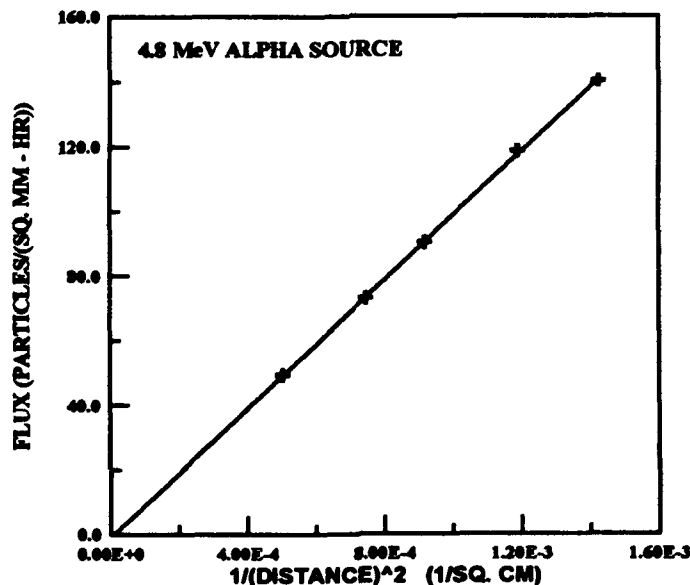


Figure 12. Particle flux versus inverse square distance for the 4.8 MeV alpha source.

Energy Calibration of a Source:

Obtain two sources with known energies. Dr. Fjeld in the ESE department can supply you with these sources. Using the two known sources and a SBD to calibrate the energy of a source is described below.

1. Make a SBD charge collection measurement using one of the known sources (Chapter 6).
2. Place the right mark at the peak position (e.g., *MARK SPAN* key).
3. Set the right mark energy value (keV) to the energy of the known source (e.g., *RI^5870*).
4. Place the left mark at the zero channel (e.g., *LM^26*). This channel is determined from a dead channel calibration of the MCA.
5. Set the left mark energy value (keV) to zero (e.g., *LE^0*).
6. Make a SBD charge collection measurement using the other known source. The peak position should be near the known energy of the source.
7. Make a SBD charge collection measurement of the source that is to be calibrated. The peak position is the energy of the source.

Using two sources with known energies verifies that the MCA is properly calibrated and that the known source energies agree. One source can be used if the source energy is calibrated. Doing steps 2 through 5 defines the energy per channel calibration of the MCA.

Energy Representation Calibration of the Pulse Generator:

The voltage pulse produced by the pulse generator is enhanced by the pre-amplifier and moves through the electronics just as if it originated in a DUT. Calibrating the pulse generator to a specific voltage is the same as calibrating it to represent a specific energy deposition. After the pulse generator is calibrated it is used to send a specific voltage pulse through the electronics. Knowing the energy deposition represented by the pulse generator allows one to make an energy per channel calibration of MCA.

Perform the following steps to make an energy representation calibration of the pulse generator.

1. Make a SBD charge collection measurement using a calibrated source (Chapter 6).
2. Do not exhaust the vacuum chamber. Do not remove the SBD. Do not change the high bias supply setting, HP power supply setting, settings on the shaping amplifier or the settings on the ADC.
3. Place the cursor at the peak position.
4. Set the pulse generator dials and switches to the values defined in Chapter 4. The frequency dial should be set to EXT. This is the off position.
5. Set the ATTEN switches to times five.
6. Change groups (*GRP* key).
7. Turn the pulse generator frequency dial to 1kHz.
8. Turn the red knob at the center of the frequency dial all the way clockwise, then turn it counter-clockwise one half of a turn.
9. Press *INIT+ACQ*.
10. Adjust the LLD (Chapter 2).

11. Adjust the amplitude dial on the pulse generator so that the pulse generator peak position is located in the same channel as the SBD peak position. Pressing the *INIT+ERAS* keys will clear the data stored in the active ADC group.

After performing these steps, the pulse generator will be calibrated to the energy of the source.

Assume that a 4.8 MeV alpha source was used to calibrate the pulse generator. Then a different DUT is connected to the PHA system. This changes the total capacitance seen by the preamplifier, changing the effective gain. Therefore, the energy per channel calibration of the MCA is not the same. Connecting the new DUT to the electronics does not change the voltage pulse produced by the pulse generator. Sending the pulse from the pulse generator through the electronics emulates the voltage pulse that a 4.8 MeV strike would generate. The pulse produced by the pulse generator is used to make the energy per channel calibration of the MCA when a microelectronic device is connected to the system.

Energy per Channel Calibration of the MCA:

The steps used to make an energy per channel calibration of the MCA are defined below.

1. The DUT is connected to the electronics and the vacuum chamber is exhausted.
2. Turn on all the components.
3. All the shaping amplifier settings, except possibly for the gain, should be set to the same values used when the pulse generator was calibrated.
4. All the pulse generator settings should be set to the same values used when it was calibrated.
5. Turn the pulse generator frequency dial to 1kHz.
6. Turn the red knob at the center of the frequency dial all the way clockwise, then turn it counter-clockwise one half of a turn.
7. Press *INIT+ACQ*.
8. Adjust the LLD (Chapter 2).
9. Adjust the shaping amplifier gain so that the pulse generator peak position appears in the largest possible channel.
10. Place the right mark at the peak position (e.g., *MARK SPAN* key).
11. Set the right mark energy value (keV) to the energy of the pulse generator (e.g., *RI^4800*).
12. Place the left mark at the zero channel (e.g., *LM^26*). This channel is determined from a dead channel calibration of the MCA.
13. Set the left mark energy value (keV) to zero (e.g., *LE^0*).

Dead Channel Calibration of the MCA:

Relatively small voltage pulse heights will appear in the channels on the left. As the voltage pulse height tends towards zero there is a channel number that represents a zero voltage pulse height. All the channels less than or equal to this channel are considered to be dead channels. To determine the number of dead channels, follow the steps outlined below.

1. Connect the oscilloscope to the MCA (Figure 7).
2. Power up all the components.
3. Turn the pulse generator frequency dial to 1kHz.

4. Turn the red knob at the center of the frequency dial all the way clockwise, then turn it counter-clockwise one half of a turn.
5. Press *INIT+ACQ*.
6. Adjust the LLD (Chapter 2).
7. Adjust the amplitude dial on the pulse generator so that the peak position appears near channel 800.
8. Use the oscilloscope to measure the voltage pulse height.
9. Record the channel number that locates the peak position.
10. Record the voltage pulse height.
11. Decrease the output of the pulse generator.
12. Repeat steps 6 through 8 until the peak position is near the noise.
13. Create a plot of the channel number versus the voltage pulse height. The y intercept is the number of dead channels (zero channel).

Figure 13 is a plot of the channel number versus the voltage. The number of dead channels is close to 26.

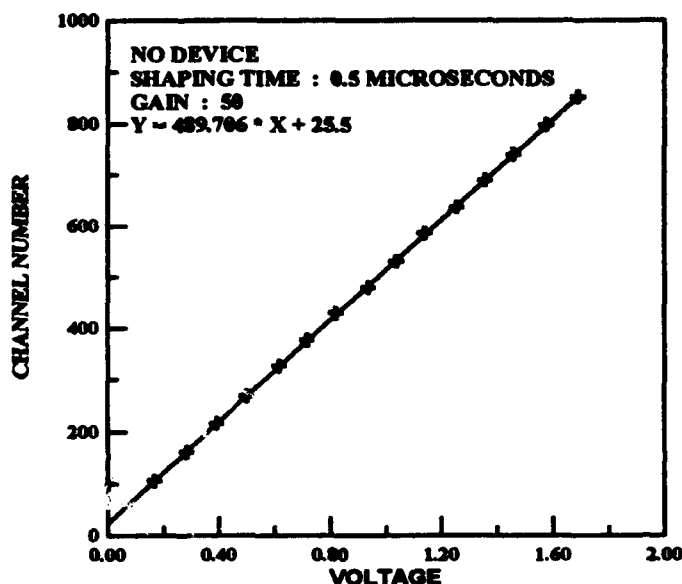


Figure 13. Determination of the number of dead channels.

Calibration of the goniometer:

Calibration of the goniometer is contained in Robert Reed's masters thesis.

CHAPTER 8: OTHER DUT's

Performing charge collection measurements on memory devices and other microelectronic chips is one of the main focuses of our group. The instruction set listed below is a general guide for performing memory device charge collection measurements. Some of the steps may vary, depending on the type of device being tested.

Memory Device Charge Collection Measurement:

A. Mount the device onto the Goniometer Assembly:

1. Mount the proper device bracket (Figure 9) onto the goniometer alignment pilot (Figure 6). The bracket to use is determined by the direction of rotation of the DUT. Make certain that the alignment pins are inserted into the correct holes. There should be an ink mark on the device bracket that is to be aligned with the ink mark on the alignment pilot. Do not force the device bracket onto the alignment pilot.
2. Mount a Zero Insertion Force (ZIF) socket onto a vector board. Make sure that the DUT can be aligned with the centering marks on the device bracket (Figure 9).
3. Solder the appropriate pins to an alpha cable (remember the centering marks). Typically, V_{SS} is connected to ground (the outer wire) and V_{DD} is connected to power (the inner wire). Solder a Mircodot connector onto the other end of the cable. The inner wire is soldered into the center hole and the outer wire is soldered onto the Mircodot connector.
4. Mount the vector board onto the device bracket (Figure 14) so that the plane of the die is in the plane of rotation (Figure 9). Make certain that the die is aligned with the centering marks.

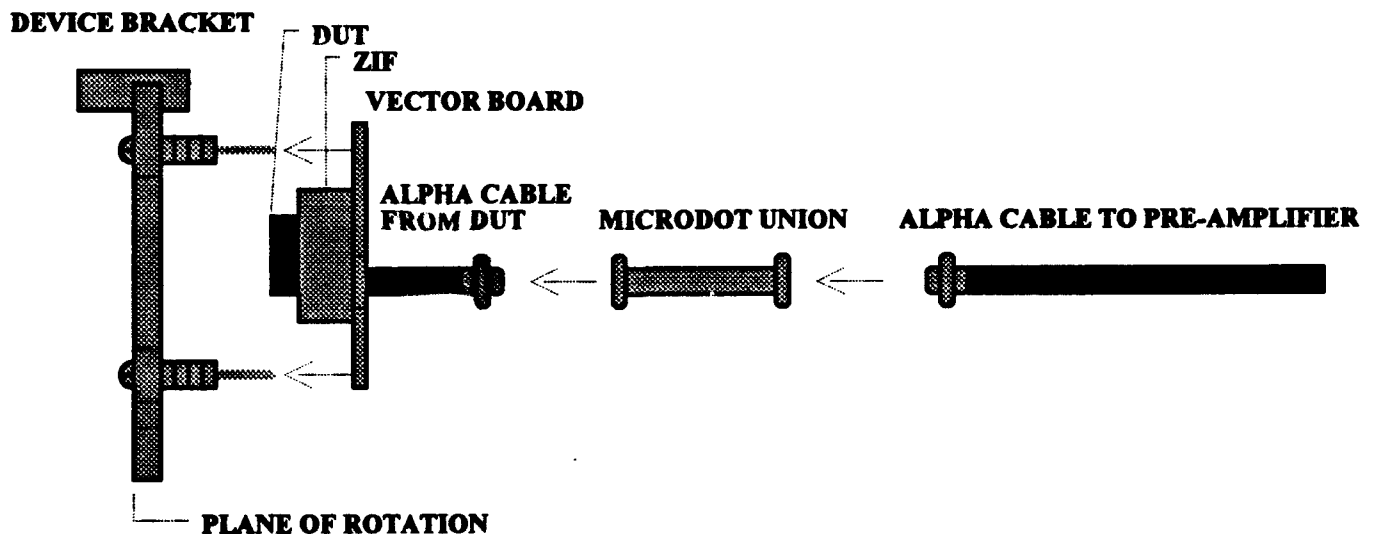


Figure 14. Schematic of SBD mounting.

- B. Place the goniometer assembly on the proper vacuum chamber opening. Make certain that the alignment tab is inserted into the alignment slot (Figures 5 and 6).
- C. Connect the Microdot connections shown in Figure 14.
- D. Place the pre-amplifier BNC plate on to proper vacuum chamber opening.
- E. Mount a flange around the BNC plate.
- F. Exhaust the vacuum chamber.
- G. Set the angle of incidence to the desired value. Make certain not to pull on any of the alpha cables.
- H. Position the die in the center of the chamber. If the die is aligned with the centering marks then the distance X in Figure 6 is 1.72 Inches.
- I. Cover all the view ports with aluminum foil.
- J. Use alligator clip wires to ground all the components.
- K. Make all the connections described in Chapter 5. Detach the alpha cable between the high bias supply and the BNC plate.
- L. Turn on the MCA, NIMBIN, HP power supply, multimeter and oscilloscope (optional).
- M. Initialize the MCA (Chapter 2).
- N. Set the shaping amplifier dials and switches to the values recommended in Chapter 4.
- O. Set the shaping time to 10 μ sec.
- P. Set the shaping amplifier gain to the estimated value.
- Q. Set the pulse generator frequency dial to EXT.
- R. Use the multimeter to measure the output of the HP power supply. Disconnect the multimeter to reduce the noise to signal ratio.
- S. Perform an energy per channel calibration of the MCA (Chapter 7).
- T. Turn the pulse generator off.
- U. Press *INIT+ERAS*.
- V. After a sufficient amount of data has been collected press *INIT+ACQ* keys. This stops the data acquisition process.
- W. Save the data (Chapter 2). *TRA^1,FILENAME.RAW*

Record in your lab book the HP power supply setting, angle of incidence, shaping time, gain, peak position of the pulse generator and the livetime.

Noise reduction is necessary when the peak appears near the noise level. Techniques that could possibly reduce the signal to noise ratio include: (1) grounding (2) shaping time setting (3) disconnecting the multimeter (4) cooling the DUT and (5) impedance matching. The pulse generator calibration is different for each shaping time. Using the desired shaping time to make an energy representation calibration of the pulse generator will ensure that the MCA energy calibration is correct.

If no data is being collected, check the items listed below.

1. All electrical connections.
2. Move the ACQ-STRB switch on the ADC to the off position then back to the ACQ position.
3. Angle of incidence.
4. The active ADC group is the acquiring ADC group.
5. The POS-NEG switch on the shaping amplifier may need to be changed.
6. Some devices have a small active area. Wait 15 minutes and check the data again.

CHAPTER 9: ND_NEWER.EXE

ND_NEW.EXE is a program that was written by David Roth (see his masters thesis for a complete program listing). It converts the binary format used by ND77 to an ASCII format. ND_NEWER is a later version with only a slight modification in the way data is computed and stored. A configuration file with the extension CNF is used as input for the program. The format for the configuration file is:

new	{Identifies the cnf file as a ND_NEWER cnf file}
9	{Incident ion number}
C:\RH6504\DEC91\RHCN00.RAW	{Input data path and file name}
C:\RH6504\DEC91\DATA\RHCN00.DAT	{Output data path and file name}
3	{Compression factor}
479	{Calibration peak position channel number}
4.80	{Calibration energy in MeV}
140.00	{Incident ion energy in MeV}
26	{Number of dead channels}
0.00	{Angle of incidence}
7.0123E+05	{Fluence}

The first entry must be entered at the top of the file. To convert more than one raw file, repeat lines 2 through 11 for each file. ND_NEWER.EXE does not use the angle of incidence and fluence entries. The path for the output data must exist.

APPENDIX F

MODELING CHARGE COLLECTION AND SINGLE EVENT UPSETS IN MICROELECTRONICS

Modeling charge collection and single event upsets in microelectronics ^{*,§}

P.J. McNulty, W.G. Abdel-Kader and J.E. Lynch

Department of Physics and Astronomy, Clemson University, Clemson, SC 29634-1911, USA

Received 23 January 1991

Single event upsets (SEU) result when modern microelectronic circuits are exposed to energetic charged particles in space, around accelerators and in the various natural or manmade radiation environments encountered by computers on earth. Estimating a circuit's SEU sensitivity at an early stage of system design requires detailed understanding of the physical phenomena through which upsets are induced, the localized generation of charge, its collection at the SEU-sensitive junction and the circuit's response. The amount of charge collected depends on the contribution from drift, field funneling and diffusion as well the removal of charge through recombination. Decreasing the area of the junction through improvements in lithography increases the complexity of the charge collection in a way which significantly complicates modeling.

1. Introduction

Soft errors or single event upsets (SEU) are charges in the logic state of microelectronic circuit elements which occur when ionizing particles traverse SEU-sensitive reverse-biased junctions on the device. They are induced by the heavily ionizing cosmic-ray nuclei of deep space, the heavily ionizing nuclear fragments from spallation reactions in the inner radiation belts, or the alpha particles emitted by the materials making up the device and its packaging. The standard models [1-3] for SEUs assume that circuit elements charge their electrical, and hence their logic, states when more than some critical charge is collected at the junction within a response time which is determined by the circuit parameters. The charge collected has two fast drift components, the charge generated in the depletion region of the junction and the charge brought in by funneling [4,5]. This is followed by a slow component of charge arriving gradually by ambipolar diffusion from regions further along the particle trajectory.

Accurate calculations of the error rates to be expected when a given device is flown in space requires quantitative knowledge of the various radiation environments of space, the physical mechanisms leading to the

generation of intense ionization trails along the charged-particle trajectories, the fraction of that charge arriving at the SEU-sensitive junction and the response of the circuit element to the resulting swing in potential. Algorithms currently used to predict error rates replace the SEU-sensitive junction by an equivalent volume and predict SEU rates by estimating the rate at which ionizing particles generate more than a threshold amount of charge within the sensitive volume. This threshold value of the charge collected is the so-called critical charge; its value differs for different circuits as does the dimensions of the sensitive volume which should be used in calculations.

There were five objectives in preparing this paper. First, outline the current states of charge collection at reverse-biased junctions thereby predicting the probability of upsetting the logic state of the cell. Second, provide equations for determining the dimensions of the sensitive volume to be used in calculations of error rates for a specific device. Their use must require only the type of information typically available regarding the masks and doping. Third, propose a simple experimental procedure for determining the proper value of the critical charge to be used in calculations. Fourth, illustrate these procedures using test data available for Intel's 2164A, an NMOS DRAM device. The procedure described in this paper is based on our current understanding of charge generation and collection at reverse-biased junctions. Since these are the SEU-sensitive targets in all device types, the procedures should be applicable to CMOS and bipolar circuits with appropriate modification for differences in circuit re-

^{*} First presented at the Tenth Conference on the Applications of Accelerators in Research and Industry, Denton, TX, November 7-9, 1988.

[§] Supported in part by the Air Force Systems Command and Defense Nuclear Agency.

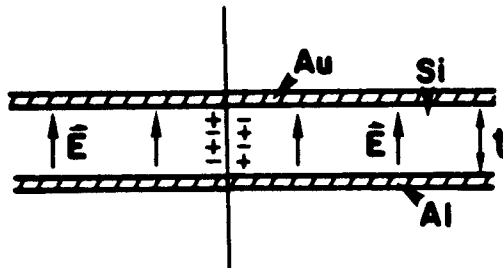


Fig. 1. Transmission-type solid state particle detector.

sponse. The final objective is to discuss the uncertainties in error-rate calculations resulting from the failure of the models used to predict the substantial deviations from a step function increase in SEU cross section as a function of the linear energy transfer (LET) of the incident particle.

2. First order model of soft errors

Current algorithms assume that an SEU-sensitive junction responds to being traversed by a charged particle in a manner similar to a solid-state particle detector of the transmission type shown in fig. 1. When sufficient bias is applied, the detector is fully depleted and all the charge generated within the silicon slab, except for a thin dead layer, is collected to form a transient voltage pulse between the gold and aluminium electrodes. If the measured charge collection is plotted versus the LET of the traversing particle, one obtains for a fully depleted detector a linear relationship of the type shown in fig. 2. The slope is the thickness of the sensitive volume, i.e., the thickness of the slab minus the dead layer.

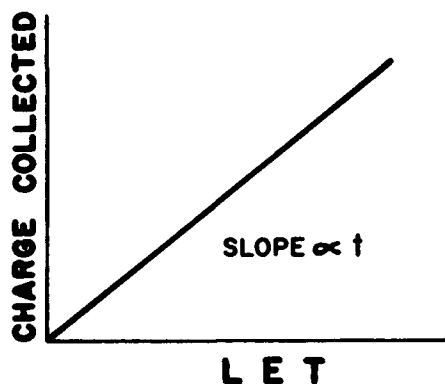


Fig. 2. Charge collection versus LET for detector of fig. 1. If the charge collected is expressed in units of energy deposition MeV and the LET is expressed in units of MeV/ μm , the slope is the path length through the sensitive volume.

The first order model for soft errors in microelectronics replaces the SEU-sensitive junction by a volume of silicon with dimensions chosen so that the charge generated within the sensitive volume equals the charge collected at the junction. The lateral dimensions of the sensitive volume are slightly larger than those of the junction, but the thickness is harder to specify. For bulk CMOS, NMOS and bipolar devices, the junctions behave like partially depleted detectors with the important difference that the junction area for a microcircuit element is so small that the charge generated along the portion of the trajectory within the sensitive volume may be comparable to the charge stored in the depletion region. As a result, the onset of charge collection from a heavily ionizing track may interfere with subsequent collection thereby destroying the linear relationship shown in fig. 2 [6]. For circuits using CMOS/SOI technology the sensitive volume should be confined to the region between the junction and the insulator substrate.

3. Dimensions of the sensitive volume

When a charged particle traverses a partially depleted junction of the type shown in fig. 3, the charge collected in the depletion region of the junction forms only a fraction of the total charge collected. Larger components are collected either by drift along the segment of charge adjacent to the junction (field funneling) or by diffusion from further along the track. This means that, at least for particles incident perpendicular to the surface, the detector of fig. 3 can be divided into three layers of charge collection corresponding to prompt and efficient collection by drift in the depletion and funneling layers and slower and inefficient collection from the rest of the detector. Expressions for the thickness of the depletion layers in terms of the doping concentration on both sides of the junction and the applied bias are given in most texts on semiconductor physics [7]. Hu [8] and Oldham and McLean [9] have derived expressions for the charge collection by funneling which are in reasonable agreement with experimental measurements. Accor-

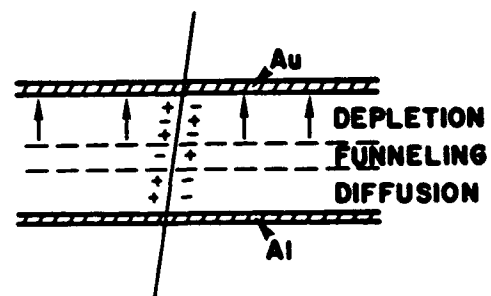


Fig. 3. Partially depleted solid state particle detector.

ding to Hu there is a linear relationship between the charge collected and the LET while for Oldham and McLean the relationship is a power law of the LET where the charge collected is proportional to LET^y , with $1 \leq y \leq 4/3$. There has been some preference for using Hu's expression in determining the dimensions of the equivalent sensitive volume because Hu's model leads to thickness of the drift layers which are independent of the stopping power or linear energy transfer (LET) of the incident particles. In many important device technologies, the largest component of the charge collected arrives by diffusion. Previous estimates of this component and the corresponding thickness of the sensitive volume involved random walk modeling using computer simulations [10]. We present here a simple equation for estimating the strength of the diffusion component of the charge collected and an expression for the thickness of the diffusion layer of the equivalent sensitive volume.

Typically, the lateral dimensions (length \times width) of the SEU-sensitive junction are taken to be the corresponding dimensions of the sensitive volume. The thickness of the sensitive volume is chosen such that the charge which would be generated in this equivalent sensitive volume equals the charge collected at the real junction. This collected charge has three contributions: (1) charge collected by drift in the depletion layer, (2) charge collected by field funneling from outside, and (3) charge that diffuses into the depletion region after the funneling of charge has ceased.

Random walk is assumed to be the characteristic of motion of the carriers arriving by diffusion. The simplest assumption is that the probability that a charge will arrive at the junction depends on the solid angle subtended by the junction. The solid angle subtended by a circular junction of radius a from the location of a point charge newly generated a distance z along its axis of symmetry is given by:

$$\Omega(z) = 2\pi \left(1 - \frac{z}{\sqrt{z^2 + a^2}} \right), \quad (1)$$

where Ω is the solid angle and z is the depth of collection. When $z \gg a$ eq. (1) can be approximated by:

$$\Omega(z) = \pi a^2 / z^2.$$

The probability of collection is the ratio $P(z)$ between the solid angle and 4π :

$$P(z) = \frac{\Omega(z)}{4\pi} = \frac{1}{2} \left[1 - \left(1 + \frac{a^2}{z^2} \right)^{-1/2} \right]. \quad (2)$$

The charge collected by diffusion Q_d can then be estimated from

$$Q_d = \int_{l_f}^{v_d \tau} \frac{dQ}{dz} P(z) dz, \quad (3)$$

where v_d is the diffusion velocity, τ is the minority carrier lifetime, l_f is the funneling length and

$$\frac{dQ}{dz} = \frac{LET(z)}{w},$$

where w is a conversion factor from MeV to picocoulomb (22.5 MeV/pC for silicon and 30.0 MeV/pC for gallium arsenide). The LET in the above equations is expressed in MeV/ μ m.

If the LET along the primary particle's track is constant then eq. (3) can be written

$$Q_d = \frac{LET}{2w} \left[v_d \tau - l_f - (v_d^2 \tau^2 + a^2)^{1/2} + (l_f^2 + a^2)^{1/2} \right]. \quad (4)$$

This expression was derived for particles incident along the axis of symmetry perpendicular to the junction but provides at least an approximation for particles striking the junction off center. The equivalent thickness t_3 of the layer of the sensitive volume corresponding to diffusion is, therefore:

$$t_3 = \frac{Q_d w}{LET} = \frac{1}{2} \left[v_d \tau - l_f - (v_d^2 \tau^2 + a^2)^{1/2} + (l_f^2 + a^2)^{1/2} \right]. \quad (5)$$

Eq. (5) represents the diffusion equivalent thickness t_3 . It depends on the doping concentration and the area of the device. The product of the diffusion velocity and the carrier lifetime $v_d \tau$ must be $\leq R$, where R is the particle track length. If $v_d \tau > R$ then the upper limit of the integral of eq. (3) must be equal to the track length R . If the circuit has a time constant such that the charge must be collected within that interval and the time constant is less than the recombination time, then that value should be used in eq. (5).

The thickness of the depletion region t_1 is given by the following expression:

$$t_1 = W = \left[\frac{2\epsilon}{e} \left(\frac{1}{N_a} + \frac{1}{N_d} \right) (V_{bi} - V) \right]^{1/2}, \quad (6)$$

where ϵ represents the permittivity which is equal $11.9\epsilon_0$ for silicon and $13.1\epsilon_0$ for gallium arsenide. The value of ϵ_0 is 8.85419×10^{-12} (C² N⁻¹ m⁻²). Also, e represents the electronic charge. N_a and N_d are the acceptor and donor doping levels, V_{bi} is the built-in voltage, and V is the applied bias to the junction. For the case of p-type substrate, $1/N_a$ can be neglected with respect to $1/N_d$ because of $N_a \gg N_d$ and vice versa for n-type substrate.

The funneling length l_f can be estimated from the expression given by Hu [8] for p-type substrate:

$$t_2 = l_f = (\mu_n / \mu_p) t_1, \quad (7)$$

where μ_n and μ_p are the electron and hole mobilities. For n-type substrate, the ratio μ_n / μ_p in eq. (7) becomes μ_p / μ_n . The total thickness of the sensitive volume t can

Table 1.

A comparison between the thickness of the sensitive volume calculated from eq. (8) and the one calculated from the ratio of the critical charge to the threshold LET for two devices.

Device	Area [μm^2]	Effective thickness	
		Eq. (8) [μm]	$Q_{\text{crit}}/\text{LET}_{\text{th}}$ [μm]
I2164A	140	3.5	3.4
TMS4256	31	2.1	N/A

be estimated as the sum of the drift and diffusion components:

$$l = l_1 + l_2 + l_3. \quad (8)$$

Consider the following example in which the thickness is calculated for Intel's 2164A DRAM by using the information available from the manufacturer which includes the area of the sensitive junction ($140 \mu\text{m}^2$), the depletion width ($l_1 = W = 0.18 \mu\text{m}$) at 5 V, and the fact that the substrate is p-doped. Using eq. (6) to determine the doping concentration for the substrate of the Intel 2164 A given the thickness of the depletion region at 5 V given above, one obtains $N_d = 2.65 \times 10^{17} \text{ atoms/cm}^3$. Fig. 3.28 of ref. [11] can be used to estimate the carrier lifetime as $1.45 \times 10^{-6} \text{ s}$ for p-substrate. The μ_n and μ_p are estimated from fig. 18 of ref. [7] as $550 \text{ (cm}^2 \text{ V}^{-1} \text{ s}^{-1})$ and $243 \text{ (cm}^2 \text{ V}^{-1} \text{ s}^{-1})$, respectively. The value of l_2 then calculated from eq. (7) is $0.41 \mu\text{m}$. Eq. (5) is used to estimate the thickness equivalent to diffusion l_3 . For the Intel 2164A DRAM, $a = 6.67 \mu\text{m}$. The product of v_d and τ is equal to the diffusion length $L_D = \sqrt{D_n \tau_n}$, where $D_n = \mu_n KT/q$ and $KT/q = 0.0259 \text{ V}$ at room temperature. The value of $L_D = 45.55 \mu\text{m}$ for electrons. The value obtained for l_3 is $2.89 \mu\text{m}$. The sum of the three thickness from eq. (8) is $3.5 \mu\text{m}$ which can be taken as the estimate of the thickness of the equivalent sensitive volume.

This value agrees reasonably well with the value of $3.4 \mu\text{m}$ estimated by the ratio of the critical charge 149 fC from the manufacturer and the threshold LET as determined by the heavy ion data [12]. Values of the thickness of the sensitive volume estimated this way are given for two DRAMs in table 1.

4. Determining the critical charge

The standard method for determining the critical charge is to irradiate the device by energetic ions over a wide range of LET values obtaining a plot of the SEU cross section vs effective LET similar to that shown in fig. 4 for Intel's 2164 A, a DRAM. Threshold occurs when the SEU cross section rises with LET until reaching a plateau value which should approximate the area

of sensitive junction. The data for this device was chosen for illustration because the manufacturer has provided an estimate of the critical charge as well as the other circuit data needed for modeling. The plateau cross section agrees with the area of the storage cell. The threshold LET at normal incident can be obtained from the ratio of the critical charge and the thickness of the sensitive volume. The latter is obtained from eqs. (4) through (8). The critical charge was provided by the manufacturer. The triangle in fig. 4 has this threshold LET for an abscissa value and 50% of the plateau value for its ordinate. It appears to be consistent with the heavy ion data in fig. 4. The data from fig. 4 formed the basis of Monte Carlo simulations using the CUPID codes [13] to predict the proton SEU cross section at a number of incident energies and the values obtained were in agreement with the experiment [12].

Given the consistencies listed above, it appears reasonable that the critical charge can be properly estimated from the product of the LET and the path length through the sensitive volume. The problem with this approach is that heavy ion irradiations are expensive and tedious. There is an alternative procedure which requires only a single irradiation with protons. It consists of a proton irradiation carried out to determine the SEU cross section at a given incident energy for comparison with a simulation of the charge-collection spectra for the same irradiation using the CUPID simulation codes. The CUPID codes have been shown to accurately predict charge-collection spectra in well defined sensitive volumes having an area of 25 mm^2 and thickness ranging from 2.5 to $97 \mu\text{m}$. Fig. 5a shows the simulated charge collection spectra for a sensitive volume having the cross sectional area of the sensitive junction listed in table 1 for the 216A and the calculated thickness of $3.6 \mu\text{m}$ exposed to protons incident at

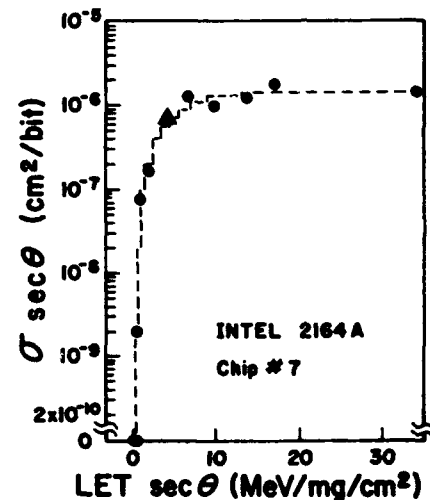


Fig. 4. SEU cross section vs effective LET for Intel's 2164A.

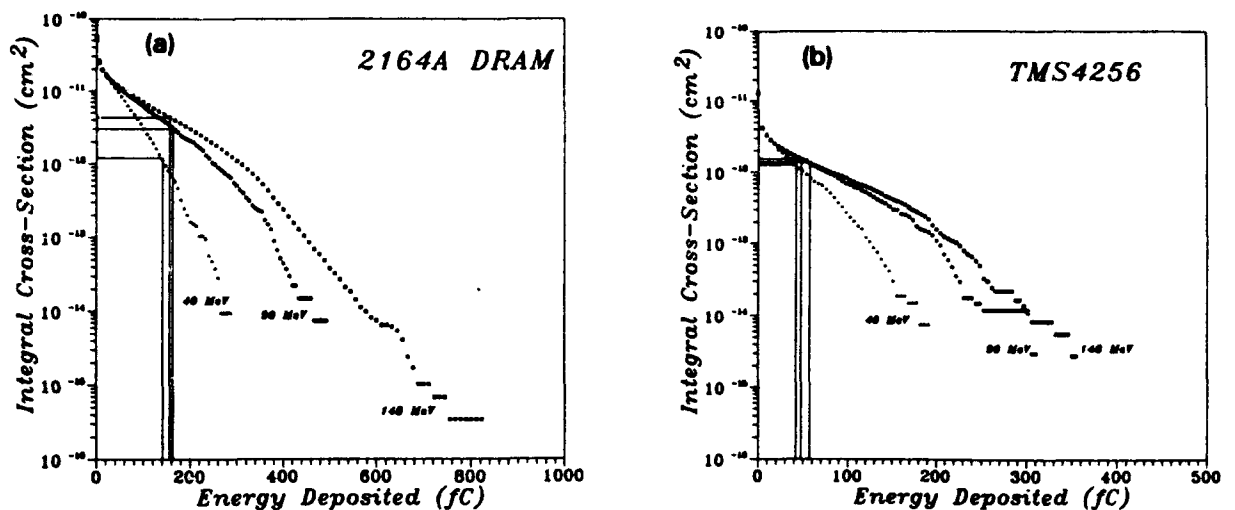


Fig. 5. SEU cross section vs charge collected. Data represents values obtained from simulations using CUPID for two devices (a) Intel 2164A, a 64K DRAM and (b) Texas Instruments TMS 4256, a 256K DRAM. Simulations are shown for 40, 90 and 148 MeV. Horizontal lines are SEU cross sections and corresponding vertical lines are the estimated values of the critical charge.

energies of 40, 90 and 148 MeV. The spectra are plotted as an integral spectra, i.e., the cross section for generating at least some value of the charge is plotted against that value of the charge. The measured SEU cross section for that device is represented by a horizontal line in fig. 5a drawn until it reaches the simulation curve; the vertical line drawn from this point of intersection marks the value of the critical charge on the abscissa. Despite the significant difference in the three spectra and the SEU cross sections, the values obtained for the critical charge appear to be consistent. Fig. 5b illustrates the same approach for the TMS 4256. Table 2 illustrates the value of the critical charge obtained this way for the 148 MeV protons irradiation for both devices along with the value estimated from the manufacturer for the Intel 2164A. The values obtained for Intel 2164A at 40 and 90 MeV protons are 141 and 163 fC, respectively. The values obtained for the Intel device are consistent with the manufacturer's estimate and also with the value obtained from the product of the threshold LET in fig. 4 and the thickness of the sensitive volume calculated from eqs. (4) through (8). The

values obtained for TMS4256 at 40 and 90 MeV protons are 42 and 57 fC, respectively. Unfortunately, a theoretical estimate of the critical charge for the TMS 4256 was not available. Manufacturer's estimates of the charge that can be stored in a full cell is also listed in table 2 for both devices

5. Complications in the first order model

The modeling approach described above assumes that the charge collected is the same as the value obtained from the product of the LET and the path length through the sensitive volume and that the dimensions of the sensitive volume are independent of LET. This ignores a possible increase in the funneling component of the thickness with LET [9] and a possible decrease in thickness with LET due to recombination increasing with LET. Significant reductions in the calculated thickness with LET have been observed for charge collection measurements obtained with the 2164A [6] but with the storage cells in the full rather than empty state. The

Table 2.

A comparison of the critical charge (Q_c) from the manufacturer with the value estimated using CUPID calculations and experimental SEU cross section for 148 MeV protons.

Device	Stored charge [fC]	SEU cross section $\times 10^{-12}$ [cm ² /Bit]	Q_c (manufacturer) [fC]	Q_c (CUPID) [fC]
I2164A	435	4.35	149	156
TMS4256	250	1.54	N/A	48

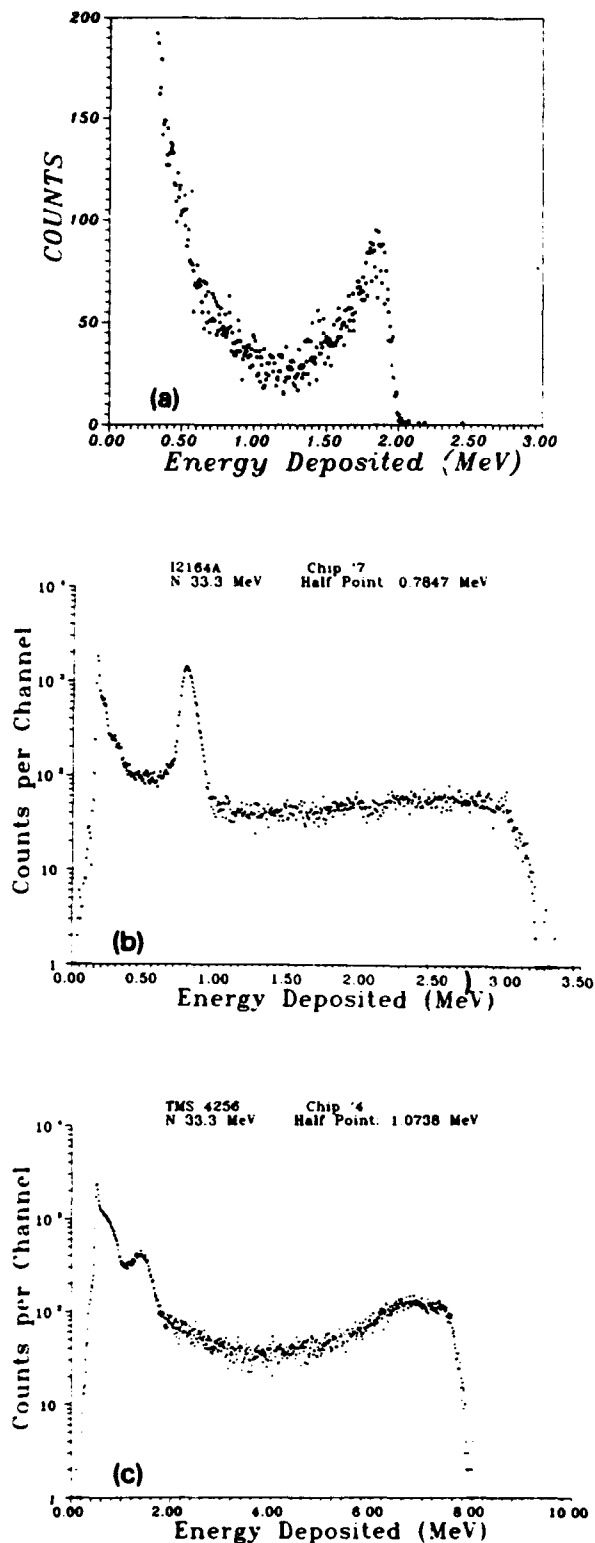


Fig. 6. Charge collection spectra obtained for three devices with junction areas: (a) $3 \times 10^3 \mu\text{m}^2$, (b) $140 \mu\text{m}^2$, and (c) $31 \mu\text{m}^2$. The first spectrum is measured from a test structure while the latter two are measured from the power lines of DRAMs.

depletion width is approximately 30% lower for the full state than it is for the empty state. This reduction with increasing LET may also be the result of the small area of the junctions for two reasons. First, the fact that the charge injected is comparable to the total charge stored in the depletion region of a small area junction may reduce the drift contributions from the values obtained with larger area junctions [7–9]. Second, the charge arriving at the depletion region of a small area junction must travel close to the trajectory, thereby increasing changes of recombination. It is most important that the question of whether the charge collected is proportional to the LET be settled by experiment for CMOS and other important junctions. A second complication is that the charge collected upon exposure to monoenergetic ions in a narrow range of LET values is a sharply peaked spectra only for large area junctions. The spectra obtained for three junctions with areas of 3×10^3 , 140 and $31 \mu\text{m}^2$ are compared in fig. 6. The first junction is a single test structure while the data for the latter two junctions were measured off the power lines of working DRAMs following the techniques described for DRAMs in ref. [6] and NMOS SRAMs in ref. [14]. The broad band of events to the right of the peaks are due to particles hitting input/output structures outside the memory array.

The peaks in the spectra of fig. 6b and c are due to traversals of the memory array [6]. The dimensions of the junctions in fig. 6c approach those typical of CMOS. The peak is smaller and broader for the smaller junctions. As the junctions decrease in size their charge collection properties become complicated. The number of particles traversing the central region of the sensitive volume (central hit) decrease relative to the number hitting the edges of missing the junction entirely [15]. Hits on the edge have been shown to result in enhanced charge collection. When the particles miss the junction some charge still arrives at the junction by diffusion. These events should appear to the left of the peaks in figs. 6b and c while edge-effect events should lie to the right of the peaks. Unfortunately, the region to the right of the peaks in fig. 6c are dominated by hits in the input–output circuitry.

5.1. Threshold dependence on LET

This charge-collection spectra observed for small area junctions may be the basis of the slow rise in SEU cross section with LET seen in fig. 4 and in many other data sets. When the product of path length and LET is below the critical charge there are still some events which induce upsets, presumably because the charge collected exceeds threshold. This suggests that the shape of the cross section versus LET curve should depend on the area of the junction. It is imperative that the reason for the slow rise of the SEU cross section with LET be

Table 3.

A comparison of the upset rate calculations using a single threshold with the more detailed calculation.

Algorithm predictions for 2164A (Adams 90% worst case environment)	
Technique	Upsets/bit-day
Single (50%)	3.3×10^{-5}
Multiple	2.7×10^{-4}

understood sufficiently to allow quantitative predictions because it is currently a limiting factor in SEU rate estimates for space. Table 3 compares the SEU rates predicted by the CREME program [16] for Intel's 2164A using a single sensitive volume with the dimensions estimated by the procedures described above and the predictions obtained by representing the data of fig. 4 by a weighted set of sensitive volumes, each set having different total area and different thresholds, as determined by the dashed curve fitting the shape of the rise in fig. 4. As seen in table 3, there is a difference of an order of magnitude between the single threshold result and the result of the more detailed, and presumably more correct, calculation.

The following analysis illustrates how the shape of the charge collection spectra can influence that of the threshold curve. Let it be assumed that a device having SEU-sensitive junctions which are identical to the above test structure will upset if more than some critical

charge is collected but not otherwise. Let it be further assumed that the value of the critical charge corresponds to the position on the pulse-height spectra marked Q_c in fig. 7. Let particles be incident with LET values of x , $2x$ and $3x$. The lower figure illustrates how the cross section for pulses exceeding Q_c varies with the incident particle's LET. Since for an LET value of x none of the pulses deliver more charge than Q_c , the number of events in which threshold is exceeded for that LET must be zero. If the particle's LET is doubled to $2x$, the pulse-height spectrum shifts to higher energies as shown in the middle figure on top of fig. 7 so that the peak position coincides with the critical charge. This means there will be a sharp rise in the number of times that threshold is exceeded between $LET = x$ and $LET = 2x$, as illustrated in the lower figure, and that the steep rise continues until LET values are reached where the entire peak lies to the right of Q_c , as it does for $LET = 3x$.

The shape of the threshold response curve in the lower figure of fig. 7 is determined by the shape of the peaks in the pulse-height spectra for the device. The cross section would be zero for LET values up to and including x . It remains zero until the LET values are reached where a few enhanced charge-collection events exceed the critical charge. The cross section at this point is much smaller than the geometric cross section of the junction. As the LET increases so that a fraction of the events making up the peak exceed the critical charge, the cross section increases rapidly. The ratio of the number of events under the peak in fig. 7 to the fluence should be the area of the junction as it was earlier for the particle detector. Therefore, the cross section after the sharp rise in LET should be just above the geometric cross section of the junction A, as shown in the lower figure. Beyond $LET = 3x$ the cross section continues to increase, but the rise is now more gradual. This gradual increase is due to the events in which the particle misses the junction, but the charge collected by diffusion still exceeds the critical charge.

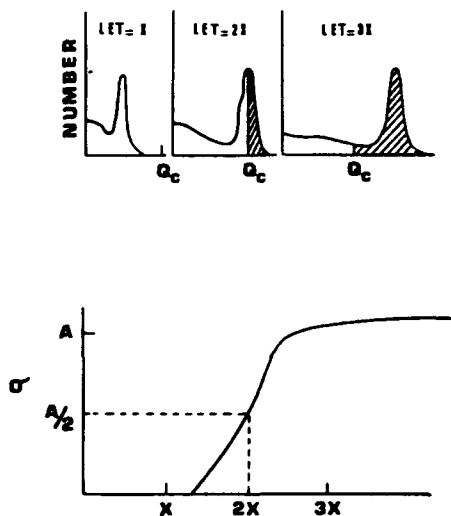


Fig. 7. Schematic representation of pulse-height spectra obtained by exposure of the same device to particles at an $LET = x$, $LET = 2x$, and $LET = 3x$. Q_c represents the critical charge for that device. The bottom plot is of the cross section for depositing at least Q_c vs LET for the same device. The shape of the cross section curve is determined by the shape of the peak in the charge-collection spectra shown above.

6. Multiple-upset events

Fig. 8 shows a pattern of upsets obtained from an irradiation of the Intel 2164A with heavy ions. The location of each upset is plotted according to its topological location on the die. The pins of the chip package are shown for orientation. No events are seen in the external right hand portion of the memory array because of the shadowing of the beam by an obstacle. The pattern in the exposed area appears to show more clumping than expected from a random distribution. In fact the computer reports numerous multiple-error events despite the fact that the data was taken with the beam particles incident at an angle of 60° to the

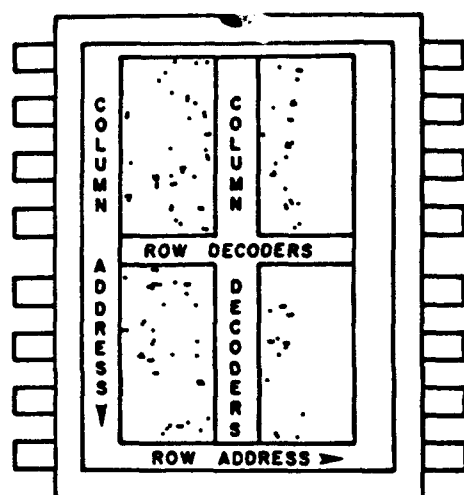


Fig. 8. Topographical map of errors on Intel 2164A for heavy ions incident at 30° above plane of die, multiple errors evident as clumps.

surface. At this angle of incidence, each particle traverses only one junction. Multiple-error events are also common at normal incidence. Multiple-error events have also been reported in VLSI CMOS where the sensitive junctions are not adjacent as in DRAMS. One possible explanation is that the field funneling does not start until the tracks have expanded by ambipolar diffusion sufficiently to trigger simultaneous funnels at different junctions [17]. An alternative explanation may be suggested in the spectra of fig. 6. If the peak value is above threshold the same particle trajectory may be a "hit" for one junction and a "miss" for a number of other neighboring junctions. The "missed" junctions for which the charge collection exceeds the critical charge will also be upset. Whatever the explanation turns out to be multiple-error events are increasing in importance as the junction area shrinks.

7. Summary

Current algorithms for calculating SEU rates require specification of the dimensions of a critical volume to be associated with each SEU-sensitive junction and the value of the critical charge which must be generated within the volume for an upset to occur. Theoretical and experimental procedures are provided for determining those parameters. The value of the critical charge estimated using the measured SEU cross section and the CUPID code simulations for the same incident proton energies agree with the manufacturer's estimate and the heavy-ion data for the Intel 2164A. Equations are presented which estimate the thickness values for the

equivalent sensitive volume. The value of the critical charge given by the product of the SEU threshold LET measured with heavy ions and the estimated thickness agrees with the proton estimates and the value given by the manufacturer. The charge collection spectra measured on microelectronic circuits are distributed about the value given by the product of LET and path length through the sensitive volume. This distribution may provide an explanation for the gradual rise in SEU cross section with LET. There is still a large inaccuracy inherent in assuming a single step function threshold without taking the shape of the rise in cross section with LET into account.

Acknowledgements

This work was funded in part by the Defense Nuclear Agency under contract DNA001-86-C-0076 and the Air Force System Command under Boston College subcontract 940-1 P0141-976. We gratefully acknowledge help from J. Beauvais, W. Weber and M. Yaktien of our laboratory. The cooperation of the staff of the Harvard Cyclotron and the Pittsburgh Tandem Van de Graaff are also appreciated.

References

- [1] D. Binder, E.C. Smith and A.B. Holman, IEEE Trans. Nucl. Sci. NS-22 (6) (1975) 2675.
- [2] J. Pickel and J.T. Blandford, Jr., IEEE Trans. Nucl. Sci. April (1980) 1006.
- [3] P.J. McNulty, G.E. Farrell, R.C. Wyatt, P.L. Rothwell, R.C. Filz and J.N. Bradford, IEEE Trans. Nucl. Sci. NS-27 (6) (1980) 1516.
- [4] C.M. Shieh, P.C. Murley and R.R. O'Brien, IEEE Electron Dev. Lett. EDL-2 (1981) 103.
- [5] C.M. Shieh et al., Proc. IEEE Int. Reliability Phys. Symp. Orlando Florida, April (1981) 38.
- [6] P.J. McNulty and J.E. Lynch, in preparation.
- [7] See for example, S.M. Sze, Physics of Semiconductor Devices, 2nd edition (Wiley/Interscience, New York, 1981).
- [8] C. Hu, IEEE Electron Dev. Lett. EDL-3 (1982) 31.
- [9] F.B. McLean and T.R. Oldham, IEEE Trans. Nucl. Sci. NS-29 (1982) 2018.
- [10] W.G. Abdel-Kader, P.J. McNulty, S. El-Teleaty, J. Lynch and A.N. Khondker, IEEE Trans. Nucl. Sci. NS-34 (1987) 1300.
- [11] H.F. Wolf, Semiconductors, 1st edition (Wiley/Interscience, New York, 1971).
- [12] J. Bisgrove, J.E. Lynch, P.J. McNulty, W.G. Abdel-Kader, V. Kletnieks and W.A. Kolasinski, IEEE Trans. Nucl. Sci. NS-33 (6) (1986) 1571.
- [13] P.J. McNulty, G.E. Farrell and W.P. Tucker, IEEE Trans. Nucl. Sci. NS-28 (6) (1981) 4007.

- [14] P.J. McNulty, D.R. Roth, W.J. Beauvais, W.G. Abdel-Kader and D.C. Ding, Nuclear Tracks and Radiation Measurements, to be published.
- [15] P.J. McNulty, Predicting Single Event Phenomena in Space, 1990 IEEE Shortcourse: Microelectronics for the Natural Radiation Environments of Space, ed. P.J. McNulty (IEEE, Reno Nevada, 1990).
- [16] J.H. Adams, Jr., IEEE Trans. Nucl. Sci. NS-30 (1983) 4475.
- [17] G. Messenger, private communication.

APPENDIX G

COMPARISON OF THE CHARGE COLLECTING PROPERTIES OF JUNCTIONS AND THE SEU RESPONSE OF MICROELECTRONIC CIRCUITS

COMPARISON OF THE CHARGE COLLECTING PROPERTIES OF JUNCTIONS AND THE SEU RESPONSE OF MICROELECTRONIC CIRCUITS

P.J. McNulty, D.R. Roth, W.J. Beauvais, W.G. Abdel-Kader and D.C. Dings

Department of Physics and Astronomy, Clemson University
Clemson, SC 29634-1911, U.S.A.

ABSTRACT

The transient voltage swings which result from the collection of charge across junctions traversed by heavy ions can be measured from the power and ground pins of static RAMs using pulse-height analysis systems similar to those used for solid state detectors. Procedures for estimating the dimensions of the sensitive volumes to be associated with the SEU-sensitive junctions from the pulse-height data are described along with a simple procedure for estimating the critical charge from a comparison of the SEU cross section measured with protons and the pulse-height spectra obtained with the CUPID simulation codes. These procedures are demonstrated on the IDT 6116V, an RMOS SRAM.

KEYWORDS

SEU; critical charge; RMOS; SRAM; microelectronic; reverse-biased junction.

INTRODUCTION

Manufacturers increase the number of logic elements on modern microelectronic circuits by decreasing the average size of the individual circuit elements. As their dimensions approach microscopic values, the elements become sensitive to ionising radiation in an entirely new way. It was discovered that the electrical state, and hence the logic state, of these elements could be altered as a result of a single interaction with an energetic cosmic-ray particle (Binder et al., 1975). This phenomenon is known as a single event upset (SEU). The logic states of circuit elements become more sensitive to SEUs as their dimensions decrease because correspondingly smaller differences in charge storage on these junctions separate the two logic states of the element. Information is represented on some modern devices by such small amounts of energy that it can be altered by the passage of a particle as lightly ionising as an alpha particle.

The algorithms currently in use for predicting SEUs require, as input, the dimensions of the equivalent sensitive volume associated with each SEU-sensitive junction and the threshold value of the charge (critical charge) which must be generated within the sensitive volume to upset the circuit element (Pickel et al., 1980; McNulty, 1990). Because the number of ion pairs generated is proportional to the energy deposited for most radiations, the critical charge can also be expressed as a threshold energy deposited. This article demonstrates simple experimental procedures for estimating the dimensions of the sensitive volume. It also describes a simple procedure for estimating the critical charge for a device by means of a single irradiation by protons. These procedures are illustrated and tested by analysis of the IDT 6116V RMOS SRAM. The paper begins with a brief discussion of reverse-biased junctions and their use in particle detector systems.

REVERSE-BIASED JUNCTIONS

The reverse-biased junction formed at the interface between regions of a silicon crystal which have different doping characteristics is the basis for both the diode action required for the operation of the transistors forming modern microelectronic circuits and the particle detection characteristics which lead to SEUs. A depletion region consisting of layers of positive and negative charges appears on opposite sides of the junction, as shown in Fig. 1. The depletion region grows thicker when the junction is reverse biased, becoming thinner in the absence of bias and thinning to the point of disappearance as the junction is forward biased. The charges in the layers making up the depletion region are fixed to the donor and acceptor atoms on either side of the junction and, consequently, the thickness of the depletion region depends on the doping levels on both sides. The higher the doping density, the thinner the depletion region is on that side of the junction. Strong electric fields connect the charges on either side, and the direction of the field lines orient perpendicular to the junction. In the absence of external disturbances, the electric field does not extend beyond the depletion region. Charges generated as electron-hole pairs within the

depletion region or individual charges wandering into the depletion region are accelerated under the force of the field with electrons and holes attracted to opposite sides. This flow of current across the junction results in a measurable decrease in the voltage difference across the junction. This voltage swing is the basis of the operation of solid-state silicon and germanium particle detectors as well as the mechanism for SEUs in microelectronic circuits.

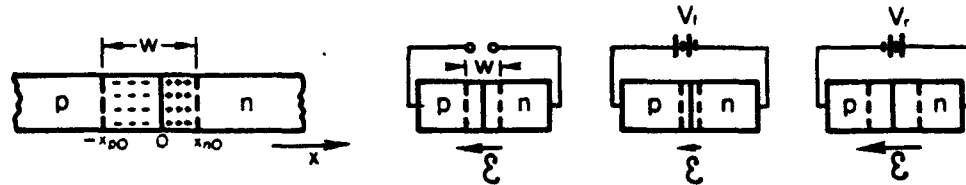
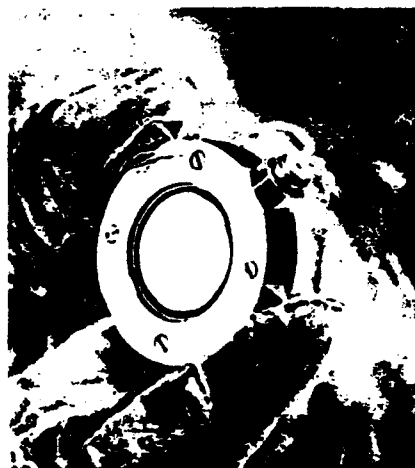


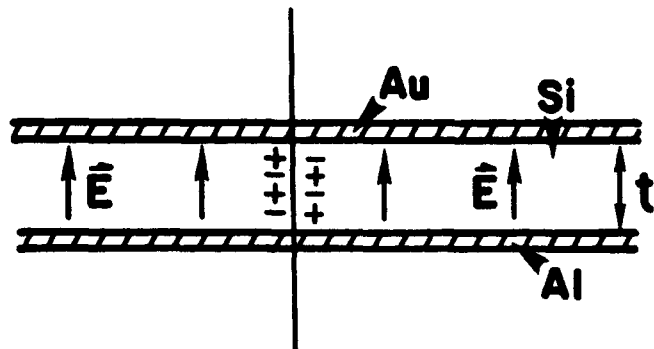
Fig. 1. Schematic of a reverse-biased junction.

Particle Detectors

The fully depleted surface barrier detector is the easiest example of charge collection to analyze quantitatively. A photograph of a silicon surface-barrier detector consisting of a biased p-n junction with metallic surface electrodes is shown in Fig. 2 along with a schematic cross-sectional view. The circuitry necessary to measure and record the amount of charge collected as a result of the junction being traversed by a charged particle is outlined in Fig. 3. If the detector is fully biased, the depletion region fills almost the entire volume of the silicon, and all the electrons and holes are accelerated under electric fields toward their respective terminals. The result is a fast voltage pulse. The preamplifiers used in pulse-height analysis have long time constants relative to the time required for the charge collection and the time constants of the device. As a result, the pulse height of the signal emerging from the preamplifier is proportional to the integral over time of the current pulse from the detector, which means that the signal entering the amplifier is proportional to the total charge collected across the junction. The shaping amplifier increases the pulse height so that it lies within a range of values suitable for sorting by the pulse-height analyzer. See Knoll (Knoll, 1989) for a complete discussion of the operation of particle detectors and pulse-height analyzers.



a



b

Fig. 2. a) Photograph of a surface barrier detector. b) Schematic of a fully depleted version in cross section.

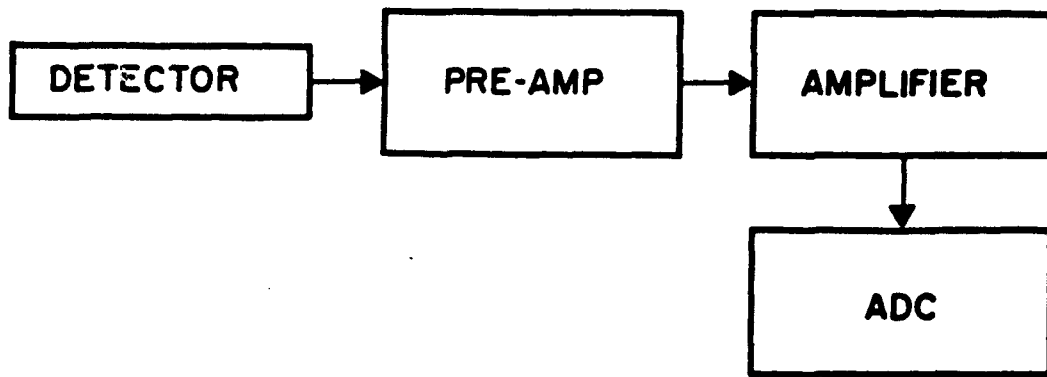


Fig. 3. Circuit used for pulse-height analysis.

Figure 4 shows a typical pulse-height spectrum obtained when the detector in Fig. 2 is irradiated with identical monoenergetic heavy ions, in this case 4.8 MeV alphas. Charge collection is plotted on the abscissa in the units of energy deposition typically used in radiation physics. The equivalence between charge collected and energy deposited is based on the fact that for most particles the number of electron-hole pairs generated along the path of an ionising particle is proportional to the energy deposited along the trajectory. The average energy deposited per pair generated is 3.6 eV for silicon and 4.8 eV for gallium arsenide with the result that 1 pC is the charge collected when 22.5 MeV energy is deposited in silicon and 1 pC in gallium arsenide requires an average deposition of 30 MeV.

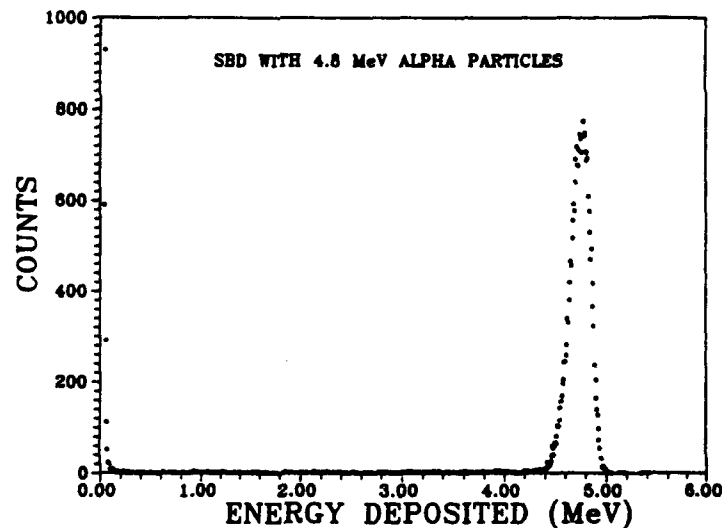


Fig. 4. PHA spectrum for a fully depleted detector exposed to 4.8 MeV alphas at room temperature.

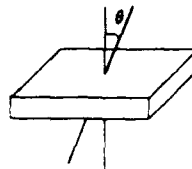
Dimensions of the Sensitive Volume

A spectrum of the type shown in Fig. 4 can be used to confirm the area of the sensitive volume of the detector. The sensitive volume is defined to be that region of the silicon within which the charges generated by the traversing particles are efficiently collected at the junction. For the surface-barrier detector, the sensitive volume is virtually the entire slab of silicon. Only the charges generated within the ultrathin dead layers formed by the highly doped regions of the ohmic contacts are not collected. The ratio of the number of events under the peak to the fluence of incident particles equals the cross-sectional area of the sensitive volume of the detector. The thickness can be obtained from the peak position in the spectrum using range-energy tables.

The charge collected across a junction traversed by an ionizing particle depends on the density of charge generated along the particle's trajectory. The linear energy transfer (LET) represents both the energy deposited in the medium per unit pathlength and the number of pairs generated per unit pathlength. A related concept often used in characterizing the SEU-sensitivity of a device is the "Effective LET" which is defined in Fig. 5. If the position of the peak of the pulse-height spectra is plotted versus the Effective LET of the high-energy incident particle, the result for a fully depleted detector is a linear relation that passes through the origin, as illustrated in Fig. 6. The slope of the curve is the product of the density of silicon 2.32 g/cm^3 and the thickness of the sensitive volume of the detector. Therefore, for fully depleted detectors at least, there are different ways of experimentally determining the dimensions of the active (or sensitive) volume of the silicon.

EFFECTIVE LET

$$\text{LET}_{\text{EFF}} = \text{LET} \sec \theta$$



Equivalent to the LET times the pathlength divided by the thickness.

Fig. 5. Definition of effective LET for a thin detector.

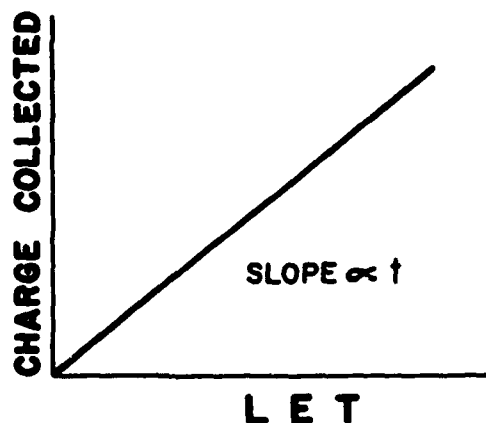


Fig. 6. Charge collection versus LET for thin fully depleted silicon insurface barrier detectors exposed to energetic heavy ions.

One advantage of working with thin fully depleted detectors is that models of energy deposition by different radiations can be tested in well defined sensitive volumes. An example is shown in Fig. 7 where the measured integral energy deposition spectrum is compared with the results of the CUPID (Clemson University Proton Interactions in Devices) simulation codes (Hamm *et al.*, 1981). The curves are integral plots i.e., they are plots of the cross section for depositing at least some energy E versus E . This format is useful for data analysis because, according to the sensitive-volume approach, a circuit element upsets when more than a threshold amount of energy (critical charge) is deposited within the sensitive volume. The ordinate then becomes the cross section for upsetting a device with a critical charge given by the abscissa. Data taken in this manner has been used for comparison to other Monte Carlo and analytic models (McNulty *et al.*, 1981, Hamm *et al.*, 1981).

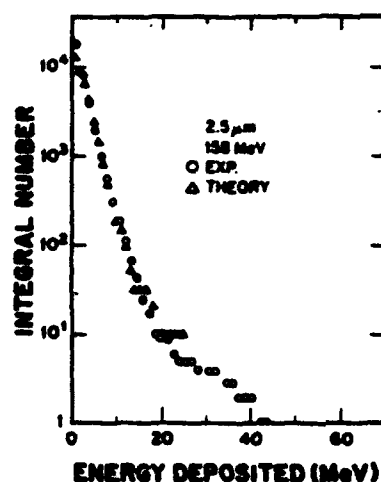


Fig. 7. Integral number of events in which at least energy E is deposited in a detector versus E . The active sensitive volume of the detector is a cylindrical disk with a cross sectional area of 25mm^2 and a thickness of $2.5\text{ }\mu\text{m}$. The experimental data was obtained with an Ortec surface barrier detector and the theoretical simulations were carried out using CUPID.

Microelectronic Junctions

The charge collection at an SEU-sensitive junction in a microelectronic circuit is more complicated than it was for the fully depleted junctions discussed above because the circuit junctions are only partially depleted and they are much smaller in area than those on the detectors. The phenomena involved in charge collection across a small partially depleted junction are outlined in Fig. 8. The passing particle generates numerous electrons and holes along its trajectory. This cylindrical sheath of charge acts as an electrical short through the depletion region. The entire column of charge expands radially by ambipolar diffusion until the charge density level reaches the doping density of the medium. At that point the electric fields penetrate the sheath and accelerate the charges toward their respective electrical contacts. This latter is the so-called funneling action (Hu, 1982; McLean et al., 1982; Oldham et al., 1983 and 1986). Eventually the funnel collapses and subsequent charge is collected by the slow random motion typical of diffusion. As a result, the pulse across such a junction has a time sequence which is quite different from the case of the fully depleted detector discussed earlier. Figure 8b illustrates the drift and diffusion components of the charge-collection current as a function of time. Diffusion contributes a slowly arriving component to the total charge collected at the junction which would not be present in the fully depleted detector.

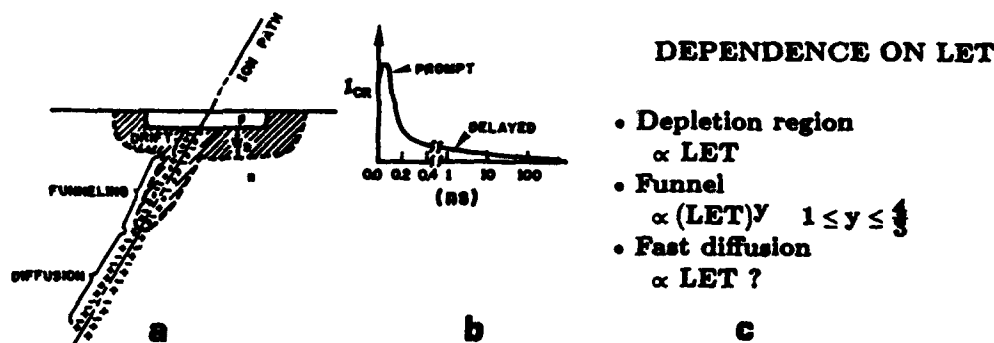


Fig. 8. a) Schematic of a particle traversing a junction showing portions of the trajectory where charge is collected by drift and diffusion. b) Charge collection across junctions versus time. Portions of the pulse due to drift and diffusion are illustrated. c) Dependence of the charge collection components on LET.

A simplifying assumption, which is presently being made for most SEU-rate predictions, is that the threshold for upsetting a given circuit is determined by the total charge collected within a period of time determined by the time constants of the circuit. This is the so-called critical charge. With the circuits typical of today's technology, the critical charge includes all of the depletion-region and funnel portions of the drift component and some part of the diffusion component. Estimating what fraction of the diffusion component of the charge collected contributes to upsetting the device requires comparison of oscilloscope traces of the charge-collection pulses with the circuit's relevant time constants. Circuits like DRAMS in the static mode include all the diffusion as well as the drift components, while circuits with switching speeds of a few nanoseconds or less would include little or no diffusion. It is difficult to specify the appropriate time constants for determining the fraction of the charge collected which contributes to upsetting the device. It must be less than the switching speed, but how much less is not easily known, by the purchaser of the device. Circuits currently flying in space have switching speeds of from twenty to hundreds of nanoseconds and so some portion of the charge arriving by diffusion must be included. Abdel-Kader *et al.* (1987) discuss the relative contributions of the drift and diffusion components of the charge collected for a small junction in bulk silicon.

There are other complications in the charge collection at partially depleted junctions beyond the extension of the temporal pattern induced by the diffusion component. The charge collected from the depletion region should on average increase linearly with LET until the LET values are so high that recombination becomes important or the charge collected approaches the fixed charge making up the junction and the depletion region collapses. The drift component from outside the depletion region is taken as linear by Hu (Hu, 1982) and as nonlinear by Oldham and McLean (McLean *et al.*, 1982, Oldham *et al.*, 1983 and 1986) but their later paper does not rule out linearity. This is an important point. Fully depleted detectors showed a linear relation and the detector could be modeled as a sensitive volume of silicon where the charge generated within the sensitive volume equals the charge collected across the junction. A nonlinear dependence on LET would mean that the dimensions of the sensitive volume depend on the LET of the incident particle.

The charge collection by junctions which have microscopic dimensions is further complicated by the phenomena illustrated in Fig. 9a which shows particles hitting the depletion region of a junction, hitting the edge, and missing the junction entirely. Particles traversing the central region of the junction provide a number of events with about the same value of charge collected. These events form the peak in the pulse-height spectrum of Fig. 9b which was obtained with a test-structure of a CMOS drain-substrate junction. The peak in the spectrum is clearly observable at the high-energy end of the spectrum. Particles traversing unprotected edges of the junction experience enhanced charge collection. As junctions decrease in size, the events at the edge become a larger fraction of the spectrum. Defects in the junction are another possible cause of enhanced charge collection. Events in which the particle misses the junction, so that either no drift component or a reduced drift component occurs, may still have a significant amount of charge collected at the junction through diffusion. These events lie on the low energy side of the peak in Fig. 9b. A small number of enhanced charge collection events on the high-energy side of the peak are also visible.

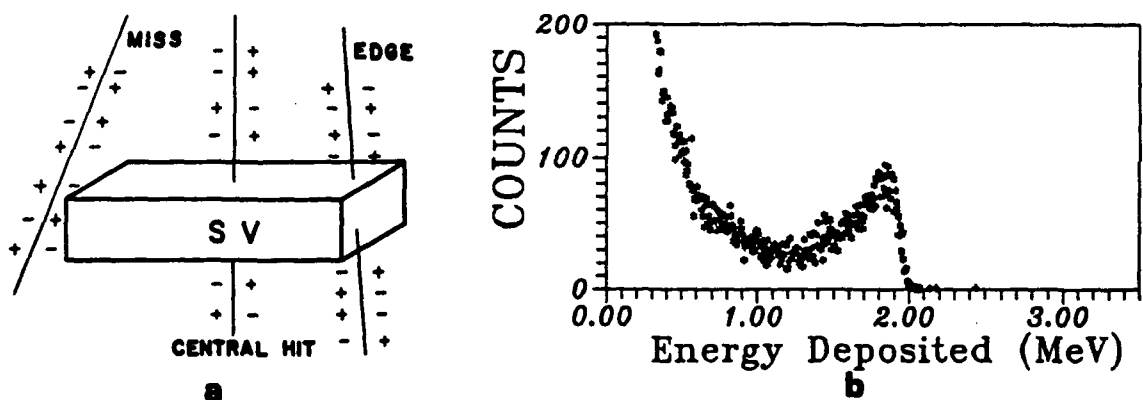


Fig. 9. a) Sensitive Volume illustrating direct hit, miss and edge-hit events. b) Measured pulse-height spectrum for a drain-substrate test structure junction of a CMOS circuit exposed to 4.8 MeV alphas.

MEMORY CELLS

The transistors that make up logic circuits are composed of p-n junctions of the type described above. Given the proper process information the charge collecting characteristics of the SEU-sensitive junctions making up the device may be estimated theoretically (Abdel-Kader et al., 1987). However, such information is often not available and, if available, does not take lot-to-lot variations into account. For certain technologies, approximate information can be obtained directly from the devices through pulse-height measurements between the power line and ground obtained while the device is being exposed to monoenergetic charged particles. This is illustrated below for a 16K resistor-load NMOS (RMOS) memory exposed to alphas from an Americium source. This technology was chosen to illustrate the procedures because their spectra are simple and easy to interpret. In addition to being an important technology in its own right, RMOS is important because its SEU-sensitive structure, the drain-substrate junction, is similar in construction to the SEU-sensitive drain-substrate junction in CMOS. CMOS is an essential component of most spacecraft systems because of its low power requirements. The memory latch for an RMOS SRAM used in space is typically the resistor-load four transistor cell of the type shown in Fig. 10a.

Figure 10b shows one of the RMOS FETs in cross section. The SEU-sensitive junctions in each memory cell of the RMOS SRAM is the drain-substrate junction which is reverse biased because the corresponding FET is turned off. In normal operation, there is only one reverse-biased drain-substrate junction in each memory latch with the SEU sensitivity alternating between junctions as the memory states switch. If the device is not under bias, all the junctions become reverse-biased to the extent of the built-in biases across the junctions. Moreover, particle strikes across the junctions connected between VDD and VSS result in transient voltage swings between those lines, even in the absence of external bias. If the VDD and VSS pins of an RMOS SRAM are connected to the same electronics as used for detectors, as illustrated in Fig. 11a, the SRAM should behave like a parallel array of partially depleted particle detectors with the detector junctions being the potentially SEU-sensitive drain-substrate junctions (McNulty, 1989, McNulty et al., 1991).

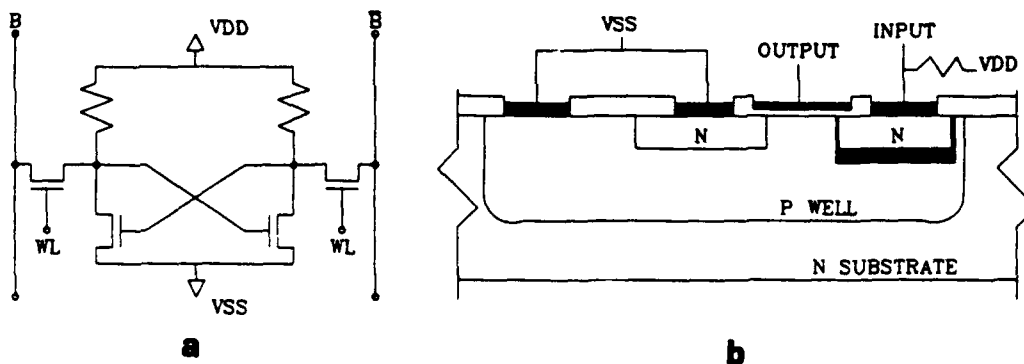


Fig. 10. a) Schematic of a resistor-load NMOS memory cell. b) Cross section of one of the inverters.

Dimensions of the Sensitive Volume

The pulse-height spectrum obtained when the memory cells of an RMOS SRAM are exposed to 4.8 MeV alphas is shown in Fig. 11b. The spectrum consists of events at 32,768 similar junctions, each junction having dimensions of roughly $10\text{ }\mu\text{m}$ on a side. The cross sectional area of the individual junctions can be estimated from the following expression:

$$\text{Area} = \text{Events}/(\text{Fluence} \times \text{Number of Junctions})$$

The results are consistent with each junction having an area of about $137\text{ }\mu\text{m}^2$ in area. This value is represented by a horizontal line on the plot of SEU cross section versus effective LET in Fig. 12. The value of the area of the junction estimated above agrees with the value of $160\text{ }\mu\text{m}^2$ obtained from the plateau value of the SEU cross section (Koga et al., 1988) within the limits imposed by the uncertainty in the fluence.

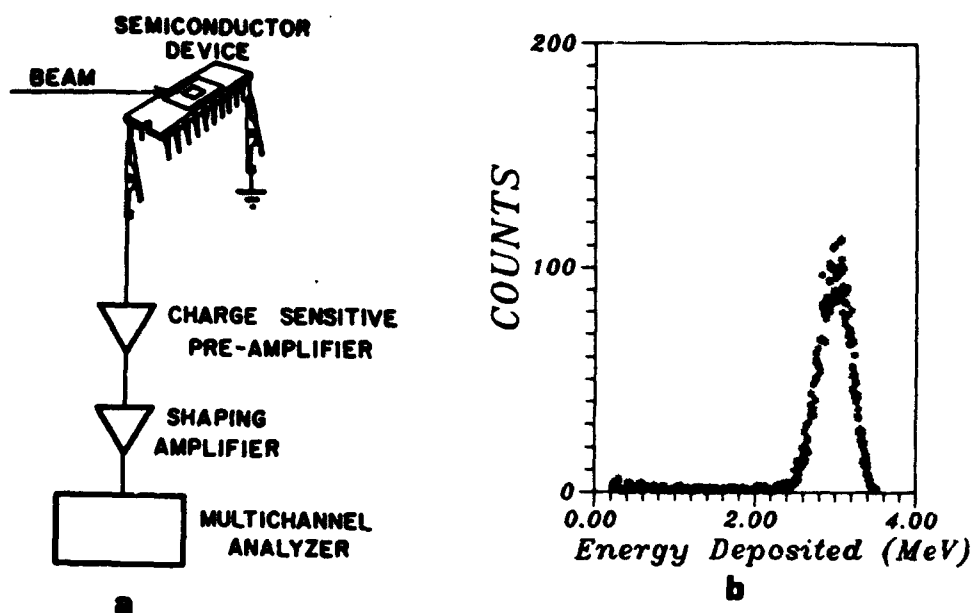


Fig. 11. a) Experimental configuration used for pulse-height analysis on the power lines of the memory cells. b) Pulse-height spectrum obtained when a portion of the memory cells of an NMOS SRAM (IDT6116V) is exposed to 4.8 MeV alphas.

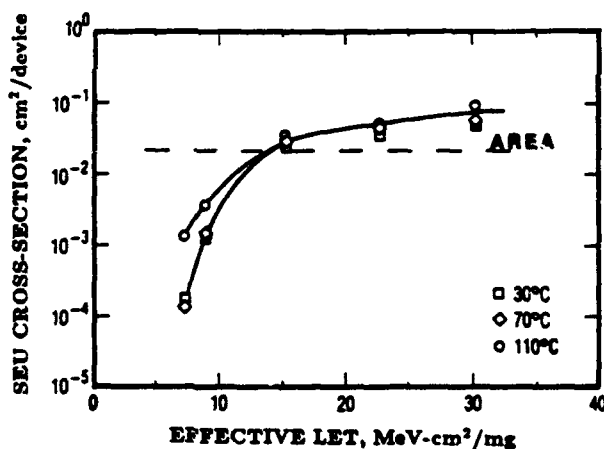


Fig. 12. SEU cross section versus effective LET for the RMOS device IDT 6116V exposed to heavy ions.

The thickness of the sensitive volume can be estimated from range-energy tables. If $R(E_i)$ is the range of the particle entering the sensitive volume with energy E_i and $R(E_i - E_d)$ is the residual range of the particle after it deposited energy E_d in traversing the sensitive volume, the pathlength ℓ through the sensitive volume can be estimated from:

$$\ell = R(E_i) - R(E_i - E_d)$$

At normal incidence, this pathlength should equal the thickness of the sensitive volume. The value obtained for the thickness of this device is 13.6 μm .

AD-A285 581

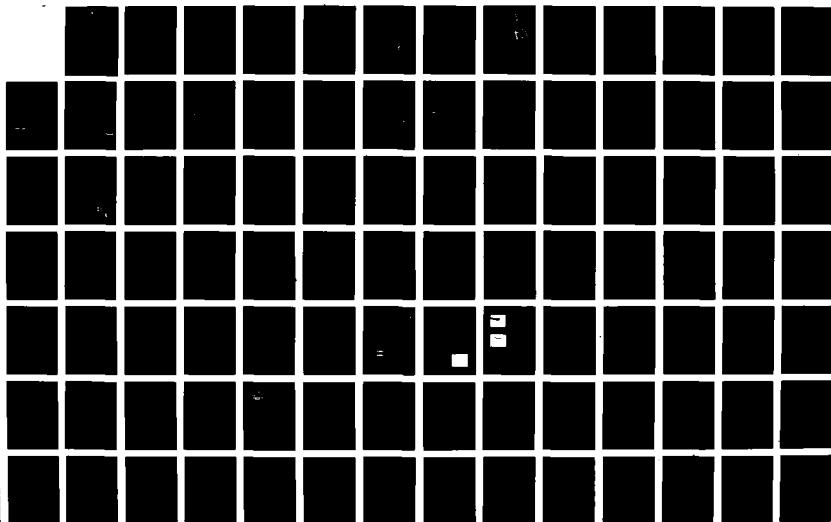
INVESTIGATION OF SINGLE EVENTS UPSETS IN SILICON AND
GAAS STRUCTURES USING REACTION CALCULATIONS(U) CLENSON
UNIV SC KINARD LAB OF PHYSICS P J MCNULTY 1 SEP 94

374

UNCLASSIFIED

DNA-TR-92-163 DNA001-88-C-0189

NL

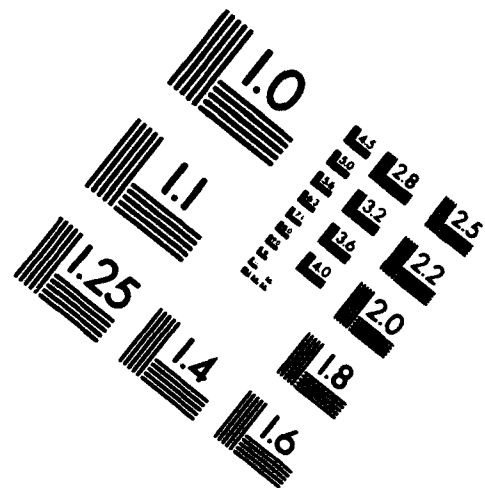
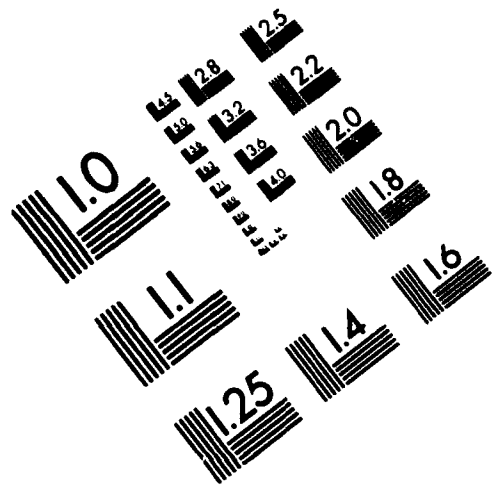




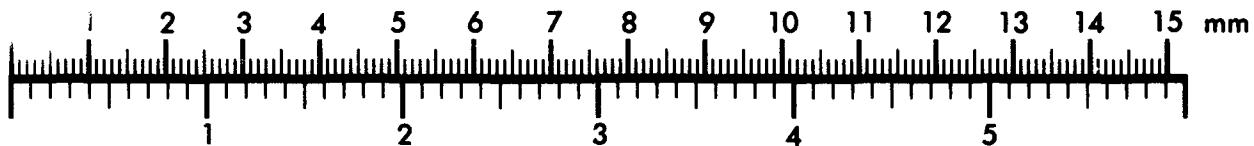
AIIM

Association for Information and Image Management

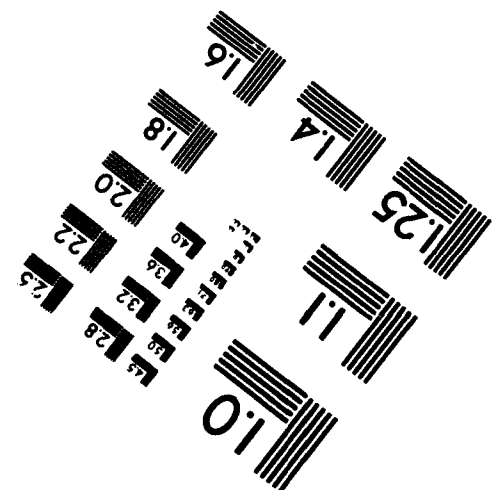
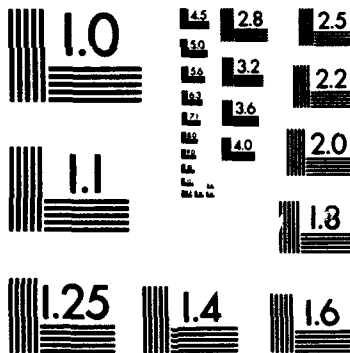
1100 Wayne Avenue, Suite 1100
Silver Spring, Maryland 20910
301/587-8202



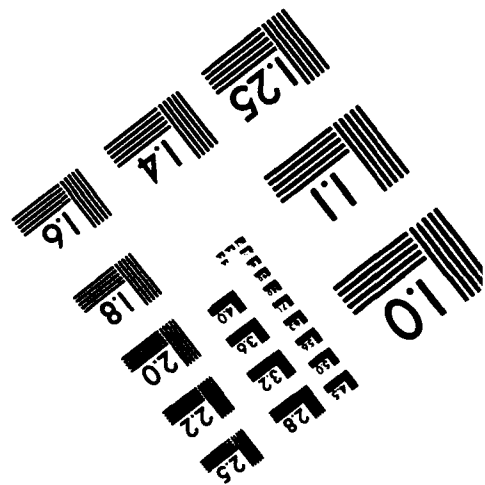
Centimeter



Inches



MANUFACTURED TO AIIM STANDARDS
BY APPLIED IMAGE, INC.



An independent check on whether these procedures provide useful estimates of the dimensions of the sensitive volume can be obtained by comparing the pulse-height spectrum obtained by exposing the device to 148 MeV protons with the results of simulations of the energy-deposition spectrum obtained from CUPID. The simulations assume the dimensions of the sensitive volume obtained above. The comparison is shown in Fig. 13. The agreement is quite reasonable considering the error in the area introduced by the uncertainty in the fluence of the alpha source.

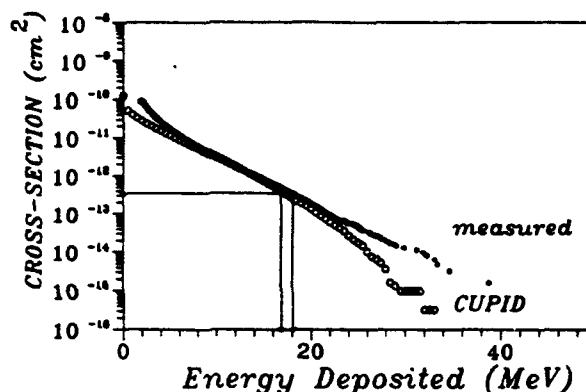


Fig. 13. Integral cross section for depositing at least energy E versus E . The horizontal curve marks the SEU cross section measured for that device. The values on the abscissa where it intersects the theoretical and experimental spectra which are marked by vertical lines represent the corresponding estimates of the critical charge.

Determination of Critical Charge

The SEU cross section for the IDT 6116V RMOS SRAM was measured using 148 MeV protons. The value obtained is represented in Fig. 13 by a horizontal line. The values of the abscissa corresponding to where the SEU cross section intersects the two curves represent the values of the energy deposited for which the cross section for depositing at least that energy equals the measured SEU cross section. Therefore, these values are estimates of the threshold energy deposition (or critical charge) for that device. The threshold LET for this device has been determined experimentally (Koga et al., 1988) following the standard procedures using heavy ions. The value obtained was $6 \text{ MeV cm}^2/\text{mg}$. The energy deposited by such an ion in a pathlength of $13.6 \text{ }\mu\text{m}$ of silicon, the thickness of the sensitive volume, is 18.9 MeV. The estimates from the intersection of the measured SEU cross section and the CUPID and measured curves in Fig. 13 are 17.5 MeV and 18.1 MeV. The agreement among the three estimates is within 10%.

SUMMARY AND CONCLUSIONS

The algorithms currently in use for predicting SEU rates in space require as input the dimensions of the equivalent sensitive volume for each SEU-sensitive junction on the device as well as the value of the energy which must be deposited in that volume in order to upset the circuit element. This latter value is known as the threshold energy deposition or critical charge. Non-destructive procedures for using exposures to monoenergetic ions to estimate the dimensions of the sensitive volume were demonstrated for the IDT 6116V, an RMOS SRAM, using 4.8 MeV alphas from a lightly shielded Americium source. The value of the cross sectional area obtained for the sensitive volume was consistent with measurements of the plateau SEU cross section for that technology.

A simple procedure for estimating the critical charge from a single SEU measurement with energetic protons combined with either measurements or theoretical simulations of the energy-deposition spectra in the sensitive volume was demonstrated for the same device. The values of the critical charge obtained from the proton SEU cross section agreed within 10% with the value estimated from published heavy ion measurements for the same technology.

Estimates of the critical charge and the dimensions of the sensitive volume obtained using the procedures described in this paper produce agreement between SEU measurements on protons and heavy ions.

ACKNOWLEDGEMENT

Supported by the Defence Nuclear Agency under contract # 001-88-C-0189.

REFERENCES

- Abdel-Kader, W. G., P. J. McNulty, S. El-Teleaty, J. E. Lynch and A. N. Khondker (1987). Estimating the Dimensions of the SEU Sensitive Volume. *IEEE Trans. Nucl. Sci.*, **NS-34**, 1300-1304.
- Binder, D., C.E. Smith and A. B. Holman (1975). Satellite Anomalies from Galactic Cosmic Rays. *IEEE Trans. Nucl. Sci.*, **NS-22**, 2675-2680.
- Hamm, R. N., M. L. Rustgi, H. A. Wright and J. E. Turner (1981). Energy Spectra of Heavy Fragments in the Interactions of Protons with Communication Materials. *IEEE Trans. Nucl. Sci.*, **NS-28**, 4013-4017.
- Hu, C. (1982) Alpha Particle Induced Field and Enhanced Charge of Carriers. *IEEE Electron Device Lett.*, **EDL-3**, 31-34.
- Knoll, G. F. (1989). *Radiation Detection and Measurements*, John Wiley and Sons, New York.
- Koga, R., W. A. Kolasinski, J. V. Osborne, J. H. Elder and R. Chitty (1988). SEU test Techniques for 256K Static RAMs and Comparison of Upsets Induced by Heavy ions and Protons. *IEEE Trans. Nucl. Sci.*, **NS-35**, 1638-1643.
- McLean, F. B. and T.R. Oldham (1982). Charge Funneling in N- and P- Type Substrates. *IEEE Trans. Nucl. Sci.*, **NS-29**, 2018-2023.
- McNulty, P. J., G. E. Farrell and W. P. Tucker (1981). Proton-Induced Nuclear Reactions in Silicon. *IEEE Trans. Nucl. Sci.*, **NS-28**, 4007-4012.
- McNulty, P. J. (1989). Track Structure Effects at P-N Junctions in Microelectronic Circuits. *Nucl. Tracks and Radiat. Meas.*, **16**, 197-204.
- McNulty, P. J. (1990). Predicting Single Event Phenomena in Natural Space Radiation Environments in Microelectronics for the Natural Radiation Environments of Space. *IEEE, Sandia National Laboratory*.
- McNulty, P. J., W. J. Beauvais, D. R. Roth and J. E. Lynch (1991). Determination of SEU Sensitivity of CMOS Devices by Charge Collection Measurements. (Submitted for publication).
- Oldham, T. R. and F. B. McLean (1983). Charge Collection Measurements for Heavy Ions Incident on N- and P- Type Silicon. *IEEE Trans. Nucl. Sci.*, **NS-30**, 4493-4500.
- Oldham, T. R., F. B. McLean, and J. M. Hartman (1986). Revised Funnel Calculations for Heavy Particles with High dE/dx. *IEEE Trans. Nucl. Sci.*, **NS-33**, 1646-1650.
- Pickel, J. C. and J.T. Blandford, Jr. (1980). Cosmic Ray Induced Errors in MOS Memory Cells. *IEEE Trans. Nucl. Sci.*, **NS-28**, 3962-3967.

APPENDIX H

MICROBEAM ANALYSIS OF MOS CIRCUITS

Microbeam Analysis of MOS Circuits

P.J. McNulty, W.J. Beauvais, D.R. Roth, and J.E. Lynch

Department of Physics and Astronomy

Clemson University

Clemson SC 29634-1911

A.R. Knudson and W.J. Stapor

Naval Research Laboratory

Washington, D.C. 20375-5000

Abstract

Irradiation of MOS SRAMs by energetic heavy ions results in pulses on the power lines of the device. Pulse-height analysis shows a series of peaks when the irradiation consists of identical particles incident in the same direction. Analysis through a microbeam shows that the pulses are generated by traversals of the p-n junctions making up the transistors of the device. Junctions in the memory array were found to dominate the spectrum from a CMOS device while those of the support circuitry dominate the spectrum from a DRAM.

INTRODUCTION

When MOS SRAMs are irradiated by heavy ions, pulses appear on the VDD and VSS pins of the device. These pulses are the result of interactions in which charge is generated and collected across the p-n junctions making up the transistors of the SRAM. When the pulses resulting from exposure to a beam of identical monoenergetic ions are analyzed according to pulse height, the result is a series of peaks in the spectrum, each peak presumably being the result of traversals of a different junction type (1-3). Since the junctions making up the transistors of the memory cells occupy the major portion of the total area on the die, one assumes that these junctions will contribute significantly to the observed spectrum, if not dominate it. If one assumes that each of the peaks in the spectrum corresponds to a single junction type and the number of junctions of each type are known, then the dimensions of the equivalent sensitive volume to be associated with each of those junctions can be simply calculated. The area of the junction is given by the ratio of the number of events under the peak to the product of the fluence and the number of junctions of that type. The thickness of the sensitive volume can be obtained from the position of the peak in the spectrum by using range-energy curves to determine the pathlength necessary to generate the amount of charge measured as being collected at the junctions. Alternatively, the thickness can be obtained from the slope of a plot of peak position versus effective LET ($LET \times \sec\theta$), when the LET is expressed in the appropriate units.

The procedure for determining the dimensions of the sensitive volume described above is based on two assumptions: First, that the peaks are due to hits on the different junctions making up the transistors in the memory array. Second, that the pulses from similar junctions outside the

array, do not contribute significantly to the size or shape of the peaks. This paper attempts to address the question of the source of the peaks for two technologies, CMOS SRAMs and NMOS DRAMs.

CMOS SRAM

Figure 1a shows a spectrum obtained by irradiating an advanced-technology CMOS SRAM by 4.8 MeV alphas under conditions in which the entire chip is exposed. Two peaks appear in the spectrum. Figure 1b shows the same chip exposed to the same fluence of alpha particles though a collimator which allows only a small portion of the chip to be exposed at one time. When the beam is restricted to the memory array, the only change in the pulse-height spectrum is the apparent splitting of the lower peak into two, as seen in Fig. 1b. When the input/output structures, the row decoders, and the sense amplifiers are exposed in turn, the same two peaks are seen as appear in Fig. 1a, but there are far fewer events. This can be seen by comparing the spectra in Figs. 1c through 1e with the memory array spectrum of Fig. 1b and the entire-chip spectrum of Fig. 1a. Comparison shows further that all three peaks are generated mostly within the memory array with only a small contribution from the junctions making up the support circuitry. This leaves the question of whether the different peaks correspond to hits on the different junctions making up the memory-cell transistors.

A series of exposures were carried out at the NRL heavy-ion accelerator using the NRL microbeam facility. The beam passed through a 2.5 μm diameter collimator before striking the die surface. The experimental configuration is shown in Fig. 2; except for the presence of the collimator and the difference in the incident particles, the measurements were carried out in the same manner as the entire-chip exposures. Because the spacing between the aperture and the die surface was estimated to be at least a few millimeters, the diameter of the beam spot on the die surface should be approximately 10 μm in diameter. In any event, the beam diameter is smaller than the dimensions of the memory cell but larger than the smallest dimensions of the junctions making up the transistors of the memory cells. The beam particles were Oxygen nuclei of about 20 MeV.

Because of the short range of 20 MeV Oxygen in silicon and the uncertainty in the thickness of the SiO_2 layer which covers the die, the energy of the incident ion arriving at the

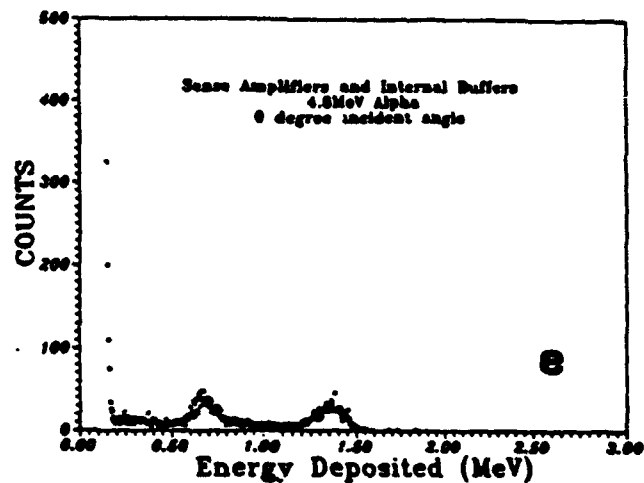
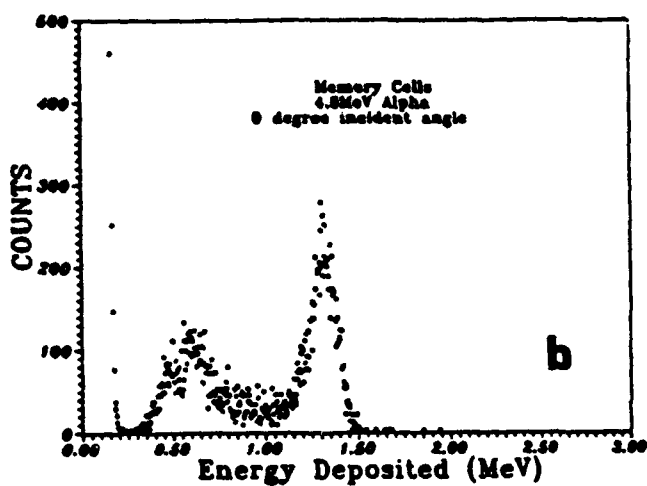
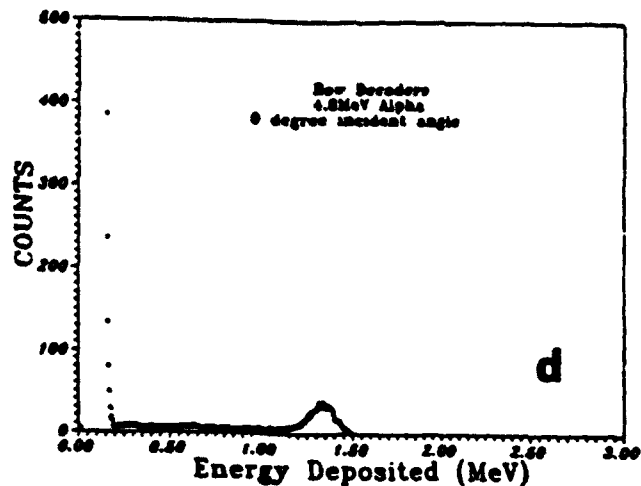
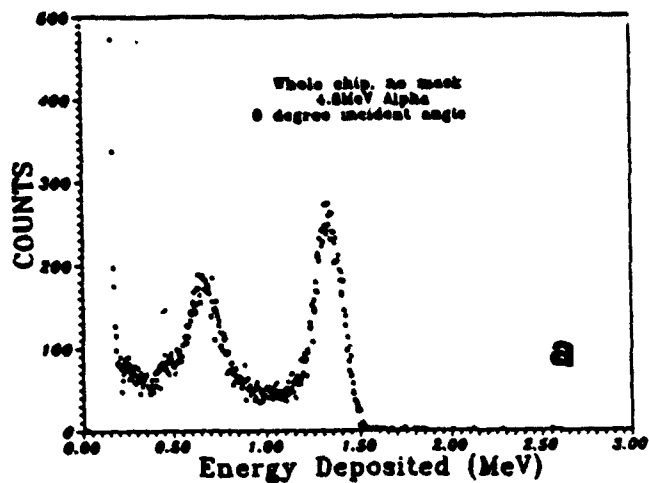


Fig 1. d) row decoders and e) sense amplifiers and internal buffers.

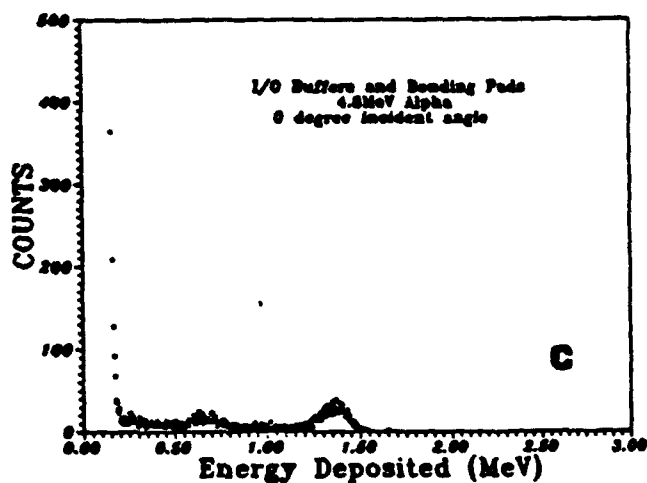


Fig. 1. Pulse-height spectrum measured off the power line of an advanced-technology CMOS SRAM when exposed to 4.8 MeV alphas. The number of events per channel is plotted versus the charge collected in the event expressed in energy units (1MeV = 44 fC). The fluence was the same for all exposures and the beam was restricted to the area of the die specified a) whole chip exposed b) memory array c) buffers and bonding pads,

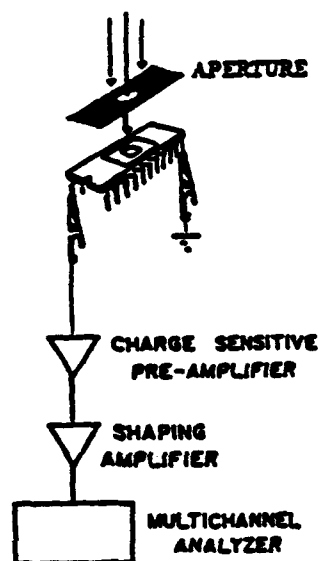


Fig. 2. Experimental configuration for measuring the pulse-height spectra from working MOS RAMs exposed through the microbeam collimator. The pulse-height spectra are measured across the power and ground pins of the RAM.

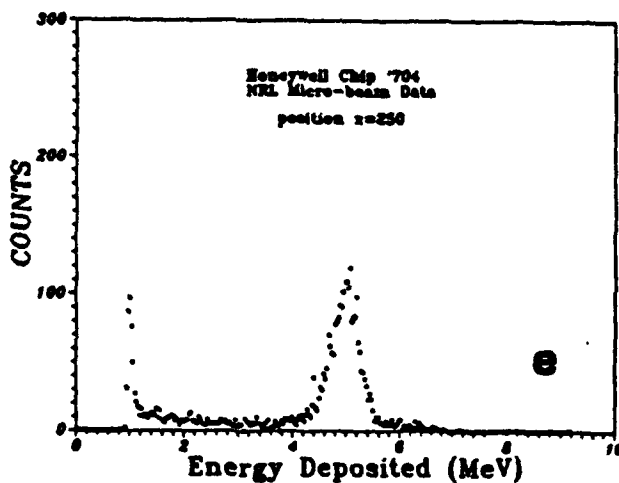
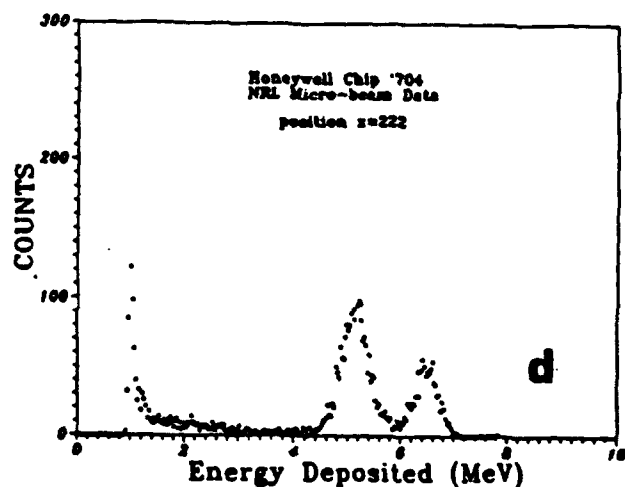
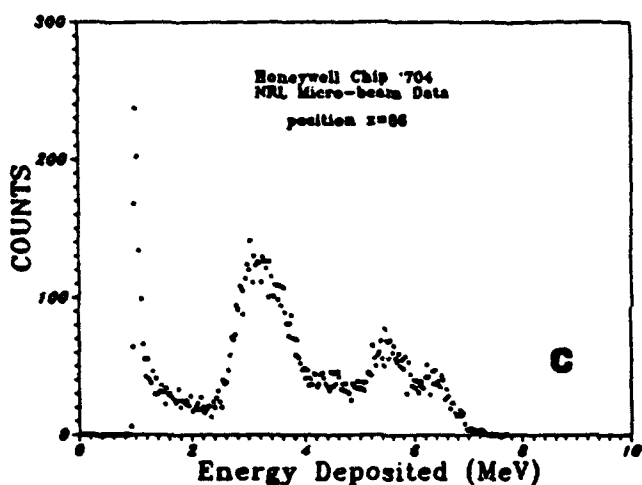
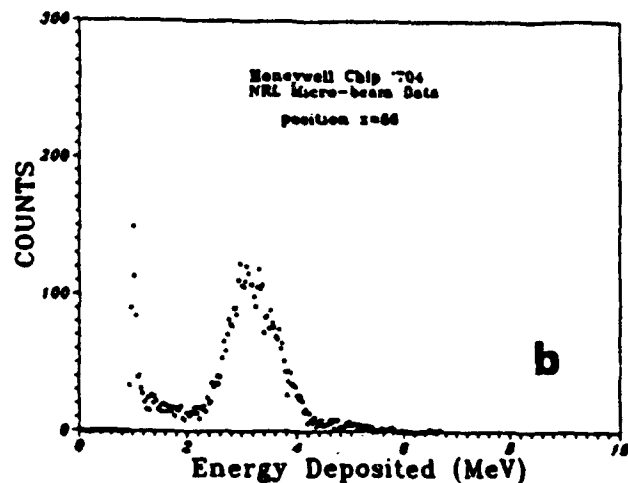
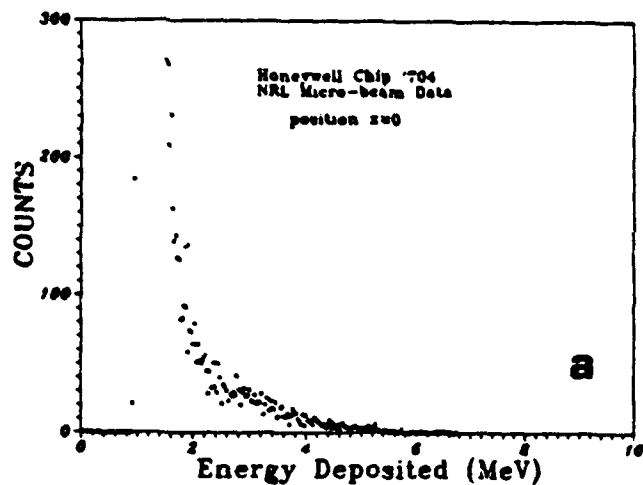


Fig. 3. Pulse-height spectra observed at different locations along one of the scans. Three peaks are observed - each predominates at different locations along the scan. a) $x = 0$ b) $x = 66$ c) $x = 86$ d) $x = 222$ e) $x = 250$.

level of the sensitive junctions cannot be specified with any accuracy. Nor can we be sure that the oxygen ions completely traverse the sensitive volumes of all the junctions, especially the one associated with the well-substrate junctions. Even if they did completely penetrate, the ions would be changing LET too rapidly for accurate use of range-energy tables. As a result, the locations of the peaks in the figure (Fig. 3) cannot be relied upon to estimate of the thicknesses of the sensitive volumes. Nor can their relative spacing on the spectra be used to calculate relative thicknesses. This would not be true, of course, if higher energy ions were used, and the NRL microbeam is routinely used at different accelerator facilities. With more penetrating particles, the thickness of the sensitive junctions can be easily obtained. What is important here, and in what follows, is that the microbeam can localize the source of the powerline signals to within a single junction.

Two scans of the device were carried out in the same direction within different portions of the memory array. During each scan, pulse-height spectra were measured at locations 4 μm apart. Sample spectra measured at different locations along one of these scans are shown in Fig. 3. Three separate peaks are observed in these spectra. At some locations only individual peaks are observed, while at others multiple peaks are apparent. Two of the peaks in Fig. 3 can be isolated at certain locations along the scan. Irradiating the entire chip, i.e., removing the collimator results in the same type of spectrum that is observed at locations where all three junctions are contributing strongly.

The pattern of the peaks along the scan can be seen more clearly in the three dimensional composite (Fig. 4) made by positioning the individual pulse height spectra according to where they were generated along the scan. The relative spacing of the peaks can be clearly seen. Obviously, range-energy tables could be used to transform spectra of this type taken with long-range particles into three dimensional reconstructions of the sensitive volumes associated with the junctions.

NMOS DRAM

The NMOS DRAM was probed by the microbeam in two ways: First, the beam was used to irradiate a number of locations on the die while SEU measurements were carried out. This ensured that we knew exactly where we were probing on the die.

The spectrum obtained from irradiating the entire DRAM with monoenergetic Nitrogen ions is shown in Fig. 5 to be a broad spectrum with only a small peak emerging from the background. The results of probing the various regions of the chip with the microbeam oxygen ions are shown in Fig. 6. Here it is obvious that the largest pulses are generated in portions of the support circuitry. Only a single low-energy peak is generated in the memory array.

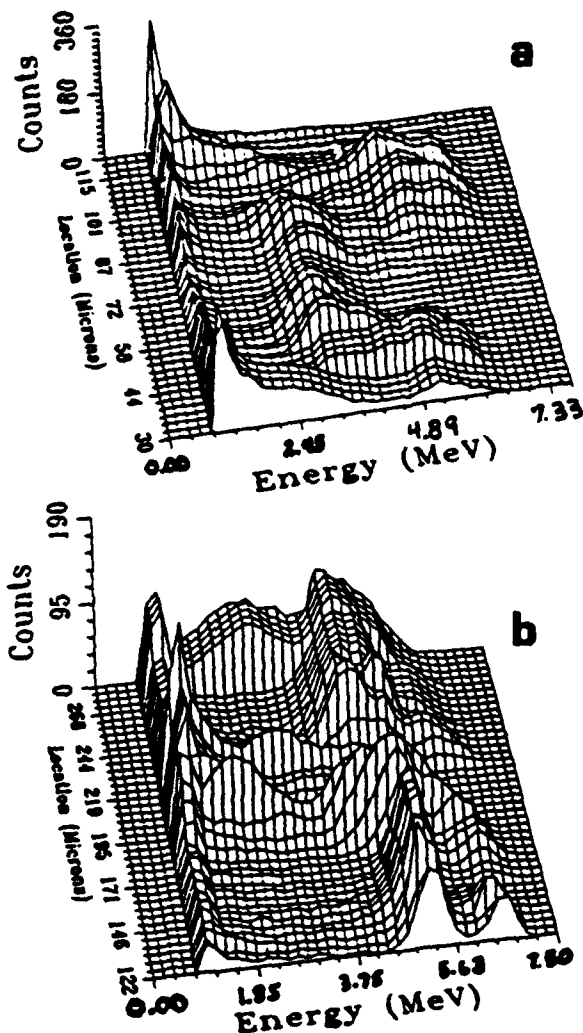


Fig. 4. Composite of pulse-height spectra positioned according to where each spectrum was generated along the scan. The results of two scans are presented. Obviously, the peaks are generated at different locations within the memory cell.

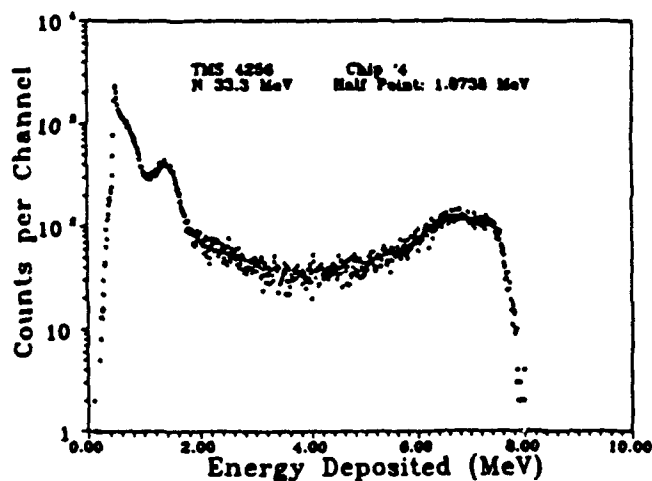


Fig. 5. Pulse-height spectrum obtained by irradiating the DRAM TMS4256 with energetic heavy ions where all regions of the die were exposed.

SUMMARY

When unbiased MOS devices are irradiated by monoenergetic identical ions, pulses appear on the VDD and VSS pins of the device which are the result of interactions in which charge is collected across the p-n junctions making up the device. Comparison of pulse height spectra obtained with the entire chip exposed to spectra obtained with small regions of the circuitry exposed showed that the spectra characterizing CMOS SRAMs are dominated by signals from the memory array. The spectrum characterizing a 256 K DRAM appears to be dominated by signals from the peripheral circuitry. Charge collection spectra measured while the chip is irradiated by 20 MeV ions confined to a 10 μm beams spot show the individual peaks of the CMOS SRAM spectra appearing and disappearing as the beam location spot moves across the memory cells.

References

1. P.J. McNulty, D.R. Roth, W.J. Beauvais, W.G. Abdel-Kader, and D.C. Dings, "Comparison of the Charge Collecting Properties of Junctions and the SEU Response of Microelectronic Circuits" to be published in *Nuclear Tracks and Radiation Measurements*.
2. P.J. McNulty, "Predicting SEU Phenomena in Space" in *1990 IEEE Short Course: Microelectronics for the Natural Radiation Environments of Space* (IEEE Nuclear Radiation Effects Committee, 1990). pp 3-1 to 3-23.
3. P.J. McNulty, W.J. Beauvais, and D.R. Roth, "Determination of SEU Parameters of CMOS SRAMs by Charge Collection Measurements" *IEEE Trans. Nuclear Science*, to be published.

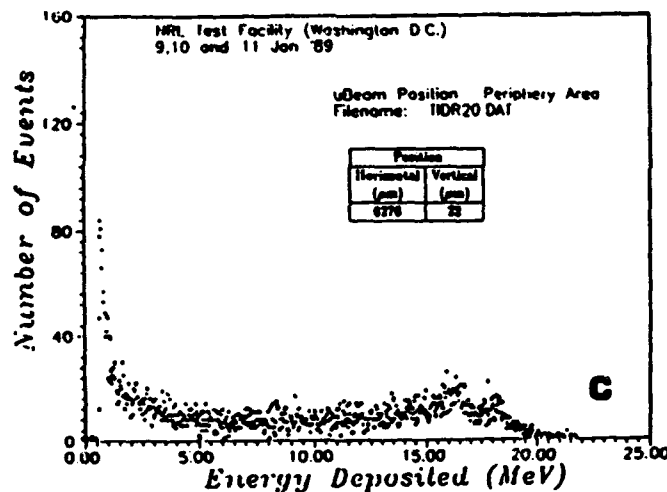
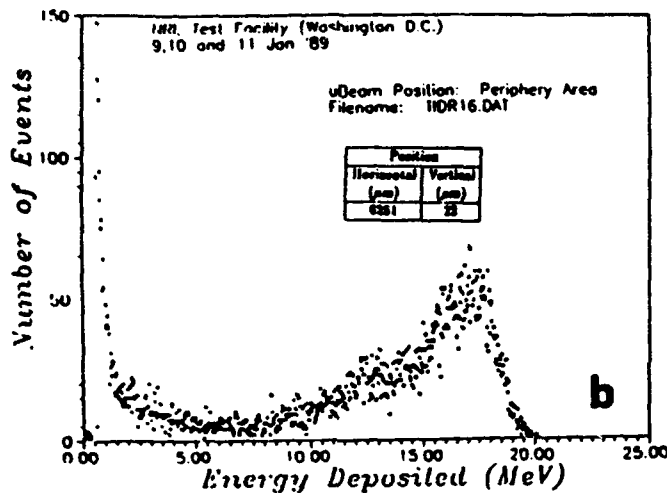
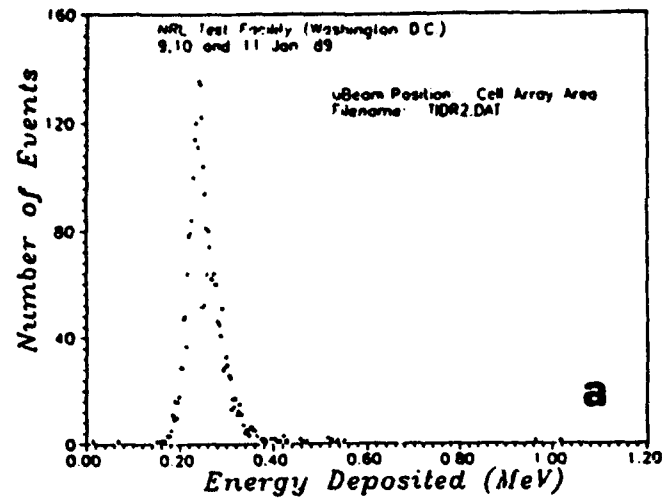


Fig. 6. Pulse-height spectra obtained when the DRAM is irradiated through a 2.5 μm diameter collimator so that only specific regions of the die are exposed. a) Memory array b) one region of the periphery c) a second region of the peripheral circuits.

APPENDIX I

CHARGE COLLECTION AT LARGE ANGLES OF INCIDENCE

CHARGE COLLECTION AT LARGE ANGLES OF INCIDENCE

P.J. McNulty, W.J. Beauvais, R.A. Reed, and D.R. Roth

Department of Physics and Astronomy

Clemson University

Clemson SC 29634-1911

and

E.G. Stassinopoulos

NASA Goddard Space flight Center

Greenbelt, MD

and

G.J. Brucker

Long Branch, NJ

ABSTRACT

Charge collection exhibited by p-n junctions, which have at least one small dimension, deviates from the geometric assumptions commonly used in SEU testing. The amount of charge collected did not increase with the secant of the angle of incidence. The number of events under the peak in the charge collection spectrum did not decrease as the cosine of the angle of incidence. Both the position of the peak and the number of events under the peak measured at a given angle of incidence depended upon which symmetry axis of the device was chosen to be the axis of rotation.

INTRODUCTION

Standard SEU testing carried out at heavy ion accelerators often involves varying the "effective LET" of ions of a given energy by changing the angle of incidence (1). Effective LET is the product of the particle's LET and the secant of its angle of incidence. This geometric correction corresponds to the presumed increase in the charge collection at the SEU-sensitive junction as the particle's trajectory within the sensitive volume increases. The concept of effective LET was adopted at a time when it could be assumed that the sensitive volume was a thin large-area rectangular parallelepiped. The upset cross section is also assumed to decrease with the cosine of the angle of incidence in the same way that the area of the SEU-sensitive junction projected onto a plane perpendicular to the beam direction decreases. As a result of these assumptions, it is standard practice to display SEU test data as the product of the measured SEU cross section and the secant of the angle of incidence plotted versus the product of the LET and the secant of the angle of incidence (1,2). Most SEU tests also involve rotations about only one of the symmetry axes despite the fact that the SEU-sensitive microjunctions have shapes which are either more complicated than rectangular parallelepipeds or at least are not square. Typically, they have one dimension which is considerably shorter than the other.

The purpose of this study was to measure the charge collection as a function of the angle of incidence for rotations about two mutually perpendicular symmetry axes in the plane of the device. If the geometric assumptions described above are valid, they should also hold for the charge collection events since the single event upsets are initiated by charge collection at certain SEU-sensitive microjunctions. Thus, studying charge collection as a function of the angle of incidence provides a simple test of whether the geometric assumptions apply to modern testing. Petersen et al (3) have suggested that, for modern microjunctions, the angular dependence of the SEU cross section would decrease with the angle of incidence faster than the cosine of the angle of incidence.

Earlier studies (4,5) did, in fact, indicate that the number of events under the peaks in the charge collection spectra corresponding to the SEU-sensitive junction decreased with increasing angle of incidence faster than the cosine. However, those studies did not rule out systematic errors in the angle of incidence due to the initial orientation of the device or problems with the goniometer. In this study, the angles of incidence extend over the entire range of angles up to grazing, include both positive and negative rotations, and include rotations about the two mutually perpendicular symmetry axes of the device. All the measured spectra showed two clearly distinguishable peaks: A large peak corresponding to events in which the particles traverse a large junction whose cross section is nearly that of the entire memory cell, and a smaller peak corresponding to charge collection at a junction with a smaller cross section, one that has asymmetric lateral dimensions typical of drain and substrate junctions on devices. The geometric assumptions are shown to hold for charge collection events at the junction with the large area and not to hold for charge collection events at the smaller junction.

EXPERIMENTAL METHODS

The measurements were carried out on a Harris 6504RH, a CMOS SRAM. Figure 1 shows a schematic of an inverter typical of p-well CMOS devices. In the absence of bias, both

transistors are off. All ions will traverse the epi-substrate junction with most electrons going to VDD through the substrate. The heavily doped substrate is biased at VDD and is used to distribute power over the chip. In the absence of applied bias, the gates are off and the depletion widths across the junctions are due only to the built-in bias resulting from the doping profile across the junction. Under normal bias, it is the n-channel drain which is sensitive to upsets. Removing the bias lowers the charge collection across a microjunction by about 20% (1,6). Since the source is connected to VSS, events in which the ions traverse the source will have some fraction of the electrons go to VSS, thereby, reducing the size of the measured pulse.

The pulse-height spectra were measured between the VDD and VSS pins of the unbiased device in a manner described previously (4-7). The polarity was set for unipolar pulses corresponding to electrons flowing toward VDD. The angle of incidence was varied by rotations about two mutually perpendicular axes, the long and short symmetry axes of the device, as shown schematically in Fig. 2. The preamplifier and amplifier circuits used are the same as those used for pulse-height measurements with nuclear detectors. The time constants of the preamplifier should be chosen such that the charge collection is integrated over times comparable to the switching speeds of the circuit.

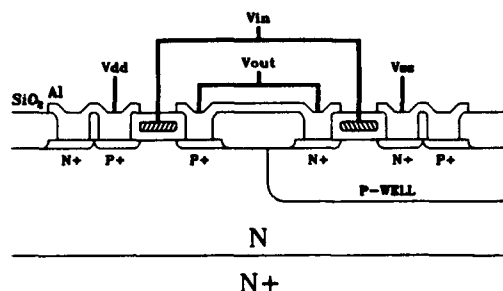


Fig. 1. Cross section of an inverter typical of p-well type CMOS circuits.

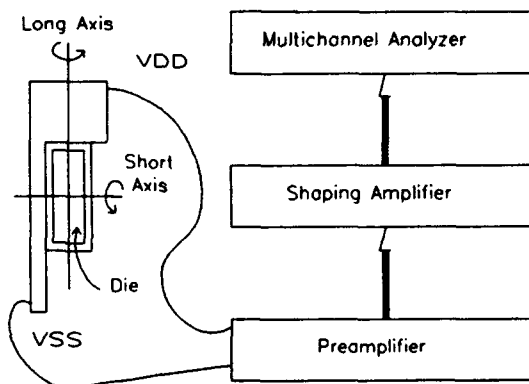


Fig. 2. Schematic of the experimental configuration showing the rotations about the axes parallel to the long and short dimensions of the device.

Fig. 2 Schematic of the experimental configuration showing the rotations about the axes parallel to the long and short dimensions of the device.

The measurements were carried out under vacuum using the SEU Test Facility at the Tandem Van de Graaff at Brookhaven National Laboratory. At that facility, rotations can be carried out about the "long" and "short" axes of Fig. 2 without breaking vacuum. The exposures were to 140 MeV Fluorine ions. The chip packages were cut to expose the die to the beam at angles up to near grazing for rotations in the negative direction about both axes of the device. The Fluorine ions have a range of over one hundred microns at this energy, an important consideration if it is to be ensured that the ion trajectories do not terminate within the sensitive volume at large angles of incidence.

RESULTS

A typical pulse-height spectrum measured on the Harris 6504RH is shown in Fig. 3. Two peaks are evident at this and all other angles. The shape and position of both peaks change as the angle of incidence changes, as can be seen in Fig. 4, which shows the spectra obtained in measurements at a series of angles about the long axis. At very large angles the peaks become broader and less well defined. At these large angles, the value of the effective LET would not adequately characterize the distribution of charge collection events or be a reliable indicator of the probability of an upset.

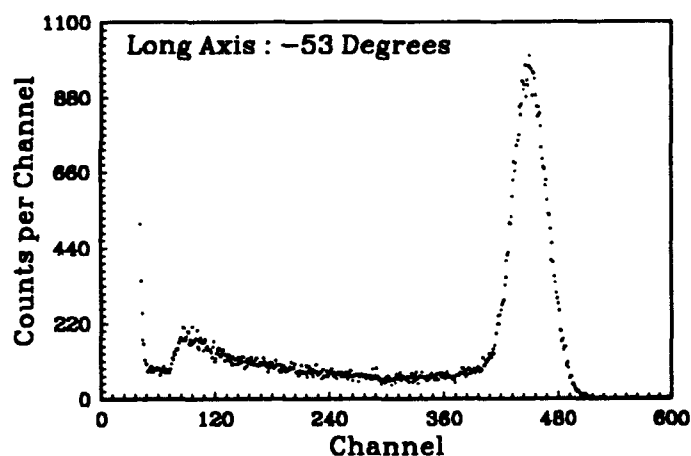


Fig. 3. Pulse-height spectrum measured off the power line of an a Harris 6504RH CMOS SRAM. The number of events per channel is plotted versus the charge collected in the event expressed in energy units (1MeV = 44 fC).

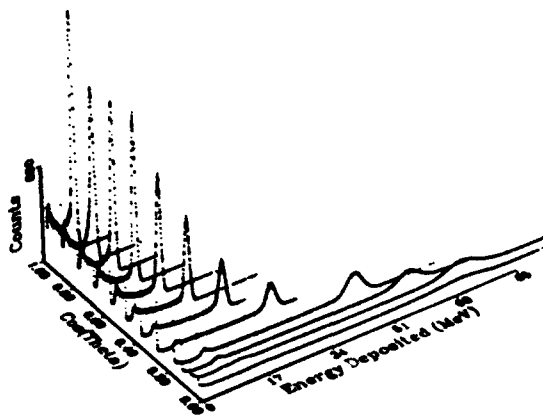


Fig. 4. Pulse-height spectra obtained at different angles of incidence for rotations about the long axis.

The total effective cross sectional area of the sensitive volume can be estimated at each angle of incidence from the ratio of the number of events to the fluence, and the distribution of the particle's path lengths through the sensitive volume can be obtained from the shape and position of the peak using range energy tables. Confining the beam particles to specific regions of the die using masks or to small beam spots using microbeams has demonstrated that the peaks observed in CMOS correspond to particles hitting different junctions within the memory cells. (8).

Large Peak

In n-well CMOS, the large peak at large energy depositions corresponds to hits on the well-substrate junctions while the smaller peak at low energy depositions corresponds to hits on the drain-substrate and source-substrate junctions. (4). In p-well CMOS of the type used in the 6504RH, the large peak in a spectra should correspond to ions traversing the epi-substrate junction. The interpretation of the small peak is more complicated, as will be discussed below.

Since the large peak is generated by ions traversing a large area structure such as the epi-substrate junction, the events under this peak serve to check and calibrate the goniometer, and the measuring system. The standard geometric assumptions should hold reasonably well for this junction, i.e., the number of events under the peak should decrease proportional to the cosine of the angle of incidence, and the peak position should increase proportional to the secant. The position of the large peak is plotted versus the secant of the angle of incidence in Fig. 5a for rotations in both the positive and negative directions about both axes of rotation. For angles of incidence below 73 degrees, the relationship is one of proportionality, as expected, and independent of the axis and direction of rotation. Measurements at larger angles in the negative direction show the position of the large peak increasing proportional to the secant of the angle until reaching the saturation imposed by the finite range of the incident ions. The ratio of the counts under

the large peak and the fluence are plotted versus the cosine of the angle of incidence in Fig. 5b. Again, there is a proportionality, in agreement with the standard geometric assumptions.

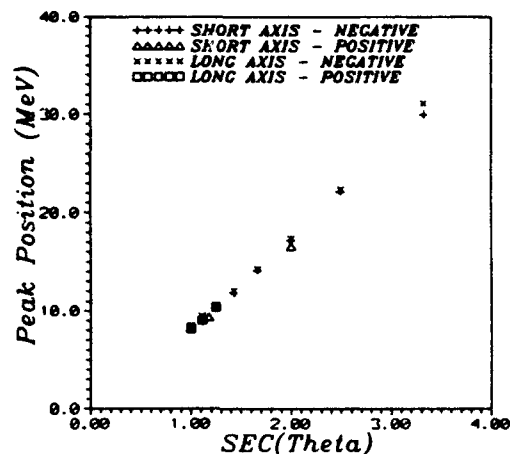


Fig. 5a. Peak position of the large peak versus the secant of the angle of incidence for rotations about two mutually perpendicular symmetry axes in the plane of the chip surface. The plot includes all measurements below an angle of 73 degrees. The peak position shifts with the secant of the angle of incidence for rotations about both axes. This data is consistent with the energy deposition increasing with the increase of the path length through a parallelepiped with large lateral dimensions.

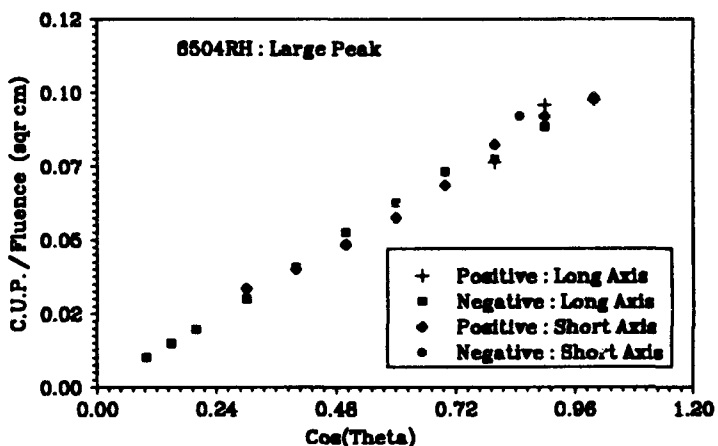


Fig. 5b. Ratio of counts under the large peak to the fluence plotted versus the cosine of the angle of incidence for rotations about both axes.

Small Peak

The small peak corresponds to events where the charge collection through the substrate is reduced. The obvious candidate is the source because electrons collected across the source junction would generate a pulse with the opposite polarity from the main signal generated at the epi-substrate

junction. The source junction is rectangular in shape with its long dimension parallel to the short symmetry axis of the device. Differences in the lateral dimensions of the small junctions should be reflected in differences in the variation of the charge collection with angle of incidence for rotations about the two axes. This difference is clearly evident in Fig. 6 where the spectra measured for rotations of 53 degrees about the two axes are compared. The two spectra were measured for different durations which were chosen to generate about the same number of events under the small peak. The large peaks differ only slightly in position and shape between the two spectra. However, the small peaks are in completely different positions and have different shapes. Both differences result from differences in the dependence of the charge collection on the angle of incidence. This is further illustrated in Fig. 7 which compares the regions in the spectra about the small peak for the two axes of rotation for angles up to 73 degrees. Measurements were only continued above 73 degrees for rotations about the long axis. The small peaks differ in shape as well as position. The small peak divides into two peaks at angles above 66 degrees for rotations about the short axis but not until 84 degrees for rotations about the long axis. These spectra should provide valuable information about the geometry of the effective sensitive volume once the appropriate tomographic software is developed.

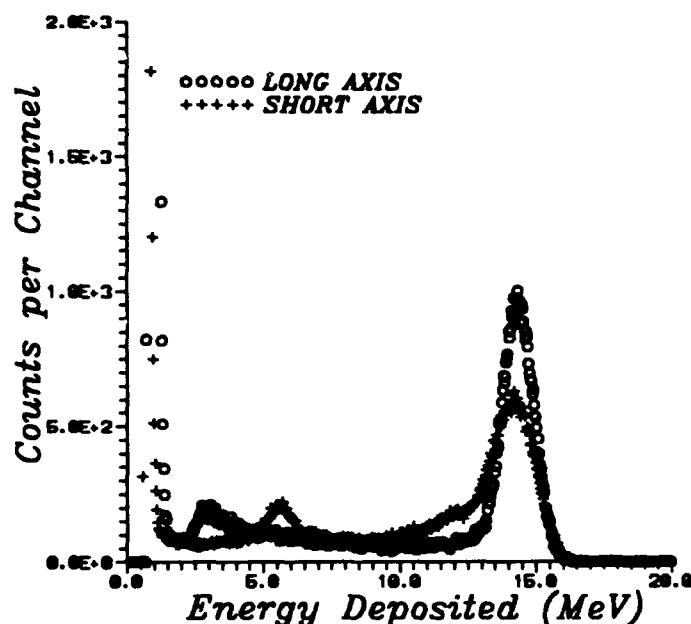


Fig. 6. Pulse-height spectra measured at the same angle of incidence for rotations about the two mutually perpendicular symmetry axes in the plane of the die. The exposures were of different duration so that the small peaks had a similar number of events. The large peaks appear to have nearly the same position and shape while the small peaks have different shapes as well as different positions.

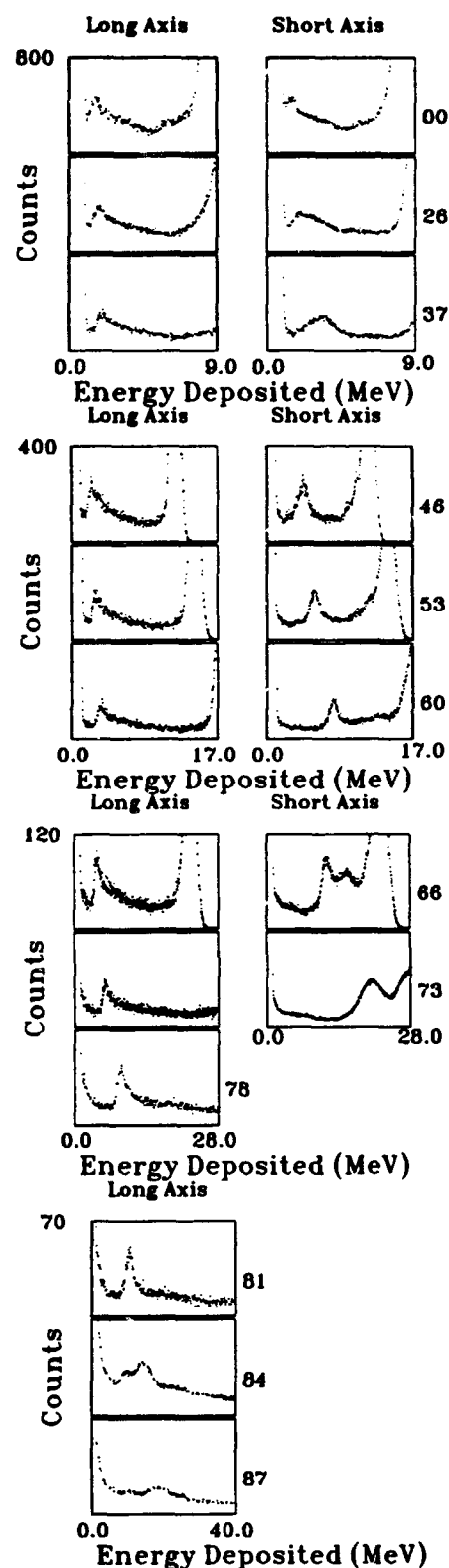


Fig. 7. Comparison of the regions of the pulse-height spectra about the small peak for rotations about the long and short axes. The angles of incidence are: a) 0, 26 and 37 degrees; b) 46, 53, and 60 degrees; c) 66, 73, and 78 degrees; and d) 81, 84, and 87 degrees.

Even without the sophisticated software which needs to be developed for tomographic scans of the effective sensitive volume, some important conclusions can be drawn relative to the concept of effective LET. The position of the small peak is seen in Fig. 8a to increase with the secant of the angle of incidence for rotations about the long axis while the position of the small peak is seen to increase in Fig. 8b with the square of the secant of the angle of incidence for rotations about the short symmetry axis. Since the path length through a rectangular parallelepiped can increase by at most the secant, a faster increase suggests that the peak position reflects the competition between the source-well junction and the epi-substrate junction, with the collection at one junction increasing with angle of incidence while relative collection at the other decreases. However, it is not clear why the peak position, and hence the charge collected, should increase with the square of the secant. Perhaps it is evidence of bipolar amplification.

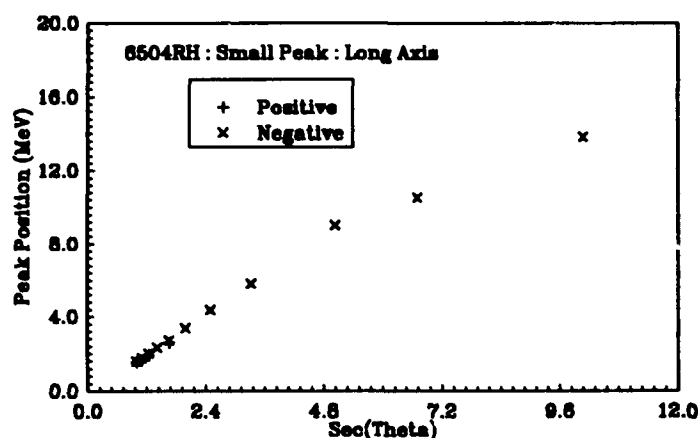


Fig. 8a. Position of the small peak versus the secant of the angle of incidence for rotations about the long axis.

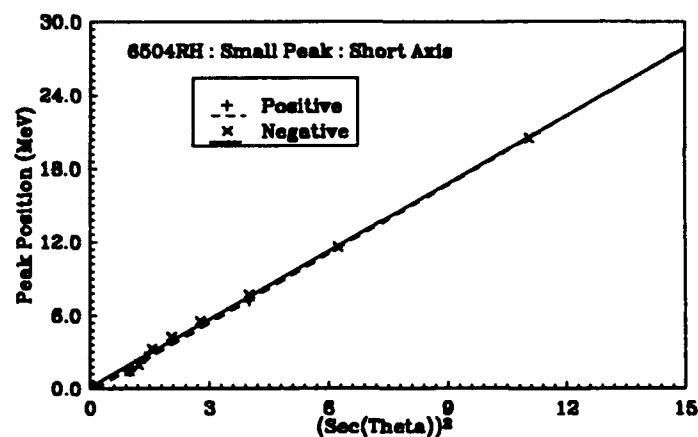


Fig. 8b. Position of the small peak versus the square of the secant of the angle of incidence for rotations about the long axis.

If SEUs are the result of ion traversals of junctions like the drain, which is similar structure to the source, one might expect

some SEU test results to depend on which axis was chosen for rotations. These SEU measurements for rotations about the two axes are in progress.

Dependence on Algorithms

The estimates of the cross sectional area of the effective sensitive volume depend on the number of events under the small peak. The value obtained can depend somewhat on the algorithm used. In order to determine this sensitivity, two quite different approaches were tried. The first program, labeled P1, produces a graphic output of an uncompressed pulse-height spectrum. It allows the user to define two levels of the background at the upper and lower margins of the peak, as illustrated in Fig. 9a. The other program, labeled P2, compresses the pulse-height spectrum to provide sharper contrast which should make it easier to set the margins. It also allows the user to define multiple estimates of background as shown in Fig. 9b. The user can estimate the number of events under the peak of either spectrum by integrating between the full margins as illustrated in Fig. 9a, or by taking the area of the box drawn between the half-maximum margins shown in Fig. 9b. The various combinations which can be used are listed in Table 1. The numbers are used to label a specific method. Table 1 also serves as a legend for the plots of Figs. 10 and 11.

	FULL BREADTH		HALF-MAX	
	BACKGROUND SUBTRACTION		BACKGROUND SUBTRACTION	
	YES	NO	YES	NO
P1	1 : ♦	2 : +	3 : x	4 : x
P2	5 : ▲	6 : •	7 : □	8 : ■

Table 1.

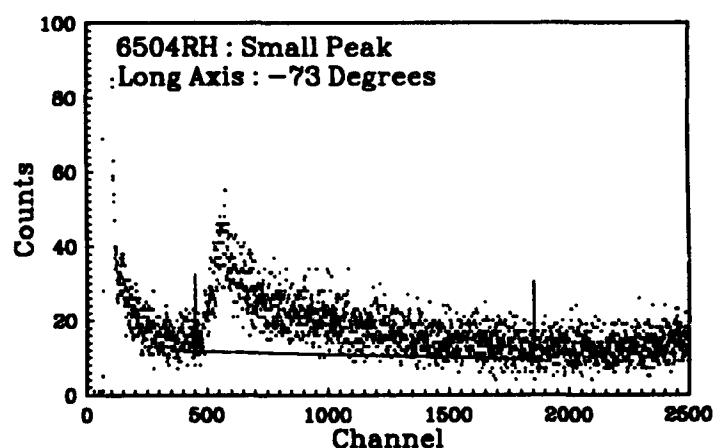


Fig. 9a. Small-peak region of an uncompressed pulse-height spectrum. The vertical lines mark the margins of the peak while the near horizontal line provides an estimate of the background contribution to the peak. The counts under the peak

are obtained by integrating between the margins with and without subtracting background.

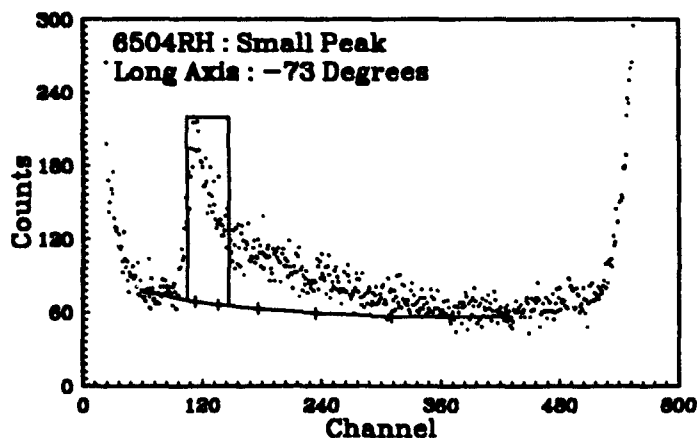


Fig. 9b. The same spectrum compressed as described in the text. Again, the background contribution is estimated from the line extending between the margins. The vertical lines represent the locations of the half-maximum values. Here, the counts under the peak is estimated from twice the number between the half-maximum margins.

All the methods yield roughly the same values for the large peak because the background is relatively small and the peaks well defined. This is illustrated in Fig. 10a where the proportional relationship is independent of the method used. The different methods do produce different estimates of the cross sectional area from the small peak as illustrated in Figs. 10b and 10c for the two axes of rotation. However, all the methods show cross sectional area decreasing with the cosine of the angle for rotations about the long axis and roughly with the square of the cosine for rotations about the short axis.

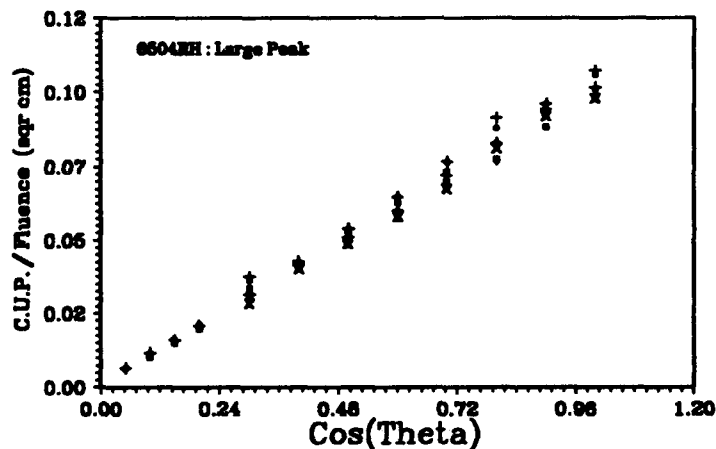


Fig. 10a. Ratio of the counts under the large peak and the fluence versus the cosine of the angle of incidence using the methods labeled in Table 1.

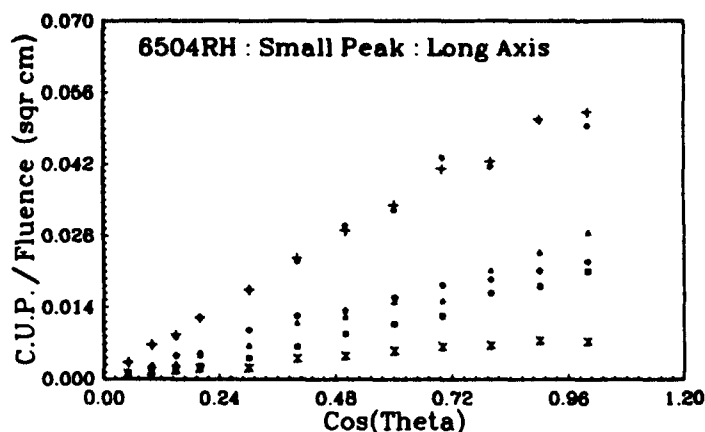


Fig. 10b. Same as 10a for the small peak and rotations about the long axis.

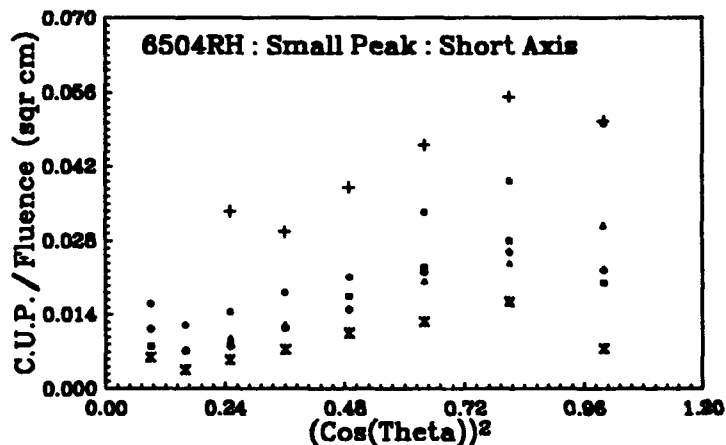


Fig. 10c Ratio of the counts under the small peak and the fluence versus the square of the cosine of the angle of incidence using the same methods.

The method employed to estimate the counts under the peak in what follows was P2 using the area of the box drawn between the half-maximum margins with background subtracted, i.e., method 7 of Table 1. The ratio of the number of counts under the peak to the fluence is plotted versus the cosine of the angle for rotations about the long axis in Fig. 11a. The relationship appears to be linear for both positive and negative rotations indicating that the long dimension of the junction is perpendicular to the long axis of the device. All the data appears consistent with the linear relationship with the best-fit lines intercepting the ordinate near the origin.

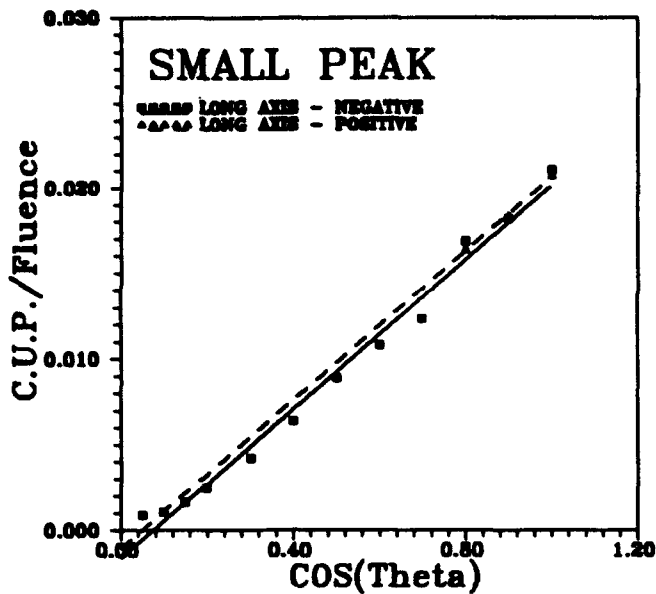


Fig. 11a. Ratio of the counts under the small peak and the fluence estimated using method 7 versus the cosine of the angle of incidence for rotations about the long axis. The curves represent best linear fits with the data for rotations in the positive and negative directions.

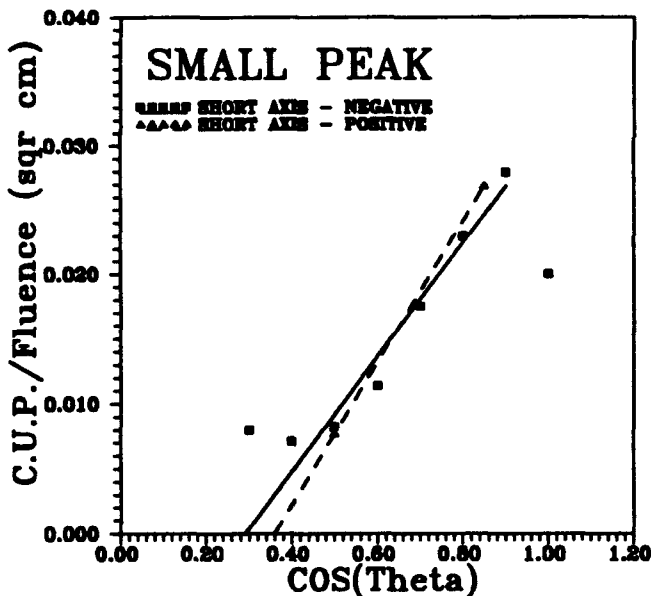


Fig. 11b. Same as 11a for rotations about the short axis.

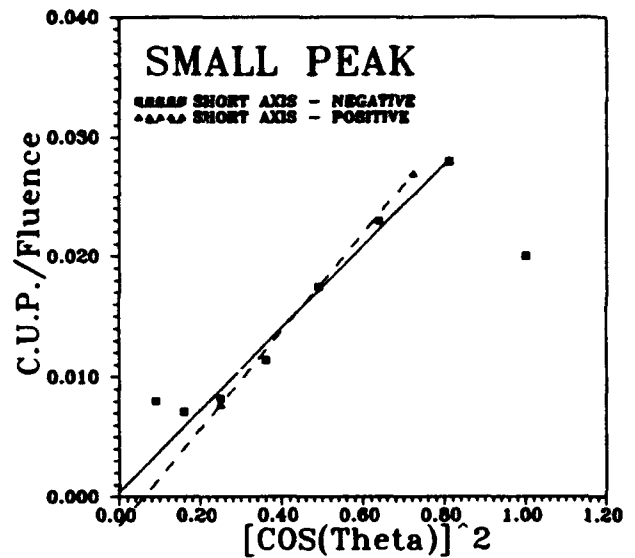


Fig. 11c. Same as 11b except the plot is versus the square of the cosine of the incident angle.

The data for rotations about the short axis is more ambiguous. As we saw earlier, the proportionality is closer to the square of the cosine rather than to the cosine, the relationship which is assumed in most SEU testing. However, when the ratio estimated by method 7 is plotted versus the cosine of the angle of incidence, as in Fig. 11b, there is good agreement with a linear relationship with a large intercept for all but the 0 degree and 73 degree data points. This means that the data is not consistent with the proportionality with the cosine assumed in most testing, but it is at least qualitatively consistent with the geometrical explanations described in the appendix of Ref. 7. The data can be fit quite simply by assuming that the number of events decrease with the square of the cosine as illustrated in Fig 11c.

Relevance to SEU

Unlike the situation for n-well CMOS, the small peak for the 6504RH is the result of traversals of the source rather than the SEU-sensitive drain. However, the thickness of the effective sensitive volume should be the same for the source and drain. It can be estimated from the position of the small peak to be about 4.5 microns. The shape of the drain is more "L" shaped than the rectangular source, and as a result, the dependence on the axis of rotation may be more complicated.

The ratio of the counts under the small peak and the fluence measured at normal incidence agrees with the total area occupied by the n-type source junctions. Since the n-type drains have similar dimensions with different orientations and more complicated shapes, the measured SEU response curve shown in Fig. 12 may be different if the rotations are carried about different symmetry axes. This may explain differences in the shapes of the response curves reported on the same devices.

The horizontal line in Fig. 12 represents the area estimated from these measurements of the source area which is then scaled by the ratio of the drain area to the source area.

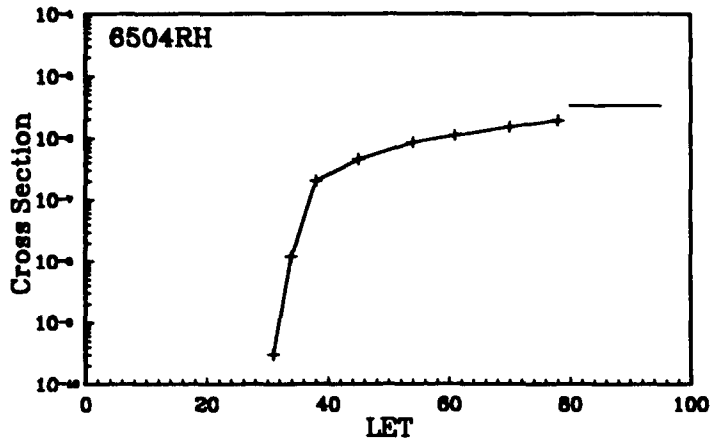


Fig. 12. The measured SEU cross section plotted versus effective LET for rotations about the long axis. The horizontal line represents the estimate of the SEU-sensitive drain as estimated from this study.

CONCLUSIONS

The charge collection by junctions with at least one small dimension was observed to vary with angle of incidence in a manner quite different from the large junction when the rotations were about the short symmetry axis of the Harris 6504RH SRAM but not when the rotations were about the long axis. Since the SEU-sensitive junction on CMOS devices typically has at least one small dimension, these results suggest that different SEU response curves may be obtained for rotations about the two mutually perpendicular symmetry axes of the device.

The nonlinear variation in peak position with the secant of the angle of incidence differs from the standard assumptions and may reflect some as yet not understood effect of competition for charge between the source and well-substrate junctions. However, even with the complication of competing junctions, the charge collection spectra can provide the projection of the cross sectional area for different angles of incidence and the distribution of path lengths through the effective sensitive volume.

These results suggest that care must be taken in correcting both the effective LET and the SEU cross section when either of the lateral dimensions of the sensitive volume is not much greater than the thickness. Since the charge collection spectra can be measured using the same setup as is used to measure the SEU cross sections, the best approach would be to make both measurements together. The appropriate corrections for the SEU cross sections can be determined from the charge collection spectra. The nonlinear dependence described above

may provide a simple physical explanation for at least some of the so-called "track effects" which have been reported.

REFERENCES

- [1.] P.J. McNulty, "Predicting SEU Phenomena in Space" in 1990 IEEE Short Course Microelectronics for the Natural Radiation Environments of Space (IEEE-NPSS Nuclear Radiation Effects Committee, 1990) pp 3-1 to 3-93.
- [2.] F. Sexton, "Measurement of Single Event Phenomena in Devices and ICs" in 1992 IEEE Short Course: Measurement and Analysis of Radiation Effects in Devices and ICs (IEEE-NPSS Radiation Effects Committee, 1992) pp 3-1 to 3-55.
- [3.] E. L. Petersen, J. B. Langworthy, and S.E. Diehl, "Suggested Single Event Upset Figure of Merit", IEEE Trans. Nucl. Sci., NS-30, No. 6, 4533-4539, Dec. (1983).
- [4.] P.J. McNulty, W.J. Beauvais, and D.R. Roth, "Determination of SEU Parameters of CMOS SRAMs by Charge Collection Measurements", IEEE Trans. Nucl. Sci., NS-38, No. 6, 1463-1470, Dec. (1991).
- [5.] P.J. McNulty, D.R. Roth, W.J. Beauvais, and W.G. Abdel-Kader, "Charge Collection Spectroscopy Applied to MOS RAMs", in Proceedings of the 1991 Single Event Upset Symposium, T. Cousins, Ed. (Defense Research Establishment Ottawa, 1991) pp 3.1-1 to 3.1-13.
- [6.] P.J. McNulty, D.R. Roth, W.J. Beauvais, W.G. Abdel-Kader, and D.C. Dinger, "Comparison of the Charge Collecting Properties of Junctions and the SEU Response of Microelectronic Circuits" Int. J. Radiat. Instrum., Part D, Nucl. Tracks Radiat. Meas., 19, Nos. 1-4, 929-938 (1991).
- [7.] P. J. McNulty, W.G. Abdel-Kader, and J.E. Lynch, "Modeling Charge Collection and Single Event Upsets in Microelectronics", Nuclear Instruments and Methods in Physics Research, B61, No. 1, 52-60, (1991).
- [8.] P.J. McNulty, W.J. Beauvais, D.R. Roth, J.E. Lynch, A.R. Knudson, and W.J. Stapor, "Microbeam Analysis of MOS circuits", in RADECS 91, First European Conference on Radiation and Its Effects on Devices and Systems, J.P. Charles, L. Adams, and A. Holmes-Siedle, Eds. (IEEE, Piscataway, NJ, 1991) pp 435 - 439.

APPENDIX J

DETERMINATION OF SEU PARAMETERS OF NMOS AND CMOS SRAMS

Determination of SEU Parameters of NMOS and CMOS SRAMs

P. J. McNulty, W. J. Beauvais, and D.R. Roth

Department of Physics and Astronomy

Clemson University

Clemson SC 29634-1911

ABSTRACT

Procedures for determining the SEU parameters for advanced memory devices are demonstrated for CMOS and resistor-loaded NMOS SRAMs. The dimensions of the sensitive volume are either obtained from charge collection measurements on test structures or estimated from similar measurements on the SRAMs themselves. Values of the critical charge determined from simple proton measurements agree with the values obtained for three SRAMs from extensive heavy-ion data.

INTRODUCTION

The algorithms currently in use for predicting SEUs require, as input, the dimensions of the equivalent sensitive volume associated with each SEU-sensitive junction and the threshold value of the charge (critical charge) which must be generated within the sensitive volume to upset the circuit element [1]. Since the number of ion pairs generated is proportional to the energy deposited for most radiations, the critical charge can also be expressed as a threshold energy which must be deposited. Obtaining the value of the critical charge with suitable accuracy normally requires tedious and expensive irradiations with heavy ions. This article describes simple procedures for estimating the dimensions of the sensitive volume with a minimum of beam time and procedures for estimating the critical charge for a device by means of one, or at most two, irradiations by protons. These nondestructive procedures are illustrated, first, for test structures and, then, for NMOS and CMOS SRAMs.

A reverse-biased junction forms at the interface between n and p doped regions of a silicon crystal. This space-charge region is the basis for the operation of the transistors which make up modern microelectronic circuits. It is also the basis for the particle detection characteristics which lead to SEUs [1,2]. The sensitive volume associated with the junction is a mathematical artifice whose dimensions are chosen such that the charge generated within the sensitive volume equals the charge actually collected across the junction. The dimensions used in calculations of SEU rates for SRAMs are often rough estimates. The dimensions parallel to the die surface should be only slightly larger than the lateral dimensions of the junction, but such process information is often not available. The thickness of the sensitive volume is difficult to estimate, even when the masks used in processing are available, because the thickness of the sensitive volume generally does not correspond to that of any identifiable structure. As a result, the thickness is usually the least known dimension.

MEASUREMENTS ON TEST STRUCTURES

Recent studies with test structures show that dimensions of the equivalent sensitive volume to be associated with a reverse-biased junction can be obtained with relatively simple procedures involving the taking of pulse-height measurements while irradiating the junction with heavy ions [2,3]. Figure 1 is a schematic of the experimental arrangement used for pulse-height measurements. The preamplifier is a charge-sensitive amplifier with a time constant comparable to the switching speeds of modern SRAMs, i.e., 20 to 500 nsec. The polarity of the signals accepted by the amplifier was set for negative pulses across the junction of interest. The pin connections for the test structure measurements were to the drain and substrate sides of the junction. Figure 2 shows the pulse-height spectra obtained across a drain-substrate junction for two different values of the bias across the junction: 0 V and 5 V. The junction is reverse-biased at zero bias due to the built-in potential induced by the abrupt change in doping across the junction. Comparison of the two spectra shows that the peak retains its shape but shifts in position about 20% toward higher energy depositions as a result of the increase in the bias to 5 V. The latter is a typical bias across the SEU-sensitive junction of a working circuit.

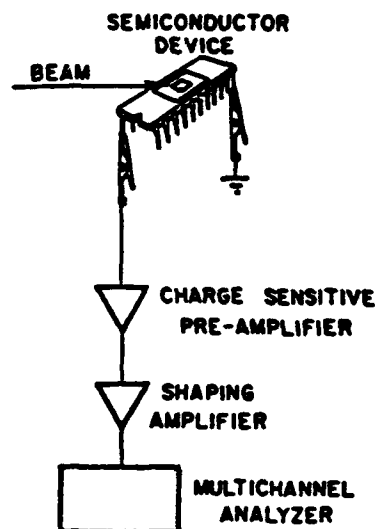


Fig. 1. Experimental configuration for measuring pulse-height spectra.

Measurements taken at zero bias provide useful information about how the junction collects charge at full bias. The ratio of the number of events making up the peak to the fluence of the incident particles should equal the cross

sectional area of the sensitive volume. The value obtained from the 0 V spectrum would be the same as that obtained at 5 V since every particle striking the junction generates a pulse in each case. The value of the energy most often deposited in the sensitive volume is given by the position of the peak in Fig. 2. The ratio of the energy deposited in MeV to the LET of the incident particles in MeV/ μm equals the pathlength of the particle's trajectory through the sensitive volume, assuming a constant LET over that distance. If that assumption does not hold, the thickness of the sensitive volume can still be estimated from the peak position using range-energy tables [2]. The shift in the peak position in Fig. 2 corresponds to that predicted by calculating the increase in the width of the depletion region with bias. Therefore, measurements at zero bias provide a reasonable estimate the thickness of the sensitive volume at full bias.

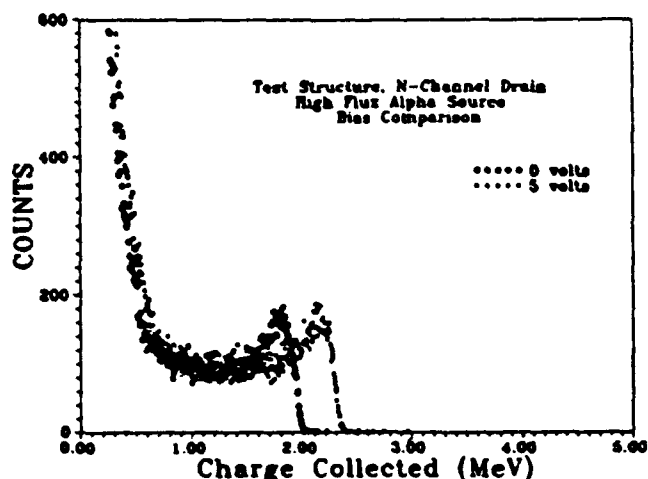


Fig. 2. Pulse-height spectra obtained across a single drain-substrate junction at two different biases: 0 V and 5 while the device was exposed to 4.8 MeV alphas from an Am-241 source. The test structure belongs to the same advanced technology bulk CMOS as CMOS circuits described later but has a larger area than the drains used in circuits.

This shift in peak position is relatively small because there is a large contribution from diffusion as well as drift [4]. Using preamplifiers with time constants comparable to the switching speeds of the circuit ensures that the peak position reflects only charge that arrives time to contribute to upsetting the device.

APPLICATION TO SRAMS

The test-structure studies led the recent proposal of an experimental approach for estimating the dimensions of the equivalent sensitive volume associated with junctions in operable devices [1,2]. Unfortunately, the application of bias during these measurements results in sufficient noise to flood the spectrum. This noise is not observed in test structures and presumably reflects changes in the electrical state of the circuit elements. The measurements are carried out at zero bias, and the results are, according to Fig. 2, somewhat thinner than the values obtained from test

structures at full bias. However, the values obtained in these nondestructive tests provide estimates suitable for accurate SEU-rate predictions. The procedure involves measuring the pulse-height spectrum between the power and ground pins of the device while the device is being irradiated by a parallel beam of monoenergetic ions. The experimental configuration is the same as that shown for test structures in Fig. 1 except that the measurements are now made between the power pins of the device. Pulse-height spectra obtained with MOS SRAMs typically exhibit one or more peaks corresponding to ions traversing different p-n junctions connected to the power line [3]. The size of the peaks reflect the total area occupied by that type of junction. The tallest peaks should correspond to those junctions which occupy the greatest area on the die, i.e., those which make up the transistors of the memory cells. This results in a form of charge collection spectroscopy where the different peaks in the spectrum correspond to traversal of different junction types. The junction type associated with each peak can be identified by analysis and comparison with data obtained on appropriate test structures.

As with the peak obtained with the test structure, the ratio of the number of particles under a peak to the fluence should equal the product of the junction area and the number of junctions of that type. The position of each of the peaks reflects the pathlength through the equivalent sensitive volume for the corresponding junction. The value of the thickness can be obtained either using range-energy tables on a single measurement at normal incidence or from the slope of a plot of peak position versus LET [1].

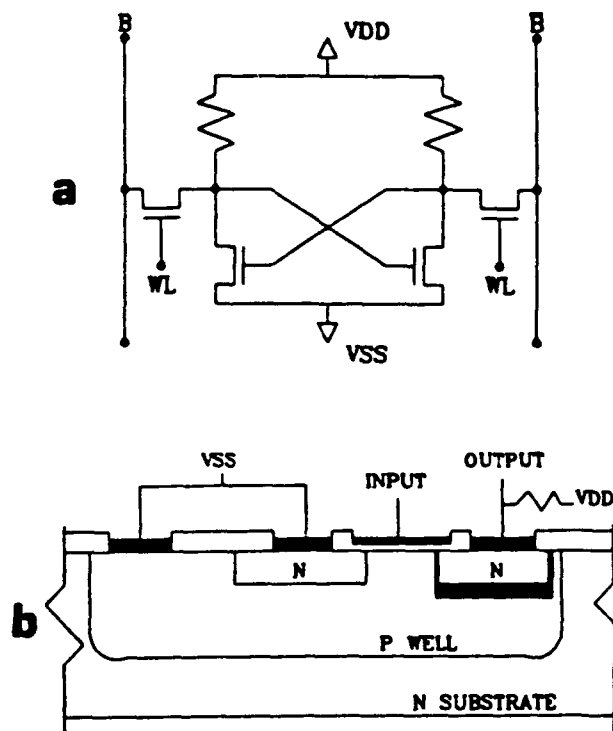


Fig. 3. a) Memory element on an RMOS device and b) a cross sectional view of one of the transistors.

Single Event Characterisation of an RMOS SRAM

The simplest spectra obtained with memory devices have been observed with resistor-load NMOS (RMOS) SRAMs which exhibit only a single large peak in their charge collection spectra. The typical memory latch of an RMOS SRAM is the four transistor cell shown in Fig. 3a. One of its transistors is shown in cross section in Fig. 3b. Some but not all RMOS transistors have a well, as is shown in Fig. 3b. The pulse-height spectrum obtained with an RMOS SRAM, the IDT6116V, is shown in Fig. 4. The spectrum contains a single peak suggesting either the absence of a well or that hits on the well are in separable from hits on the drain. The area calculated from the peak in Fig. 4 was previously shown to agree with the experimentally measured SEU cross section for that device [1,2] showing that the observed peak provides the correct area of the sensitive volume. It should be noted that the memory circuits are generally produced using same implants and diffusion as some other circuits on the die. As a result, the observed peaks would contain contribution from junctions outside the memory array. However, it was possible to mask the chip such that portions of the die were exposed, and it was found that the peak in Fig. 4 was

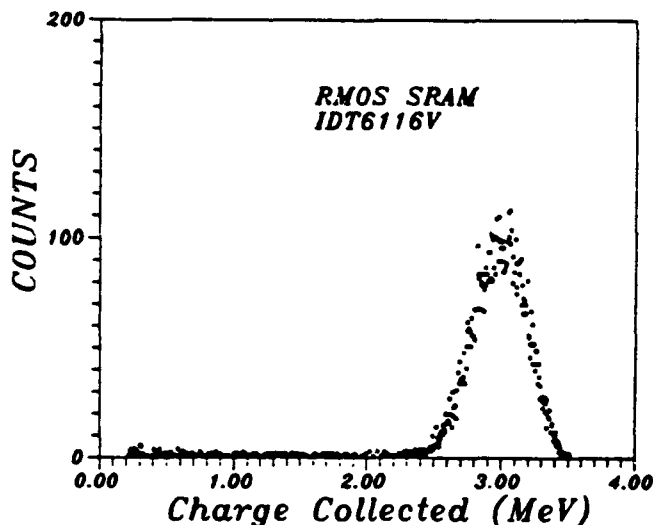


Fig. 4. Pulse-height spectrum measured between the power pins of an RMOS SRAM, the IDT6116V, measured at zero bias. The peak corresponds to charge collection from the 32,768 reverse-biased junctions on the unbiased device.

almost entirely due to the memory cell. The procedures used for isolating the memory and peripheral circuitry are described in Ref. 5. The thickness was obtained using range-energy tables. The dimensions of the sensitive volume were then used as input for CUPID simulations of the charge collection spectrum to be expected upon exposure to 148 MeV protons. Since the pulse-height spectrum obtained from the RMOS device is dominated by events at a single junction type, the proton-induced charge collection spectra at that junction can be measured directly and compared with the predictions of CUPID. The agree-

ment between theory and experiment is apparent in Fig. 5 where the cross section for depositing at least energy E is plotted versus the value of E . This represents the first test of CUPID against partially depleted silicon microstructures. Since the dimensions of RMOS drain-substrate junctions are similar in design to the SEU-sensitive junctions in CMOS, this agreement is evidence that CUPID can be used successfully to model charge collection at drain-substrate junctions in both CMOS and RMOS.

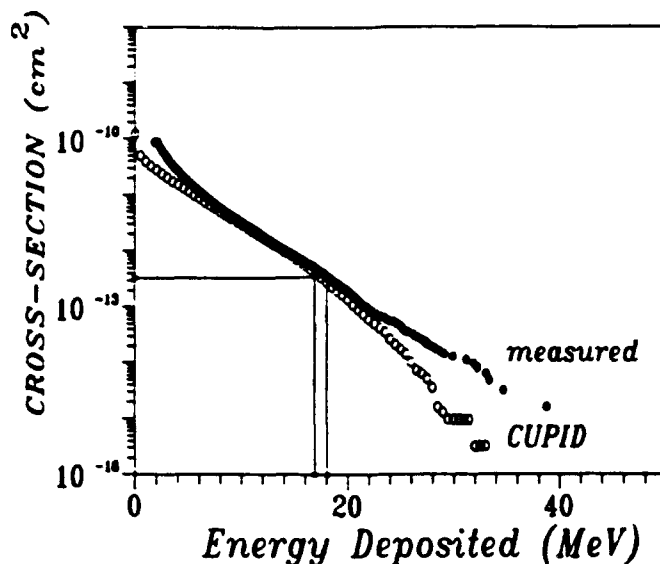


Fig. 5. Comparison of CUPID simulations of proton induced spallation reactions with experimental measurements of the pulse-height spectrum measured between the power and ground pins of an IDT6116V exposed to 148 MeV protons. The data from both the experiment and the simulations are plotted as the cross section for depositing at least some energy E within a sensitive volume of the RMOS device (11.7 microns \times 11.7 microns \times 13.6 microns) is versus E .

Figure 5 also illustrates how simple measurements of pulse-height spectra from the power lines of working microelectronic circuits can be combined with single SEU measurements made with energetic protons, or simulations of such spectra, to determine the critical charge. The single SEU cross section measurement made on these devices exposed to 148 MeV protons is represented by the horizontal line in the figure. Vertical lines drawn from the intersections of the horizontal line with the theoretical and experimental curves represent the corresponding estimates of the critical charge. This simple procedure provides a new technique for estimating the critical charge without expensive and tedious heavy-ion SEU testing. However, charge collection measurements are required to determine the thickness of the sensitive volume. Data, like that shown in Fig. 8, suggest that heavy ions provide more accurate estimates than would alphas, but only a single ions species is needed for this measurements. The critical charge of the IDT6116V obtained with protons is compared to that determined by Koga et al [4] from heavy ion testing in Table 1. The agreement is quite good.

Table 1.

Heavy Ion LET (MeV-cm ² /mg)	Equivalent Q _{crit} 13.6μm MeV	Proton Q _{crit} (MeV)
6 \pm 1	19 \pm 1	18 \pm 1

The critical charge can be determined from proton irradiation. Only a single incident energy because the complex proton induced spallation reactions result in a wide spread in energy depositions. As a result, a significant fraction of the events will result in charge collection above and below threshold at most proton energies. The measured SEU cross section at a given energy identifies the fraction of the charge collection events which exceed threshold at that energy and upset the device. This, in turn, determines the value of the threshold or critical charge when the device exposed to monoenergetic heavy ions, the charge collection spectrum is quite narrow, and for most values of LET all events are either above or below threshold. Therefore, many heavy ion measurements are required to identify the transition region.

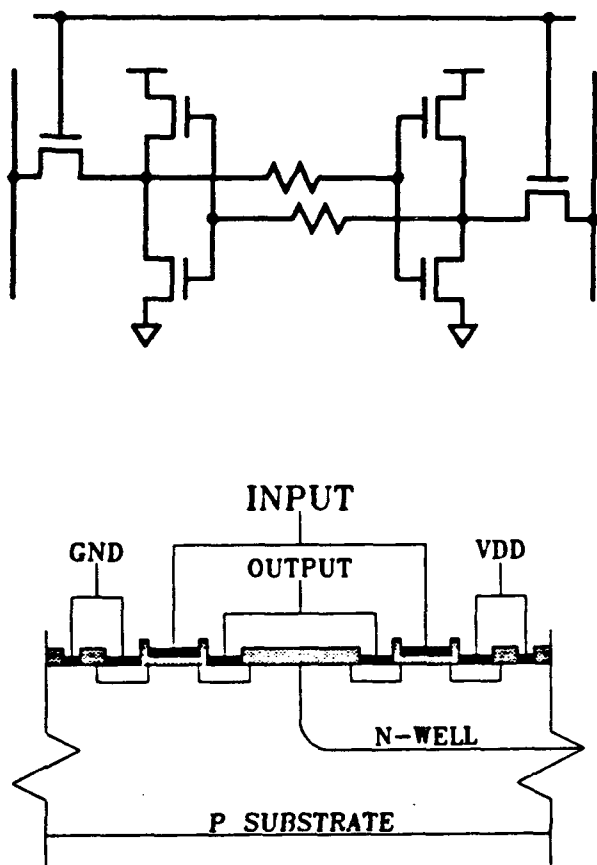


Fig. 6. Memory element of a CMOS SRAM and a cross sectional view of one of the inverters.

Characterisation of CMOS Devices

Measurements on CMOS devices are carried out in the same way as for RMOS. The difference is that the CMOS spectra typically exhibit more than one peak because of the increased number of junction types within the memory cell [3]. A CMOS inverter which makes up half a memory cell is shown schematically in Fig. 6. The p-channel transistor is on with zero bias on the gate resulting in a direct electrical connection between VDD and the drain-well and drain-substrate junctions. The well-substrate junction is directly connected to VDD. Figures 7a through 7c show the spectra obtained from CMOS SRAMs irradiated with various ions. Two and sometimes three peaks are present in CMOS spectra. In all three cases, the spectrum observed when the entire chip was irradiated was the same as that observed when the beam was collimated to a portion of the memory array [5]. The lower energy peaks are sometimes pronounced in an alpha spectrum but not always. These peaks become clearly visible when the device is exposed to heavy ions incident at higher values of LET. This improvement with higher LET particles is evident when Figs. 7c and 7d are compared. The poorly defined low energy peak in Fig. 7c resolves into two clearly defined peaks upon exposure at the higher LET. This splitting into two may reflect differences in the geometry of the two drain-substrate junctions in the memory circuit.

A microbeam analysis [5] shows that the three peaks in Fig. 7d are generated within the memory cell at different locations separated by distances which are consistent with their being generated at the different junctions which make up the transistors of the memory cell. The largest energy peak corresponds to ions traversing the well-substrate junction. The lower peaks correspond to traversals of the drain-substrate junctions, presumably the SEU-sensitive junction. Comparison to data obtained with test structures from the same technology suggests that the lower-energy peak should, in general, correspond to the drain-substrate junction while the larger peak should be generated at the well-substrate junction. The much larger area of the well results in many more events (larger peak) and more charge collected across that junction both from the substrate and from within the well. Again, the ratio of the number of events under the peak to the fluence is the product of the the number of junctions and the area of each. Since the measurements are carried out under no bias, all 131,072 of the drain-substrate junctions are reverse-biased because of their built-in potential and contribute signals to the spectrum. Only 65,536 of the junctions in a working circuit would be reverse biased and connected to the power line.

Dependence of Thickness on LET and Angle of Incidence

Figure 8a is a plot of the position of each peak in the pulse-height spectra versus the effective LET ($LET \times \sec\theta$) for exposures of the CMOS device of Fig. 7a to Am²⁴¹ alphas and 178 MeV chlorine ions. The slope of the best-

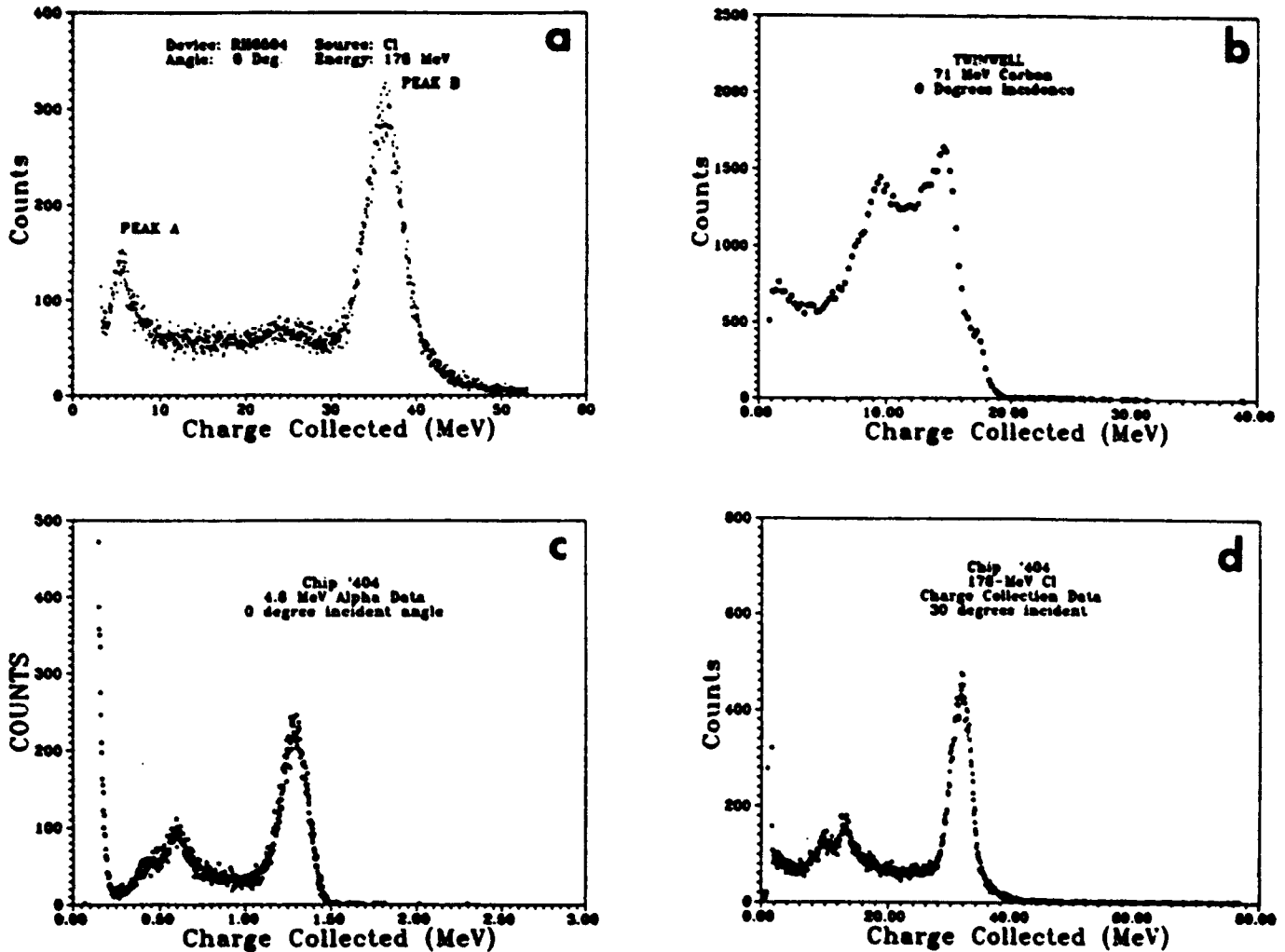


Fig. 7. a) Pulse-height spectrum obtained from a Harris CMOS circuit, the 6504RH, exposed to 178 MeV Cl. b) Spectrum from Texas Instruments HC5517A, 71 MeV carbon. c) Spectrum obtained from an advanced technology CMOS device, 4.8 MeV alphas. d) Spectrum from the previous device exposed to 178 MeV chlorine ions incident at an angle of 30 degrees to the normal to the die surface.

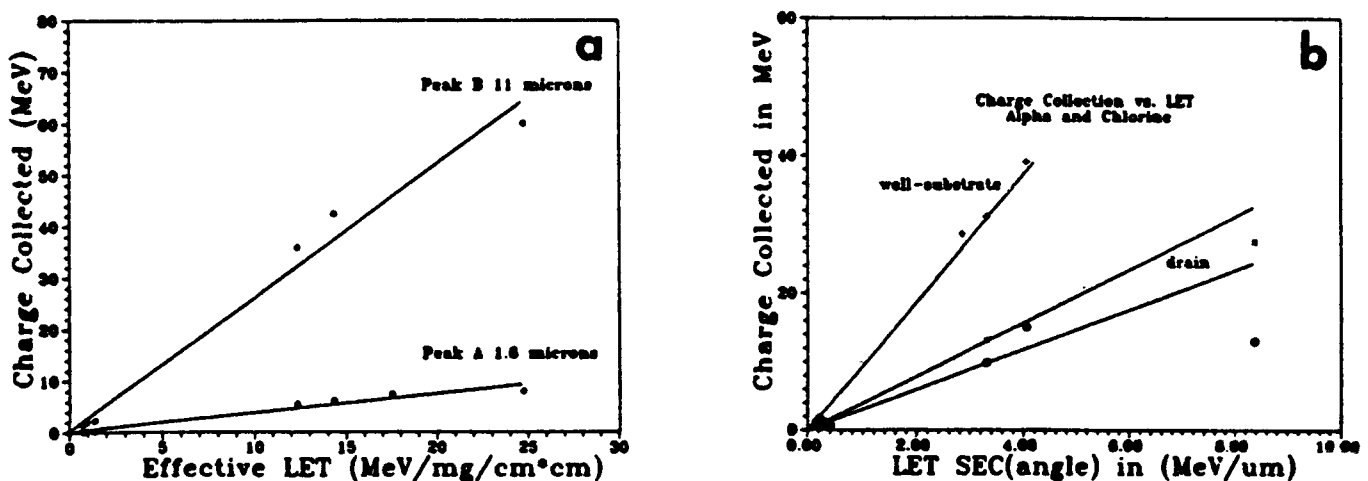


Fig. 8. Position of the peak in the charge-collection spectrum versus the effective LET ($LET \times sec\theta$) of the incident particle. a) RH6504 b) Advanced CMOS process.

At straight line for the events generated at each junction should be the product of the thickness of that sensitive volume and the density of silicon. The thickness of the sensitive volume obtained from the slope for the drain-substrate junction of this device was $1.6 \mu\text{m}$; this makes the sensitive volume relatively thin and disk shaped, which is consistent with the data fitting a linear curve up to angles of 60° . Figure 8b shows a similar plot for the advanced CMOS process of Figs. 7c and 7d. The peak at lower energy depositions splits into two well defined peaks as the angle of incidence increases. This may reflect small differences in the two drain substrate junctions. The curve with the large slope was used in our calculations. The values of the drain slopes yield thickness values of 3.0 and $3.8 \mu\text{m}$. These values are comparable to at least one of the other two dimensions of the sensitive volume. They are also consistent with the observed fall off from linearity apparent at the highest angle of incidence because the pathlengths through a sensitive volume with this shape would begin to decrease at higher angles. The linear relation between charge collection and effective LET confirms that the thickness of the sensitive volume is independent of the LET of the incident particle - a relationship which is inherent in all the standard algorithms used for SEU-rate predictions but has not previously been tested experimentally on silicon microstructures.

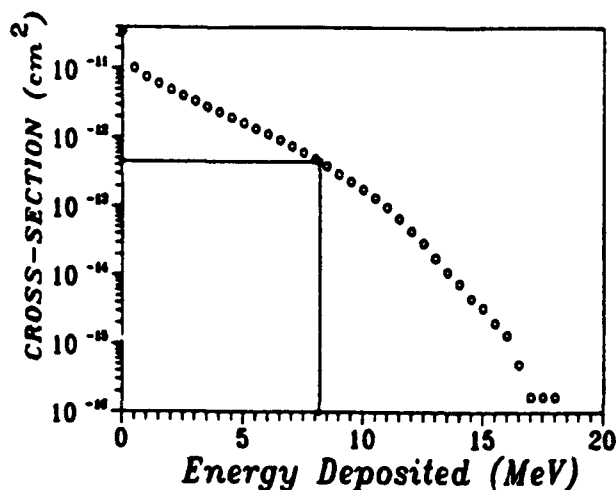


Fig. 9. Cross section for depositing at least some energy E versus E , as simulated for the HC5517A by CUPID. The horizontal line represents the measured SEU cross section. The intersection of the vertical line with the abscissa marks the estimated critical charge.

Proton Simulations and the Critical Charge

The charge collection spectrum was predicted by the CUPID simulation codes for interactions of 148 MeV protons in a sensitive volume having the dimensions which were determined for the Texas Instruments CMOS SRAM of Fig. 7b. The results are plotted in Fig. 9 as an integral spectrum, i.e., a plot of the cross section for depositing at least some energy E versus E . The SEU cross section was measured for the same irradiation with the function-

ing device. The result is plotted as a horizontal line in Fig. 9. A vertical line drawn from where it intersects the theoretical curve marks the value of the critical charge on the abscissa. Although the proton simulation results in a broad spread of energy depositions, the procedure results in an unambiguous estimate of the critical charge of the device.

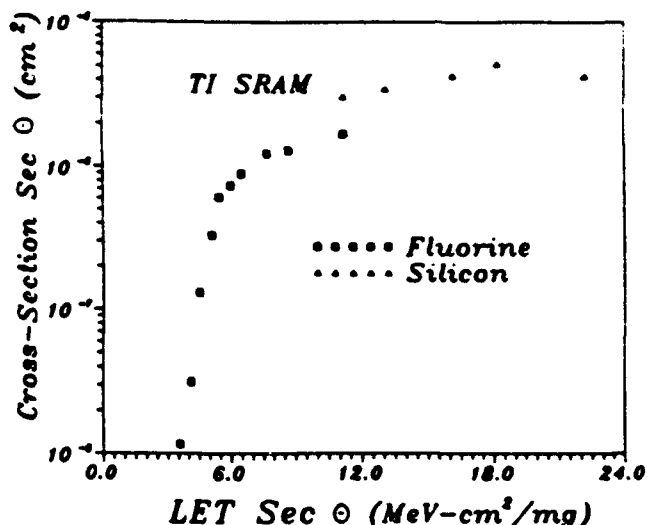


Fig. 10. Measured SEU cross section versus effective LET for the HC5517A.

SEU cross sections were measured on the Texas Instruments' HC5517A exposed to energetic heavy ions at different values of effective LET. A plot of the measured SEU cross section versus the effective LET is given in Fig. 10. The critical charge can also be obtained from the threshold value of the LET needed to upset the device by multiplying threshold by the ion's pathlength through the sensitive volume. Unfortunately, threshold is not unambiguously defined in plots such as that of Fig. 10. This is because of the slow rise in the cross section with increasing LET. This laboratory defines threshold as the value of the LET when the SEU cross section rises to 50% of the value it reaches on the early portion of the plateau. See Refs. 1 and 6 for an explanation of the shape of the curve. The value of the critical charge obtained this way is compared in Table 2 with the value obtained from protons using the procedures described above. The agreement is excellent.

Table 2.

Heavy Ion LET (MeV-cm ² /mg)	Equivalent Q_{crit} $5 \mu\text{m}$ MeV	Proton Q_{crit} $8.1 \times 8.1 \times 5.0 \mu\text{m}^3$ (MeV)
5 ± 0.5	8.5 ± 1.6	8.2 ± 0.2

The procedures described above for determining circuit parameters were repeated for the advanced technology CMOS device. The dimensions of the sensitive volume were determined from the pulse height spectrum of Figs. 7c and 7d by the above procedures. The SEU cross section measured as a function of the effective LET [7] was used to

determine the value of the threshold LET which, in turn, was multiplied by the pathlength to determine the critical charge. The SEU cross section was measured for 148 MeV incident protons and used on a CUPID plot to estimate the critical charge. All the procedures were carried out in a manner similar to those described above. Table 3 compares the values of the critical charge obtained with protons and heavy ions - again, the agreement is excellent.

Table 3.

Heavy Ion LET (MeV-cm ² /mg)	Equivalent Q _{crit} 3.8μm MeV	Proton Q _{crit} 9.2 × 9.2 × 3.8μm ² (MeV)
15±2	13±2	16±2

There is a significant difference evident in Fig. 10 between the SEU cross sections measured at the same effective LET with two different ions. The value measured with ions incident at the lower LET and higher angle of incidence yield lower cross sections than those measured at normal incidence and correspondingly higher LET. The problem doesn't appear to be with the correction applied to the abscissa values to generate the effective LET. The use of the effective value of the LET, obtained by multiplying the LET by the secant of the angle of incidence, is consistent with the linear relationships seen in Fig. 8 and should be appropriate. The other angular correction, which is routinely applied to SEU measurements (automatically at BNL), corrects for the fact that the cross sectional area of the junction projected on a plane perpendicular to the beam direction should decrease as the angle of incidence increases. Since the number of beam particles crossing the junction should decrease with the cosine of the angle of incidence, multiplying the measured cross section by the secant should raise it to the value it would have had at normal incidence. This correction works for large area junctions like those in nuclear detectors. This correction, which was applied to the data of Fig. 10, may not be appropriate for many modern circuits with their small SEU-sensitive junctions.

The numbers of events under the low-energy peak in the pulse-height spectra for the 6504RH were measured for the same fluence, but at different angles of incidence. The numbers are shown plotted versus the cosine of the angle of incidence in Fig. 11. The number of events falls off much faster with increasing angle than the cosine. This has been found to be true for a number of different device types tested [3]. It may be due to the small junction size, although a measuring artifact which would affect all our devices at two facilities has not been ruled out. In either event, SEU measurements would be affected the same way, and the standard correction would clearly be wrong for any of the devices we tested. The implication is that the standard geometric correction significantly underestimates the cross section at normal incidence. This provides an explanation for jumps in the cross section as ion species

are changed like that seen in Fig. 10. This mechanism does not depend on differences in track structure.

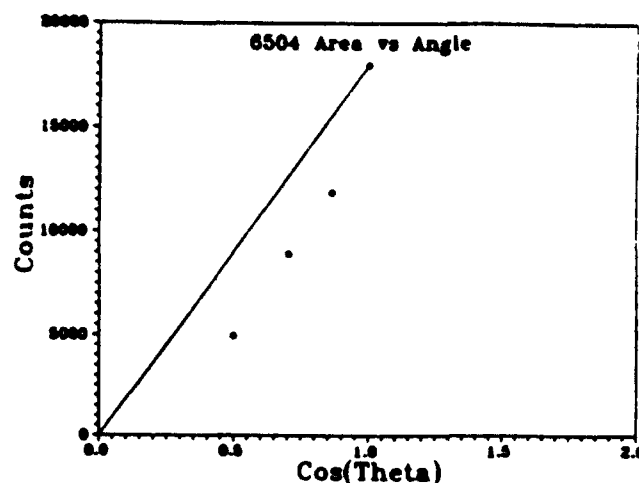


Fig. 11. Number of events under the peak versus the cosine of the angle of incidence for the Harris 6504RH. The solid curve assumes that the number of events is proportional to the cosine of the angle. This assumption is the basis for the geometric correction routinely made at accelerators.

SUMMARY AND CONCLUSIONS

When heavy ions traverse the reverse-biased junctions that form the transistors of modern SRAMs, the current flowing across the junction results in a pulse which can be seen on the power lines of the device. The spectrum is easily measured using pulse-height analyser setups which are similar to those used in nuclear spectroscopy. The peaks in the pulse-height spectra obtained with parallel identical ions are the result of traversals of different types of p-n junctions. The number of events under the peak is used to estimate the cross sectional area of the sensitive volume as seen from that angle of incidence. The position of the peak provides the value of the most common pathlength through the sensitive volume. The shape of the peak yields the pathlength distribution. With a sufficient number of measurements and the appropriate software, a detailed profile of shape of the sensitive volume in any plane can be obtained. Tomographic images similar to medical CAT scans is possible.

The value of the critical charge for RMOS devices is obtained from a comparison of the measured proton SEU cross section with the measured pulse-height spectrum with the device exposed to protons at the same incident energy. A similar comparison using CUPID simulations instead of a measured pulse-height spectrum determines the critical charge for CMOS SRAMs.

The standard methods of generating curves of SEU cross sections versus the effective LET may have to be modified so that proper corrections for angle of incidence can be made to the measured SEU cross sections. Charge collection measurements could determine the exact corrections to use as a function of angle.

REFERENCES

- [1] P.J. McNulty, "Predicting SEU Phenomena in Space" in 1990 IEEE Short Course: Microelectronics for the Natural Radiation Environments of Space (IEEE Nuclear Radiation Effects Committee, 1990).
- [2] P.J. McNulty, D.R. Roth, W.J. Beauvais, W.G. Abdel-Kader, and D.C. Dingo, "Comparison of the Charge Collecting Properties of Junctions and the SEU Response of Microelectronic Circuits" to be published in Nuclear Tracks and Radiation Measurements.
- [3] P.J. McNulty, D.R. Roth, W.J. Beauvais, and W.G. Abdel-Kader, "Charge Collection Spectroscopy Applied to MOS RAMS," to be published in the proceedings of the 1991 Single Event Symposium, Ottawa, Canada.
- [4] R. Koga, W.A. Kolaszinski, J.V. Osbourne, J.H. Elder, and R. Chitty, "SEU Testing for 256K Static RAMs and Comparison of Upsets Induced by Heavy Ions and Protons," *IEEE Trans. Nucl. Sci.* NS-35, 1638-1643 (1988).
- [5] P.J. McNulty, W.J. Beauvais, D.R. Roth, J.E. Lynch, A. Kaudson, and W. J. Stapor, "Microbeam Analysis of CMOS SRAMs" to be published in the proceedings of the RADECS Conference, September 9-12, Montpellier, France.
- [6] P.J. McNulty, W.G. Abdel-Kader, and J.E. Lynch, "Modeling Charge Collection and Single Event Upsets in Microelectronics", *Nuclear Instruments and Methods in Physics Research B61*, 52-60 (1991).
- [7] E.G. Stassinopoulos, private communication.

APPENDIX K

CHARGE COLLECTION AND SEU SENSITIVITY FOR GaAs BIPOLAR DEVICES

CHARGE COLLECTION AND SEU SENSITIVITY FOR Ga/As BIPOLAR DEVICES*

M.H. Yaktien, P. J. M^cNulty, J.E. Lynch and D.R. Roth
Department of Physics and Astronomy
Clemson University
Clemson, SC 29634-1911

J.F. Salsman and J.H. Yuan
Texas Instruments

ABSTRACT

Charge collection was measured across the base-emitter heterojunction to test certain assumptions of the standard "sensitive volume" models for calculating SEU rates. The observed dependence of charge collection on the LET (linear energy transfer) and the angle of incidence of alphas and 20 MeV Oxygen ions is consistent with the hypothesis that the charge collected equals the product of LET and pathlength through a sensitive volume of fixed dimensions. The data suggest that the switch from MBE to MOCVD processing resulted in an increase in the thickness of the sensitive volume from 0.11 to 0.25 microns.

of incidence in determining the threshold value of LET for inducing upsets. The assumptions of the SV hypothesis have never been tested experimentally in GaAs.

This paper reports on a study of the charge collection measured during exposure to 4.4 MeV alphas and 20 MeV Oxygen ions. A verifiable consequence of the SV hypothesis for a large area junctions like the H^2L base-emitter heterojunction is that the charge collected following traversals by energetic particles should be proportional to the LET of the particle and the secant of the angle of incidence as long as the particles are sufficiently energetic that the LET remains relatively constant within the SV.

INTRODUCTION

The observed insensitivity of bipolar H^2L circuits implemented in GaAs against SEUs (1) has been attributed to the restricted collection of charge at the base-emitter heterojunction, the junction believed to be the most vulnerable to upsets. Previous measurements (2) suggested that charge collection at the base emitter heterojunction increased when the fabrication process changed from MBE to MOCVD. Suggested alternative explanations of the data included a nonlinear relationship between charge collection and LET and the inappropriateness of the sensitive volume hypothesis to GaAs bipolar circuits, as well as the possibility of experimental error.

The Sensitive Volume (SV) is a mathematical artifice common to the algorithms most used for SEU-rate calculations (3-5). The location, orientation, and dimensions of the SV are chosen such that the charge generated along the segment of the initial particle's trajectory which lies within the SV equals the charge collected across the junction following the particle's traversal. If the charge generated within the SV exceeds the critical charge for that junction, the element upsets. The dimensions of the SV are assumed to be the same for every particle, independent of the incident particle's charge, energy, and angle of incidence. This assumption is the same as saying that the charge collected across the junction equals the convolution of the product of the LET and the pathlength across the SV. This is why SEU cross sections are typically plotted versus the product of the LET and the secant of the angle

EXPERIMENTAL METHODS

The test structure used in this study consisted of an array of 20 H^2L transistors bonded out in parallel as shown in Fig. 1. A cross sectional view of the H^2L transistor is shown in Fig. 2. The emitters were all tied to ground through the substrate (See Fig. 1), the collectors were held to 2 V, and the bases were held to 0.7 V to approximate the SEU-sensitive "off" state of the H^2L transistor.

A schematic of the circuit used for measuring the pulse-height spectra across the base-emitter heterojunction is given in Fig. 3. The peak amplitude of the preamplifier output is proportional to the charge collected within the time constant of the preamplifier circuit which in this case was a few hundred nanoseconds. Since the recombination time in GaAs is on the order of a few nanoseconds, the signal recorded for each event should be proportional to the total charge collected at the junction.

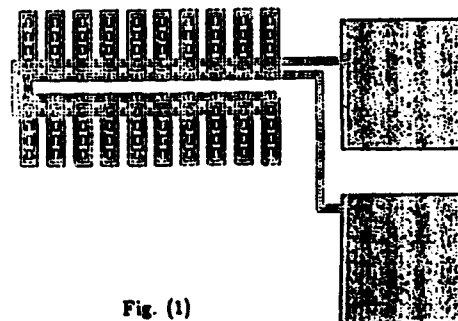


Fig. (1)

*Supported in part by the Defense Nuclear Agency and the Air Force Systems Command

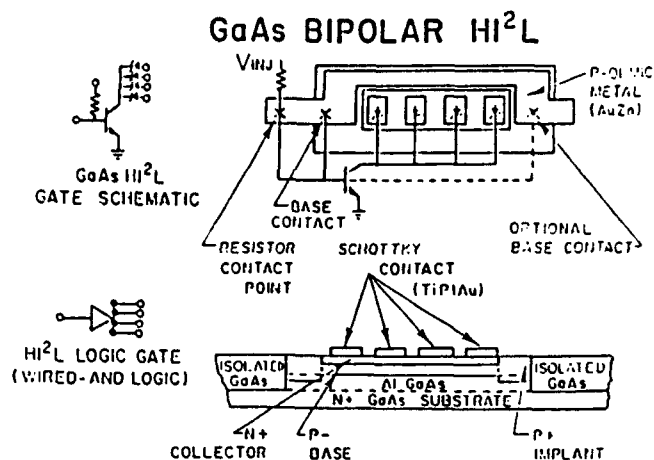


Fig. (2)

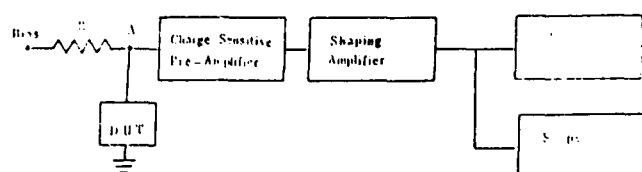


Fig. (3)

The exposures were carried out in vacuum; the 4.4 MeV alpha irradiations were carried out in our laboratory using a 1 mCi Americium 241 source. An intense source allowed us to obtain data in reasonable intervals but required such a thickness of radioactive material as to distort the spectrum as can be seen in Fig. 4.

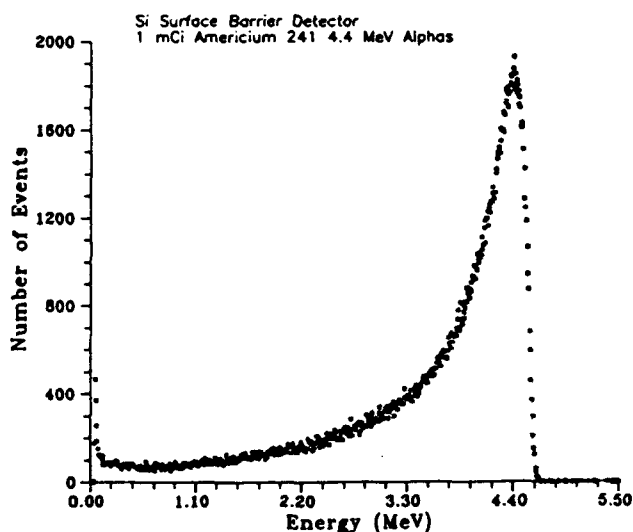


Fig. (4)

The package including the die was split without breaking the bond wires to facilitate exposures at large angles of incidence.

RESULTS AND DISCUSSION

The pulse-height spectrum measured between the base and emitter leads is shown in Fig. 5a for 4.4 MeV alphas incident normal to the surface. The abscissa is expressed in energy units, the traditional units for pulse-height analysis, but the values can be converted to charge collected in pC by 30 MeV. Two peaks are observed in the spectrum. The peak labelled (1) is a tall sharp peak at low energies close to the noise (The upper edge of the noise is seen just above where the lower-level discriminator was set). This position of this peak is the same as that observed earlier (2) on a single transistor. The second, peak (2), is a small peak at high energies which was not seen in measurements on an isolated transistor (2) or in the spectra obtained with the same transistor array exposed to 20 MeV Oxygen (See Fig. 6).

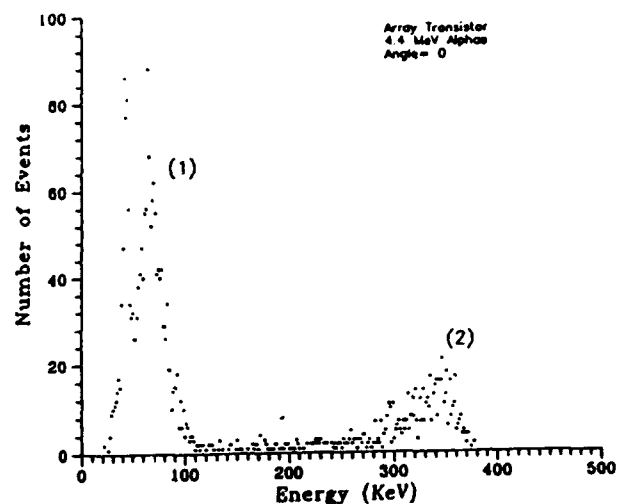


Fig. (5.a)

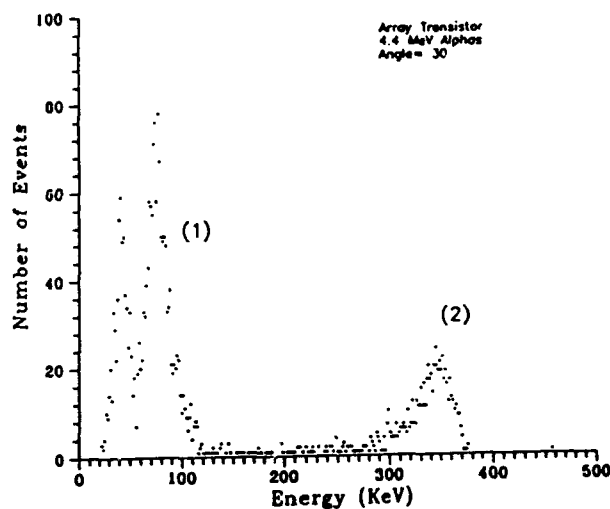


Fig. (5.b)

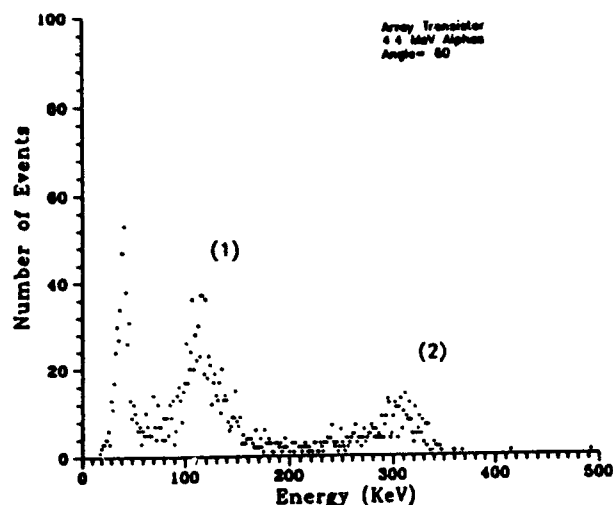


Fig. (5.c)

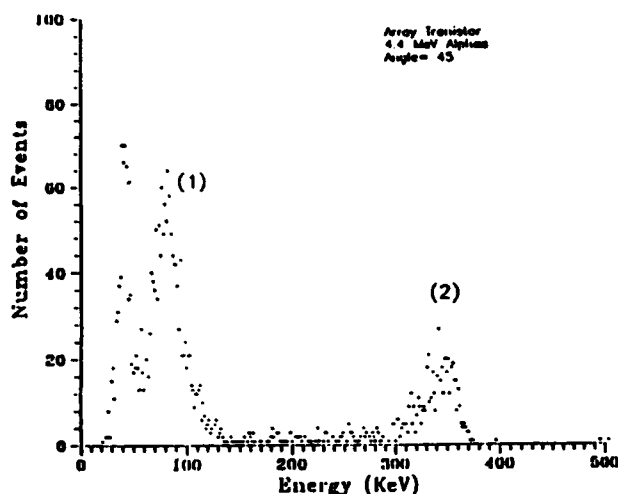


Fig. (5.d)

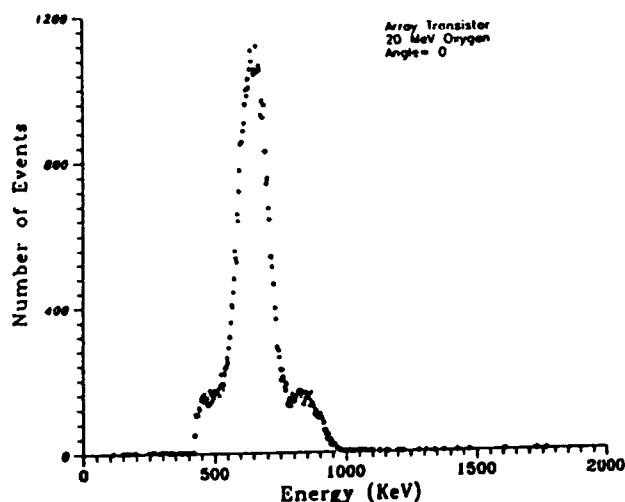


Fig. (6)

The effect on the alpha spectrum of changing the angle of incidence is illustrated in Figs. 5a through 5d for angles of incidence of 0°, 30°, 45°, and 60°, respectively. There

is a clear shift in peak (1) towards higher energies as one might expect for traversals of a thin large-area sensitive volume. Peak (2) is not particularly sensitive to the angle of incidence, suggesting that it may result from some other junction, possibly one not having a planar structure. Since the position of the low-energy peak agrees with the earlier isolated transistor and the position of the peak in the pulse-height spectra changes with angle of incidence as expected for a large area junction, we assume in what follows that it represents signals from the base-emitter heterojunction.

The positions of both peaks in the pulse-height spectra are plotted versus the angle of incidence for exposure to 4.4 MeV alphas in Fig. 7. As mentioned above, the small high-energy peak falls off with increasing angles while the large low-energy peak increases with angle similar to the secant of the angle of incidence. Testing whether increases in pathlength produce the same change in charge collection at the junction as equivalent increases in LET, requires that the value of the particle's LET at the SV be calculated for each angle of incidence.

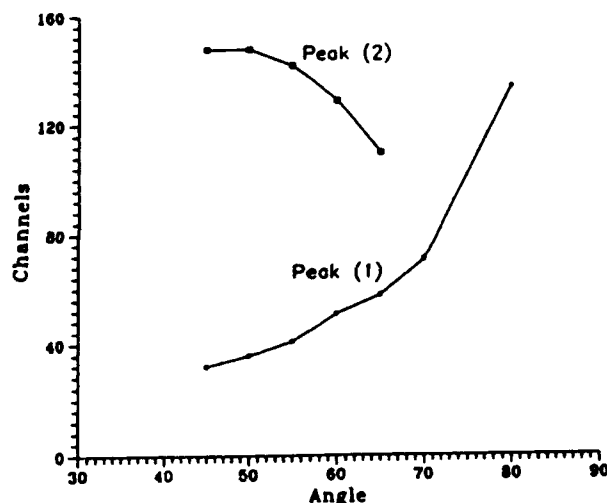


Fig. (7)

Calculating LET at the Heterojunction

Both the alphas and the oxygen ions have enough range to penetrate to the heterojunction with considerable residual energy at normal incidence. However, since that energy is quite different from what the particles had entering the top of the material, the LET values at the junction may be different from what they were at the surface. Moreover, as the angle of incidence is increased, the pathlength through the overlying material is longer and the energy with which the particle arrives at the junction is correspondingly lower. As a result, the LET a particle has at the heterojunction must be calculated for each angle of incidence. The values obtained depend on the thickness of the layers of material lying above the sensitive volume. These layers include the collector as well as the metal contacts and the passivation layers holding the interconnects. We assume in what fol-

lows that these overlying layers are equivalent to a layer of GaAs $D = 3 \mu\text{m}$ thick. Tables 1 - 3 summarise the results of the calculations outlined below. Tables 1 and 2 present results for two different devices exposed to 4.4 MeV alphas and Table 3 presents the results for exposure to 20 MeV Oxygen ions.

Array Transistor / Chip A
Ion: He
E = 4.4 MeV
Range = 15.0 μm

Angle	S	R_{in}	E_{in}	LET	LETsec θ	CC	E_{peak}	R_{peak}	s	d
0°	3.00	12.00	3.71	0.48	0.48	0.066	3.64	11.77	0.23	0.23
30°	3.46	11.54	3.59	0.49	0.56	0.075	3.51	11.24	0.30	0.26
45°	4.24	10.76	3.39	0.50	0.71	0.082	3.31	10.44	0.32	0.23
60°	6.00	9.00	2.92	0.53	1.10	0.112	2.81	8.63	0.37	0.19

Table(1)

Array Transistor / Chip B

Ion: He
E = 4.4 MeV
Range = 15.0 μm

Angle	S	R_{in}	E_{in}	LET	LETsec θ	CC	E_{peak}	R_{peak}	s	d
45°	4.24	10.76	3.39	0.50	0.71	0.096	3.29	10.39	0.37	0.26
50°	4.67	10.33	3.28	0.51	0.80	0.107	3.17	9.91	0.42	0.27
55°	5.23	9.77	3.13	0.52	0.90	0.113	3.00	9.37	0.40	0.23
60°	6.00	9.00	2.92	0.53	1.10	0.135	2.79	8.55	0.45	0.23
65°	7.10	7.90	2.60	0.56	1.33	0.152	2.45	7.38	0.52	0.22
70°	8.77	6.23	2.10	0.60	1.75	0.179	1.92	5.67	0.56	0.19
75°	11.59	3.41	1.13	0.69	2.66	0.221	0.91	2.81	0.60	0.16

Table(2)

Array Transistor / Chip A

Ion: O
E = 20.0 MeV
Range = 10.0 μm

Angle	S	R_{in}	E_{in}	LET	LETsec θ	CC	E_{peak}	R_{peak}	s	d
0°	3.00	6.97	13.35	4.50	4.50	0.66	12.70	6.70	0.28	0.28
30°	3.46	6.51	12.28	4.50	5.20	0.73	11.54	6.20	0.31	0.27
45°	4.24	5.73	10.45	4.44	6.27	0.83	9.62	5.38	0.35	0.25
60°	6.00	3.97	6.43	4.13	8.26	1.03	5.41	3.50	0.47	0.24

Table(3)

After the particle arriving at an angle θ with respect to the normal traverses a pathlength S where:

$$S = D \sec \theta$$

through this overlying material, it arrives at the heterojunction with residual range R_{in} :

$$R_{in} = R_o - S$$

where R_o is the original range in μm . The energy the particle has at the heterojunction was obtained from Ziegler's Range-Energy Tables (8) and the values listed as column 4 in Tables 1 - 3. The value of the LET at the heterojunction was then obtained from Ziegler's Tables and listed in column 5 in the tables. According to these calculations, there was very little change in LET over the range of angles studied. Column 7 list the peak position (CC) in the measured charge collection spectrum (See Figs. 5a through 5d) for each angle of incidence.

The values of the peak position are plotted versus the values of the product LET sec θ in Fig. 8a for two different sets of test structures (A and B) exposed to 4.4 MeV alphas and in Fig. 8b for set A exposed to 20 MeV Oxygen. Since the calculated LET at the junction varies only slightly, with angle of incidence, the plots in Fig. 8 test the dependence of charge collection on the secant of the angle of incidence. The curves represents a best fit of the points

to a straight line. The fits to straight lines appear to be good. The alpha data on two different devices are in relatively good agreement. All three curves have similar slopes but the y-intercept is much higher for the heavy-ion data set. The heavy ion data set and the low-angle alpha data were obtained on the same device. The slopes for the two data sets are similar but the y-intercepts are quite different. The much higher y-intercept for the Oxygen data may be related to the much higher electronic noise observed on the circuit at the accelerator.

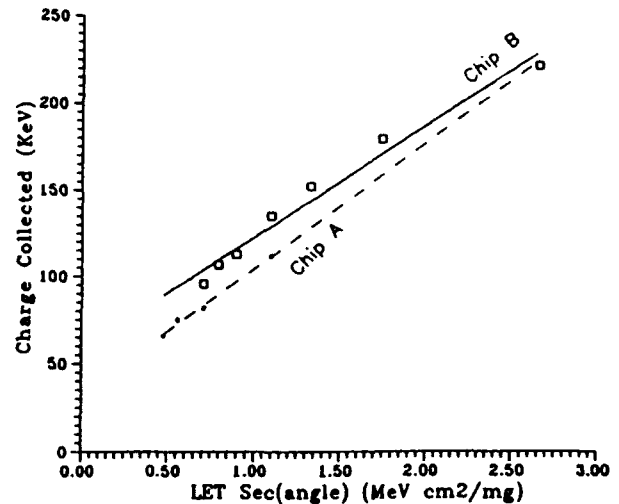


Fig. (8a)

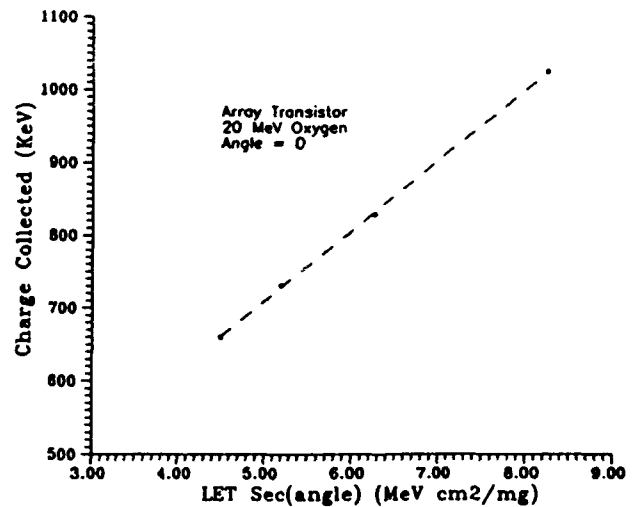


Fig. (8b)

To test the dependance on LET, we consider only the heavy-ion data and alpha data taken on the same device. In Fig. 9 the positions of the large low-energy peak in the charge collection spectra are plotted versus LET for the alpha and Oxygen data and compared to a "best fit" straight line to all the data. This plot is in strong agreement with the assumption of proportionality between the charge collected and the value of LET sec θ of the incident particle. However, this result is based on data obtained at only two values of LET and should eventually be con-

firmed with data over a wider range of LET values. The proportionality between charge collected at the junction and $LET \sec \theta$ is the basis for calculating SEU rates using the concept of sensitive volumes. It appears to hold true for bipolar circuits in GaAs but should also be tested on other technologies including those implemented in silicon.

Estimates of Thickness of Sensitive Volume

One value of the thickness of the sensitive volume can be obtained from the slope of the straight line in Fig. 9. The slope of a plot of measured peak energy (CC) in MeV versus the LET in MeV/mg/cm² is the product of the thickness of the sensitive volume t and the density ρ . Therefore,

$$t = (1/\rho) \text{SLOPE}$$

The value obtained from Fig. 9 is 0.25 μm .

The value of the thickness determined this way relies somewhat on the accuracy of our estimates of the thickness of the passivation layers, the calibration of our pulse-height measuring system, as well as the accuracy of Ziegler's Tables. Some feeling for the consistency, if not the reliability, of this approach can be obtained by estimating the value of the thickness from the individual data points as shown below.

The energy the particle has leaving the sensitive volume is then

$$E_{\text{out}} = E_{\text{in}} - CC$$

The values obtained for each angle of incidence and the corresponding range from Ziegler's Tables, R_{out} , are listed in Columns 8 and 9 in Tables 1 and 2. The path length through the SV is then

$$s = R_{\text{in}} - R_{\text{out}}$$

Finally, the thickness of the SV is given by

$$d = s \cos \theta$$

the values obtained for which are given in Column 11. The thickness estimates obtained this way are, again, grouped around 0.25 μm .

SUMMARY AND CONCLUSIONS

The position of the peak in the charge-collection pulse-height spectra measured during irradiation with 4.4 MeV alphas and 20 MeV Oxygen ions was found to vary linearly with the secant of the angle of incidence. Moreover, the data appears to be consistent with the charge collection being proportional to the value of $LET \sec \theta$ the particle has arriving at the level of the SEU-sensitive junction. There-

fore, for HI^2L technology at least, changes of $\sec \theta$ produce roughly the same change in the charge collected as an equivalent change in LET at least up to angles of 70°. This is an important confirmation in light of current practices in determining SEU thresholds where the angle of incidence is changed more often than the LET. If this assumption did not hold for HI^2L technology where the sensitive volume is a thin large area disk, one could certainly not apply it with confidence to CMOS where the sensitive volumes are typically more compact. The implied proportionality of charge collection with LET provides considerable support for the common assumption in SEU rate calculations of a sensitive volume with dimensions independent of the LET of the incident particle.

A procedure is described for determining the thickness of the sensitive volume from charge collection measurements at different values of LET. The value obtained for HI^2L implemented by MOCVD was 0.25 μm which is thicker than the 0.11 μm measured earlier for transistors implemented by MBE. Both data sets need to be repeated before one can conclude that less than half the charge is collected at the MBE heterojunction than at one implemented with MOCVD. Differences would presumably be due to the very different doping level profiles obtained with the two techniques. Since a thinner sensitive volume results from less charge collection for the same ion traversal, these results suggest that MBE may have a significant advantage over MOCVD in SEU hardening if the critical charge for upset remains the same.

REFERENCES

- 1 J.F. Salzman, P.J. McNulty, and A.R. Knudson, "Intrinsic SEU Reduction From Use of Heterojunctions in GaAs Bipolar Circuits" IEEE Trans. Nucl. Sci. *NS* - 34, 1676-1679 (1987).
- 2 P.J. McNulty, M.H. Yaktieen, J.E. Lynch, W.M. Weber, H.T. Yuan, and J.F. Salzman, "Charge Collection in HI^2L Bipolar Transistors" IEEE Trans. Nucl. Sci. *NS* - 35, 1613-1618 (1988).
- 3 J. Pickel and J.T. Blandford, Jr., "Cosmic Ray Induced Errors in MOS Devices" IEEE Trans. Nucl. Sci., *NS* - 27, 1006-1015 (1980).
- 4 J.H. Adams Jr. IEEE Trans. Nucl. Sci. *NS* - 30, 4475 (1983).
- 5 P. Shapiro, Naval Research Laboratory Memorandum Report 5901 (1986).

APPENDIX L

PROTON-INDUCED SPALLATION REACTIONS

PROTON INDUCED SPALLATION REACTIONS

PETER J. McNULTY, WAGIH G. ABDEL-KADER and GARY E. FARRELL

Department of Physics and Astronomy, Clemson University, Clemson, SC 29634-1911, U.S.A.

Abstract—Proton-induced upsets are becoming an important problem for modern digital electronics used on satellites that traverse the inner radiation belts. The mechanism for this single event phenomenon is the proton-induced spallation reaction. Computer simulations are used to illustrate the kinematics of the spallation reaction and the resulting energy deposition in microvolumes which have dimensions typical of the elements comprising modern devices.

INTRODUCTION

Protons have been shown to be a leading cause of single-event upsets (SEU) in satellites whose orbits intersect the inner radiation belts (Goka *et al.*, 1991; Dyer *et al.*, 1991; Campbell, 1991). Many of the protons trapped in the belts by the earth's magnetic field have sufficient energy to penetrate the satellite's shielding and arrive at the electronic components with more than enough energy to induce SEUs. Goka *et al.* (1991) have recently observed proton-induced single event latchup (SEL) in space, and it has been observed subsequently in a variety of commercial devices on the ground (Adams *et al.*, 1992; D. Nichols and D. R. Roth, private communication).

The relative importance of proton-induced SEUs versus those induced by cosmic rays depends on the satellite's orbit as well as the sensitivity of the devices. This has been demonstrated by the SEU and SEL studies which flew as part of the Microelectronics Package experiment on the CRRES satellite. The CRRES satellite flew an elliptical orbit inclined at 18.2° with a perigee of 348 km and an apogee of 33,582 km. Therefore perigee was below the inner belts and apogee was above geosynchronous altitudes. This orbit is similar to the transfer orbits used to lift satellites to geosynchronous orbits, and requires 9.87 h for completion. A number of digital electronic components in the Microelectronics Package experiment were monitored for SEU and SEL events. The SEUs observed in relatively sensitive parts during the short time in which the spacecraft traversed the proton belts far exceeded the event rate in deep space where the cosmic rays were more plentiful, and the spacecraft spent most of its time. In the deep space portion of the orbit, the cosmic rays were the dominant source of SEUs for all parts. Preliminary analysis of a few carefully characterized devices shows the relatively high proton event rates are consistent with the NASA models of the environment and the standard models for calculating upset rates (McNulty *et al.*, 1991c).

Single event upsets

The experimental configuration used to measure single event upsets (SEU) is shown in Fig. 1. Characterizing a part fully in terms of its SEU sensitivity requires both proton and heavy ion testing. When the measurements are made with energetic protons, no vacuum is required, and the incident energy can be varied quickly with degraders. This makes proton testing much faster than heavy-ion testing particularly in terms of beam time. Proton SEU testing can, therefore, be the least expensive of the SEU tests needed to fully characterize a part. Moreover, the results of proton measurements, properly interpreted, can be used to predict the heavy-ion sensitivity of a device, thereby considerably reducing the need for heavy-ion beam time. Figure 2 plots the measured SEU cross section versus incident proton energy for two well known devices which were included in the Microelectronics Package Experiment on the CRRES satellite. A third device, the CMOS 6504RH did not upset in our tests which included proton energies up to 800 MeV. Figure 2 shows that the three devices have completely different dependencies on incident proton energy, and any model of the proton-induced SEUs must explain these differences as well as predict the SEU rates in space. The shapes of the curves in Fig. 2 reflect differences in the SEU parameters of the devices and, consequently, proton measurements can provide valuable information regarding the values of the SEU parameters to be used for different devices.

This paper discusses the mechanism for the most common single-event phenomena, the SEU. It discusses how protons can generate the large energies needed to upset devices through the spallation reaction. A simulation model, the CUPID (Clemson University Interactions In Devices) code, is used to illustrate the kinematics of the spallation reactions, to predict the reaction products, and to demonstrate how the probability of upsetting a circuit element depends on the dimensions of the sensitive volume associated with each element. This code has been

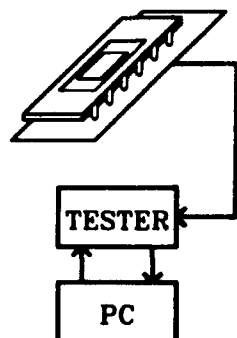


Fig. 1. Experimental configuration used to measure SEUs.

tested in the sense that it has successfully predicted proton-induced SEU rates from heavy-ion data (Bisgrove *et al.*, 1986), and it has accurately predicted the charge collection spectrum in a SRAM memory device (McNulty, 1990; McNulty *et al.*, 1991b).

First order model of SEU

Single event phenomena do not occur in commercial electronics in the absence of high LET (linear energy transfer) particles. This implies that there is a threshold amount of charge which must be generated locally in order to induce an event. The First Order Model (McNulty, 1990) assumes that this charge must be generated within the dimensions of a sensitive volume associated with that SEU-sensitive circuit element. The sensitive volume is a mathematical artifice used to simplify calculations and does not necessarily correspond to a structural entity on the device. The dimensions are chosen so that the charge generated within the sensitive volume equals the charge collected at the SEU-sensitive junction. Typically, the area can be taken from the plateau value of the SEU cross section measured with heavy ions at high values of the LET. In circuits with only one SEU-sensitive junction per cell, this area typically agrees with the lateral dimensions of the sensitive junction. The thickness can be estimated by simple modeling (McNulty *et al.*, 1991a) if the details of the device manufacture are known or using charge collection techniques if they are not known (McNulty *et al.*, 1991b). It will be shown below that predictions of proton SEU cross sections are consistent with the First Order Model and are very sensitive to the thickness of the sensitive volume.

SPALLATION REACTION SIMULATIONS

In modeling spallation reactions, the target nucleus is viewed as two non-interacting Fermi gases (neutrons and protons) in a potential well. The proton-induced spallation reaction with a target nucleus of mass number A is modeled as occurring in two stages. In the first, the cascade stage, the incident proton enters the nucleus, a sphere of radius $1.3 A^{1/3}$ fm, collides with another nucleon and these in turn strike others. This sets up a cascade within the nucleus

which ends with some nucleons being ejected from the nucleus, which is left in an excited state. This stage is over within $\sim 10^{-20}$ s. In the second or evaporation stage, the nucleus is modeled as a Fermi gas of neutrons and protons confined in a potential well with some excitation energy. The excitation energy is shared by the nucleons in the well, and the system can be characterized by a nuclear temperature. Occasionally, a nucleon near the edge and moving in the right direction will have enough energy to escape from the potential well. The two stages of the spallation reaction are represented schematically in Fig. 3. Both stages are completed within $\sim 10^{-6}$ s, long before the recoil has moved an appreciable distance, and as a result, the momentum of the recoiling nuclear fragment has contributions from both stages. The details of simulating spallation reactions are different for different Monte-Carlo codes. What follows is based on the CUPID (Clemson University Proton Interactions in Devices) codes developed in this laboratory (McNulty *et al.*, 1981).

Cascade stage

In passing through the nucleus, the proton may or may not collide with another nucleon. Metropolis *et al.* (1958) devised empirical relations for n-p cross sections. From these, an average cross section can be calculated as $\sigma_{av} = [(A - Z)\sigma_n + Z\sigma_p]/A$, where σ_n and σ_p are the cross sections of the incident particle with the neutrons and protons, respectively. The proton's mean free path in nuclear matter is then $\lambda = 1/(\rho\sigma_{av})$ where ρ is the density of nucleons within the nucleus.

When the incident proton enters the nucleus, a path length is randomly assigned as $\lambda \ln(1/p_n)$, where p_n is a random number. If the chosen path length, measured from the point of impact at the nuclear surface, carries the proton beyond the boundaries of the nucleus, there is a collision. Upon entering the nucleus, the particle picks up the nuclear potential in addition to its kinetic energy. The nuclear potential

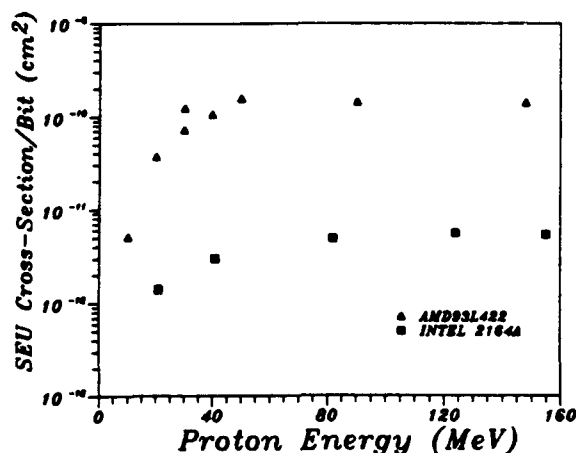


Fig. 2. Measured SEU cross sections versus incident proton energy for the AMD 93L422, the Intel 2164A.

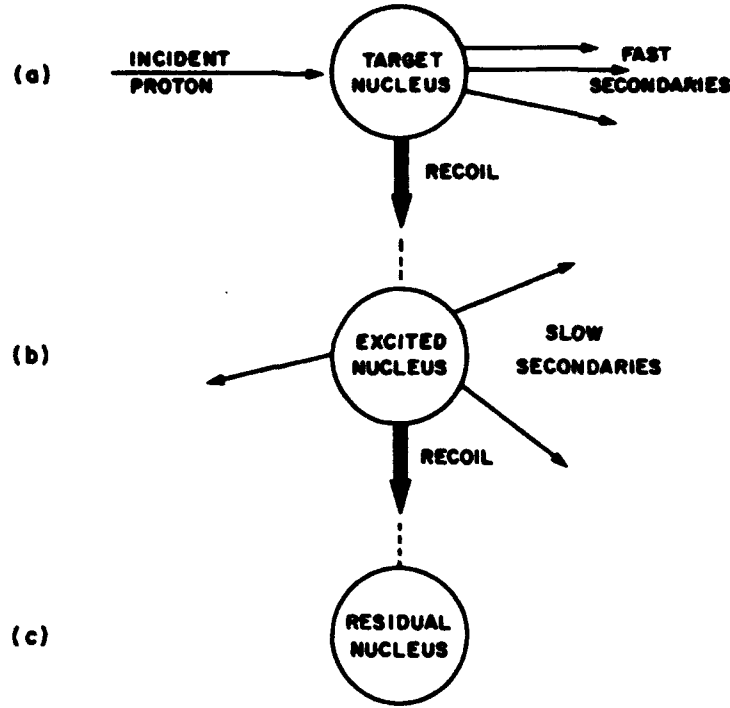


Fig. 3. Three stages of a spallation reaction. (a) The cascade stage involving collisions between nucleons and later (b) the evaporation stage in which secondaries are isotropically emitted and (c) the recoil of the residual nuclear fragment.

is taken to be the sum of the Fermi energy and the binding energy. This potential is the depth of the well confining the nucleons, and the target nucleons have all energies up to the Fermi energy subject to the Pauli exclusion principle.

The kinematics of the collision are handled relativistically. Neutrons and protons are treated as having equal masses. The components of the momentum of the incident particle are already known. To obtain the momentum of the target nucleon, the momentum distribution is assumed to be a sphere in momentum space with a radius equal to the Fermi momentum, $P_F = (\hbar/2\pi)(3\pi^2 N/V)^{1/3}$, where V is the nuclear volume and N is the number of neutrons or protons. Three random numbers within this sphere are chosen for the momentum coordinates of the target nucleon. The momenta of the incident and target nucleons are transformed to the center of momentum frame. The distribution of scattering angles is given by:

$$d\sigma/d\Omega = K[A \cos^4 \theta + B \cos^2 \theta + 1]$$

where A and B depend on the relative velocity and the identity of the nucleons (McNulty *et al.*, 1981). The value of θ is chosen from this distribution by random number generator and the momenta of the scattered particles calculated and transformed back to the laboratory frame. If either of these is less than the Fermi momentum, the collision is forbidden by the Exclusion Principle. If the collision is permitted, path lengths are chosen for both particles and the

procedure is repeated for each until all nucleons leave the nucleus.

Whenever a nucleon leaves the nucleus, the nuclear potential is subtracted from the nucleon's energy. When the energy of a nucleon falls below the sum of the nuclear potential and the Coulomb barrier for a proton, the cascade stage is terminated for that nucleon. Particles with less than this cutoff energy will undergo many potential collisions before the Exclusion Principle allows an emission to occur. A transition is made in the model to the evaporation stage where further particle emission is handled statistically.

Evaporation stage

At the end of the cascade stage, the residual nucleus has an excitation energy:

$$U = T_0 - \sum_{i=1}^{i=N} T_i - (N-1)B - T_N \quad (1)$$

where T_0 is the energy of the incident proton, T_i is the kinetic energy of cascade particle i , N is the number of cascade particles, B is the binding energy of a nucleon and T_N is the kinetic energy of the residual nucleus. The evaporation calculation closely follows the model of Dostrovsky *et al.* (1959). The relative probabilities for neutron and charged particle emission are given in equations (2) and (3):

$$\begin{aligned} \Gamma_n &= (2\pi m r_0^2 A_n^{2/3} g_n \alpha / a_n^2 \hbar^2) \exp\{2(a_n R_n)^{1/2} \\ &\quad - 2[a_n(U - \delta_n)]^{1/2}\} \\ &\quad \times \{2a_n R_n - (3/2 - a_n B)[2(a_n R_n)^{1/2} - 1]\} \end{aligned} \quad (2)$$

$$\Gamma_j = (2\pi m r_0^2 A_j^{2/3} g_j [1 + C_j]) / (a^2 h^2) \exp\{2(a, R_j)^{1/2} - 2[a_0(U - \delta_0)]^{1/2}\} \times \{2a, R_j - (3/2)[2(a, R_j)^{1/2} - 1]\} \quad (3)$$

where m represents the mass of the emitted particle; Γ_n and Γ_j denote the relative probabilities neutron and charged particle emission, respectively; the subscripts 0 represents the original nucleus, and n or j represents the residual nucleus; g represents the number of spin states of the particle; $\beta = (2.12A^{-2/3} - 0.05)/\alpha$; $\alpha = 0.76 + 2.2A^{-1/3}$; δ is the pairing energy for that isotope; the value $A/8$ was used for a , the level density parameter; $r_0 = 1.3A^{1/3}$ fm is the radius of the target nucleus; the C_j are constants chosen to fit the inverse nuclear cross sections; R is the kinematic upper limit to the energy available for emission, i.e. the excitation energy minus the separation energy, the pairing energy, and in the case of charge particles, the energy needed to overcome the Coulomb barrier. Equation (3) was calculated for protons, deuterons, tritons, He^3 and α 's. The identity of the evaporated particle is chosen by random number weighted by the relative probabilities calculated from equations (2) and (3). The kinetic energy ϵ is chosen for each evaporation emission by random number from the distribution (Dostrovsky *et al.*, 1959):

$$P_n(\epsilon) d\epsilon = \{[8\pi^2 g_n m r_0^2 A_n^{2/3} \epsilon \alpha (1 + \beta/\epsilon)] / h^3\} \times \exp\{2[a_n(R_n - \epsilon)]^{1/2} - 2[a_0(U - \delta_0)]^{1/2}\} d\epsilon. \quad (4)$$

The evaporation particles are assumed to be emitted isotropically in the frame of the nucleus. Two more random number choices determine the angle of emission.

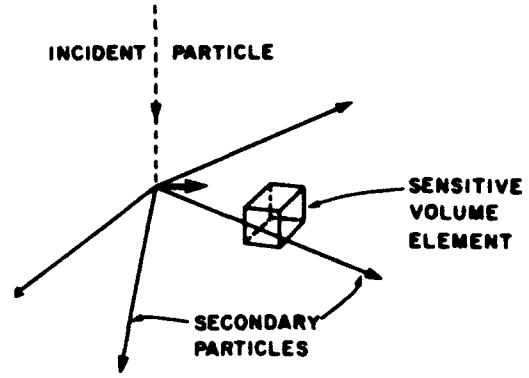


Fig. 4. Spallation reaction with some secondary particles traversing the sensitive volume.

The excitation energy eventually falls to a level (≈ 10 MeV) which is too low for additional particle emission. Further deexcitation would occur by γ emission which is not considered in the computer codes. The direction and energy of the residual nucleus is found from momentum conservation. The ranges of the cascade particles, the evaporation particles, and the residual nucleus are found from range-energy tables.

Energy deposited in the sensitive volume

In CUPID, two nested volumes are specified by the user, a large outer volume and a small inner volume. The latter is the sensitive volume. The spallation reaction is assumed to occur anywhere within the outer volume including inside the sensitive volume. The trajectories of the primary and each of the charged secondaries, including the recoil, are monitored to determine which enter the sensitive volume,

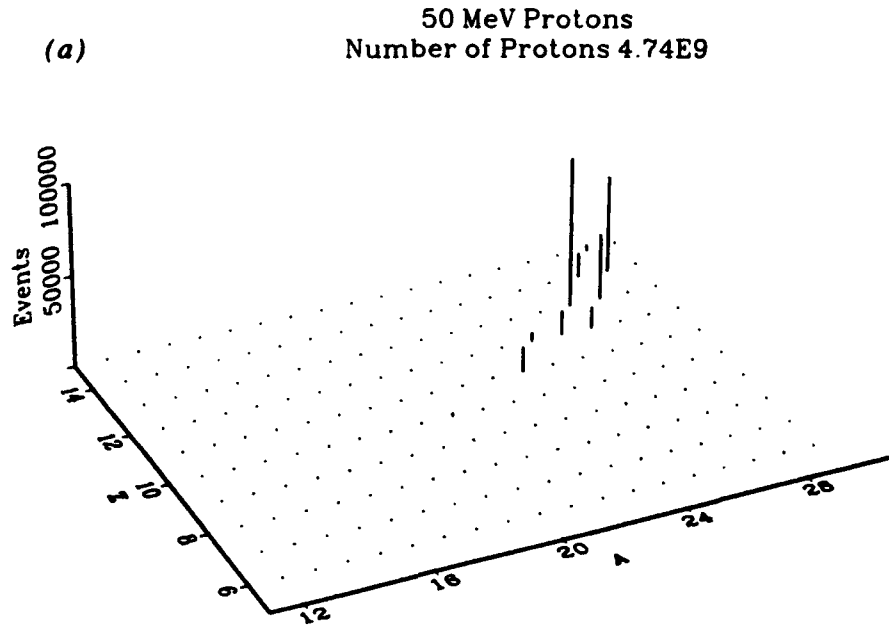


Fig. 5(a).

(b) 100 MeV Protons
Number of Protons 4.74E9

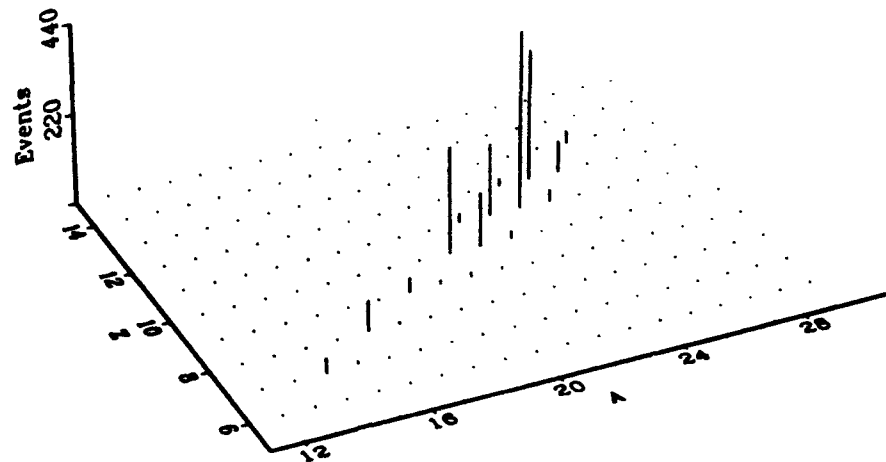


Fig. 5(b).

(c) 150 MeV Protons
Number of Protons 4.74E9

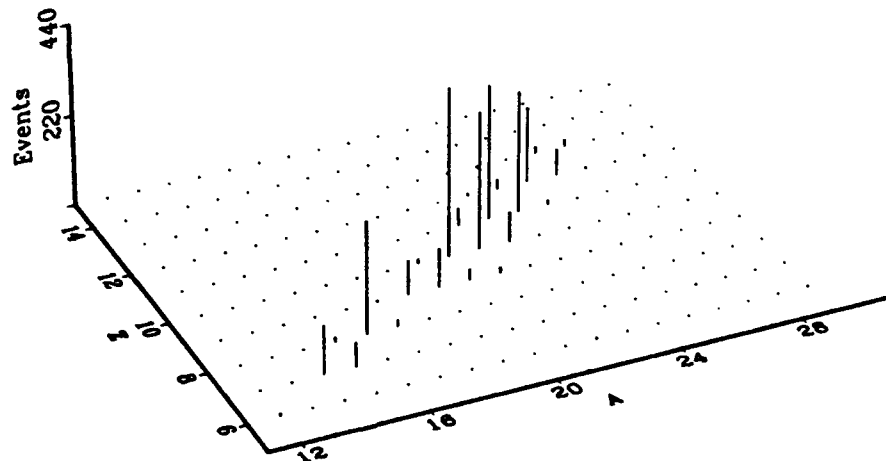


Fig. 5(c).

and if they do, where they exit or stop within the sensitive volume. This is shown schematically in Fig. 4. The energy deposited within the sensitive volume is then calculated for each of the secondaries, and the total energy deposited determined. For sensitive volumes with dimensions typical of microelectronics, 90% of the energy is deposited by the nuclear recoil. Therefore, the outer volume does not need to extend beyond the sensitive volume in any direction greater than the range of a nuclear recoil. This approximation saves considerable computer time.

RESULTS OF THE SIMULATIONS

Residual nuclear fragment

Since typically 90% of the energy deposited in a volume element having dimensions typical of microelectronics is deposited by the recoiling residual nuclear fragment, it is important to consider the nature and kinematics of these fragments. Figure 5 shows the isotopes emerging from spallation reactions between silicon target nuclei and protons incident at 50, 100 and 150 MeV. The calculations were carried out

for the same number of incident protons. The number of events increases sharply with increasing energy between 50 MeV and 100 MeV, and it continues to increase to 150 MeV. The degree of fragmentation increases with energy also with significant amounts of ^{16}O being generated above 100 MeV.

According to the First Order Model, SEUs are caused by the highest energy depositions. The fluences used to generate Fig. 5(a-c) typically would generate on the order of 100 events in a modern

commercial device. Figure 5(d-f) are the recoil spectra for the events which resulted in the 200 highest energy depositions. There is surprise agreement between the relative abundances of the fragments emerging from the SEU events and the entire set of nuclear recoils. The differential energy spectrum of the recoiling nuclear fragments are shown for the three incident energies in Fig. 6. The fluences are much higher than for the spectra in Fig. 5 in order to have reasonable statistics in the region of energy

(d) 50 MeV Protons
6 MeV Energy Deposited or More

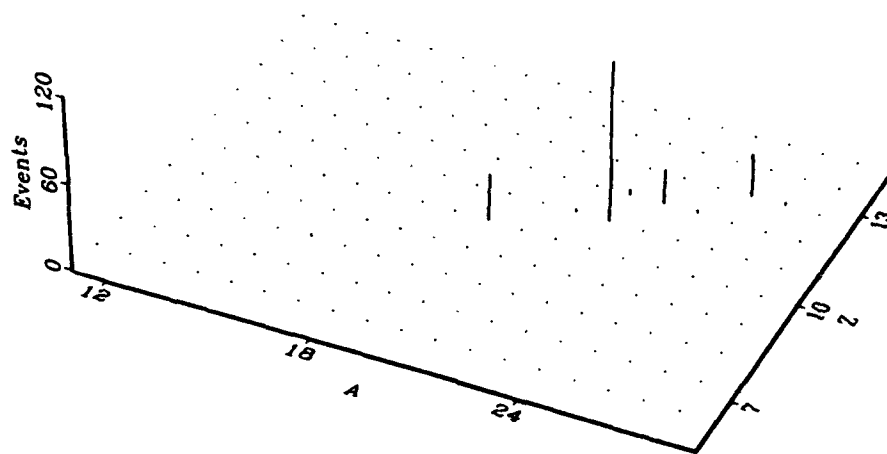


Fig. 5(d).

(e) 100 MeV Protons
9 MeV Energy Deposited or More

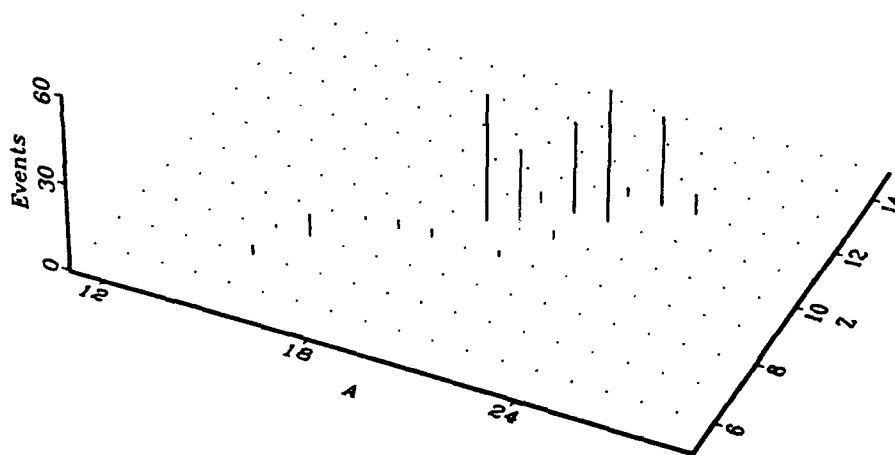


Fig. 5(e).

150 MeV Protons
(f) 11 MeV Energy Deposited or More

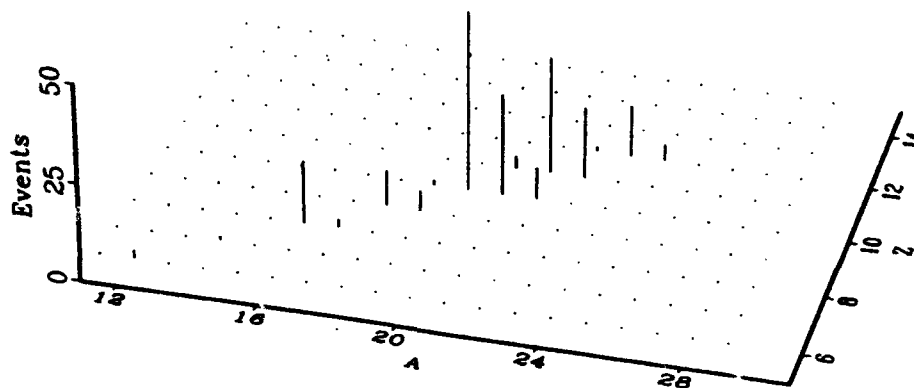


Fig. 5(f).

Fig. 5. Relative isotropic abundances of the recoiling residual nuclear fragments following spallation reactions between target silicon nuclei and protons incident at (a) 50 MeV, (b) 100 MeV, (c) 150 MeV. The relative isotopic abundances for the same reactions but restricted to the highest 200 or so events: (d) 50 MeV incident energy and more than 6 MeV deposited; (e) 100 and 9 MeV; (f) 150 and 11 MeV.

depositions likely to cause upsets. At low incident energies, the spectrum is very narrow and restricted to low energies. By 100 MeV, the energy spectrum is much broader, and some rare fragments recoil with more than half the incident energy. The tendency of the nuclear fragments to recoil with larger fractions of the incident energy increases up to at least 150 MeV.

Energy deposited in the sensitive volume

The possibility of an upset depends on whether at least some critical amount of energy is deposited (charge generated) within the sensitive volume. Obviously, the amount deposited depends on the dimensions of the sensitive volume as well as the kinetic energy of the incident proton. For the small structures being considered, the probability of a spallation reaction within the sensitive volume is proportional to the volume, but energy can also be deposited within the volume by charged secondaries from spallation reactions initiated outside the sensitive volume. The dimensions of the sensitive volume also determine what fraction of the energy carried by the emerging charged secondaries will be deposited within it. The energy deposited is a complicated function of the dimensions and the relative orientation of the trajectory. This will be illustrated by some simple calculations. In all these calculations, the proton is assumed to be incident parallel to the thickness or third dimension of the sensitive volume.

Figure 7 illustrates how the energy deposited depends on the lateral dimensions of the sensitive

volume. The curves are plots of the integral cross sections, i.e. the cross section for depositing at least some energy E_d plotted versus E_d . This form is used because the First Order Model assumes that an upset occurs whenever more than some critical or threshold amount of energy is deposited within the sensitive volume. If the threshold energy deposition required for an upset (the critical charge in energy units) is found on the abscissa, the predicted SEU cross section is the coordinate obtained off the ordinate axis. Integral cross section plots are shown for four sensitive volumes all having the same thickness. The spectra are obviously not exactly parallel, but the cross section does scale at least roughly with the cross sectional area. The shape of the cross section of the sensitive volume does not appear to be important in these calculations, as is illustrated in Fig. 8. The cross sectional area and the thickness are the same for all calculations in Fig. 8, but the arrangements of the lateral dimensions are different. The data points all lie on one curve suggesting that the cross sectional area is important but the shape of that area is less so.

The dependence on thickness is more complicated. This is illustrated in Fig. 9 where the integral spectra are plotted for sensitive volumes having the same cross sectional area but different values of the thickness. It is clear that these curves do not scale with the thickness in any simple manner. Mistakes in what value to use for the thickness would obviously seriously impact SEU rate calculations.

The probability of an upset also depends upon the orientation of the incident particle's trajectory. This

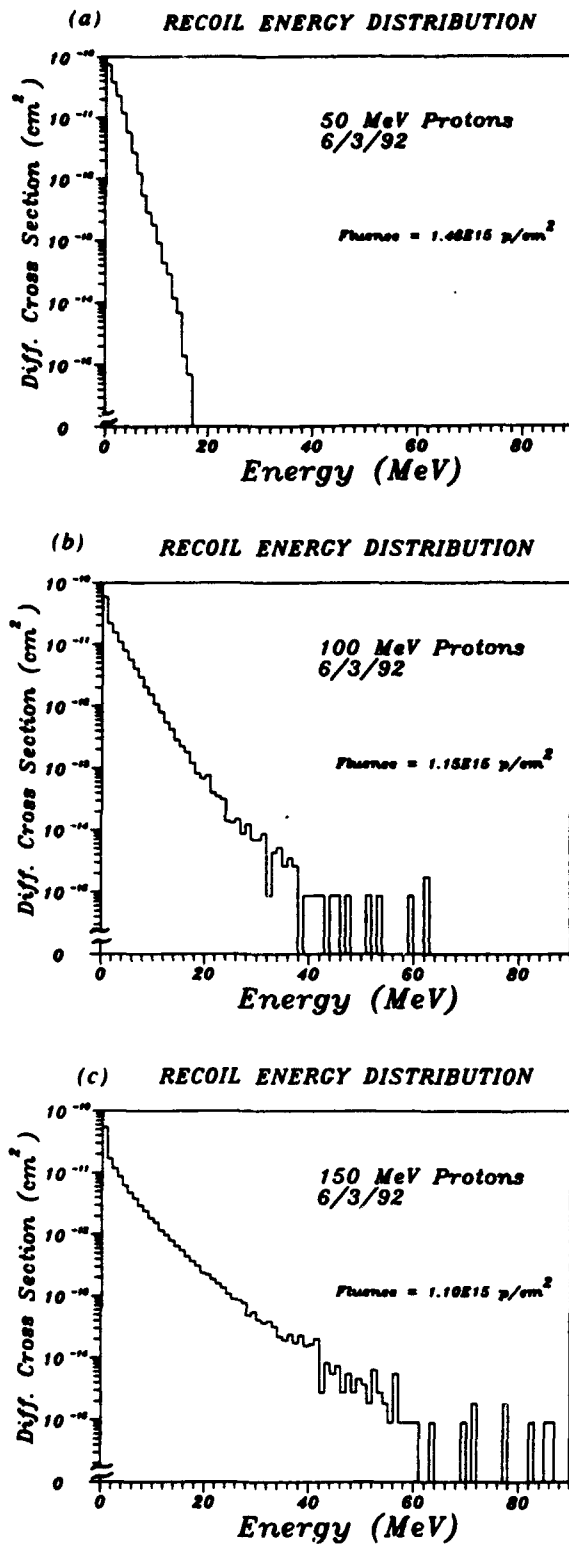


Fig. 6. Differential energy spectra of recoiling nuclear fragments following spallation reactions between target silicon nuclei and protons incident at (a) 50 MeV, (b) 100 MeV, (c) 150 MeV.

can be seen from the comparison in Fig. 10 of the integral cross section spectra obtained for 63 MeV protons incident in two mutually perpendicular direc-

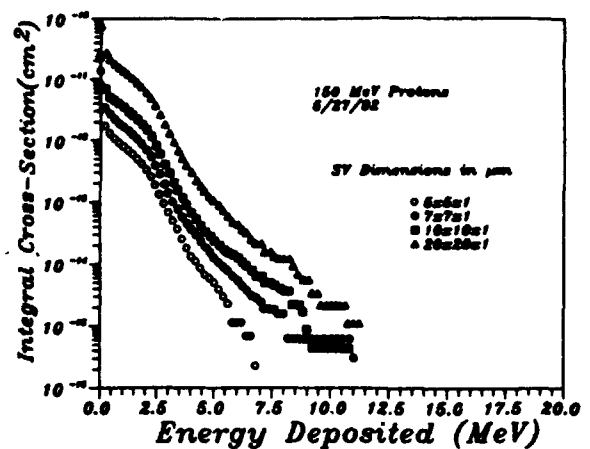


Fig. 7. Integral cross sections for depositing energy $> E_d$ versus E_d for four sensitive volumes having the same thickness, $1 \mu\text{m}$. The beam is incident parallel to the third dimension, the thickness with a kinetic energy of 150 MeV.

tions. In one case, the protons are incident parallel to the short dimension, and in the other case, parallel to the long dimension. The cross sections are dramatically different. This is a direct result of the angular distribution of the recoiling residual nuclear fragments. They have a tendency at this energy to be oriented in the forward direction. This is illustrated in Fig. 11 which shows the angular distribution of the recoiling fragments for protons incident at the same energy. Fragments recoiling in the forward direction deposit more energy when that direction is parallel to one of the long axes of the sensitive volume. Asymmetric sensitive volumes should in general exhibit significant differences between SEU cross sections measured parallel to and perpendicular to the short dimension of the sensitive volume. Testing should be carried out in a worst case situation, i.e. with the beam protons incident parallel to the longest axis of the sensitive volume.

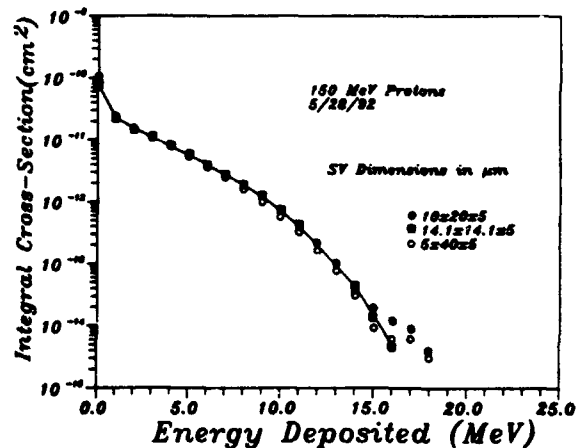


Fig. 8. Integral cross section for depositing $> E_d$ versus E_d for four sensitive volumes having the same thickness and cross sectional area but different shapes. The protons are incident in 150 MeV.

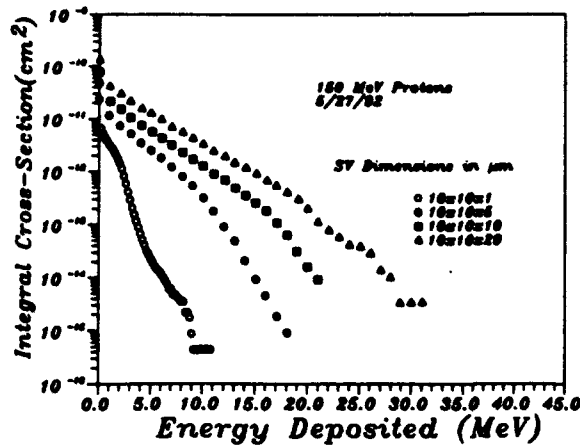


Fig. 9. Integral cross section for depositing energy $> E_d$ for sensitive volumes with $100 \mu\text{m}^2$ cross sectional area and different thicknesses. The protons are incident at 150 MeV.

It is not practical to test every detail of a simulation program, but there is limited data on energy deposition in thin silicon detectors (McNulty *et al.*, 1981) and in the sensitive volumes of NMOS SRAMs (McNulty *et al.*, 1991a). The fits between CUPID and the experimental data were all quite good. For example, the comparison between the simulated energy deposition cross section and the charge collection spectrum measured off the power lines of an NMOS SRAM is shown in Fig. 12. The fits described in McNulty *et al.* (1981, 1991b) and illustrated in Fig. 12 give some confidence, not only in CUPID's description of the details of the energy deposition process described above, but in the possibility of using cupid to determine the SEU parameters from proton measurements in the manner discussed in the next section.

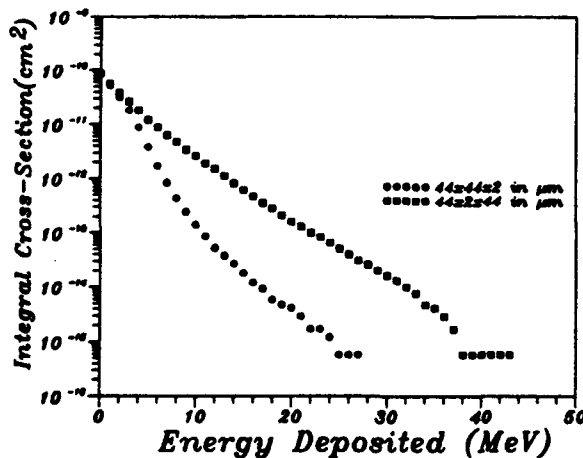


Fig. 10. Integral cross section for depositing $> E_d$ versus E_d for protons incident on the identical volume at different orientations. The beam particles enter the sensitive volume parallel to the third dimension. The beam particles are incident at 148 MeV and are uniformly distributed.

RECOIL ANGULAR DISTRIBUTION

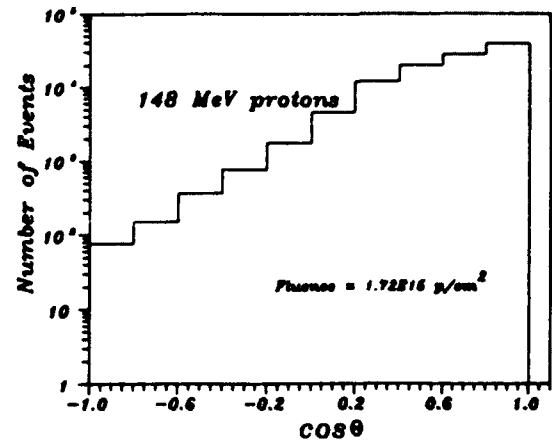


Fig. 11. Angular distribution of the recoiling nuclear fragments following proton-induced spallation reactions between 148 MeV protons and silicon nuclei at rest.

PROTON DETERMINATION OF SEU PARAMETERS

The SEU parameters which must be specified when using the standard algorithms for determining the SEU rates in space (e.g. CREME and CUPID) are the dimensions of the sensitive volume and the critical charge. The critical charge is traditionally given in units of energy deposition with the conversion being 3.6 eV per electronic electron-hole pair generated. Each pair is assumed to result in one electronic charge being collected across the junction. Simulations show that the proton cross sections are very sensitive to the dimensions of the sensitive volume, particularly the thickness. The lateral dimensions are typically the dimensions of the SEU-sensitive junction which can be obtained from the masks used to manufacture the devices or estimated from inspection of the devices by optical or electron microscopy. The thickness can be obtained from charge collection measurements carried out with heavy ions (McNulty, 1990; McNulty *et al.*, 1991b) or modeling (McNulty *et al.*,

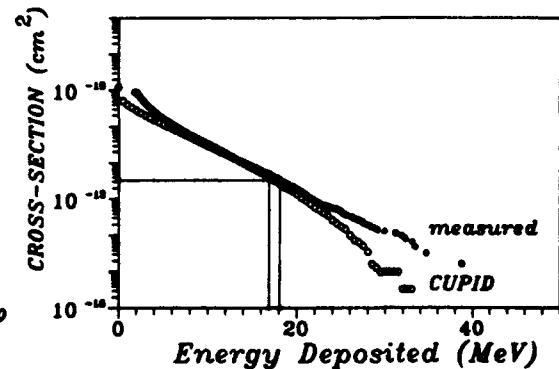


Fig. 12. Comparison between the charge collection in spectrum measured between the power lines of an NMOS SRAM and the predictions of the CUPID simulation code (McNulty *et al.*, 1991a).

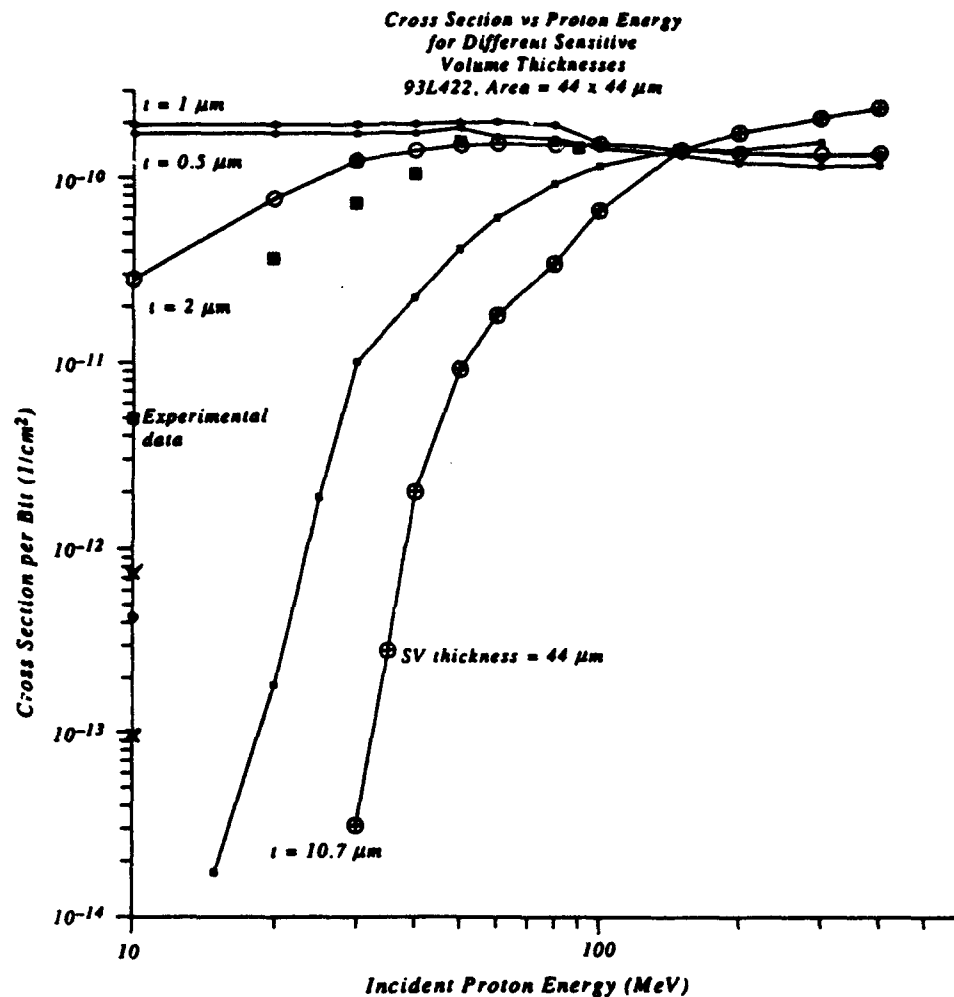


Fig. 13. SEU cross section versus incident proton energy. The experimental data are from Shimano *et al.* (1989) and Nichols and Price (1982).

1991a). Alternatively, both the thickness of the sensitive volume and the value of the critical charge can be obtained from SEU measurements carried out with protons at different incident energies and angles. This latter approach is illustrated by application to the 93L422, a bipolar RAM. The approach will be detailed in (McNulty *et al.*, 1993).

Thickness of the sensitive volume

The integral energy-deposition spectra were generated for sensitive volumes having the lateral dimensions of the sensitive volume with different thicknesses. The results were similar to those given for 100 μm^2 in Fig. 9. The value of the measured SEU cross section at 148 MeV was located on the ordinate and drawn as a horizontal line. The abscissa values corresponding to where the line intersects each of the curves should be the value of the critical charge in energy units for that value of the thickness. The value of the critical charge and the dimensions of the sensitive volume are independent of the species and

the energy of the particle depositing the energy if, and only if, the dimensions chosen for the sensitive volume are correct. The SEU cross sections generated by CUPID are plotted in Fig. 13 versus the incident proton energy using the value of the critical charge determined at 148 MeV for each assumed thickness. The shapes of the curves have a strong dependence on thickness, and the measured proton SEU cross sections for the 93L422 fit closer to the 2 μm curve than to the others. This agrees with the manufacturer's information that the device is made with a 2 μm epilayer. A more rigorous comparison would involve changes of angle of incidence as well as the energy of the incident particle. Obviously, only a sensitive volume with a thickness between 2 and 5 μm would fit the measured 93L422 cross sections showed in Fig. 13 with the same value of the critical charge at all energies. The value of the critical charge determined from the proton data is consistent with the value estimated from the heavy-ion tests on this same part assuming a similar thickness.

Table 1.

Device		Critical charge (MeV)	
Company	Part number	Heavy ion	Proton
IDT	6116V	21 (+4/-7)	19 (± 1)
Intel	2164A	3.3 (± 8)	3.5 (± 0.2)
Honeywell	HC6116RH	13 (± 2)	16 (± 1)
Texas inst.	HC5517A	8.5 (± 1.6)	9.8 (± 0.5)
AMD	93L422	1.1 (± 0.3)	1.2 (± 0.2)

Critical charge

An independent check of the cross sectional area of the SEU-sensitive junction can usually be obtained quickly and inexpensively from charge collection measurements with a calibrated α source (McNulty, 1990; McNulty *et al.*, 1991b). Simulations using the correct dimensions of the sensitive volume will then yield unambiguous values of the critical charge. The location of the SEU threshold on an integrated energy-deposition curve, such as those in Figs 7-10, has as coordinates the measured SEU cross section on the ordinate and the value of the critical charge on the abscissa. Given the simulated curve and the critical charge, the predicted SEU curve can be obtained from the ordinate. Alternatively, given the measured SEU cross section, the prediction for the critical charge can be obtained from the abscissa.

Table 1 compares values of the critical charge determined for five devices using protons with the values determined using traditional heavy ions. In both cases, the uncertainties in the values determined with protons were comparable or less than the uncertainties in the heavy-ion determinations.

CONCLUSIONS

Proton SEU cross sections are functions of the dimensions of the sensitive volume and the value of the critical charge. Simulations using CUPID show that predictions of the dependence of the proton SEU cross section on incident energy or angle of incidence change dramatically with the assumed value of the smallest dimension of the sensitive volume usually the thickness. The thickness appears to determine the shape of the dependence while the correct cross sectional area is required for predicting the total number of events, but the correct shape of that area is not required. The dependence of the SEU cross section on the angle of incidence also depends on the relative dimensions. Because of this sensitivity to the area, thickness and angle of incidence, experimental SEU measurements with protons can be used in conjunction with simulation programs such as CUPID to estimate the proper dimensions to be used in SEU-rate calculations. Given the proper set of dimensions, a single SEU measurement at any energy determines the correct value of the critical charge to be used. The accuracy of this value is limited by the

accuracy of the simulations and one measured cross section rather than the resolution of a series of data points. Hence, proton determination of SEU parameters should involve less accelerator beam time than comparable determinations with heavy ions.

Acknowledgements—This work was partially supported by the Defense Nuclear Agency under Contract No. DNA0011-88-C-0189-P00003. Discussions with and help from W. J. Beauvais and D. R. Roth from Clemson and L. Adams from ESA/ESTEC were helpful and are gratefully acknowledged.

REFERENCES

- Adams L., Daly E. J., Harbre-Sorensen R., Nickson R., Haines J., Schafer W., Conrad M., Greich H., Merkel J., Schwall T. and Henneck R. (1992) A verified proton induced latch-up in space. *IEEE Trans. Nucl. Sci.* NS-39, 1804.
- Biggrove J., Lynch J. E., McNulty P. J., Abdel-Kader W. G., Kleitnieks V. and Kolasinski W. A. (1986) Comparison of soft errors induced by heavy ions and protons. *IEEE Trans. Nucl. Sci.* NS-33, 1571.
- Campbell A. B. (1991) SEU flight data from the CRRES MEP. *IEEE Trans. Nucl. Sci.* NS-38, 1647-1654.
- Dostrovsky I., Fraenkel Z. and Friedlander G. (1959) *Phys. Rev.* 106, 683.
- Dyer C. S., Sims A. J., Farren J., Stephen J. and Underwood C. (1991) Radiation environment measurements and single event upset observations in Sun synchronous orbit. *IEEE Trans. Nucl. Sci.* NS-38, 1700-1707.
- Goka T., Kuboyama S., Shimano Y. and Kawanishi T. (1991) The on-orbit measurements of single event phenomena by the ETS-V spacecraft. *IEEE Trans. Nucl. Sci.* NS-38, 1693-1699.
- McNulty P. J. (1990) Predicting SEU phenomena in space. In *1990 IEEE Short Course Microelectronics for the Natural Radiation Environments of Space*, Reno, Nev., pp. 3.1-3.93. IEEE-NPSS Nuclear Radiation Effects Committee.
- McNulty P. J., Abdel-Kader W. G. and Beauvais W. J. (1993) SEU parameters and proton-induced upsets. To be published.
- McNulty P. J., Abdel-Kader W. G. and Lynch J. E. (1991a) Modeling charge collection and single event upsets in microelectronics. *Nucl. Instrum. Meth. Phys. Res. B61*, 52-60.
- McNulty P. J., Farrell G. E. and Tucker W. P. (1981) Proton induced nuclear reactions in silicon. *IEEE Trans. Nucl. Sci.* NS-28, 4007.
- McNulty P. J., Roth D. R., Beauvais W. J., Abdel-Kader W. G. and Ding D. C. (1991b) Comparison of the charge collecting properties of junctions and the SEU response of microelectronic circuits. *Nucl. Tracks Radiat. Meas.* 19, 929-938.
- McNulty P. J., Beauvais W. J., Abdel-Kader W. G., El-Teaty S., Mullen E. G. and Ray K. P. (1991c) Test of SEU algorithms against preliminary CRRES satellite data. *IEEE Trans. Nucl. Sci.* NS-38, 1642-1646.
- Metropolis N., Bivins R., Storm M., Turkevich A., Miller J. N. and Friedlander G. (1958) *Phys. Rev.* 110, 185.
- Nichols D. K. and Price W. P. (1982) *IEEE Trans. Nucl. Sci.* NS-29, 2081.
- Shimano Y., Goka T., Kuboyama S., Kawachi K., Kanai T. and Takami Y. (1989) The measurement and prediction of proton upsets. *IEEE Trans. Nucl. Sci.* NS-36, 2344-2348.

APPENDIX M

SEU PARAMETERS AND PROTON-INDUCED UPSETS

SEU PARAMETERS AND PROTON-INDUCED UPSETS

W.J. Beauvais, P.J. McNulty, W.G. Abdel Kader, and R.A. Reed

Department of Physics and Astronomy
Clemson University, Clemson, SC 29634-1911

ABSTRACT

The variation of SEU cross section with incident proton energy and angle of incidence is very sensitive to the thickness of the sensitive volume and the critical charge required for upset. This paper provides a method to determine accurate estimates of these important parameters, the critical charge and the sensitive volume thickness, using simple SEU measurements for a number incident proton energies.

INTRODUCTION

Most modern microelectronic circuits are sensitive to proton-induced single event upsets. The use of proton sensitive devices in space should increase with the trend toward SEU-tolerant designs. However, designing tolerant circuits requires accurate SEU-rate predictions. The models currently used for SEU-rate predictions require that the user specify certain SEU parameters for the device, the dimensions of the sensitive volume and the critical charge. Experience with CRRES and other satellites has shown the difficulty in using limited ground test data to predict SEU rates without accurate knowledge of these parameters. The commonly used SEU model assumes a rectangular parallel-piped sensitive volume, (SV). All the charge generated within the sensitive volume by an energetic particle passing through it is assumed to be collected and contribute to the probability of an upset. All charge generated outside the SV is not collected. If the charge collected from a single event is larger than a specific critical charge, then the circuit will be upset. The three necessary parameters for the application of this model are the area of the SV, the thickness of the SV, and the critical charge required to upset the circuit.

DIMENSIONS OF THE SENSITIVE VOLUME

The area of the SV is normally found by taking the saturated cross section from a plot of measured SEU cross section vs. LET obtained by exposing a device to heavy-ions. An example of such a plot is shown in Fig. 1. The area can also be found by looking at a mask diagram of the chip. If it can be determined which structure on the device is radiation sensitive, the area of this structure can be determined directly from this scaled layout drawing. A third method for determining the SV area is to use a charge collection spectrum measured off the power lines of a device. The charge collection spectrum for the device studied in this paper is shown in Fig. 2. The large broad peak at 20 MeV is assumed to correspond to the SEU sensitive junctions. The area is the ratio of the number of events under the peak to the fluence [1,2]. The other two parameters, the sensitive volume, the

thickness, and the critical charge, are interrelated and much more difficult to determine.

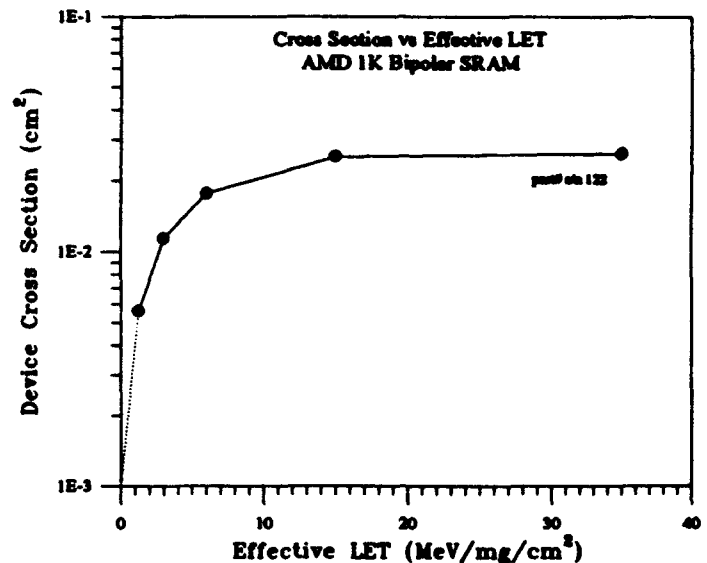


Figure 1. Heavy ion cross section vs. LET for Bipolar SRAM[14].

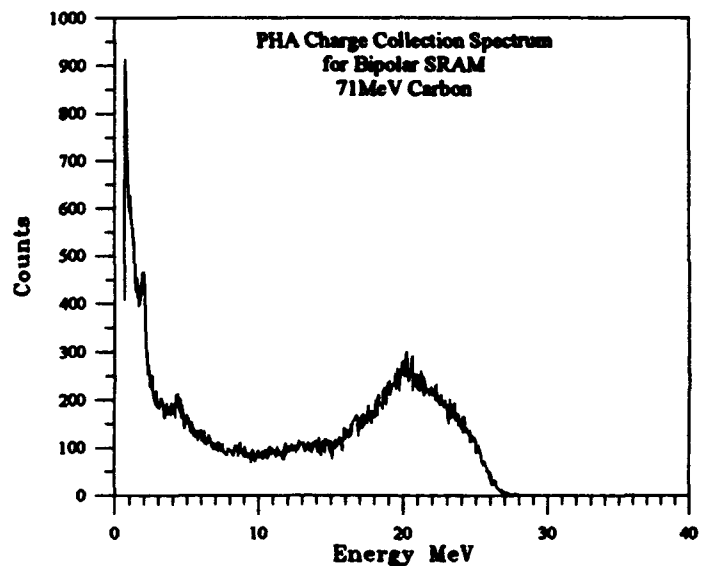


Figure 2. Charge collection spectrum for a Bipolar SRAM.

The SV is just a mathematical artifice and thus its dimensions do not necessarily correspond to any actual physical structures on the device. This means that except for SOS and possibly SOI technology, the thickness of the

sensitive volume can not be accurately determined by just using processing and circuit design information. Techniques have been developed for obtaining the thickness of the SV from the peak position using range-energy tables [1,2], but signals from a bipolar SRAM may be amplified by the bipolar transistors.

At first glance, it may not seem necessary to determine a specific critical charge and sensitive volume thickness as long as their ratio, the threshold LET, can be determined. The threshold LET is the value of the Linear Energy Transfer, of an incident particle crossing the sensitive volume, that is required to upset the device. The normal way of determining this value is to use the heavy-ion cross section vs. LET curve shown in Fig. 1. The threshold LET is determined by taking the LET value from the curve at a certain percentage of plateau. A conservative approach often taken in predicting SEU rates is to use the lowest value of LET which led to an upset, the onset of threshold LET. Others use 25% of the saturation value. More precise calculations require taking the shape of the response curve into account [2]. For purposes of comparing heavy-ion and proton data, it is necessary to use for the critical charge, a value likely to result in upset. We prefer the traditional value of threshold, i.e., the value of the LET corresponding to a cross section of 50% of the saturation value [2]. The saturation value should be estimated from the early portions of the plateau rather than its value at high LET [2]. Difference in the approach used to determine threshold can lead to substantially different values of threshold LET depending upon the shape of the response curve.

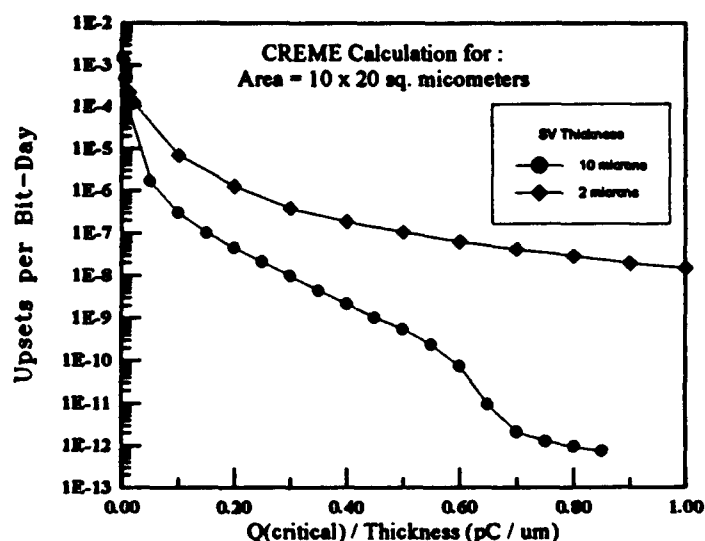


Figure 3. CREME calculations for various parameters.

Fig. 3 compares SEU rate calculations for a device plotted as a function of the critical charge for two different assumed thicknesses of the SV for cosmic-ray-induced upsets. The abscissa is scaled by dividing the critical charge by the sensitive volume thicknesses in order that a measured

threshold LET corresponds to the same abscissa value on both curves. The curves clearly indicate that for devices with equivalent threshold LETs, the thicker device is less sensitive, especially for high values of the threshold LET. This figure demonstrates that accurate knowledge of the sensitive volume thickness, as well as the value of the critical charge, is necessary for predicting the upset rate of a device in deep space.

CRRES SEU data has shown that proton induced SEU dominate the cosmic-ray-induced SEUs for proton sensitive devices flying in satellites that traverse the inner proton belts even when the satellite spends only a small fraction of its orbit there [3]. Proton-induced upset rates are also quite sensitive to the thickness of the sensitive volume. This is illustrated by following the dashed lines on the curves shown in Fig. 4. The integral energy deposition curves shown there were calculated by CUPID [4,5] and are plotted for sensitive volumes having the same lateral dimensions and different thicknesses. At each thickness, the integral spectra for both 148 MeV and 30 MeV normally incident protons are shown for an area of 44 μm by 44 μm . The curves in Fig. 4 are plots of the cross section for a proton-induced spallation reaction which results in at least the energy deposition given by the abscissa. The curves can be used to relate the upset cross section to the critical charge. The dashed lines on each graph show that for a given arbitrary critical charge of 10 MeV, the cross sectional upset rate on the ordinate axis can vary considerably for different SV thicknesses. The 1 micron thick SV has an upset cross section of around $3\text{E-}14$ while the 10.7 micron thick SV has an upset cross section of about $4\text{E-}11$. So in this particular case, the 10.7 micron device would have an upset rate 1000 times higher than the 1 micron device for the same proton fluence.

The prior illustrations illustrate how that fairly precise values of both sensitive volume thickness and critical charge are necessary for accurate upset rate predictions. The common way for each to be determined is to estimate one or the other and use the heavy ion threshold LET relationship to determine the unknown one. The only way to estimate the critical charge is through SPICE or other circuit simulations which are somewhat complex and whose results are often suspect. Consequently, the SV thickness is usually estimated first, and then, the critical charge is calculated from the threshold LET. The SV thickness is often estimated by using a given value for a specific type of technology such as NMOS, Bipolar or CMOS. Other times the SV thickness is estimated by the location of a physical structure on the chip such as the epi-layer depth or the junction depletion depth. McNulty et. al. [1] have used a charge collection method to determine the SV thickness of devices. This method has been found to work well for NMOS devices [1,2], and for CMOS devices but the latter can require some very complex interpretation [6]. The method is inaccurate for BIPOLAR devices due to internal amplification of the signal. Figure 2 shows a charge collection spectrum from a very common and widely studied [7,8] bipolar SRAM, the one used in this study.

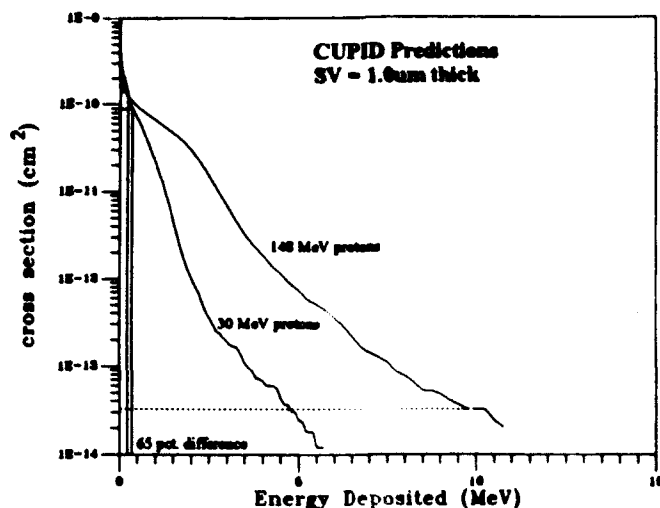


Figure 4a.

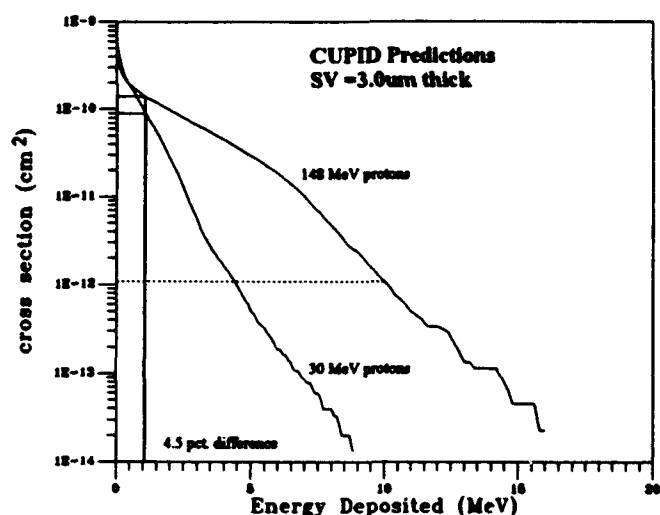


Figure 4b.

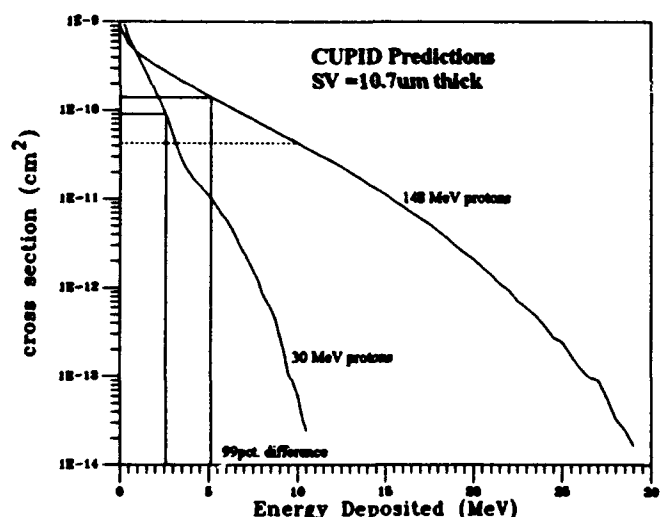


Figure 4c.

Figure 4. Integral cross section for depositing at least the energy deposited given by the abscissa versus the energy deposited. Curves are for protons incident at 30 MeV and 148 MeV on sensitive volumes with thicknesses of a) 1 μm , b) 3 μm and c) 10.7 μm .

Using the energy of the peak position and range energy tables of the incident ion, the thickness of the charge collecting SV is found to be 44 microns. This large value is assumed to be due to the amplification of the ion generated signal by the bipolar transistor the ion crosses. This amplification causes the curve to be shifted to the right to higher energies. If the amplification factor of the transistor was known, then the spectrum could be normalized and the data would be more useful but, the factor can not be easily determined at this time.

DETERMINATION OF SV THICKNESS

This paper presents a method for determining both the critical charge and SV thickness for a device using simple proton SEU cross-section measurements and CUPID simulations of the device. The basic idea behind this method can be seen by referring to the graphs in Fig. 4. The critical charge of an SRAM cell is circuit design dependent only and should be independent of the particle generating the charge. This means that the critical charge is the same for different incident proton energies. The two horizontal solid lines from the ordinate axis in the figures represent measured proton-induced SEU cross section values for 30 and 148 MeV normally incident protons. These upset cross sections are traced across to the appropriate CUPID simulation curve and then down to the abscissa which determines the corresponding critical charge. The graphs show that the curves for a thickness of 10 microns yield two clearly different values of critical charge which differ by a factor of two while the curves for a thickness of 3 microns yield values that differ by less than 5%. If the correct SV thickness is used, then each different proton energy should correspond to approximately the same constant critical charge.

The procedure to be used is to measure SEU cross sections of a device at a variety of incident proton energies. CUPID simulations of the integral spectra are then calculated for each incident proton energy for a variety of assumed thicknesses. For each thickness, the values of critical charge are obtained for each proton energy using the CUPID curves and experimentally obtained cross sections. The thickness value with the least dispersion of critical charge is the best estimate of the thickness of the SV.

This procedure was applied to the same type of 1 kbit bipolar SRAM described previously. SEU cross sections measurements for this part were done by Shimano [9] and Smith [10]. CUPID simulations were performed for SV thickness values ranging from 0.5 micron to 44 microns. Values of the critical charge were found for each thickness from the appropriate CUPID curve.

Fig. 5 plots the value of the critical charge versus the incident proton energy for each value of assumed thickness.

The relationships appear to be linear when plotted on a log-log scale. A value of the critical charge which is independent of energy would give a horizontal line on this graph so the SV thickness that corresponds closest to a horizontal line should be the correct thickness.

The average and standard deviation of the critical charge distribution were calculated for each thickness. The standard deviation was divided by the corresponding average to normalize the values for each distribution. Figure 6 shows this dispersion estimate plotted versus the value of the thickness. A cubic spline best fit was applied to the data to generate the curve. The minimum of this graph is the thickness with the smallest dispersion of critical charge, and thus, is the most appropriate value of the SV thickness. The average value of the critical charge at this thickness is the critical charge that should be used for upset rate calculations.

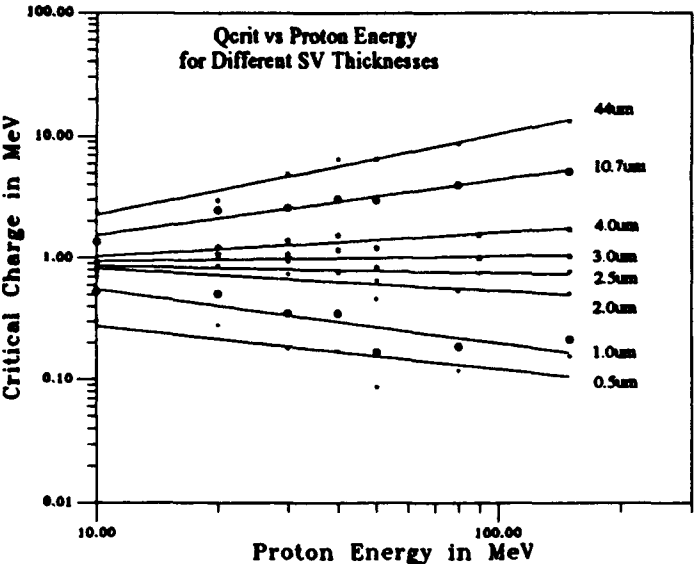


Figure 5. Critical charge vs. proton energy for Bipolar SRAM.

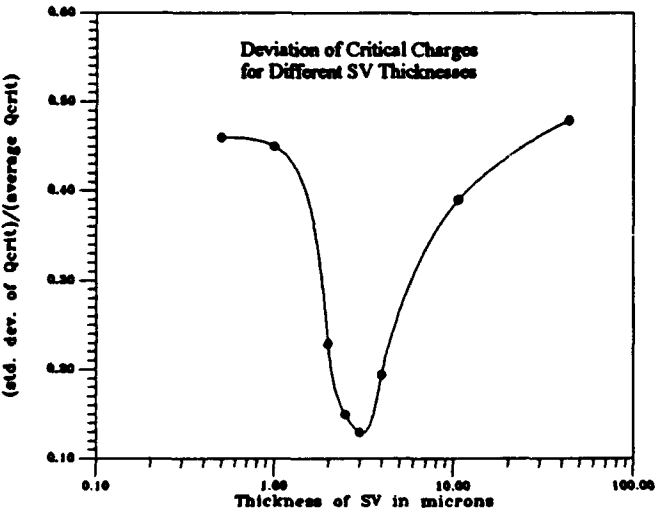


Figure 6. Dispersion of critical charge at each SV thickness.

Figure 7 compares the experimental measured SEUcrosssections from Refs. [9,10] against the results of the simulations. The average value of the critical charge obtained previously was used for each thickness. An interesting feature of the simulations is that the SEU cross section at 40 MeV appears to be independent of the thickness assumed. At low energies, using too small a thickness in simulations results in an overestimate of the cross section, and using too large a

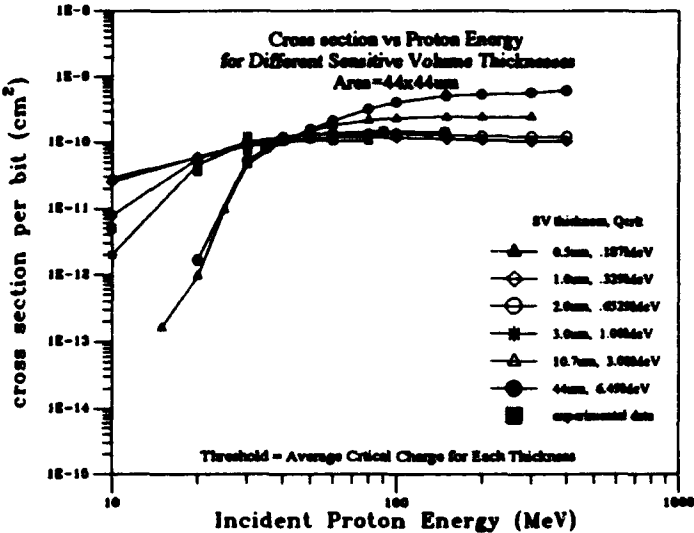


Figure 7. SEU cross section versus incident proton energy. Experimental measurements from Refs. 9 and 10 are plotted as squares. The theoretical curves are based on CUPID simulations for sensitive volumes with different thicknesses. The value of threshold was taken to be the average value of the critical charge which fit its measured cross sections as shown in Fig. 4.

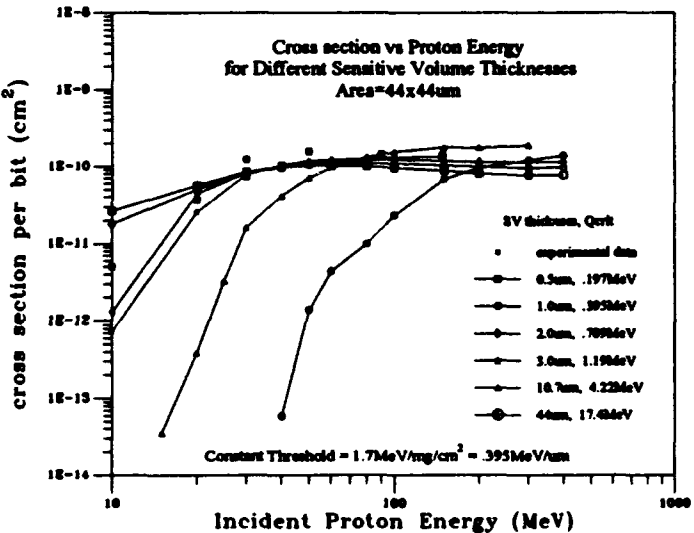


Figure 8. Same as Fig. 7 with the threshold based on the threshold LET of 1.7 MeV-cm² /mg obtained from Refs. 7 and 11.

thickness causes an underestimate of the cross section at low energies and an over estimate at high energies. the best fit is between two and three microns.

The question arises as to how well the curves would fit the experimental data if the threshold LET from heavy-ion data was used to determine each critical charge instead of using proton data.

Figure 8 shows the plots of this using a threshold LET of 50% of plateau which is about 1.7 MeV/mg/cm^2 from Ref. [11,14]. As one can see, the fits are all are below the experimental data. The best fit is with the thinnest values of SV thickness.

DISCUSSION

We have shown how proton SEU data can be used to obtain SV thickness and critical charge parameters for a device. The only drawback of this procedure is that some of today's leading-edge rad-hard devices are immune to proton upsets. This problem may be at least partially overcome by making SEU measurements at reduced biases [12]. However, most of the commercial devices used in satellite systems are proton sensitive so the method should be applicable for many devices of interest. We have also modified this approach to uses protons at different angles of incidence instead of different energies [12,13]. It has also recently been applied to latch-up [13].

Of course, the most important application of this method would be to produce more accurate upset rate predictions. CREME, which calculates upset rates for heavy ions in space, requires precise values of the SEU parameters for accurate and consistent upset rate predictions. Calculation of proton upset rates in space, like those illustrated in [3], also benefit from accurate determination of critical charge and SV thickness.

One important implication of this procedure is the prediction of the effects of radiation with different angles of incidence. Once the area and thickness of the sensitive volume are known exactly, then variation of SEU cross section with different angles of incidence can be calculated. Nearly all heavy-ion testing is done within a vacuum with particles that have ranges in silicon of much less than 100 microns. This limited range typically only allows angles of less than 60 degrees measured from normal incidence to be used before the packaging around the die starts to shadow the beam or the beam penetration depth becomes too small to traverse the sensitive volume. Accurate knowledge of the critical charge and SV dimensions can be used to predict upset rates at high angles of incidence by calculating the chord length distributions of particle crossings of the SV at a particular angle of incidence.

The value of the critical charge estimated using this procedure can predict the threshold LET for heavy ion experiments. Table 1 compares the threshold LET estimated from the data of Refs. [11,14] and from the method described in this paper.

TABLE 1.

Part#	Threshold LET, MeV/mg/cm^2	
	Heavy-ion	Proton
93L422	1.7 ± 1	$1.44 \pm .05$

CONCLUSION

A procedure is described for determining the critical charge and the sensitive volume thickness of a device using proton upset cross sections and CUPID simulations. Proton SEU cross sections are obtained for a device at a variety of proton energies. CUPID simulations are then performed for these energies for various SV thicknesses. For each SV thickness, critical charges are found from the simulation curves for that thickness using the experimental SEU cross section for each proton energy. The dispersion of critical charge is the found for the thickness by dividing the standard deviation of the values of critical charge obtained at different energies for this thickness by the average value. The proper thickness of the SV is the one with the minimum dispersion of critical charge. Accurate estimation of the SV dimensions and critical charge can lead to more accurate SEU rate predictions.

REFERENCES

- [1] P.J. McNulty, D.R. Roth, W.J. Beauvais, W. Abdel-Kader, and D.C. Dinger, "Comparison of the Charge Collecting Properties of Junctions and the SEU Response of Microelectronic Circuits", *Int. J. Radiat. Instrum., Part D Nucl. Tracks and Radiat. Meas.*, Vol. 19, Nos 1-4, pp. 929-938, (1991).
- [2] P.J. McNulty, "Predicting SEU Phenomena in Space" in 1990 IEEE Short Course Microelectronics for the Natural Radiation Environments of Space (IEEE-NPSS Nuclear Radiation Effects Committee, 1990) pp. 3-1 to 3-93.
- [3] P. J. McNulty, W.J. Beauvais, W. G. Abdel-Kader, S. S. El-Teleaty, E. G. Mullen, and K. P. Ray, "Test of SEU Algorithms Against Preliminary CRRES Satellite Data," *IEEE Trans. Nucl. Sci.*, **NS-38**, No. 6, 1642-1646, December (1991).
- [4] G.E. Farrell and P.J. McNulty, "Microdosimetric Aspects of Proton Induced Nuclear Reaction in Thin Layers of Silicon," *IEEE Trans. Nucl. Sci.* **NS-28**, 4007-4012 (1981).
- [5] G.E. Farrell, P.J. McNulty, and W. Abdel Kader, "Microdosimetric Analysis of Protons-Induced Reactions in Silicon and Gallium Arsenide", *IEEE Trans. Nucl. Sci.* **NS-31**, pp. 1073-1077 (1984).
- [6] R.A. Reed, P.J. McNulty, W.J. Beauvais, and D.R. Roth, "Charge Collection Spectroscopy" *IEEE Trans. Nucl. Sci.*, Dec. (1993), to be published.

- [7] M. Shoga, P. Adams, D.L. Chenette, R. Koga, and E.C. Smith, "Verification of Single Event Upset Rate Estimation Methods with On-orbit Observations," IEEE Trans. Nucl. Sci., NS-34, No. 6, (1987)
- [8] D. Binder, "Analytic SEU Rate Calculation Compared to Space Data," IEEE Trans. Nucl. Sci., NS-35, No. 6, (1988)
- [9] Y. Takami, F. Shiraishi, T. Goka, Y. Shimano, M. Sekiguchi, K. Shida, N. Ishida, H. Kadotani, T. Kikuchi, N. Hoshino, S. Murakami, H. Anayama, and A. Morio, "Investigation of Single Event Upset Subject to Protons of Intermediate Energy Range," IEEE Trans. Nucl. Sci., NS-37, No. 6, (1990)
- [10] E.C. Smith, private communication.
- [11] E.G. Stassinopoulos, NASA Goddard Spaceflight Center, Greenbelt, MD 20771, private communication.
- [12] D.R. Roth, P.J. McNulty, L. Strauss, and E.G. Stassinopoulos, "Monitoring SEU Parameters at Reduced Bias" IEEE Trans. Nucl. Sci., December (1993), to be published.
- [13] P.J. McNulty, W.G. Abdel Kader, and W.J. Beauvais, "Simple Model for Proton-Induced Latch-up," IEEE Trans. Nucl. Sci., December (1993), to be published.
- [14] D.K. Nichols, private communication.

APPENDIX N

**TEST OF SEU ALGORITHMS
AGAINST PRELIMINARY CRRES SATELLITE DATA**

Test of SEU Algorithms Against Preliminary CRRES Satellite Data

P. J. McNulty, W. J. Beauvais, W.G. Abdel-Kader, and S. S. El-Teaty

Department of Physics and Astronomy

Clemson University

Clemson SC 29634-1911

E.G. Mullen and K.P. Ray

Space Physics Division

Air Force Geophysics Laboratory

Hanscom AFB, MA 01731

ABSTRACT

The CRRES satellite's highly elliptical orbit exposes the SEU-sensitive devices within the Microelectronics Package to both the trapped protons of the inner radiation belts and the cosmic rays of deep space. Preliminary data from sensitive devices show more upsets due to protons than due to cosmic rays on this type orbit. This is consistent with pulse-height spectra measured from a photodiode within the package. Preliminary data obtained with the Ratemeter experiment in the inner radiation belts are in reasonable agreement with predictions based on the trapped proton spectra given by the NASA AP8 model for solar maximum combined with CUPID simulations of the spallation reactions near the sensitive volumes of the memory elements. The more limited data from deep space is in agreement with the CREME calculations for cosmic ray traversals. CUPID is also in relatively good agreement with the pulse-height spectra measured in the inner belts as part of the PHA experiment.

INTRODUCTION

The purpose of the Microelectronics Package on CRRES (Combined Release Radiation Effects Satellite) is to use and monitor a wide variety of microelectronic components. Its design includes dosimeters and thermistors to measure the radiation exposure and temperature at a large number of positions within the instrument. The cumulative effects of total dose and the single event phenomena induced by the radiation are constantly monitored. The objective of the Microelectronics Package is to test and improve space radiation models which predict exposure and device models which predict the effects of that exposure. This paper describes the preliminary results from two experiments within the Microelectronics Package which were designed to provide an early test of the models used for single-event upset (SEU) predictions: the Pulse-Height - Analyser (PHA) experiment and the Ratemeter experiment.

Since circuits are upset by current flow across sensitive junctions traversed by cosmic rays [1] or by current flow initiated by nuclear spallation reactions [2], the environmental models to be tested concern the cosmic rays and the energetic protons trapped in the inner radiation belt.

Successful SEU-rate prediction requires accurate prediction of the charge-collection events at the sensitive p-n junctions on a device as well as accurate prediction of the response of the circuit to the subsequent voltage swings. In the PHA experiment the energy-deposition events measured in a cylindrical volume of known dimensions are pulse-height analyzed. The PHA spectra provide an independent test of the environmental models generating the primary radiation events.

The Ratemeter experiment consist of ten 64K DRAMs (Intel's 2164A) which have been extensively studied regarding their SEU response to both heavy ions and protons. Both the heavy-ion and proton SEU data obtained at accelerators with this device has been fitted [1] using a single set of parameters: the dimensions of the sensitive volume and the critical charge. All the devices tested were from the same lot as the CRRES parts, and there was very little variation in their SEU response. The device is relatively insensitive to total dose compared to most DRAMS. Moreover, the proton SEU cross section for the 2164A has been shown not to be sensitive to the cumulative total dose. Finally, the sensitive volume has dimensions close to those typical of modern CMOS devices.

The Ratemeter and PHA experiments were designed into the Microelectronics Package as modeling targets which can provide the type and amount of data necessary to characterize the various regions of space and solar flares according to their SEU risks. They also provide a quick test of the primary radiation-effects models of the natural environments.

To facilitate comparison of theory and experiment, the orbit has been divided into two major segments; deep space and the inner radiation belts. The inner radiation belts have some electromagnetic shielding against cosmic-ray particles, but they contain the energetic trapped protons which produce large energy-deposition events through spallation reactions. Deep space, on the other hand, contains few trapped protons, but the satellite is exposed to the natural abundance of the energetic heavy ions of the cosmic rays.

RATEMETER EXPERIMENT

Methods and Materials

Ten 64K-bit DRAMs were located in the Microelectronics Package Experiment, 5 on each experimental bus. They were assigned to cells 8 and 17 of the inner board of experimental section 1. The DRAMs are read out once per second. The memory array is then reset periodically. Figure 1 shows a schematic of the logical organisation of each half of the Ratemeter experiment. No identification of the bit in error is made. The Intel 2164A was used as the test chip because it had been carefully characterised in terms of SEU sensitivity and was the available DRAM with the least sensitivity to total dose effects.

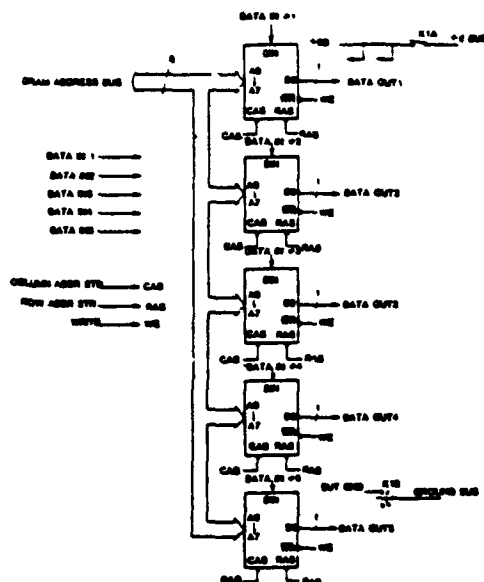


Fig. 1. Test circuit used for measurements of SEUs in the DRAMs of the Ratemeter experiment in the Microelectronics Package experiment on the CRRES satellite.

Characterisation of SEU Response

Model calculations of the SEU rate for the Ratemeter DRAMs were based on the trapped proton environment calculated by the NASA model AP8 [2] with the orbital parameters of apogee=36000km, perigee=360km, and an inclination of 21 degrees. The energy spectrum averaged for the trapped protons over many orbits is given in Fig. 2. The energy-deposition events induced in the circuit elements were simulated using the CUPID (Clemson University Proton Interactions in Devices) codes [3]. Using these codes to calculate SEU rates required knowing the dimensions of the sensitive volume and the critical charge (or threshold energy deposition - $1 \text{ pC} = 22.5 \text{ MeV}$) for the DRAM. These were determined by irradiating the delidded part with heavy ions. Figure 3 shows the cross section for upsetting the Intel 2164A plotted versus the effective LET of the incident heavy ion [1]. The triangle represents the predicted threshold LET, plotted as 50% of plateau, based on the ratio of the manufacturer's estimate of the critical charge and our estimate of the thickness of the sensitive volume. Two estimates of the thickness, one theoretical

following the procedures of Ref. 4 and the other experimental using the charge collection procedures outlined in Ref. 5 were found to be in agreement. The area of the sensitive volume is given by the value of the SEU event cross section [1] measured on the early portion of the plateau. The second method of determining the thickness involved estimating it from the peak in the spectrum shown in Fig. 4. The fact that the peak in the spectrum corresponds to traversals of the memory cell was confirmed by probing the DRAM with the heavy-ion microbeam, as described in Ref. 6.

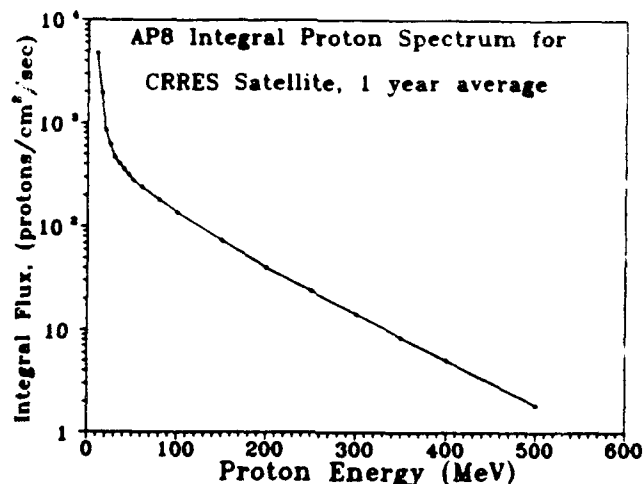


Fig. 2. Integral spectrum of the trapped protons in the inner radiation belts averaged over many orbits as given by NASA's AP8 model for solar maximum [2].

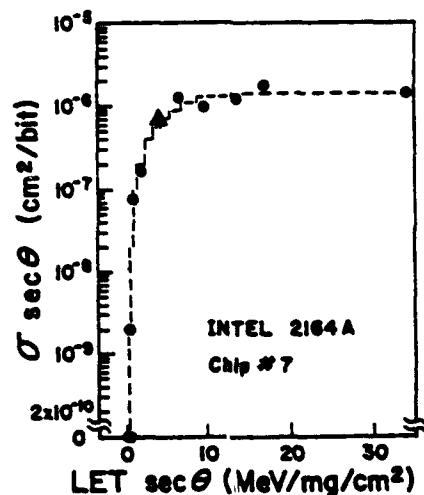


Fig. 3. SEU event cross section versus effective LET for the Intel 2164A. The plateau in the cross section at high values of LET agrees with the estimates of the memory cell area obtained from optical measurements [1].

The same SEU parameters, the dimensions of the sensitive volume and the critical charge were used in CUPID simulations of the SEU cross sections to be expected when the DRAM was exposed to energetic protons. The parameters used were a sensitive volume area of $140 \mu\text{m}^2$, a sensitive volume thickness of $3.58 \mu\text{m}$, and a critical charge of 3.3 MeV . Figure 5 compares the SEU cross sections as a

function of incident proton energy as given by theory with the measured values, showing very good agreement. This consistency of the laboratory data and the model predictions made the Intel 2164A the ideal sensitive part to use to test our environmental and interaction algorithms for this orbit. Moreover, fewer than 10% of the SEUs induced in our proton tests were multiple upset events, which simplifies the comparison of space data with theory.

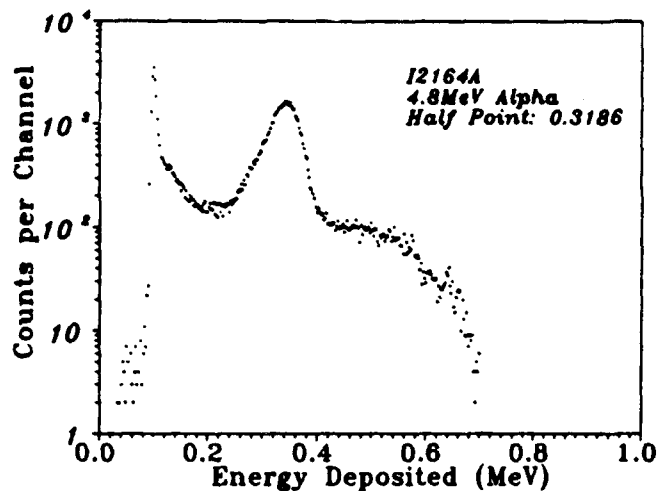


Fig. 4. Pulse-height spectrum measured on the Intel 2164A following the techniques described in Ref. 5. The peak corresponds to hits on the memory cells while the broad background is dominated by interactions in the support circuitry.

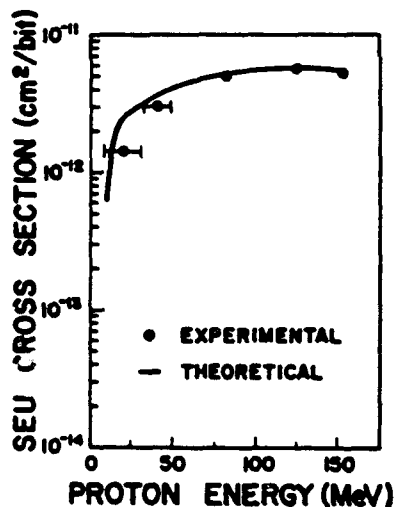


Fig. 5. Measured SEU cross section versus incident proton energy for the Intel 2164A. The solid curve represents the results of simulations using CUPID.

Results - Inner Radiation Belt

The SEU rates were calculated for this orbit by using CUPID to simulate the energy-deposition (charge collection) spectra for a number of incident energies. The incident particles were assumed to have first traversed a thickness of shielding before arriving at the DRAM. Figure 6 is a plot of the SEU rate for the CRRES orbit as a function of the thickness of a spherical shield surrounding it. The error

rate is not terribly sensitive to the shielding after the first thin layer of aluminum. The DRAMs had an equivalent shielding of 886 mills of Al on one side and an estimated 20gm/cm² on all other sides. The calculated upset rate is compared to the value measured in over 450 orbits in Table 1. The agreement is good with the calculated upset rate being a factor of two lower than the actual rate. AP8 had only been expected to be accurate within a factor of two when compared to data averaged over periods exceeding one year.

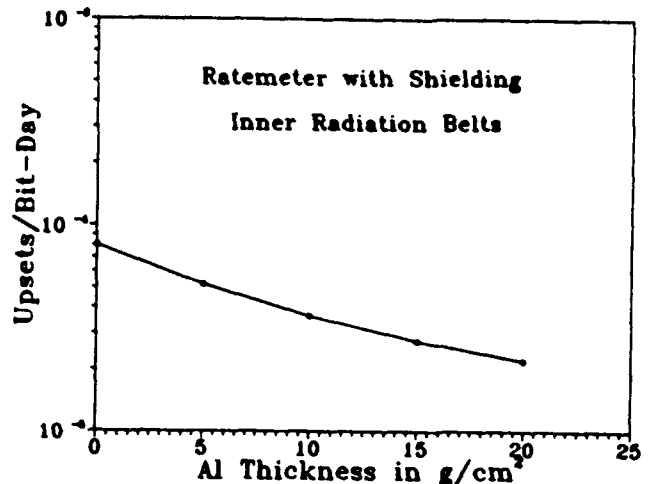


Fig. 6. Simulated SEU rate for the 2164A DRAM in the inner belts as a function of spherical shielding thickness.

Table 1.
Ratemeter Predictions
(Inner Radiation Belts).

	Upsets/Bit-Day
CALCULATED	$(0.35 \pm 0.04) \times 10^{-4}$
OBSERVED	$(0.81 \pm 0.02) \times 10^{-4}$

Deep Space - Ratemeter

The CREME codes were used to simulate the energy deposition in the DRAM's sensitive volumes as a result of cosmic-ray traversals. No corrections were included for the removal of lower energy cosmic rays due to deflection by the earth's magnetic field. The error rate due to cosmic rays is also not particularly sensitive to the thickness of the shielding around the circuit after the first thin layer. This can be seen in Fig. 7 where the SEU rate due to cosmic rays is plotted versus the thickness of the spherical shielding assumed in the CREME calculations. Table 2 compares the predictions with the upset rate measured in the deep-space segment of the orbit. The experimental data shown in this table is for only the first 33 orbits. Again, the agreement is better than expected considering the accuracy of the model for this short a period. In a highly elliptical transfer orbit like that of CRRES, the spacecraft spends only a small fraction of its 10.6 hour orbit within

the inner radiation belts. Despite this, comparison of the SEU rates in the inner belts (Table 1) with the rates observed in the remainder of the orbit (Table 2) shows that the protons pose the greater hazard to sensitive parts in a transfer orbit.

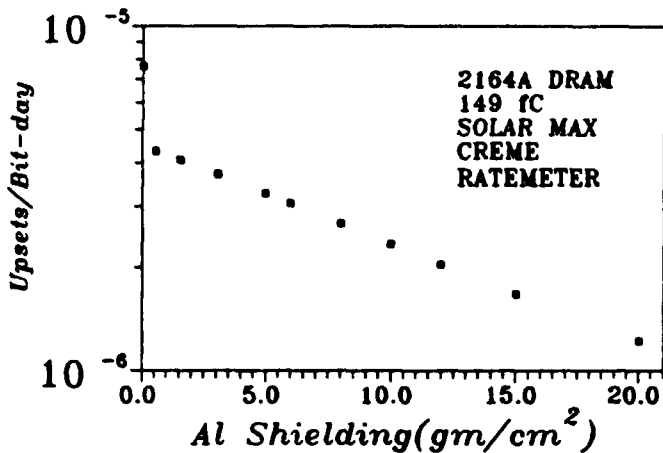


Fig. 7. CREME predictions of the upset rate for the 2164A DRAM as a function of shielding thickness.

Table 2.
Ratemeter Predictions.
(Deep Space)
(5gm/cm² Al Shielding)

	Upsets/Bit-Day
CALCULATED	$(1.5 \pm 0.6) \times 10^{-6}$
OBSERVED	$(1.4 \pm 0.3) \times 10^{-6}$

PULSE HEIGHT ANALYZER EXPERIMENT

The Pulse-Height Analyzer experiment was designed into the CRRES satellite in order to test our ability to model the radiation environment and the primary interactions which lead to SEUs without involving the SEU response of specific devices. The logic diagram for the PHA is shown in Fig. 8. It involves monitoring the pulses generated

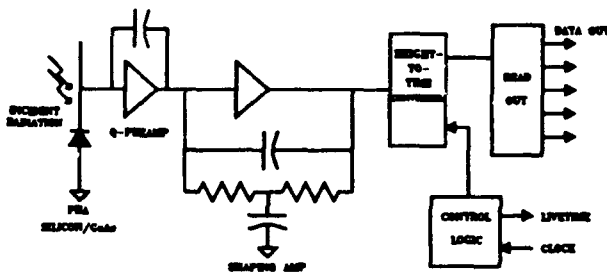


Fig. 8. Circuit used for the pulse-height analyzer experiment on CRRES.

across within a partially depleted PIN diode which has a well-characterized equivalent sensitive volume, an area of .051cm² and a thickness of 50 microns. If one cannot predict the shape of the spectrum observed in the PHA experiment, then agreement with specific devices would be suspect as fortuitous or due to multiple errors. CUPID's ability to predict the charge collection spectra for a number of incident proton energies before launch using the Harvard Cyclotron. An example of such a comparison is shown in Fig. 9.

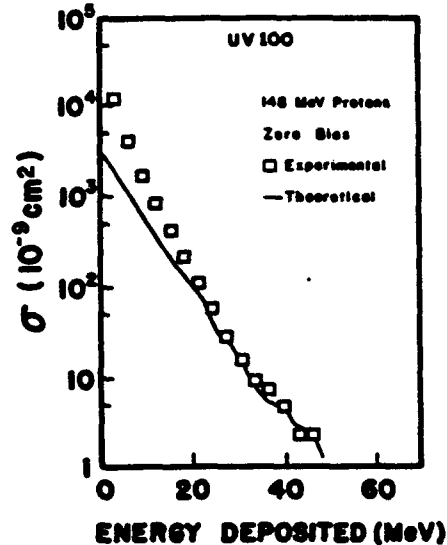


Fig. 9. Measured cross section for depositing at least energy E in the sensitive volume of the UV100 photodiode used in the PHA experiment plotted versus E. The theoretical curve represents the predictions of the CUPID codes for that incident energy.

Results - Inner Radiation Belt

The PHA experiment was on the outermost circuit board. The detector is a UV100 photodiode. The shielding on one side of the detector was only equivalent to a 75 mills thickness of aluminum. We estimate the shielding for ions incident in all other directions to be 20 gm/cm² thickness of aluminum. Using this shielding estimate, a PHA spectrum was calculated from a set of theoretical PHA response curves from CUPID, similar to the one shown in Fig. 9, and the theoretical proton spectrum from AP8 shown in Fig. 2. Figure 10 shows this theoretical spectrum compared against the actual spectrum measured during the inner radiation belt segments of 408 orbits. The shape of the spectra agree, but the theoretical curve is at least a factor of 4 below the measurements. Comparisons over longer time intervals would be helpful in determining the significance of this disagreement. The few high energy events, larger than 80 MeV, seen in the proton belts are most likely from heavy-ion cosmic rays. The total number of these large events is consistent with the number that would be expected if there was little reduction in the cosmic rays by the earth's magnetic fields.

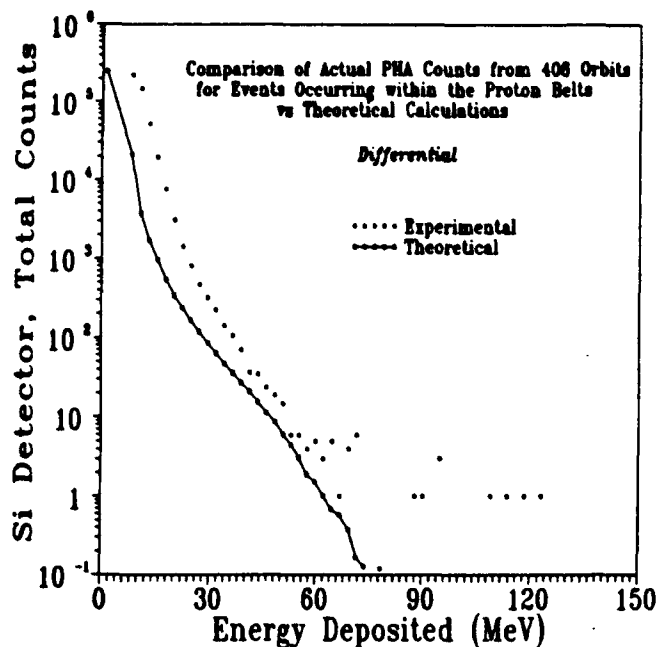


Fig. 10. Differential PHA spectrum measured in the inner radiation belt segments of 408 orbits.

Deep Space - PHA

There were considerably fewer events recorded outside the inner radiation belt than inside, either in the microelectronic devices or in the PHA detector. Figure 11 gives the pulse-height spectrum observed for the first 408 orbits outside the inner belts. There are far fewer low-energy events in the deep space segments of the orbits than was observed in the inner belts but somewhat more high energy events. For the more SEU-sensitive devices, therefore, the inner radiation belts represent a harsher environment than the cosmic-ray environment of deep space.

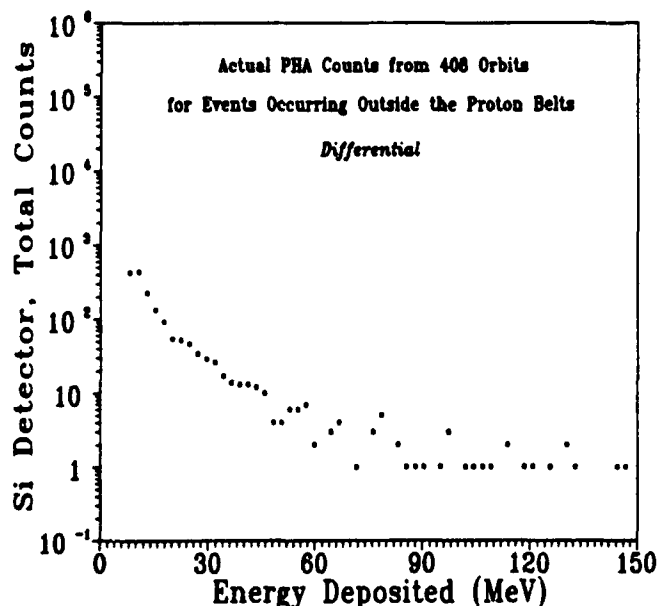


Fig. 11. Pulse-height spectrum measured outside the inner radiation belts over 408 orbits.

SUMMARY AND CONCLUSIONS

The Ratemeter experiment on the CRRES satellite exhibits many more SEUs due to energetic trapped protons than due to cosmic rays. Fairly accurate theoretical predictions of proton induced events were made by combining the NASA AP8 model of the protons trapped in the inner radiation belt and the energy-deposition spectra from CUPID code's simulation of the nuclear spallation reactions. The number of upsets predicted for the Ratemeter DRAMs was only a little over a factor of two lower than what was seen on the satellite. Similarly, comparison of the events outside the inner belt with the predictions of CREME, with no corrections for magnetic deflection, yield good agreement. A more detailed test of proton modeling came from comparing the simulations with the experimental energy-deposition spectrum measured in the inner radiation belts as part of the PHA experiment. The theoretical simulation of the integral pulse-height spectrum had the same shape as the experimental spectrum, but the simulation was about a factor of four lower in total count rate. Since AP8 and CREME are expected to be accurate within a factor of two only when averaged over intervals longer than a year, and the experimental data represents just under six months of flight time, the agreement is considered to be quite good.

ACKNOWLEDGEMENTS

We would like to acknowledge the contributions of our colleagues on the CRRES Microelectronics Working Group who contributed greatly to the design of both experiments. We especially thank E.G. Stassinopoulos for his calculations of the yearly averaged proton spectrum from AP8.

REFERENCES

- [1] J.M. Bisgrove, J.E. Lynch, P. J. McNulty, W.G. Abdel Kader, V. Kletnieks, and W.A. Kolasinski, "Comparison of Soft Errors Induced by Heavy Ions and Protons", IEEE Trans. Nucl. Sci. *NS-33*, 1571-1576, Dec. (1986).
- [2] E.G. Stassinopoulos, private communication
- [3] P.J. McNulty, G.E. Farrell, and W.P. Tucker, "Proton-Induced Nuclear Reactions in Silicon", IEEE Trans. Nucl. Sci. *NS-28*, 4007, (1981).
- [4] W. G. Abdel-Kader, P. J. McNulty, S. El-Teaty, J. Lynch and A. N. Khondker, "Estimating the Dimensions of the SEU-Sensitive Volume", IEEE Trans. Nucl. Sci., *NS-34*, 1300, (1987).
- [5] P.J. McNulty, W.G. Abdel-Kader, and J.E. Lynch, "Modeling Charge Collection and Single Event Upsets in Microelectronics", Nuclear Instruments and Methods in Physics Research B61, 52-60, (1991).
- [6] P.J. McNulty, W.J. Beauvais, D.R. Roth, J.E. Lynch, A. Knudson, and W. Stapor, "Microbeam Analysis of CMOS Circuits" to be published in IEEE RADECS proceedings Sept. 91.

APPENDIX O

PROTON-INDUCED SEU IN CMOS/SOS

PROTON-INDUCED SEU IN CMOS/SOS

J. C. Pickel
IRT Corporation

B. Lawton
SAIC

A. L. Friedman
SAIC

P. J. McNulty
Clarkson University

ABSTRACT

Experiments on proton-induced SEU in 16 K CMOS/SOS RAMs have shown that nuclear-reaction-induced upset can occur in this technology with significant probability at total dose and dose rate well below damage or dose rate upset levels. Analytical predictions based on circuit analysis and Monte Carlo analysis for nuclear-reaction-induced upset are consistent with the experimental results. The approach, results, and implications for SOI-type technologies are discussed.

INTRODUCTION

CMOS/SOS is the chosen technology for many system applications which require low SEU rates or high dose rate operate-through capability. The transient hardness of silicon-on-sapphire (SOS) relates to the smaller volume from which ionization-generated charge can be collected. A similar hardening is realized with silicon-on-insulator (SOI), of which SOS is a special case.

The data retention of CMOS/SOS RAMs in a high flux proton beam is of interest from the standpoint of neutral particle beam (NPB) weapon lethality and survivability. Previous studies of proton-induced SEU in CMOS/SOS RAMs have been confined to exposure of RAMs up to 1 K-bit size at cyclotrons using relatively low fluxes¹. No upset had been observed up to total fluences of 10^9 p/cm²; the upset cross-section was placed at less than 10^{-12} cm²/bit and it was generally assumed that proton-induced SEU in SOS could not occur or would be of insignificant probability. However, with a larger RAM (e.g., 16 K-bit) and a more total dose tolerant technology it is possible to measure the proton-induced upset cross-section in CMOS/SOS at levels as low as 10^{-15} cm²/bit. Such a low upset cross-section is not insignificant for some applications.

This paper reports a study of proton-induced upset in 16 K CMOS/SOS RAMs. Commercial technologies from both RCA and Marconi were studied in experiments at the 200 MeV proton Linac at the Radiation Effects Facility (REF) at Brookhaven National Laboratory (BNL) and at the Harvard Cyclotron Laboratory (HCL). The initial

emphasis of the study was to experimentally verify modeling predictions that multiple event upset (MEU) should not occur in the RAMs. However, after SEU was observed in the proton Linac testing, a careful set of experiments and analyses were performed to isolate the upset mechanism. While the emphasis was on upset, the associated total dose associated acquired during the measurements was considered in the data analyses.

Test data was also obtained on several types of non-SOS 16 K RAMs including unhardened (bulk) and hardened (epitaxial) versions of the IDT6116 and the hardened (epitaxial and feedback resistors) version of the Harris 65C262.

UPSET MECHANISMS

Upset in RAMs is due to dose rate effects which generate non-equilibrium carrier concentration, leading to voltage disturbances and bit-flips. Upset mechanism can be generally divided into global dose rate upset and local dose rate upset. Global dose rate upset occurs when a relatively uniform dose rate across the chip exceeds the upset threshold for most memory cells or initiates a disturbance on a common input; this is the usual upset effect encountered in the prompt ionization from nuclear weapons. Global dose rate upset is indicated by large numbers of bit errors with commonality to rows and columns. Local dose rate upset is indicated by single, or relatively few, isolated bit errors. Possible causes for this type of upset can be postulated as either "weak" memory cells for which a uniform dose rate across the chip exceeds the upset threshold for a few cells, or a locally non-uniform dose rate at an isolated cell. For the latter case in a proton beam, the possibilities that can be considered are non-uniform ionization due to multiple particle effects (i.e., the multiple event upset or MEU effect) or localized ionization due to a recoil from proton-induced nuclear reactions in the chip.

Global dose rate upset was not observed in any of the 16 K CMOS/SOS RAMs tested. This is not surprising since the upset threshold for SOS is usually greater than 10^{10} rad/s and the peak dose rate during our experiment was mid 10^9 rad/s. However, SEU was observed. The "weak" cell postulate was eliminated by observing that upset

locations were random and non-repetitive. The thrust of the experiments and analyses was then to isolate the mechanism to either MEU or to nuclear-reaction-induced SEU (NRSEU).

The MEU mechanism relates to the fact that at relatively low fluxes, there is a statistical probability that multiple particles will penetrate a sensitive node in a device within a time period that is comparable to the time required for the node to recover. The charge deposited by two or more protons is then integrated and is indistinguishable from the charge deposited by a heavier ion. If the differential between the instantaneous charge deposition on the two nodes of a bistable latch become sufficiently large, a bit flip may occur. MEU from a NPB weapon is analogous to SEU from the natural environment, but there are important differences. The relatively high flux required for a significant probability of multiple particles traversing a nodal collection region within the circuit integration time causes concurrent ionization in all devices in the circuit. NPB pulses which are long compared to the nodal integration times in a circuit result in a steady-state background ionization that generates photocurrents at PN junctions and causes photoconduction in both the semiconductors and the insulators. These synergistic dose rate effects may affect the critical charge for upset of the circuit. Statistics dictate that occasionally a particular collection region will be penetrated by multiple particles above the background rate (the average particle hit rate to all the collection regions within the circuit) within the integration time. If the multiple particles generate the critical charge of the circuit, as modified by the background ionization, the circuit will upset; if the flux is less than that which leads to upsets induced by dose rate effects, this is the MEU effect. At sufficiently high fluxes, dose rate effects will dominate the circuit failure mechanisms. At sufficiently high fluences, total dose, nuclear-reaction-induced SEU or displacement effects will dominate. Thus, MEU effects need to be considered only up to the flux or fluence at which other effects dominate.

The MEU effect in CMOS/SOS was analyzed in detail in Reference 2, with consideration for the synergistic effects discussed above. The results of this analysis showed that it is not a viable mechanism, since the large differential in the particle traversal through the two sides of the memory cell could not be achieved before global dose rate upset levels were reached. The MEU model indicates a strong dose rate dependence of MEU probability, with a super-linear dependence of probability of MEU with increasing dose rate.

Nuclear-reaction-induced upset from protons is a well established phenomenon. For a typical traversal length of the active region of a micro-electronic device, approximately 1 to 10^5 protons can be expected to undergo a nuclear reaction with the Si. The excited nucleus then emits other particles and recoils. The net effect is to transfer energy from a low linear energy transfer (LET) proton to a high LET particle. An SEU can occur if the reaction occurs sufficiently close to the sensitive charge collection

volume and the recoiling heavy particle traverses sufficient path length in the sensitive volume. Nuclear-reaction-induced SEU depends on independent reactions between a single proton and a Si nucleus; consequently, the probability for NRSEU is independent of dose rate, in contrast to the probability for MEU which has a strong dose rate dependence. NRSEU had not been previously observed in CMOS/SOS technologies.

EXPERIMENTAL MEASUREMENTS

Measurement of NRSEU or MEU in SOS device presents a challenging experimental problem since these are very low probability phenomena. The high fluence that may be needed for statistically significant observation of NRSEU may cause total dose damage to the chip and care must be taken to ensure that the synergism of the total dose damage does not affect the results. The high flux that would be required for MEU may be just below the threshold for global dose rate upset and the synergism of the global dose rate ionization may affect the critical charge and change the NRSEU probability.

Total dose hardened 16 K CMOS/SOS RAMs provide a good test vehicle for these effects, since they have a high dose rate upset threshold, and provided they have sufficient total dose hardness, the large number of memory cells allow low probability events such as NRSEU to be detected. For these tests, commercial versions of 16 K CMOS/SOS RAMs from RCA (RCA-6167) and Marconi (MA-6116) were measured. The RCA-6167 has a 5-transistor memory cell, while the MA-6116 utilizes a 6-transistor cell design. The RCA device was stated to be total dose hard to approximately 200 krad(Si) and the Marconi device to approximately 50 krad(Si).

The tests were performed primarily at the proton Linac at the Radiation Effects Facility (REF) at Brookhaven National Laboratory (BNL), with some low dose rate testing performed at the Harvard Cyclotron Laboratory (HCL). The REF tests utilized proton energies at 190 MeV and pulse widths from 2 to 300 μ s. The cyclotron tests utilized a continuous beam with proton energies at 40, 90, and 149 MeV. The experiments at the two facilities provided a span in the average dose rates from 10^3 to 10^9 rad/s.

TEST APPROACH

The experiments consisted of measurements of the static RAMs after exposure to a known fluence of protons from the accelerator (either the proton Linac at BNL or the proton cyclotron at HCL). All exposures were made in air with the package lid in place. The approach was to write a pattern into memory, expose it to a known fluence of protons, and then read the memory and compare to the written pattern. Any discrepancy was counted as a bit error and the location in memory was noted. Functionality was verified by writing and reading the complement of the previous pattern, and then the exposure sequence was continued. The electrical test setup is shown schematically in Figure 1.



set of exposures. A second foil was located at the exit of the shielding collimator hole for some runs to check on uniformity. The fluence uniformity across the DUT was estimated at 10 percent and the accuracy of the fluence calculation from the activation foils was 5 percent⁴. The carbon diffuser reduced the 200 MeV proton beam to 190 MeV at the DUT. The Linac was operated in the single pulse mode with several seconds between pulses.

The test setup at HCL consisted of locating the DUT at a calibrated position and exposing it to the continuously pulsing beam for a measured time period. Typical run times were 10 to 20 minutes. The fluence at the DUT was determined by integrated current monitor counts provided by the facility.³ The Harvard Cyclotron is a very stable machine with well calibrated dosimetry. The current probe calibration was performed by the facility using both a Faraday cup and an integrated Si diode current response. The calibration was determined at the three energies for which data was taken — 149, 90 and 40 MeV.



The setup in the proton Linac exposure room is illustrated in Figure 2. Upon exiting the Linac drift tube, the beam was passed through a carbon diffuser and a one-inch diameter aluminum collimator. A current probe was used to integrate the charge in the beam pulse. A PIN diode was placed directly behind the device under test (DUT) and was used for real time monitoring of dose rate and pulse width. Aluminum activation foils were located directly in front of the device for each major



DOSIMETRY

The primary dosimetry data was the proton fluence (p/cm^2). If the energy is known, the average dose can be calculated. The dose rate calculation requires consideration for the microstructure associated with the accelerator beam. The protons in the beam from both the Linac and Cyclotron do not arrive in continuous fashion, but rather, are bunched into micropulses. Figure 3 illustrates the parameters associated with the dose rate calculation. During a beam pulse, the protons are allowed to strike the target for a period of time equal to the pulse width. An average dose rate (or flux) during the pulse can be defined by

$$R_{av} = \frac{D}{PW}$$

where

D = the integrated dose (or fluence) during the pulse, and

PW = is the pulse width.

The peak dose rate (or flux) occurs during the micropulses and can be determined by

$$R_{max} = R_{av} \left(\frac{T}{W} \right)$$

where

T = the period for the micropulse

W = the full width at half maximum for the micropulses.

Table 1 lists the pertinent values for dose rate calculations for the proton Linac and the Harvard Cyclotron, based on beam microstructures parameters provided by the facilities.^{4,5}

Table 1.
Dose Rate Calculation Parameters.

Test	PW(μs)	T(ns)	W(ns)	R_{max}/R_{av}
Proton Linac	2-300	5	1.67	3
Harvard Cyclotron	200	40	7	5.7

The maximum dose rate calculation results in Table 1 assume that the micropulses are all of equal amplitude. However, a detailed study indicated that this is not the case at the proton Linac, as discussed in the following.

LINAC MICROSTRUCTURE

In order to evaluate mechanisms causing upsets, beam microstructure characteristics must be understood. It is imperative that maximum dose rates encountered during beam testing be quantified at the microstructural level to be able to assess the potential for dose rate upset (global or "weak" memory cell) during each exposure.

The microstructure of the beam is determined by characteristics of the ion source and RF field. The basic beam structure at the source is a series of 320 ps proton bunches with a spacing of 5 ns. Analysis by BNL person-

nel predicted that the full-width half-maximum (FWHM) pulse widths at the device under test would spread to 1.7 ns as a result of momentum distribution and time of flight through the approximately one-half mile travel through the beam vacuum line to the exposure cell. Up to the time of these tests, the proton Linac beam characteristics had not been measured in real time. To accomplish these measurements, a Unitrode 9441 PIN diode was used as an ionization detector.

A wide bandwidth data capture and recording capability is necessary to view beam characteristics; an oscilloscope rise time of less than 350 ps, or an equivalent bandwidth of greater than 1 GHz, is needed. Since beam durations in the hundreds of microseconds do not allow sampling techniques to be used, a single shot mode of data capture is required. The use of a Tektronix 7104 oscilloscope, 7A29 pre-amp, and 7B10 time base, in addition to a DCS01 digitizing camera system provided the 1 GHz bandwidth and recording capability for the measurements to be accomplished. This combination of instrumentation was the widest bandwidth available at the time of the test. While somewhat limiting the recording fidelity of waveforms encountered, the equipment was suitable for viewing the beam parameters important for upset testing and analysis.

Figures 4 through 6 reveal beam characteristics. These figures were recorded with constant baseline settings and vertical calibration. Figure 4 shows the basic beam microstructure of 2 ns pulse (FWHM) with 5 ns spacing. These pulse widths are in good agreement with BNL predictions. Figure 5 shows the maximum pulse width of 300 μs . The enlarged waveform shown in Figure 6, which was captured by the DCS01 at 200 ns per division, is useful for examining structural detail.

The conclusion that can be reached from examination of the data is that the average peak dose rate during the 300 μs pulse is one division of the PIN diode response. The photos also reveal that the typical structure consists of a series of pulses with amplitude of one large division with occasional peaks of greater amplitude. The max-

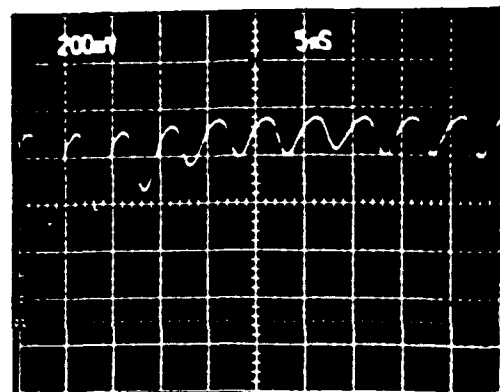


Figure 4. Linac beam microstructure of 5 nanosecond/division.

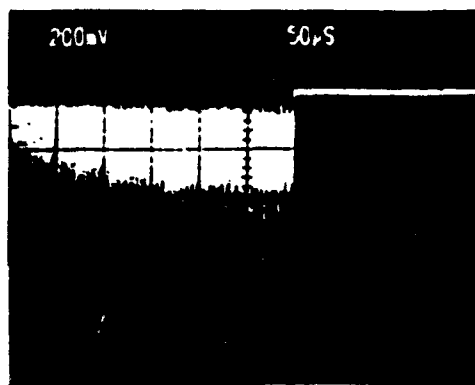


Figure 5. Linac micropulse variation during 300 microsecond pulse width.

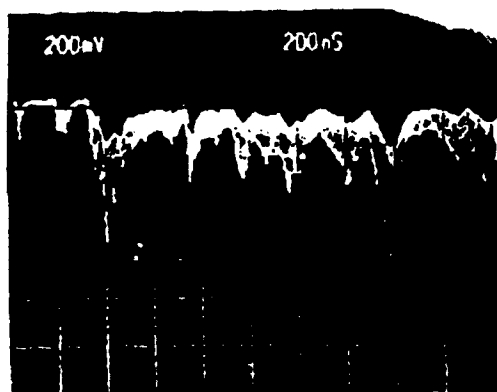


Figure 6. Linac beam microstructure at 200 nanosecond/division.

imum dose rate per microstructure pulse found in these occasional anomalously large peaks captured in the photos is at least 4 divisions. Activation foils were used for dosimetry during these tests. Such dosimetry integrates the dose over the total beam pulse width. If a rectangular approximation is used to represent the average dose rate during the beam interval, the ratio of peak-to-average dose rates is 2.86. This figure is derived by approximating the typical beam structure as a series of triangular pulses with base widths of 3.5 ns and whose peaks occur at 5 ns intervals. The ratio is determined by equating these triangular areas to rectangles of 5 ns width, thus, creating a dc level representing the foil integration. The maximum peak-to-average dose rate per pulse is then the product of the ratios of 2.76×4 which is 11.4. This compares to a nominal peak-to-average dose rate ratio of about 3, based on the theoretical beam parameters provided by the facility, assuming constant amplitude micropulses.

ANALYSIS APPROACH

Detailed analyses were performed on the RCA 6167 memory cell to determine the critical charge for upset and to predict MEU and NRSEU effects in the high flux proton beam environment at the REF proton Linac.

Circuit Analysis

The RCA 6167 16 K static RAM is based on 3 micron CMOS/SOS technology. The memory is designed using memory cells with five transistors, an internal voltage multiplier, and a pre-charge of bit lines and sense amplifiers. The processing approach results in buried contact diodes located at the drains of transistors of P1 and P2 as shown in Figure 7. As a result, a P1 or P2 ion hit is relatively insensitive to SEU because the diodes act as large non-linear resistors during the ion charge collection transient, effectively decoupling the inverter nodes.⁶

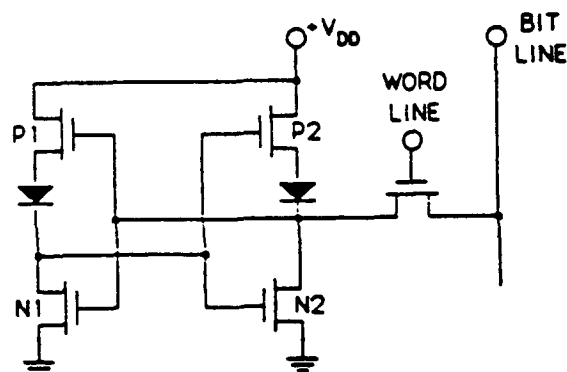


Figure 7. RCA 5-transistor memory cell circuit.

A modular version of SPICE (SPICE-PAK) was used to analyze the memory cell circuit for critical charge. The code was modified to automatically search for the critical charge, Q_c , needed to upset a memory cell and the synergistic effects of the proton beam were included.

The principal difference between analysis for critical charge in a proton beam environment (as in a NPB weapon) and a heavy ion environment (as in natural environment SEU) is that the entire circuit is ionized in the former, while only a single PN junction has the effects of ionization in the latter. The synergistic effects due to concurrent ionization in all PN junctions and all insulators must be considered in calculating critical charge. These effects include junction photocurrent, substrate photoconductivity, gate oxide photoconductivity and total-dose-induced shift of circuit parameters (threshold voltage shift and leakage currents). The proton beam irradiation has pulse widths on the order of several microseconds compared to the CMOS circuit time constant (i.e., the time required for a circuit node to recover after being disturbed by

a voltage transient) on the order of nanoseconds. Therefore, the particle flux from the proton beam can be treated as steady-state background ionization.

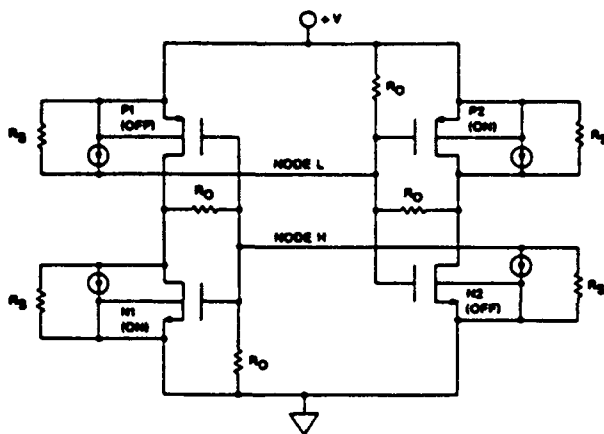


Figure 8. SPICE model for MEU analysis.

The simulation circuit used to determine the critical charge for upset is shown in Figure 8. The analysis was performed by applying a current pulse to node "L", simulating an ion hit or a multiple proton differential hit to N2. The current pulse amplitude was varied to find the threshold. The calculation was performed as a function of proton flux with an effective average background ionization rate determined for each flux level. The assumed proton energy was 100 MeV, which gives results representative of the energy range (40-190 MeV) over which testing was performed.

The current generators in parallel with the drain junctions simulate steady-state (during the wide proton pulse) photocurrent generated by the ionization. The collection volume was assumed to be the silicon under the gate and photocurrent was calculated from the generation rate, $6.4 \text{ A/cm}^2\text{-(rad/s)}$. The resistors R_s between the drain and source of the transistors represent sapphire photoconduction due to the background ionization. A sapphire photoconduction model based on Reference 7 was used. The resistors R_0 represent ionization-induced conductivity through the gate oxide. Analysis showed that this effect was negligible for the dose rates analyzed.

The results of the SPICE analyses for a hit to N2 and worst-case assumptions for end-of-range protons are given in Figure 9 where the node voltage and the critical charge are plotted as a function of proton flux. The analysis shows a Q_c of 250 fC without the background ionization from the proton flux with a significant decrease beginning above 10^{10} rad/s . At these dose rates, global dose rate upset mechanisms begin to dominate. Consequently, the analysis shows that for this device and for the proton energies and dose rates used in the testing, the synergistic effects of the proton beam on Q_c are not important.

The key effect which determines MEU is the coincident (within the circuit integration time) arrival at a junction of a sufficient number of particles to generate the critical charge. The required number of coincident particles is determined by the ratio of the charge generation per particle and the critical charge. The charge deposition per particle depends on path length through the collection region and the LET of the particle, which is energy dependent. Near the end of the particle range, LET goes through a maximum of approximately 0.1 MeV/micron; for protons in silicon, this occurs at less than 100 keV. However, due to the statistical variation in the proton range (straggling), there is no significant probability of multiple protons coincidentally arriving at a thin collection

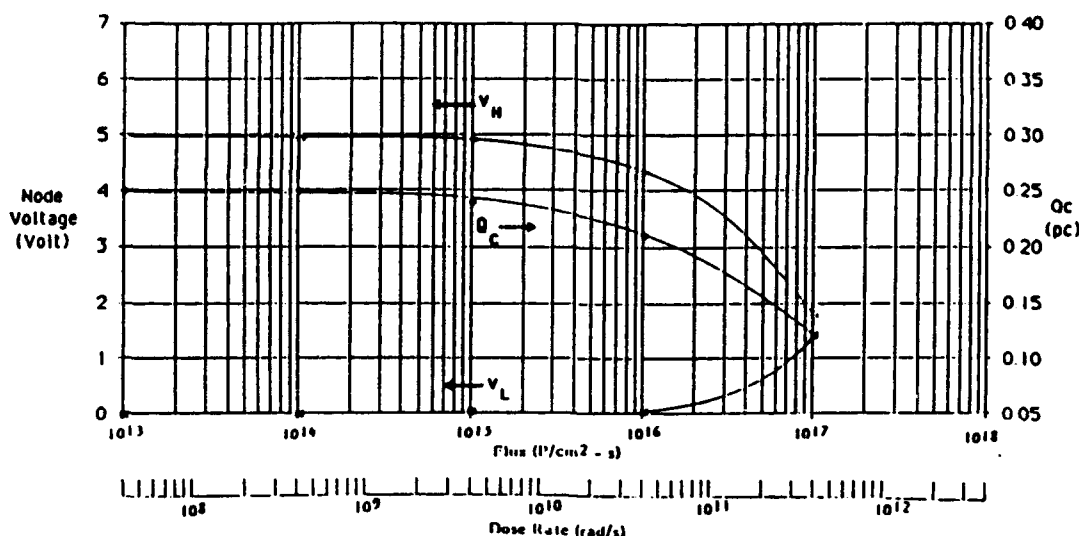


Figure 9. Node voltage and critical charge versus flux for RCA-transistor CMOS/SOS cell (N2 hit, end of range protons).

volume with the same energy. The net effect of the range straggling is to reduce the maximum average LET for a proton beam near the end of range to about 0.01 MeV/micron. For the end-of-range case, approximately 190 coincident proton hits would be required to generate the critical charge. For the proton tests at the Linac and cyclotron, energies in the range from 40 to 190 MeV were used; for this case the applicable LET is approximately 0.0014 MeV/micron and the analysis shows that approximately 1,500 coincident proton hits would be required for upset.

The MEU effect depends on integrating the charge generation from multiple particles which strike a junction coincidentally within the circuit integration time. The memory cell integration time was estimated by calculating the critical charge as a function of pulse width. As the pulse becomes wider and exceeds the integration time, the apparent Q_c (total charge in the pulse) increases because significant recovery occurs during the pulse as charge is restored through the associated "on" transistor. For narrow pulses, Q_c is independent of pulse width. From these data, it was determined that the integration time is on the order of 1 ns for the SOS memory cell circuits.

Given the projected area of the charge collection region in the direction of the beam and the circuit integration time, the probability of getting the required number of coincident particles for upset can be readily determined, since the events obey discrete Poisson statistics. The statistical analysis shows that, due to the required large number of coincident hits, the probability of MEU for the CMOS/SOS device is insignificantly small for the experimental case, even for the end-of-range case where the LET is at a maximum.

NRSEU Analysis

The CUPID codes were used to simulate proton-induced nuclear reaction SEU, based on the calculated critical charge of 250 fC. The Monte-Carlo-based CUPID codes simulate nuclear reactions that occur at random positions in a larger surround volume and keep track of energy deposition within a smaller sensitive volume embedded in the surround volume. The geometry is illustrated in Figure 10. The type of reaction and the identities and energies of the secondary particles emitted are the consequences of simulated events occurring during the cascade and evaporation stages of the nuclear reaction.^{8,9} The resulting residual nuclear fragment is the most important secondary as far as SEUs are concerned. Its charge and mass are determined by the secondaries emitted in the reaction, with the kinetic energy being determined by kinematics.

The sensitive volume is a mathematical artifice whose dimensions are chosen so that the charge generated in the sensitive volume equals the charge collected at the actual junction. For this case, the lateral dimensions were determined by the gate area and the thickness was determined by the silicon epitaxial thickness.

The larger surround volume is assumed to extend 4 microns beyond the sensitive volume on all sides. The

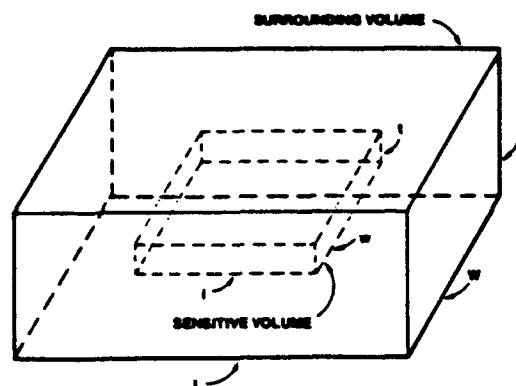


Figure 10. Geometry for Monte Carlo simulation.

contribution from secondary particles emitted from nuclear reactions located more than 4 microns from the sensitive volume is relatively small for upsets requiring a significant critical charge. This results from the reduced probability of the residual nuclear fragment traversing the sensitive volume from large distances and the fact that it would arrive at the sensitive volume after having lost a considerable fraction of its kinetic energy. For this analysis, the configurations used were a $3 \times 4.5 \times 0.5$ micron³ volume, representative of the charge collection volume in a single N-channel transistor of the memory cell. There are 16,384 sensitive volumes on the chip. A $5 \times 5 \times 5$ micron³ volume, typical of the collection volume in a bulk device, is also analyzed for comparison. In both cases, the sensitive volume was centered in the larger surrounding volume extended by 4 microns on each side to represent the material in the substrate or overlayer. The analysis was performed for proton energies in the range from 36 to 200 MeV.

The calculated results for 200 MeV protons are given in Figure 11 for the SOS volume and Figure 12 for the typical bulk volume. The ordinate represents the cross section per bit for events in which the charge generated in the sensitive volume exceeds the value given by the abscissa. Charge is converted from energy at 3.6 eV/carrier pair. The analysis was run until a statistically significant number of events were recorded at the calculated Q_c of 250 fC. Figure 11 shows an SEU cross section of approximately 10^{-14} cm² at $Q_c = 250$ fC. There is a sharp decline for higher Q_c as the required energy deposition in the thin epitaxial silicon layer begins to exceed that available from the secondary particles. For the comparative bulk case shown in Figure 12, the effect of the larger volume can be seen with a cross section of approximately 10^{-13} cm² at $Q_c = 250$ fC.

The effect of proton energy on the upset cross section for $Q_c = 250$ fC is shown in Figure 13 for the thin and thick volumes. The shapes of the two curves are quite different. There is a large drop in the cross section, as

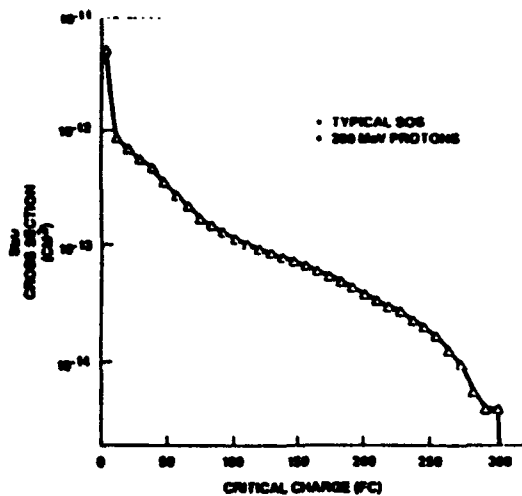


Figure 11. Integral upset cross-section versus critical charge for $3 \times 4.5 \times 0.5$ micron³ volume.

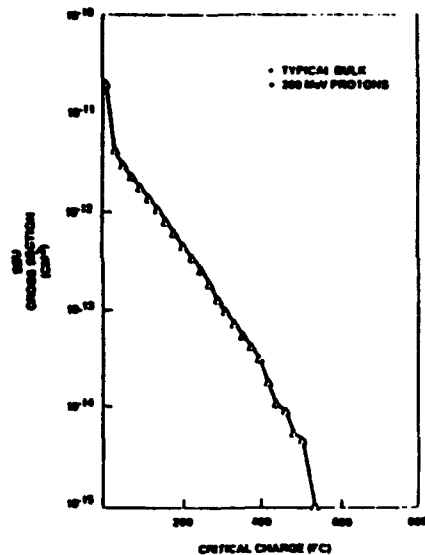


Figure 12: Integral upset cross-section versus critical charge for $5 \times 5 \times 5$ micron³ volume.

proton energy decreases, for the thick volume that is absent for the thin volume.

An unusual feature of the data is the fact that the thick and thin cross sections differ by less than a factor of two at 36 MeV despite the tenfold difference in thickness. (For the 40 MeV proton beam, the energy loss in the package lid resulted in an energy of 36 MeV at the chip.) The effect was examined further by repeating the 36 MeV simulations for both volumes with no surround. The integral cross section versus energy deposition spectra are compared in Figure 14. Here the ratio of the total number of events should go as the ratio of the volumes, as it does. It is much easier to deposit larger energies in larger volumes and Figure 14 shows the curves diverge quickly

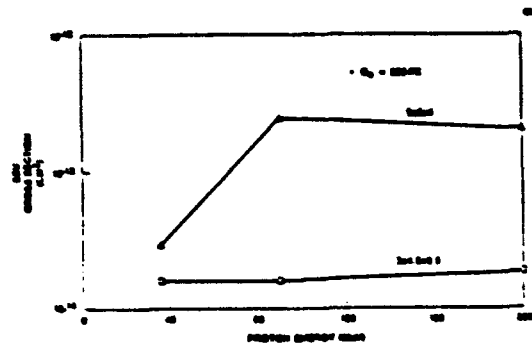


Figure 13. Calculated upset cross-section versus proton energy.

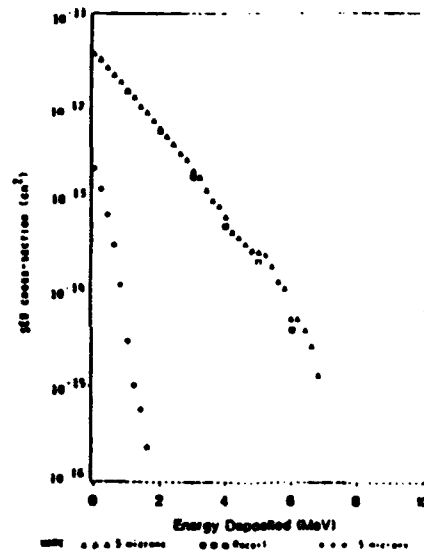


Figure 14. Cross-section versus energy deposited by nuclear recoil alone compared to total energy deposited (for no surround material) for 36 MeV proton.

as expected. The results suggest that all of the large energy events initiate outside the sensitive volume. The integral cross section versus the energy deposited by the nuclear recoil alone in the larger volume is plotted as squares in Figure 14 for comparison with the integral cross section versus the total energy deposited. Obviously, the recoiling nuclear fragment dominates over all other values of the energy deposited up to 6.0 MeV.

RESULTS AND DISCUSSION

No upset (SEU or dose rate) was seen in the Harris 16 K RAM (65C262RH) and one part survived a total dose of 5×10^5 rad(Si). This device has feedback resistors in the memory cell which raise the critical charge for

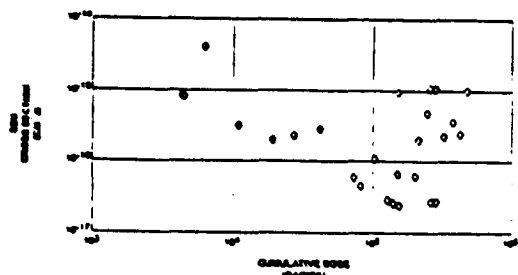


Figure 15. Measured RCA RAM upset cross section versus cumulative dose.

upset to values beyond what can be generated by any nuclear reaction. No SEU cross-section measurements were obtained on the unhardened IDT RAMs (IDT-6116) because all parts either suffered global dose rate upset (scrambled memory) or failed permanently. For the hardened IDT RAMs (IDT-6116RH), both global dose rate upset and SEU was seen. The SEU cross-section measurements ranged from $1.9 \times 10^{-8} \text{ cm}^2/\text{bit}$ to $3.9 \times 10^{-10} \text{ cm}^2/\text{bit}$. No dose rate upset was seen in either of the CMOS/SOS 16 K RAM types — the RCA 6167 or the Marconi MA-6116 — however, SEU was seen. The SEU cross-section measurement ranged from $3 \times 10^{-17} \text{ cm}^2/\text{bit}$ to $4 \times 10^{-15} \text{ cm}^2/\text{bit}$ for the 13 RCA devices tested and ranged from $5 \times 10^{-17} \text{ cm}^2/\text{bit}$ to $3 \times 10^{-16} \text{ cm}^2/\text{bit}$ for the 7 Marconi devices tested.

The data do not indicate any total dose enhancement of the SEU cross-section as can be seen by comparing the upset cross-section results for multiple measurements on 13 RCA devices with increasing cumulative dose as shown in Figure 15. Upsets were seen at cumulative dose as low as 4 krad for the RCA devices and as low as 16 krad for the Marconi devices. These upsets occurred at cumulative dose levels well below the dose failure levels.

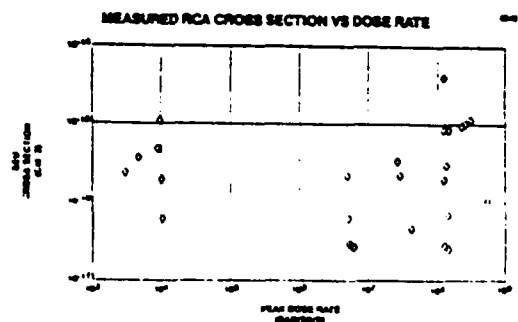


Figure 16. Measured RCA RAM upset cross section versus dose rate.

Having eliminated total dose effects as a likely contributor to the observed upsets, the next issue to be considered is the possibility of dose rate or MEU effects. This was approached experimentally by determining the upset cross section as a function of dose rate. No global upset was seen in the CMOS/SOS devices; this result is consistent with the reported dose rate upset level of 10^{10} rad/s for the device. The possibility of "weak" memory cells was eliminated by observing that the same memory cell location never repeated an upset in subsequent exposures; the location of the SEUs appeared to be random.

The possibility of MEU effects was eliminated by observing no dose rate dependence of the upset cross section. This is shown in Figure 16 for the RCA devices and Figure 17 for the Marconi devices, where the peak dose rate during the microstructure is determined based on the nominal parameters from Table 1. For some anomalously large micropulses, the peak dose rate could be a factor of 3 to 4 higher, as discussed above. The data are shown for multiple measurements on 13 RCA devices and 7 Marconi devices. For 3 of the Marconi devices, no upsets were observed before failure due to total dose effects. Analysis of the MEU probability for the RCA memory cell indicated that there should be a strong dependence on dose rate. For example, the worst-case predictions for probability of MEU show a reduction of approximately 7 orders-of-magnitude as the flux is varied from 10^{15} to $10^{10} \text{ p/cm}^2\text{-s}$. However, the upset cross-section versus dose rate shown in Figure 16 shows an essentially constant value over the range of $10^{16} \text{ p/cm}^2\text{-s}$ ($6 \times 10^8 \text{ rad/s}$) to $5 \times 10^9 \text{ p/cm}^2\text{-s}$ ($3 \times 10^2 \text{ rad/s}$). A similar lack of dependence of upset cross-section on dose rate is shown in Figure 17 for the Marconi RAMs. The results shown in Figures 16 and 17 convincingly demonstrate that the upsets were not due to the MEU effect.

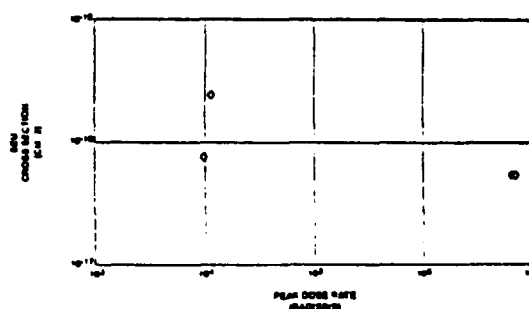


Figure 17. Measured Marconi RAM upset cross section versus dose rate.

The above analysis of the test results suggests that nuclear reaction-induced SEU is the probable cause of the observed upsets. The results of the Monte Carlo calculation can be compared to the experimental measurement for the RCA device. The SPICE analysis indicated that the critical charge for upset was approximately 250 fC. The calcula-

tion results shown in Figure 13 for proton energies of 36, 90 and 200 MeV, respectively, indicate an upset cross section of approximately $2 \times 10^{-14} \text{ cm}^2$ over the energy range for $Q_c = 250 \text{ fC}$. Only a slight increase in Q_c results in a large drop in the upset cross section as shown in Figure 11. The measured data in Figure 16 show an upset cross section ranging from mid 10^{-17} to mid- 10^{-15} cm^2 ; however, from the steep drop off in the cross section with increasing Q_c , it can be seen that the modeling predictions are in reasonable agreement with the measurements if Q_c is assumed to be slightly higher. For example, a 10 percent increase in Q_c (0.275 pC) causes the predicted cross section to drop by more than an order-of-magnitude to approximately 10^{-15} cm^2 , in agreement with the measurements. Considering the accuracy to which the critical charge can be calculated and the poor statistics in the experimental data, the Monte Carlo prediction results appear to be consistent with the experimental measurements.

These results point out that caution should be exercised in concluding that insulated substrate technologies such as SOS or SOI are inherently insensitive to SEU without taking steps to increase the critical charge. For other device technologies which have larger charge collection volumes such as bulk MOS or bipolar, and also have sufficiently low critical charges, nuclear-reaction-induced SEU could be an even more significant upset mechanism.

ACKNOWLEDGMENT

The support of Dr. James Young in the development of the SPICE models and the support of James Blandford, Jr. in the MEU modeling is gratefully acknowledged. Much credit goes to Brian Christensen for his laborious analysis of the test data. The support of the facility crews at the REF, Brookhaven National Laboratory and the Harvard Cyclotron is greatly appreciated. Special thanks go to Dr. Tom Ward at Brookhaven for his support through several difficult test sessions.

REFERENCES

1. Nichols, D.K., et al., "Single Event Upset in Semiconductor Devices—A Summary of JPL Test Data," *IEEE Trans. Nucl. Sci.*, Vol. NS-30, No. 6, p. 4520, December 1983.
2. Pickel, J.C. and B.L. Christensen, "Modeling and Analysis of Neutral Particle Beam Weapon Effects in Microelectronic Circuits," Final Report under P.O. 3616 to Questron Corporation in Support of AF Contract F04704-86-C-0060, September 1987.
3. Missile Guidance Electronics NPBW Vulnerability Study, Questron Corporation Final Report for Contract F04707-86-C-0060.
4. Ward, Tom, Brookhaven National Laboratory, Private Communication.
5. Koehler, Andy, Harvard Cyclotron Laboratory, Private Communication.
6. Pridmore, J.S., et al., "An SEU Hardening Technique for CMOS Static RAMs," *Journal of Radiation Effects*, 1986.
7. Amatea, R., "Interline Resistance of SOS due to Radiation," RCA Memorandum, April 1985.
8. Farrell, G.E. and P.J. McNulty, *IEEE Trans. Nucl. Sci.*, NS-29, 2012, 1982.
9. Petersen, E.L., *IEEE Trans. Nucl. Sci.*, NS-27, 1494, 1980.

APPENDIX P

**PROTON AND HEAVY-ION UPSETS
IN GaAs MESFET DEVICE**

PROTON AND HEAVY ION UPSETS IN GaAs MESFET DEVICES

T.R. Weatherford, L. Tran
SFA Inc.
1401 McCormick Drive
Landover, MD 20785

W.J. Stapor, E.L. Petersen, J.B. Langworthy, D. McMorrow
Naval Research Laboratory
4555 Overlook Avenue SW
Washington, DC 20375-5000

W.G. Abdel-Kader, P.J. McNulty
Department of Physics and Astronomy
Clemson University
Clemson, SC 29634-1911

ABSTRACT

Proton and heavy SEU data has been obtained for devices made by several GaAs MESFET manufacturers. Proton energy dependence and proton and heavy ion upset cross sections are reported. Measurements of charge collection from latches designed with various gate widths show that charge collection depths appear deeper than the 1 μm depth expected. Critical charge does not scale linearly with area. Proton upset cross sections are reduced with increased device width.

INTRODUCTION

The opportunity to use digital GaAs integrated circuits (ICs) in spacecraft applications has improved vastly in recent years. Costs have reduced, yields and densities improved, and several suppliers are offering not only memories, but also gate array and standard cell options. GaAs ICs provide a significant reduction in power dissipation and a magnitude improvement in clock speeds over silicon ECL devices. GaAs ICs also operate at speeds not yet available with BiCMOS technology devices. Even though BiCMOS does provide considerable power savings for the performance, these circuits may be hampered by low total dose hardness and possible latchup susceptibility. All of these technologies appear to have high SEU vulnerability due to small device capacitances required for high performance.

SEU experimental data has been reported previously on a few GaAs integrated circuits including, a JFET SRAM,[1,2] E/D MESFET logic,[3] and a HBT shift register.[4] This work updates the GaAs SEU database with respect to proton, neutron and heavy ion radiation. This work benchmarks several GaAs FET processes and designs including gate arrays, standard cells and memories. Gate arrays incorporate a single gate design which is modified for

different logic functions while standard cells use different gate designs for various logic functions. This work also examines the effects of device width on critical charge.

Previous work has shown GaAs SEU sensitivity to be higher than initially expected from circuit simulation.[5] Experiments have shown enhanced charge collection and also sensitive areas larger than device dimensions.[6] This work examines some possible explanations for high vulnerability in GaAs MESFET logic.

Parts from four foundries were examined. Table I gives a description of the devices tested. Foundry A provided a 1K SRAM, standard cell and a gate array design; the devices are fabricated in an enhancement/depletion (E/D)

Table I - Experimental Devices.

Foundry	Technology	Devices
A	MESFET	SRAM gate array std cell
B	MESFET	SRAM std cell
C	MESFET recess gate	custom/ std cell
D	JFET	SRAM

MESFET process. The 1K SRAM was examined for proton energy and flux dependent upset cross section, neutron upset cross section and heavy ion upset cross section.

Table III - Trends showing improvements with capacitive techniques in JFET SRAMs.

JFET SRAM Design	Cell Capacitance (fF)	Q _e Improvement Estimate	Soft Error Rate Improvement	
			Heavy Ion Estimate	Proton Measured
Standard	50	1		1
MIS	300	6	36	28
Diode (p-n)	550	11	121	118

at Brookhaven National Laboratory Tandem Van de Graaff. Effective LETs ranged from 0.76 MeV/(mg/cm²) to 9.35 MeV/(mg/cm²). Laser irradiations were performed at the Naval Research Laboratory with a 600 nm source. An alpha emitting radioactive source (²⁴¹Am) at Clemson University was used to determine collection depths.

SIMULATIONS

The test chip incorporating the various gate widths and the circuit hardening approach was simulated for critical charge using GAASPICE.[8] I-V and gate characteristics from depletion and enhancement FETs were used to develop parameters for the GAASPICE device model. The appropriate FETs, enhancement driver widths (30 μm) and depletion loads of the standard sized cell were scaled by a factor of two and three to model the 60 μm and 90 μm gate widths of the larger latches.

CUPID [9] was run to predict a critical charge from the measured proton upset cross sections. Measurements of collection depth were used as input with assumptions from previous work on determining the sensitive area. An integral charge spectrum is produced from the simulation from which a critical charge can be obtained from a measured upset cross section or visa-versa.

RESULTS AND DISCUSSION

Proton and heavy ion upset measurement results are shown in Table II. Results are shown for 61 MeV proton upset cross section, heavy ion onset LET and saturated upset cross section with the respective calculated soft error rates. Heavy ion and proton error rates were calculated for a 600 nmi orbit at an inclination of 63°. Heavy ion upset rates in this orbit are about one half that of geosynchronous. Proton

rates were calculated using the two parameter Bendel model whenever more than one proton energy cross section could be acquired, otherwise the one parameter model was used.[10,11] Heavy ion rates were calculated from the upset cross section curves with an estimation of collection depth for each process (The heavy ion error rate was not strongly dependent on the range of estimated collection depths). The four vendors are referred as 'A' through 'D' in the first column.

Figure 1 shows the proton energy dependence on upset cross section of the 'A' SRAM. The measured neutron cross section is also plotted on this graph. The observed 60 MeV neutron upset cross section is approximately a factor of 2 larger than the 60 MeV proton upset cross section. The neutron upset cross section is consistent with the general behavior of neutron reaction cross sections in this energy region. The Bendel one and two parameter model is fitted

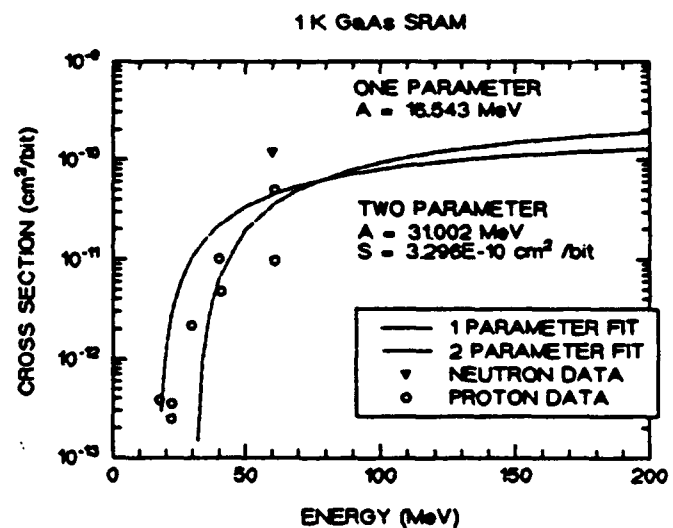


Figure 1. Proton and neutron upset cross sections versus energy for 1K GaAs MESFET SRAM. Also shown are one and two parameter Bendel model fits to the proton data.

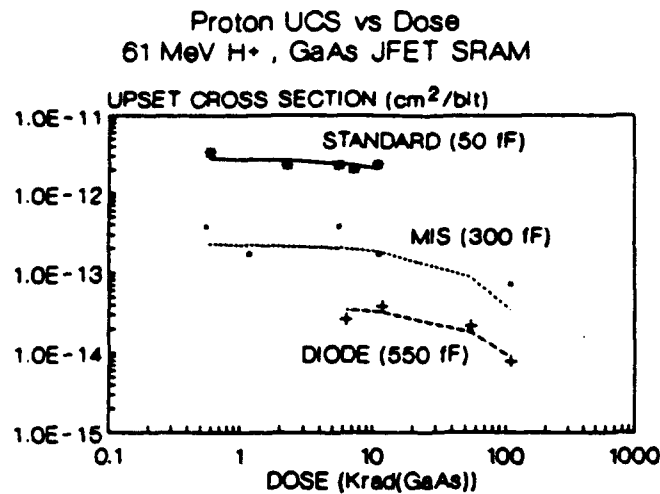


Figure 3. Proton upset cross section versus total dose for a 1K C-E/JFET GaAs SRAM. Results from standard memory and two capacitive hardening techniques are shown.

sections of a resistive decoupled E-JFET cell are comparable to the upset cross section measured for the capacitive hardened cell incorporating the p-n diode when the different proton energy upset cross sections are taken into account.[12,13] It should be noted that both the resistive and capacitive techniques do provide improved SEU immunity but at a significant loss of memory write times (> 50 ns).

A standard cell circuit incorporating latches of varying gate widths was examined from foundry D. The four latches are defined as 30 μ m HD, 30 μ m, 60 μ m, and 90 μ m; corresponding to a 30 μ m gate width circuit hardened latch, a 30 μ m gate width standard latch, a 60 μ m gate width latch and a 90 μ m gate width latch. The circuit hardening approach of using D-FETs to decouple the inverters has been described in other work.[5] The results of proton upset cross section, LET data, CUPID simulations, SPICE predicted critical charge and laser irradiation is shown in Table IV.

The standard cell part was examined under alpha particles to calculate charge collection depth. Each collection event corresponds to a specific particle energy and thus an

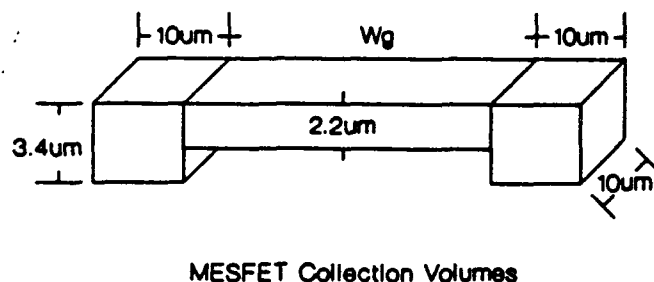


Figure 4. The sensitive charge collection volumes used in the CUPID simulations for the varied GaAs MESFET gate width latches.

appropriate particle range. A collection depth is associated with each peak in the energy spectrum data. Two energy peaks were observed which would correspond to depths of 2.2 μ m and 3.4 μ m. This data suggests charge collection by diffusion or funneling can occur to depths greater than 1 μ m when a minimum field exists on the unbiased FET. The field in the unbiased FET is due to the built-in gate junction field (a biased FET has an increased field due to a positive drain voltage, therefore collected charge in the depleted regions of the FET would expected to be larger in the biased case). These results show suggest larger collection depths that previously presented.[2,14] This value is comparable to a diffusion length in the semi-insulating substrate. The diffusion length can vary widely by the substrate and channel doping. The diffusion length l is defined in Equation 1, where D is diffusivity, and τ is the carrier lifetime. The channel depth

$$l = \sqrt{D \cdot \tau} \quad (1)$$

is less than 0.2 μ m, therefore the majority of diffusion should occur in the substrate where D is approximately 220 cm^2/s for electrons in an undoped substrate. The electron lifetime in the substrate is approximately 10 ns.[15] This corresponds to a diffusion length of 14.8 μ m, larger than the measured collection depth. If the calculated collection depth of 2.2 μ m (corresponding to a direct hit on the gate-to-drain) is used with the threshold LET of 1.5 MeV/(mg/cm²) this corresponds to 57.9 fC, very close to the predicted SPICE value of 57.8 fC. The SPICE simulation uses an exponential pulse with a fall time of 250 ps. Calculations by Hughlock et al. [3] suggest charge collection occurs within 0.3 ns. The SPICE simulation shows the reversal of logic nodes to occur at 0.5 ns. Approximately 86% of the charge has been collected at the drain from the exponential shaped pulse at 0.5 ns. Settling of the logic levels occurs at approximately 2 to 3 ns. These results do suggest charge collection may be deeper than previously expected.

The calculated upset parameters of this device are presented in Table IV. The increase in of critical charge with gate width is shown by four methods in the table. SPICE simulations were used to determine a critical charge from circuit parameters. A critical charge was produced from CUPID simulations using the measured proton upset cross sections. Specifications for the collection volumes are shown in Figure 4. Onset LET was measured from heavy ion experiments. Laser-induced charge collection measurements are shown normalized in the fourth column under calculated critical charge in Table IV. The measured proton upset cross sections are shown in Table IV with cross sections predicted from CUPID using SPICE calculated critical charges as inputs(values are in parenthesis in Table IV). Figure 5 shows the trend of critical charge with gate width.

Soft Error Rates for various technologies

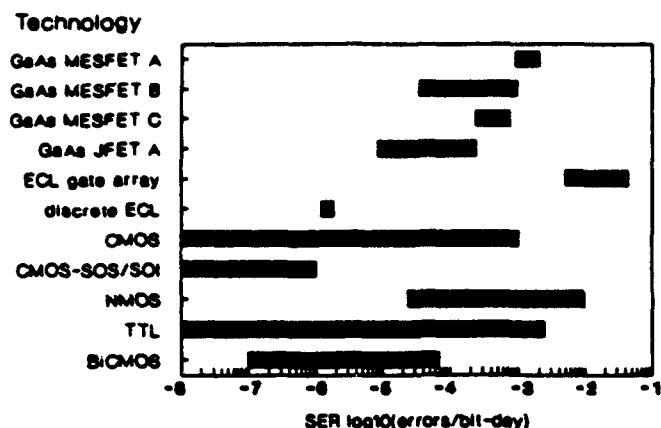


Figure 6. Soft error rate (SER) comparison for several device technologies. These results are calculated for an orbit which contains protons and heavy ions.

ACKNOWLEDGEMENTS

The authors would like to acknowledge Al Knudson, and Art Campbell for helpful discussions. Jim Mann and Dave Wilson assisting in performing experiments. We also thank Barry Hughlock and George LaRue of Boeing for providing the gate width test latch. We would like to thank the Naval Center for Space Technology for funding this work. We also appreciate assistance from Vitesse, Unisys, Martin Marietta, Gigabit Logic, McDonnell Douglas, Triquint, and DARPA.

REFERENCES

- [1] P. Shapiro, A.B. Campbell, J.C. Ritter, R. Zuleeg, and J.K. Northoff, "Single Event Upset Measurements of GaAs E-JFET RAMs," *IEEE Trans. on Nucl. Sci.* Vol. NS-30, No. 6, December 1983.
- [2] R. Zuleeg, J.K. Northoff, D.K. Nichols, "SEU of Complementary GaAs Static RAMs Due to Heavy Ions," *IEEE Trans. on Nucl. Sci.* Vol. NS-31, No. 6, December 1984.
- [3] B.W. Hughlock, G.S. LaRue, and A.H. Johnston, "Single-Event Upset in GaAs E/D MESFET Logic," *IEEE Trans. on Nucl. Sci.*, Vol. 37, No. 6, December 1990.
- [4] J.F. Salzman, P.J. McNulty, and A.R. Knudson, "Intrinsic SEU Reduction from Use of Heterojunctions in Gallium Arsenide Bipolar Circuits," *IEEE Trans. on Nucl. Sci.*, Vol. NS-34, No. 6, December 1987.
- [5] T.R. Weatherford, J.R. Hauser, S.E. Diehl, "Comparisons of Single Event Vulnerability of GaAs SRAMs," *IEEE Trans. on Nucl. Sci.*, Vol. NS-33, No. 6, December 1986.

- [6] P.J. McNulty, W. Abdel-Kader, A.B. Campbell, A.R. Knudson, P. Shapiro, F. Binea, and S. Roonild, "IEEE Trans. on Nucl. Sci., Vol. NS-31, No. 6, December 1984.
- [7] P.J. McNulty, W.J. Beauvais, D.R. Roth and J.E. Lynch, "Determination of SEU Parameters of CMOS SRAMs by Charge Collection Measurements on Working Devices," to be published in this issue.
- [8] J.M. Golio, J.R. Hauser, and P.A. Blahy, "A Large-Signal GaAs MESFET Model Implemented on SPICE," *IEEE Circuits and Devices*, September 1985, 1,21.
- [9] P.J. McNulty, G.E. Farrell, W.P. Tucker, "Proton-Induced Nuclear Reactions in Silicon," *IEEE Trans. on Nucl. Sci.*, Vol. NS-28, No. 6, December 1981.
- [10] W.J. Stapor, J.P. Meyers, J.B. Langworthy, and E.L. Petersea, "Two Parameter Bead Model Calculations for Predicting Proton Induced Upset," *IEEE Trans. on Nucl. Sci.*, Vol. NS-37, No. 6, December 1990.
- [11] W.L. Bendel and E.L. Petersea, "Proton Upsets in Orbit," *IEEE Trans. on Nucl. Sci.*, Vol. NS-30, No. 6, December 1983.
- [12] R. Zuleeg, "Radiation Effects in GaAs FET Devices," *Proc. of the IEEE*, Vol. 77, No. 3, March 1989.
- [13] S.E. Diehl, A. Ochoa, P.V. Drenthorfer, R. Koga, and W.A. Kolasinski, "Error Analysis and Prevention of Cosmic Ion-Induced Soft Errors in Static CMOS RAMs," *IEEE Trans. on Nucl. Sci.*, Vol. NS-29, No. 6, December 1982.
- [14] M.A. Hopkins and J.R. Srouer, "Charge Collection Measurements on GaAs Devices Fabricated on Semi-Insulating Substrates," *IEEE Trans. on Nucl. Sci.*, Vol. NS-31, No. 6, December 1984.
- [15] S.M. Sze, "Physics of Semiconductor Devices," John Wiley & Sons, 1981, pg. 851.
- [16] B.W. Hughlock, personal communication.
- [17] L.D. Flesser, "Gate Charge Collection and Induced Drain Current in GaAs FETs," *IEEE Trans. on Nucl. Sci.*, Vol. NS-32, No. 6, December 1985.
- [18] A.R. Knudson, A.B. Campbell, D. McMorro, S. Buchner, K. Kang, T.R. Weatherford, V. Srinivas, G.A. Swartzlander Jr., and Y.J. Chen, "Pulsed Laser-Induced Charge Collection in GaAs MESFETs," *IEEE Trans. on Nucl. Sci.*, Vol. 37, No. 6, December 1990.
- [19] Y. Liu, R.W. Dutton, M.D. Deal, "Sidegating Effect of GaAs MESFETs and Leakage Current in a Semi-Insulating GaAs Substrate," *IEEE Elec. Dev. Lett.*, Vol. 11, No. 11, November 1990.
- [20] D.C. D'Avanzo, "Proton Isolation for GaAs Integrated Circuits," *IEEE Trans. Electron Devices* Vol. ED-29, No. 7, 1051 July 1982.

APPENDIX Q

QUANTITATIVE COMPARISON OF SINGLE EVENT UPSETS INDUCED BY PROTONS AND NEUTRONS

QUANTITATIVE COMPARISON OF SINGLE EVENT UPSETS INDUCED BY PROTONS AND NEUTRONS

Eugene Normand
Boeing Defense & Space Group
P. O. Box 3999, MS 2T-50
Seattle, WA 98124

William J. Stapor
Naval Research Laboratory
Washington, D. C. 20375-5000

Peter McNulty, W. G. Abdel-Kader and M. H. Yaktieen
Clemson University
Seneca, South Carolina 29678

Abstract

The SEU susceptibility of microchips induced by neutrons and protons has been examined on both experimental and theoretical grounds. Experimental energy deposition spectra in surface barrier detectors by 14 MeV neutrons are compared against theoretical predictions based on considering individual neutron reactions and using ENDF-V cross sections. These results are compared with recent SEU measurements on 3 RAM devices made separately with 67 MeV neutrons and protons.

Introduction

Single event upsets (SEUs) in microchip devices can be caused both directly, by high energy charged particles, and indirectly, by secondary reaction products generated by the interaction of incoming particles with atoms in the chip [1]. These incoming particles may be protons or neutrons. This has been demonstrated both theoretically [1] and experimentally [2].

The purpose of this paper is to examine the SEU susceptibility induced by neutrons and protons quantitatively, and more accurately than has been done previously. The intention is to allow SEU cross section data made with sources of both particle types to be used in concert. On the theoretical end, the early comparison made by Ziegler [1] used old and coarse cross section data. The later results obtained by C. H. Tsao et al [3,4] apply only to the integration of the upset model with specific energy spectra of incident particles. We will utilize the up-to-date proton interaction model developed by McNulty [5-7] and combine it with the improved neutron interaction calculations carried out by Normand [8]. On the experimental end, we will examine: a) integral energy deposition spectra in silicon barrier detectors generated by a beam of 14 MeV neutrons and b) older and newer measurements of SEU cross sections in microchip devices

by monoenergetic beams that will allow direct comparisons between induced rates by neutrons and protons.

Neutron and Proton Induced SEU Cross Sections

Compared to measured heavy ion SEU cross section data, there is a very limited set of experimental cross sections for SEU induced by protons [9], and even less for those due to neutrons. The proton measurements are hampered by the limited number of proton accelerator facilities available to perform testing, as well as by cost. Neutron-induced SEU measurements have been made using at least three different types of neutron sources: an accelerator [2], PuBe source [10] and a 14 MeV neutron generator which provides an essentially monoenergetic beam [2,11,12].

SEU measurements using neutrons, especially those made with a 14 MeV generator, have several potential advantages: greater availability, simplicity of operation and lower cost. The major disadvantage is that it provides data at only one energy, 14 MeV, and that energy is relatively low compared to the energies needed for specific applications. Nevertheless, the neutron generator can be very useful for expanding the existing data base of proton-induced SEU measurements. The major obstacle that has limited making additional use of 14 MeV neutron measurements is lack of a firm understanding of the relationship between proton-induced and neutron-induced SEU cross sections. This paper intends to provide a better understanding of that relationship from both theoretical and experimental perspectives.

Surface Barrier Detector Measurements and Predictions

Over the last decade, McNulty and his coworkers have made extensive measurements of the integral energy deposition spectra in silicon surface barrier detectors (SBDs) bombarded by beams of various particles [5-7].

These measurements are important because they allow comparisons to be made with the predictions from various particle interaction models. In a parallel effort, the group developed a computer simulation model that calculates the energy deposited by incoming protons within a microscopic sensitive volume [5-7]. Their calculations have given very good agreement with the SBD measurements [7] and the model has been formalized into the CUPID computer code. The proton-induced nuclear reactions utilized in the code have been described previously [5].

Heretofore, only the SBD measurements made with proton beams have been published [5-7]. However, the same SBD detector system was also used to make a series of measurements using a 14 MeV neutron generator to provide the beam of energetic particles. The results of these measurements will be examined in some detail.

In Figure 1 integral spectra in the same SBD ($5000 \times 5000 \times 2.5 \mu^3$) are compared that result from beams of 14 MeV neutrons and 37 MeV protons. It should be noted that the proton beam isn't truly monoenergetic, having a FWHM of 10 MeV [5]. Furthermore the neutron energy produced by a neutron generator operated at 150 kV (D,T reaction) varies from 13.5-14.7 MeV, depending on the angle of emission [13]. For standard irradiation configurations, such as used in the SBD measurements, the neutrons strike the target essentially head on, hence the energy is 14.7 MeV, that for 0° emission angle. Throughout this paper neutrons from a 14 MeV generator will be regarded as having an energy of 14.7 MeV.

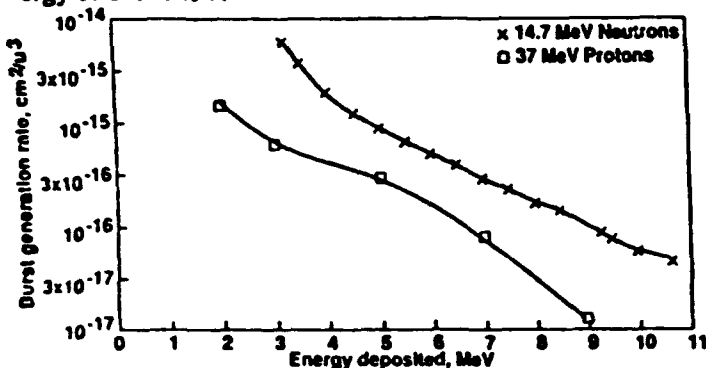


Figure 1. Comparison of Burst Generation Rate Measured in 2.5μ Thick Silicon Barrier Detector by 14 MeV Neutrons and 37 MeV Protons.

The SBD data has previously been presented as the number of events per incident number of protons incident on a volume of specified size, in which energy above a threshold level has been deposited by the reaction products [5]. We reformulated it into the form of the burst generation rate, BGR or $B(E_p \text{ or } E_n, E_r)$, in units of $\text{cm}^2/\text{micron}^3$ [1]. The BGR is the partial macroscopic cross section that quantifies the rate at which secondary reaction products of energy E_r or greater, are produced by incoming protons of energy E_p or neutrons of energy E_n .

From Figure 1 it is evident that for energy deposition > 3.2 MeV, the 14.7 MeV neutron beam deposits

at least 3 times as much as energy as the 37 MeV proton beam. The 14.7 MeV neutron energy deposition spectrum begins at 3.2 MeV due to limitations of the neutron generator facility that was used. It required that a discriminator setting of 3.2 MeV be used in order to avoid spurious counts.

The CUPID code was able to predict the energy deposition spectrum by protons very well [7], however it was not designed to model neutron interactions. In the most recent approaches for neutrons [3,8,14], the BGR has been calculated in two different ways, depending on the energy of the neutron. For neutrons with $E_n < 20$ MeV, the detailed neutron cross section data of the ENDF-V library have been used [8]. For neutrons with $E_n > 50$ MeV, a probabilistic approach has been used, based on calculations with the HETC code [14]. For energies in between, extrapolations or interpolations have been used [8].

To calculate the energy deposition spectra induced by 14.7 MeV neutrons in a SBD such as the results in Figure 1, we utilized the approach in [8] based on the neutron cross section data from the ENDF-V library [15]. In this approach we account for each individual neutron-silicon reaction separately and sum up the contributions. As indicated in [8], for those reactions in which a charged particle is emitted, e.g., the (n, α) reaction, energy deposition results from both the heavy and light reaction products, in this case the Mg recoil and the alpha respectively. Because the sensitive volume is so large in the SBD, compared to the depletion region of a typical memory device, the energy deposited by the light reaction product is very significant. This can be seen in Figure 2 where we have plotted the energy deposited by a 14.7 MeV neutron in the (n, α) reaction as a function of the scatter angle. This is predicated on a scatter point on the centerline of an SBD having dimensions of $5000 \times 5000 \times 4.2 \mu^3$. The α particle has a limited range (about 55 - 80 μ), depending on the energy it emerges with after the reaction (8.35-11.7 MeV). Since the scatter angle is directly related to the α particle's energy through the reaction kinematics, the scattering angle is vital in determining how much of its energy the α deposits within the sensitive volume.

By focusing on the energy deposition spectrum above 4 MeV, we only have to consider three reactions, namely (n, α), (n,p) and (n,d) in order to calculate the energy deposition spectrum. None of the other 6 reactions can deposit 4 MeV. Figure 3 shows the total energy deposited by the (n,p) reaction for the same configuration as Figure 2. Because the range of protons is so much larger than that of alpha particles (about 620 - 850 μ for proton energies ranging between 9.17 - 10.84 MeV), the deposition is very narrowly peaked. Only (n,p) reactions with scatter angles nearly 90° will produce long enough path lengths to deposit most of the proton energy. Energy deposited by the (n,d) reaction is similar but midway between the two, less peaked than the (n,p) curve but not as broadened as the (n, α) curve.

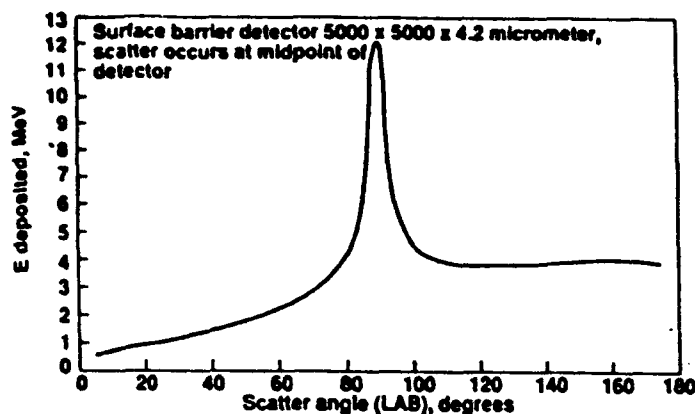


Figure 2. Energy Deposition from (n,α) Reaction by 14.7 MeV Neutrons in 4.2 μ Thick Surface Barrier Detector As a Function of Scatter Angle.

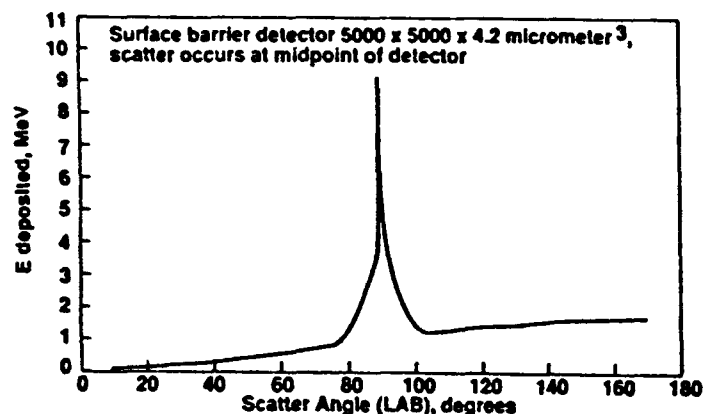


Figure 3. Energy Deposition from (n,p) Reaction by 14.7 MeV Neutrons in 4.2 μ Thick Surface Barrier Detector As a Function of Scatter Angle.

Using the energy deposition curves such as Figures 2 and 3, and assuming that all three differential reaction cross sections are isotropic with scatter angle, we can calculate the combined burst generation rate. This is shown in Figure 4 along with the measured values obtained by the McNulty group for the same size SBD. The agreement is quite good. In these calculations the vast majority of the energy deposited is from the (n,α) reaction.

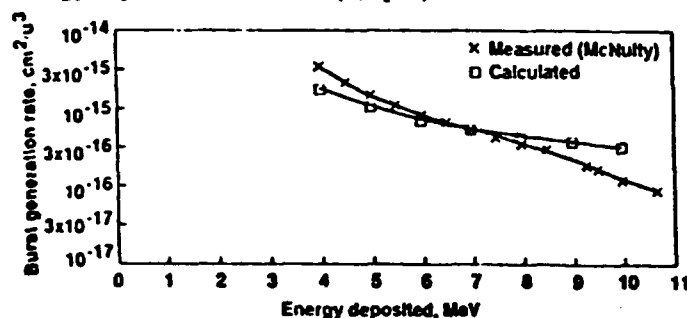


Figure 4. Comparison of Calculated and Measured Burst Generation Rate in 4.2 μ Thick Silicon Barrier Detector by 14.7 MeV Neutrons.

The good agreement between the calculated and measured burst generation curves means that our simplified model based on an interaction point along the SBD centerline is valid. Since the SBD is so thin, in this case 4.2 micrometers, compared to the alpha particle range, moving the interaction point up or down should not affect the calculated result very much. The overprediction for large energy depositions is attributed to the lack of isotropy in the actual (n,α) differential cross section. These large energy depositions are due to (n,α) reactions of almost 90°. While we haven't found measured (n,α) differential cross sections in silicon for 14.7 MeV neutrons, we have found such data for aluminum [16], and it is shown in Figure 5. Neutron behavior in aluminum and silicon are very similar, and so Figure 5 will be applied to silicon. From Figure 5 we see that the (n,α) differential cross section is peaked in the forward and backward directions, and is smallest for scatter angles between 60° - 120°. Thus our simplified model overestimates the almost 90° (n,α) contributions.

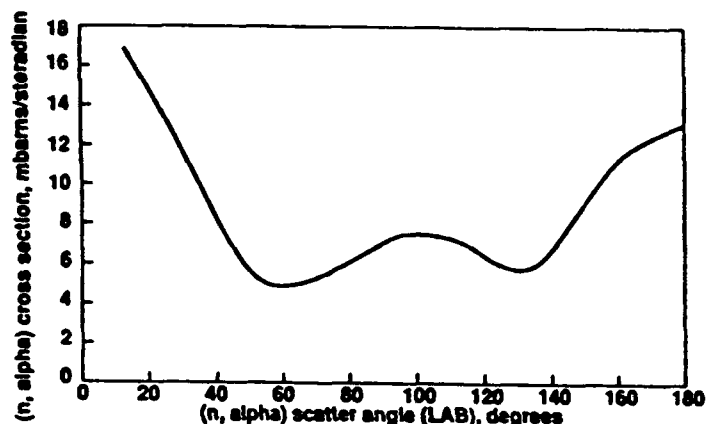


Figure 5. Variation of the (n,α) Differential Cross Section in Aluminum As a Function of the Scatter Angle.

As indicated, energy deposition by the alpha particle is the dominant mechanism and it is appreciable even for path lengths of half or a third of the alpha particle range. In our model the energy deposition is treated in the manner of Burrell and Wright [17]. Following [17], the range for each particle type is obtained as a function of energy in the form of the 3-parameter fit for parameters a, b and r.

$$R = (a/2b) \ln(1 + 2bE^r) \quad (1)$$

An initial particle of energy E, on traversing a distance x, deposits energy ΔE

$$\Delta E = E - [(E' - \alpha) / \beta]^{1/r} \quad (2)$$

where

$$\beta = \exp(2bx/a) \quad \text{and} \quad \alpha = (\beta - 1)/2b \quad (3)$$

The McNulty group measured integral energy deposition spectra by 14.7 MeV neutrons in a series of SBDs. The surface barrier detectors had the same cross section but different thicknesses. According to our simplified model of a single interaction point at the center and isotropic differential interaction cross sections, the energy deposition is proportional to the \cos (scatter or interaction angle). For a path length just contained within the SBD, the \cos (angle) is proportional to the half-thickness of the SBD, i. e., $\cos(\text{angle}) = (1/2) \cdot \text{Range}$ (see Inset in Figure 6). To test the validity of this model we have plotted the measured energy deposition cross sections for the four different SBD thicknesses, 2.5, 4.2, 25 and 50 μ , as a function of the SBD thickness, and normalized the cross sections to that for the 50 μ SBD. Such normalized cross sections are plotted in Figure 6 for three different energy depositions. If the simplified model is valid, the normalized cross sections should be proportional to the ratio of the SBD thickness. Figure 6 indicates that the simplified model is generally valid, but the actual energy deposition is more complex. Complications arise for SBD's which are thick compared to the alpha particle range, because the single interaction point is no longer representative, and because of the anisotropy of the differential interaction cross sections.

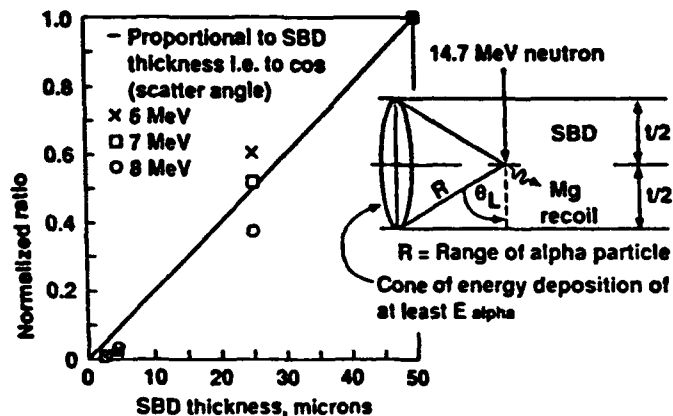


Figure 6. Normalized Ratios for Energy Deposition Cross Sections Measured in Various Thicknesses of SBDs with 14.7 MeV Neutrons.

A better test of the model for a thick SBD is seen in Figure 7 which shows the measured and calculated burst generation rate for a 50 μ SBD. The agreement is considerably poorer than that in Figure 4 for the 4.2 μ SBD. In Figure 7 two calculated curves are shown, one for the interaction point along the centerline of the SBD volume, and one for the interaction point at the top. For the top interaction point we also accounted for the anisotropy of the (n, α) reaction) using Figure 5. Figure 7 shows that for

silicon volumes that are thick compared to the alpha particle range, the energy deposition has to be treated more accurately than our simplified model, e.g., by means of either J. Ziegler's approach in the TRIM code [18] which accounts for range straggling and uses higher order fits to the range, or the Effective Interaction Volume (EIV) model of our earlier paper [8].

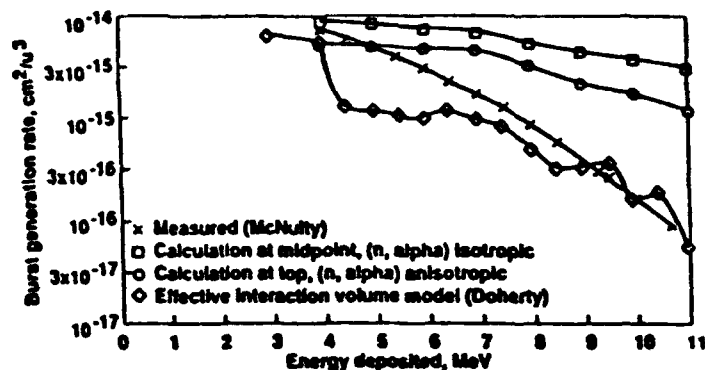


Figure 7. Comparison of Calculated and Measured Burst Generation Rate in 50 μ Thick Silicon Barrier Detector by 14.7 MeV Neutrons.

The EIV model was upgraded and applied to the 50 μ SBD, and the results from such preliminary calculations are shown in Figure 7. While there appear to be some numerical convergence problems, the shape of the curve matches the experimental data much better than the simple model, as would have been expected. The EIV model incorporates the pathlength distribution for the device as a function of angle and integrates over the reaction volume [8] to provide a much better representation of the geometry. The model uses a 5-parameter fit to the range, and in this application, it also included the anisotropy of the (n, α) reaction as shown in Figure 5. We conclude that, despite its limitations, the simplified model gives useful results for many silicon volume configurations of interest, and that the EIV model can be used to improve the predictions for more difficult geometries.

SEU Measurements with Proton and Neutron Beams

The SBD energy deposition spectra, both measured and calculated, are very useful in evaluating the success of our model in predicting the underlying interactions involved. They are limited however, by the fact that the SBD involves a very large volume ($5000 \times 5000 \times 4.2 \mu^3$) of silicon relative to that of the sensitive depletion region volume in a microchip device (often taken as $10 \times 10 \times 5 \mu^3$ [3], but much smaller e.g., $5 \times 5 \times 2 \mu^3$, in some current devices). To compare neutron and proton induced upsets in microchips we will rely primarily on SEU measurements, but at the same time derive some generalizations from the SBD measurements and calculations.

The earliest SEU measurements with neutrons [2]

also made a few measurements with protons on two 16K RAMs. The proton beam was nominally monoenergetic (32 MeV) but most of the neutron measurements were with broad-spectrum neutron beams from a cyclotron. For one RAM, the Motorola MCM 4116L20, measurements were also made with a monoenergetic 14 MeV neutron generator. The resulting SEU cross sections were $1.5\text{E-}12\text{ cm}^2/\text{bit}$ for the 32 MeV protons, and $3.3\text{E-}13\text{ cm}^2/\text{bit}$ for the 14 MeV neutrons.

The higher SEU cross section for protons compared to neutrons from this data is opposite to the SBD measurements in Figure 1 which show the neutron cross section to be higher. However, the geometry of the sensitive volume plays a very important role. We have already shown that in the large volume of the SBD, having dimensions that are large compared to the range of the alpha particle, complete deposition of the alpha particle's energy occurs within the cone of alpha particle deposition, and large energy deposition is also possible outside the cone (see Fig. 6). In the depletion region of a memory device, even for the often-used $10 \times 10 \times 5\text{ }\mu^3$, the dimensions are considerably smaller than the alpha particle range (55 - 80 μ), so most of the energy is deposited by the Mg recoil and the recoils from the other neutron-silicon reactions.

We have made preliminary calculations for 50 MeV protons and 14.7 MeV neutrons interacting with a small $20 \times 20 \times 4.2\text{ }\mu^3$ subvolume, using the CUPID and ENDF reaction cross section methods respectively. For energy deposition up to about 2 MeV, the 14.7 neutrons deposit more energy than the 50 MeV protons. However, the maximum energy the neutron can deposit is 4.2 MeV, and for energy depositions of between 2- 4.2 MeV, the protons contribute more than the neutrons. At 4 MeV, the probability of energy deposition by the protons is about 5 times greater than for the neutrons. Thus, in general terms, we can conclude that for the Motorola part the critical charge was likely to have been about 0.2 pC (equivalent to a critical energy deposition of about 4.5 MeV).

Eleven years later a more careful experiment was carried out specifically to measure the upset cross section in three 1990's vintage RAM devices using separate beams of 67 MeV protons and neutrons (the proton energy was actually 62.5 MeV). This experiment was performed at the UC Davis Cyclotron [19]. The proton upsets were measured first using small increments of fluence on the target device to keep the particle and total dose damage negligible. The results are shown in Table 1 for the three devices: a 16K NMOS SRAM, a 256K bipolar-CMOS RAM and a 1K GaAs RAM. Statistical uncertainties for the proton and neutron measurements were relatively large because few total upsets were observed for each run. In all three cases the per bit neutron upset cross section was larger than that for the protons by a factor of 2 to 10. It was the GaAs device that showed the largest increase, a factor in the range of 5 - 10, between the neutron and proton cross sections.

Simple explanations for the higher neutron upset

	Upset Cross Section, $\sigma_{up}(cm^2/bit)$		
	MDT 6116 NMOS 2K x 8	MDT 71256 BIMOS 32K x 8	Vitesse V833422 1K x 1
62.5 MeV proton	1.82×10^{-14}	3.70×10^{-14}	$1 - 2 \times 10^{-11}$
67.0 MeV neutron	5.81×10^{-14}	7.10×10^{-14}	1.10×10^{-10}
σ_n/σ_p	3.2	1.9	5 - 10

Table 1. Comparison of Neutron and Proton Induced SEU Upset Cross Sections.

cross section are inadequate to explain the large differences. For example, by ignoring the contribution from elastic scattering we can estimate the proton and neutron cross sections for all other reactions in silicon at energies of 62.5 and 67 MeV respectively. We find for silicon that $\sigma_{\text{reaction}} \sim 0.505$ barns for 62.5 MeV protons [20,21], based on silicon and aluminum measurements, and $\sigma_{\text{non-elastic}} \sim 0.55$ barns for 67 MeV neutrons [22]. The neutron/proton ratio of non-elastic cross sections is ~ 1.1 , not nearly large enough to explain the much larger ratio of upset cross sections.

Conclusions

We have examined two sets of measurements, integral energy deposition spectra in SBDs by 14.7 MeV neutrons, and SEU upset cross sections in three RAM devices by both 67 MeV neutrons and protons. The SBD measurements allowed us to evaluate the accuracy of a simplified neutron interaction model, just as McNulty and his coworkers have previously confirmed the applicability of the CUPID proton interaction code against similar SBD measurements [5-7]. We then shifted emphasis from the relatively large silicon subvolumes of the SBDs to the small subvolumes in memory devices. SEU upset cross sections were measured separately with beams of 67 MeV neutrons and protons, and the neutron per bit cross sections were consistently higher. We have not, however, applied the models, CUPID for protons and the ENDF reaction cross section or HETC approaches for neutrons, to calculate the SEU cross sections. To do so would have required additional information, namely the critical charge, Q_c (equivalent to a critical energy deposition), and the sensitive volume for each device in order to calculate the upset rates using the aforementioned modeling codes.

Acknowledgement

The authors wish to thank the following individuals for their assistance: W. R. Doherty for providing the EIV calculations, C. Casteneda for the 67 MeV irradiations, and T. R. Weatherford for the upset measurements in the GaAs RAM.

References

- 1) J. L. Ziegler and W. A. Lanford, "Effect of Cosmic Rays on Computer Memories," Science, **206**, 776, Nov, 1979
- 2) C. S. Guenzer, E. A. Wolicki and R. G. Allas, "Single Event Upset of Dynamic RAMs by Neutrons and Protons," IEEE Trans. Nucl. Sci., **NS-26**, 5048, 1979
- 3) C. H. Tsao, R. Silberberg and J. R. Letaw, "A Comparison of Neutron-Induced SEU Rates in Si and GaAs Devices," IEEE Trans. Nucl. Sci., **NS-35**, 1634, 1988
- 4) R. Silberberg, C. H. Tsao and J. R. Letaw, "Neutron Generated Single Event Upsets in the Atmosphere," IEEE Trans. Nucl. Sci., **NS-31**, 1183, 1984
- 5) G. E. Farrell and P. J. McNulty, "Microdosimetric Aspects of Proton-Induced Nuclear Reactions in Thin Layers of Silicon," IEEE Trans. Nucl. Sci., **NS-29**, 2012, December, 1982
- 6) S. El Teleaty, G. E. Farrell and P. J. McNulty, "Charge-Deposition Spectra in Thin Slabs of Silicon Induced by Energetic Protons," IEEE Trans. Nucl. Sci., **NS-30**, 4394, 1983
- 7) S. El Teleaty et al, "Soft Fails in Microelectronic Circuits due to Proton-Induced Nuclear Reactions in Material Surrounding the SEU-Sensitive Volume," Nucl. Inst. Methods, **B40**, 1300 1989
- 8) E. Normand and W. R. Doherty, "Incorporation of ENDF-V Neutron Cross Section Data for Calculating Neutron-Induced Single Event Upsets," IEEE Trans. Nucl. Sci., **NS-36**, 2349, 1989
- 9) W. J. Stapor et al., "Two Parameter Bendel Model Calculations for Predicting Proton Induced Upset," IEEE Trans. Nucl. Sci., **NS-37**, 1966, 1990
- 10) E. Normand et al, "Use of PuBe Source to Simulate Neutron-Induced Single Event Upsets in Static RAMs," IEEE Trans. Nucl. Sci., **NS-35** 1523, 1988
- 11) R. E. Morgan, "Neutron Induced Upset in the TMS 32020 and 320C25 Microprocessors," Paper presented at the 7th SEE Symposium, Los Angeles, April, 1990
- 12) D. L. Oberg, W. R. Doherty, E. Normand and J. L. Wert, "Test Report for SEU and NSEU Upsets of IDT 7132/7142 Bulk Dual Port RAM and IDT 7130/7140 Epitaxial Dual Port RAM," Boeing Report D180-317-74-1, September, 1989
- 13) J. Csikai, CRC Handbook of Fast Neutron Generators, Vol I, CRC Press, 1987
- 14) J. R. Letaw, "Burst Generation Rates in Silicon and Gallium Arsenide from Neutron-Induced Nuclear Recoils," SCC Report 87-02, Severn Communications Corp, 1987
- 15) R. Kinsey, "ENDF-102, Data Formats and Procedures for the Evaluated Nuclear Data File, ENDF," BNL-NCS-50496, Oct, 1979
- 16) D. I. Garber et al "Angular Distributions in Neutron-Induced Reactions, Volume I," BNL 400, 1970
- 17) M. O. Burrell and J. J. Wright, "The Estimation of Galactic Cosmic Ray Penetration and Dose Rates," NASA TN D-6600, March 1972
- 18) J. F. Ziegler, TRIM-90, "The Transport of Ions in Matter," IBM Corporation, 1990
- 19) K. M. Murray, W. J. Stapor and C. Casteneda, "Calibrated Charged Particle Radiation System with Precision Dosimetric Measurement and Control," Nucl. Instr. and Meth., **A281**, 616 (1989)
- 20) N. H. Kwong and J. Hufner, "The Energy Dependence of Nuclear Reaction Cross Sections," Phys. Letters, **146B**, 370, 1984
- 21) W. F. McGill et al, "Measurements of the Proton Total Reaction Cross Section for Light Nuclei Between 20 and 48 MeV," Phys. Rev., **C10**, 2237, 1974
- 22) R. G. Alsmiller, Jr. et al, "Neutron-Photon Multigroup Cross Sections for Neutron Energies < 400 MeV," ORNL/TM-9801, 1986

APPENDIX R

SOFT FAILS IN MICROELECTRONIC CIRCUITS DUE TO PROTON- INDUCED NUCLEAR REACTIONS IN MATERIAL SURROUNDING THE SEU- SENSITIVE VOLUME

SOFT FAILS IN MICROELECTRONIC CIRCUITS DUE TO PROTON-INDUCED NUCLEAR REACTIONS IN MATERIAL SURROUNDING THE SEU-SENSITIVE VOLUME *

S. EL-TELEATY, P.J. McNULTY **, W.G. ABDEL-KADER and W.J. BEAUVAIS **

Physics Department, Clarkson University, Potsdam, NY 13676, USA

Charge collection in silicon surface barrier detectors resulting from proton-induced nuclear reactions have been measured for a number of incident proton energies with and without various surrounding materials. The results are in agreement with the predictions of the CUPID simulation codes over the range of incident proton energies from 37 to 154 MeV. Proton spallation simulations which ignore the contribution from reactions in the surround can seriously underestimate the SEU rates.

1. Introduction

Proton-induced nuclear reactions are an important source of soft fails or single-event upsets (SEUs) in microelectronic circuits flown on satellites in low earth orbits. If more than a threshold or critical amount of charge is collected at certain reversed-biased n-p junctions on a device, the logic state of the corresponding cell will be changed. The CUPID (Clarkson University proton interactions in devices) codes [1] were developed to simulate proton-induced spallation reactions in well defined silicon microvolumes in order to predict SEU cross sections. They are available in a user-friendly form suitable for running on an IBM-AT-type computer and are beginning to be used to estimate SEU cross sections for devices.

The codes were previously tested by comparing their predictions with the pulse-height spectra obtained in a series of fully depleted surface barrier detectors for a variety of thicknesses [2]. That study confirmed the code's ability to simulate charge generation within a sensitive volume due to spallation reactions within that volume. Unfortunately, simulations for geometries corresponding to real devices show that more than half of the SEU-inducing events result from nuclear reactions occurring outside the sensitive volume [3]. This study provides the first attempt to test the code's ability to handle the charge generated within the sensitive volume as a result of nuclear reactions which occur outside.

CMOS/SOS and CMOS/SOI are technologies that can be accurately represented in the manner of a fully depleted detector, i.e. all the charge of a given sign

generated within the sensitive volume is collected across the junction while the charge generated outside is not. This simplicity results from the SEU-sensitive regions being isolated by either sapphire in CMOS/SOS or SiO₂ in CMOS/SOI. Bulk CMOS, bipolar, and NMOS technologies more closely resemble partially depleted detectors in that the charge collected at the junction includes contributions due to drift from the depletion region, field-assisted drift or funneling from portions of the track just outside the depletion region [4,5] and diffusion of charges from further out [6,7]. These contributions are too complicated to model easily. The currently accepted procedure is to simply increase the thickness of the sensitive volume beyond the depletion region by an amount estimated to be necessary so that the simulated charge generated within the new sensitive volume equals the amount actually collected at the junction [8].

In order to restrict the experimentally observed charge-collection signals to the charge generated within the sensitive volume, fully depleted SBDs were separated from the surrounding material by a small gap in vacuum. This allowed energetic spallation products from reactions in the surround to jump the gap and traverse

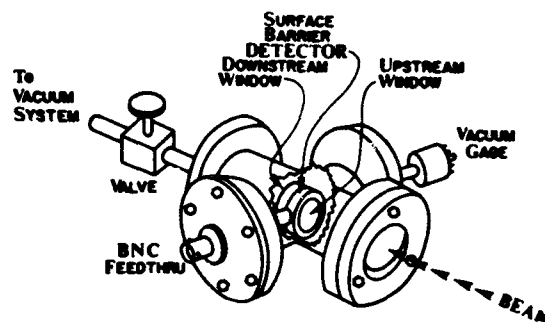


Fig. 1. Schematic diagram of the experimental setup.

* Work supported by the Air Force Geophysics Laboratory and the DNA/DARPA Single Event Radiation Effects Program.

** Now at Clemson University, Clemson, SC 29634-1971, USA.

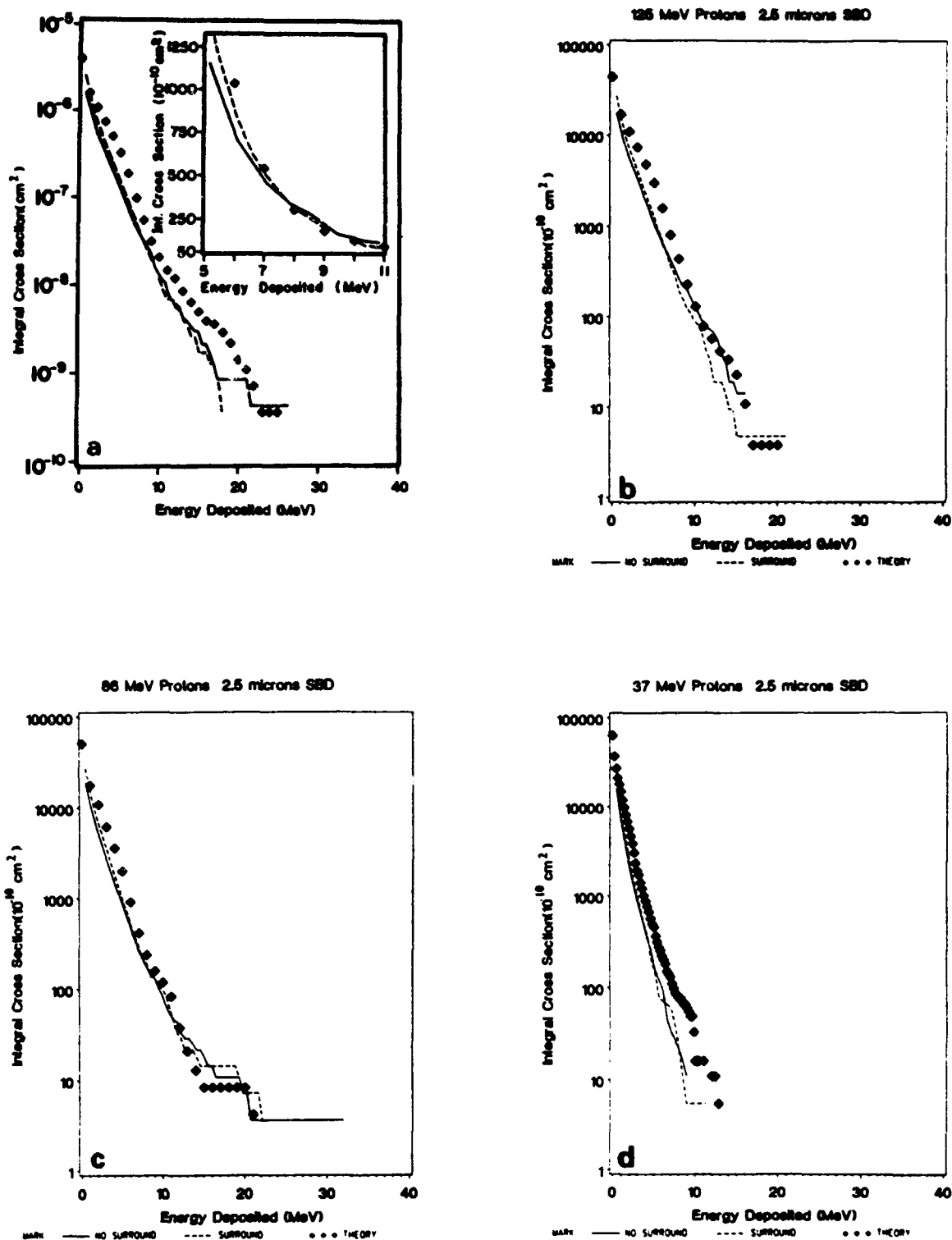


Fig. 2. (a) Pulse height spectra of 154 MeV protons for a 2.5 μm surface barrier detector. Solid line, dashed line and solid diamonds represent the detector without surround, the detector with two slabs of silicon and the theoretical calculation, respectively. In the top right corner are the comparisons with the corrected theoretical calculations for the gap. (b) Comparison between the three sets of data as in (a), with a proton energy of 125 MeV. (c) Comparison between the three sets of data as in (a) with a proton energy of 86 MeV. (d) The comparison between the three sets of data as in (a) with a proton energy of 37 MeV.

XI. DETECTORS/CALIBRATION

the detector, but restricted the electrons collected at the junction to those generated as electron-hole pairs within the detector volume.

2. Experimental procedures

The experimental setup is shown schematically in fig. 1. A surface barrier detector is placed in a vacuum "tee" with slabs of material placed upstream and downstream of the detector. The detector is a fully depleted slab of silicon separated from the surround materials by the ultrathin metallizations which serve as electrical contacts and vacuum gaps of 3.8 mm. The separation ensures that there is no drift or diffusion of charge from the surround to the detector.

Charge generated in the 2.5 μm layer of silicon is collected through the BNC connector to a charge-sensitive preamplifier which in turn feeds through an amplifier to a pulse-height analyzer. Pulse-height spectra were obtained with various materials forming the surround and for different thicknesses of the sensitive volume.

3. Results for a silicon surround

The experimental data are presented in the form of integrated spectra where the cross section for collecting at least some amount of charge is plotted against collected charge. The collected charge is expressed in terms of equivalent energy deposition E where 22.5 MeV is equivalent to 1 pC of collected charge. Figs. 2a-d compare the experimental results for a 2.5 μm thick detector (area = 25 mm^2) surrounded by silicon slabs

(dashed curve) with the corresponding spectra obtained in the absence of surround (solid curve). There is a statistically significant difference between the integral spectra at low-energy depositions but not at large energies.

The effect of the surround would be greater without the introduction of the gap which reduces the solid angle subtended by the detector as seen from points along the trajectory where nuclear reactions are generated in the surround. As a result, a smaller fraction of the recoiling nuclear fragments from the spallations reach the sensitive volume than would be the case if the surround was immediately adjacent to the sensitive volume. This is illustrated in fig. 2 by the standard CUPID simulations which ignore the gap between detector and surround. They predict a significant increase in the spectra (solid diamonds) compared to the no-surround case.

Correcting for the effects of the gap requires some knowledge of the angular distribution of the recoiling nuclear fragments emerging from the spallations. This information can also be estimated from the simulations. The angular distributions obtained from CUPID for protons with incident energies from 37 MeV and 154 MeV are shown in fig. 3. These distributions can be used to calculate the fraction of the recoils that reach the detector. The corrected theoretical spectra are plotted for 154 MeV at the top right corner in fig. 2a. The agreement between the simulations corrected for the gap and the surround data is quite good.

The dependence on the thickness of the sensitive volume is illustrated in fig. 4 which compares the integral spectra obtained experimentally for surface barrier detectors of different thicknesses exposed to 154

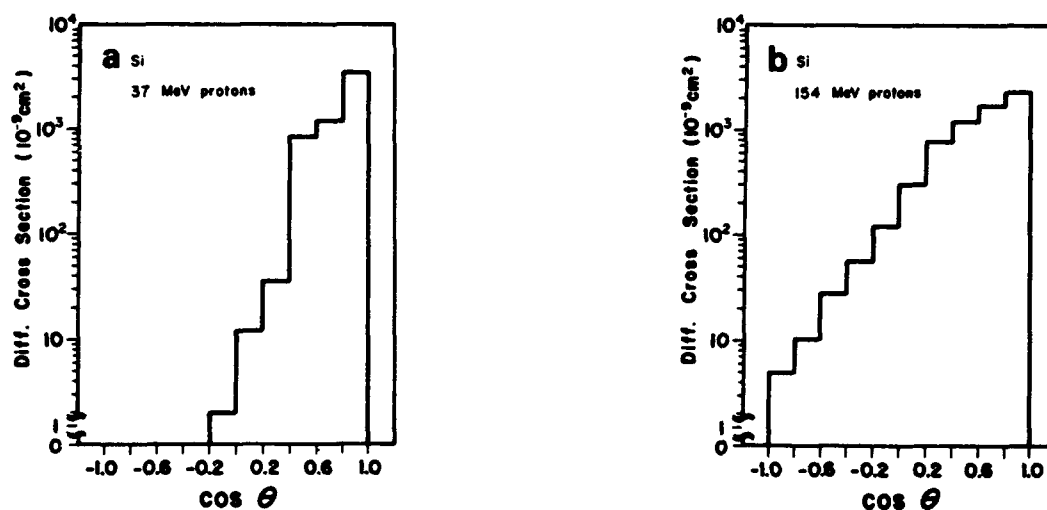


Fig. 3. The angular distribution of the recoil nuclei from nuclear reactions induced by protons incident at (a) 37 MeV and (b) 154 MeV, respectively.

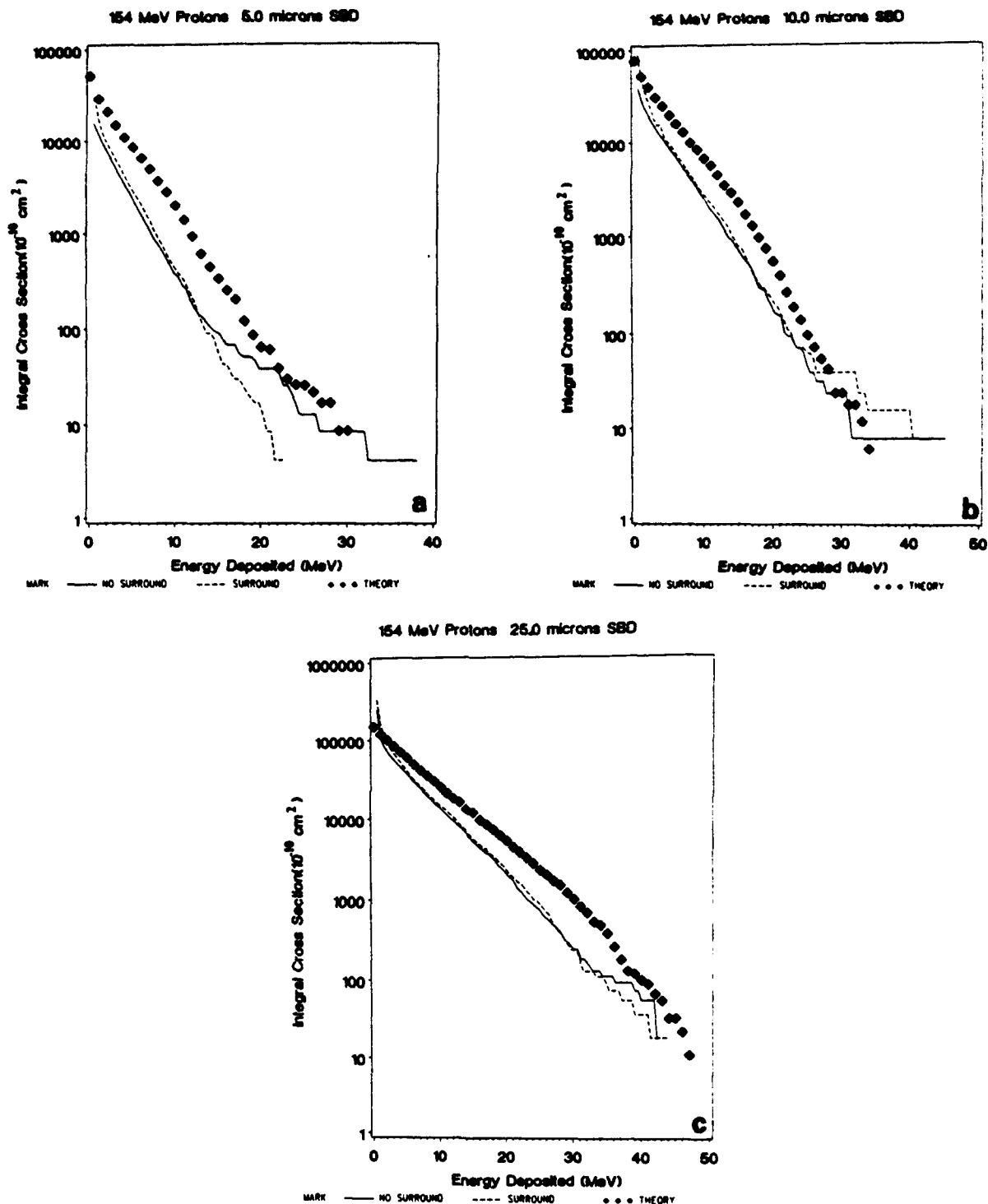


Fig. 4. Comparison between the two experimental measurements and the theoretical calculations similar to fig. 2a for 154 MeV proton exposure on surface barrier detectors with thickness (a) 5 μm , (b) 10 μm and (c) 25 μm , respectively.

MeV protons. The measured effect with the gap is small in all cases compared to what the CUPID simulations predict for the no-gap case.

The effect of nuclear reactions in silicon surrounding a silicon-sensitive volume which has dimensions more typical of devices is illustrated in fig. 5 which compares

XI. DETECTORS/CALIBRATION

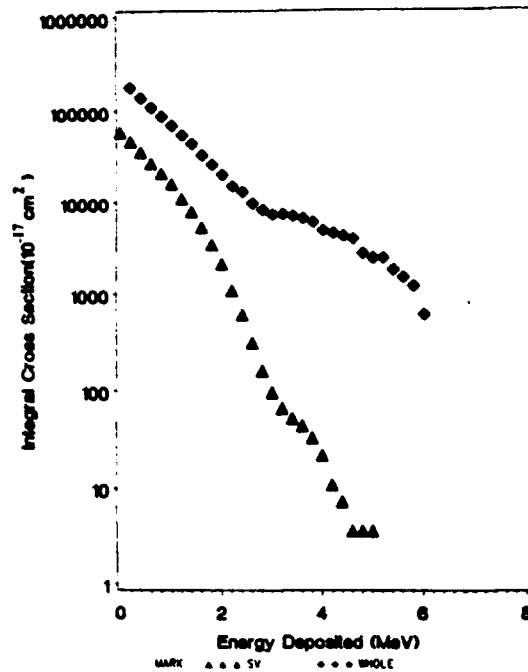


Fig. 5. Integral cross section vs energy deposited with 60 MeV protons incident on a sensitive volume with dimensions of $2 \times 10 \times 1 \mu\text{m}^3$ with and without including reactions in the surround. The solid triangles represent the pulse height spectra obtained from only reactions in the sensitive volume itself. The solid diamonds represent the combined contributions from all the reactions in the sensitive volume and a larger volume extending $4 \mu\text{m}$ beyond each face, i.e. the large volume dimensions are $10 \times 18 \times 9 \mu\text{m}^3$.

simulation results for 60 MeV protons incident on a sensitive volume with dimensions of $2 \times 10 \times 1 \mu\text{m}^3$ with and without including reactions in the surround. The solid triangles represent the pulse-height spectra obtained from only reactions in the sensitive volume itself. The solid diamonds represent the combined contributions from all the reactions in the sensitive volume and a larger volume extending $4 \mu\text{m}$ beyond each face (see fig. 6a). There is predicted almost a doubling of the total cross section due to the presence of the surround and an increase of one or two orders of magnitude predicted for the larger-energy depositions. Ignoring the surround in simulating proton-induced SEU rates therefore, seriously underestimates the true rates, even when the program correctly simulates energy depositions in the sensitive volume itself. The contributions from reactions occurring in the top layer of the surround, the sides and the bottom are shown separately. The majority of surround events are initiated by spallations in the top but the bottom layer is the major source for the

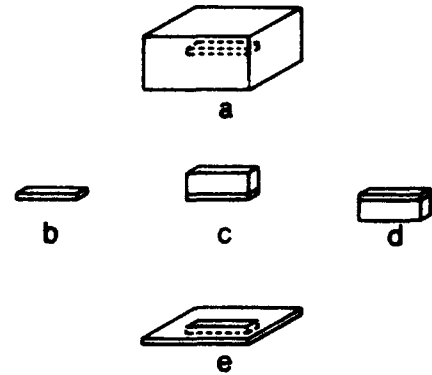


Fig. 6. Schematic diagram representing the possible cases for the surround materials. These cases are: (a) all, (b) sensitive volume (no surround), (c) top, (d) bottom, (e) side.

large-energy depositions necessary to induce upsets in typical circuits.

4. Other materials

If portions of the surround consist of materials of higher atomic weight than silicon, the contribution of the surround will be less, because the heavier recoiling nuclear fragments have less energy to deposit in the

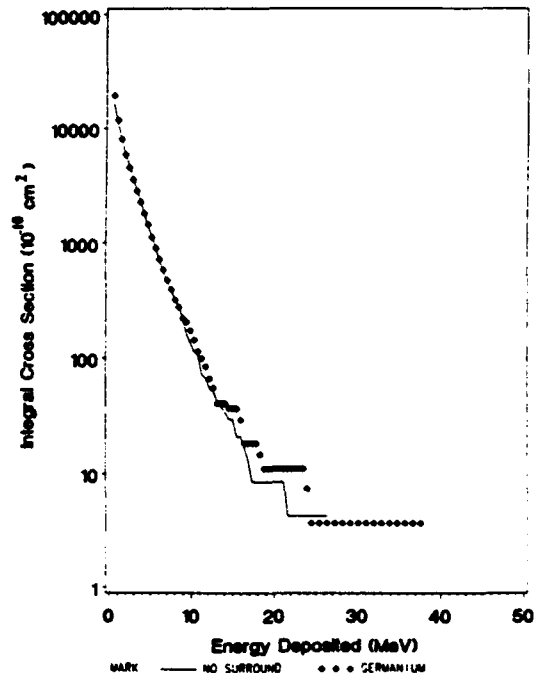


Fig. 7. Integral spectra obtained experimentally with and without surround are compared for the case of the same $2.5 \mu\text{m}$ silicon detector and germanium surround with 154 MeV incident protons.

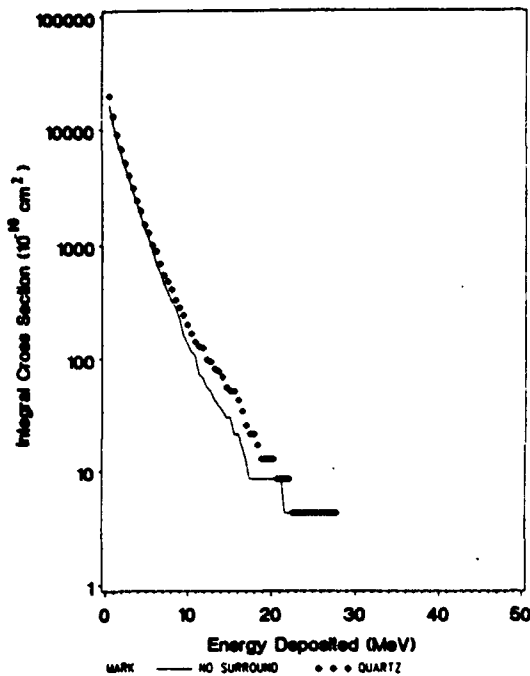


Fig. 8. Integral spectra obtained experimentally with and without surround are compared for the case of the same 2.5 μm silicon detector and quartz surround with 154 MeV incident protons.

sensitive volume. This is illustrated in fig. 7 where the integral spectra obtained experimentally with and without surround are compared for the case of the same silicon detector and germanium surround. No significant differences are observed.

Materials of lower atomic weight, on the other hand,

produce recoils with higher energies which can deposit more energy in the sensitive volume. Fig. 8 shows a small effect seen experimentally in the surface barrier detector when the sensitive volume is surrounded by quartz.

5. Summary and conclusions

CUPID simulations predict a contribution to the pulse-height spectra measured in a surface barrier detector due to spallation reactions occurring outside the sensitive volume which is roughly the same as the contribution from reactions occurring within the sensitive volume.

References

- [1] G.E. Farrell and P.J. McNulty, *IEEE Trans. Nucl. Sci.* NS-29 (1982) 2012.
- [2] S. El-Teleaty, G.E. Farrell and P.J. McNulty, *IEEE Trans. Nucl. Sci.* NS-30 (1983) 4394.
- [3] G.E. Farrell, P.J. McNulty and W.G. Abdel-Kader, *IEEE Trans. Nucl. Sci.* NS-31 (1984) 1073.
- [4] C. Hu, *IEEE Electron Devices Lett.* EDL-3 (1982) 31.
- [5] F.B. McLean and T.R. Oldham, *IEEE Trans. Nucl. Sci.* NS-29 (1982) 2018.
- [6] S. Kirkpatrick, *IEEE Trans. Electron Devices* ED-26 (1979) 11.
- [7] G.A. Sai-Halasz and M.R. Wordeman, *IEEE Electron Devices Lett.* EDL-1 (1980) 10.
- [8] P.J. McNulty, W. Abdel-Kader and J.M. Bisgrove, *IEEE Trans. Nucl. Sci.* NS-32 (1985) 4180.

APPENDIX S

SINGLE AND MULTIPLE PROTON-INDUCED NIEL EVENTS IN SILICON

SINGLE AND MULTIPLE PROTON-INDUCED NIEL EVENTS IN SILICON

L. Chen, P.J. McNulty, and W. G. Abdel-Kader
Department of Physics and Astronomy
Clemson University
Clemson, SC 29634-1911

T.L. Miller, and D. A. Thompson
Federal Systems Division
Eastman Kodak Company
901 Elmgrove Rd.
Rochester, NY 14650

ABSTRACT

Computer simulations of proton-induced spallation reactions predict the deposition of as much as 200 KeV of non ionizing energy loss (NIEL) within the active regions of CCD pixels as the result of individual spallation reaction interactions. Peaks in the NIEL -deposition spectra correspond to the recoils of different nuclear fragment isotopes. The increase in pixel dark current from such events is a design constraint for the use of CCDs in satellite communications, hyperspectral imaging and other applications which require low noise imaging. Individual pixels can be functionally impaired from single-event NIEL even with minimal exposure, contributing both transient signals and permanent changes in the performance of specific pixels. At high fluence, the spallation reactions will be responsible for at least half the increased pixel noise and dominate the shape of the measured noise spectra. Calculations show good agreement with previously measured spectra. We presently are evaluating the effects of such reactions, as generated by alpha particles, on bare KAF-0400 CCDs from Eastman Kodak.

Displacement damage in silicon in or near the depletion regions of reverse-biased junctions results in increased noise currents across the junction. Measurements with protons have involved high proton fluence where the noise appears to increase gradually with continued exposure (1-3). The damage and the induced dark current are proportional to the Non-Ionizing Energy Loss (NIEL) deposited in the sensitive volumes associated with the junctions (4). Individual spallation events can generate significant amounts of NIEL within individual pixels of CCDs, CIDs, and similar photometric devices which suggest that, for low noise applications such as satellite communication and hyperspectral imaging, the amount of dark current generated by a single spallation reaction may interfere with reliable pixel function.

The CUPID simulation codes have been used extensively to predict the kinematics of proton-induced spallation reactions. In calculations, all secondary particles are followed to determine the energy deposition by the incident proton and all secondaries within the sensitive volume. The sensitive volume has microscopic dimensions typical of the sensitive volumes associated with the junctions of modern microelectronic circuits. The agreement between measured charge-collection spectra and CUPID simulations for surface-barrier particle detectors (5) and SRAM memories (6) give some confidence in the code's ability to predict the kinematics of the nuclear interaction with silicon as the target nucleus and to determine the subsequent energy loss in the sensitive volume. The code was modified to calculate the NIEL component of the energy deposition and record it so that the displacement damage and the consequent noise currents could be predicted.

Figure 1 is a plot of the ionization loss and the NIEL components of the LET as a function of the particle's incident energy. The NIEL is concentrated at low ion energies near the end of the particle's range. As a result, the NIEL measured for a given ion species doesn't depend strongly on the incident energy as long as the particle stops in the active region of the detector and the active region is large enough to contain the portion of the trajectory with significant NIEL. This is illustrated in Fig. 2 where the NIEL spectra are shown for different thicknesses of the sensitive volume. The peaks become pronounced as the thickness increases. These simulated spectra do not take the accumulated effect of exposure of the pixels in an array where the effects of elastic scatters and multiple spallation events must be taken into account.

To examine these effects, the code was modified to distribute the spallation events randomly among the pixels of an array of 10,000 pixels. Figure 3a shows the NIEL spectra for the spallation reactions following an exposure of $1.4 \times 10^{11} \text{ cm}^{-2}$. Each pixel has experienced the average of more than ten spallation reactions. There is only a slight hint of the peaks due to the different isotopes. Each pixel would also have been subject to hundreds of elastic scattering events with very little energy transfer per event. Figure 3b shows the effect of including the elastic and inelastic events in one spectrum. The peak position has shifted considerably compared to Fig. 3a, suggesting that the total NIEL has roughly equal contributions from elastic and inelastic interactions. However, the shape of the spectrum is determined by the spallation reactions alone.

Figure 4 compares the simulation spectrum with the experimental measurements of Marshall et al (3) carried out with a silicon CID circuit exposed to protons incident at 63 MeV. The measured and calculated spectra were normalized to the same total number of events. The simulations are in excellent agreement with the measured spectrum. Marshall et al (3) were able to fit their spectrum with a statistical approach valid when the mean number of spallation reactions exceeds ten. The current model is not restricted to high multiple spallation events. The final paper will include predictions of the NIEL spectra for a range of fluence from the region where there is less than one per pixel up to ten or more. These predictions will be compared with the results of the measurements currently being made on the Kodak CCDs, where the device and model geometry are similar.

REFERENCES

1. J.R. Srour, S.C. Chen, S. Othmer, and R.A. Hartmann, "Radiation Damage Coefficients for Silicon Depletion Regions" IEEE Trans. Nucl. Sci. NS-26, 4784 (1979)
2. E.A. Burke, "Energy Dependence of Proton-Induced Displacement Damage in Silicon", *ibid.* NS-33, 1276 (1986).
3. P.W. Marshall, C.J. Dale, and E.A. Burke, "Proton-Induced Displacement Damage Distributions and Extremes in Silicon Microvolumes", *ibid.* NS-37, 1776 (1990).
4. G.P. Summers, E.A. Burke, C.J. Dale, E.A. Wolicki, P.W. Marshall, and M.A. Gehlhausen, "Correlation of Particle-Induced Displacement Damage in Silicon," IEEE Trans. Nucl. Sci. NS-34, 1134 (1987).
5. P.J. McNulty, G.E. Farrell, and W. P. Tucker, *ibid.* NS-28, 4007 (1981).
6. P.J. McNulty, D.R. Roth, W.J. Beauvais, W.G. Abdel-Kader, and D.C. Ding, "Comparison of the Charge Collecting Properties of Junctions and the SEU Response of Microelectronic Circuits", Int. J. Radiat. Instrum., Part D, Nucl. tracks Radiat. Meas. 19, 929-938 (1991).

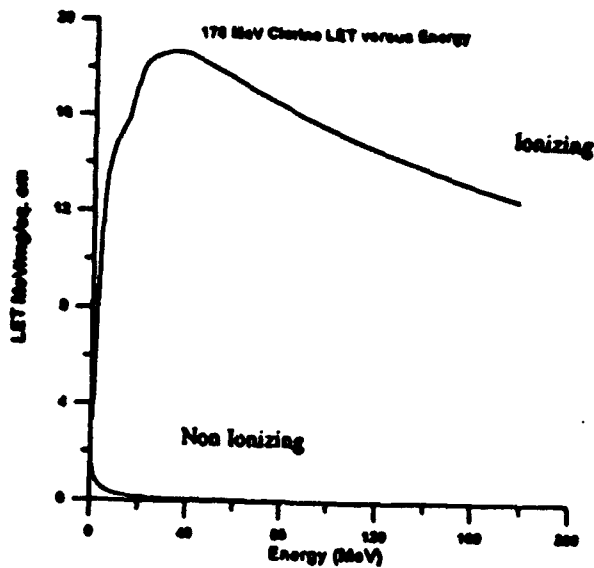


Fig. 1. Plots of the ionization loss and the non ionizing energy loss components of the LET as a function of incident energy.

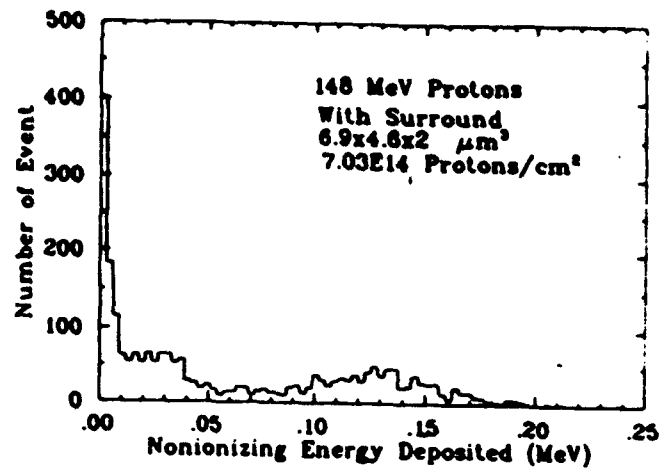


Fig.2a

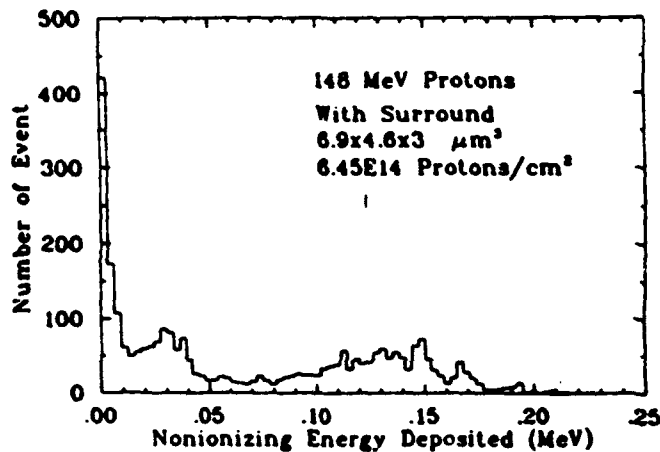


Fig.2b

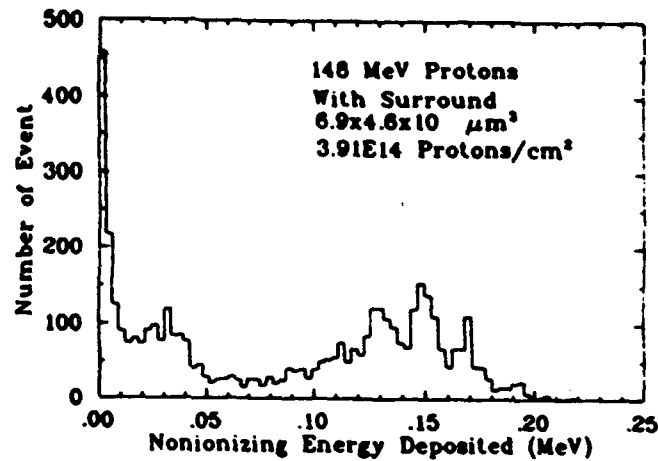


Fig.2c

Fig.2. Number of events versus the non ionizing energy loss per event for sensitive volume with the same but different thickness exposed to the same number of protons. The thickness are $2 \mu\text{m}$, $3 \mu\text{m}$, $10 \mu\text{m}$.

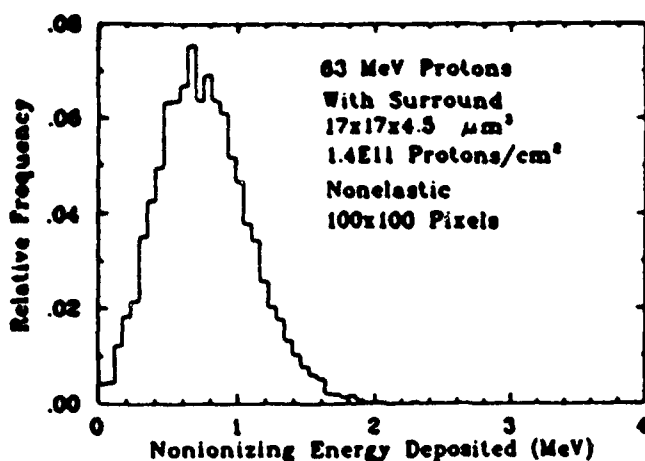


Fig.3a

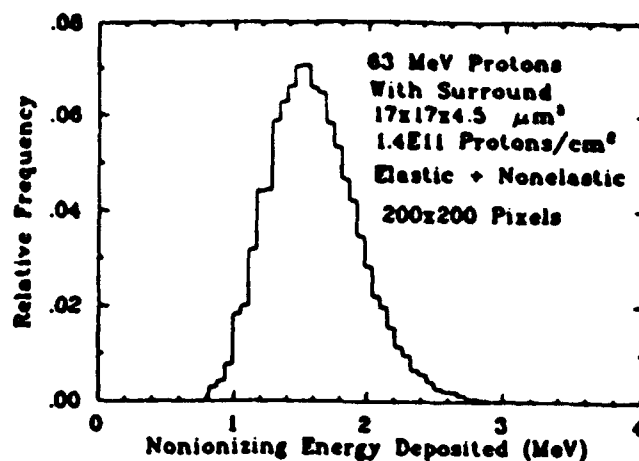


Fig.3b

Fig3. Multiple event NIEL spectra for an array of 200x200 pixels exposed to a proton fluence of $1.4 \text{E}11 \text{ cm}^{-2}$, a) Spallation reactions only, b) Elastic scattering reactions and spallation reactions.

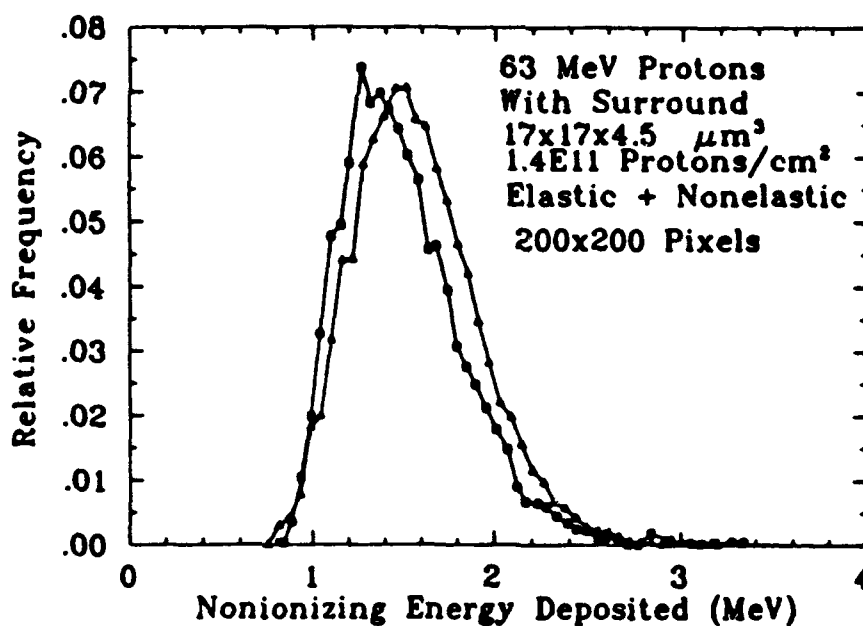


Fig.4. Comparison of the simulation spectrum with the experimental measurements of Marshall et al(3) carried out with a silicon CID circuit exposed to protons incident at 63 Mev. Square represents experimental data and triangle represents calculation data.

APPENDIX T

SIMPLE MODEL FOR PROTON-INDUCED LATCH-UP

SIMPLE MODEL FOR PROTON-INDUCED LATCH-UP

P.J. McNulty, W.G. Abdel-Kader, and W.J. Beauvais
Clemson University, Clemson SC 29634-1911
and

L. Adams, E.J. Daly, and R. Harboe-Sorensen
ESA-ESTEC, Noordwijk, Netherlands

ABSTRACT

Computer simulations show that the strong angular dependence exhibited by proton-induced single-event latch-up can be explained by a simple mechanism. Latch-up occurs if, and only if, more than some threshold amount of energy is deposited within the sensitive volume. A procedure for determining the SEU parameters by comparing SEU cross sections and CUPID simulations at different incident energies and angles of incidence is described. The thickness of the sensitive volume and the value of the critical charge determined for the NEC 4464, a 64 Kbit CMOS SRAM, agrees with the measured thickness of the p-well and the value of the threshold LET determined with heavy ions.

INTRODUCTION

Proton-induced Single Event Latch-up (SEL) is a recent phenomena first observed when modern commercial microelectronics were flown in orbits that intercept the inner radiation belts (1,2). This paper outlines a simple model for SEL that strongly resembles the First-Order Model for single event upsets (3). The model assumes that there is a sensitive volume associated with each memory cell and of the energy deposited (*i.e.* charge generated) within the sensitive volume contributes to the probability of an upset while none of the charge deposited outside the sensitive volume contributes. A latch-up occurs if, and only if, more than some threshold amount of energy is deposited within the sensitive volume. This model provides a simple explanation for the large increase in the proton-induced SEL cross section with increasing angle of incidence (2). The sensitive volume for SEL is, in general, different than the sensitive volume associated with SEU, and the amount of energy which must be deposited to initiate an SEL is different than the value required for SEU in the same device. For the NEC 4464 it is slightly smaller. The value of the critical charge (in pC) required for latch-up can be obtained, as for SEU, from the threshold energy (in MeV) by dividing the latter by 22 MeV/pC.

Procedures are described for determining the SEL parameters, the dimensions of the sensitive volume and the value of the critical charge, by comparing the measured SEL cross sections with CUPID simulations (4) at different incident energies and angles of incidence. For the NEC 4464, the area of the sensitive volume was already known from

measurements of SEL cross sections with fission fragments and heavy ions (5). It remained to determine the thickness of the sensitive volume and the threshold energy. This requires a minimum of two SEL measurements, in this case data was available at an incident energy of 60 MeV, at normal and grazing incidence (2).

CUPID SIMULATIONS OF SPALLATION REACTIONS

The CUPID simulation model (4,6) is used in what follows to apply the model to the test data for the NEC 4464, a 64 Kbit SRAM known to latch-up in space, and for which proton and heavy-ion test data exist. The standard output of CUPID is a plot of the cross section for depositing at least energy ϵ versus ϵ . Such a plot is labeled "all" in Fig. 1 for 60 MeV protons incident on a sensitive volume typical of some devices. Also included for comparison are calculations of the cross sections for events in which the recoil or secondary alphas deposit at least energy ϵ . Clearly, it is the recoil which is responsible for most of the large localized energy depositions which initiate SEL and SEU events.

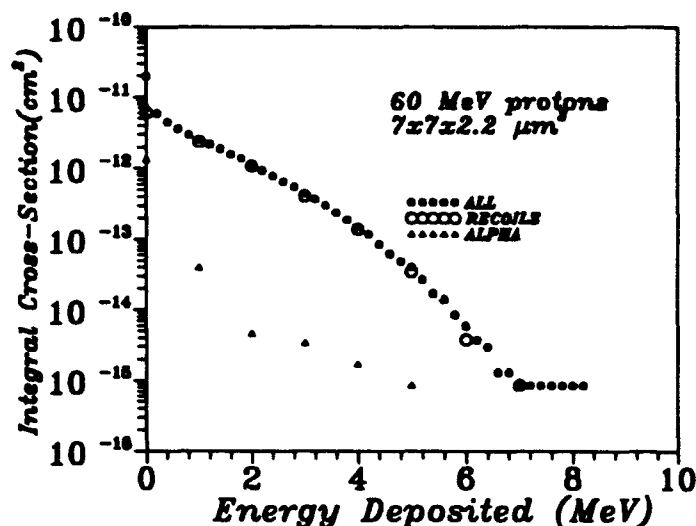


FIGURE 1. Cross section for depositing at least energy ϵ versus ϵ for 60 MeV protons incident on a sensitive volume of silicon having dimensions of 7 μm x 7 μm x 2.2 μm surrounded on all four sides by a thickness of 4 μm. Plots are drawn for the relative contributions from all charged secondaries, the recoiling nuclear fragments alone, and the secondary alphas alone.

The dominance of the nuclear recoil mandates a closer look at the kinematics of the recoiling nuclear fragments. Figure 2 is the energy spectrum for the fragments recoiling after spallation reactions induced by 60 MeV protons incident on silicon target nuclei. The nuclear fragment can sometimes recoil with a significant fraction of the incident proton's energy, something not possible in elastic interactions. The recoil has a very short range and deposits all its energy locally.

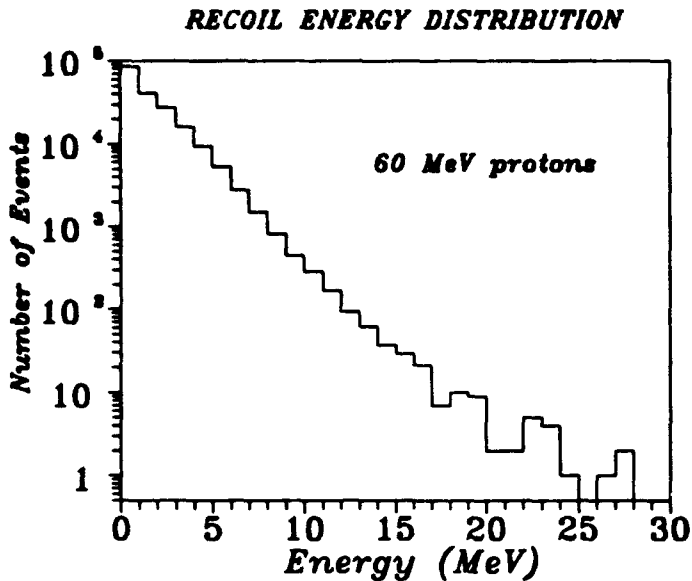


FIGURE 2. Energy spectrum of the residual nuclear fragments recoiling after spallation reactions induced by 60 MeV protons incident on silicon target nuclei.

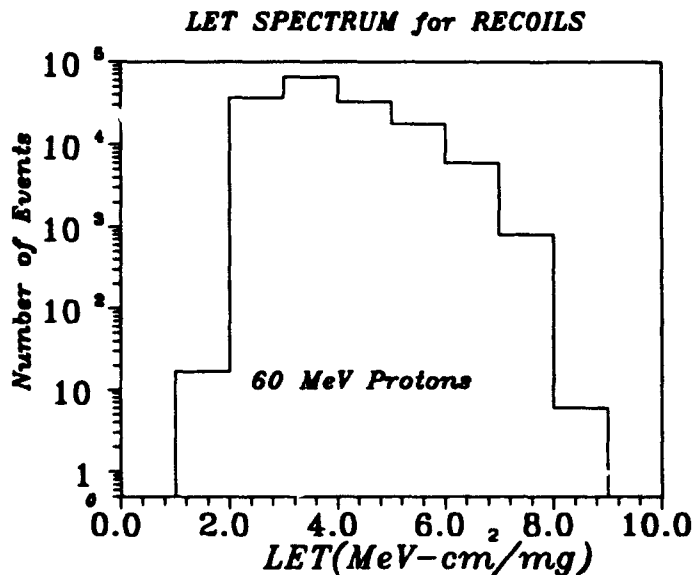


FIGURE 3. Average LET for the recoiling nuclear fragments following spallation reactions between 60 MeV protons and silicon target nuclei.

The value of the LET of these recoils change rapidly as they progress through the sensitive volume, but an average LET can be defined as the ratio of the recoil energy and the particle's range. The distribution of average LET for these recoiling nuclear fragments is shown in Fig. 3. The LET of recoiling nuclear fragments of silicon are limited to values below 9 MeV-cm²/mg as can be seen in the figure. This is sometimes erroneously interpreted as indicating that a part will be insensitive to protons if the threshold LET measured with heavy ions is above 10 MeV-cm²/mg. Proton-induced SEL and proton-induced SEU are both problems in space for the NEC 4464 despite the fact that the threshold LET for both phenomena are above 10 MeV-cm²/mg. 10 MeV / cm² / mg is a proper upper limit to the LET of recoiling nuclear fragments from spallation reactions, those fragments typically enter the sensitive volume at some angle of incidence, and there effective LET can be considerably higher depending on the dimensions of the sensitive volume and the orientation of the trajectory.

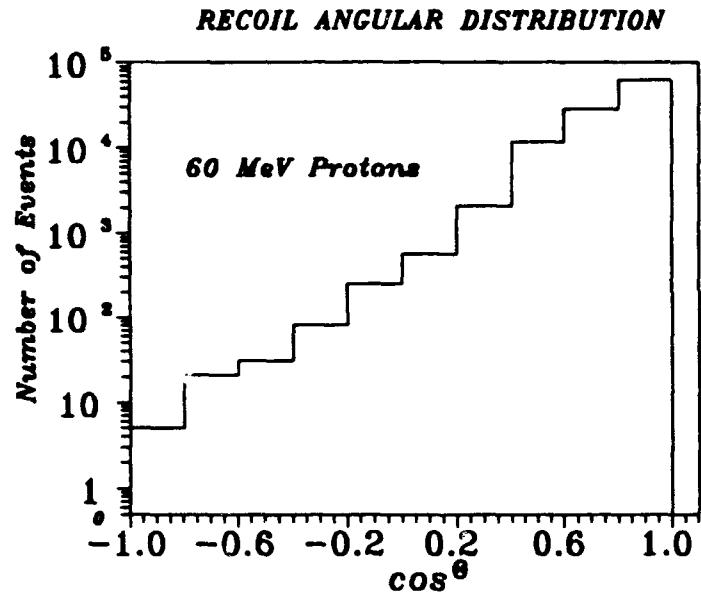


FIGURE 4. Angular distribution of the recoiling nuclear fragments following spallation reactions between 60 MeV protons and silicon target nuclei.

The kinematics of the recoiling fragment explain the dependence of the SEL cross section on angle of incidence observed with the NEC device (2). Figure 4 shows the angular distribution of the nuclear recoils emerging from the spallation reactions at 60 MeV plotted as number of events versus cosine of the angle of the recoil relative to the incident direction. The residual nuclear fragments clearly recoil in the forward direction. If the sensitive volume is thin compared to its lateral dimensions, much less energy will be deposited in spallation reactions initiated by protons incident parallel to the small dimension than will be deposited in reactions where the protons are incident parallel to one of the long dimensions. On the other hand, if the sensitive volume is

shaped more like a cube, there will be little or no angular dependence. This sensitivity of the angular dependence of the SEL cross section forms the basis for determining the correct value of the thickness of the sensitive volume. However, more detailed calculations are required to explain the angular dependence quantitatively because only a small fraction of the recoils in Fig. 4 deposits enough energy to induce latchup.

DIMENSIONS OF THE SENSITIVE VOLUME

Measurements by Goka et al (1,5) using heavy ions show a plateau in the SEL cross section plotted versus LET of 0.18 cm^2 per device or $275 \text{ } \mu\text{m}^2$ per bit. This device was also examined under SEM and optical microscopes at the National Microelectronics Research Centre at Cork (Ireland). They determined the area of the memory cell to be $380 \text{ } \mu\text{m}^2$. The measured SEL cross section is more than half the area of the memory cell, and it is consistent with the area of the p-well since the p-well contains the n-channel transistor which is usually larger than the p-channel transistor. The latch-up is normally assumed to be due to a current in the base (p-well) which turns on two parasitic transistors creating a low resistance path between power and ground. In what follows, we have used plateau value of the per bit SEL cross section measured with heavy ions to estimate the area sensitive volume. Further we assume that the sensitive volume is a square parallelepiped. The p-well is more likely to be a rectangular parallelepiped, and it may have at least one very long dimension because in high density devices the p-wells are typically not isolated. Furthermore, the charge collection from an ion strike at a given LET will depend on position because of the well resistance to ground contact varies with position. The effect of this position dependence results in broadening in the peak of the charge collection spectrum at the well junction and stretches the threshold region of the response curve for SEL cross section versus LET. The effect of a very long dimension for the well is probably important for proton testing because each cell biases its own ground contacts which determines the response of that cell, and the recoiling nuclear fragments which dominate the SEL response typically have ranges less than $20 \text{ } \mu\text{m}$. Simulations were found not to be very sensitive to whether the area of the well was assumed to be square or rectangular with in the values typical of CMOS SRAMs.

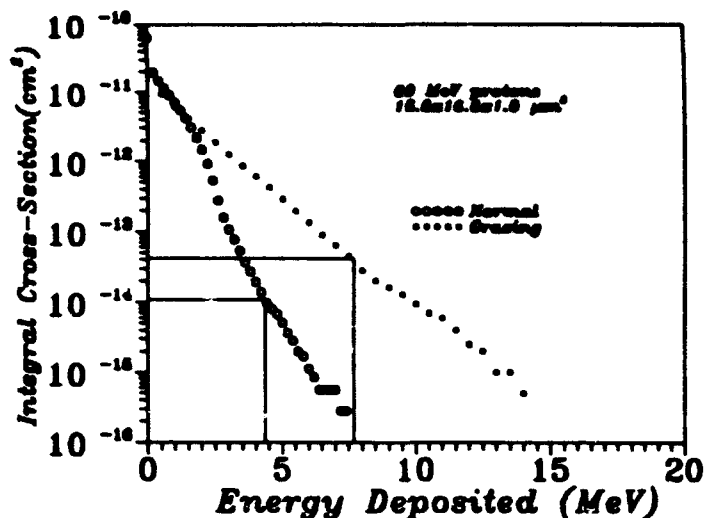


FIGURE 5a. Cross section for depositing at least energy ϵ plotted versus ϵ for protons incident on a sensitive volume having dimensions $16.6 \text{ } \mu\text{m} \times 16.6 \text{ } \mu\text{m} \times 1 \text{ } \mu\text{m}$. Curves are drawn for normal and grazing incidence. The horizontal lines are the measured SEU cross sections, and they terminate on the curve for the corresponding angle of incidence at point where the abscissa coordinate equals the critical charge.

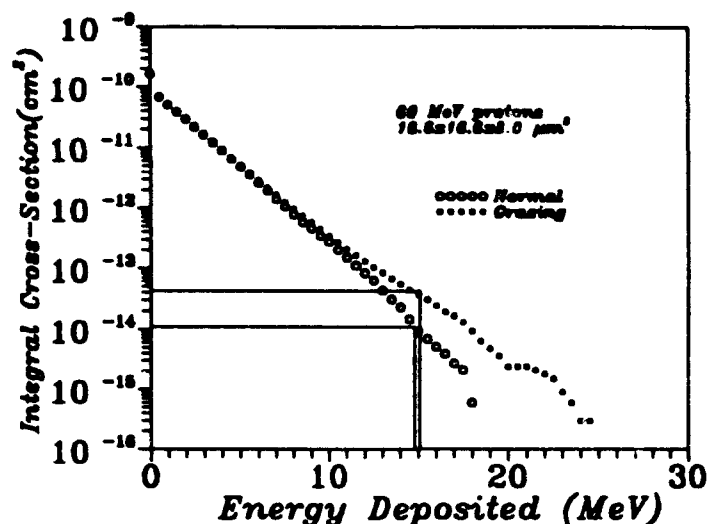


FIGURE 5b. Same plots for a sensitive volume having dimensions $16.6 \text{ } \mu\text{m} \times 16.6 \text{ } \mu\text{m} \times 8.0 \text{ } \mu\text{m}$.

The simulations show the latch-up cross section to be sensitive to both the thickness and the angle of incidence. This can be used to obtain an independent check on the thickness of the sensitive volume. This is illustrated in Fig. 5 where the integral energy-deposition spectrum is plotted as the cross section for depositing more than some energy ϵ versus ϵ for normal and grazing incidence. The sensitive volume is assumed to be a square parallelepiped with the protons incident either normal to the square surface or grazing, i.e., at right angles to the normal. Both the simulated and the measured SEL cross sections were different for the two cases.

The measured values of the SEL cross section are plotted as horizontal lines originating at the ordinate and terminating at the simulation curve corresponding to that angle of incidence. The coordinate on the abscissa marking this termination (vertical line) is the threshold energy deposition estimated for that thickness, and the critical charge can be obtained by dividing by 22 MeV/pC. However, the critical charge should not depend on the angle of incidence. When the thickness is 1 μm , as it is in Fig. 5a, the estimates of threshold are quite different for normal and grazing incidence. However, when the thickness is assumed to be 8 μm , as in Fig. 5b, the estimates for the two angles of incidence are in good agreement. Presumably, the correct thickness is closer to 8 μm than 1 μm . This leads to a simple analysis to obtain a value of the thickness which best fits the data.

Figure 6 plots the magnitude of the difference between the threshold values obtained for grazing and normal incidence versus the value of the thickness assumed for the sensitive volume. The values are fit by a simple second-degree polynomial shown as a solid curve. The curve's minimum is at 6.7 μm and this thickness is in excellent agreement with the value of 7.1 μm for the depth of the p-well measured using SEM (7).

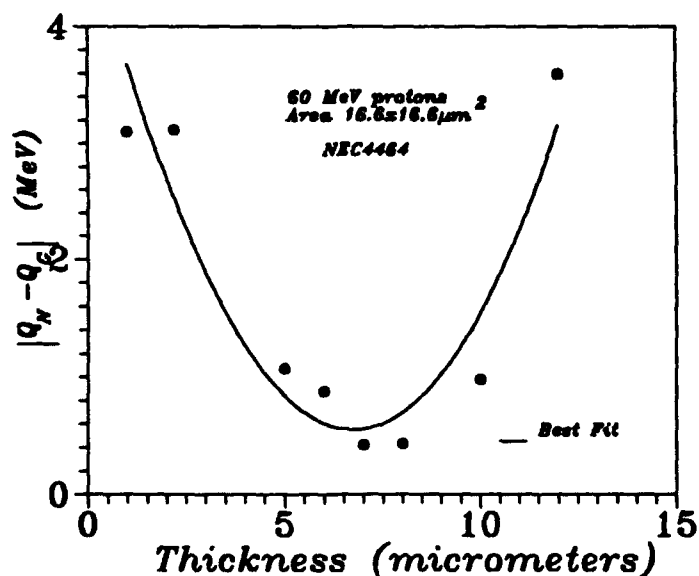


FIGURE 6. Magnitude of the difference between the normal and grazing estimates of the critical charge. The correct dimensions of the critical charge should result in the minimum difference.

DETERMINATION OF THE CRITICAL CHARGE

Assuming a thickness of 6.7 μm , the value of the threshold energy needed for latch-up is 14.2 MeV as obtained from a curve similar to Fig. 5b. The corresponding value of the critical charge obtained by dividing by 22 MeV/pC is 0.65 pC. To initiate latchup at normal incidence, a heavy ion must deposit of 14.2 MeV along a segments of trajectory of 6.7 μm

which corresponds to a threshold LET (for 50% of the plateau cross section) at normal incidence of $9 \pm 1 \text{ MeV-cm}^2/\text{mg}$. The value the LET corresponding to 50% of plateau obtained from the data of Goka et al (1,5) combined with the data of Adams et al. (2) is $11 \pm 3 \text{ MeV-cm}^2/\text{mg}$. This agreement is quite good considering the fact that Goka's data is on different devices than the one tested with protons.

APPLICABILITY TO SEU

The procedures described above for determining the values of the thickness of the sensitive volume and the critical charge can be applied to any single event effect (SEE) for which the First-Order Model is applicable. Table 1 summarizes the comparisons of the thickness obtained with this procedure to date with values obtained from charge collection spectroscopy (CCS), SEM, and the epi thickness plus 1 μm , an approximation for the upper limit of the possible thickness of the sensitive volume. It appears that this procedure gives a good estimate of the thickness in cases where the area of the sensitive volume is already known. If data set is expanded by including other incident energies and angles of incidence about two symmetry axes of the device, it should be possible to determine all three dimensions of the sensitive volume from measurements of proton SEE cross sections alone. In that case, it should be the standard deviation of the values of the critical charge obtained which should be minimized.

TABLE 1: THICKNESS.

DEVICE	CCS (μm)	PROTON (μm)	EPI+1 (μm)	SEM (μm)
IDT6116	13.6	13.1		
NEC4464		6.7		7.1
HC 6364	5.0	5.3		
AMD 93L422	*	3.1	3.0	

* Not available because of Bipolar amplification

PREDICTIONS OF THRESHOLD LET

If the values of the threshold energy ϵ required for an SEE and the thickness of the sensitive volume t are known, the threshold LET (50% of plateau) for a material of density ρ can be estimated from the following:

$$\text{LET} = \epsilon / t \times \rho$$

The values of the threshold LET obtained with these procedures are compared in Table 2 to values measured with heavy ions and available in the literature (8). The agreement is good within the error limits of the heavy ion data. More study is required before estimates of the error limits can be put on the proton values, but the preliminary results are encouraging.

TABLE 2: THRESHOLD LET.

DEVICE	CUPID (MeV-cm ² /mg)	HEAVY-IONS (MeV-cm ² /mg)	SEE
NEC 4464	9±1	11 ± 3	Latchup
IDT 6116	5.8	6.0 ± 1.0	Upset
AMD93L422	1.4	1.8	Upset
HC 6364	10	<18**	Upset

** No measurements are available for LET below this value. No evidence of threshold at this value or above.

CONCLUSIONS

Simulations show that proton-induced SEL can be explained by localized concentrations of energy deposition resulting from spallation reactions. The increase in SEL cross section observed with increasing angle of incidence is consistent with the First-Order Model which assumes that SEL occurs, if and only if, at least a threshold amount of energy is deposited within a sensitive volume with dimensions which are independent of the type of radiation incident. The sensitivity of the SEL cross section to the energy of the incident proton and the angle of incidence allows for the dimensions of the sensitive volume to be determined by matching the data to CUPID simulations at each angle and energy. The correct dimensions of the sensitive volume are those which result in the smallest variation in the values of the threshold energy (critical charge) at which the simulations match the measured cross sections. In this manner all the SEU parameters can be determined. A limited trial was carried out for the NEC 4464, a CMOS SRAM for which proton and heavy-ion SEL data were available. The values of the thickness of the sensitive volume is in agreement with the thickness of the p-well measured by SEM. The threshold LET (50% of Plateau) to be expected for heavy ions at normal incidence determined from the thickness of the sensitive volume and the critical charge obtained with protons is in excellent agreement with the value measured with heavy ions. This agreement is consistent with the results of a parallel analysis of SEU (8). This analysis was meant to be a test of whether the First-Order Model could be applied to SEL. The model forms the basis for predictions of SEU rates in space using CREME for heavy ions and CUPID for protons. The results presented here and in the analysis of SEU in reference 8 indicate that the First-Order Model is sufficient to fit the data without corrections for funneling as long as proper techniques are followed to estimate the proper dimensions to be used in the sensitive volume. Funneling and diffusion are only included in the model indirectly in term of thickness of the sensitive volume that is generally much thicker than the depletion region.

REFERENCES

- 1 T. Goka, S. Kuboyama, Y. Shimano, and T. Kawanishi", IEEE Trans. Nucl. Sci. NS-38, 1693 (1991).
- 2 L. Adams, E.J. Daly, R. Harboe-Sorensen, R. Nickson, J. Haines, W. Schafer, M. Conrad, H. Greich, J. Merkel, and T. Schwall, IEEE Trans. Nucl. Sci. NS-41, 1804 (1992).
- 3 See for example... P.J. McNulty, "Predicting Single Event Phenomena in the Natural Space Environments", in Microelectronics for the Natural Radiation Environments of Space, P.J. McNulty Ed., (IEEE Short Course for the 1991 International Nuclear and Space Radiation Effects Conference, Reno Nevada) pp. 3-1 to 3-93.
- 4 P.J. McNulty, G.E. Farrell, and W.P. Tucker, IEEE Trans. Nucl. Sci. NS-28, 4007 (1981)
- 5 T. Goka, private communication
- 6 P.J. McNulty, W.G. Abdel-Kader, and G.E. Farrell, "Proton Induced Spallation Reactions" in Radiation Physics and Chemistry: Special Issue on Space Radiation Environment and Effects, to be published.
- 7 NMRC report to ESA-ESTEC 'NEC 64 Kbit SRAM Reverse Engineering Report' Part 2, MTS-010
- 8 P.J. McNulty, W.J. Beauvais, and W.G. Abdel-Kader, "SEU Parameters and Proton-Induced Upsets," to be presented at the RADECS Conference in San Malo, France.

APPENDIX U

MICRODOSIMETRY IN SPACE USING MICROELECTRONIC CIRCUITS

MICRODOSIMETRY IN SPACE USING MICROELECTRONIC CIRCUITS

P.J. McNulty, D.R. Roth, W.J. Beauvais, W.G. Abdel-Kader ¹ and
E. G. Stassinopoulos ²

¹ Department of Physics and Astronomy
Clemson University
Clemson, SC 29634-1911

² NASA Goddard Space Flight Center
Greenbelt, MD 20771

ABSTRACT

Single event phenomena in biological organisms are compared with similar phenomena in microelectronic circuits and the similarities and differences are discussed. Both types of phenomena appear to obey the same model, at least to first order. The general applicability of this first-order model appears to reflect the need to operate despite the noise inherent in the storage and processing of information within microscopic volume elements. Arrays of p-n junctions, each having dimensions of a few microns, are proposed as solid-state microdosimeters.

INTRODUCTION

Modern microelectronic circuits respond to the heavily ionizing radiations of space in ways which resemble the effects the same radiations have on biological organisms (McNulty, 1983, 1988 and to be published). These similarities first became pronounced when circuit designers began to design spacecraft systems around microelectronic chips whose transistors had dimensions in the size range typical of biological cell nuclei. At that point, circuits exhibited single-event phenomena initiated either by the traversal of sensitive microstructures by individual cosmic-ray ions or by one or more particles from a nearby nuclear reaction (McNulty, 1983). Moreover, there are similarities in the response curves when the cross sections for single-hit phenomena are plotted versus the LET of the incident heavy ion. In this paper, we explore the possibility that these similarities in response may form the basis for using microelectronic circuits as microdosimeters for astronauts flying on future space missions. We will also demonstrate that accelerator exposures of microstructures can generate the data necessary to test those models which predict the energy deposition within sensitive microvolumes.

A circuit is proposed for measuring the energy-deposition events in an array of as many as two million junctions where each volume element has dimensions typical of biological cell nuclei. Furthermore, commercial lithographic techniques can be used to customize the dimensions and shape to represent different target structures.

Analogs with Radiobiological Effects

Single-event phenomena are those which are initiated by a single energetic particle. The normal macroscopic units of exposure, dose and dose equivalent, cannot easily be applied to single-event phenomena because they do not predict the probability that a given microstructure will be traversed by an ionizing particle or the probability that its being traversed will produce an effect, with the trivial exception of predicting the exposure to identical monoenergetic particles whose effects have already been measured. In other words, the measured response from exposure to one type of heavily ionizing radiation cannot be used to predict the response to another type of radiation. Single-event phenomena involving damage or a permanent change in at least one microstructure on a device are called hard errors. Chromosome aberrations are biological single-event hard errors. Errors are said to be soft when information or logic flow is altered without any direct damage to any part of the circuit. The device works as well after a soft error as before, only it is now processing erroneous information. Since more data is available for soft errors than for damaging events, they will be emphasized in what follows.

Two types of soft errors are known to have biological analogies. A single event upset (SEU) is said to occur when the information stored in a memory cell is altered without direct damage to the microstructures involved. Its biological equivalent is the somatic mutation which involves changes in the genetic code stored in the DNA. Both types of soft error can have catastrophic effects on the system. Mutations in cells which remain healthy can be harmless or can lead to serious organic illnesses like cancer. Similarly, the loss of information stored in a memory can be important if it is part of a critical instruction. The second type of soft error known to have a biological equivalent is the single-event transient (SET). The SET is a transient signal generated by a radiation event. The SET is treated as a valid logic signal by the system and may lead to some unforeseen consequence. Both SEUs and SETs have been known to trigger catastrophic results such as unscheduled rocket firings, system shutdowns, and loss of contact with the ground station (McNulty, 1991). The visual phenomena experienced by Apollo astronauts are examples of biological SETs (Pinsky *et al.*, 1974).

The propagation of errors resulting from an isolated SEU or SET in a logic network is

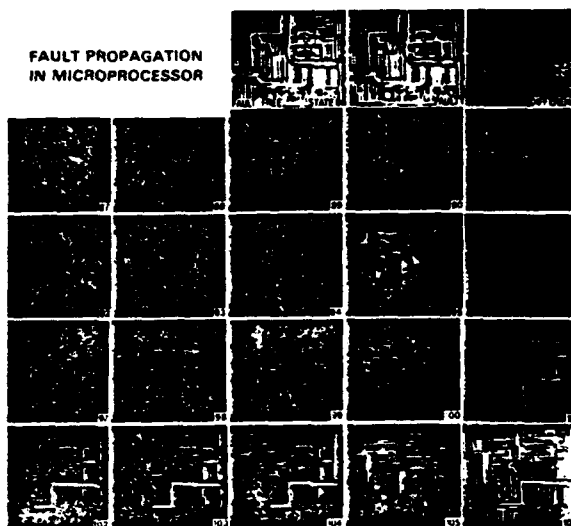


Figure 1. Error Propagation in the Intel 806186 Microprocessor. Light and Dark Areas Represent Different Voltage States on the First Two SEM Photographs (Pinsky *et al.*, 1974).

illustrated for the Intel 80186 microprocessor in a series of electron microscope photographs (Fig. 1) taken by Tim May (May, 1984). The voltage levels and, therefore, the logic states of the gates of the microprocessor are represented as light and dark areas on the photographs of Fig. 1. The fault free micrograph of the device taken after machine cycle 86 of a programmed sequence is shown in the image on the left in the top row. The next image shows the micrograph taken after step 86 and a single error has been introduced. No difference between such complicated photographs is noticeable to the eye. The third image on the top row is the difference between the first two, i.e., lighted points in the third image represent those pixels which appear lighted in one of the preceding images but not the other. The light spot in the third image on the top row, then, represents the location of the original error. Unfortunately, a single point is barely distinguishable from the photographic reproducing noise in Fig. 1. The microprocessor then operated normally and micrographs were taken after each machine cycle. Each image numbered above 86 in Fig. 1 represents the difference between the fault image and the fault-free image after the same number of machine cycles. The error points spread over the images, contract, then spread again in complicated patterns. It takes a large number of machine cycles, in this case twenty, before any of the errors reach a bond pad. Only after an error reaches the edge of the die is the problem observable to the world outside the chip. The outside world sees a pattern of erroneous information on the pins of the device that bear little resemblance to the simple change that was first introduced. The complications to the system caused by an error of this type are not the direct result of the error but rather the result of the system operating on the false information subsequently generated.

Astronauts experienced SETs in the form of visual experiences both while in deep space during the Apollo program (Pinsky et al, 1974) and while in low earth orbit on Skylab and Shuttle missions (Pinsky et al, 1975). One feature of the light flash phenomena which puzzled workers during the Apollo program can now be seen as similar to what has just been described for logic circuits. Descriptions of the visual experiences given by astronauts on Apollo and those given by scientists exposed under controlled conditions at accelerators typically included features, both physical and temporal, which clearly differed from the physical events at the retina. Figure 2 shows the two types of particle events known to induce visual experiences in space. Traversals of the retina by cosmic rays in deep space generated streaks and large bright flashes (Budinger, Lyman and Tobias, 1972; McNulty et al, 1972) while nuclear reactions induced by protons in the portion of the radiation belt known as the South Atlantic Anomaly produced point flashes (Pinsky, 1975; Rothwell, Filz and McNulty,

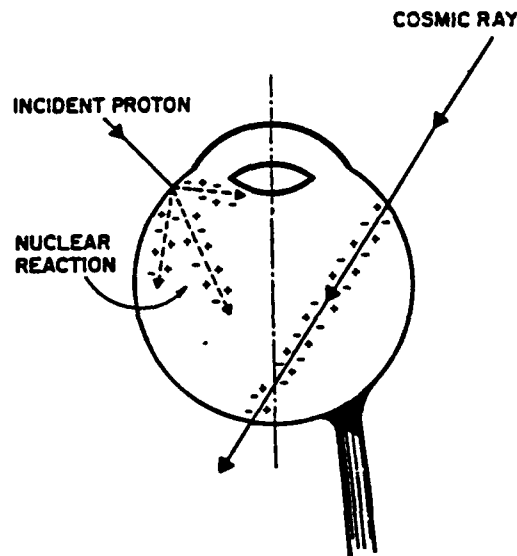


Figure 2. Cosmic Ray Incident on the Retina of the Human Eye and a Nuclear Spallation Reaction. These are the Two Physical Events Known to Initiate Visual Phenomena in Astronauts Flying in Space.

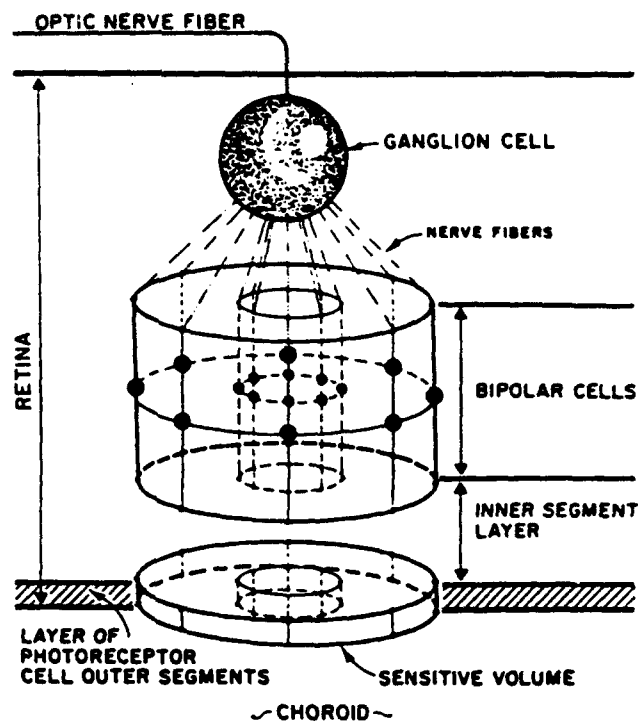


Figure 3. Schematic of the Functional Visual Signal Processing Unit on the Peripheral Retina. The Axons of the Ganglion Cells Form the Optic Nerve Fibers which Lead to the Central Nervous System.

1976). The nuclear events generated short-range recoiling nuclei which deposited a relatively large amount of energy within a small region of the retina. The fact that such localized generations of ionizations result in the experience of point flashes of light was predictable. However, the streaks observed in deep space and at accelerators did not appear to correlate so nicely with the physics of the inducing events. The streaks often had curvature and were broken in two or three places. Large bright flashes sometimes were followed by slower streaks elsewhere. This temporal sequence was consistently reported despite the fact that the particle events were obviously instantaneous compared to the time constants of any neural processing. Moreover, their trajectories were straight and intersected the retina at one, or at most, two places. These apparent discrepancies clearly result from neural processing by the retina and the central nervous system.

The First-Order Model

The prediction of soft-error rates in space began with the light-flash phenomena. The organization of the retina and its response to optical light at near threshold intensities were well known and this provided a basis for developing a model of its response to ionizing radiation. The functional unit of the peripheral retinal, shown schematically in Fig. 3, corresponds roughly to the region monitored by a single ganglion cell. The lateral dimensions of this region, known as a summation area, can be determined by probing with small spots of light. The thickness of this sensitive volume is just that of the layer of the rod cell outer segments. These outer segments contain the rhodopsin molecules which absorb the photons and initiate the electrical response. Photons absorbed within this sensitive volume contribute to the detection of light; those absorbed outside this volume do not contribute and, if they are absorbed within adjacent sensitive volumes, can inhibit detection.

The first-order model assumes that a visual experience occurs if a threshold number rhodopsin isomerizations occur within the sensitive volume and not otherwise. The isomerizations must be generated within the time constants of the unit, called the summation

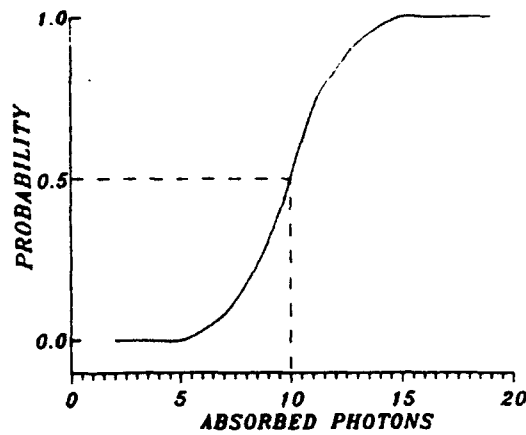


Figure 4. Response Curve for the Probability that a Human Observer Will Detect a Small Spot of Light on the Retina Versus the Average Number of Photons within the Sensitive Volume at that Intensity.

time, which is about 0.1 sec for a dark-adapted retina. This model is known to work well for optical vision. A response curve typical of the threshold or "S" shaped curves measured for vision is shown in Fig. 4.

The response of the visual unit to any type of ionizing radiation localized to within a single sensitive volume could be predicted knowing that the the visual response to ionizing radiation also follows a threshold response curve (Lipetz, 1953) and assuming that the relationship between large area and small area exposures is the same for ionizing radiation as it is for optical light. The results were in good quantitative agreement with accelerator data and the more limited data available from space (Rothwell, Filz and McNulty, 1976). This was the first time that the response of a biological system to quite different types of ionizing radiation could be explained quantitatively using a single set of parameters, the dimensions of the sensitive volume and the threshold number of ionizations (more correctly, the threshold amount of energy deposited) required for a visual response. This appears to be the essential test for all soft-error modeling, whether in biological systems or in circuits - that a single set of parameters can be used to predict the response to radiations which are quite different. In the visual system, the geometry of the sensitive volume was known from studies with visible light, and the value of threshold energy which had to be deposited in the sensitive volume could be estimated from the X-ray data. Another important characteristic of all soft errors was illustrated by the light flashes: it is a systems effect and the consequences of the soft error can only be measured in a complete organism.

SINGLE EVENT UPSETS

Since microelectronics fly in the same regions of space as the astronauts, the physical mechanisms leading to their soft errors are the same: cosmic-ray traversals and nuclear spallation reactions. The SEU-sensitive structures in microcircuits are small reverse-biased n-p junctions. Besides being the building blocks of microelectronic circuit elements, these junctions are also used as the sensors of silicon particle detector systems. One such system is shown schematically in Fig. 5. The sensitive volume in a detector is the region in the silicon immediately surrounding the depletion region formed at the reverse-biased junction. In a fully depleted detector, it is the entire volume of the silicon. Pulses are generated at the junction and shaped by the nearby circuit elements, and those which exceed some threshold value set by the discriminator are counted while lesser pulses are not. This operation is very similar to the first-order model for the retina's detection of photons and, as a result, it is not surprising that two independent groups attempting to model SEUs, one using the retina as a model (Wyatt et al, 1979; McNulty et al, 1980) and the other silicon detectors (Pickel and Blandford, 1980; 1981), arrived at essentially the same set of assumptions, now known as the first-order model.

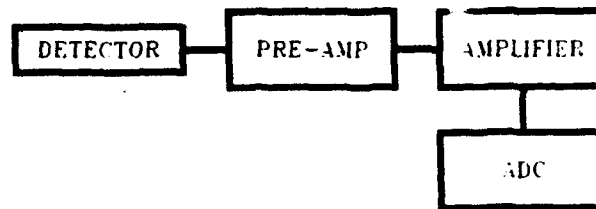


Figure 5. Schematic of a Silicon Particle Detector System.

First-Order Model for SEUs

The first assumption is that there is a sensitive volume associated with each SEU-sensitive junction on a microelectronic circuit whose dimensions are chosen such that the charge generated within this volume equals the charge collected across the junction. The dimensions of the sensitive volumes on the retina and the one within the fully depleted detector are known because they correspond to actual structures. Unfortunately, the sensitive volumes in microelectronic devices often differ in at least one dimension from identifiable microstructures, usually the thickness measured normal to the crystal surface. Moreover, it has only recently been shown that this dimension is independent of LET (McNulty, Beauvais and Roth, 1991) for circuit elements, a necessary condition for the concept of a sensitive volume to be useful quantitatively. Of course, the lateral dimensions of the sensitive volume should be only slightly larger than those of the junction but the value of the thickness could, until only recently, be estimated for most devices.

The second assumption is that there is a threshold number of ionizations which must be generated within the sensitive volume to induce an upset. This value is known as the critical charge. Since the number of ionizations is proportional to the energy deposited, the value of the critical charge is often listed in energy units where the conversion is the W value for silicon, 3.6 eV.

Luckily, both the area and the thickness of the sensitive volume can now be estimated from pulse-height measurements made on signals generated at the junction. Figure 6 shows the circuit used for these measurements. It is a modified version of the pulse-height system used in nuclear spectroscopy. The time constants of the charge-sensitive preamplifier should approximate the time constants of the circuit in order to collect only that charge which would

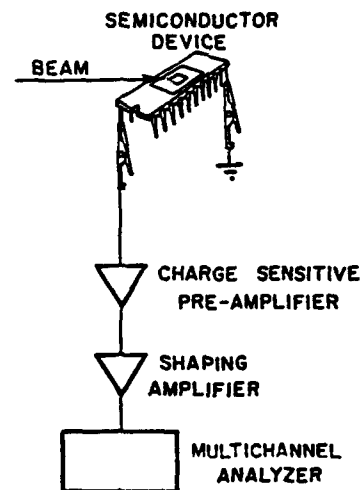


Figure 6. Schematic of Circuit Used for Pulse-height Measurements between the Power Pins of Static Memories.

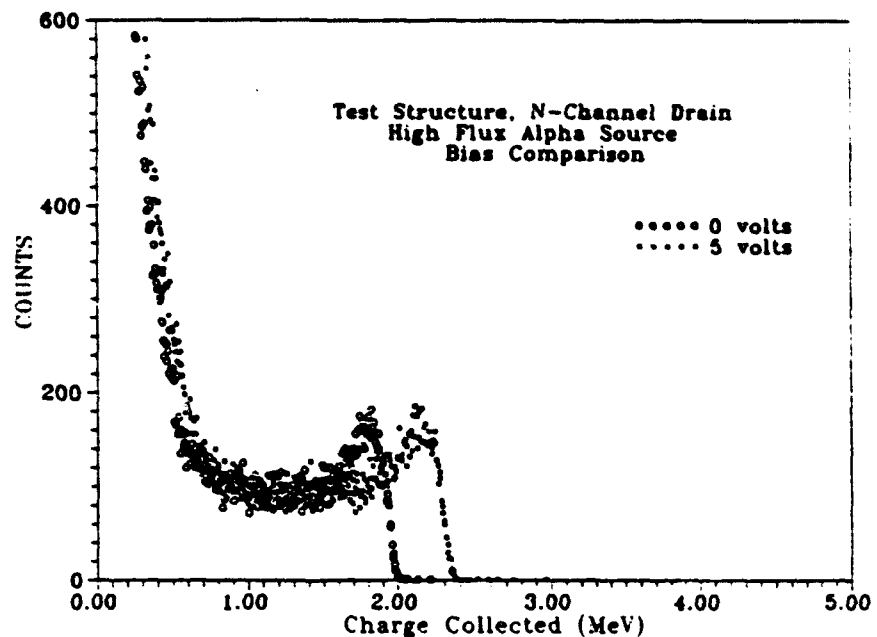


Figure 7. Pulse-height Spectra Measured across a Single n-p Junction of the Type Used in Microelectronic Circuits. Measurements are Plotted for Two Values of the Applied Bias, 0 V and 5 V.

contribute to upsetting the device. Figure 7 shows the pulse-height spectrum measured from a single n-p junction exposed to 4.8 MeV alphas. The junction has dimensions similar to the SEU-sensitive junctions in memory cells. Measurements are plotted for two values of the applied bias: 0 V and 5 V. A spectrum is obtained at zero bias because of the built-in potential across the metallurgical junction resulting from the differences in doping levels on either side. Increasing the bias to a working voltage of 5 V produces only a 20% shift in the spectrum toward higher energies with little or no change in the shape. This is important because the dimensions of the sensitive volume can be obtained from the pulse-height spectrum and, for reasons given below, they are usually estimated at zero bias.

Since particles initiate pulses by traversing the sensitive volume, the area can be estimated from the ratio of the number of events under the peak and the fluence. The thickness can be estimated from the position of the peak in the spectrum. If the energy of the incident particle is E and the peak position corresponds to a deposition of energy ΔE in the sensitive volume, then the thickness t of the sensitive volume can be estimated using range-energy tables and the formula:

$$t = R(E) - R(E - \Delta E)$$

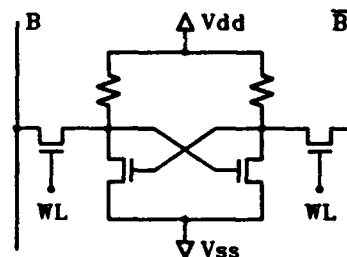


Figure 8. Memory Element of a Resistor-loaded NMOS Static Random Access Memory (SRAM) Device.

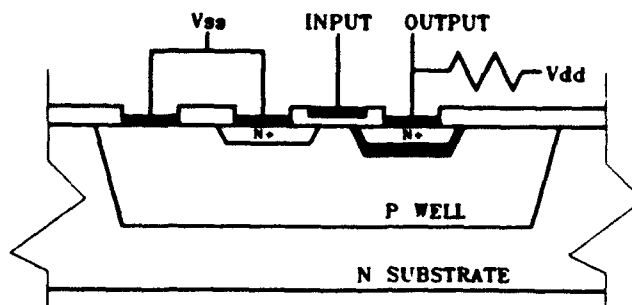


Figure 9. Cross Section of an Inverter in a Resistor-loaded NMOS SRAM.

where $R(E)$ is the range of the particle entering the sensitive volume and $R(E - \Delta E)$ is the range of the incident particle after traversing the sensitive volume.

SEUs in Static RAMs

The resistor-loaded NMOS SRAM is the memory circuit best suited to illustrate the analysis of SEUs in working devices. The circuit diagram of a memory element of an NMOS static RAM is shown in Fig. 8. The cell consists of two cross-coupled inverters held between high voltage V_{DD} and ground. The sensitive junction for this device is the reverse-biased drain-substrate junction. There are two drains shared by the four transistor cell. When the cell is powered up in either state, only one of these junctions is reverse-biased, but at zero bias both junctions in the cell are reverse-biased as a result of the built-in potential. The structure of a single inverter is shown in cross section in Fig. 9. When the chip is irradiated, the pulses at the drain-substrate junction can be monitored through the power (V_{DD}) and the ground lines of the device. The experimental configuration for measuring these pulses is shown in Fig. 6. By selecting only those pulses of the appropriate polarity, the spectrum obtained should be dominated by a peak due to particles traversing the drain-substrate junctions. Pulses due to hits on other junctions have a different polarity and are ignored. Figure 10 shows the pulse-height spectrum measured between the V_{DD} and ground pins of an IDT 6116V, a 16K

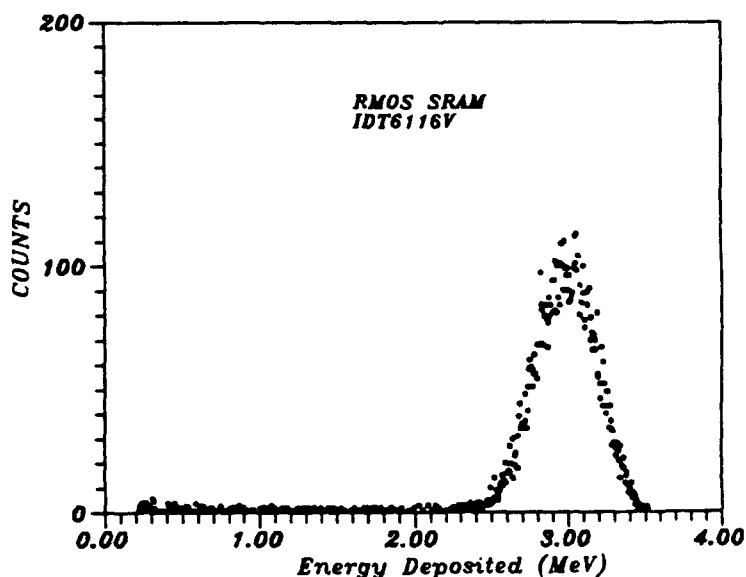


Figure 10. Pulse-height spectrum measured between the power and ground pins of an IDT 6116V resistor-loaded NMOS SRAM.

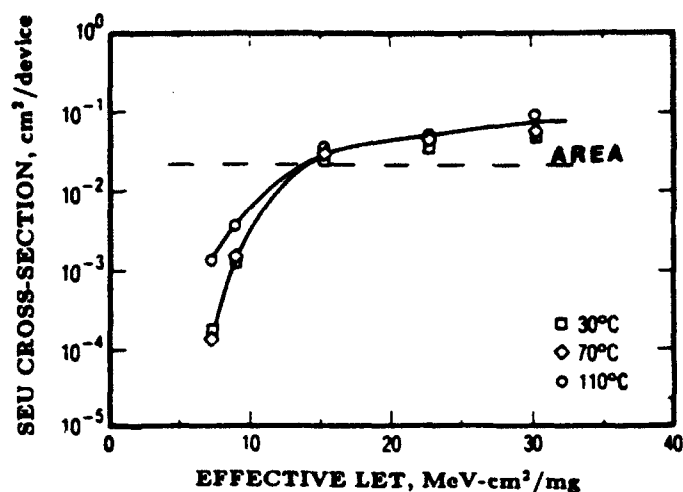


Figure 11. SEU Cross Section Versus LET for Heavy Ions Incident on the IDT 6116V at Different Temperatures. The Horizontal Curve is the Cross Sectional Area of the Sensitive Volume Determined from Fig. 10.

memory device with over 32,000 reverse-biased drain-substrate junctions in its unbiased state. As with test structures, the area of the junction can be found from the ratio of the number of events under the peak to the product of the fluence and the number of junctions. This area is also the cross sectional area of the target which must be hit to upset the memory cell. The thickness of the equivalent sensitive volume for this junction is obtained from the position of the peak in the spectrum as described earlier.

SEU Cross Section Measurements

For heavy ions the probability that an individual energetic particle will induce an SEU is expressed in terms of the per-bit SEU cross section which is typically determined from experimental measurements of the number of upsets induced by a parallel beam of accelerator particles. (See McNulty, 1991 for a recent review of the literature.) The per-bit cross section is defined to be the ratio of the number of SEUs generated to the product of the fluence and the number of memory cells in the device. Since all circuits are designed to work error free in the natural environment at sea level, they do not upset to particles incident with very low LET. At sufficiently high values of LET, any commercially available microcircuit will upset every time an SEU-sensitive junction is traversed. Then, the response curve of an SRAM exposed to particles of intermediate LET should be similar to the response curve of the retina to increasing number of photons, i.e., at low numbers of ionizations (low LET) the SEU cross section is zero, rising quickly at threshold to approximately the junction area and then continuing to rise slowly with LET as the cells begin to upset even with near misses (McNulty, 1991).

The response curve for the IDT 6116V was measured by Koga et al (1988) at different temperatures, and the results are plotted in Fig. 11. The horizontal line is the estimate of the junction area obtained from the pulse-height measurements described above. This value is in excellent agreement with the value of the SEU cross section at the point of transition between fast and slow rise in cross section. If this data, or any of the more complete data sets we are familiar with, were replotted as the probability that a heavy ion traversing one of the junctions caused an upset versus the number of ionizations generated by the ion as it traversed the sensitive volume (obtained by dividing the product of the LET, the density and the thickness of the sensitive volume by the average energy deposited per ion pair for silicon), the resulting curve would have the shape of the response curve of Fig. 4 except that the units of the abscissa would be number of ionizations instead of photon absorption.

SEU Measurements for Protons

A Monte-Carlo code called CUPID (McNulty, Farrell and Tucker, 1981) simulates the energy deposition in silicon microvolumes as a result of nearby proton-induced nuclear spallation reactions. It was developed following the approach of our earlier code for predicting proton-induced events in the retina (Rothwell, Filz and McNulty, 1976). The results of calculations for a sensitive volume having the dimensions obtained earlier for the IDT 6116V and exposed to 148 MeV protons are compared in Fig. 12 to experimental pulse-height measurements between power and ground on that device (McNulty et al, 1991). The plots are of integral cross section versus energy, i.e., the cross section for depositing at least some energy E in the microvolume versus E . The agreement between theory and the experimental curve is quite good. The horizontal line in Fig. 12 is the experimental SEU cross section. The locations on the abscissa which mark where the cross-section line intersects the curves are theoretical and experimental estimates of the value of the threshold energy deposition required to upset the device. The values are very close. The ratio of either value to the thickness of the sensitive volume is in good agreement with the threshold LET measured by Koga et al (1988) for heavy-ion data.

Universality of the First-Order Model

Similar studies have been carried out for CMOS static memories (McNulty, Beauvais and Roth, 1991) and NMOS dynamic memories (McNulty, Abdel-Kader and Lynch, 1991). The spectra for these technologies are more complicated, but the peak due to ion hits on the SEU-sensitive junctions can usually be identified and the dimensions of the SEU sensitive volumes determined. The proton SEU cross sections for more complicated devices must be compared to simulations of the energy-deposition in the sensitive volume rather than experimental measurements because, with spallation reactions, events on the SEU-sensitive junctions cannot be differentiated from other events. It has been shown for a variety of devices having different microstructures that the heavy-ion SEU cross sections and the proton SEU cross sections can be fit by a single set of parameters: the dimensions of the sensitive volume and the value of threshold for upset (critical charge). Events which generate fewer than a critical number of ionizations, or deposit less than a threshold amount of energy, do not upset the device. Events which exceed threshold always result in upsets. The shape of the response curve of cross section versus LET has been explained as being due primarily to the spread of energy-deposition events observed at a single LET (McNulty, Abdel-Kader and Lynch, 1991) just as the shape of the visual response curve has been attributed to quantal fluctuations at low intensities.

Bond and Varma have developed a variation on the first-order model for somatic mutations in biological cells (Bond and Varma, 1983). Since the dimensions of the sensitive

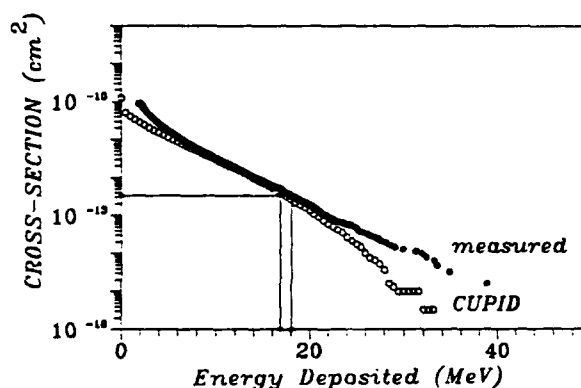


Figure 12. Cross Section as Calculated by CUPID for Depositing at Least Energy E within the Sensitive Volume of the IDT 6116V Plotted Versus E . The Experimental Curve Represents the Values Obtained from the Pulse-height Spectrum Measured between the Power and Ground Pins while the Unpowered Device is Irradiated by 148 MeV Protons.

volume are poorly defined for mutations, available data defining a response curve (probability of a mutation versus LET) cannot be used with confidence to specify the value of the threshold energy which must be deposited. It has been shown (Sondhaus, Bond and Feinendegen, 1990) that a wide range of mutations and chromosome aberrations have response curves which are similar in shape to the curve of Fig. 12, again with ionizations within the sensitive volume replacing photon absorption on the abscissa. An interesting exercise, then, would be to try estimating the size of the sensitive volume following the procedure outlined earlier for SEUs. The per-cell cross sections for mutations are needed to do this. They are obtained for heavy ions at various values of LET from the ratio of the number of mutations to the product of the fluence of incident particles and the number of cells at risk. The values of the per-cell cross sections would have to be plotted versus LET as the SEU data plotted in Fig. 11. The value of the cross section that marks the transition between the region of fast rise in cross section with LET and the region of slower increases with LET is the cross sectional area of the sensitive volume, just as the corresponding value of the SEU cross section in Fig. 11 was the junction area. Assuming that the sensitive volume is a sphere, the radius of the sensitive volume and the the pathlength distribution through the sensitive volume can also be calculated.

It is not clear that the model of Bond and Varma can be adequately tested without at least approximate dimensions for the sensitive volume being known. If the sensitive volumes have submicron feature sizes, the energy-deposition spectra may be dominated by events where the particle missed the target (Dicello, private communication). This is also true for large volumes when there is a low value of threshold. In this regime, the plateau in the cross section may reflect track structure effects more than the dimensions of the sensitive volume. Our experiences with the retina and microcircuits suggest that, if the first-order model is valid for mutations, the proper dimensions of the sensitive volume would be those which when combined with the corresponding value of the threshold would fit data for two different radiation types. Nuclear reactions and traversals by heavy ions might be the logical place to start, but they are not the only radiations which should give consistent results.

We know why the SEU response of microelectronic circuits follows the first-order model: circuits are deliberately designed not to upset in the natural environment at ground level. This environment includes thermal fluctuations as well as background radiations. So circuits are designed not to upset at low values of LET, but the information stored in random access memories is meant to be stored and recalled easily at low power. This makes the circuits sensitive to ion hits at higher LET. It seems clear that evolutionary processes also designed a threshold into the human visual system. Individual photoreceptors respond electrically to individual photons but, if a visual experience resulted from individual photon absorptions, the visual system would be swamped by the infrared radiation of the thermal background. Both types of systems have adjusted to a signal to noise problem. If there is a threshold in radiation induced mutations, perhaps it is also an evolutionary response to a signal to noise problem. Mutations are necessary for evolutionary progress, but to be too sensitive would make organisms vulnerable.

Circuits are designed with different threshold values depending on how harsh the intended environment is expected to be. Increasing the level of protection typically involves trade offs in performance: usually speed. Often, protection is designed in at the system level rather than by hardening individual components. Redundancy of stored information and voting logic are frequently used. The genetic code also incorporates redundancy. Comparisons in this area may be fruitful.

APPLICATIONS TO MICRODOSIMETRY

Parallel arrays of p-n junctions have been proposed as a microdosimetry tool for characterizing complex radiation environments for microelectronic circuits (McNulty et al, 1990). The pulse-height spectra measured from an array containing over two million junctions is shown in Fig. 13. The pulse-height spectrum measured at a microjunction having a sensitive volume with dimensions similar to the circuit of interest would certainly be a better predictor of the risk of SEUs in a given environment than any other form of dosimetry including detailed measurements of the charge and energy of the particles making up the

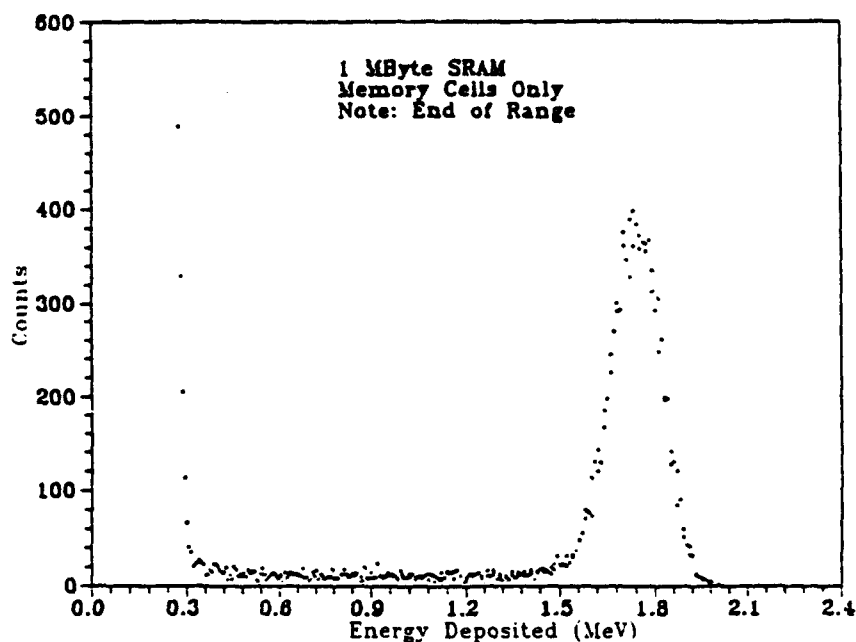


Figure 13. Pulse-height Spectrum Obtained from an Array of over Two Million Junctions in Bulk CMOS.

environment. Clearly, such arrays would also be useful in predicting light flash rates if proper corrections for the differences in composition were taken into account in selecting the dimensions to use for the sensitive volume. The possibility of using microelectronics to characterize a radiation environment for risk of mutations is less obvious. We do not know the shape or size of the tissue equivalent volumes that must be approximated. Although not essential for the space radiations mentioned above, a good general purpose microdosimeter should have all the individual sensitive volumes isolated from one another. Technology is now available to do just that. Figure 14 shows the pulse-height spectrum obtained with a parallel array of 2,316 junctions from a Texas Instruments test chip where the sensitive volume associated with each junction is completely surrounded by dielectric except where the electrical contacts are made.

Even in the absence of clearly specified dimensions for the sensitive volumes for biological mutations, microelectronic junction arrays still have important potential advantages in characterizing a radiation environment in terms of radiobiological risk. Sensitive volumes can be scaled to the size of biological cell nuclei, a probable upper limit to any sensitive volume. The pulse-height spectra would separate the high-energy-deposition events from the low-energy ones. These spectra could then be used to calculate dose equivalents based on quality factors or equivalent quantities determined by the NCRP or ICRP. Battery operated personnel dosimeters small enough to fit into shirt pockets can be made with commercially available devices and dosimeters as small as a film badge can be constructed using modern lithographic techniques.

CURRENT TESTING OF MODELS IN SPACE

The accuracy of predictions of single event phenomena strongly depends on the accuracy of the environmental models and the transport calculations for handling the effects of shielding. Solar flares and magnetic disturbances result in dramatic temporary changes in the radiation incident on spacecraft and consequently the error rates. There is a slow variation in the environments from solar minimum to solar maximum which should result in corresponding increases in SEU rates over the poles and decreases in the portions of the low earth orbits where spacecraft penetrate the radiation belts. This is an eleven year cycle and

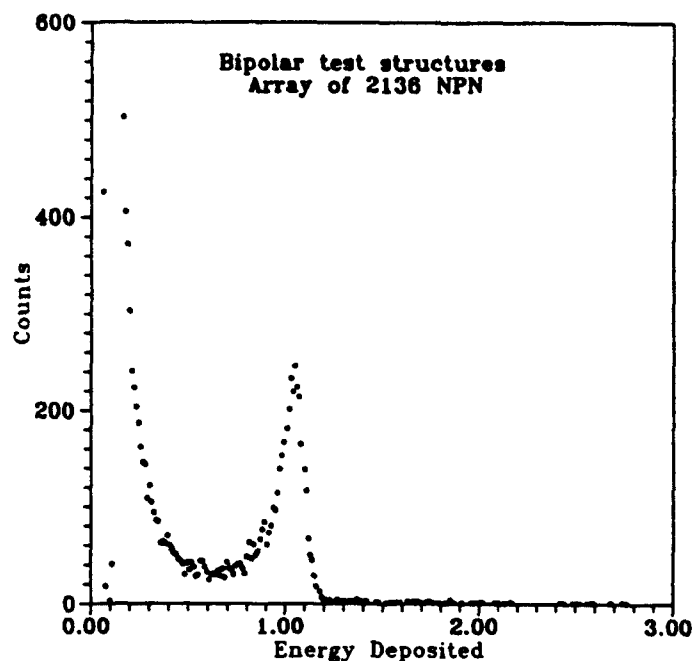


Figure 14. Pulse-height Spectrum Obtained with an Array of 2316 Microjunctions where Sensitive Volume is Surrounded by a Layer of Dielectric Isolation. Energy in MeV.

longer trends cannot be ruled out. Current NASA models of the radiation environments are static models which only incorporate the dynamic variations described above by long-term averaging. The model for the cosmic-ray environment is probably valid to within a factor of two for averages of the environment in excess of a year. It is necessary, of course, to provide the proper mix of the solar maximum and the solar minimum in calculations. Also, AP8, the NASA code of the trapped proton environment, may have an error of a factor of two in the high energy proton flux for low-earth orbits. The J* dosimeter recently characterized the low-earth orbit of the DMSP satellite in terms of the energetic nuclear reactions which would lead to SEUs in microelectronic devices (Gussenhoven et al, 1987). The data was found to agree with predictions of the AP8 model of the proton environment combined with CUPID's predictions of the number of spallation events which deposit at least 40 MeV and 75 MeV in the detectors (Beauvais et al, to be published).

Relatively good agreement between predictions based on heavy-ion accelerator data and cosmic-ray spaceflight data have been reported by Binder (1988), Smith and Simpson (1987) and Blake and Mandel (1986). These predictions were for a small number of devices in different satellite programs and included geosynchronous orbits and low-earth polar orbits.

The CRRES satellite is an entire satellite dedicated to measuring the radiation environments and correlating them with the effects on circuit components. The orbit is a highly elliptical orbit typical of the transfer orbits used to shift satellites from low-earth orbit to a geostationary orbit. Analysis is just beginning, but data sufficient for careful test of environmental and transport codes is being made available.

PREDICTING PROTON RESPONSE FROM HEAVY ION DATA

The procedure for using heavy-ion data to predict the proton cross section versus incident energy response function is discussed in Bisgrove et al, 1986. As described earlier, for this the work, the dimensions of the sensitive volume must be determined from charge collection measurements. The critical charge can then be estimated from the threshold LET measured in the heavy ion data. The agreement obtained using CUPID was excellent for the

device reported on by Bisgrove et al , (1986) and for a number of devices tested later. Bion and Bourrieau (1989) have developed simulation codes of the same general type as CUPID. They also find that the heavy-ion data can be used to predict the proton data. It is important to note that, in all of these calculations, the detailed shape of the response curve must be taken into account for accurate calculations. Errors of an order of magnitude result from ignoring the shape of the response curve in predicting SEU rates in space Brucker and Stassinopoulos, 1991).

SUMMARY AND CONCLUSIONS

The single event upset phenomena induced in circuits flown in space have response curves in plots of SEU cross section versus LET which exhibit a threshold behavior similar to the response curves reported for the light flash phenomena experienced by astronauts and mutations in biological cells. It is possible to independently determine the dimensions of the sensitive volume for a visual unit on the retina and for a memory cell in a circuit, but not for mutations. Knowledge of these dimensions and the threshold energy that must be deposited in the sensitive volume is sufficient to predict the response to a variety of radiation types. The first-order model assumes that if more than a threshold amount of energy is deposited within the sensitive volume, an event is induced, but not otherwise. Knowledge of the dimensions of the sensitive volumes would be essential for testing whether mutations obey similar models.

ACKNOWLEDGEMENTS

Conversations with V.P. Bond, J. Booz, and L.E. Feinendegen are gratefully acknowledged.

REFERENCES

- Beauvais, W.J. , P.J. McNulty, S. El-Teleaty, W. G. Abdel-Kader, M.S. Gussenhoven, E.G. Mullen, and G.E. Farrell, Comparison of Spallation-Reaction Simulations with DMSP Satellite Data , IEEE Trans. Nucl. Sci., to be published.
- Binder, D., 1988, Analytic SEU Rate Calculation Compared to Space Data, IEEE Trans. Nucl. Sci., NS-35: 1570-1572.
- Bion, T. and J. Bourrieau, 1989, A Model for Proton-Induced SEU, IEEE Trans. Nucl. Sci., NS-36: 2281-2286.
- Bisgrove, J.M., J.E. Lynch, P.J. McNulty, W. Abdel-Kader, V. Kletnieks, and W.A. Kolasinski, 1986, Comparison of Soft Errors Induced by Heavy ions and Protons, IEEE Trans. Nucl. Sci., NS-33: 1571-1576.
- Blake, J.B. and R. Mandel, 1986 On-Orbit Observations of Single Event Upsets in Harris HM-6508 1K SRAMs, IEEE Trans. Nucl. Sci., NS-34: 1616-1619.
- Bond, V.P., and M.N. Varma, 1983, Low-Level Radiation Response Explained in Terms of Fluence and Cell Critical Volume Dose, in Eight Symposium on Microdosimetry, (Julich West Germany; Commission of the European Communities) pp 423-439.
- Brucker, G. J. and E.G. Stassinopoulos, 1991, Prediction of Error Rates in Dose-Imprinted Memories on Board CRESS by Two Different Methods, IEEE Trans. Nucl. Sci., NS-38: 913-922.
- Budinger, T.F., J.T. Lyman, and C.A. Tobias, 1972, Visual Perception of Accelerated Nitrogen Nuclei Interacting with the Human Retina, Nature 239: 209-211.
- Gussenhoven, M.S., E.G. Mullen, R.C. Filz, D.H. Brautigam, and F.A. Hanser, 1987, New Low-Altitude Dose Measurements, IEEE Trans. Nucl. Sci., NS-34: 676-683.
- Koga, R., W.A. Kolasinski, J.V. Osborne, J.H. Elder, and R. Chitty, 1988, SEU Test Techniques for 256K Static RAMS and Comparison of Upsets Induced by Heavy Ions and Protons, IEEE Trans. Nucl. Sci., NS-35: 1638-1643.

Lipetz, L.E., Ph.D. Thesis, 1953, University of California Radiation Laboratory Report No. 2056.

May, Tim; 1984, Dynamic Fault Imaging of VLSI Logic Devices, presented at the International Reliability Symposium, Los Vegas, Nevada April 2-5, 1984.

McNulty, P.J. ; 1983, Charged Particles Cause Microelectronic Malfunction in Space , Physics Today (Guest Comment) 36: 9.

McNulty, P.J.; 1988, New Directions in Space Dosimetry; In Terrestrial Space Radiation and Its Biological Effects P.D. McCormack, C.E. Swenberg, and H. Buckner, Eds. (Plenum Publishing Co.) pp 819 - 840.

McNulty, P.J. ; Single Event Upsets in Microelectronics, Radiation Research, to be published.

McNulty, P. C.; Predicting Single Event Phenomena in the Natural Space Environments ; in Microelectronics for the Natural Radiation Environments of Space P.J. McNulty, ed., (IEEE Short Course for the 1991 International Nuclear and Space Radiation Effects Conference, Reno, Nevada) pp 3-1 to 3-93.

McNulty, P.J. , W.G. Abdel-Kader, and J.E. Lynch, 1991, Modeling Charge Collection and Single Event Upsets in Microelectronics," Nuclear Instruments and Methods in Physics Research, B61, No. 1: 52-60.

McNulty, P.J., W.J. Beauvais, and D.R. Roth, 1991 Determination of SEU Parameters of CMOS SRAMS by Charge Collection Measurements on SRAMS, IEEE Trans. Nucl. Sci., NS-38: 1463-1470, Dec..

McNulty, P.J., G.E. Farrell, and W.P. Tucker, 1981, Proton-Induced Nuclear Reactions in Silicon, IEEE Trans. Nucl. Sci., NS-28: 4007-4012.

McNulty, P.J. , V.P. Pease, L.S. Pinsky, V.P. Bond, W. Schimmerling and K.G. Vosburgh; 1972, Visual Sensations Induced by Relativistic Nitrogen Nuclei, Science 178: 160-162.

McNulty, P.J. , D.R. Roth, W.J. Beauvais, W.G. Abdel-Kader, and D.C. Dinger, 1991, Comparison of the Charge Collecting Properties of Junctions and the SEU Response of Microelectronic Circuits, Int. J. Radiat. Instrum., Nuclear Tracks and Radiation Measurement, 19, Nos. 1-4: 929-938.

McNulty, P.J., D.R. Roth, E.G. Stassinopoulos, and W.J. Stapor, 1990, Characterizing Complex Radiation Environments Using MORE (Monitor of Radiation Effects), in Proceedings of The Symposium on Detector Research and Development for The Superconducting Super Collider, (Fort Worth, Texas, October 15-18, 1990) pp 690-692.

Pickel, J.C. and J.T. Blandford, Jr., 1980, Cosmic Ray Induced Errors In MOS Memory Cells, IEEE Trans. Nucl. Sci., NS-27: 1006-1015; 1981, CMOS RAM Cosmic Ray Induced Error Rate Analysis, IEEE Trans. Nucl. Sci., NS-28: 3962-3967.

Pinsky, L.S., W.Z. Osborne, J.V. Bailey, R.E. Benson, and L.F. Thompson; 1974, Light Flashes Observed by Astronauts On Apollo 11 Through Apollo 17, Science 183: 957 - 959.

Pinsky, L.S., W.Z. Osborne, R.A. Hoffman, and J.V. Bailey, 1975 Science 188: 928.

Rothwell, P. , R. Filz, and P.J. McNulty; 1976, Light Flashes Observed on Skylab IV - The Role of Nuclear Stars, Science 193: 1002.

Smith, E.C. and T.R. Simpson, 1987, Prediction of Cosmic-Radiation-Induced Single-Event Upsets in Digital Logic Devices On Geostationary Orbit, TRW Final Report, November 21, 1987.

Sondhaus, C.A., V.P. Bond and L.E. Feinendegen, 1990, Cell Oriented Alternatives to Dose, Quality Factor, and Dose Equivalent for Low-Level Radiation, Health Physics 59: 35-48.

Wyatt, R.C. , P.J. McNulty, P. Toumbas, P.L. Rothwell, and R.C. Filz, 1979, Soft Errors Induced by Energetic Protons, IEEE Trans. Nuc. Sci., NS-26: 4905-4910; McNulty, P.J. , G.E. Farrell, R.C. Wyatt, P.L. Rothwell, R.C. Filz, and J.N. Bradford, 1980, Upset Phenomena Induced by Energetic Protons and Electrons, IEEE Trans. Nucl. Sci., NS-27: 1516-1522.

APPENDIX V

CHARACTERIZING COMPLEX ENVIRONMENTS USING MORE (MONITORING OF RADIATION EFFECTS)

CHARACTERIZING COMPLEX RADIATION ENVIRONMENTS USING MORE (MONITOR OF RADIATION EFFECTS)

P.J. McNulty and D.R. Roth

Department of Physics and Astronomy, Clemson University, Clemson SC 29634-1911

E.G. Stassinopoulos

NASA Goddard Spaceflight Center, Greenbelt MD

W.J. Stapor

Naval Research Laboratory

Beltsville, MD 20375-5000

Abstract

The MORE instrument can be used for testing microelectronic technologies for use in complex radiation environments such as those inside SSC detector assemblies or operational satellites.

1. Introduction

Particle detector assemblies proposed for the SSC resemble electronic systems flown on operational satellites in that they must be designed to operate for long periods in complex radiation environments with few if any opportunities for repairs. There are long lead times between the design of a system and its implementation in orbit or on the beam line. The radiation threats to microelectronics in both cases include the all-or-nothing single-event effects as well as the gradual degradation due to cumulative exposure. Like satellite system designers, SSC experimentalists will be forced into difficult choices between the guaranteed survivability obtained by building systems around rad-hard components and the greater performance at lower cost associated with commercial devices. The rad-hard approach will probably be followed in the earliest versions of the detector components, but the desire to improve will be almost immediate. Use of any commercial parts requires that one be able to predict with some accuracy both the single-event effects and the gradual degradation due to accumulated absorbed dose. This requires radiation testing of critical components combined with detailed knowledge of the particles making up the environment. Detailed measurement of the environment is not feasible. Nor can standard test procedures be corrected easily for dose-rate effects or synergistic effects. Trials of critical components in the identical or similar radiation environments would appear desirable before committing to specific technologies.

We describe in this paper an instrument designed to allow experimenters to characterize complex radiation environments in terms of their effects on microelectronic components of interest to the experimenter while simultaneously measuring the absorbed dose. This instrument, the Monitor of Radiation Effects (MORE) is designed to measure the rate of single event upsets (SEU), monitor how these rates would vary with device sensitivity, and measure circuit degradation due to chronic or acute exposures. It is designed to operate on operational satellites or within the limited empty spaces inside functioning SSC detectors.

2. Instrument Design

The proposed instrument has three separate components designed to carry out different types of measurements: The first component measures the SEU rate on an array of SRAMS. Soft errors or single event upsets are the most common form of single event phenomena in space, and they are the form most likely to be observed in microelectronics used inside detector assemblies. The name single event upsets comes from the fact that the upsets are typically the result of individual interactions. They can occur in logic as well as memory circuits, but they are most easily studied in memories. Often the electrical (and hence logic) states of more than one circuit element are changed as a result of one event. This is taken into account because the instrument provides the memory location, type of error, and time of occurrence for each event. Large memory arrays can be used in order to obtain reasonable statistics in the shortest possible time. Figure 1 is a schematic diagram of the SEU tester component of MORE. It requires only 6 chips including one of the memory devices being tested. An essential feature of this component is that the devices under test are interchangeable - the SRAMs can be of any technology from 4K to 256K (or higher when available). Changing SRAMs only requires switching socket adapters and the ROM chip.

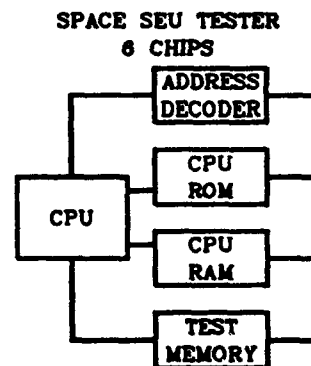


Fig. 1. Schematic of SEU tester of MORE.

Soft errors are believed to be a threshold phenomena with threshold being determined by the size of the pulse generated across the drain-substrate junction for most NMOS and CMOS devices. The cross section for SEU events is plotted in Fig. 2 versus the LET (or stopping power) of the incident particle for the IDT 6116V, a device used for testing the prototype of MORE. While the data taken from Ref. 1 appears to depend on the ion species, it does exhibit a threshold behavior in that there are no upsets at low LET values and then a sharp rise to a cross section which roughly equals the total cross sectional area of the array of SEU-sensitive junctions. The gradual increase beyond threshold is due to multiple upset events. The device has also been shown to upset when exposed to protons incident at energies as low as 30 MeV. The proton-induced upsets in SRAMs are due to spallation reactions at or near the SEU-sensitive junctions.

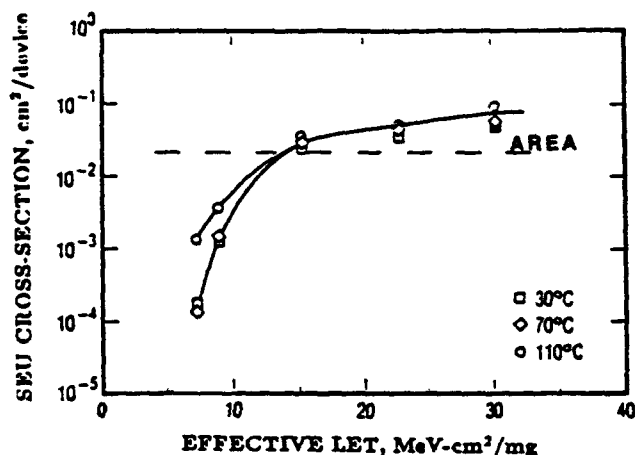


Fig. 2. Cross section for SEU events versus LET for the IDT 6116V. Data is from Ref. 1.

The second component of MORE conducts a pulse-height analysis of the pulses generated at the microjunctions of a parallel array of circuit elements as a result of radiation-induced events. The junctions used are identical or at least similar to the SEU-sensitive junctions of the SRAMs monitored by the first component. The SRAM used in the prototype was an NMOS device, the IDT 6116V, and the pulse height spectra were measured off the power pins of an identical device. In both cases, the events of interest are due to interactions at junctions from similar arrays. For CMOS devices, the pulse-height spectra must be measured from a parallel array of drain-substrate junctions. These test structure arrays are often available from the vendors since they are used as test structures in yield studies. The experimental configuration used for the pulse-height measurements is shown schematically in Fig. 3. The pulse-height spectrum obtained with the prototype exposed to 4.8 MeV alphas is shown in Fig. 4. This spectrum was measured on an array of 32,678 junctions, each having dimensions of about 11 μm on a side. The area of the junctions drawn in Fig. 2 as a horizontal line was obtained from the ratio of the number of events under the peak in Fig. 4 to the fluence. This agreement between the

area and the measured SEU cross section provides some confidence for using this arrangement for characterizing more complex radiation environments.

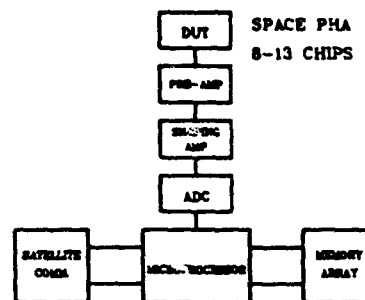


Fig. 3. Experimental configuration used for pulse-height measurements in MORE.

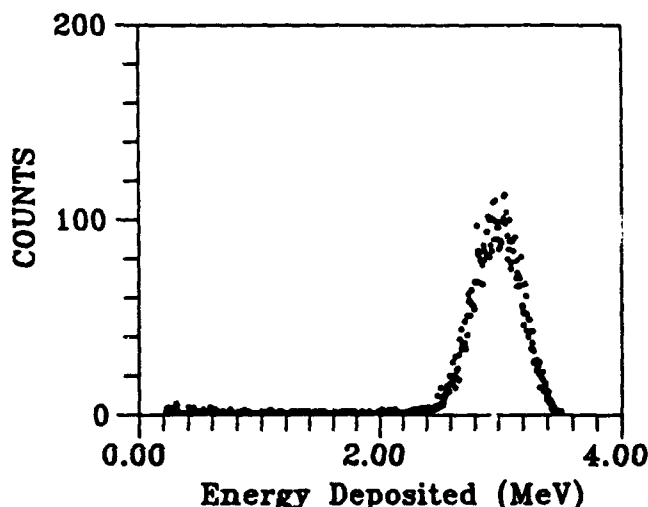


Fig. 4. Differential pulse-height spectrum obtained with more prototype exposed to 4.8 MeV alphas.

The pulse-height spectra obtained when the prototype was exposed to 148 MeV protons is shown in Fig. 5 where the data is plotted in integral form as the cross section for depositing at least a given energy E versus E . This spectrum is roughly typical of the form spectra will take in regions around the beam line within a detector assembly except that, cross sections cannot be determined in a complex radiation environment. Instead, the plots will be the number of events in which at least E is deposited versus E . Cross section cannot be calculated because the identity of the incident particles are not known. However, even without knowing the particles making up the incident radiation, the threshold for the device can be determined. This is illustrated in Fig. 5 where the SEU cross section measured for the IDT 6116V is represented as a horizontal line. The energy corresponding to threshold is marked on the abscissa where the line intersects the experimental curve. In a complex environment, the numbers of SEUs (scaled to the same junction area) should correspond to the largest events on the spectrum. Again, comparison of the measured SEU rate and the spectrum yields the value of threshold.

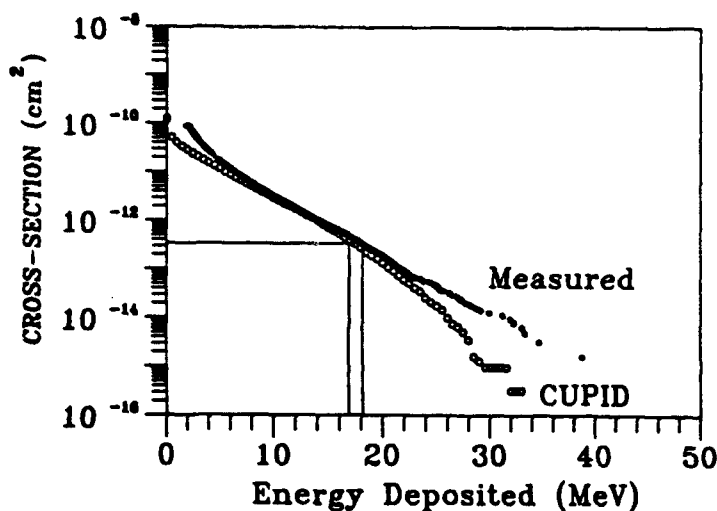


Fig. 5. Integral pulse-height spectrum obtained from exposure to 148 MeV protons.

The theoretical curve represents the simulations from CUPID (2) for the sensitive volume associated with the SEU-sensitive junction of the IDT 6116V with the dimensions of the sensitive volume obtained from the position of the peak and the number of events in Fig. 4 (3). The agreement between theory and experiment, besides testing the simulation model, provides some confidence in the use of pulse-height arrays to determine the SEU parameters of a technology.

The third component of MORE measures the total dose absorbed in SiO_2 while monitoring the effects on a test structure from a device made with the technology to be tested. The total dose is obtained by measuring the turn-on voltage on calibrated PMOS transistors following the procedures outlined by Holmes Siedle et al (4). The same procedures are used to measure the turn-on voltage on the test structures. A schematic cross section of a MOS transistor is shown in Fig. 6. The gate bias required to turn on or off the test structure is monitored. Changes in the turn-on voltage is the dominant failure mode for MOS devices exposed to ionizing radiation at low and moderate dose rates. It is principally the result of the buildup of positive charge in the thin oxide under the gate and negative interface states at the SiO_2/Si interface.

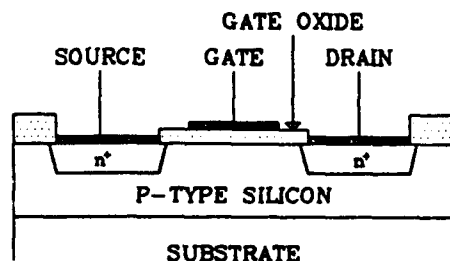


Fig. 6. Schematic cross section of a MOS transistor.

3. Specifications

The SEU, PHA, and Total Dose components of MORE require 2 W, 2.5 W, and 1.5 W of power, respectively. The total weight of the package is 6 lbs and fits inside a box having dimensions of 8" x 6" x 4".

4. Summary and Conclusions

The radiation problems within the the detector assemblies proposed for the SSC will be similar to those experienced on operational satellites. Because of the absence of heavily ionising cosmic rays around accelerators, the environment should be less severe than in deep space. However, both the single event upsets and gradual device degradation due to accumulated dose is to be expected. The use of rad-hard components developed for military systems flown in space should be sufficient for SSC applications for any locations except in or very close to the beam line. Use of commercial devices is risky even when the candidate parts are tested if the SEU rate to be expected must be accurately known. The MORE instrument allows trials of a technology of devices in complex radiation environments. Problems of synergistic effects and dose-rate effects are automatically included in the test data using this approach.

5. Acknowledgements

This work was funded in part by the Defense Nuclear Agency.

6. References

1. R. Koga, W.A. Kolasinski, J.V. Osborne, J.H. Elder, and R. Chitty, *IEEE Trans. Nucl. Sci.* **NS-35**, 1638 (1988).
2. P.J. McNulty, G.E. Farrel, and W.P. Tucker, *IEEE Trans Nucl. Sci.* **NS-28**, 40007 (1981).
3. P.J. McNulty, D.R. Roth, W.J. Beauvais, W.G. Kader, and D.C. Ding, *Nuclear Tracks and Radiation Meas.*, to be published.
4. A. Holmes-Siedle and L. Adams, *Radiat. Phys. Chem.* **28**, 235 (1986).

APPENDIX W

USERS MANUAL FOR THE CUPID CODES

THE

CUPID

CODE

Contents

1	Introduction	4
2	Getting Started	5
2.1	The goal of this manual	5
2.2	Installing the CUPID code	5
2.3	Running the CUPID code	5
2.4	The I/O routine	6
2.5	How to use the menus	6
3	The Parameters Menu	7
3.1	Overview	7
3.2	Specific operation	9
3.2.1	Proton energy	9
3.2.2	Output energy interval	9
3.2.3	Number of iterations	9
3.2.4	Volume dimensions	9
4	Other Main Menu Options	10
4.1	Target Volume	10
4.2	Saving parameters	10
4.3	Loading parameters	10
4.4	Running the CUPID code	12
4.5	Loading an output file	13
4.6	List output	13
4.7	Graph output	13
4.8	Make X-Y data file	13
4.9	Printing the output	14
5	Miscellaneous	16
5.1	File name and directory conventions	16
5.2	About the mouse	17
5.3	Changing the colors	17
5.4	Saving the colors	17
5.5	CUPID.BAT	17
5.6	Computer Requirements	17

5.7	Cost	18
5.8	Problems or Comments	18

List of Figures

2.1	The Main Menu.	6
3.1	The Parameters Menu.	8
3.2	The Prameters menu with an error.	8
4.1	The Target Volume	11
4.2	Example file screen	11
4.3	Run selection screen	12
4.4	Example output printed on screen	13
4.5	Example output graphed on screen	14
4.6	Printing Screen	15
5.1	Directory Screen	16

Chapter 1

Introduction

The CUPID code is a proton-induced spallation reaction simulation code which determines the SEU cross section as a function of the critical charge for a sensitive volume of defined dimensions. The code requires several inputs: the most important of these are the dimensions of the sensitive volume in which the charge is generated and the energy is deposited. Other inputs are the dimensions of the surrounding volume within which the nuclear reactions can occur, the number of iterations, and the incident proton energy. The output is the integral cross section for depositing some energy E versus E . The output is given in this form because the SEU cross section should be the cross section for events in which more than some threshold energy (critical charge) is deposited.

The CUPID code consists of two programs. The "main" CUPID code does the actual calculations, while the CUPID I/O routine feeds the main routine with the required information to run properly. The I/O routine is user friendly and menu driven.

Chapter 2

Getting Started

2.1 The goal of this manual

The goal of this manual is to outline to the intermediate DOS user how to use the CUPID I/O routines.

2.2 Installing the CUPID code

The CUPID code is installed by copying all the files on the distribution disk into a subdirectory called CUPID. The CUPID code may be installed into a different subdirectory but the CUPID.CNF file must reflect the directory in which CUPID is installed. The second line in CUPID.CNF contains the path where the CUPID code is installed. The path should also indicate the drive in which CUPID is installed. The default path in CUPID.CNF is "C:\CUPID". To easily install the program, you should type the following from the DOS prompt:

```
md cupid {enter}
cd cupid {enter}
Place the distribution disk in drive A.
copy a:.*/*b {enter}
```

The knowledge DOS user may install the CUPID code in any manner that is convient.

2.3 Running the CUPID code

There are many ways to run the CUPID code. The simplest way is to type the following from the DOS prompt:

```
cd cupid {enter}
cupid {enter}
```

The knowledgeable DOS user may employ any convenient manner.

1. Enter-Edit Parameters
2. Look at Target Volume
3. Save Parameters to Disk
4. Load Parameters from Disk
5. Run CUPID Codes
6. Load Output File from Disk
7. List Output to Screen
8. Look at Graph of Output
9. Make X-Y Data File
10. Print Output to Printer

Figure 2.1. The Main Menu.

2.4

The I/O routine

The I/O routine was developed to help the user create the required files to run the CUPID code. It generates the files which contain the basic information necessarily to run the CUPID code. The I/O routine is menu driven. The menus can be broken up into three basic types. The first type contains the items used to develop input files which feed the CUPID code. The second type is the menu item which instructs CUPID which simulations to perform. The third type contains the items which control the analysis of the data after the running of the CUPID code.

2.5

How to use the menus

The menus are one level deep for simplicity. Menu entries may be selected from the main menu (see Figure 2.1) by any of four different ways. The function keys F1- F10 can immediately select the corresponding option. The keys 1-9 are mapped to the corresponding function keys with 0 mapped to F10. Therefore, the keys 1-9,0 work the same as the function keys. Another method is to simply to use the arrow keys to highlight the desired option and then press enter. The final method is to move the mouse up or down to highlight the desired option and press enter or the left mouse button. The left mouse button is always mapped to the enter key. To regain the main menu simply press escape. The right mouse button is always mapped to the escape key.

Chapter 3

The Parameters Menu

3.1

Overview

The parameters menu is where the information for each run is entered (see Figure 3.1). Entering information can be accomplished by moving the highlighted area over the parameter you wish to change. Typing the entry will cause an input window to appear so that you can see and edit your value as you enter it. The backspace key can be used to correct errors. Press the enter key to end the entry. If the value is out of range or has an error, the input window will automatically reappear and a new input is required. The escape key will not work from any input frame.

The sensitive volume is a parallelepiped nested within a larger parallelepiped, the outer volume. The dimensions of the sensitive volume and the outer volume are set using the parameters menu. It is possible to enter dimensions which physically cannot exist. When this occurs a star appears to the left of dimensions which have the error. For example (see Figure 3.2), if a sensitive volume thickness of $5\mu\text{m}$ is chosen, an offset from the top of the outer surface of $4\mu\text{m}$ is chosen and a total outer thickness of $8\mu\text{m}$ is chosen then all the thickness dimensions will be flagged as having an error. The total outer dimension must always be larger than the sensitive dimension plus its associated offset dimension. It is possible to save parameters which are not physically possible and eventually run them. The only safeguard against these types of errors is that they are flagged when entered.

Our experience has been that an offset dimension of $4\mu\text{m}$ is a useful compromise between accuracy of calculation and computer time. A nuclear recoil may enter the sensitive volume from outside the sensitive volume and deposit energy inside the sensitive volume. Four microns of surrounding material around the sensitive volume is usually sufficient for capturing there recoils from outside the sensitive volume that enter the sensitive volume and deposit large amounts of energy.

The easiest way to set the dimensions is to enter in the sensitive volume dimensions and go to the outer dimensions and press "c" or "C"; the offset dimensions are automatically set to $4\mu\text{m}$ as a default. This will select an outer volume dimensions and center the sensitive volume in the outer volume. The centering hot key may also be used to select the offset dimensions. The centering hot key is not active on the sensitive volume dimensions.

```

Proton Energy in MeV   =   148
Output Energy Interval = 0.500
Number of Iterations  = 1000000

Outer Volume Dimensions in microns

    Thickness = 13.000
    Length    = 13.000
    Width     = 13.000

Sensitive Volume Dimensions in Microns
    Thickness = 5.000
    Length    = 5.000
    Width     = 5.000

Outer Volume to Sensitive Volume Offsets

    Top of SV   = 4.000
    Front of SV = 4.000
    Right of SV = 4.000

```

Figure 3.1. The Parameters Menu.

```

Proton Energy in MeV   =   148
Output Energy Interval = 0.500
Number of Iterations  = 1000000

Outer Volume Dimensions in microns

    * Thickness = 8.000
    Length      = 13.000
    Width       = 13.000

Sensitive Volume Dimensions in Microns
    * Thickness = 5.000
    Length      = 5.000
    Width       = 5.000

Outer Volume to Sensitive Volume Offsets

    * Top of SV   = 4.000
    Front of SV   = 4.000
    Right of SV   = 4.000

```

Figure 3.2. The Prameters menu with an error.

3.2

Specific operation

The following subsections give the information needed for each parameter entry.

3.2.1

Proton energy

The proton energy is the energy of the incident proton. The proton energy is limited to positive energies and energies less than or equal to 400 MeV. The purpose for the 400 MeV limit is because pion interactions above that energy are not included in the code. (If you wish to extend your calculations above 400 MeV please contact us.) The proton energy must be entered in a integer form.

$$0 < \text{Proton energy} \leq 400 \text{ (Integer)}$$

3.2.2

Output energy interval

The output data file is split into 100 channels. Each channel is the cross section for at least that channel's energy being deposited. The output energy interval times 100 is the largest energy deposited CUPID can record. The output energy interval is limited to positive values less than or equal to 4.

$$0 < \text{Output energy interval} \leq 4 \text{ (Real)}$$

3.2.3

Number of iterations

The number of iterations is proportional to the number of protons incident on the large volume. For volumes typical of microelectronics 5,000,000 iterations usually yields reasonable statistics. The number of iterations should not be confused with the number of incident protons or the number of interactions. It is an intermediate between the two values. A 25Mhz 486DX machine processes about 2,000,000 iterations per hour. A 33Mhz 386DX with a Weitek 3167 processes about 1,700,000 iterations per hour. A 25Mhz 368DX with a Intel 387 processes only about 600,000 iterations per hour. More benchmarks are available upon request. The number of iterations must be a positive integer less than 4 billion. (I do not recommend attempting 4 billion iterations.)

$$0 < \text{Number of iterations} < 4 \text{ billion (Integer)}$$

3.2.4

Volume dimensions

The only limitation on the volume dimensions is that they be greater than zero, except for the offset dimensions which may be set to zero. Dimensions less than $0.001\mu\text{m}$ are not displayed on the parameters menu screen. CUPID does not work well with small dimensions. Therefore the resolution of the I/O routine is better than the CUPID code can handle.

$$0 < \text{Volume Dimension (Real)}$$

Chapter 4

Other Main Menu Options

4.1

Target Volume

The second entry on the main menu allows the user to get a rough view of the target volume. CUPID assumes all protons are incident from the top of the larger cube. This view is a simplified view (see Figure 4.1). The thickness dimension is in the vertical direction, the width dimension is in the horizontal direction, and the length dimension is in the depth of the screen. This view is a basic orthographic representation of the target volume. The sizes observed are only relative sizes. This option is provided to give a quick check of desired volume. If the dimensions selected are physically impossible this view will clearly show it. To exit back to the main menu simply press escape.

4.2

Saving parameters

This menu option is provided so that the user may save the information entered on the parameters screen. When this option is selected all the files with the ".INP" extension are displayed on the screen (see Figure 4.2). These files are in alphabetical order. To save the current information on the parameters screen in an existing file simply move the cursor over the file name and press enter. To save the information on the parameters screen to a new non-existing file simply press the space bar and an input window will appear. Any valid DOS file name may be entered; only the 8-character limit is used (see Section 5.1). If there are more files than the screen can hold you may simply scroll to them. The arrow, Home, End, PgUp and PgDn keys are all active for aiding movement around the file names. The I/O routine can handle up to 2048 file names, but it cannot locate the 2049th input file. This limitation should not be a problem.

4.3

Loading parameters

This menu option is provided so that the user may load input files which have already been created and saved. This option allows the user to modify an existing file. When this option is selected all the files with the extension ".INP" will appear on the screen (see Figure 4.2). To load a desired file simply move the cursor over the desired file and press enter. If there are

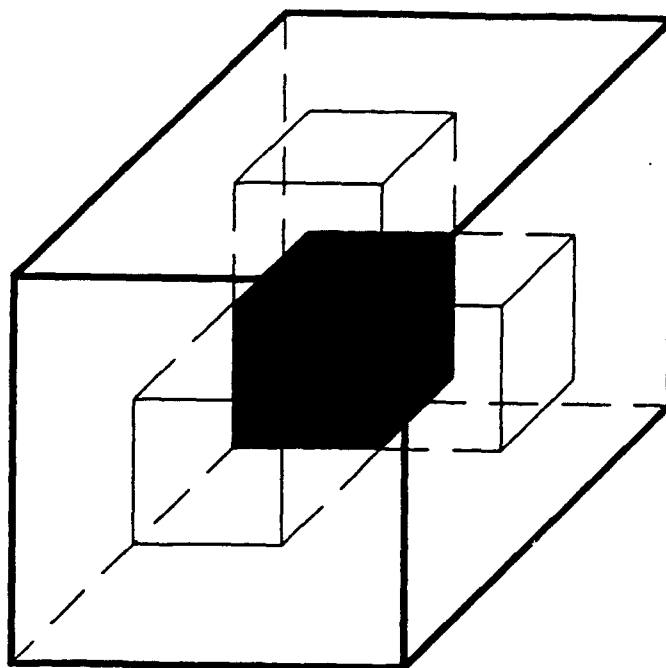


Figure 4.1. The Target Volume.

A8T10E04	A8T10E05	A8T10E06	A8T10E08	A8T10E10	A8T10E15	A8T10E20	A8T10E30
A8T10E40	A9T10E04	A9T10E05	A9T10E06	A9T10E08	A9T10E10	A9T10E15	A9T10E20
A9T10E30	A9T10E40	A9T15E04	A9T15E05	A9T15E06	A9T15E08	A9T15E10	A9T15E15
A9T15E20	A9T15E30	A9T15E40	A9T44E04	A9T44E05	A9T44E06	A9T44E08	A9T44E10
A9T44E15	A9T44E20	A9T44E30	A9T44E40	AATEST	AM02T040	AM02T050	AM02T060
AM02T080	AM02T100	AM02T148	AM02T150	AM02T200	AM02T300	AM02T400	AM44T040
AM44T100	AM44T148	AM44T400	AT10E025	AATEST	CR1E100	CR1E148	CR1E200
CR1E300	CR1E400	CR1E50	CR1E60	CR1E80	CR2E100	CR2E148	CR2E200
CR2E300	CR2E400	CR2E50	CR2E60	CR2E70	CR2E80	CRTEST3	CRTST20
CRTST6	CRTST	D2164E11	D2164E15	D2164E20	D2164E30	D2164E4	D2164E40
D2164E6	D2164E8	DAVETST	DM1-100	DM1-120	DM1-148	DM1-200	DM1-300
DM1-400	DM1-50	DM1-60	DM1-80	DUD	GTES2	GTEST	HASSLE
HIT1	I130J23	MTEST	NP010	NP015	NP020	NP025	NP030
NP040	NP050	NP060	NP080	NP100	NP148	NP200	NP300
NP400	NPG010	NPG015	NPG020	NPG030	NPG040	NPG050	NPG060
NPG080	NPG100	NPG120	NPG148	NPG200	NPG300	NPG400	NPHN148
R6504T	RH65042	RH6504	S110	S148	S36	S80	T40
TEST40	TEST	TEST42	TEST445	TEST44	TEST50	TTHICK3M	TTHICK
Y100U148	Y100U30	Y100U50	Y100UM	Y40U148	Y40U30	YAG100	YAG148
YAG200	YAG300	YAG400	YAG50	YAG60	YAG80	YGRAZ148	

Figure 4.2. Example file screen.

A8T10E04	A8T10E05	A8T10E06	A8T10E08	A8T10E10	A8T10E15	A8T10E20	A8T10E30
A8T10E40	A9T10E04	A9T10E05	A9T10E06	A9T10E08	A9T10E10	A9T10E15	A9T10E20
A9T10E30	A9T10E40	A9T15E04	A9T15E05	A9T15E06	A9T15E08	A9T15E10	A9T15E15
A9T15E20	A9T15E30	A9T15E40	A9T44E04	A9T44E05	A9T44E06	A9T44E08	A9T44E10
A9T44E15	A9T44E20	A9T44E30	A9T44E40	AATEST	AM02T040	AM02T050	AM02T060
AM02T080	AM02T100	AM02T148	AM02T150	AM02T200	AM02T300	AM02T400	AM44T040
AM44T100	AM44T148	AM44T400	AT10E025	ATEST	CR1E100	CR1E148	CR1E200
CR1E300	CR1E400	CR1E50	CR1E60	CR1E80	CR2E100	CR2E148	CR2E200
CR2E300	CR2E40					CRTEST3	CRTST20
CRTST6	CRTS					D2164E4	D2164E40
D2164E6	D2164E					DM1-200	DM1-300
DM1-400	DM1-5					GTEST	HASSLE
HIT1	I130J2					NP025	NP030
NP040	NP05					NP200	NP300
NP400	NPG01					NPG050	NPG060
NPG080	NPG100	NPG120	NPG148	NPG200	NPG300	NPG400	NPHN148
R6504T	RH65042	RH6504	S110	S148	S36	S80	T40
TEST40*****TEST		TEST42	TEST445	TEST44	TEST50	TTHICK3M	TTHICK
Y100U148	Y100U30	Y100U50	Y100UM	Y40U148	Y40U30	YAG100	YAG148
YAG200	YAG300	YAG400	YAG50	YAG60	YAG80	YGRAZ148	

Press one of the following keys:

Press A - append current run

Press N - start a new run

Figure 4.3. Run selection screen.

no input files in the directory the main menu will just stay on the screen. If there are more files than the screen can hold you may simply scroll to them. The arrow, Home, End, PgUp and PgDn keys are all active for aiding movement around the file names. The I/O routine can handle up 2048 file names, but it cannot locate the 2049 input file. This limitation should not be a problem.

4.4 Running the CUPID code

The I/O routine builds a file called CUPID.IDT which establishes the number of files to be run and the associated file names for each run. This menu option allows the user to select which of the input files are to be run. When this option is selected all the files with the ".INP" extension will appear on the screen. To select a file for a run simply move to that file and press enter. A set of asterisks will appear in front of that file name to mark that this file has been selected (see Figure 4.3); note files with asterisks. To deselect the file simply highlight the file and press enter. Once all your files have been selected simply escape back to the main menu. Pressing escape cause the input window in figure 4.3 to appear. There are two options: one, press "n" or "N" to start a new run. This option erases the current CUPID.IDT file and places only the new files selected in CUPID.IDT. The second option is to press "a" or "A". This option places all the selected files on the bottom of CUPID.IDT. This allows the user to select files from several different directories. If you enter this menu option by mistake and do not wish to change the CUPID.IDT file simply deselect all files which may have been selected and press escape. It is possible to have that more ".INP" files than the screen can hold. To access files not on the screen simply scroll to them. The arrow, Home, End, PgUp and PgDn keys are all active for moving around the file names. The I/O routine can handle up 2048 file names, it cannot locate the 2049 input file. When the run is completed, the output is placed in a file with the same name, but with a ".OUT" as an extension.

File "RH65042"
Proton Energy = 148 MeV
Number of Iterations 10000000

	Outer Volume Dimensions	Thick	Length	Width
	Sensitive Volume Dimensions	9.600	13.000	13.000
	Volume Offsets	1.600	5.000	5.000
		4.000	4.000	4.000

Energy Deposited MeV	Upset Crossection cm*cm	Statistical Error	
		+	-
7.80	1.22000E-15	8.34400E-16	1.60600E-15
8.00	7.32100E-16	4.33200E-16	1.03100E-15
8.20	7.32100E-16	4.33200E-16	1.03100E-15
8.40	6.10100E-16	3.37300E-16	8.83000E-16
8.60	4.88100E-16	2.44000E-16	7.32100E-16
8.80	4.88100E-16	2.44000E-16	7.32100E-16
9.00	4.88100E-16	2.44000E-16	7.32100E-16
9.20	3.66100E-16	1.54700E-16	5.77400E-16
9.40	3.66100E-16	1.54700E-16	5.77400E-16
9.60	3.66100E-16	1.54700E-16	5.77400E-16
9.80	2.44000E-16	7.14800E-17	4.16600E-16
10.00	2.44000E-16	7.14800E-17	4.16600E-16
10.20	2.44000E-16	7.14800E-17	4.16600E-16

Figure 4.4. Example output printed on screen.

4.5 Loading an output file

This option is exactly like loading parameter files with one exception. The exception is that ".OUT" files are loaded instead of ".INP" files. This allows the user to view and print out the results of a run at will.

4.6 List output

Once an output file has been selected the user may look directly at the numbers in the output file (see Figure 4.4). The arrow, home, end, PgUp, and PgDn keys are all active so that you may scroll through the numbers. To exit back to the main menu press the escape key.

4.7 Graph output

Once an output file has been selected the user may look at a graph of the numbers on the screen (see Figure 4.5). There are no user changeable parameters on the graph. To exit back to the main menu press the escape key.

4.8 Make X-Y data file

Once an output file is selected the user may make an X-Y data file. This is simply done by selecting the option. The screen never leaves the main menu. The only indication that the file was created is that your hard drive light turned on. When this option is selected a

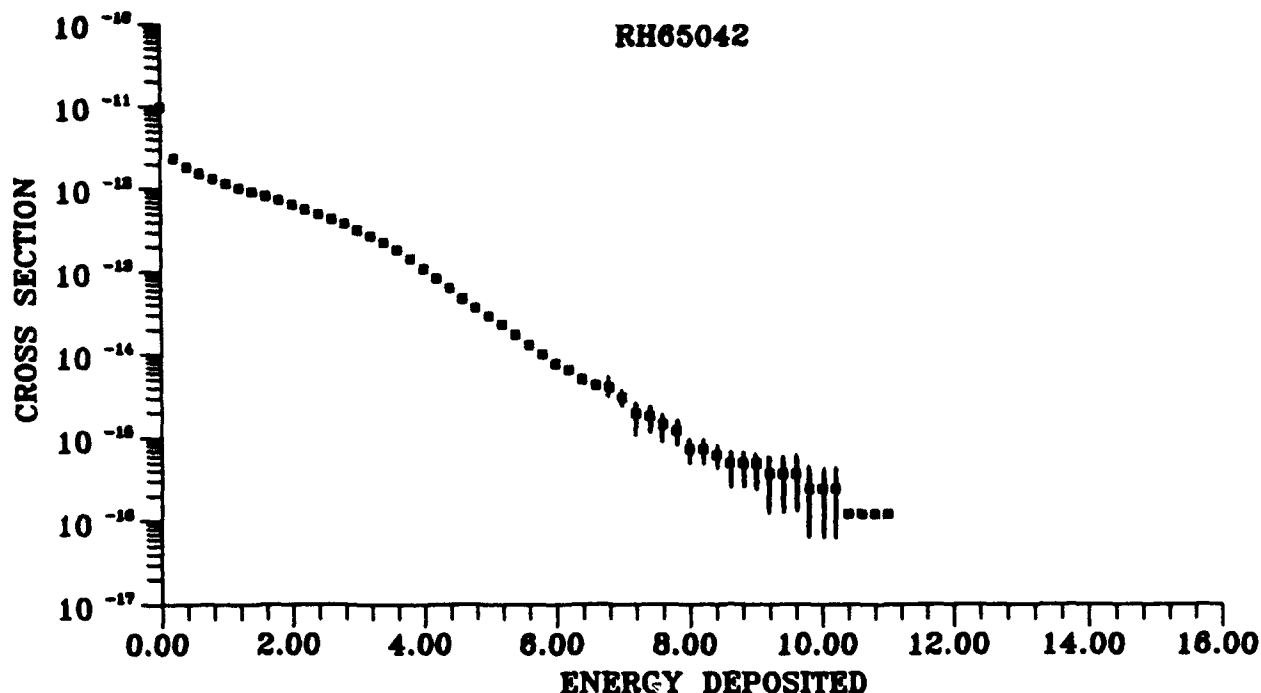


Figure 4.5. Example output graphed on screen.

partial image of the output file is copied to the current directory under the same name with a ".DAT" extension (see 5.1). This image file has two columns of numbers. The first column is the energy. The second column is the cross section of depositing at least the energy indicated in the first column. This option is provided because most graphing software expects this format.

4.9

Printing the output

Once an output file is selected this option allows the user to print the output. When selected the screen in figure 4.6 appears. This just manually checks to see if a printer is hooked up to LPT1. The output is similar to directly viewing the number on the screen. This option automatically returns to the main menu after printing.

1. Enter-Edit Parameters
2. Look at Target Volume
3. Save Parameters to Disk

Press one of the following keys:

Press Y - you have a printer

Press N - no active printer

8. Look at Graph of Output
9. Make X-Y Data File
10. Print Output to Printer

Figure 4.6. Printing Screen.

Chapter 5

Miscellaneous

5.1 File name and directory conventions.

There are three file name conventions. The input files always have an extension of ".INP". An input file contains the dimensional information and other information pertaining to one particular run. The output files always have an extension ".OUT". The output file contains the data of the corresponding input file. The forename of an output file is the same forename as the corresponding input file. X-Y data files can be created from output files. These X-Y data files always have the extension ".DAT" and the forename is the same as the output file which was used to create it. A X-Y data file is a file of two columns of numbers in ASCII format. The first column is the energy in MeV. The second column is the cross section of that energy or greater being deposited in the sensitive volume. The X-Y data file option was added to give the user a file format which most graphing software readily accepts. Therefore a particular run may have three files associated with it. The forename on all three files are the same and the extensions indicate what information is contained in the file.

The CUPID I/O routines can access files from any directory of the installed disk. Why change directories? This allows the user to separate files on any criteria. For example, information about SOI devices may be in one directory while bulk CMOS in another. To change directories simply press "d" or "D" and a special directory screen will appear (see Figure 5.1). Then simply move to the desired selection and press enter. The "root" directory

ROOT	BACK ONE	ACAD	AXUM	BIN	BORLANDC	CUPID	DOS
DR11	FORTTRAN	GRAPHER	PCTEX	PROCOMM	QB45	TP	USERS
WINDOWS	WP51	XTALK					

Figure 5.1: Directory Screen

option will change the directory to the root option similar to the DOS command "cd\". The "back one" option will change the directory back one level similar to the DOS command "cd..".

5.2 About the mouse.

A Microsoft or Logitech mouse have demonstrated to work fine with the I/O routine. Any Microsoft compatible mouse should work without difficulty. The left key is always mapped to the enter key and the right key is always mapped to the escape key. The movement of the mouse is mapped to the arrow keys. In the absence of a mouse, the I/O routines work with the keyboard.

5.3 Changing the colors.

To change the foreground color simply press "z" or "Z". The background color is always a compliment of the selected foreground color. The color maybe changed and saved from any screen.

5.4 Saving the colors.

To save the current color set as the default color set simply press "s" or "S". The default color is the color which the I/O routine start with.

5.5 CUPID.BAT

The CUPID.BAT file is a DOS batch file which runs the I/O routine and then the main CUPID code. If you wish just to run the I/O routine type CUPIDIO and press the enter key (from the installed directory). This may be convenient to do when analyzing a just completed run. If you wish to run the just the main CUPID code type CUPIDF and press the enter key. The experienced DOS user may find several easy shortcuts around the I/O routines.

5.6 Computer Requirements

- 486, 386, or 386SX MICROCOMPUTER with a DOS operating system
- 2 MEGABYTES OF RAM
- CGA, EGA, VGA, or Hercules VIDEO SYSTEM
- MATH COPROCESSOR (not required with a 486 system)

80387 or COMPATIBLE COPROCESSOR

3167 WEITEK COPROCESSOR
COPROCESSOR TYPE MUST BE SPECIFIED WHEN ORDERING

5.7

Cost

The price of \$2,495.00 covers our costs for license fees, future updates, and maintenance of the CUPID code.

5.8

Problems or Comments

If you have any questions or comments concerning these programs please contact:

Peter J. McNulty
or
David Roth
Department of Physics and Astronomy
Clemson University
Clemson, SC 29634-1911

DISTRIBUTION LIST

DNA-TR-92-163

DEPARTMENT OF DEFENSE

ADVANCED RESEARCH PROJECT AGENCY
ATTN: ASST DIR ELECTRONIC SCIENCES DIV
ATTN: R REYNOLDS

ASSISTANT TO THE SECRETARY OF DEFENSE
ATTN: EXECUTIVE ASSISTANT

DEFENSE ELECTRONIC SUPPLY CENTER
ATTN: DESC-E

DEFENSE INFORMATION SYSTEMS AGENCY
ATTN: JNGO

DEFENSE INTELLIGENCE AGENCY
ATTN: DIW-4
ATTN: DT-1B

DEFENSE NUCLEAR AGENCY
2 CY ATTN: IMTS
ATTN: RAES

DEFENSE TECHNICAL INFORMATION CENTER
2 CY ATTN: DTIC/OC

FIELD COMMAND DEFENSE NUCLEAR AGENCY
ATTN: FCINI
ATTN: FCTO
ATTN: FCTT-T W SUMMA
ATTN: FCTT DR BALADI

DEPARTMENT OF THE ARMY

ARMY RESEARCH LABORATORIES
ATTN: AMSRL-WT-NG
ATTN: AMSRL-WT-NJ

PED MISSILE DEFENSE SFAE-MD-TSD
ATTN: CSSD-SL

U S ARMY MISSILE COMMAND
ATTN: AMCPM-HA-SE-MS

U S ARMY NUCLEAR & CHEMICAL AGENCY
ATTN: MONA-NU DR D BASH

U S ARMY RESEARCH OFFICE
ATTN: R GRIFFITH

U S ARMY STRATEGIC SPACE & DEFENSE CMD
ATTN: CSSD-SA-E
ATTN: CSSD-SD-A

U S MILITARY ACADEMY
ATTN: LTC-AL COSTANTINE

USAISC
ATTN: ASOP-DO-TL

DEPARTMENT OF THE NAVY

DEPARTMENT OF THE NAVY
ATTN: CODE H21 F WARNOCK

NAVAL COMMAND CONTROL & OCEAN
SURVEILLANCE CTR
ATTN: CODE 250

NAVAL POSTGRADUATE SCHOOL
ATTN: CODE 52 LIBRARY

NAVAL RESEARCH LABORATORY
ATTN: CODE 4600 D NAGEL
ATTN: CODE 4653 A NAMENSON
ATTN: CODE 4682 D BROWN
ATTN: CODE 6613 A B CAMPBELL
ATTN: CODE 6813 N SAKS
ATTN: CODE 6816 H HUGHES

NAVAL SURFACE WARFARE CENTER
ATTN: CODE H-21

NAVAL TECHNICAL INTELLIGENCE CTR
ATTN: LIBRARY

NAVAL WEAPONS SUPPORT CENTER
ATTN: CODE 6054 D PLATTETER

NAWCWPNSDIV DETACHMENT
ATTN: CLASSIFIED LIBRARY

PROGRAM EXECUTIVE OFFICE
ATTN: AIR-536T

STRATEGIC SYSTEMS PROGRAM
ATTN: JIM HOWARD SP-23

DEPARTMENT OF THE AIR FORCE

AERONAUTICAL SYSTEMS CENTER
ATTN: ASD/ENSS

AIR FORCE CTR FOR STUDIES & ANALYSIS
ATTN: AFSAA/SAI

AIR UNIVERSITY LIBRARY
ATTN: AUL-LSE

PHILLIPS LABORATORY
ATTN: PL/VTE
ATTN: PL/VTEE S SAMPSON

ROME LABORATORY
ATTN: ESR

USAF ROME LABORATORY TECHNICAL LIBRARY FL2810
ATTN: RBR

2242 AVIONICS CIR STE 17
ATTN: WL/ELE
ATTN: WRDC/MTE

DEPARTMENT OF ENERGY

DEPARTMENT OF ENERGY
ALBUQUERQUE OPERATIONS OFFICE
ATTN: NESD

LAWRENCE LIVERMORE NATIONAL LAB
ATTN: J YEE
ATTN: G POMYKAL
ATTN: W ORVIS

LOS ALAMOS NATIONAL LABORATORY
ATTN: E LEONARD

SANDIA NATIONAL LABORATORIES
ATTN: DEPT 1332 F SEXTON
ATTN: L D POSEY DIV 9351
ATTN: ORG 2146 T A DELLIN
ATTN: P WINOKUR DIV 1332
ATTN: T F WROBEL DIV 9341
ATTN: 2140 J WOODARD

OTHER GOVERNMENT

CENTRAL INTELLIGENCE AGENCY
ATTN: OSWR/NED 5S09 NHB
ATTN: OSWR/STD/MTB 5S09 NHB

DEPARTMENT OF TRANSPORTATION
ATTN: ARD-350

NASA
ATTN: CODE 313 V DANCHENKO
ATTN: CODE 900 E STASSINOPOULOS

NATIONAL INSTITUTE OF STANDARDS & TECHNOLOGY
ATTN: P ROITMAN

DEPARTMENT OF DEFENSE CONTRACTORS

ADVANCED RESEARCH & APPLICATIONS CORP
ATTN: R ARMISTEAD

AEROSPACE CORP
ATTN: C RICE
ATTN: D SCHMUNK
ATTN: G CUEVAS
ATTN: K G HOLDEN
ATTN: LEE MENDOSA
ATTN: N SRAMEK
ATTN: R KOGA
ATTN: S MCGREGOR

ALLIED-SIGNAL, INC
ATTN: DOCUMENT CONTROL

ANALYTIC SERVICES, INC (ANSER)
ATTN: A HERNDON
ATTN: A SHOSTAK

BOEING CO
ATTN: D KINGSBURY
ATTN: D EGELKROUT
ATTN: ROS WOOD
ATTN: O MULKEY

BOEING TECHNICAL & MANAGEMENT SVCS, INC
ATTN: E NORMAND
ATTN: P R MEASEL
ATTN: W C BOWMAN
ATTN: W G BARTHOLET

BOOZ ALLEN & HAMILTON INC
ATTN: D VINCENT
ATTN: L ALBRIGHT

CALIFORNIA INSTITUTE OF TECHNOLOGY
ATTN: C BARNES

CHARLES STARK DRAPER LAB, INC
ATTN: J BOYLE
ATTN: N TIBBETTS

CLEMSON UNIVERSITY
2 CY ATTN: P J MCNULTY

COMPUTER PRODUCTS A DIVISION OF AMPEX
ATTN: B RICKARD
ATTN: K WRIGHT

DAVID SARNOFF RESEARCH CENTER, INC
ATTN: R SMELTZER

E-SYSTEMS, INC
ATTN: MAIN LIBRARY

EATON CORP
ATTN: R BRYANT

ELECTRONIC INDUSTRIES ASSOCIATION
ATTN: J KINN

GENERAL ELECTRIC CO (ASD)
ATTN: D SWANT
ATTN: D TASCA
ATTN: H O'DONNELL
ATTN: J ANDREWS
ATTN: J LINNEN
ATTN: J LOMAN

GENERAL ELECTRIC CO
ATTN: B FLAHERTY
ATTN: L HAUGE

GENERAL RESEARCH CORP
ATTN: A HUNT

GEORGE WASHINGTON UNIVERSITY
ATTN: A FRIEDMAN

HARRIS CORPORATION
ATTN: E YOST
ATTN: W ABARE

HONEYWELL INC
ATTN: C SANDSTROM

HONEYWELL, INC
ATTN: MS 725-5

HUGHES AIRCRAFT COMPANY
ATTN: E KUBO

IBM CORP
ATTN: DEPT L75

IBM CORP
ATTN: A SADANA

IBM CORP
ATTN: N HADDAD

INSTITUTE FOR DEFENSE ANALYSES
ATTN: TECH INFO SERVICES

JAYCOR
ATTN: D WALTERS

JAYCOR
ATTN: CYRUS P KNOWLES
ATTN: R SULLIVAN

JAYCOR
ATTN: R POLL

JOHNS HOPKINS UNIVERSITY
ATTN: R MAURER

KAMAN SCIENCES CORP
ATTN: DASIAC

KAMAN SCIENCES CORPORATION
ATTN: DASIAC
ATTN: R RUTHERFORD

KEARFOTT GUIDANCE AND NAVIGATION CORP
ATTN: J D BRINKMAN

LITTON SYSTEMS INC
ATTN: F MOTTER

LOCKHEED MISSILES & SPACE CO, INC
ATTN: TECHNICAL INFO CENTER

LOCKHEED MISSILES & SPACE CO, INC
ATTN: E HESSEE
ATTN: G LUM
ATTN: J CAYOT
ATTN: L ROSSI
ATTN: P BENE

LOCKHEED SANDERS, INC
ATTN: BRIAN G CARRIGG

LOGICON R & D ASSOCIATES
ATTN: D CARLSON

LORAL AERONUTRONIC
ATTN: TECHNICAL LIBRARY

LTV AEROSPACE & DEFENSE COMPANY
2 CY ATTN: LIBRARY EM-08

MARTIN MARIETTA
ATTN: J MILLER

MARTIN MARIETTA DENVER AEROSPACE
ATTN: P KASE
ATTN: RESEARCH LIBRARY

MARTIN MARIETTA TECHNOLOGIES INC
ATTN: J TANKE
ATTN: TIC/MP-30

MARTIN MARIETTA TECHNOLOGIES, INC
ATTN: H SCHISLER

MARYLAND, UNIVERSITY OF
ATTN: H C LIN

MAXWELL LABORATORIES INC
ATTN: J M WILKENFELD

MCDONNELL DOUGLAS CORPORATION
ATTN: P ALBRECHT

MISSION RESEARCH CORP
ATTN: D ALEXANDER

MISSION RESEARCH CORP
ATTN: J LUBELL
ATTN: W WARE

MITRE CORPORATION
ATTN: J R SPURRIER
ATTN: M FITZGERALD

NORDEN SYSTEMS, INC
ATTN: N RIEDERMAN
ATTN: TECHNICAL LIBRARY

NORTHROP GRUMMAN CORPORATION
ATTN: J R SROUR

PACIFIC-SIERRA RESEARCH CORP
ATTN: H BRODE

PHYSITRON INC
ATTN: MARK CHRISTOPHER

PHYSITRON INC
ATTN: MARION ROSE

RAYTHEON CO
ATTN: D D LEE
ATTN: JOSEPH SURRO

RESEARCH TRIANGLE INSTITUTE
ATTN: M SIMONS

ROCKWELL INTERNATIONAL CORP
ATTN: V DE MARTINO

SCIENCE APPLICATIONS INTL CORP
ATTN: D MILLWARD
ATTN: DAVID LONG

SCIENCE APPLICATIONS INTL CORP
ATTN: W CHADSEY

SCIENCE APPLICATIONS INTL CORP
ATTN: P ZIELIE

SCIENTIFIC RESEARCH ASSOC, INC
ATTN: H GRUBIN

SUNDSTRAND CORP
ATTN: C WHITE

SYSTRON-DONNER CORP
ATTN: SECURITY OFFIC

TECHNOLOGY DEVELOPMENT ASSOCIATES
ATTN: R V BENEDICT

TELEDYNE BROWN ENGINEERING
ATTN: G R EZELL
ATTN: LEWIS T SMITH

TEXAS INSTRUMENTS, INC
ATTN: J SALZMAN

THE RAND CORPORATION
ATTN: C CRAIN

DNA-TR-92-163 (DL CONTINUED)

TRW
ATTN: M J TAYLOR

TRW INC
ATTN: TIC

TRW S. I. G.
ATTN: C BLASNEK

TRW SPACE & DEFENSE SECTOR
ATTN: D M LAYTON

UNISYS CORPORATION-DEFENSE SYSTEMS
ATTN: P MARROFFINO

VISIDYNE, INC
ATTN: C H HUMPHREY
ATTN: W P REIDY